

Alma Mater Studiorum – Università di Bologna

DOTTORATO DI RICERCA IN

Meccanica e Scienze Avanzate dell'ingegneria

Ciclo XXXV

**Settore Concorsuale: 09/A3 - PROGETTAZIONE INDUSTRIALE, COSTRUZIONI  
MECCANICHE E METALLURGIA**

**Settore Scientifico Disciplinare: ING-IND/21 – METALLURGIA**

Optimization of an innovative T6 heat treatment for the  
AlSi10Mg alloy processed by Laser-based Powder Bed  
Fusion: effect on microstructure, mechanical properties,  
and tribological behavior

**Presentata da:** Gianluca Di Egidio

**Coordinatore Dottorato**

Prof. Lorenzo Donati

**Supervisore**

Prof.ssa Lorella Ceschini

**Esame finale anno 2022**

Il gol e l'assist. L'oro e l'argento. Il campione e il gregario... Non tutti sono primi. Non tutti vogliono esserlo. Bollati come perdenti, i secondi raggiungono, comunque, la meta. A suon di sconfitte e (poche) vittorie, di denti stretti e testa bassa, di fatica e umiltà. Valori, in un certo senso secondi, perché in apparenza poco importanti di questi tempi. Storie da prima pagina, quelle dei numeri uno. Altre storie, invece, quelle dei numeri due, i quali spesso non amano nemmeno raccontarle. Eppure anche queste sono pervase di lotta, di duro lavoro, di impegno per cambiare un pezzetto, magari piccolo, di mondo. I secondi non vincono mai. Ma sono comunque, a modo loro, degli eroi. Dipende da quale angolazione si guardano.

< La bellezza dei numeri due, Nicoletta Masetto >

# Abstract

Laser-based Powder Bed Fusion (L-PBF) technology is one of the most commonly used metal Additive Manufacturing (AM) techniques to produce highly customized and value-added parts in the biomedical, energy, aerospace, and automotive industries. It is receiving significant attention as it overcomes many limitations that were once considered inherent in mass production, i.e., the design of easily customizable structures, the production of complex geometries, and the achievement of significant weight savings while maintaining structural integrity.

Al alloys are perfect candidates for industrial applications that involve the L-PBF process: in particular, the AlSi10Mg alloy has received more and more attention due to its good printability, high strength/weight ratio, corrosion resistance, and relatively low cost. However, despite the extensive work that has been completed on the mechanical properties of the L-PBF AlSi10Mg alloy, a solid understanding of the effect of heat treatments on this alloy's metastable microstructure is still required in order to develop or optimize tailored heat treatments.

Therefore, the first part of the Ph.D. thesis aims to carry out a complete literature review in order to assess the state of the art concerning the effect of process parameters and heat treatment conditions on microstructure, strengthening mechanisms, and damage modes of the L-PBF AlSi10Mg alloy and to identify the primary relationships between the mechanical performance and the microstructure of the alloy.

The second part of the Ph.D. thesis focused on developing tailored heat treatments for the L-PBF AlSi10Mg alloy to overcome the limits of the as-built condition. Several authors have already investigated the effects of conventional heat treatment on the microstructure and mechanical behavior of the L-PBF AlSi10Mg alloy but often overlooked the peculiarities of the starting supersaturated and ultrafine microstructure induced by rapid solidification. In particular, the effects of innovative T6 heat treatment (T6R) on the microstructure and mechanical behavior of the L-PBF AlSi10Mg alloy were assessed. The short solution soaking time (10 min) and the relatively low temperature (510 °C) reduced the typical porosity growth at high temperatures and led to a homogeneous distribution of fine globular Si particles in the Al matrix. In addition, it increased the amount of Mg and Si in the solid solution available for precipitation hardening during the aging step.

The third part of the thesis aimed to evaluate the mechanical (at room temperature and 200 °C) and tribological properties of the T5 and T6R heat-treated alloy. The results of this characterization were correlated to the specific microstructures induced by the L-PBF or heat treatment. Results showed that the innovative T6R alloy exhibits the best mechanical trade-off between strength and ductility, the highest fatigue strength among the analyzed conditions, and interesting tribological behavior. Furthermore, the high-temperature behavior, particularly of the T5 alloy, makes the heat-treated L-PBF AlSi10Mg alloy suitable for structural components operating in mild service conditions at 200 °C.

## List of symbols and abbreviations

<p>Thermal diffusivity (a)</p> <p>Artificial aging (AA)</p> <p>As-built (AB)</p> <p>Aluminium-Silicon (AlSi)</p> <p>Additive manufacturing (AM)</p> <p>Al solid solution (Alss)</p> <p>Contact area substrate/liquid metal (<math>A_{SM}</math>)</p> <p>Contact area at the S/L interface (<math>A_{SL}</math>)</p> <p>Real area of contact (<math>A_r</math>)</p> <p>Nominal area of contact (<math>A_n</math>)</p> <p>Projected contact area (<math>A(h_c)</math>)</p> <p>Bright Field (BF)</p> <p>Binder Jetting (BJ)</p> <p>Beam Parameter Product (BPP)</p> <p>Backscattered Electron (BSE)</p> <p>Liquid compositions (<math>C_L</math>)</p> <p>Solid compositions (<math>C_s</math>)</p> <p>Bulk composition at the beginning of solidification (<math>C_0</math>)</p> <p>Nominal composition (<math>C_0</math>)</p> <p>Computer-aided Design (CAD)</p> <p>Copper Mold Casting (CMC)</p> <p>Coefficient of Friction (CoF)</p> <p>Diffusivity of the solute in the liquid (<math>D_L</math>)</p> <p>Design for Additive Manufacturing (DAM)</p> <p>Direct Energy Deposition (DED)</p> <p>Department of Industrial Engineering (DIN)</p> <p>Electron Beam Melting (EBM)</p> <p>Electron Backscatter Diffraction (EBSD)</p> <p>Young's modulus (E)</p> <p>Young's modulus tribo-element 1 (<math>E_1</math>)</p> <p>Young's modulus tribo-element 2 (<math>E_2</math>)</p> <p>Energy Density (ED)</p> <p>Linear Energy Density (<math>ED_l</math>)</p> <p>Superficial Energy Density (<math>ED_s</math>)</p> <p>Volumetric Energy Density (<math>ED_v</math>)</p> <p>Energy-dispersive X-ray Spectroscopy (EDS)</p> <p>Electrode Induction Gas Atomization (EIGA)</p> <p>Elastic Recovery Parameter (ERP)</p> <p>Elongation to failure (<math>e_f</math>)</p> <p>Normal load (<math>F_n</math>)</p> <p>Seizure load (<math>F_s</math>)</p> <p>Field Emission Gun (FEG)</p> <p>Focused Ion Beam (FIB)</p> <p>Temperature gradient (G)</p> <p>Grain Boundary Densities (GBD)</p> <p>Gibbs free energy (<math>G_{T,P}</math>)</p> <p>Gas Atomization (GA)</p> <p>Glow Discharge Optical Emission Spectroscopy (GD-OES)</p> <p>Cooling rate (<math>G^*R</math>)</p> <p>Hatch distance (h)</p> <p>Contact depth (<math>h_c</math>)</p> <p>Depth at the maximum load (<math>h_{max}</math>)</p> <p>Hardness (H)</p> <p>Heat Affected Zone (HAZ)</p> <p>Hot Isostatic Pressure (HIP)</p> <p>High-Pressure Die-Cast (HPDC)</p> <p>Equilibrium distribution coefficient (k)</p> <p>Curvature / Strength coefficient (K)</p> <p>Thermal conductivities of tribo-element 1 (<math>k_1</math>)</p> <p>Thermal conductivities of tribo-element 2 (<math>k_2</math>)</p> <p>Latent heat per unit volume (<math>L_v</math>)</p> <p>Equivalent heat diffusion distances tribo-element 1 (<math>l_1</math>)</p> <p>Equivalent heat diffusion distances tribo-element 2 (<math>l_2</math>)</p> <p>Long-Infrared (LIR)</p> <p>Lack-of-Fusion (LoF)</p>	<p>Laser-based Powder Bed Fusion (L-PBF)</p> <p>Slope of the liquidus line (<math>m_L</math>)</p> <p>Material Extrusion (MEX)</p> <p>Material Jetting (MJ)</p> <p>Melt Pool (MP)</p> <p>Melt Pool Border (MPB)</p> <p>Melt Spinning (MS)</p> <p>Miniaturized Tensile sample (MT)</p> <p>Strain-hardening exponent (n)</p> <p>Near-Infrared (NIR)</p> <p>Overaging (OA)</p> <p>Post-OA at high temperatures (200 °C) (OA - 200T)</p> <p>Optical Microscopy (OM)</p> <p>Laser power (P)</p> <p>Average pressure (<math>p_{average}</math>)</p> <p>Maximum Hertzian contact pressure (<math>p_{max}</math>)</p> <p>Maximum applied load (<math>P_{max}</math>)</p> <p>Powder Bed Fusion (PBF)</p> <p>Peclet number (Pe)</p> <p>Particle Size Distribution (PSD)</p> <p>Drouzy, Jacob e Richard Index (<math>Q_{DJR}</math>)</p> <p>Din, Rashid e Campbell Index (<math>Q_{DRC}</math>)</p> <p>Nucleus radius / radius tribo-contact region (r)</p> <p>Solidification rate (R)</p> <p>Radius of curvature tribo-element 1 (<math>R_1</math>)</p> <p>Radius of curvature tribo-element 2 (<math>R_2</math>)</p> <p>Average Roughness (<math>R_a</math>)</p> <p>Root-mean-square roughness (<math>R_q</math>)</p> <p>Radius of tribo-element 1 (<math>R_1</math>)</p> <p>Radius of tribo-element 2 (<math>R_2</math>)</p> <p>Regions of Interest (ROI)</p> <p>Rapid Prototyping (RP)</p> <p>Residual Stress (RS)</p> <p>Room temperatue tensile test (RT)</p> <p>Scanning Electron Microscope (SEM)</p> <p>Slope of the unloading curve (S)</p> <p>Solution treatment (SHT)</p> <p>Benchmark solution treatment (SHTB)</p> <p>Rapid solution treatment (SHTR)</p> <p>Sheet Lamination (SL)</p> <p>Selective Laser Melting (SLM)</p> <p>Selective Laser Sintering (SLS)</p> <p>Stress relieving/Stress relieved (SR)</p> <p>Scanning Transmission Electron Microscopy (STEM)</p> <p>Surface Tessellation Language (STL)</p> <p>Solid/Liquid interface (S/L)</p> <p>Layer thickness (t)</p> <p>Aging Soaking time (<math>t_{AA}</math>)</p> <p>Aging Temperature (<math>T_{AA}</math>)</p> <p>Flash temperature at the contact interface (<math>T_f</math>)</p> <p>Liquidus temperature (<math>T_L</math>)</p> <p>Equilibrium temperature for a sphere of radius r (<math>T_L^r</math>)</p> <p>Melting temperature (<math>T_M</math>)</p> <p>Bulk temperature (<math>T_0</math>)</p> <p>Overaging temperature (<math>T_{OA}</math>)</p> <p>Overaging soaking time (<math>t_{OA}</math>)</p> <p>Average surface temperature (<math>T_s</math>)</p> <p>Stress relieving Soaking time (<math>t_{SR}</math>)</p> <p>Stress relieving Temperature (<math>T_{SR}</math>)</p> <p>Solution Soaking time (<math>t_{SHT}</math>)</p> <p>Solution Temperature (<math>T_{SHT}</math>)</p> <p>T5 heat treatment/heat treated (T5)</p> <p>T5 heat-treated alloy post-OA (<math>T5_{OA}</math>)</p> <p>T5 heat-treated alloy at room temperature (T5 - RT)</p>
---	---

T5 heat-treated alloy post-OA at 200 °C for 48 h (T5 - 200 °C)	Yield strength (YS)
T5 heat-treated alloy post-OA at 210 °C for 48 h (T5 - 210 °C)	Building direction (Z)
T5 heat-treated alloy post-OA at 245 °C for 48 h (T5 - 245 °C)	Distance from the surface corresponding to $\tau_{\max}$ value ( $Z_{\tau_{\max}}$ )
T5 heat-treated alloy at high-temperature (200 °C) (T5 – 200T)	Angle between the scan direction and the normal to the solid/liquid interface ( $\alpha$ )
T5 heat-treated alloy at high-temperature (200 °C) post-OA (T5 <sub>OA</sub> - 200T)	Angle between the scan direction and preferential growth direction ( $\beta$ )
T6 heat treatment/heat treated (T6)	Precursors strengthening phases of the Mg <sub>2</sub> Si equilibrium phase ( $\beta''$ and $\beta'$ )
T6 Benchmark heat treatment/heat treated (T6B)	Surface tension per unit area at metal/liquid substrate interface ( $\gamma_{ML}$ )
T6 Rapid heat treatment/heat treated (T6R)	Surface tension per unit area at solid nucleus/liquid interface ( $\gamma_{SL}$ )
T6R heat-treated alloy post-OA (T6R <sub>OA</sub> )	Surface tension per unit area at solid nucleus/metal substrate interface ( $\gamma_{SM}$ )
T6R heat-treated alloy at room temperature (T6R - RT)	Gibbs-Thomson coefficient ( $\Gamma$ )
T6R heat-treated alloy post-OA at 200 °C for 48 h (T6R - 200 °C)	Surface free energy change per unit area ( $\delta G_S$ )
T6R heat-treated alloy post-OA at 210 °C for 48 h (T6R - 210 °C)	Free energy variation for homogeneous nucleation ( $\Delta G_{Het}$ )
T6R heat-treated alloy post-OA at 245 °C for 48 h (T6R – 245 °C)	Free energy variation for homogeneous nucleation ( $\Delta G_{Hom}$ )
T6R heat-treated alloy at high-temperature (200 °C) (T6R – 200T)	Superficial change of free energy ( $\Delta G_S$ )
T6R heat-treated alloy at high-temperature (200 °C) post-OA (T6R <sub>OA</sub> – 200T)	Volumetric change of free energy ( $\Delta G_V$ )
Transmission Electron Microscopy (TEM)	Entropy for melting ( $\Delta S_F$ )
Ultimate Tensile Strength (UTS)	Undercooling ( $\Delta T$ )
Scanning speed ( $v$ )	Constitutional (solutal) undercooling ( $\Delta T_C$ )
Fixed sliding speed of tribological sample ( $v$ )	Kinetic undercooling ( $\Delta T_K$ )
Volume (V)	Pressure undercooling ( $\Delta T_P$ )
Beam speed ( $V_b$ )	Curvature undercooling ( $\Delta T_R$ )
Grain growth rate ( $V_{hkl}$ )	Thermal undercooling ( $\Delta T_T$ )
Nominal growth rate ( $V_n$ )	Change in volume ( $\Delta V$ )
Local grain growth velocity ( $V_s$ )	Inter-particle spacing variation ( $\Delta \lambda$ )
Vacuum Inert Gas Atomization (VIGA)	Total strain ( $\epsilon_{tot}$ )
Tub Photopolymerization (VPP)	Elastic strain ( $\epsilon_{elastic}$ )
Plastic work ( $W_p$ )	Plastic strain ( $\epsilon_{plastic}$ )
Elastic work ( $W_e$ )	Necking strain ( $\epsilon_{necking}$ )
Wear Depth (WD)	Inter-particle spacing ( $\lambda$ )
X-ray diffraction (XRD)	Maximum shear stress ( $\tau_{\max}$ )
Building platform plane (XY)	Poisson coefficient tribo-element 1 ( $\nu_1$ )
	Poisson coefficient tribo-element 2 ( $\nu_2$ )
	High-temperature tensile test (200 °C) (200T)

# Index

<b>Introduction</b>	9
References	13
<b>Chapter 1 – AlSi10Mg alloy produced by Laser-based Powder Bed Fusion – Process, microstructure, and mechanical properties</b>	
1.1 Additive Manufacturing	14
1.2 Introduction to Powder Bed Fusion	16
1.3 Laser-based Powder Bed Fusion	18
1.3.1 Feedstock powder features	21
1.3.2 Laser sources	25
1.3.3 Laser beam-powder bed interaction	27
1.4 Influence of the L-PBF process parameters on defect formation	31
1.4.1 Pore formation	34
1.4.2 Balling phenomenon	37
1.4.3 Spattering phenomenon	39
1.4.4 Oxide formation	41
1.4.5 Residual stress, crack, and delamination	42
1.4.6 Optimization of the L-PBF process parameters for operating window	45
1.5 L-PBF AlSi10Mg alloy: microstructure and mechanical properties	51
1.5.1 Solidification theory	54
1.5.2 Hierarchical structure induced by rapid solidification	63
1.5.3 L-PBF AlSi10Mg microstructure	71
1.5.4 L-PBF process parameters: influence on microstructure and strengthening mechanisms	77
1.5.5 Heat treatment: influence on microstructure and mechanical properties	82
References – Chapter 1	92

## **Chapter 2 – Optimization of innovative heat treatments for the L-PBF AlSi10Mg alloy: a new perspective**

2.1	Aim	100
2.2	Experimental procedure	102
2.3	Results and discussion	110
2.3.1	Rapid solution optimization	110
2.3.1.1	Density measurement	110
2.3.1.2	X-ray diffraction	111
2.3.1.3	Microstructure	113
2.3.1.4	Aging curves	119
2.3.2	Static mechanical characterization	121
2.3.3	Nano-mechanical characterization	128
2.3.4	In-situ mechanical characterization	131
2.3.5	Cyclic mechanical characterization	149
2.4	Conclusion	156
	References – Chapter 2	158

## **Chapter 3 – Tribological behavior of the as-built and heat-treated L-PBF AlSi10Mg alloy**

3.1	Aim	163
3.2	Experimental procedure	165
3.2.1	Samples production and characterization	165
3.2.2	Dry sliding tests	166
3.2.3	Microstructural and micromechanical characterization after dry sliding	167
3.3	Results and discussion	168
3.3.1	Microstructural analysis	168
3.3.2	Dry sliding tests	174
3.3.3	Sub-surface characterization	178
3.3.3.1	Thermo-mechanical analysis	178
3.3.3.2	Morphological and micromechanical analysis of the sub-surface zone	180
3.4	Conclusion	188
	References – Chapter 3	189

## **Chapter 4 – High-temperature behavior of the heat-treated and overaged L-PBF AlSi10Mg Alloy**

4.1	Aim	194
4.2	Experimental procedure	196
4.3	Results and discussion	199
4.3.1	Effects of overaging on hardness and microstructure	199
4.3.2	Static mechanical characterization	205
4.3.3	Cyclic mechanical characterization	212
4.3.4	Comparison between the high-temperature performance of the L-PBF AlSi10Mg alloy and AlSi cast alloys	219
4.4	Conclusion	222
	References – Chapter 4	223
	<b>Conclusions</b>	226

# Introduction

The fourth industrial revolution, also known as the "Industry 4.0" era, represents a turning point in achieving flexible and ecologically sustainable industrial production through combining physical and digital technologies [1]. In this context, Additive manufacturing (AM) has managed to become the fulcrum of an innovative industrial development thanks to its more efficient and adapting production model compared to conventional processes (Figure 1), aimed at quickly satisfying the growing market demand for high-performance and custom-made components [2]. Due to the inherent advantages of this technology, including its one-piece flow capability and near-infinite design freedom, the AM has recently also been described as "the manufacturing technology that will change the world" [3].

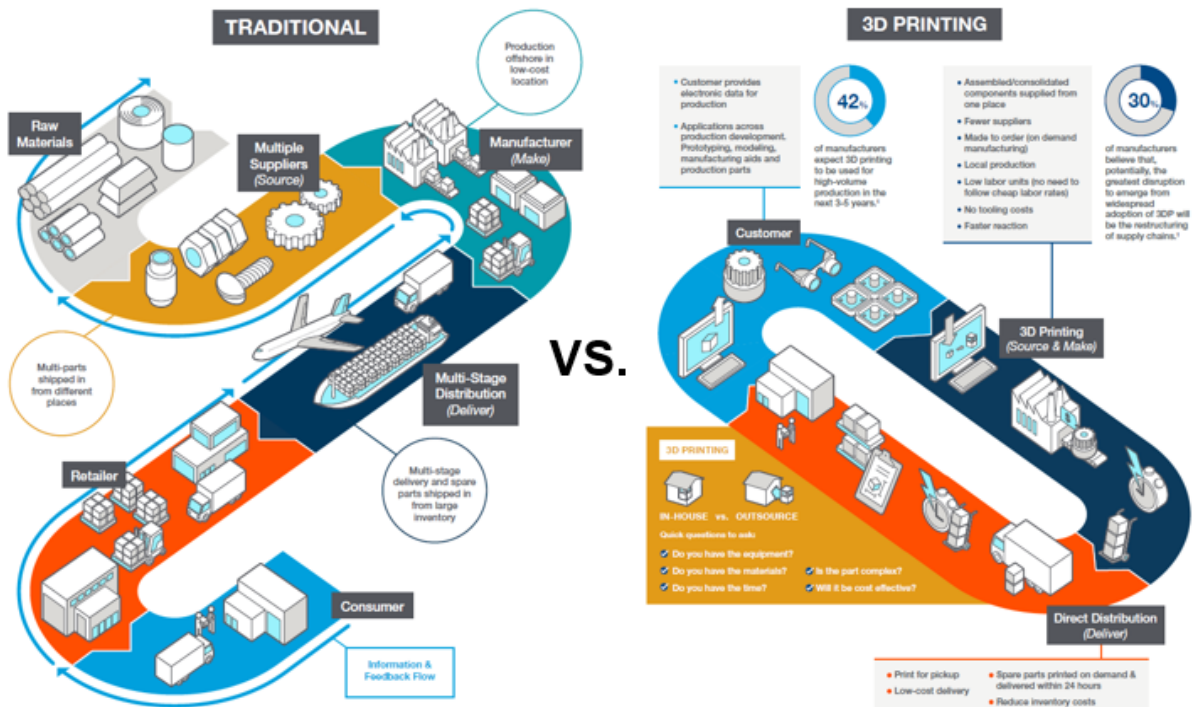


Fig. 1. Infographic between conventional and AM production chain. Adapted from [4].

The growing development to which AM technologies have been subjected is evident. Starting from the first Rapid Prototyping (RP) process developed to produce a 3D multilayer component starting from a Computer-Aided Design (CAD) model in the 1980s [5] up to modern equipment currently used in industrial production (Figure 2), the AM underwent an impressive industrial development that led it to cover a market of over 21 billion dollars in 2020 [6].

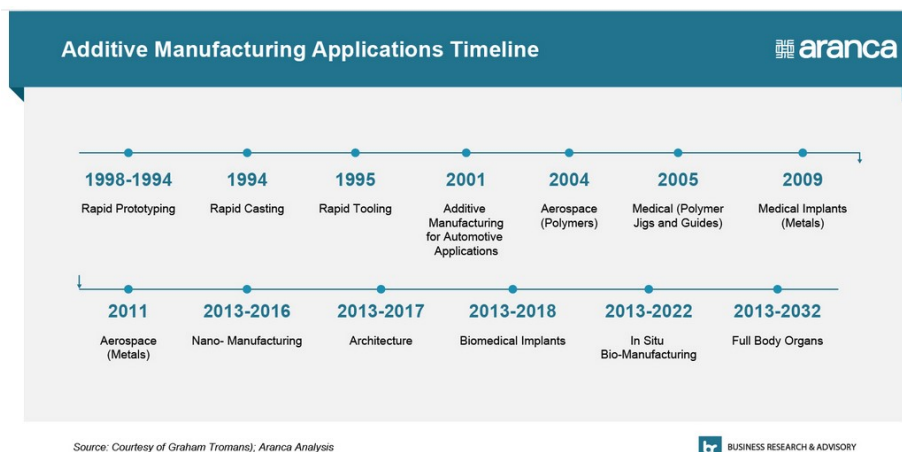


Fig. 2. Industrial evolution of the AM in the last three decades [7].

The exponential growth of scientific publications on AM over the past 10 years has been only limited by the CoVid-19 pandemic. As shown in Figure 3, from 2010 to 2022, the number of papers published annually grew by 20 times, an impressive number compared to the development of other technologies [8].

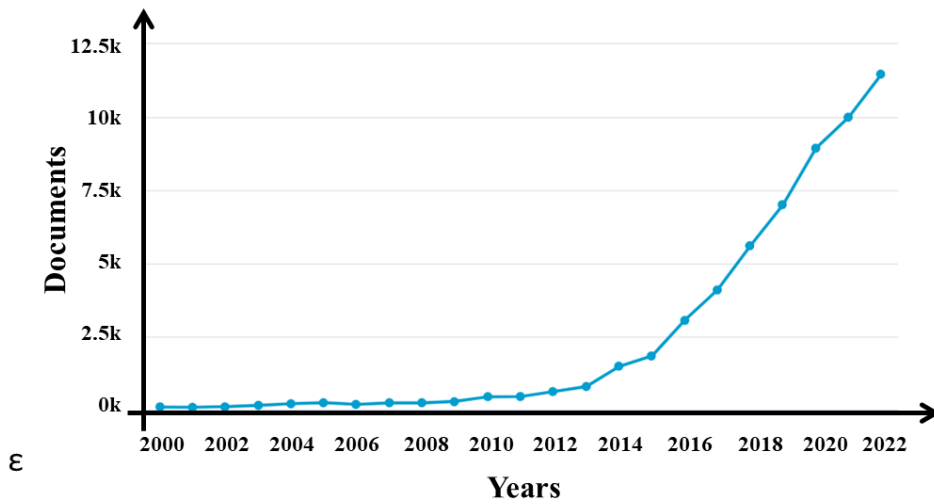


Fig. 3. Trend in the scientific research of AM by Scopus® database (accessed on December 2022).

AM's specific design and manufacturing concept reduces the anthropogenic CO<sub>2</sub> footprint by limiting energy-consuming processes, waste material, and the use of fabrication tools and joining methods, resulting in significant interest from the industrial community and scientific [9]. These advantages are due to the main features of AM: (i) reduction of production times and costs of complex-shaped parts, (ii) increase in the volume of recycled raw materials and reduction of production waste, (iii) topological optimization of mechanical components, and (iv) decrease in the number of post-production processes (Figure 4) [9-11].



Fig. 4. Brackets for Airbus A350 made by AM: with support structures (a) and without support structures following post-production treatments (b). Topological optimization resulted in a weight reduction of approximately 30% compared to the component manufactured using conventional processes. Adapted by [12].

These advantages make AM technology extremely competitive today compared to conventional processes in the small production of high-tech components and can be summarized in the three critical industrial factors: short times, reduced costs, and high production flexibility (Figure 5).

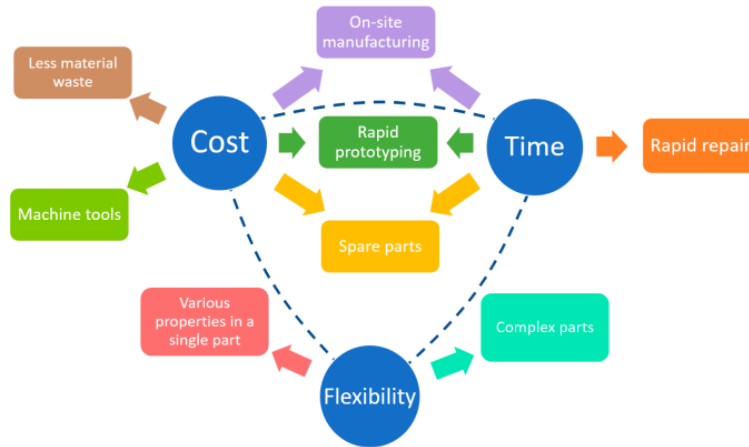


Fig. 5. Correlation between critical features and benefits of AM technology [2].

As described above, AM technologies are highly suitable for high-tech sectors, such as automotive, aeronautics, medicine, and energy. In particular, they benefit from AM technology for producing complex-shaped components characterized by light and high-performance structures obtainable through the customized design and topological optimization of mechanical parts [11,12]. Medical and dental implants, fuel injectors, heat sinks, mixing and swirling burner tips, pistons, gas turbines, and aerodynamic parts are possible AM-produced components (Figure 6) [13-15]

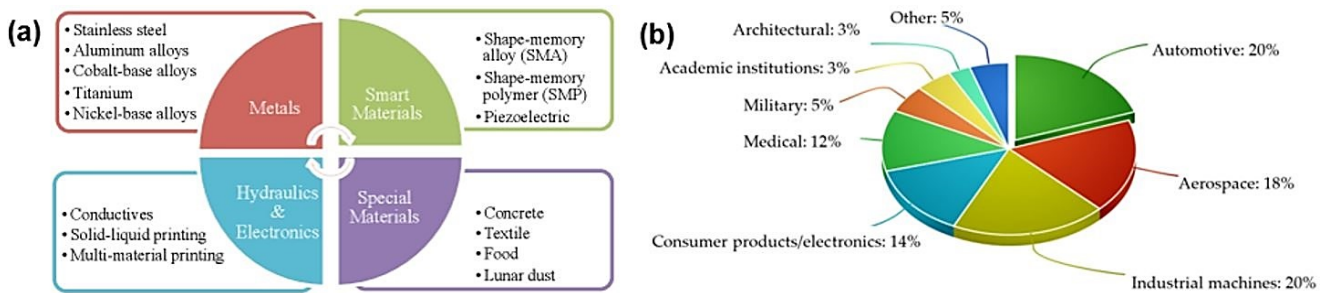


Fig. 6. Materials currently available for AM (a) [10]. AM by industrial sectors (%) in 2019 (b). Adapted by [12].

As described above, AM has a great future ahead of it. However, its large-scale industrial application is still limited by several unsolved production problems, including [2]:

- **Process limits:** Gas and lack-of-fusion (LoF) porosities, residual stresses, deformations, hot-cracking, microstructural inhomogeneities, low surface quality, and mechanical properties anisotropy are significant problems linked to the complex AM process conditions, which negatively influence the performance of the components;
- **Industrial production restrictions:** Very high costs characterize feedstock production and AM systems, which are only in part balanced through re-using materials, waste reduction, and an optimized supply chain. However, AM machines and materials costs have been reduced significantly, considering that they decreased by 51% from 2001 to 2011 [2]. Furthermore, the AM technology is currently not competitive compared to conventional processes for large production batches while being able to reduce production times for small production batches or single and customized components (Figure 7);
- **Cost and production volume trade-off:** The cost of the AM processes does not vary significantly with the part's number and complexity. Conversely, it is higher than conventional processes' production due to the high cost of raw materials. AM is currently preferred for small production batches or for single and customized parts where the high cost of raw materials is offset by a reduction in fixed costs, while conventional processes are more competitive for large production batches

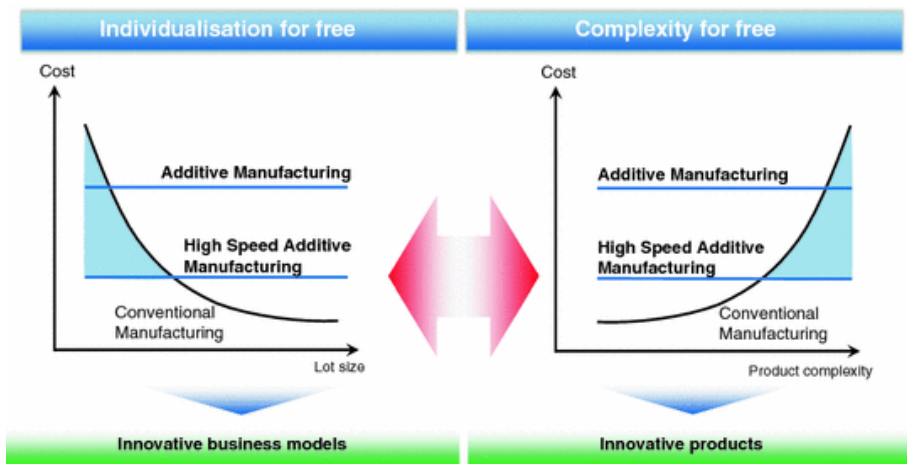


Fig. 7. Comparison between AM and conventional processes regarding production volume and cost per unit [3].

- **Design constraints:** The volume of the build chamber and the difficulties of printing some alloys, such as magnesium-based or aluminum-based alloys, are just a few of the issues that still limit the use of AM technology in numerous fields.

AM represents a technology with a substantial economic and social impact. The scientific community is moving compellingly, considering it one of the most critical technologies for achieving a new ecological and industrial transition. However, like all innovative and developing technologies, it presents numerous technological and metallurgical problems still to be solved to allow the full use of AM in the industrial sector.

This Ph.D. project moves in this highly stimulating scenario, using the scientific approach to overcome the AM limits in the industrial environment. The experimental activities were aimed at filling the gaps in knowledge relating to the effects of heat treatments on the AlSi10Mg alloy produced by Laser-based Powder Bed Fusion (L-PBF), which is one of the most used solutions in the high-tech industry, as well as developing an industrial process capable of reducing production times and costs and increase the performance of the AMed components.

The Ph.D. thesis consists of three main parts:

- The first part aims to understand the current AM scenario, particularly Powder Bed Fusion (PBF) technologies and AlSi alloys, through an extensive literature review. The survey provided the theoretical basis to evaluate the effects of process parameters and heat treatments on the microstructure and mechanical properties of the L-PBF AlSi10Mg alloy.
- The second part of the Ph.D. thesis focused on developing tailored heat treatments for the L-PBF AlSi10Mg alloy to overcome the limits of the as-built condition. This part collected the experimental activities for optimizing innovative heat treatments dedicated to the L-PBF AlSi10Mg alloy capable of exploiting the peculiarities of the supersaturated and ultrafine as-built microstructure.
- The third part of the thesis aimed to evaluate the mechanical (at room temperature and 200 °C) and tribological properties of optimized T5 and T6R heat-treated alloy. Research activities were conducted at the Department of Industrial Engineering at the University of Bologna under Prof. Lorella Ceschini. The experimental results discussed here derive from fruitful collaborations established within the RIMMEL project and with the Department of Materials and Manufacturing of the Engineering School of the University of Jönköping (Sweden), where in-situ tensile tests, Electron Backscatter Diffraction (EBSD) characterization, and nano-indentation analysis were performed.

## References

1. R. Godina, I. Ribeiro, F. Matos, T. Ferreira, B., H. Carvalho, P. Peças, Impact Assessment of Additive Manufacturing on Sustainable Business Models in Industry 4.0 Context. *Sustainability*, 12 (2020) 7066. <https://doi.org/10.3390/su12177066>.
2. M. Mehrpouya, A. Dehghanghadikolaei, B. Fotovvati, A. Vosooghnia, S.S Emamian, A. Gisario, The Potential of Additive Manufacturing in the Smart Factory Industrial 4.0: A Review. *Appl. Sci.* 9(18) (2019) 3865. <https://doi.org/10.3390/app9183865>.
3. R. Poprawe, C. Hinke, W. Meiners, J. Schrage, S. Bremen, S. Merkt, SLM Production Systems: Recent Developments in Process Development, Machine Concepts, and Component Design. In: Brecher C. (eds) *Advances in Production Technology. Lecture Notes in Production Engineering*. Springer, Cham, (2015). [https://doi.org/10.1007/978-3-319-12304-2\\_5](https://doi.org/10.1007/978-3-319-12304-2_5).
4. “3D Printing Impact on the Supply Chain | Infographic | Stratays Direct.” Stratays Direct Manufacturing, [www.strataysdirect.com/resources/3d-printing-supply-chain-infographic/](http://www.strataysdirect.com/resources/3d-printing-supply-chain-infographic/).
5. Y. Zhang, L. Wu, X. Guo, S. Kane, Y. Deng, Y.-G. Jung, J.-H. Lee, J. Zhang. Additive Manufacturing of Metallic Materials: A Review. *J. of Materi Eng and Perform*, 27 (2018) 1–13. <https://doi.org/10.1007/s11665-017-2747-y>.
6. M. K. Thompson, G. Moroni, T. Vaneker, G. Fadel, R. I. Campbell, I. Gibson, A. Bernard, J. Schulz, P. Graf, B. Ahuja, F. Martina, Design for Additive Manufacturing: Trends, opportunities, considerations, and constraints, *CIRP Annals*, 65(2) (2016) 737-760. <https://doi.org/10.1016/j.cirp.2016.05.004>.
7. <https://www.aranca.com/knowledge-library/blogs-and-opinions/business-research/additive-manufacturing-the-next-industrial-revolution>.
8. I. Gibson, D. Rosen, B. Stucker, Development of Additive Manufacturing Technology. In: *Additive Manufacturing Technologies*. Springer, New York, NY (2015). [https://doi.org/10.1007/978-1-4939-2113-3\\_2](https://doi.org/10.1007/978-1-4939-2113-3_2).
9. W. Gao, Y. Zhang, D. Ramanujan, K. Ramani, Y. Chen, C.B. Williams, C.C.L. Wang, Y.C. Shin, S. Zhang, P. D. Zavattieri, The status, challenges, and future of additive manufacturing in engineering, *Computer-Aided Design*, 69 (2015) 65-89. <https://doi.org/10.1016/j.cad.2015.04.001>.
10. U. M. Dilberoglu, B. Gharehpapagh, U. Yaman, M. Dolen, The Role of Additive Manufacturing in the Era of Industry 4.0, *Procedia Manufacturing*, 11 (2017) 545-554, <https://doi.org/10.1016/j.promfg.2017.07.148>.
11. W.E. Frazier, Metal Additive Manufacturing: A Review. *J. of Materi Eng and Perform* 23 (2014) 1917–1928. <https://doi.org/10.1007/s11665-014-0958-z>
12. A. Vafadar, F. Guzzomi, A. Rassau, K. Hayward, Advances in Metal Additive Manufacturing: A Review of Common Processes, Industrial Applications, and Current Challenges. *Appl. Sci.* 11 (2021) 1213. <https://doi.org/10.3390/app11031213>.
13. D. Herzog, V. Seyda, E. Wycisk, C. Emmelmann, Additive manufacturing of metals, *Acta Materialia*, 117 (2016) 371-392, <https://doi.org/10.1016/j.actamat.2016.07.019>.
14. T. DebRoy, H.L. Wei, J.S. Zuback, T. Mukherjee, J.W. Elmer, J.O. Milewski, A.M. Beese, A. Wilson-Heid, A. De, W. Zhang, Additive manufacturing of metallic components – Process, structure and properties, *Progress in Materials Science*, 92 (2018) 112-224. <https://doi.org/10.1016/j.pmatsci.2017.10.001>.
15. J.C. Najmon, S. Raeisi, A. Tovar, 2 - Review of additive manufacturing technologies and applications in the aerospace industry, Editor(s): F. Froes, R. Boyer, *Additive Manufacturing for the Aerospace Industry*, Elsevier, 7-31 (2019). <https://doi.org/10.1016/B978-0-12-814062-8.00002-9>

# Chapter 1 – AlSi10Mg alloy produced by Laser-based Powder Bed Fusion – Process, microstructure, and mechanical properties

## 1.1 Additive Manufacturing

The term "additive manufacturing," which was first introduced by the F42 ASTM Committee (American Society for Testing and Materials) in 2009 [1], refers to techniques characterized by “n-process of joining materials to make parts from 3D model data, usually layer upon layer, as opposed to subtractive manufacturing and formative manufacturing methodologies” [2]. In particular, the AM techniques are characterized by more efficient use of material and greater design flexibility, essential for making complex-shaped parts and thin-walled components (Figure 1.1) in a few industrial steps, which is extremely difficult or impossible to make by traditional processes, such as casting, forging or machining [3-5].

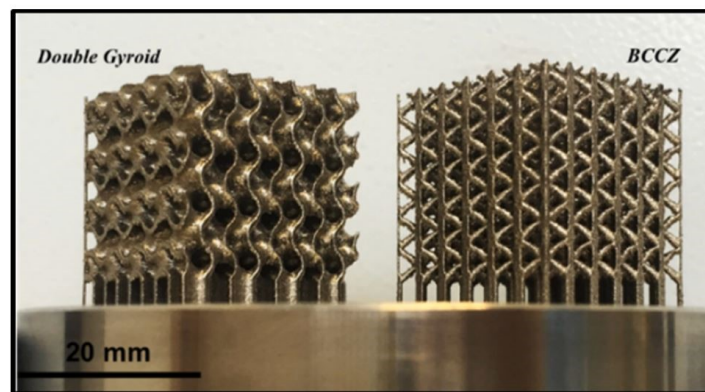


Fig. 1.1. A double gyroid lattice structure and a strut-based lattice structure fabricated using a Realizer SLM-50 [3].

ASTM International classifies AM techniques into seven different categories based on different raw materials (powder, wire, or plate) and energy sources (laser, electron beam, electric arc, or ultrasonic vibration) [5]: Material Extrusion (MEX), Vat Photopolymerization (VPP), Material Jetting (MJ), Binder Jetting (BJ), Powder Bed Fusion (PBF), Direct Energy Deposition (DED) and Sheet Lamination (SL) [6,7] (Figure 1.2). Materials, dimensional accuracy, intrinsic advantages and criticalities of the process, and the post-processing treatments necessary to complete the component influence the choice of the AM technique to be used (Table 1.1) [8].

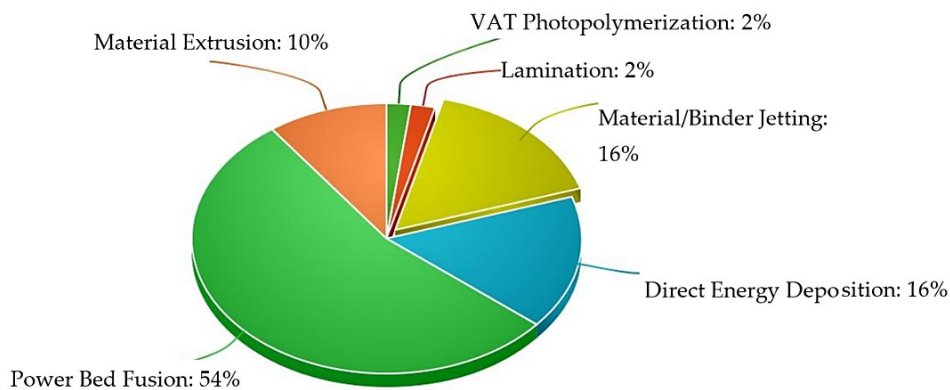
	Material Extrusion	Vat Photo-polymerization	Material Jetting	Binder Jetting	Powder Bed Fusion	Direct Energy Deposition	Sheet Lamination
Scheme							
Process	Layer by layer deposition of molten material	Selective curing of photo-curable material in a liquid container	Material deposition and subsequent curing	Selective dispense of binder for joining powder in a bed	Fusing of powder in a bed by melting the selected region	Direct fusion of the material	Bonding of individual sheets of material
Name	FDM RC MJS SFF	SLA DLP LAMP 2PP	DOD MJ NPJ	BJ	SLS SLM DMLS EBM MJF	LENS EBAM DMT	LOM UC
	Only polymers	Metals in R&D stage	Metals commercially available	Metals commercially available	Metals commercially available	Metals commercially available	Metals commercially available

Fig. 1.2. Categorization of AM processes in the current state-of-the-art and concerning metal component production. Adapted from [8].

**Table 1.1.** Application fields, usable materials, dimensional accuracy, advantages, criticalities, and post-processing treatments [8].

Technique	Materials	Application	Advantages	Challenges	Accuracy	Post-Processing
Direct Energy Deposition (DED)	Metals, ceramics	Industrial purposes, part repairing, implants, joining	High fabrication speed, high aspect ratios of parts, functionally graded materials can be obtained by several material nozzles	In some cases, the materials are burnt due to high laser power, the final part accuracy is relatively lower than SLM	100–250 $\mu\text{m}$	Heat treatment, in some cases a slight deburring
Selective Laser Melting (SLM)	Metals, ceramics	Industrial purposes, bio-applications, implants, actuators	Unlimited level of geometrical complexity, a wide range of metallic and ceramic powders, clean parts, high density	Fine powder is needed, fabrication chamber needs inert gas, slight metal evaporation in high laser powers	50–150 $\mu\text{m}$	Heat treatment, in some cases a slight deburring
Binder jetting	Polymers, ceramics, metals	Industrial purposes, research, bio-applications	High quality of the final part, high geometrical accuracy, flexibility in feedstock material	Residual thermal stresses, unwanted porosity due to using bonding materials	50–200 $\mu\text{m}$	Sintering, heat treatment
Metal jetting	Polymers, plastics	Desktop applications, research purposes, bio-applications	High speed of fabrication, high flexibility in process, low cost	Limitations in feedstock material selection, low geometrical accuracy in complex parts and it is not consistent	5–200 $\mu\text{m}$	Usually some slight deburring and residue removal with hand
Sheet lamination	Polymers, metals, and ceramics	Electronics, tissue fabrication	High speed of fabrication, low residual stresses	Low accuracy of the final product, chance of delamination under harsh thermal/mechanical conditions	Depends on the thickness of the sheets	Internal material residue removal, clamping in some cases that glue is used
Photo-polymerization	Acrylonitrile butadiene styrene (ABS), epoxy, polystyrene, acrylate	Biomedical, electronics, alpha prototyping	High geometrical accuracy, high surface quality	Limitation in feedstock material selection, low fabrication speed	<10 $\mu\text{m}$	Slight deburring
Extrusion	Thermoplastics such as ABS, Polylactic acid (PLA), polyethylene, polyether ketone, polycarbonate	Visual aids, educational models, alpha prototypes, tooling models	Simplicity, low cost, high speed	Low geometrical accuracy, low surface finish, only for polymers and thermoplastic materials	~100 $\mu\text{m}$	–

Among the AM technologies listed above, only the BJ, PBF, DED, and SL processes have the technical characteristics to be used in the industrial production of metal components [5,7]. In particular, PBF-based processes currently represent the best solutions for making structural components thanks to the excellent balance between mechanical properties and free-design solutions (Figure 1.3) [7].



**Fig. 1.3.** Distribution of AM technologies in the printer market: PBF techniques own the largest sector of the market [9].

In particular, the L-PBF process, also commercially known as Selective Laser melting (SLM), is currently the most employed solution in the industry compared to other important PBF technologies, such as Selective Laser Sintering (SLS) and Electron Beam Melting (EBM) [4,6]. This condition is related to essential advantages, including complete melting of the powder to produce almost entirely dense near-net-shape components without the need for post-processing, a wide range of materials that can be used, and mechanical components characterized by higher mechanical properties, surface finish, and high dimensional accuracy [10,11].

## 1.2 Introduction to Powder Bed Fusion

The PBF technology represents the most used AM technique in the industrial field. In particular, it produces small batches of customized components for high-tech applications [4,12]. The rapid expansion of this technology is linked to the possibility of carrying out a complete restyling of the components without the technological limits imposed by conventional processes, thus improving the distribution of the material to increase the specific strength of the part [13,14]. The Design for Additive Manufacturing (DAM) approach defines the process parameters and the print strategies to reduce production times and material waste and increase the mechanical and technological properties of the component. In any case, the production of a part by a PBF process always follows the following steps [3]:

- I. The 3D-CAD model format was converted to a Surface Tessellation Language (STL) file. The STL format uses finite element discretization through triangular vectors, each characterized by specific information about position and orientation in the space, to represent the solid parts described in the original CAD model (Figure 1.4). The resolution level of the .STL file should be optimized based on the surface finish of the 3D-printed part, considering the printing times and the design complexity.

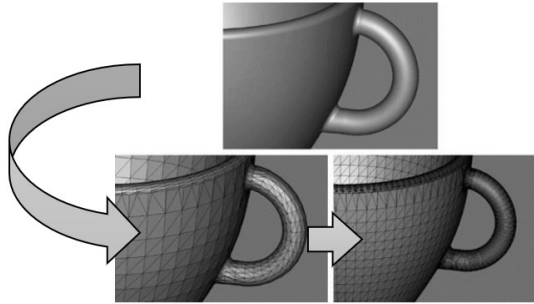


**Fig. 1.4.** Conversion from an original CAD model into a .STL file using different offset height (cusp) values. It shows how the model accuracy will change according to the triangle offset. Adapted from [15].

- II. The .STL file is virtually positioned on the building platform to obtain the optimal orientation of the components, depending on component size, heat transfer conditions, scan strategy, and support structures. The positioning directly affects the mechanical behavior of the component. The .STL file is "sliced," i.e., the component is divided into several layers through a uniform or adaptive subdivision (staircase) (Figure 1.5). The slicing operation limits the layer thickness of the powder bed and influences the surface quality and accuracy, as well as the mechanical properties of the component

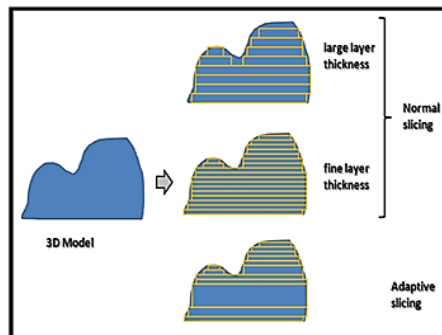


**Fig. 1.5.** Slicing operation on a 3D model. It can be normal or adaptive according to the component's complexity [15].

- III. The component is produced by a layer-by-layer deposition strategy. A build plate is usually heated to aid in heat dissipation and reduce the component's deformation and residual stress due to the high thermal gradient. Initially, the first layer of powder of a predefined thickness is spread over the build plate, and a heat source is focused on it, moving in the x-y plane to scan and melt/sinter the regions of interest selectively. The building

platform is then lowered to a distance equal to the thickness of the layer to allow subsequent deposition and continuation of the process. At the end of printing, the component is separated from any surplus support or material and subjected to post-processing operations.

As described above, several technologies are referable to PBF: (i) SLS, (ii) L-PBF, and (iii) EBM [4]. These techniques involve the use of powders as raw material and can be divided according to the method of consolidation (sintering (SLS) or fusion (SLM and EBM)) and the energy source used to produce the components (electron beam (EBM) or laser source (SLS and SLM)) (Figure 1.6).

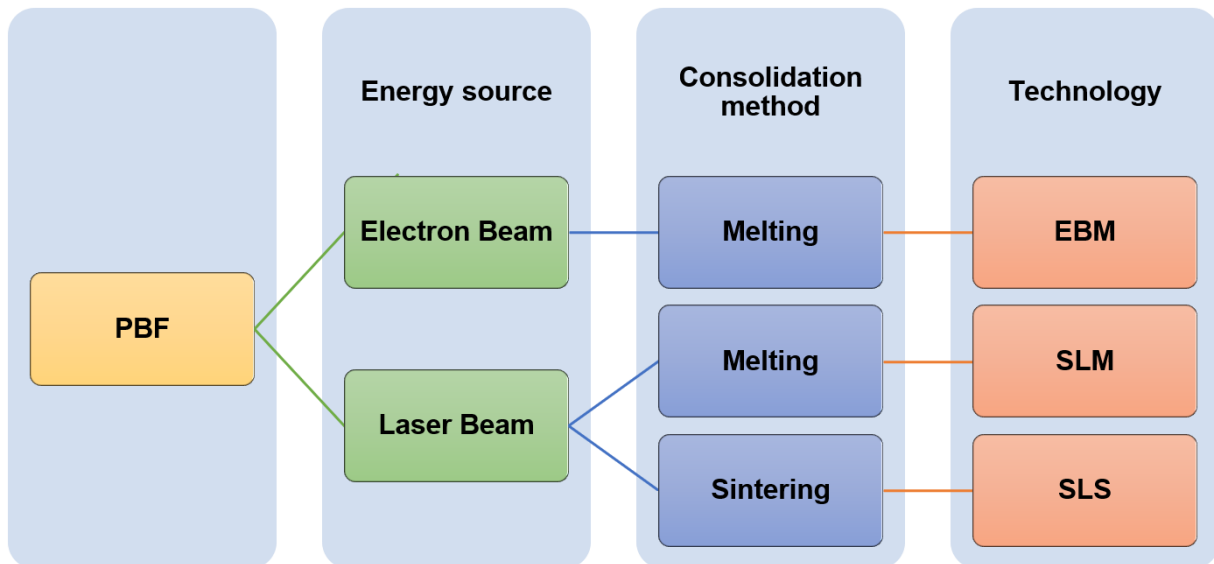


Fig. 1.6. Hierarchical tree of PBF technologies.

Only SLS technology is based on a sintering consolidation mechanism, mainly used for RP or polymeric-based composite materials [6]. On the contrary, EBM and L-PBF technologies, which are based on melting and solidification mechanisms, allow the production of structural components in metallic alloys, ceramic materials, and composites [7]. The electron beam transfers more energy than the laser beam and decreases the thermal shocks, making it highly suitable for making difficult-to-print materials such as Ti6Al4V alloy. It requires a vacuum working environment (order of  $10^{-3}$  Pa), which has some advantages, such as degassing the impurities present in the powders but preventing the use of EBM to process materials containing volatile elements, such as Mg. On the contrary, the laser beam only needs an inert protective atmosphere (Ar, N<sub>2</sub>, or He) and has a high resolution and surface finish, thanks to the focusing of a large amount of energy in a small area, and versatile, adapting very well to the processing of low-melting alloys, such as AlSi alloys [4,5]. For this reason, in recent years, the high-tech industrial sector has mainly turned to L-PBF technology, given its enormous potential, especially for producing complex-shaped and high-performance components in light alloy [12].

### 1.3 Laser-based Powder Bed Fusion

In the last decade, the L-PBF technology has represented one of the most studied AM techniques to make complex engineering structures characterized by high specific strength in a single production step [11]. This goal is made possible by depositing single layers of metal powders on the building platform and the selective melting of single Regions of Interest (ROI) using a high-energy-density laser beam according to a predefined scanning strategy [3]. The complete melting of the powders allows for obtaining a bulk material density close to that obtainable with the most common conventional processes [16]. Furthermore, the reduced production times and costs of complex-shaped parts, the low environmental impact, and the high mechanical properties of the mechanical components make the L-PBF process highly suitable for producing high-performance and custom-made components (Figure 1.7) [15].

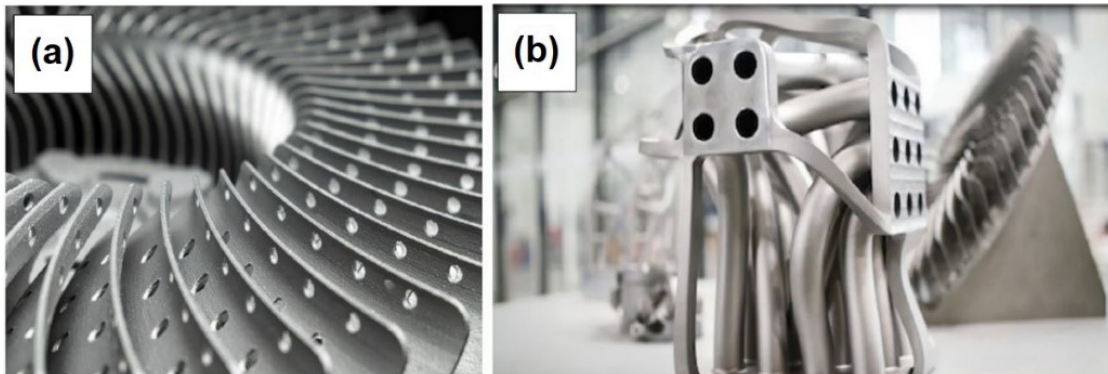


Fig. 1.7. Complex-geometry metal parts in L-PBF AlSi10Mg alloy: distributor housing (a) and large heat sink (b). Adapted from [17]

The structure of the L-PBF system is schematically reported in Figure 1.8. It uses a high-power laser beam as an energy source, guided on the x-y plane using a system of lenses and a galvanometer scanning mirror. This system is needed to direct the laser spot to a specific area to selectively melt the powder bed and produce a near full-density part [18]. Currently, the L-PBF systems are mostly equipped with active fiber laser sources (Nd: YAG) with continuous laser emission close to the wavelength of the infrared field (about  $1\ \mu\text{m}$ ) [3]. A power range between 200 W and 400 W, with a maximum peak of 1 kW, and a spot size varies between  $50\ \mu\text{m}$  and  $200\ \mu\text{m}$ , depending on the process conditions and the surface quality of the component, characterize the laser source. A closed chamber constitutes the printing system with a controlled atmosphere ( $\text{N}_2$  or Ar) to avoid the oxidation phenomena of the powders [19]. A thin layer of powders, between 20 and  $100\ \mu\text{m}$ , is distributed from a powder hopper or a feeding system on a mobile platform using a re-coater with a ceramic, steel, or rubber blade. The choice of the re-coater depends on the powder type and the component to be produced.

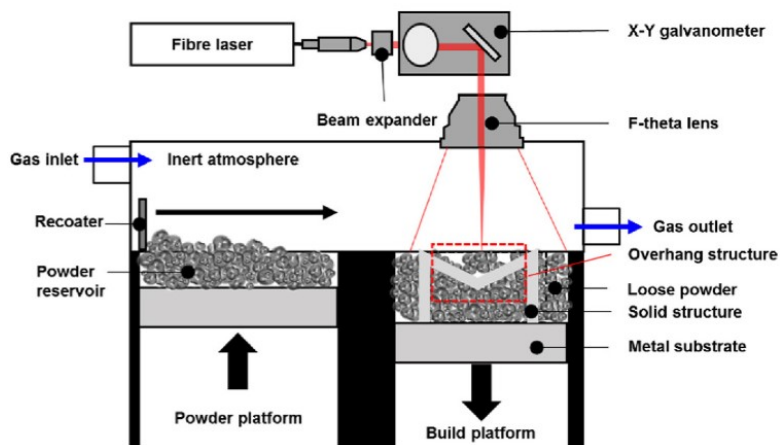


Fig. 1.8. Scheme of L-PBF printing machine. The build chamber is purged from secondary products of the process, such as weld fume and weld spatter, with a flowing inert atmosphere. The blue arrows indicate the gas flow direction [20].

A build substrate, or 'start plate', is firstly deposited on the platform to supply mechanical and thermal support to the part during the printing [4]. After deposition and scanning of the first layer, the platform is lowered by a height equal to the slicing thickness of the component (Figure 1.8). Subsequently, a new layer of material is deposited. The process repeats until the completion of the part. In the end, the unmelted powders are removed from the component's surface and re-used in subsequent print. The L-PBF technology uses overhang lattice-like structures to support the component during the printing and to promote heat dissipation (Figure 1.9) [4], which must be removed. As described in the following sections, the component can be subjected to post-processing heat treatments to relieve residual stress that could cause the failure of the part after the disengagement from the building platform. A similar strategy can be applied by heating the build platform to reduce the temperature gradient and residual stress. Therefore, the term "as-built" indicates the components extracted by the building platform; various mechanical post-processing treatments can be performed on them, such as brushing, sandblasting, and shot peening, to eliminate residual powder, reduce surface roughness and induce residual compressive stresses, respectively [21]. Therefore, four stages are fundamental in the L-PBF process: machine set-up, component building, powder recovery, and substrate removal.

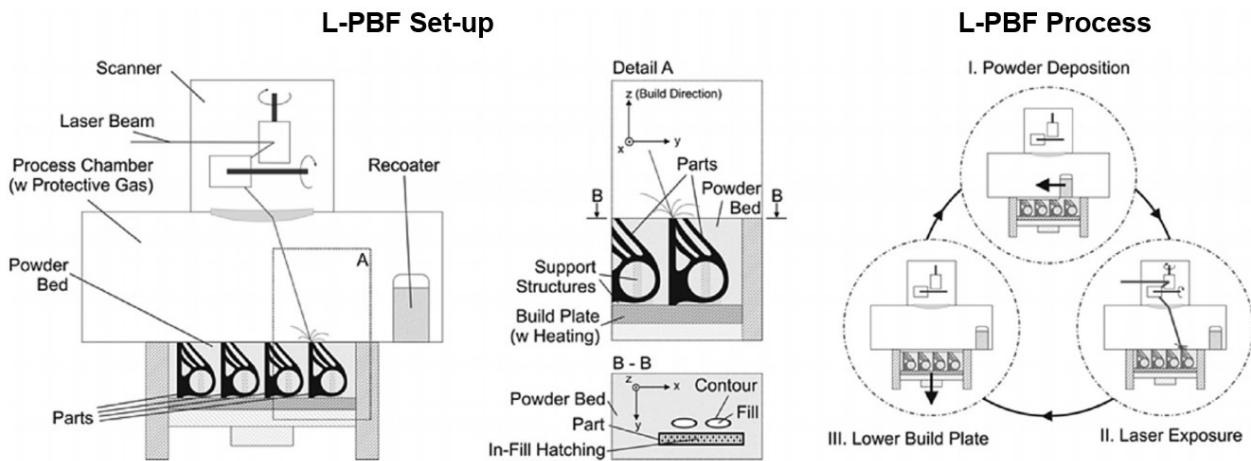


Fig. 1.9. Scheme of L-PBF printing machine (left) and support structures (center). Three process steps were iterated during the build (right) [4].

The materials used in the L-PBF process include [3-5,11,22]:

- **Steels and ferrous alloys:** In particular, most publications refer to 316L and 904L stainless steel, AISI Maraging 300 steel, 15-5 PH and 17-4 PH steels, H20 and X110CrMoVA1 8-2 tool steels. Given the high cost of L-PBF-manufactured parts, these materials are mainly used in high-value-added applications in the medical sector and the automotive and aerospace industries due to the possibility of creating lattice structures and structural lightening.
- **Ti alloys:** Commercially pure Ti alloys and Ti6Al4V are the most studied Ti-based materials. Others are Ti6Al7Nb, Ti24Nb4Zr8Sn, Ti13ZrNb, and Ti13Nb13Zr. The Ti alloys are very suitable for the L-PBF process; in fact, using an inert atmosphere and the high cooling rate in the L-PBF process reduces the critical production issues linked to their high reactivity. Furthermore, Ti alloys are mainly preferred in the biomedical field thanks to their biocompatibility, high specific strength, and elastic modulus closer to the bone than Co-Cr alloys and stainless steels. In addition, Ti6Al4V alloy is also used to produce turbine blades for aircraft engines.
- **Ni alloys:** Nickel-based alloys are a family of superalloys widely used in aeronautical and aerospace applications to produce gas turbine blades or swirling nozzles due to high corrosion resistance, high mechanical properties at high temperatures, and excellent fatigue resistance. The 718 Inconel alloy is the most used Nickel-based alloy. Other nickel-based alloys studied are Chromel, Hastelloy X, Nimonic 263, IN738LC, and MAR-M 247.

- **Al alloys:** Al alloys are used in the aerospace and automotive industries to produce high-performance components due to their high AM feasibility and specific strength. These features make them ideal for producing lightweight and thin-walled parts and more complex-shaped components subjected to high mechanical loads. Currently, the most used alloys are AlSi7, AlSi10Mg, AlSi12, AlScMg, AlCuMg, AlScZr, AlMgScZr, AlSi11CuMn, AA-2024, AA-7075, Scalmalloy®.
- **Co-Cr alloys.** The L-PBF process represents an efficient option for rapidly producing complex-shaped components in Co-Cr alloy due to the difficulty of machining these alloys. They are distinguished by their high hardness, corrosion resistance, and biocompatibility, which determine their wide use in the medical fields for producing dental, knee, and hip prostheses. The elevated high-temperature mechanical properties make them suitable for aerospace and energy applications.
- **Other materials.** Other materials have also been studied to be produced with the L-PBF process for particular applications, such as Cu-based, Mg-based, or W-based alloys or precious metals such as Au and Ag. Ceramic materials can also be used in this process, but only as a reinforcement in composite materials.

### 1.3.1 Feedstock powder features

In the L-PBF process, each powder layer is deposited on the build platform and then selectively melted to make the final component progressively. Therefore, the powder's characteristics must guarantee high performance from the L-PBF-produced component [23,24].

The raw powder manufacturing process influences the quality and Particle Size Distribution (PSD). The most common method to produce high-quality reactive alloy powders, such as Al alloys, is Gas Atomization (GA) [3]. It is a common and consolidated method to produce spherical powders, in which the raw material is first melted in an oven, placed inside an upper chamber, and then conveyed to an underlying chamber in the form of liquid metal. Within the chamber, inert gas at high pressure nebulizes the liquid metal, thus producing spherical powders (Figure 1.10).

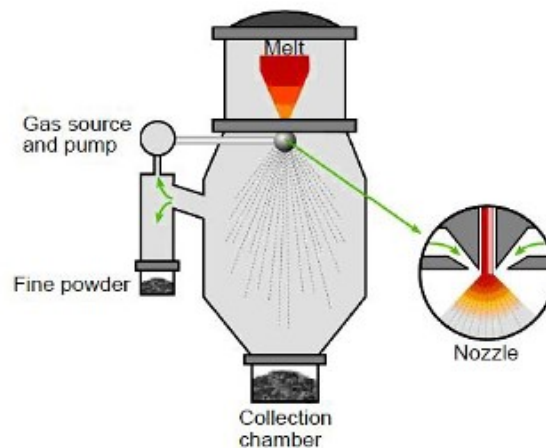


Fig. 1.10. Scheme of the GA production system [23].

The solidified metal droplets are collected in a lower chamber. Due to the high purity requirements of the powder in the high-tech industry, melting is usually performed by vacuum melting furnaces or induction melting furnaces. In particular, two different solutions exist: (i) Vacuum Inert Gas Atomization (VIGA), which produces degassed melts that pour through a basket nozzle into the atomization chamber (Figure 1.11(a)), and Electrode Induction Gas Atomization (EIGA), which uses bars as raw materials (Figure 1.11(b)). In the latter case, the rod is fed, rotated, and melted by an induction coil, so the liquid metal enters the atomization chamber directly without using a basket. This process ensures no contact with the crucible, minimizing the risk of contamination for reactive alloys.

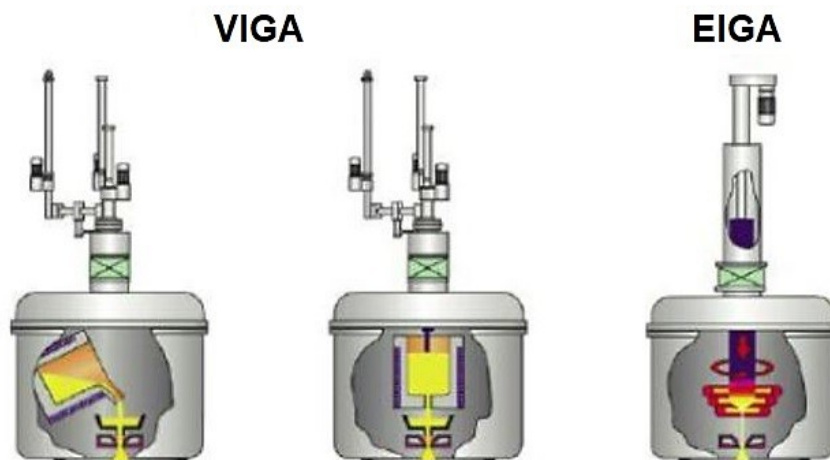
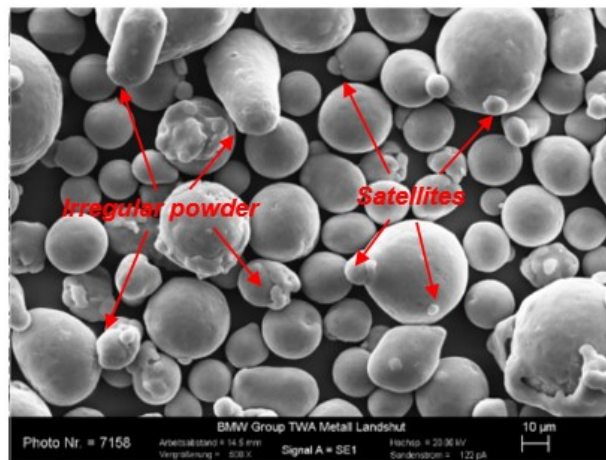


Fig. 1.11. Illustration of melting systems: (a) VIGA (tilting crucible (left) and bottom pouring crucible (right)) and (b) EIGA (induction coil) [23].

The PSD value of the final product (about 0 - 500  $\mu\text{m}$ ) can be reduced by more precise control of the gas flow and post-processing sieving. However, the formation of so-called satellites on the surface of the powders cannot be avoided

(Figure 1.12). They are surface irregularities made up of smaller particles that adhere to the surface of larger ones due to a difference in solidification rate between smaller and larger partially melted particles. Satellites reduce the morphological and technological features of the powders [25].



**Fig. 1.12.** GAed AIS10Mg powder. Morphology can be easily studied by scanning electron microscope (SEM). Adapted from [25].

The GA is characterized by higher productivity and lower cost than plasma atomization (PA), which makes it highly suitable for industrial production, despite the lower quality of the powders due to the presence of satellites and a broader PSD value [26]. The quality of the powder affects the density and the surface finish of the L-PBF-produced component. Two crucial physical characteristics define powders' quality: flowability and packing density. Specifically, they describe the ability of a powder to flow, which can be evaluated by the Hall Flowmeter method, and the ratio between the mass of the compacted powder in the container and the non-compacted powder, including the contribution of the interparticle vacuum, respectively. In particular, an increase in the packing density reduces the volume of porosity in the bulk material, while an increase in the flowability results in a more uniform powder layer, a less volume of voids among the powders, and higher absorption of laser energy [27].

The flowability and packing density depend on different powder features, including:

**Morphology:** Smooth and spherical powders are characterized by lower interparticle friction and mechanical interlocking phenomena compared to rough, irregular, and elongated particles (Figure 1.12) and, consequently, by a greater flowability and packing-density value [3]. The inner powder porosity due to the gas trapped within the powders during the GA process is another undesirable characteristic that reduces the density of the L-PBF-produced components for the release of gas during the process (Figure 1.13).

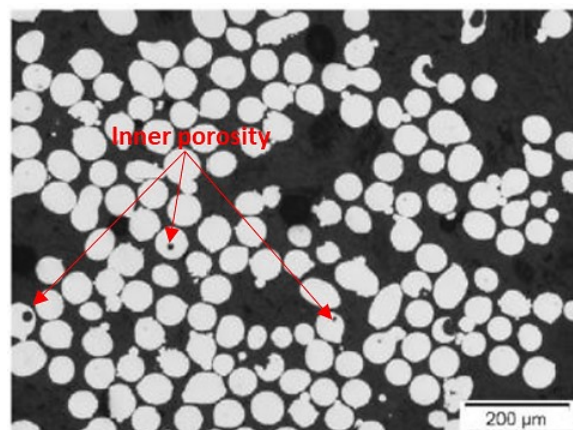


**Fig. 1.13.** OM image of polished cross-sections of GAed Inconel 718 powders. The internal porosities of the powder can be observed by a polished cross-section [25].

**Particle Size Distribution (PSD):** An increase in particle size determines a higher flowability due to the decrease of the Van Der Waals forces and the electrostatic forces that can cause agglomeration phenomena. In addition, extremely fine powders have a larger surface area and generate more inter-particle friction and lower flowability. The layer thickness limits the maximum powder size. The heterogeneous distribution of powder size leads to the maximum packing density because the finer particles settle in the interstices left by the coarser ones, thus minimizing the volume of voids within the powders (Figure 1.14) [27].

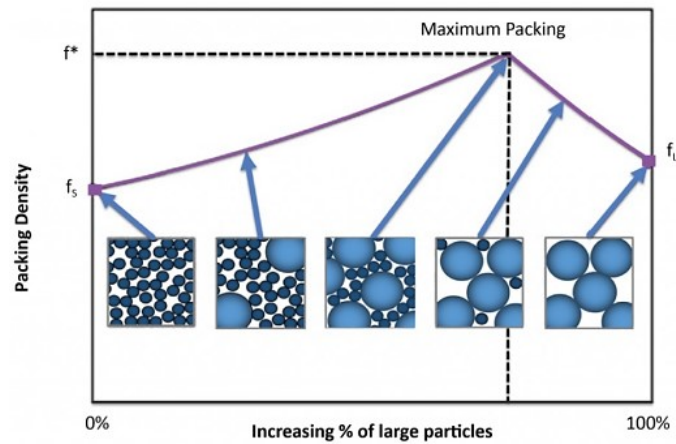


**Fig. 1.14.** A high packing density is associated with producing high-quality components with minimal defects and a relatively large PSD value [27]. A PSD between 15 - 45  $\mu\text{m}$  or 20 - 63  $\mu\text{m}$  guarantees excellent quality of the L-PBF-produced component [28]. It reduces the layer thickness and, consequently, improves the resolution and surface quality of the component (Figure 1.15). Broader PSD distribution and unsuitable layer thickness could lead to in situ segregation due to the re-coater mechanical removal of coarser particles from the powder bed [29].

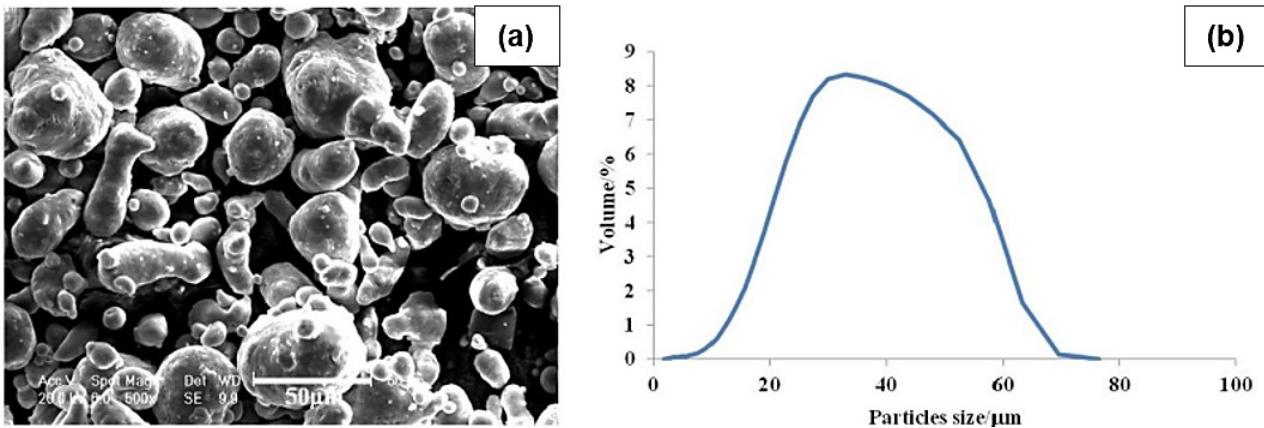


**Fig. 1.15.** SEM image of AlSi10Mg powders (a) and PSD trend (b). The PSD peak is shifted towards 35  $\mu\text{m}$  in diameter to increase the components' relative density through a larger size range (20 - 63  $\mu\text{m}$ ) and a higher content of small-size powders. Adapted from [30].

**Humidity level:** Incorrect feeding and storage conditions determine a high level of humidity and a significant reduction in both flowability and packing density due to the formation of compact agglomerates of powders, which increases inter-particle friction [24]. Furthermore, the formation of surface oxide films affects high reactivity alloys such as Al alloys, reducing the absorption of laser energy and facilitating the formation of defects. Therefore, powder drying before the L-PBF process improves the component's quality [3].

**Absorbance:** The powders' physical characteristics deeply influence the melting process of the L-PBF process. In particular, the powders' morphology and size influence the powder bed's absorbance. Absorbance is the ratio of the absorbed radiation to the radiation incident from the laser beam. Only a fraction of the incident radiation is absorbed by the external surface of the particles, while the remainder penetrates through the interparticle voids or reflects among the

powders (Figure 1.16). Thus, the absorbance directly affects the penetration depth of the laser beam and the heat absorption of the powder bed, depending on the material's particle size, packing density, and physical properties [5].

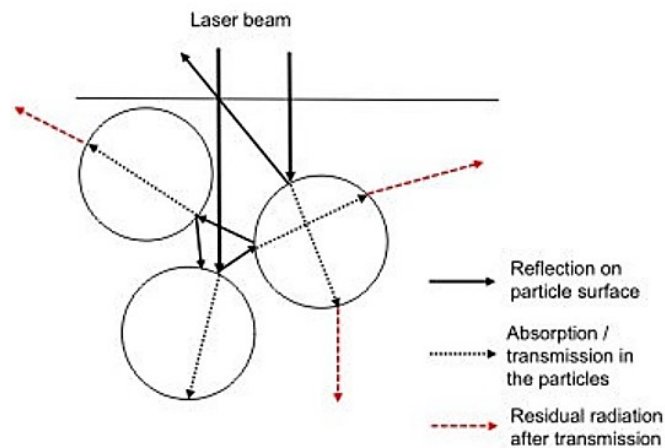


Fig. 1.16. Scheme of the laser beam penetration in a powder bed [31].

**Recyclability:** The total powder volume used within the build chamber can be significantly higher than the total volume of the final component. As a result, a large volume of unfused powder will need to be effectively recovered and reused due to the high cost of powders [32]. However, the thermal effects resulting from the process can cause physical and chemical alterations to the recycled powder. Only powders not subject to partial melting or microstructural changes can be reused due to morphology and physical characteristics similar to fresh powder [3]. In several studies [32,33], recycled and sieved vs. fresh Al powders showed similar PSD, chemical, and phase composition, almost identical surface oxide content, and powder morphology. Consequently, recycled Al powder can be used to reduce the cost of the economic impact of the L-PBF process, achieving mechanical properties equivalent to those produced with fresh powders [34]. However, particular attention should be paid to contamination by impurities or foreign bodies, which can also occur following manipulations during the pre or post-processing steps.

### 1.3.2 Laser sources

The L-PBF process uses a high-energy laser beam to melt the powders and make a full-dense component. Consequently, the type of laser source and the laser parameters directly influence the amount of energy transferred to the powder bed and the component performance [7]. The most commonly used laser source are CO<sub>2</sub>, Nd:YAG, and Yb-fiber (Figure 1.17).

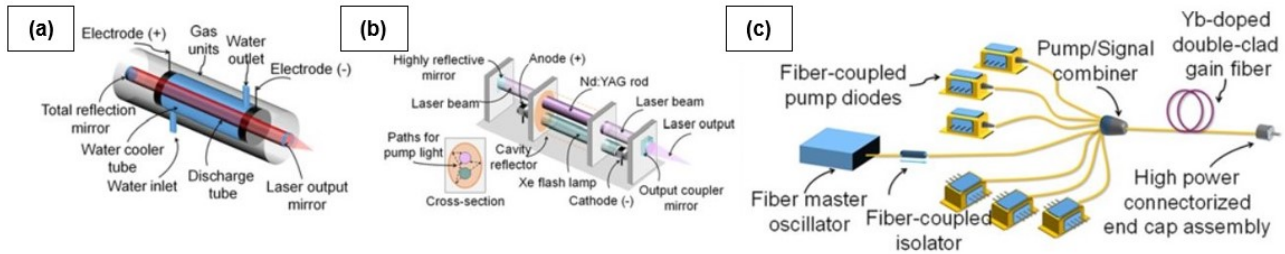


Fig. 1.17. Operative scheme of different laser sources: (a) CO<sub>2</sub>, (b) Nd:YAG, and (c) Yb-fiber. Adapted from [35].

The CO<sub>2</sub> laser was one of the first gas lasers developed. It consists of a discharge tube, an electric pump source, and an optical resonator (Figure 1.17(a)). Compared to other continuous wavelength lasers, CO<sub>2</sub> lasers provide high efficiency (5 - 20%) and high output power (0.1 - 20 kW) (Table 1.2), so they are widely used in technological processing, e.g., cutting, drilling, welding, and surface modification [35]. Although the system is simple, reliable, and low cost, its use in the L-PBF process is limited by the relatively unstable output power and Long-Infrared (LIR) output wavelength, which are not optimal for making metallic components.

Table 1.2. Specifications of the most representative lasers for L-PBF technology [35].

Laser	CO <sub>2</sub> laser	Nd:YAG laser	Yb-fiber laser
Operation wavelength	9.4 & 10.6 $\mu\text{m}$	1.06 $\mu\text{m}$	1.07 $\mu\text{m}$
Efficiency	5-20 %	Lamp pump: 1-3 %, Diode pump: 10-20 %	10-30 %
Output power (CW)	Up to 20 kW	Up to 16 kW	Up to 10 kW
Pump source	Electrical discharge	Flashlamp or laser diode	Laser diode
Operation mode	CW & Pulse	CW & Pulse	CW & Pulse
Pulse duration	Hundreds ns-tens $\mu\text{s}$	Few ns-tens ms	Tens ns-tens ms
Beam quality factor (mm-mrad)	3-5	0.4-20	0.3-4
Fiber delivery	Not possible	Possible	Possible
Maintenance periods	2000 hrs	200 hrs (Lamp life) 10,000 hrs (Diode life)	Maintenance free (25,000 hrs)

The Nd:YAG laser is a type of solid-state source that uses rod-shaped Nd:YAG crystals (Nd<sup>3+</sup>:Y<sub>3</sub>Al<sub>5</sub>O<sub>12</sub>) as a solid gain medium (Figure 1.17(b)), producing a Near-Infrared (NIR) output wavelength (Figure 1.18). It is more compact and efficient than a CO<sub>2</sub> laser and can operate in both continuous and pulsed modes for melting metal powder. However, the low energy efficiency translates into a deterioration in component quality, which has led to the replacement of the Nd:YAG laser in L-PBF applications with Yb fiber lasers, which are currently the most widely used solution in the industry [35].

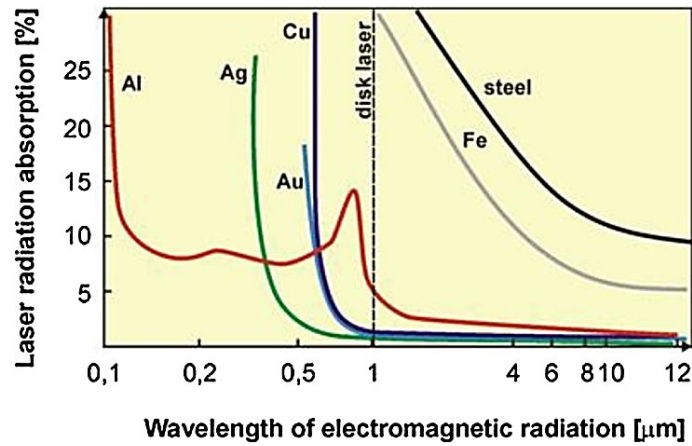


Fig. 1.18. Absorption of laser radiation as a function of wavelength and material [37].

The Yb fiber laser produces a NIR laser beam by an active gain medium consisting of optical fiber doped with rare-earth (Yb), which is pumped by laser diodes (Figure 1.17(c)). Other advantages are high electrical-to-optical efficiency, excellent beam quality, robustness against environmental disturbances, and system compactness (Table 1.2). In addition, introducing multiple lasers in a single machine, such as the SLM500, has improved part quality and scan speed. Conversely, the change in polarization due to fiber bending, vibration, and temperature changes can be detrimental to the laser's output efficiency [35].

The laser parameters influence the interaction between the laser beam and the powder bed and, consequently, the melt pool formation and the solidification process. Energy absorption depends on the characteristics of the heat source and the material and determines the deposition rate and the feature quality (Figure 1.19).

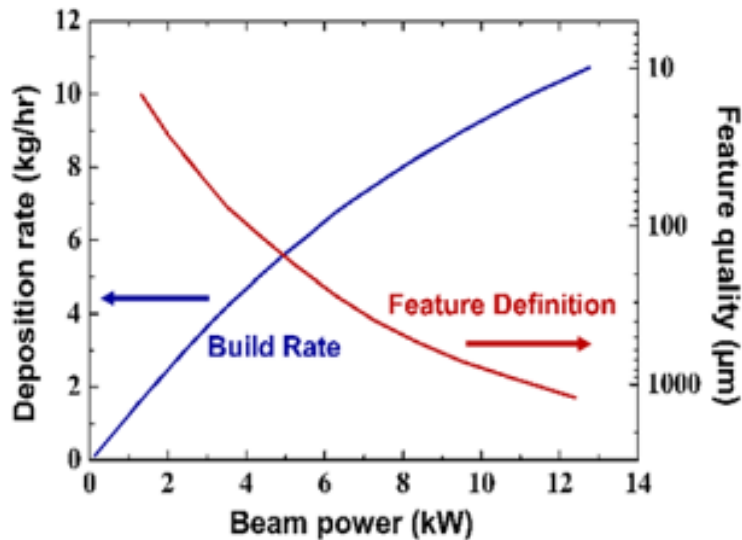


Fig. 1.19. Deposition rate and component quality trend related to the power of the laser beam [35].

First, the high reflectivity and thermal diffusivity of some alloys, such as Al-based or Cu-based alloys, make melting the metal powder difficult and require high laser power. Likewise, the deposition rate must allow for the complete melting of the metal powder and avoid poor surface finish and component defect formation. To reduce these problems, maximize the amount of energy transferred to the powder through short operating wavelengths or use various pulse durations to instantly raise the temperature of the material where it is needed while minimizing heat dissipation. Ultimately, the high quality of the beam, which is defined in terms of the Beam Parameter Product (BPP), i.e., the product of the radius and the half-angle of divergence of the beam, increases the density of energy transferred to the powder and, consequently, the component resolution and solidification rate.

### 1.3.3 Laser beam-powder bed interaction

During the L-PBF process, the laser beam irradiates the powder bed, transferring a certain amount of energy (Figure 1.20(a)): part of this energy is absorbed by the particles while the rest is dissipated by radiation and convection or reflected by the powder bed and consequently dispersed (Figure 1.20(b)) [19]. In addition, metallic powders and solidified metal act as heat dissipators so that the heat conduction through the substrate gradually decreases with the deposition of the layers [38]. Therefore, the amount of heat absorbed by the particles depends on both the characteristics of the laser source (power density and laser beam features) and the powder bed (particle size, packing density, and material properties) [11,19]. The irradiation by the laser beam leads to rapid heating of the powders and resultant localized melting, thus generating a semicircular molten pool, called "Melt Pool" (MP) (Figure 1.20(a)) [39]. The circular shape of the MP is a function of the energy transferred (asymmetric Gaussian distribution (Figure 1.20(c)) to the raw material and the substrate, which induces the morphological characteristics and the crystallographic texture of the microstructure [5,14,40]. The MP's rapid solidification ( $10^3 - 10^8$  K/s) occurs when the heat source leaves the molten region.

The solidification of the MP is a critical element: it allows the metallurgical bonding between adjacent tracks and overlapping layers according to the scanning strategy and the part's consolidation [7,12].

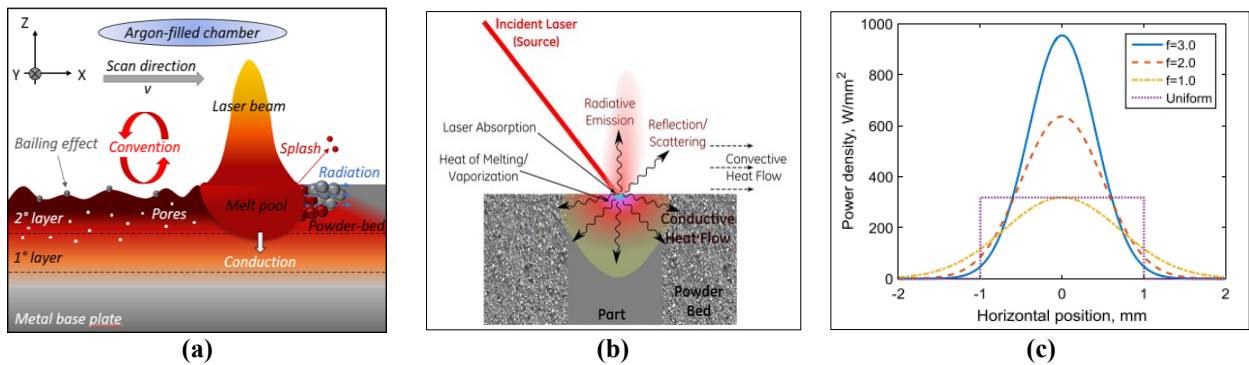


**Fig. 1.20.** Scheme of the interaction laser beam/powder bed (a). Heat transfer mechanisms in MP formation (b). The primary heat transfer mechanisms include laser irradiation to the powder bed, heat conduction from the MP to the solidified substrate and powder bed, and heat convection to the protective atmosphere, respectively [19]. Power density distribution as a function of the distribution factor  $f$  (c) [5].

The amount of energy transferred to the powder bed determines the formation mechanisms of the molten pool: generally, the higher the laser energy, the higher the penetration depth [41]. The MP formation by conduction mode occurs without metal vaporization (Figure 1.21(a)): the energy density is relatively low, and the temperature gradient promotes the formation of broad and shallow MPs. Conversely, at higher energy density, metal vaporization occurs, and the recoil pressure of the metal vapors becomes more significant than the surface tension and hydrostatic pressure of the liquid metal, leading to the formation of deep and narrow MPs (keyhole deposition mode), as shown in Figure 1.21(b). As the energy density increases, the recoil pressure of the metal vapors is too high to form voids inside the key-hole and so makes key-hole pores (Figure 1.21(c)), as will be described in section [39].

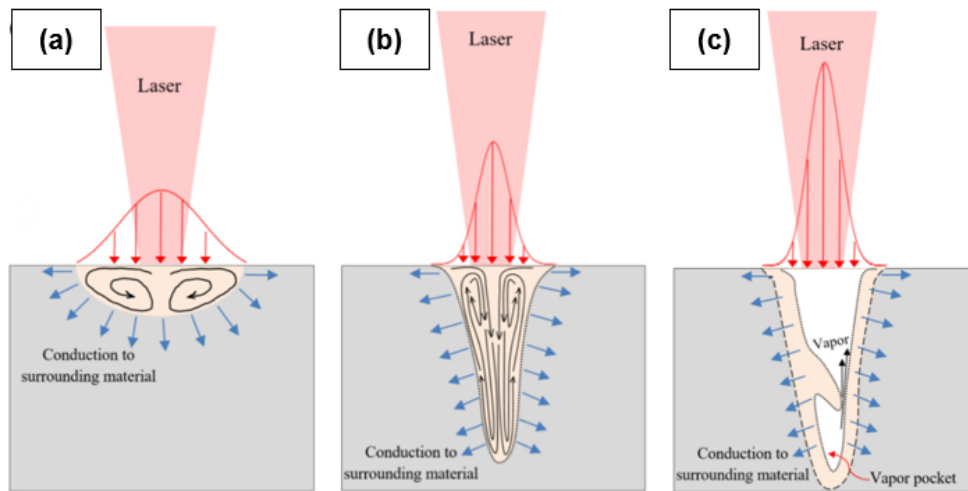


**Fig. 1.21.** MP formation mechanisms: conduction mode (a), transition mode (b), and keyhole with porosity (c) [39].

The heat transfer mechanisms involved in the MP formation are highly complex and make it difficult to predict the thermal history undergone by the material [40,41]; in fact, the energy transfer from the laser beam to the metal powders leads to the rapid melting and solidification of the material and generates a series of complex physical and chemical phenomena challenging to predict [5]. The primary phenomenon to be analyzed is the flow dynamics inside the MP, which influences the temperature distribution, the cooling rate, the solidification process, and, consequently, the morphology and dimensions of the microstructure [42-44].

As described in Figure 1.22, four main forces act on liquid metal inside the MP: buoyancy force, originating from the volume variation induced by the solid-liquid transformation, Marangoni force, developed by surface tension gradients, gravitational force, and shear force, which is generated by vapor or plasma [45]. In the presence of an electric or magnetic field, the action of the electromagnetic force on the MP, e.g., Lorentz force, must also be considered, while when evaporation occurs in the keyhole melting mode, the recoil pressure becomes the principal driving force of molten metal [39]. The interaction between the different forces that constitute the convective flow field makes it difficult to predict the microstructure deriving from the solidification of the MP through mathematical models [46,47].

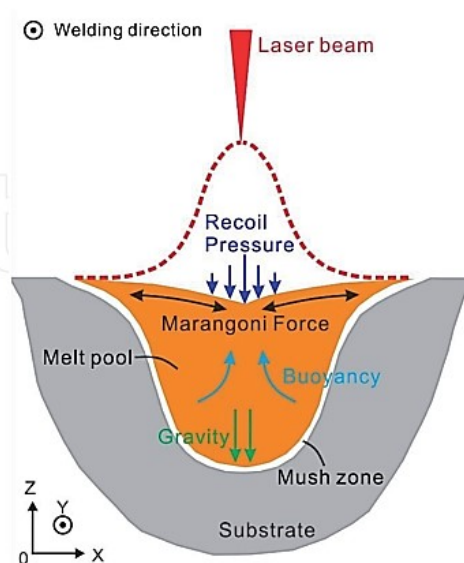


**Fig. 1.22.** Dynamic flows acting on the MP. The main forces acting on the liquid metal are highlighted: buoyancy force, Marangoni force, gravity force, and recoil pressure [45].

The Marangoni force constitutes the main contributor to the flow dynamics in the MP and is also known as thermocapillary convection flow [49]. The laser beam heats the powder bed in a limited area inducing a temperature

gradient characterized by the maximum temperature in the center of the molten pool and a rapid radial decrease (Figure 1.23(a)). This phenomenon causes a difference in surface tension ( $\gamma$ ) in the MP and a centrifugal flow of the liquid metal. Therefore, the Marangoni flow is related to the surface tension gradient on the top surface of the MP, which acts as shear stress on the free surface resulting from a convective flow (Figures 1.24(e,f)). The concentration gradient or surface-active agents are other factors that can influence the Marangoni flow [48]. As the contribution of these factors increases, it can invert the surface tension gradient (Figure 1.23(b)). The reversal of the flow and the consequent formation of a centripetal movement is harmful to proper wetting by the liquid metal, inducing the so-called balling phenomenon [50].

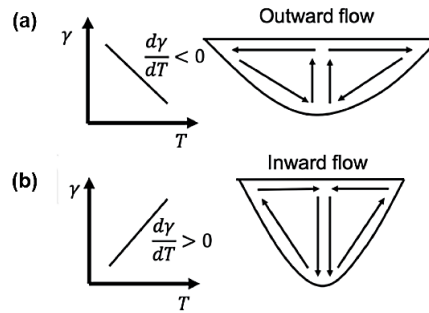


**Fig. 1.23.** Effect of the sign of the surface tension temperature coefficient on fluid flow in the weld pool [48].

The buoyancy force is essential in the flow dynamic and derives from the spatial density variation in the liquid/solid phase transition. It is known that the variation in density is inversely proportional to the temperature of the material: the temperature of the liquid metal in the upper part of the MP is higher than the bottom one and therefore determines an upward circulatory motion of the liquid metal within the MP, as shown in Figures 1.24 (a,b) [48]. However, this effect is negligible compared to the Marangoni force.

The gravitational force slightly influences the size and shape of MP due to the support provided by the solidified substrate and the unmelted powder, which delimit the volume of the liquid metal [46].

The shear stress generated by vapor or plasma is due to the evaporation phenomena from the vapor recoil pressure, which pushes the liquid towards the edge of the MP (Figures 1.24(g,h)). In the keyhole mode, the pressure of the recoil is the driving force for the liquid metal flow [5].

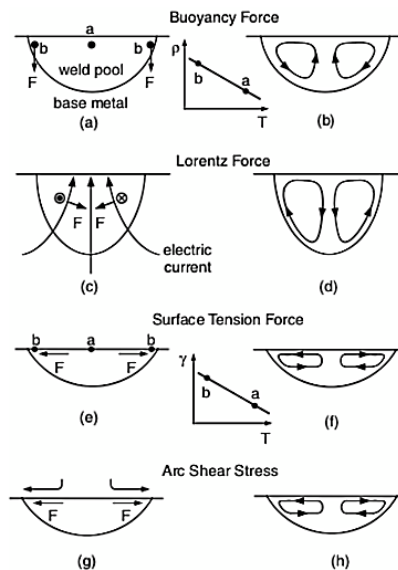


**Fig. 1.24.** Driving forces of convection flow (a,c,e,g); relative flow inside the MP (b, d, f, h) [45].

Part geometry and process parameters, such as hatch distance or scan strategy, affect the heat exchange conditions close to the MP due to the different heat transport properties between the metal powders and the solidified material (Figure 1.20(b)). The component and powder bed behave like a heat sink, and their volumes influence the conductive dissipation from the MP: the higher the solid interface, the higher the heat transferred. Therefore, in the L-PBF process, predicting and controlling the temperature gradient is extremely difficult due to the numerous parameters influencing heat transfer. The very high scanning speed modifies the morphology of the MP and increases the thermal gradient. At the same time, the amount of heat transferred to the powder bed and the heat flow control the volume of the MP (Figure 1.25) [51].

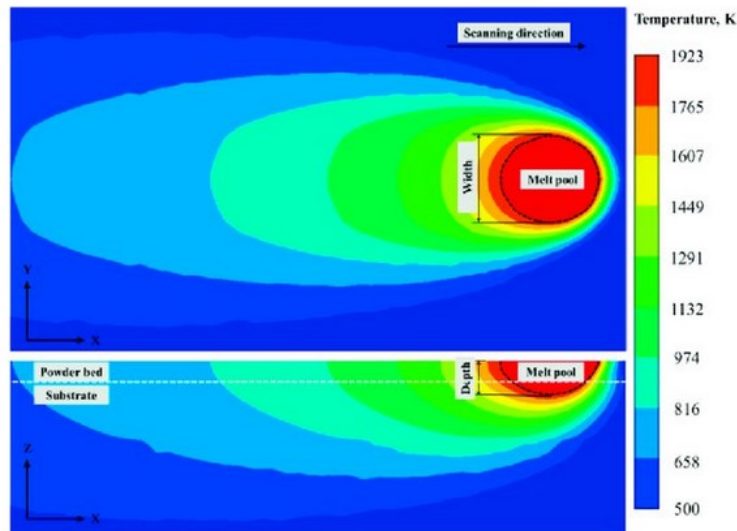


**Fig. 1.25.** Temperature distribution within the MP and along the scan track. The heat flow promotes the highest temperatures near the axis of the heat source and the lowest temperatures at the Melt Pool Boundaries (MPBs) [51].

The non-uniform temperature gradient promotes a surface tension gradient inside the MP that drives the liquid metal and influences the solidification pattern of the microstructure. In particular, the MPBs, and consequently, the contours of the thermal gradient (Heat Affected Zones (HAZs)), are stretched behind the heat source and compressed in front of it due to the high scan speed and intense Marangoni stress, which drives and stirs the flow of liquid metal within the fusion zone [42].

The shape of the fusion zone and the temperature field affect both the local solidification growth rate,  $R$ , and the temperature gradient,  $G$ , at the solid-liquid interface and influence the mechanical performance of the L-PBF-produced components. In particular, as will be further discussed, the ratio of the parameters,  $G/R$ , affects the morphology of the solidification structure, and  $G \cdot R$ , the cooling rate, affects the size and morphology of the microstructure. These parameters are essential for determining the extent of solid-state transformations induced by the subsequent thermal cycles and will be explored in the following section.

## 1.4 Influence of the L-PBF process parameters on defect formation

The L-PBF process parameters directly or indirectly influence the feasibility of the printing process, the microstructural characteristics, the distribution and morphology of the defects, and, consequently, the mechanical properties of the L-PBF-produced part [52-54]. In the L-PBF process, over 50 different variables can be involved in printing, both directly and indirectly, making optimization and control difficult [25,38]. The main important parameter analyzed in the literature can be classified into four categories [3,38,55] (Figure 1.26).

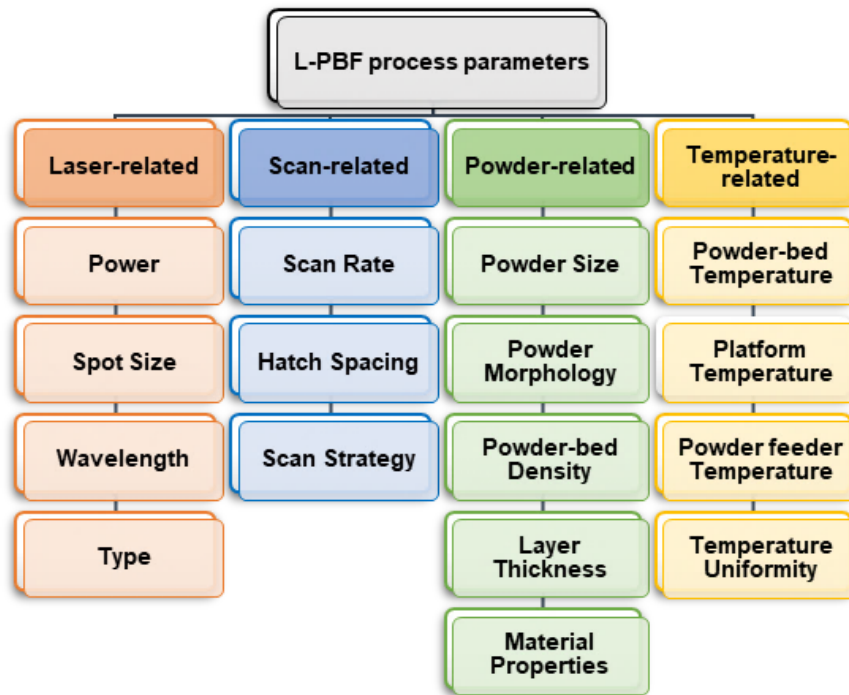


Fig. 1.26. Main important process parameters involved in an L-PBF process. Adapted from [3].

Optimizing the process parameters is fundamental to producing defect-free and fully-dense parts, thus increasing the mechanical properties of the L-PBF components produced by [52,54]. The printing system and the material strongly influence the choice of process parameters; consequently, the optimization must be implemented case by case. In particular, the laser beam and its properties, hatch spacing, scan rate, layer thickness, and scan strategy are the main parameters involved in the process and have been studied in the literature to improve the part density and mechanical properties of the material [7]. These parameters are summarized in Figure 1.27.

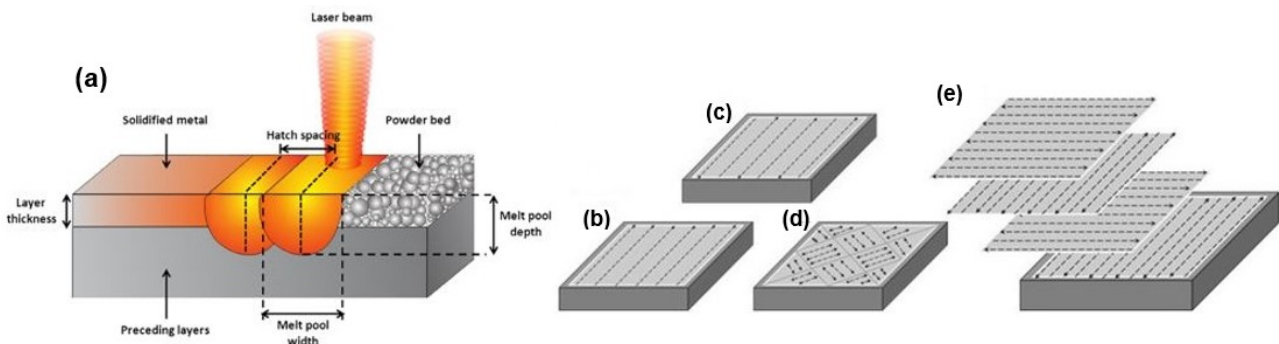


Fig. 1.27. Schematic representation of the interaction between laser beam and powder-bed and the main operating parameters involved during the L-PBF process (a) [17]. Examples of different scan patterns: meander (b), meander-bidirectional (c), and chessboard (d). A schematic presentation for rotating the scan orientation per layer is in (e) [3].

The **laser power** controls the amount of energy transferred to the irradiated material. The high reflectivity of Al alloys leads to high power levels to melt powders [13]. If the transmitted energy is insufficient, the partial melting of the powders and the incomplete filling of the MP in the solidification phase occurs, thus forming defects. In addition, the laser source properties govern the size and continuity of the scan track [20], affecting the part's structural integrity.

The **hatch spacing** provides the overlap distance between adjacent tracks, ensuring the metallurgical bonding and the consolidation of the part to be built [56]. A small hatch spacing increases production time and leads to the re-melt of a large volume of material, while a large hatch spacing imposes limitations on the maximum layer thickness, i.e., the crack starts to form due to a lack of intra-layer bonding [52,56].

The **scan speed** controls the melting and solidification rates. The slower the speed, the longer the irradiated spot is held above the MP, which takes longer to solidify, thus affecting the microstructure and defect formation [54]

The **layer thickness** is the fundamental parameter in a "layer-by-layer" deposition process, as it directly affects the final component's quality in terms of mechanical properties and surface roughness. Minimum layer thicknesses increase the surface quality and dimensional accuracy but also production times and costs, while greater thicknesses introduce defects [52], like balling and LoF pores, due to the difficulty of the laser beam in completely melting the powders [50].

The **scan strategy** defines the pattern of the laser path within a layer and the difference in scan patterns between layers, e.g., rotating layer orientations by a set angle or scanning a layer multiple times (Figure 1.27) [3]. An optimized scan strategy is oriented to minimize the defects and control the microstructural texture.

To evaluate the overall contribution of the primary process parameters, energy density (ED) was introduced as a relative term between the various parameters concerning the interaction between the heat source and the powder layer. The ED can be expressed in three different ways, depending on the portion of space affected by the laser/powder interaction.

The linear energy density  $ED_l$  is given by the ratio between the laser power (P) and scanning speed (v) (Equation 1.1):

$$ED_l = \frac{P}{v} \left[ \frac{J}{mm} \right] \quad (1.1)$$

The surface energy density  $ED_s$  is given by the ratio between the  $ED_l$  value and the hatch distance (h) (Equation 1.2):

$$ED_s = \frac{P}{v h} \left[ \frac{J}{mm^2} \right] \quad (1.2)$$

Finally, the volumetric energy density  $ED_v$  is given by the ratio between the  $ED_s$  and the layer thickness (t) (Equation 1.3):

$$ED_v = \frac{P}{v h t} \left[ \frac{J}{mm^3} \right] \quad (1.3)$$

However, the energy density term can also constitute a limit in providing an accurate approximation of the interaction between the laser beam and the powders due to the absence of essential process parameters, such as specific heat capacity of the powder bed, scan strategy, flow rate and direction of gas flow within the build chamber, and more [57]. In addition, the absence of physical phenomenon contribution (Marangoni flow, recoil pressure, hydrodynamic instability, ...), which controls the shape of each scan track, makes it challenging to obtain a reliable value of the energy transmitted.

The interaction between the laser beam and the powder bed generates a series of complex thermophysical phenomena (solid mechanics, solid-state transformation, thermal fluid dynamics, and particle dynamics [58]) during the rapid melting and solidification phases (Figure 1.28), influencing the formation of defects.

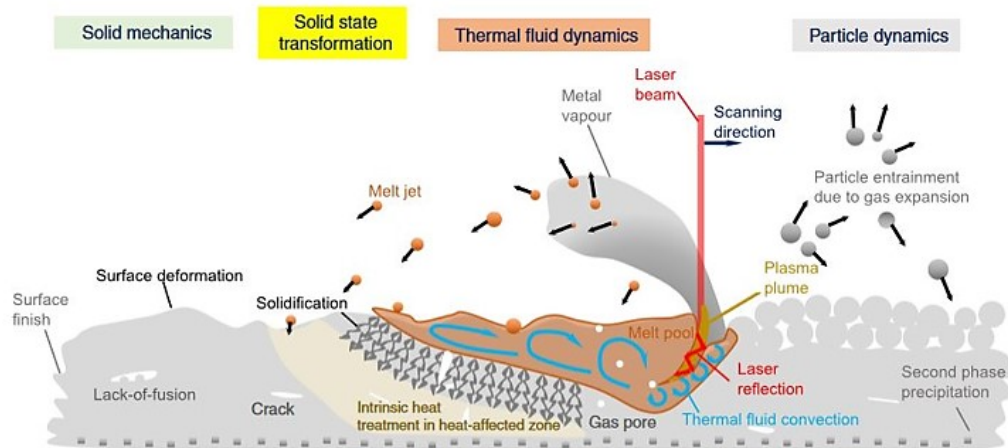


**Fig. 1.28.** Different physical effects occur during the L-PBF process, including powder particle dynamics due to gas expansion, thermal fluid dynamics capturing solid-liquid-vapor transition when interacting with laser, solid-state transformation such as precipitation once re-melting and intrinsic heat treatment, and subsequent solid mechanics to deal with damage mechanism such as cracking [58].

Defect formation (metallurgical and keyhole pores, LoF, delamination, and cracks) and damage phenomena (spattering, balling, oxide formation, and loss of low-melting temperature elements) have been extensively studied in the literature to evaluate their effects on the mechanical performances of the materials.

### 1.4.1 Pore formation

Pores represent one of the primary defects deriving from the L-PBF process; in fact, they are challenging to eliminate and negatively influence the mechanical properties of the components. The formation process defines the morphological and dimensional characteristics of the pores, dividing them into two categories: metallurgical pores (gas pores) and technological pores (LoF and keyhole pores) [52,54,55]

**Metallurgical pores**, also called **gas porosities**, are spherical in shape, and small in size (between 10  $\mu\text{m}$  and 100  $\mu\text{m}$  in diameter) (Figure 1.29(a)), and their formation is attributable to the volume of gas present inside the MP, which remains trapped during the solidification of the liquid metal leaving spherical cavities inside the bulk material [12]. The presence of gas pores inside the MP can be related to the following:

- Gases absorbed by the powders ( $\text{N}_2$ ,  $\text{O}_2$ , and  $\text{H}_2$ ) during the production and released in the MP during the melting;
- Inert gases (Ar,  $\text{N}_2$ , or He) absorbed from the protective atmosphere inside the build chamber due to the turbulence of the MP induced by convective flows;
- $\text{H}_2$  released from  $\text{H}_2\text{O}$  in the form of humidity due to incorrect storage of metal powders in humid environments;
- Air ( $\text{N}_2$ ,  $\text{O}_2$ , and  $\text{H}_2$ ) entrapped in the voids within the powder layer due to a low packing density;
- Vaporization of low-temperature melting alloying elements (including Mg and Zn).

Consequently, various factors can promote the formation of gas pores: (i) high intensity of the laser beam, which increases the temperatures of the MP and, therefore, the solubility of gases in the liquid metal, (ii) high scan speed, which increases the cooling rate and turbulence of the liquid metal, thus facilitating the trapping of the protective gas.

**Lack-of-Fusion (LoF)** defects, also known as incomplete fusion holes, have a highly irregular morphology, larger dimensions than gas porosities, and three-dimensional anisotropy, which are attributable to the formation of voids left during the solidification between the individual layers and scan tracks [52]. The maximum extension is between 50 and 300  $\mu\text{m}$ , and un-melted powders can be located inside them (Figure 1.29(c)) [3]. The number of LoFs increases in proportion to insufficient energy density, which may be associated with insufficient power or excessive scan speed, hatch distance, or layer thickness, thus not allowing a complete powder melting. More in detail, the formation of LoF is linked to various mechanisms [35,52]:

- Incomplete melting of the powder layer and the underlying solidified layers due to insufficient energy density;
- Insufficient hatch distance, resulting in the formation of voids due to a scan track overlapping, insufficient to close the strong volume decrease in the liquid-solid passage during solidification;
- Oxides formed during the L-PBF process, which avoids the powder melting and reduces the metallurgical bonding effect between solidified layers and scan tracks;
- Ejection of liquid metal droplets from the MP due to the high scanning speed of the laser source (spattering phenomena). The metal droplets fall back onto the powder bed, being incorporated into the subsequent layers. The difficult re-melting of the re-solidified particles by the laser beam determines the formation of cavities in the surrounding volume.
- Spherical metal particles formed by the combined action of the low wettability of the liquid metal on the solid substrate and the convective motions generated inside the protective atmosphere above the MP (balling phenomena). As in the previous case, the balling reduces cohesion between successive layers.

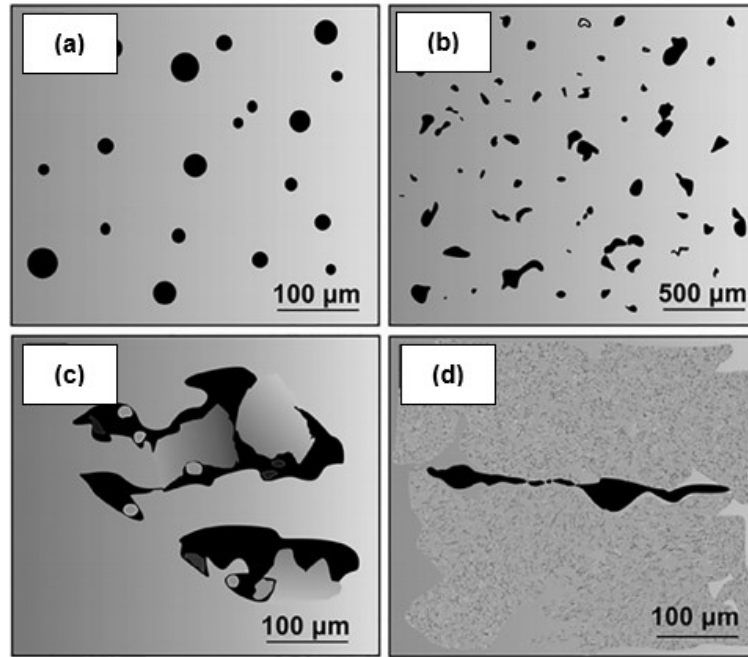


**Fig. 1.29.** Characteristic pores in L-PBF-produced parts: entrapped gas porosities (a); incomplete melting-induced porosity (b); LoFs with un-melted particles inside large irregular pores (c) and cracks (d). Adapted from [35].

**Keyhole pores** arise from MP instability and depend on the equilibrium between the two opposing pressures acting on the keyhole: (i) the ablation pressure and (ii) the capillary pressure. The first one, which constitutes the pressure necessary to keep the keyhole open, is attributable to the evaporation of the liquid metal and its expulsion from the MP. The second one is due to the surface tension along the MPB resulting from the temperature gradient, which acts to close the keyhole. [59].

As the laser power exceeds specific limit values, the evaporation rate increases proportionally to the heat absorption. The increase in the diameter and depth of the vapor plume formed inside the hole causes a consequent increase in the ablation pressure until it reaches a critical size limited by the Rayleigh instability phenomenon. In this case, the length/diameter ratio of the vapor column inside the cavity is excessively high, thus leading to closures along the axis due to the increase in surface tension and the entrapment of the outgoing vapor (Figure 1.30).

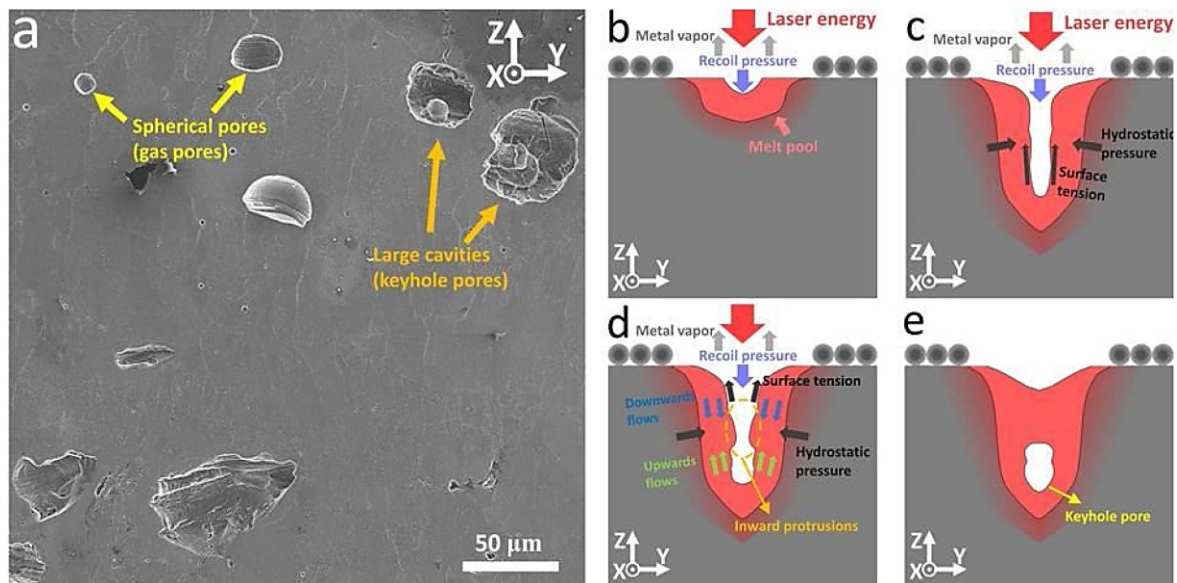


**Fig. 1.30.** Keyhole porosity in the L-PBF-produced AA 2024 alloy: (a) SEM micrograph (b-e) schematic illustration of the formation mechanism of the keyhole porosity [60].

As previously described, the keyhole formation mechanism is associated with a high energy density due to excessive power or low scanning speed. The penetration depth is significantly marked, involving many pre-solidified layers and the powder layer to be scanned, leading to partial evaporation of the material. Therefore, the high instability of the MP causes the trapping of gases inside the material, and the presence of empty volumes is attributed to the rapid solidification of the metal, which causes no complete filling of gaps with liquid metal. The dimensions depend on the process conditions but settle on the intermediate values between the gas porosities and LoFs (Figure 1.31) [61].

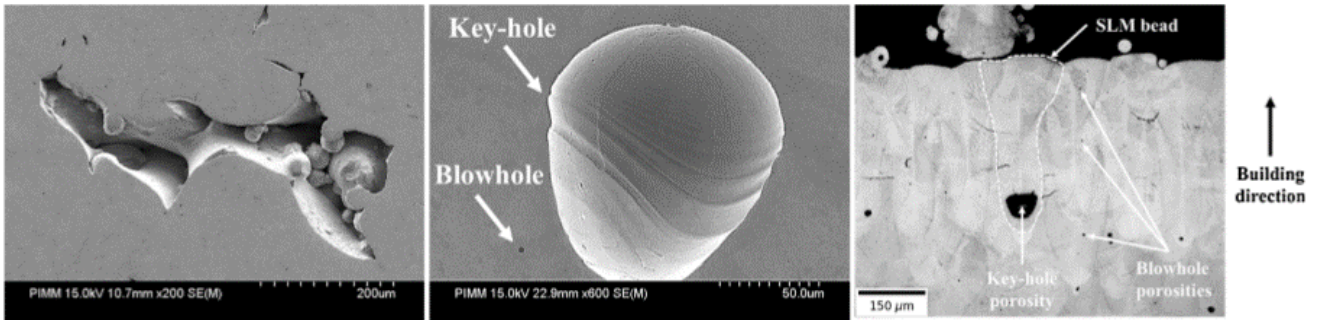


**Fig. 1.31.** Types of pores: LoF (a), blowhole (gas pore) (b), key-hole cavity (b) (c) [61].

### 1.4.2 Balling phenomenon

The term "balling" identifies a peculiar phenomenon of the L-PBF process characterized by the formation and subsequent solidification of spheroidal droplets above the pre-solidified layer due to the poor wettability between the liquid, which shrinks into a spherical shape, and the solid material. This phenomenon determines a high surface roughness (Figure 1.32) and the possible formation of voids in the bulk material, thus penalizing the tribological and mechanical qualities of the material [5].

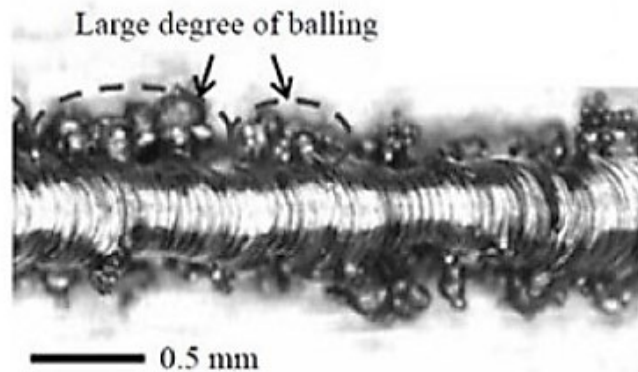


Fig. 1.32. Top view of a surface affected by balling phenomena along a single scan track [5].

To correctly analyze the balling phenomenon, the MP must be divided into two regions: a broader volume due to the melting of the powders and a smaller volume due to the re-melting of the substrate (Figure 1.33). As the volume of the MP's lower part increases, the balling phenomenon tends to decrease because the wetting angle is reduced (Figure 1.33(b)), avoiding the formation of liquid metal spheres near the scan track. On the contrary, a larger wetting angle at the solid-liquid interface due to a small volume of the lower part of the MP promotes the phenomenon of balling (Figure 1.33(a)) [3].

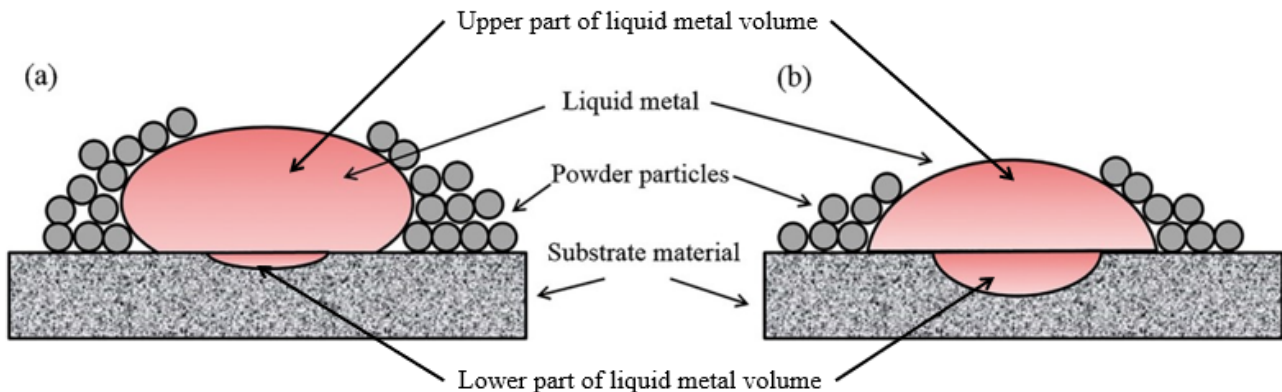
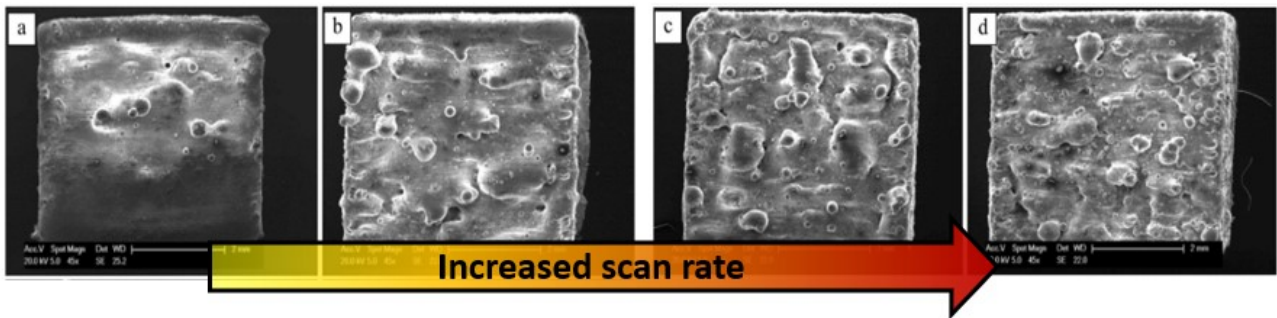


Fig. 1.33. Representation of the phenomenon of balling. Low wettability (a); high wettability (b). Adapted by [14].

The onset of the balling phenomenon generates a non-uniform layer deposition and, in the worst cases, damages the recoater due to the higher hardness of the particles and the worse surface quality of the layer [50]. In extremely reactive materials such as Al, the presence of an oxide film above the solidified material amplifies the balling phenomenon as it reduces the wettability of the liquid metal. Consequently, adequate control of the  $O_2$  level (generally less than 0.1%) allows an effective reduction of the balling [56].

Adequate laser power increases the energy density and reduces the balling phenomenon. The melting of a larger volume of the solid substrate below the deposited layer of powders leads to a consequent improvement of the wetting angle

between liquid metal and solid substrate and, therefore, a reduction in the formation of spherical surface particles. Furthermore, higher energy density corresponds to better viscosity and fluidity characteristics of the liquid metal [14]. Other techniques adopted to reduce the balling phenomenon consist in preheating the substrate, again to increase the wettability, and using a scan strategy characterized by a double scan of the single layer of powder to re-melt the spherical particles formed in the previous step. Another process parameter influencing the balling formation is the scan speed: Aboulkhair et al. [16] reported that high scan speed promotes unstable MP and the consequent formation of surface droplets (Figure 1.34).



**Fig. 1.34.** Effect of increasing scanning speed on the balling phenomenon from a minimum (a) to a maximum value (d). Adapted from [3].

### 1.4.3 Spattering phenomenon

Spattering is related to the thermodynamic, dynamic, and metallurgical instability of the MP induced by the laser beam/powder bed interaction and by the rapid melting and solidification of the material [50]. It consists of the ejection of small droplets of liquid metal from the MP due to the recoil pressure generated by the laser beam/powder bed interaction [3]. A high energy density ensures the re-melting of the previous layer and facilitates the metallurgical bonding between the layers and the melting of the powder bed. However, it can produce violent vaporization of the liquid metal and the recoil pressure on the MP. This phenomenon causes the deformation and sinking of the liquid surface and the collapse under the gravity force of the MP (Figure 1.35) [50].

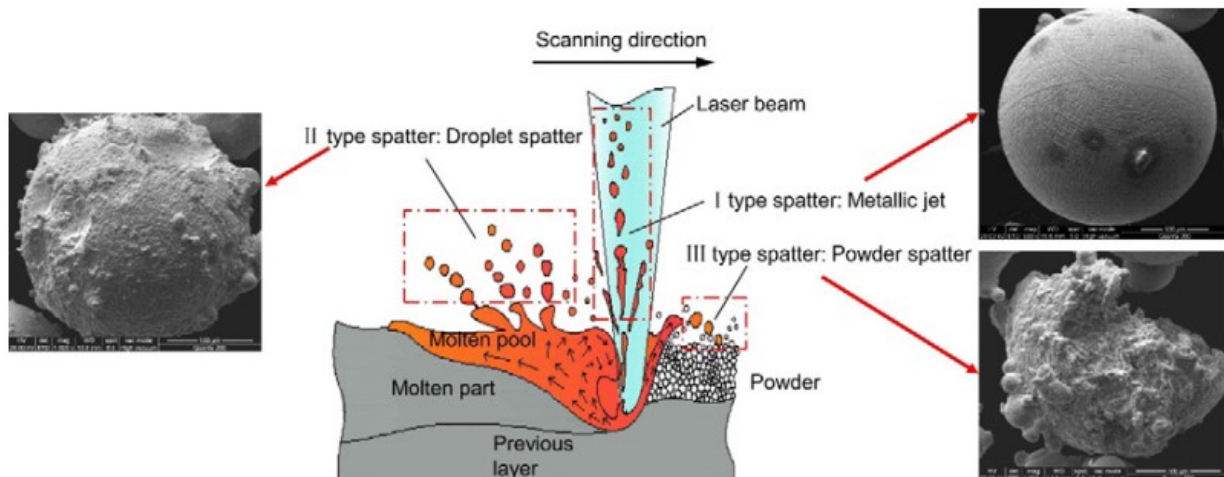


**Fig. 1.35.** Representative illustration of the spattering phenomenon and different types of spatters: (i) metallic jet, (ii) droplet spatter, (iii) powder spatter [62].

Three different types of spatter can be defined: (i) metallic jet associated with the extreme expansion of gases caused by the recoil pressure, which expels at high heights splashes coaxially to the laser beam, promoting spatter characterized by a smooth surface and excellent sphericity due to the highly rapid solidification; (ii) droplet spatter generated by the low viscosity of the liquid metal and the action of the recoil pressure that leads to the fracture in tiny drops of the liquid metal that comes out from the MP; (iii) powder spatter, i.e., non-melted powder ejected forward of the scan direction due to the accumulation of liquid metal in the front of the MP due to the intensity of the laser beam [62].

The droplets expelled from the MP oxidize in contact with the atmosphere, eventually settling on the powder bed. Defect formation occurs based on the position of the splashes on the powder bed; if they fall within an area affected by the scan track of a subsequent layer, given their large size, they are incorporated into the bulk material (Figure 1.36).

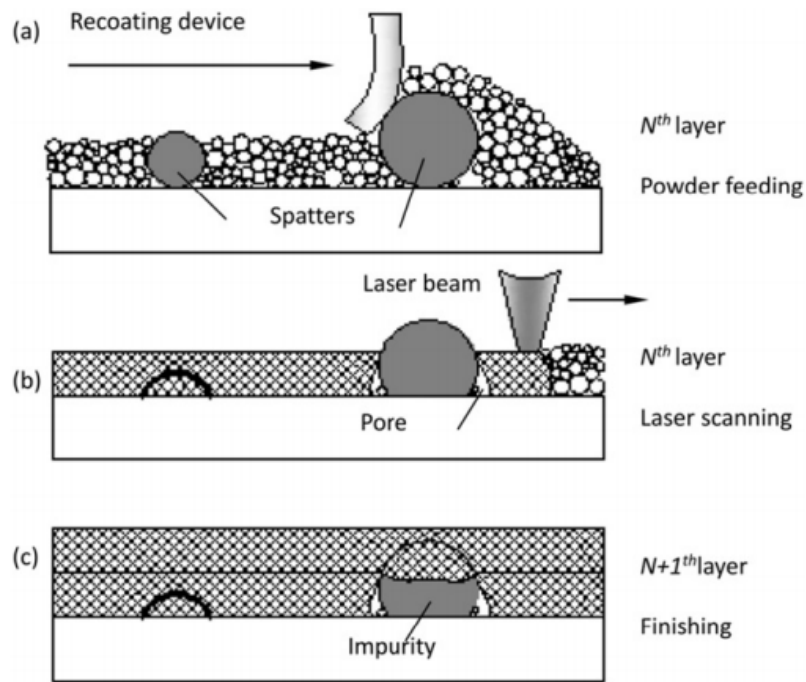


**Fig. 1.36.** The influence of spattering particles on powder recoating and internal defects of L-PBF-produced components [62].

The spatter formation determines the reduction of the mechanical properties of the L-PBF-produced parts due to voids inside the component, a low metallurgical interlayer bonding, and a worsening surface finish. Furthermore, the significant loss of low-melting elements, such as Mg, due to their lower vaporization temperature and higher volatility compared to other alloying elements, determines strong oxidation of the spatter formed in the printing of AlSi alloys caused by the high affinity of this element with  $O_2$ . The formation of oxidized spatter makes it even more challenging to re-melt them during the subsequent scanning phase (Figure 1.37).

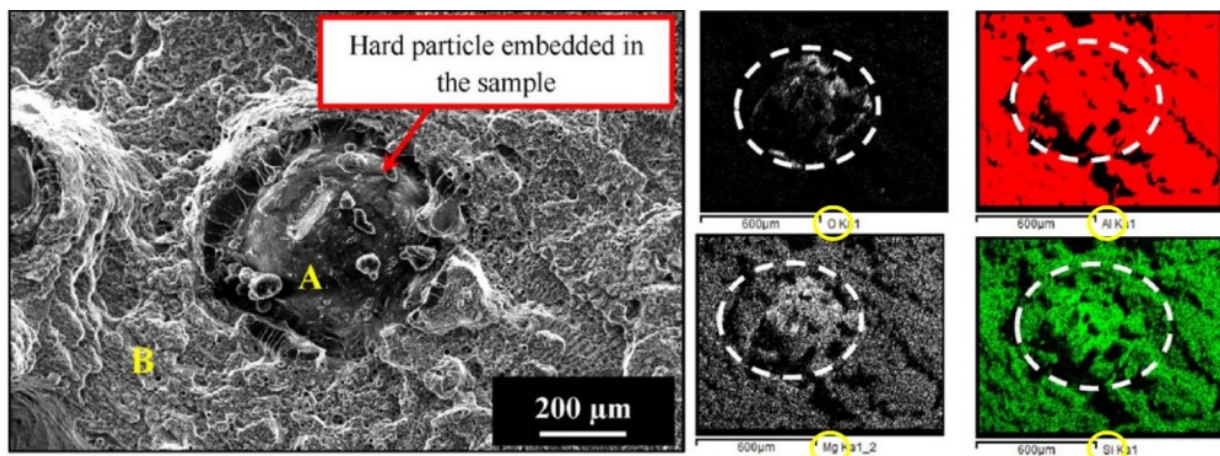


**Fig. 1.37.** The fracture surface of a component in L-PBF AlSi10Mg alloy. It has an integrated spatter formed during the printing and identified by EDS spectroscopy, which is rich in Si, Mg, and O (elements circled in yellow) [62].

As reported in [3] and [50], the spattering is evident as the scanning speed and energy density increase due to the higher turbulence and the recoil pressure on the MP. Furthermore, a suitable scanning strategy can avoid incorporating spattering in the following layers.

### 1.4.4 Oxide formation

The formation of oxides is present in almost all alloys produced with L-PBF technology. However, Al alloys are among those most subject to this phenomenon. The inclusions of Al oxide within the AlSi alloy components produced by L-PBF derive mainly from the partial oxidation of the powders and the volume of O<sub>2</sub> trapped inside the MP due to turbulent flow conditions. Despite using an inert atmosphere within the build chamber, up to O<sub>2</sub> level of 0.1 vol.%, it may still be present in the empty interstices inside the powder layer or as humidity (H<sub>2</sub>O). Al oxide in the bulk material is damaging as it promotes the phenomenon of balling and the formation of LoF, avoids the melting of the powders, and reduces the interlayer metallurgical bonding (Figure 1.38). All these factors lead to a decrease in the mechanical properties of the component [56].

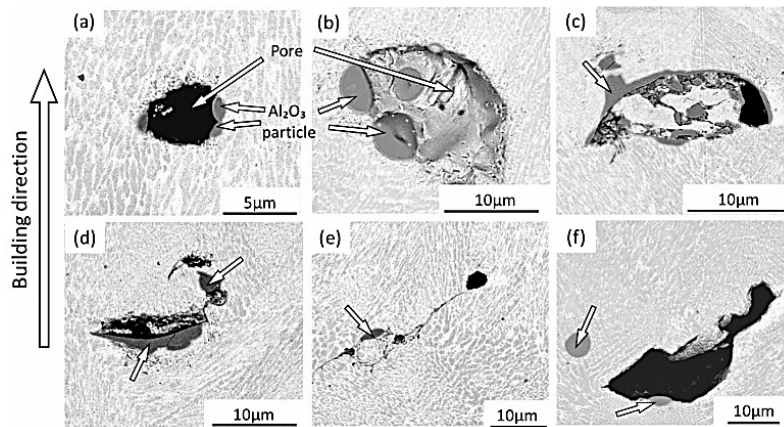


**Fig. 1.38.** Backscattered electron (BSE) images of porosity and oxide particles on polished cross-sections of as-built specimens. Most oxide particles are associated with pores and located at the pore boundary (a–d) or connected with a lap (e); some are present as isolated particles (f) [56].

The formation of oxide films along the MPBs reduces the wettability of the substrate and consequently promotes the formation of pores inside the material (Figures 1.39(a,b)). The surface tension gradient generated by the Marangoni effect leads to the oxide film breakage in the bottom region of the MP and its incorporation into the solidified material [3,12].

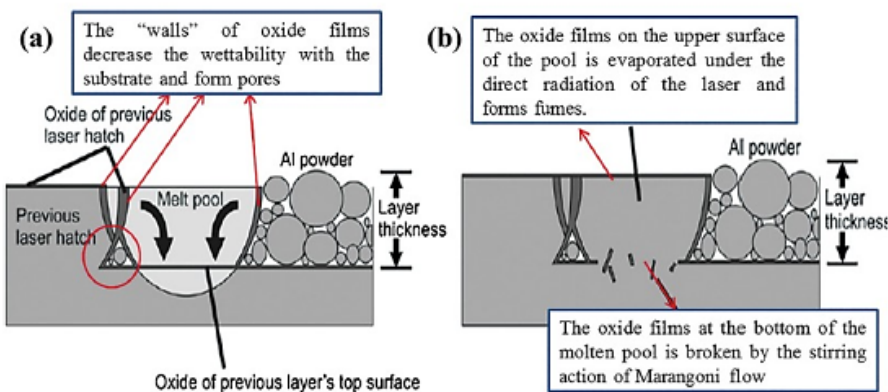


**Fig. 1.39.** Formation mechanism and morphology of oxide film [14].

The oxidation phenomenon in AlSi alloys produced by the L-PBF process is proportional to the O<sub>2</sub> level. Hence, reducing the O<sub>2</sub> content in the build chamber and using pre-drying powders reduce this problem. The humidity (H<sub>2</sub>O) present in the powders dissociates under the action of the heat source into H<sub>2</sub> (the primary source of gas pores in the material) and O<sub>2</sub> (the leading cause of oxide formation). The process parameters relating to the energy density must also be optimized to induce the vaporization of the oxide layer and produce a Marangoni effect capable of breaking the oxide film present in the lower part of the MP, evacuating it from the liquid metal.

### 1.4.5 Residual stress, crack, and delamination

The operating conditions of the L-PBF technology lead to significant residual stress: the laser beam melts only a localized volume of the powder bed, i.e. the MP. At the same time, the surrounding area is subject to a steep spatial thermal gradient (Figure 1.40(a)) and repeated heating and cooling cycles (Figure 1.40(b)) that determine a cyclic thermal expansion/contraction of the material [12]. In addition, high thermal conductivity, high coefficient of thermal expansion, and wide range of solidification temperatures further amplify this phenomenon [63].

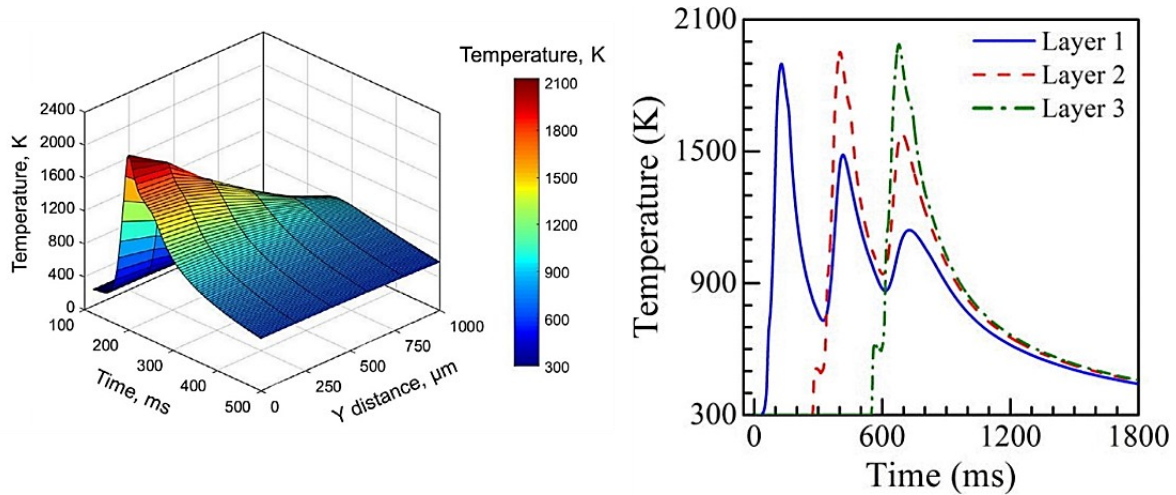


Fig. 1.40 Temperature gradient as a function of the distance from the center of the MP (Y) during the deposition of one layer (a); thermal cycles during the deposition of three layers (b) [5].

The uneven distribution of the inelastic deformations necessary to balance the force field generated by the cyclic plastic flow causes high residual stresses (RS). In particular, during the heating phase, the solidified layer that delimits the MP exerts compressive stress on the heated material, which tends to expand (Figure 1.41(a)). Subsequently, during the cooling phase, the volumetric shrinkage following the liquid metal solidification present in the MP induces tensile stress on the material delimited in the volume by the MPBs and the HAZ (Figure 1.41(b)) [44,64]. A complex RS field is formed inside the solidified alloy, which can add to the stress of the external load applied to it, amplifying both the effects on the material and causing the failure of the component at the end of the production process [4].

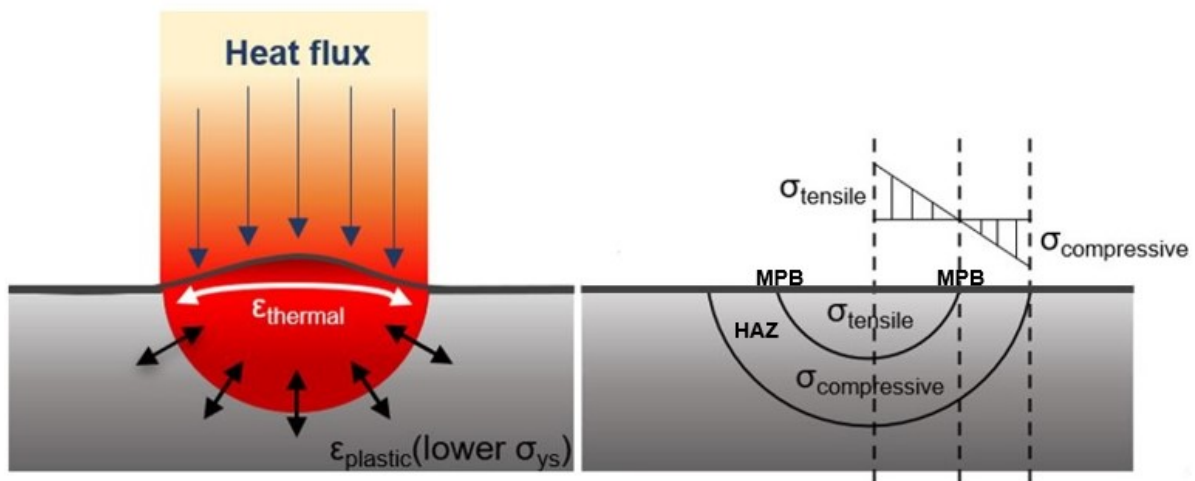
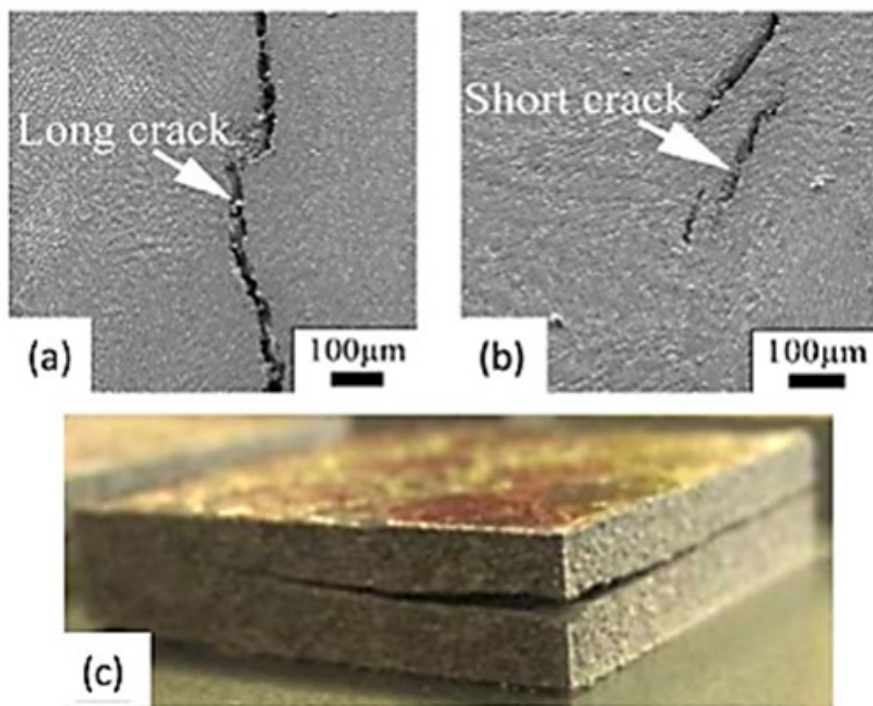


Fig. 1.41. RS field developed in the MP area during the L-PBF process. Compressive stress of the pre-solidified layers on the material directly exposed to the laser beam (a); Stress distribution at the end of the solidification process: tensile stress within the MP volume, compressive stress within the volume embedded into MPB and HAZ regions (b).

The RS can be divided into thermal stress and structural stress. The former is caused by an uneven distribution of heat which involves a different thermal expansion of the material and affects the areas surrounding the MP, while the latter is mainly due to phase transformations (liquid-to-solid) [65]. Optimizing the process conditions aims to reduce the thermal gradient and the effect of cyclic thermal on the material. In particular, it is necessary to limit the energy density and the scan speed to reduce the thermal stress and the cooling rate, respectively, and to adopt a practical scan strategy, such as counter-clockwise rotation of the scan vector by 67°, to relieve RS in-situ on each layer deposition. Furthermore, using a heated platform to control the temperature gradient represents a good solution [3,64]. Although the optimization of these parameters has drastically reduced the phenomena of deformation and cracking, the level of RS inside the components remains high [5], and heat treatments can be considered an excellent solution to reduce it, as will be described in the following sections [66,67].

The control of the process parameters is essential not only to reduce the RS and their effects on the mechanical properties of the component but also to avoid crack formation, distortion, and delamination phenomena during L-PBF printing (Figures 1.42(a,b)).



**Fig. 1.42.** Cracks formed in Al alloys during L-PBF process (a), (b); delamination phenomena (c) [5]

As for the formation of cracks, they can be classified into liquefaction and solidification cracks. For example, in the Al alloys, liquefaction cracks depend on the content of alloying elements present in the powder and, consequently, on the precipitation of the low-melting elements (Mg) that can occur in the HAZ and the overlapping area between successive layers [14]. Solidification cracks form at the interface between the eutectic-Si network and the  $\alpha$ -Al cell and are linked to both shrinkages due to solidification and thermal contraction. Alloys with a wide solidification temperature range, such as Al alloys, exhibit cracks of this type more frequently [5]. The alloy's chemical composition is modified by adding alloying elements such as Si to significantly reduce the solidification interval ( $\Delta T \sim 50$  °C) and, consequently, the RS (Figure 1.43).

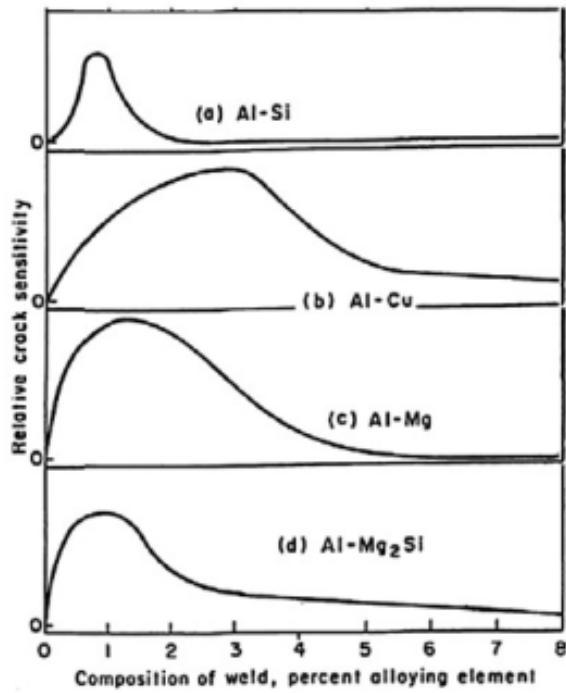


Fig. 1.43. Influence of alloying elements on crack formation in Al alloys [42]

The formation of cracks can be reduced through a correct distribution of the liquid phase during the printing process and a complete filling of the voids formed inside the material caused by the volume variations occurring during the solidification phase. This solution can be made possible by reducing the cooling rate and the thermal gradient during the printing process, as already described in the RS control [5].

Ultimately, the phenomenon of delamination (Figure 1.42(c)) consists of the complete separation of the successive layers due to the poor cohesion between them, which precludes the use of the component because it cannot be recovered in post-production [8].

### 1.4.6 Optimization of the L-PBF process parameters for operating window

The optimization of the process parameters is mainly aimed at obtaining a fully dense component and high mechanical properties. Bulk material density is a crucial indicator of the quality of parts manufactured by L-PBF: low density corresponds to low strength, ductility, and fatigue performance. At the same time, an ultrafine and homogeneous microstructure increases the mechanical properties of the material.

Fixed the powder features and the laser characteristics imposed by the machine specifications, the process parameters to be optimized are the energy density, directly proportional to the laser power, and the scan rate.

A helpful way to analyze the effects of process optimization on the part produced by L-PBF is to evaluate the graph of the laser power (P) versus the scan rate (V) at fixed process parameters. The correct operating window of an L-PBF machine is between two extreme conditions: the "Lack of fusion" zone at high scan speed and insufficient laser power and the "Keyhole porosities" zone at low scan speed and very high laser power. Gas porosities, as described above, are a type of defect typical of the L-PBF process, even in optimal conditions. However, the volume in the bulk material increases at low scanning speed and laser power due to the difficulty of the gas escaping from the MP [30]. Other operating limits are linked to the instability of the MP caused by the high laser power and scan speed, the consequent formation of "spattering" and "balling" phenomena, and an excessive loss of low melting alloy elements and volatile promoted by the high energy density corresponding to excessive laser power.

Therefore, the identification of the optimal scanning speed and laser power leads to the formation of MPs of adequate depth, amplitude, and duration, a low volume of defects, and an optimized microstructure that produces, obtaining, at the same time, an acceptable level of productivity (Figure 1.44).

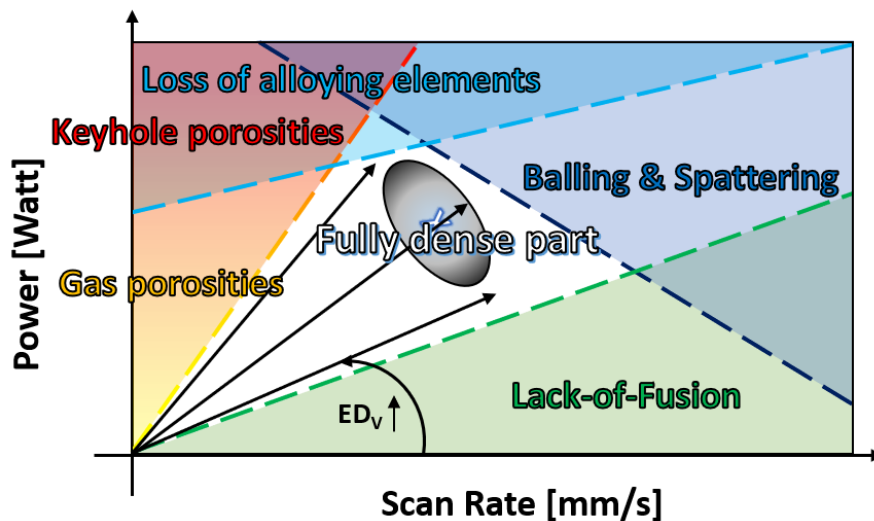
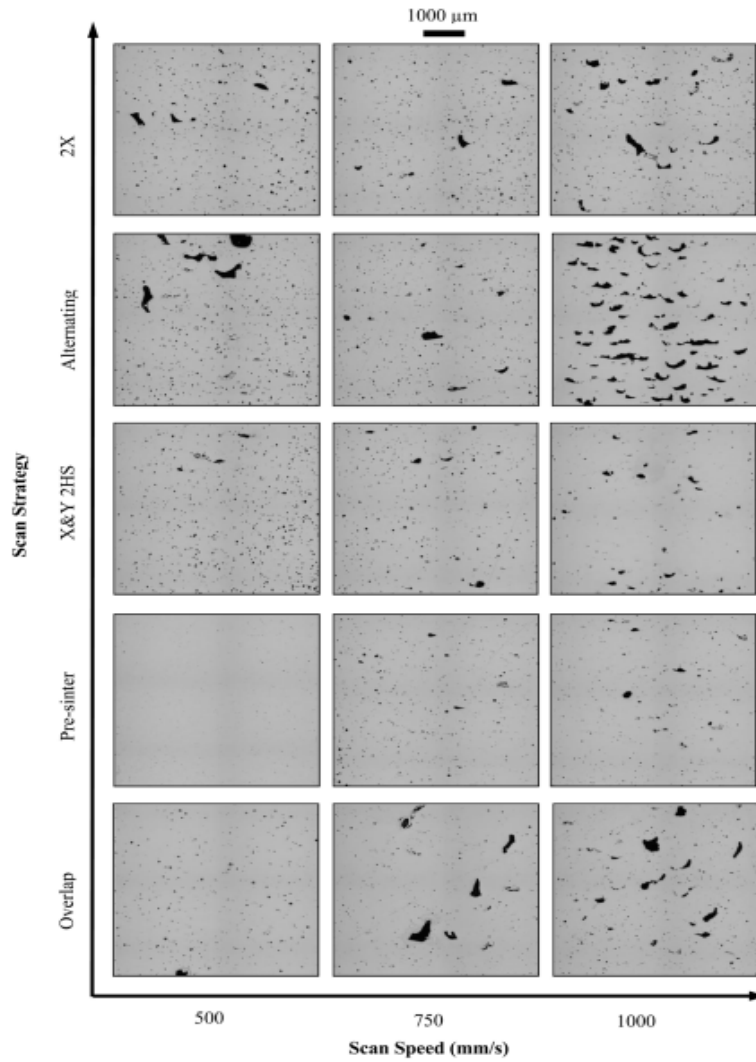


Fig. 1.44. Influence of process parameters on defect formation

Figure 1.44 assumes that energy density is governed only by laser power and scan speed. However, the analysis can be completed by introducing other process parameters, such as hatch distance. The hatch distance can be varied independently from the power and the scan speed, preserving the same energy density (Figure 1.45). However, choosing a hatch distance guarantees the right compromise between productivity and mechanical properties is essential. For example, with a higher laser power/scan speed ratio and operating conditions closer to the keyhole formation area, it is possible to keep the energy density low by increasing the hatch spacing. This optimization makes it possible to form a more extensive and deeper MP but a coarser microstructure due to the low energy density.







**Fig. 1.49** Porosity evolution in AlSi10Mg samples processed using different scan speeds and scan strategies: The “2X” denotes a unidirectional scan with a re-scan strategy. The “Alternating” strategy scans each layer in a direction that is rotated by 90° to its precursor. The “X&Y 2HS” indicates that each layer was scanned twice, having each scan perpendicular to the one before and with different hatch spacings. The “Pre-sinter” is carried out with half the power and then is followed by a second scan with full power. The “overlap” strategy was where each layer was scanned twice, with the second scan melting the overlap between every two adjacent MPs [16].

The term "hatch angle" means the angle between the scan direction of two consecutive layers, as shown in Figure 1.50 [43].

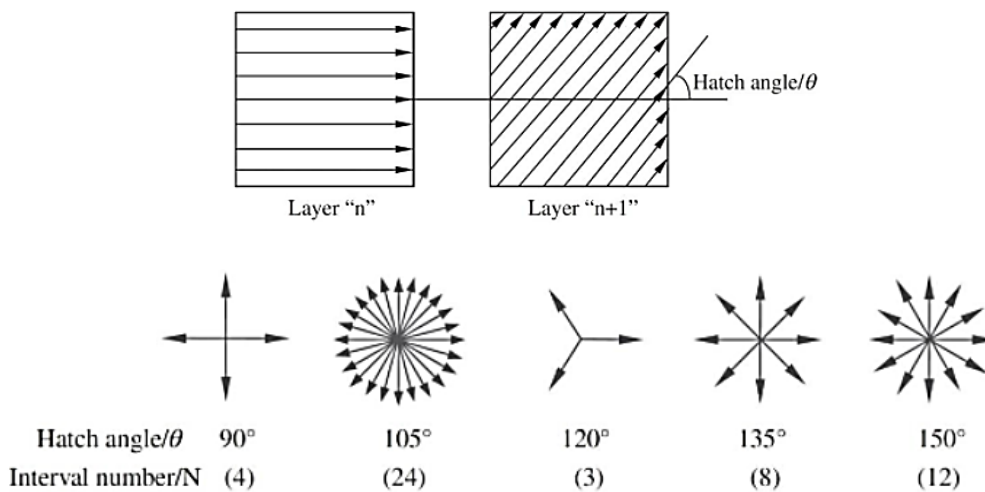
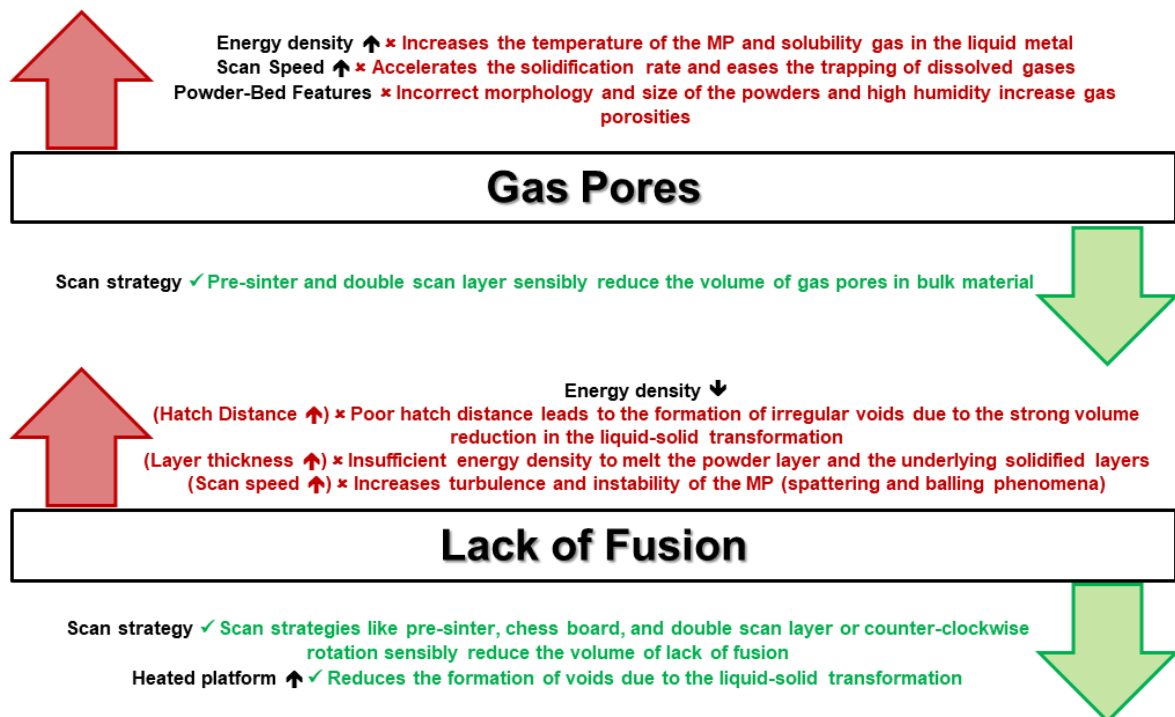


**Fig. 1.50** Rotations in lines in neighboring planes and different hatch angles [43]

Changing the hatch angle can affect the component's density, surface finish, and mechanical properties. As the rotation angle varies, the number N of layers varies, after which the direction of the scan vectors is the same as that of the first layer. For example, using a hatch angle equal to 90°, N = 4, and the limited intersection between the scan tracks induce anisotropy of the mechanical properties. Conversely, as described by Hanzl et al. [43], the use of rotation angles of 90°, 105°, 120°, 135°, and 150° results in higher mechanical performances of the material. In particular, the specimens made with a hatching angle of 105°, which maximizes the value of N, have higher mechanical performance than those obtained with different rotation angles. A relationship was therefore found between N and the material's mechanical properties. As the number of layers N increases, the mechanical properties increase. At the same time, the anisotropic characteristics decrease [70]. Currently, the most employed rotation angle is 67°, which maximizes the mechanical performance of the component, reducing the microstructural anisotropy, the number and volume of defects, and the surface roughness [71-73].

The scan strategy influences the volume and distribution of the defects between the bulk material and the contour, which is associated with the variation of the scan strategy and scan rate needed to ensure full-density bulk region, rapid build, good mechanical properties, and high surface quality [74]. Advantages are possible by reducing the scan rate and increasing the energy density. Laser power is usually unstable at the beginning and end of a scan track, and scan speed is gradually reduced, resulting in a relatively higher laser energy input and defect formation. The cross-hatching scan strategy can balance the entire laser energy input in the whole layers, effectively preventing defect accumulation.

The effect of the process parameters is resumed in Figure 1.51



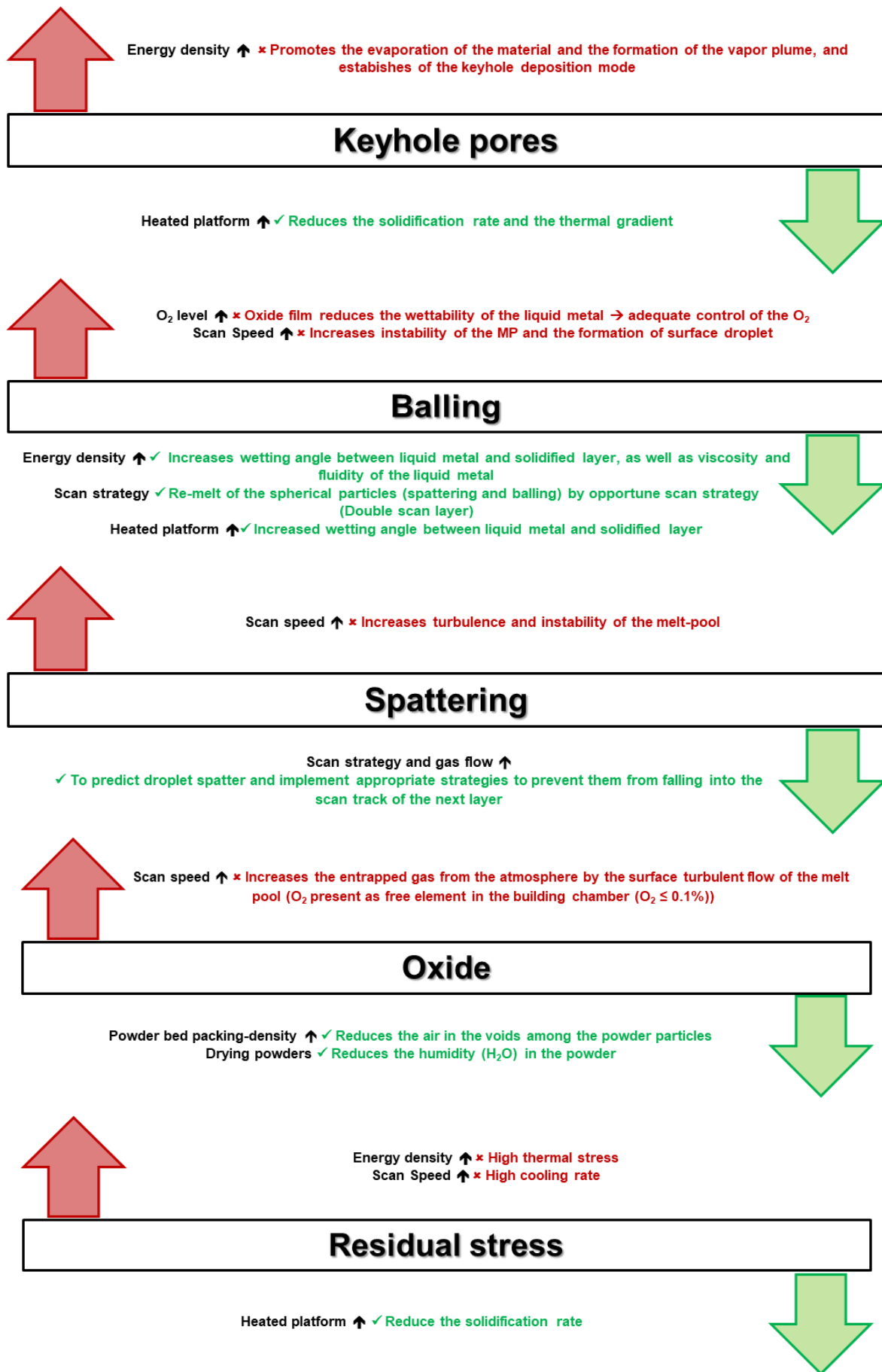


Fig. 1.51 Influence of process parameters on the defect formation in AlSi alloys.

## 1.5 L-PBF AlSi10Mg alloy: microstructure and mechanical properties

Al alloys are the second most used alloys in industry, surpassed only by steel. They are increasingly employed in automotive, aerospace, energy, and aircraft applications because of their recyclability, excellent strength-to-weight ratio, thermal and electrical conductivity, corrosion resistance, formability, and attractive appearance [12,14]. In particular, the AlSi10Mg alloy is currently the most investigated Al alloy to be processed by L-PBF (Figure 1.52) [7] due to its high AM feasibility [77] and positive response to heat treatment [78].

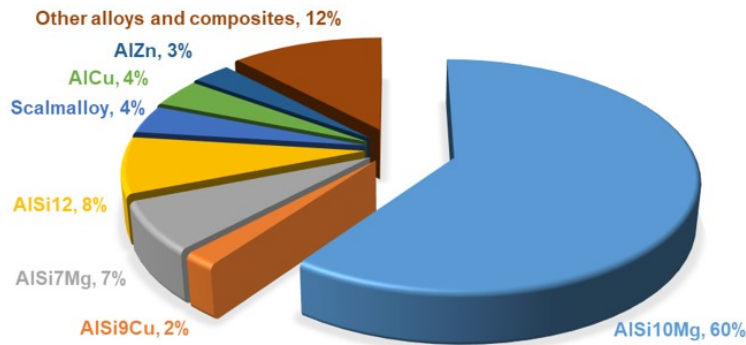


Fig. 1.52. Published papers regarding L-PBF of Al alloys in the last years (Scopus®, accessed on December 2022).

This alloy allows for complying with both mechanical (high strength-to-weight ratio) and production requirements (high fluidity and significant weldability) [4,5]. These advantageous characteristics are made possible thanks to its near-eutectic chemical composition compared to other Al cast alloys, such as the heat-resistant AlCu and AlZn alloys [75,76]. The high Si content, close to the eutectic point (Figure 1.53), reduces the solidification range and increases the laser absorption by the powder bed, thus improving the fluidity of the MP and simplifying the printing process [4]. The high Si content allows for overcoming the problems linked to the high laser reflectivity of pure Al, making it incompatible with the printing of components with the L-PBF process [3]. In addition, Mg content enables the precipitation of the precursor phases of  $Mg_2Si$ , occurring even during the L-PBF process and inducing a further strengthening of the Al-matrix [36].

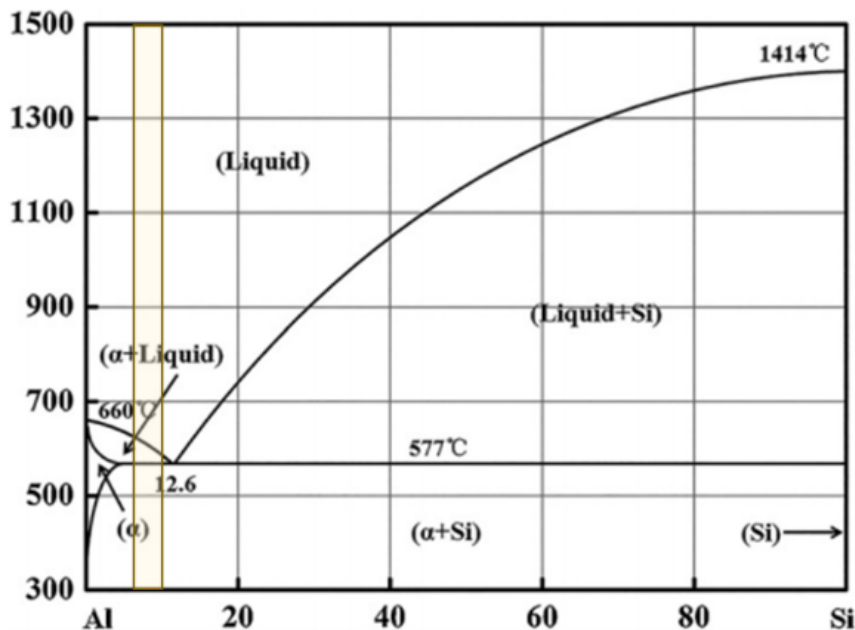


Fig. 1.53. AlSi phase diagram. The yellow area highlights a near-eutectic Si content between 9% and 11%.

These features make it ideal for producing lightweight and thin-walled parts and more complex-shaped components subjected to high mechanical loads. For these reasons, the L-PBF AlSi10Mg alloy is used in many high-tech industries, ensuring performance and lightness at a relatively low cost [3,12]. As can be appreciated in Table 1.3, which reports the nominal chemical composition of this alloy, it also has a limited content of impurity. The content of unwanted elements within the powders must be carefully checked before the process, given that pure Al is obtained from secondary processes and the extensive use of recycled powders. For example, a high Fe content can cause the formation of brittle Fe-rich intermetallics, such as  $\beta$ -Al<sub>5</sub>SiFe or other possible precipitates, during the L-PBF process [79]. The AlSi10Mg alloy is also characterized by a lower Mg and Cu content than other AlSiMg alloys used in automotive and aeronautics sectors, such as the A357 alloy. The low Mg content is due to this element's high volatility, low vaporization temperature, and high reactivity, which causes many problems related to the formation of defects, as will be discussed in the following chapters. Likewise, the Cu content is limited to promote the processability of the AlSi10Mg alloy by the L-PBF technique due to the higher reflectivity of the Cu powder compared to the Al ones and the higher sensitivity of the alloy to hot cracking and the formation of zones rich in brittle phases as the Cu content increases [3].

**Table 1.3.** Comparison between the nominal chemical compositions (wt%) of the AlSi10Mg alloy according to EN AC-43000 standard and A360 alloy according to Aluminum Association standard. The A360 alloy, a high-pressure die-cast Al alloy (HPDC), is the most compared alloy in the literature in terms of chemical composition to the AlSi10Mg alloy [77,80].

Designation	Element (wt%)										
	Al	Si	Mg	Fe	Cu	Mn	Ni	Pb	Sn	Ti	Zn
AlSi10Mg	Bal.	9 - 11	0.20 - 0.45	< 0.55	< 0.05	< 0.45	< 0.05	< 0.05	< 0.05	< 0.15	< 0.10
A360	Bal.	9 - 10	0.40 - 0.60	< 1.3	< 0.60	< 0.35	< 0.50	< 0.05	< 0.15	< 0.25	< 0.50

The peculiar solidification conditions of the L-PBF process and the chemical and physical properties of the AlSi10Mg alloy led to the formation of a hierarchical microstructure (Figure 1.54), which consists of four different structures [81]:

- Macrostructure, of the order of magnitude of  $10^{-1}$  to  $10^0$  mm, is characterized by macro-elements directly linked to the printing process, such as MPs and significant defects, i.e., LoF, cracking, and delamination phenomena;
- Mesostructure, of the order of magnitude of  $10^{-2}$  to  $10^{-1}$  mm, consists of microstructural characteristics attributable to the solidification process, such as grain size and type of grain (columnar or equiaxial, for example), without, however, distinguishing the elements making up the grain structure (see microstructure). Chemical micro-segregation areas and micro-defects such as porosity and inclusions are also part of this structure;
- Microstructure, of the order of magnitude of  $10^{-3}$  to  $10^{-2}$  mm, describes the complex grain solidification morphology (e.g., dendritic or cellular) and the size scale of the solidification microstructure (e.g., phase spacing, matrix cell size, and eutectic lamellar spacing);
- Nanostructure, of the order of magnitude of  $10^{-6}$  mm, is the level of the microstructural components of nanometric dimensions, observable only by scanning and transmission electron microscopy, therefore from the nanometric precipitates to the dislocations and single atoms;

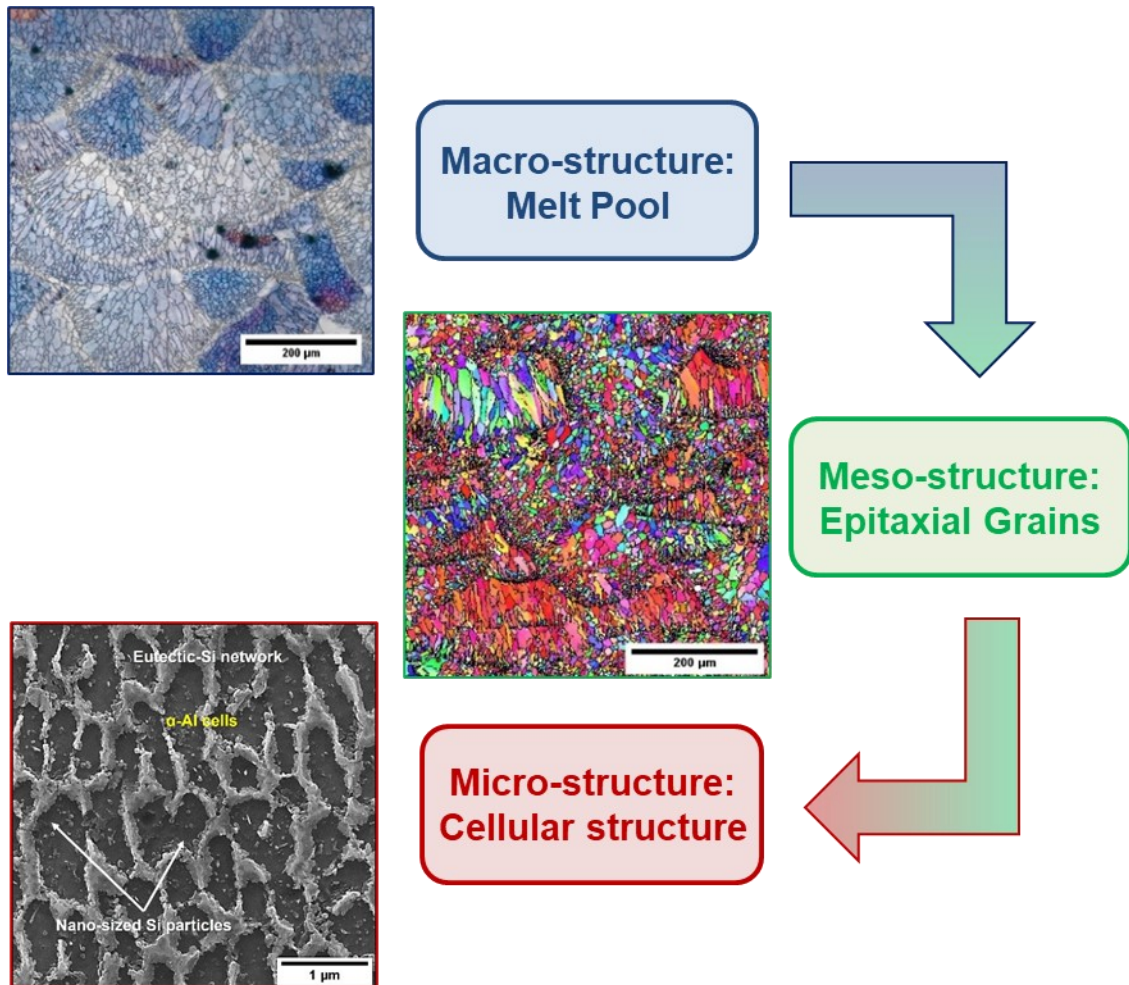


**Fig. 1.54.** Hierarchical microstructure in L-PBF-produced AlSi alloys: Macro-structure: Melt Pools; Meso-structure: columnar and equiaxed grains; Micro-structure: cellular microstructure; Nano-structure: strengthening phases

To better understand the solidification mechanisms and how they affect the microstructure characteristics and, consequently, the mechanical properties of the L-PBF AlSi10Mg alloy, it is first necessary to delve into the theory behind solidification and then apply it to the process involving solidification of MP during the L-PBF process.

## 1.5.1 Solidification theory

The microstructural evolution during the solidification process of the MP represents one of the most critical parameters to be evaluated to increase the performance of the L-PBF-produced components. Considering the AM technologies as an evolution of a currently consolidated technology such as the welding process, the latter can be used to explain its solidification mechanisms [4,12].

The unique process conditions of L-PBF technology compared to conventional processes lead to significant differences in solidification: the absence of a fine-grained cooling zone along the track boundaries, a typically curved Solid/Liquid (S/L) interface, and a preferential columnar zone formation influenced whose morphology is influenced by the speed of solidification front, which is controlled in turn by the scan speed of the heat source (Figure 1.55). The different process conditions can theoretically lead to the formation of a heterogeneous mesostructure in which the extension of the different solidification morphologies is regulated both by the extent of the constitutional undercooling to which the liquid metal is subjected and by the solidification conditions resulting from the chemical composition of the alloy and process parameters.

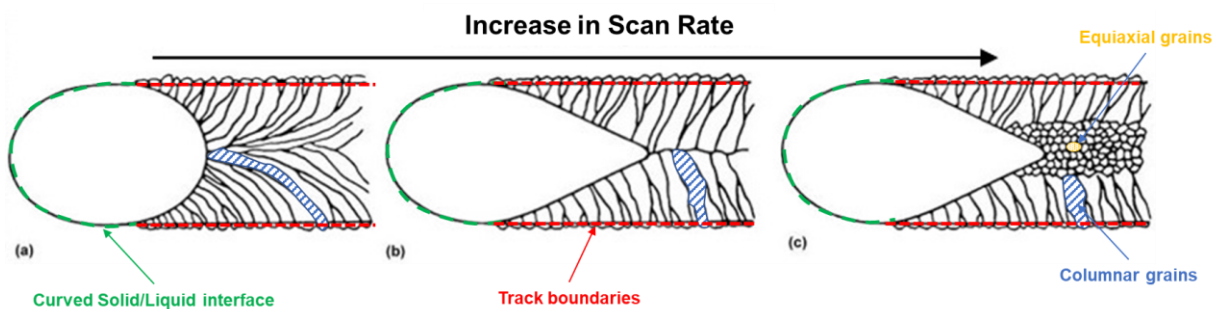


**Fig. 1.55.** Influence of the scan rate on the grain morphologies: columnar (a) (b) and columnar and equiaxed (c). Adapted from [82].

Furthermore, the solidification conditions influence not only the formation of the mesostructure but also the distribution of the alloying elements and the formation of the phase fractions during the solidification process, deeply modifying the microstructure morphology [83]. An example is shown in Figure 1.56, which represents the pattern of an extensive residual micro-segregation of alloying elements linked to the formation of a cellular microstructure that occurs in conditions of non-equilibrium solidification (as occurs in the L-PBF AlSi10Mg alloy). This microsegregation produces a relatively high fraction of intercellular eutectics and aggregated second phases according to the concepts of solute redistribution, which will be described in more detail below.

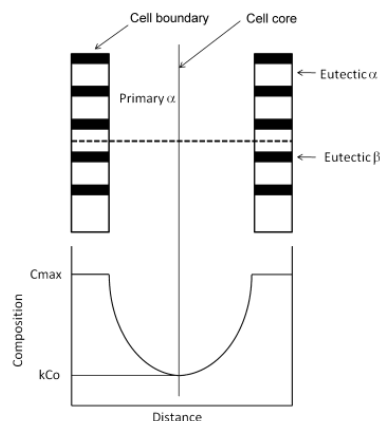


**Fig. 1.56.** Potential distribution of alloying elements and phase fractions formed by the L-PBF process. The example shown is for a simple eutectic system (AlSi alloy) which forms the primary  $\alpha$  phase and the intercellular  $\alpha/\beta$  eutectic under conditions of non-equilibrium solidification. The composition trend follows the product  $k^*C_0$ , through the primary and eutectic  $\alpha$  phase, where  $C_0$  is the nominal composition of the alloy and  $k$  is the equilibrium distribution coefficient, defined by the  $C_S/C_L$  ratio, where  $C_S$  and  $C_L$  are the solid and liquid compositions at the S/L interface [82].

The solidification process takes place into the MP and occurs, as in metal casting, in two different stages [81, 84]:

- **Nucleation:** formation of a new phase in liquid metal in the form of a cluster of atoms called embryo [85]. If it reaches a minimum critical size, the nucleus grows and coalesces. Otherwise, the nucleus re-dissolves into molten material. This process depends on thermodynamic factors;
- **Growth:** increase in the size of the initial stable nucleus and complete transformation from a liquid to a solid phase that depends on kinetic factors.

Both factors contribute to the microstructure formation and affect the bulk material's mechanical features. Starting from the nucleation process, it can occur through two different mechanisms which influence the subsequent growth of the microstructure [84]:

- **Homogeneous:** spontaneous process correlated to the continuous growth of clusters in the liquid metal, which exceed the critical size and form the first nuclei. Clusters of subcritical size are often called embryos and disappear if they lose atoms and do not reach the critical size.
- **Heterogeneous:** nucleation takes place on a substrate characterized by different chemical compositions, such as the walls of the mold or the particles attributable to insoluble impurities present in the melt added or not voluntarily to reduce the critical size of stable nuclei/embryos.

During a solidification process in non-equilibrium conditions, heterogeneous nucleation is promoted over homogeneous due to the lower energy contribution necessary to achieve it [84]. In fact, in thermochemistry, a transformation is spontaneous only if it occurs (Equation 1.4):

$$dG_{T,p} < 0 \quad (1.4)$$

i.e., the Gibbs free energy ( $G_{T,p}$ ) reduction to allow a phase transformation [86]. During the homogeneous nucleation of pure metal, the solid phase has lower free energy than the liquid phase (Figure 1.57), which is generally insufficient to guarantee stability to a small solid particle, allowing it to grow [87].

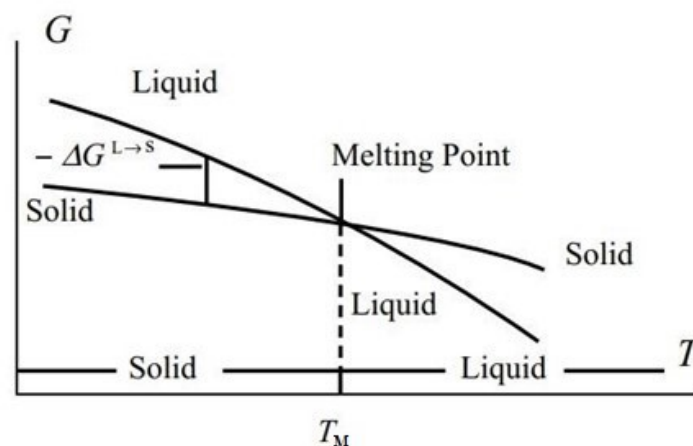


**Fig. 1.57.** Variation in molar Gibbs free energy of a metal, in solid or liquid condition, versus temperature. Homogeneous nucleation does not occur without the undercooling contribution for temperatures higher than the melting temperature ( $T_M$ ) [87].

The free energy associated with the L/S interface causes an increase in the global free energy system in the L-to-S transition, causing the initial embryo to dissolve and the solidification process to stop. A spherical nucleus in a condition of homogeneous nucleation can be considered to explain this concept (Figure 1.58).

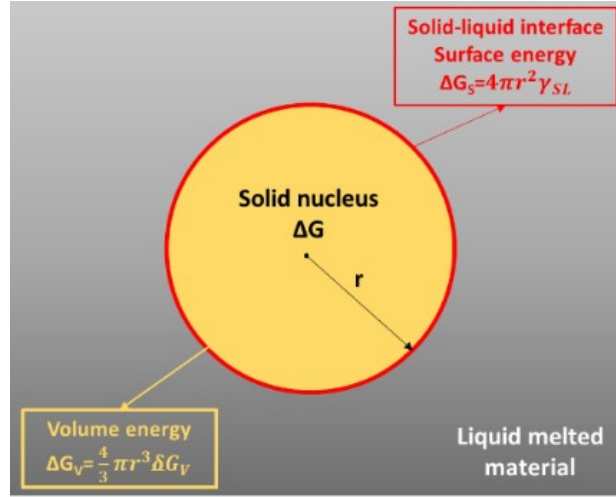


Fig. 1.58. Schematic homogeneous nucleation of a crystal in an undercooled liquid.

Thermodynamic factors drive nucleation, influencing its development. In particular, the change in free energy determines the conditions in which nucleation occurs (Equation 1.5):

$$\Delta G_{hom} = \Delta G_V + \Delta G_S = -V\delta G_V + A_{SL}\delta G_S \quad (1.5)$$

The overall change in free energy during solidification ( $\Delta G_{hom}$ ) required for homogeneous nucleation is described by Equation 1.5. In particular, it consists of two terms, the volumetric ( $\Delta G_V$ ) and superficial ( $\Delta G_S$ ) change of free energy referred to as the spherical nucleus, which depends on the volume ( $V$ ) and the contact area at the S/L interface ( $A_{SL}$ ). The first contribution is negative due to its correlation with the L-to-S phase transformation ( $\Delta G_S < \Delta G_L$ ) (Figure 1.58), while the second is positive because it represents the level of energy to be supplied to the nucleus to grow and overcome the surface tension on the S/L interface. Note that  $\Delta G_V = 0$  at the melting point, so there is no driving force for solidification at  $T=T_m$ . Therefore, undercooling is generally required to guide nucleation [81].

Undercooling is an essential factor in understanding nucleation and, consequently, the solidification process of an alloy. Focusing on a phase diagram, it describes the phase transformations in equilibrium conditions, which exist when the solidification rate is much lower than the diffusion rate, and, therefore, ideally, only for prolonged heating and cooling processes, such as to allow compliance with the conditions of thermodynamic equilibrium. In a conventional process, this usually does not happen; during the solidification process, the temperature and chemical composition at the S/L interface makes it impossible for solidification to take place in equilibrium conditions. Therefore, a liquid can solidify only in the presence of a specific contribution of undercooling, which reduces the liquid temperature below the melting temperature  $T_m$  [81]. In particular, undercooling ( $\Delta T$ ) consists of five contributions (Equation 1.6):

$$\Delta T = \Delta T_K + \Delta T_T + \Delta T_R + \Delta T_P + \Delta T_C \quad (1.6)$$

The individual factors present in Equation 1.6 are defined using complex thermodynamic concepts, of which a brief description will be provided below:

**Kinetic undercooling ( $\Delta T_K$ )** results from the difference in the atoms transported from the L to the S phase and vice versa through the solidification interface. For solidification to occur, more atoms ( $n$ ) must cross the solidification interface from L-to-S rather than in the other direction ( $(dn/dt)_{solid} > (dn/dt)_{melt}$ ). This condition occurs for a temperature ( $T^*$ ) at the interface S/L lower than the liquidus temperature ( $T_L$ ) value by an amount equal to  $\Delta T_K$ . In ideal conditions (pure metal, constant pressure, absence of thermal gradient in the liquid, and flat S/L interface), it represents the only contribution for undercooling, equal to 0.01 - 0.05 °C.

**Thermal undercooling ( $\Delta T_T$ )** considers the more significant amount of heat to be extracted from the liquid metal if the other undercooling contributions (e.g., kinetic, curvature, ...) are insufficient to start the nucleation process. Therefore, it simply considers the additional heat extraction at the S/L interface necessary for solidifying pure metal. It can be defined as (Equation 1.7):

$$\Delta T_T = T_L - T^* \quad (1.7)$$

**Curvature undercooling ( $\Delta T_R$ )** occurs in the early stages of solidification when a discrete liquid volume becomes solid, and the newly formed S/L interface produces an increase in the system's energy linked to the variation of the energy of the interface associated with volume reduction in the L-to-S phase transformation [81]. As the size of a particle decreases, its surface/volume ratio increases, and the contribution of the interface energy to the total free energy of the particle increases. This change generates a further contribution of undercooling proportional to the curvature of the solidification front, which is necessary for the solidification. Considering for simplicity a sphere of radius  $r$  (Figure 1.58), the curvature undercooling is defined as (Equation 1.8):

$$\Delta T_R = T_L - T_L^r = \Gamma K \quad (1.8)$$

Several factors are introduced:  $T_L^r$  is the equilibrium temperature for a sphere of radius  $r$ ,  $\Gamma$  represents the Gibbs-Thomson coefficient, while  $K$  is the curvature, equal to  $1/r$ .

**Pressure undercooling ( $\Delta T_P$ )** is caused by an increase in the pressure applied to the liquid,  $\Delta P$ , and can be defined as follows (Equation 1.9):

$$\Delta T_P = \frac{\Delta P + \Delta V}{\Delta S_F} \quad (1.9)$$

Where  $\Delta V$  is related to the change in volume, while  $\Delta S_F$  is the entropy for melting. For metals, the undercooling pressure is relatively small, of the order of  $10^{-2}$  K/atm, and therefore can be negligible in evaluating the overall undercooling.

**Constitutional (solutal) undercooling ( $\Delta T_C$ )** is the main contributor to the solidification of the alloys. During the solidification process, the low-melting temperature solute moves away from the solid, contributing to the general undercooling (Figure 1.59(a)) [81]. For a given interface temperature  $T^*$ , and in equilibrium conditions, the solute content in the solid,  $C_S$ , is smaller than that in the liquid,  $C_L$ . Therefore, it is possible to define both the equilibrium partition coefficient,  $k$ , equal to the ratio  $C_S/C_L$ , and the slope of the liquidus line,  $m_L$ , equal to  $dT_L/dC_L$ . The outbreak of the solute from the solid forms a boundary layer richer in solute at the S/L interface than in the bulk liquid, resulting in a significant reduction in the liquid's temperature in the solid's vicinity (Figure 1.59(b)). The heat flow from the liquid to the solid imposes a thermal gradient,  $G_T$ , through which it is possible to define the local temperature in the liquid metal. Ultimately, for a thermal gradient lower than the liquidus gradient (the tangent to  $T_L$  at the S/L interface),  $G_L$ , as shown in Figure 1.59(b), the temperature in the boundary layer will be lower than the liquidus equilibrium temperature, thus constituting a constitutional undercooled region. The amount of the local constitutional undercooling can be calculated as a function of the local composition (Equation 1.10):

$$\Delta T_C = T_L - T^* = -m_L(C_L^* - C_0) \quad (1.10)$$

Where  $C_L^*$  is the composition of the liquid at  $T_0$ ,  $C_0$  is the bulk composition of the alloy at the beginning of solidification.

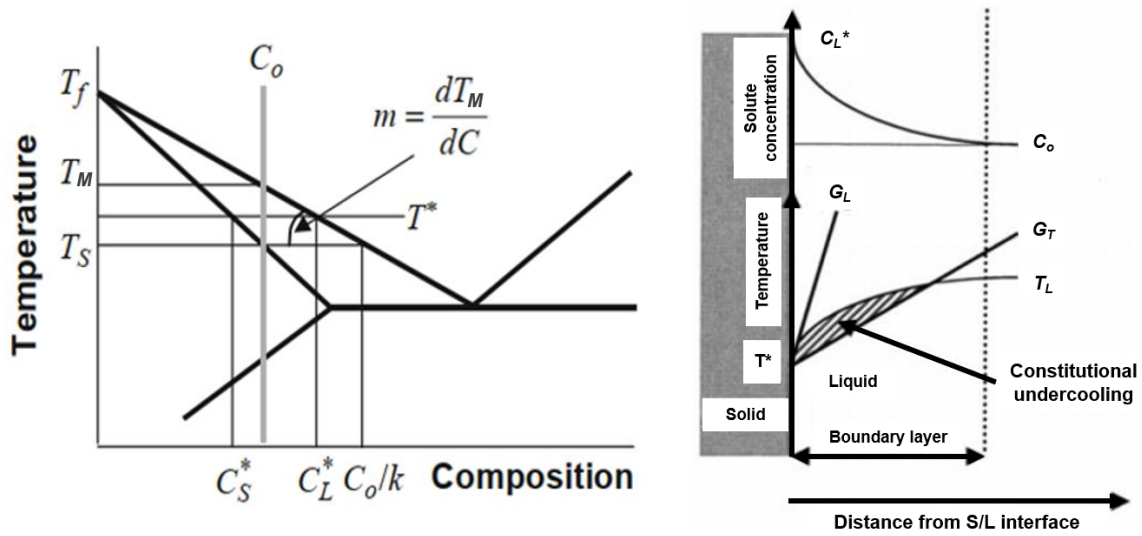
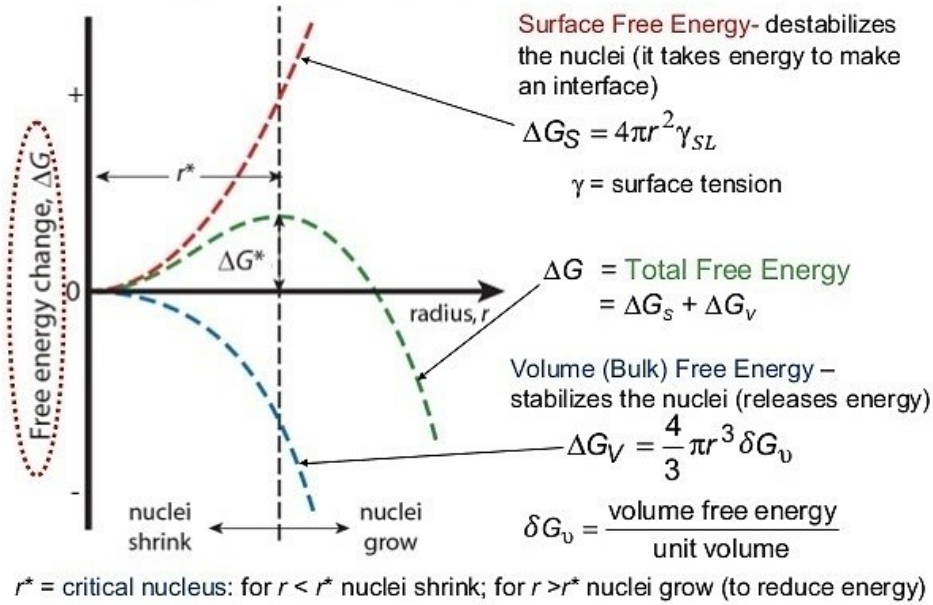


Fig. 1.59. The left corner of a phase diagram (a). A constitutional undercooled region (dashed area) is formed in the liquid next to the S/L interface due to the lower liquidus temperature produced by the higher solute content (b). Adapted from [81].

Undercooling is a fundamental condition for forming the first nuclei in the liquid. It increases the free energy variation per unit volume  $\delta G_V$  associated with the formation of the core, considering that the other contributions are the physical characteristics of the alloy (latent heat per unit volume ( $L_V$ )), thus allowing for reducing of the overall free energy of the system (Equation 1.11):

$$\Delta G_{hom} = -\frac{4}{3}\pi r^3 \frac{L_V \Delta T}{T_L} + 4\pi r^2 \gamma_{SL} \quad (1.11)$$

On the contrary, the surface free energy change per unit area ( $\delta G_S$ ), which is described by the nucleus radius ( $r$ ) and the surface tension per unit area ( $\gamma_{SL}$ ), is a positive contribution to the overall change of free energy and therefore counteracts the formation of the nucleus. The function described by Equation 1.11 reaches a maximum at the critical radius ( $r^*$ ), beyond which the reduction due to the term ( $-\frac{4}{3}\pi r^3 \frac{L_V \Delta T}{T_e}$ ) exceeds the increase associated with the term ( $4\pi r^2 \gamma_{SL}$ ). At  $r$  values smaller than  $r^*$ , the cubic dependence of  $\Delta G_V$  dominates over the quadratic dependence of  $\Delta G_S$  (Figure 1.60), and  $\Delta G_{Hom}$  achieves its maximum at the critical radius,  $r^*$ . When a thermal fluctuation causes an embryo to become more significant than  $r^*$ , the growth of the nucleus continues as a result of the decrease in the total free energy  $\Delta G_{hom}$ , with a value equal to the critical energy of activation  $\Delta G^*$  for an embryo of radius  $r^*$ . On the contrary, embryos characterized by a radius greater than  $r^*$  are stable and continue to grow to an overall reduction in the  $\Delta G_{hom}$  value. In particular, the  $\Delta G^*$  value is the maximum of the function  $\Delta G_{Hom}$ , and represents the activation energy associated with homogeneous nucleation, defined as the nucleation work [85].



**Fig. 1.60.** Variation in the terms  $\Delta G_V$ ,  $\Delta G_S$ , and  $\Delta G_{Hom}$  for an embryo as a function of its radius ( $r$ ) and undercooling ( $\Delta T$ ). Spherical embryo provides the minimum surface/volume ratio, optimizing the  $\Delta G_{Hom}$  value [88].

In summary, only by reaching a critical value ( $r^*$ ), a nucleus can grow, continuing the solidification process. The  $r^*$  value can be obtained by differentiating Equation 1.11 and then defining the maximum of the function expressed in Equation 1.12:

$$r^* = \frac{2\gamma_{SL}}{\Delta G_V} = 2\gamma_{SL} \frac{T_m}{L_V \Delta T} \quad (1.12)$$

By substituting Equation 1.12 in Equation 1.11 it is possible to obtain Equation 1.13:

$$\Delta G^* = \frac{16\pi\gamma_{SL}^3}{3(\Delta G_V)^3} = \frac{16\pi}{3} \gamma_{SL}^3 \left(\frac{T_m}{L_V \Delta T}\right)^2 \quad (1.13)$$

which represents the system's free energy change corresponding to the  $r^*$  value. From Equation 1.13,  $\Delta G^*$  tends to infinity when  $\Delta T = 0$ , indicating that nucleation cannot occur without a specific undercooling value. In particular, the more significant the undercooling, the greater the variation in the volume of free energy that leads (Equation 1.11) compared to the interfacial energy term, thus reducing the  $\Delta G_{hom}$  value. Consequently, both values,  $r^*$  and  $\Delta G^*$ , decrease as undercooling increases [89]. Random temperature fluctuations in the liquid metal capable of inducing the necessary conditions for forming crystals with a radius more significant than the critical radius  $r^*$  are very unlikely. This condition occurs because nucleation is tricky in the absence or at negligible values of undercooling [84]. Figure 1.61 shows that the solidification of a pure metal through homogeneous nucleation occurs in the early stages much below the  $T_M$  temperature. Following the L-to-S transformation, the temperature increase is proportional to the  $L_V$  value up to the  $T_M$  value.

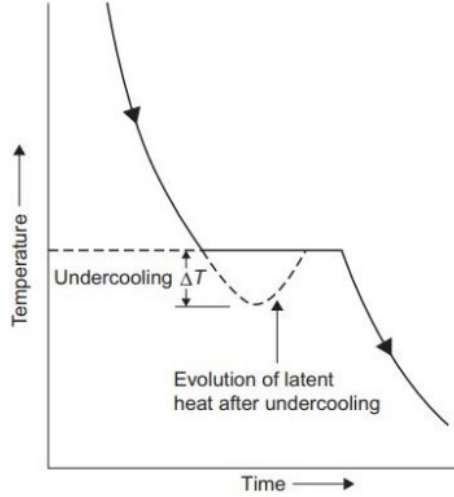


**Fig. 1.61.** The cooling curve for a pure metal shows possible undercooling [85].

Heterogeneous nucleation occurs in the presence of small contaminating particles in the liquid metal, oxides on the molten surface, or in the presence of all those conditions capable of initiating nucleation with a minimum undercooling [84]. As described below, epitaxial solidification represents particular heterogeneous nucleation caused by the interaction between a liquid and a solid substrate characterized by the same chemical composition [38].

During solidification, the system (Figure 1.62) influences the shapes of the nucleation germ according to the equilibrium conditions of the interfacial surface tension in the different areas ( $\gamma_{ML}$ : surface tension per unit area at metal/liquid substrate interface,  $\gamma_{SM}$ : surface tension per unit area at solid nucleus/metal substrate interface,  $\gamma_{SL}$ : surface tension per unit area at solid nucleus/liquid interface). Therefore, for heterogeneous nucleation, the overall variation of free energy can also be defined as (Equation 1.14):

$$\Delta G_{Het} = -V\delta G_V + \Delta G_s = -V\delta G_V + A_{SL}\gamma_{SL} + A_{SM}\gamma_{SM} - A_{SM}\gamma_{ML} \quad (1.14)$$

In Equation 1.14,  $A_{SM}$  represents the contact area substrate/liquid metal; consequently, the term  $A_{SM}\gamma_{SM}$  is the increase in the overall free energy resulting from the formation of the solid nucleus/liquid metal interface, while the term  $A_{SM}\gamma_{ML}$  is the decrease in overall free energy associated with eliminating some of the substrate/liquid metal interface due to the formation of the nucleus [82]. Remark that the interfacial energy between two solids is typically lower than that between a solid and a liquid, the term  $A_{SM}(\gamma_{SM} - \gamma_{ML})$  in Equation 1.14 is rightly negative and implies a value of  $\Delta G_{Het}$  less than  $\Delta G_{hom}$ .

The four factors expressed in Equation 1.14 depend on the shape of the nucleus and, therefore, in heterogeneous nucleation, on the wetting angle  $\varphi$  (Figure 1.62(a)), which thus plays a fundamental role in the solidification process. The value is determined by the relative values of the surface energies and, at equilibrium conditions, it is given by the force balance in the horizontal direction according to the Equations 1.15 and 1.16:

$$\gamma_{ML} = \gamma_{SM} + \gamma_{SL} \cos \varphi \quad (1.15)$$

$$\varphi = \cos^{-1}\left(\frac{\gamma_{ML} - \gamma_{SM}}{\gamma_{SL}}\right) \quad (1.16)$$

From Equation 1.16 it is clear that the  $\varphi$  value is governed by the relative values of the surface energies. Then, assuming a spherical cap-like nucleus (Figure 1.62(a)), each contribution in Equation 1.15 can be expressed as a function of the wetting angle (Equations 1.17, 1.18, and 1.19):

$$A_{SL} = 2\pi r^2(1 - \cos \varphi) \quad (1.17)$$

$$A_{SM} = \pi r^2 \sin^2 \varphi \quad (1.18)$$

$$V = \pi r^3(2 + \cos \varphi) \frac{(1 - \cos \varphi)^2}{3} \quad (1.19)$$

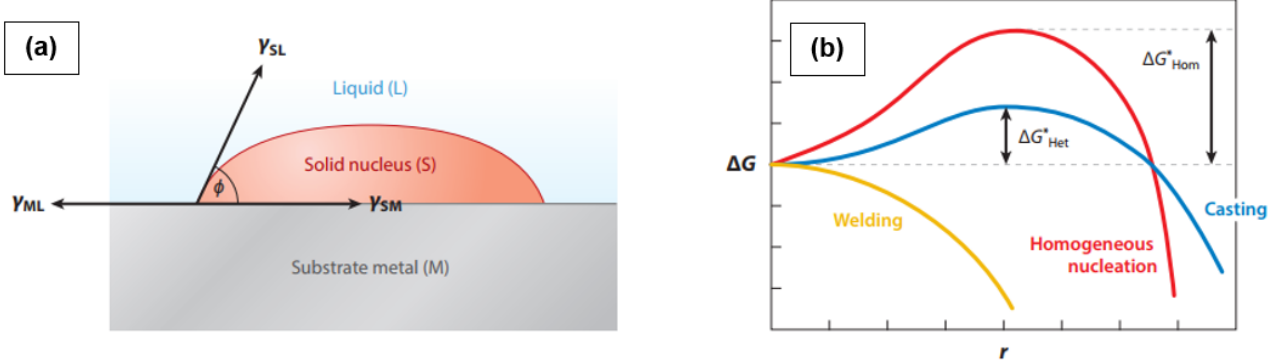


**Fig. 1.62.** Scheme of a solid nucleus in contact with substrate metal and liquid (a). Schematic of free energy change associated with heterogeneous nucleation in casting and welding along with homogeneous nucleation (b) [38].

The formation of a solid spherical-cap nucleus with a defined radius of curvature ( $r$ ) is linked to a change in free energy equal to (Equation 1.20):

$$\Delta G_{Het} = S(\varphi) \left[ -\frac{4}{3} \pi r^3 \frac{L_V \Delta T}{T_m} + 4\pi r^2 \gamma_{SL} \right] \quad (1.20)$$

Where  $S(\varphi)$  is the form factor expressible as (Equation 1.21):

$$S(\varphi) = (2 + \cos \varphi) \frac{(1 - \cos \varphi)^2}{4} \quad (1.21)$$

Note that for  $0^\circ < \varphi < 180^\circ$ , the shape factor changes proportionally as  $0 < S(\varphi) < 1$ , underlining again as  $\Delta G_{Het} < \Delta G_{Hom}$  (Figure 1.62(b)). Low values of  $\varphi$  indicate that the interfacial energy of the solid nucleus/metal substrate is low, i.e., a high wettability of the substrate, and leads to low values of  $S(\varphi)$  and small values of  $\Delta G_{Het}$ . Since the form factor depends on the value of  $\varphi$ , the energy required for heterogeneous nucleation is lower than the homogeneous one. When  $\varphi = 180^\circ$ , no substrate wetting occurs, and the nucleation takes place only in homogeneous mode ( $S(\varphi) = 1$ ) without reduction of  $\Delta G_{Het}^*$  (Figure 1.62(b)); instead, when  $\varphi \rightarrow 0^\circ$ , the system tends to a complete wetting and heterogeneous nucleation occurs (Figure 1.63), leading to a lower nucleation work [85].

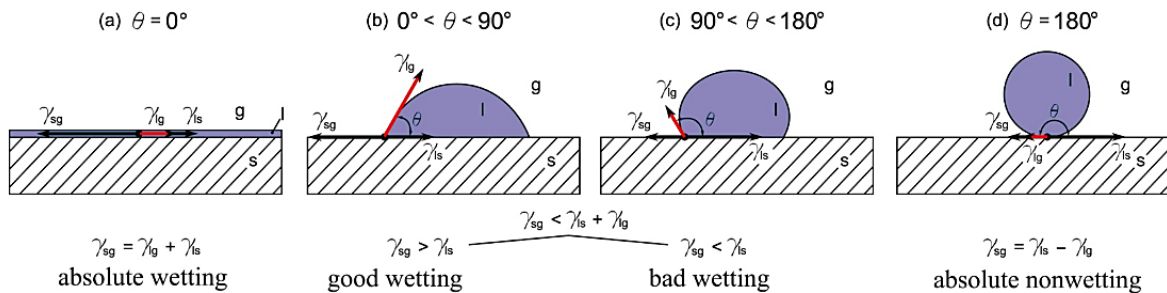


**Fig. 1.63.** Dependence of the surface wettability on the contact angle  $\theta$  [90]

It is essential to point out that similar chemical compositions and perfect crystallographic correspondence characterize the substrate and the liquid metal inside the MP process. Hence, in this case, the value of  $\gamma_{SM}$  becomes negligible, while the contributions  $\gamma_{ML}$  and  $\gamma_{SL}$  are approximately the same. This consideration leads to the following conditions (Equations 1.22 and 1.23):

$$\varphi = \cos^{-1} \left( \frac{\gamma_{ML} - \gamma_{SM}}{\gamma_{SL}} \right) = 0 \quad (1.22)$$

$$S(\varphi = 0) = 0 \quad (1.23)$$

As seen above, the formation of a solid nucleus through heterogeneous nucleation is possible only if the radius of curvature is more significant than a critical value  $r^*$ , to which a nucleation work  $\Delta G^*_{Het}$  corresponds to Equation 1.24:

$$\Delta G^*_{Het} = S(\varphi) \frac{16\pi}{3} \gamma_{SL}^3 \left( \frac{T_m}{L_v \Delta T} \right)^2 \quad (1.24)$$

Therefore, in the solidification conditions of the L-PBF process, the energy barrier at the S/L interface is infinitely smaller than that of conventional casting processes (Figure 1.62(b)) (the  $\varphi$  value almost always tends to zero), as occurs in the welding process, thus promoting the epitaxial solidification process.

## 1.5.2 Hierarchical structure induced by rapid solidification

The L-PBF technology has numerous process parameters involved in producing the final component, such as scanning speed, heat source (spot size, power, ...), powder-bed features, layer thickness, scan strategy, etc., which profoundly affect part integrity [92]. In particular, the solidification process depends on three critical variables: temperature gradient  $G$ , solidification rate  $R$ , and undercooling  $\Delta T$ . In particular, considering the term  $\Delta T$  expressed in Equation 1.6, the constitutional contribution  $\Delta T_c$  assumes a predominant role in the L-PBF process to understand not only the morphology of the solidification structure, i.e., planar, cellular, columnar, or equiaxed, but also the conditions in which the substructure of the AlSi10Mg alloy solidifies [82]. The solidification rate ( $R$ ) is determined by the scanning speed ( $V$ ) of the heat source and the shape of the MP, while the cooling rate ( $G \cdot R$ ) and temperature gradient ( $G$ ) are described primarily by the energy density ( $ED_V$ ). Three-dimensional distributions characterize the temperature gradient  $G$  and the solidification rate  $R$  as a function of position and time. The first follows the non-linear spatial temperature distribution, oriented in the opposite direction and perpendicular to the direction of the heat flow (Figure 1.64), while the second depends on the change in growth direction between the S/L interface within the MP and the laser source direction.

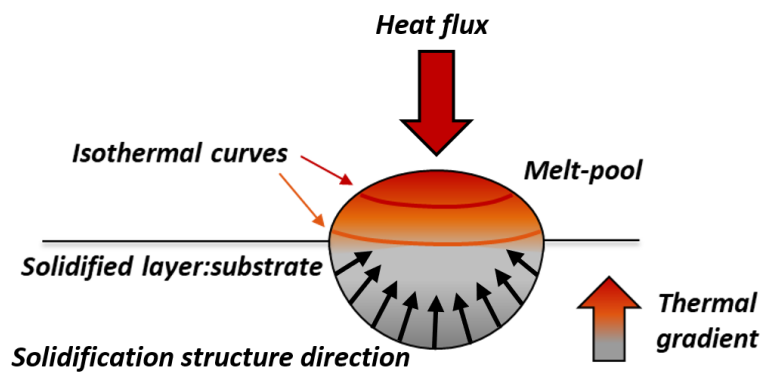


Fig. 1.64. Direction of the temperature gradient  $G$  and the solidification rate  $V$  in a single scan processed by L-PBF technology.

In the production of a real component, the evaluation of the trend of the  $G$  and  $V$  values becomes extremely more complex than a single scan track. The cross-weaving of the MPs, the continuous heating and cooling cycles, and the structure's consolidation make prediction difficult (Figure 1.65) [77].

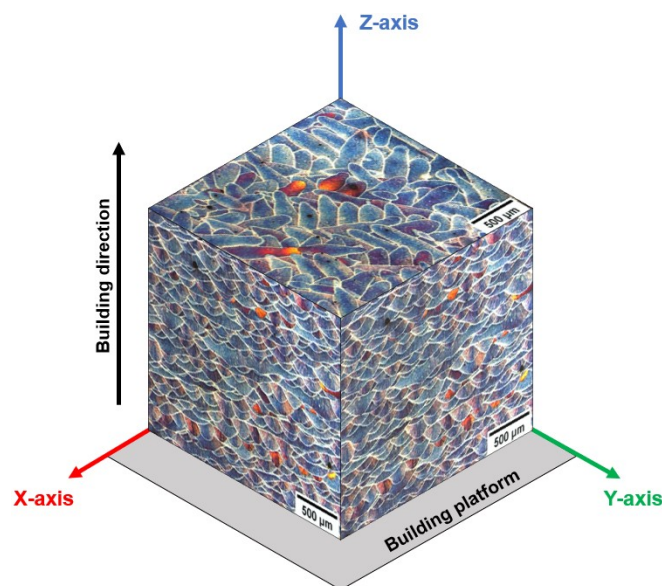
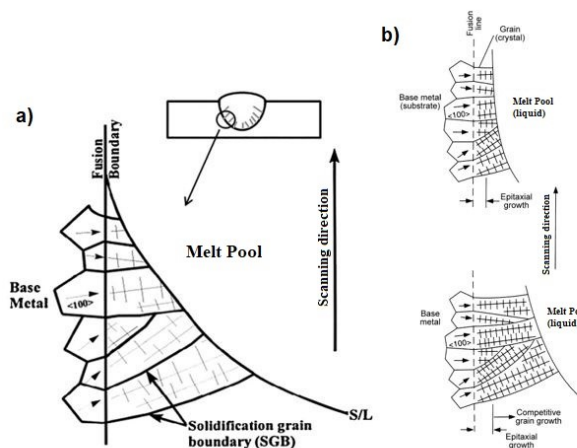


Fig. 1.65. Three-dimensional macrostructure of the as-built L-PBF AlSi10Mg alloy.

As previously introduced, the solidification process in L-PBF technology is based on the epitaxial grain growth starting from the substrate at the MPB (Figure 1.66). The grain growth occurs during solidification from previously solidified layers and ultimately determines the crystallographic nature of the L-PBF structure through a partial or complete fusion of the previously formed underlying layer. The penetration of the heat flow re-melts the previous layers, consolidating the part, removing surface contaminants, breaking down the oxide films, and providing a clean S/L interface at the atomic level [38]. In this process, the favorable crystalline orientation determines whether or not the grains grow in the epitaxial process, making it a competitive growth process. In particular, it is controlled by two main factors:

- **Heat flow:** the grain growth orientation is antiparallel to the maximum direction for heat extraction. This phenomenon derives from the transportation of the latent heat of solidification along the temperature gradient in the colder base metal. Along the direction perpendicular to the S/L interface, the temperature gradient is higher; consequently, the resulting heat flow will be higher. Hence, the grain growth direction will tend to be perpendicular to the S/L interface;
- **Easy-growth crystallographic directions:** the preferred crystallographic directions for solidification are along the  $\langle 100 \rangle$  directions for face-centered and body-centered cubic materials [5]. It is related to the thermal stability phenomena of the crystallographic planes at the S/L interface.



**Fig. 1.66.** Epitaxial solidification and competitive growth in the MP zone. Schematic illustrations of the competitive grain growth in the L-PBF process: initial step near the melting line (a); successive growth of the favorably oriented grains (b). Adapted from [14,38]

These solidification conditions induce competitive growth in which the favorably oriented growth grains will be characterized by an easy growth direction aligned to a normal direction at the S/L interface compared to grains whose growth is instead inhibited. In the L-PBF process, the shape of the MP formed during the process has a curved S/L interface constantly in motion as it follows the heat source, thereby heavily influencing the grain orientation. (Figure 1.66(b)) [38]. The epitaxial grains along the MPB may initially be oriented in a direction favorable to growth, but their direction may become unfavorable due to the movement of the laser source and the change in the position of the curved S/L interface. Consequently, the grains mentioned above can be hampered by favorably oriented grains following the movement of the S/L interface along the scanning direction, thus inhibiting their growth. In this case, the columnar structures most aligned with the temperature gradient outweigh the slower-growing misaligned structures (Figure 1.67). This process is defined as “competitive grain growth.”

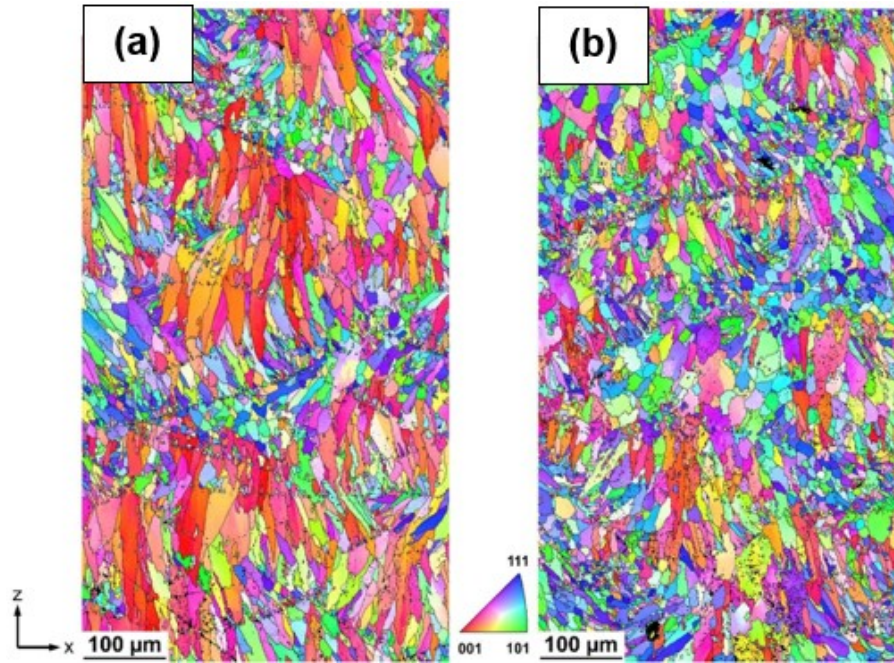


**Fig. 1.67.** EBSD IPF images along the building direction of two different samples characterized by two different printing orientations, vertical (a) and horizontal (b), to the building platform. It is visible the competitive growth of the epitaxial grains [92]

The growth rate  $R$  depends on the heat-source scan speed (Figure 1.68). This relationship can be expressed in terms of the angles  $\alpha$  and  $\beta$ , which represent the angle between the scan direction and the normal to the solid/liquid interface and the angle between the scan direction and preferential growth direction, respectively (Table 1.4). In polycrystalline alloys, the crystallographic growth during solidification occurs along with preferential directions according to the maximum heat flow direction at the solid/liquid interface, dependent on the local curvature of the MPB (Figure 1.68).

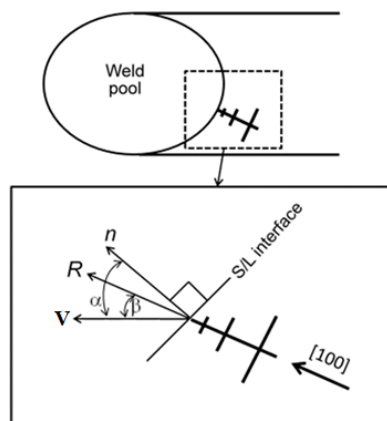


**Fig. 1.68.** Relation between the heat-source scan speed ( $V$ ) and growth rate ( $R$ ) [82].

**Table 1.4.** Easy growth directions for materials with various crystal structures [5].

Crystal structure	Easy-growth direction	Examples
Face-centered-cubic (fcc)	$\langle 100 \rangle$	Aluminum alloys, austenitic stainless steels
Body-centered-cubic (bcc)	$\langle 100 \rangle$	Carbon steels, ferritic stainless steels
Hexagonal-close-packed (hcp)	$\langle 10\bar{1}0 \rangle$	Titanium, magnesium
Body-centered-tetragonal (bct)	$\langle 110 \rangle$	Tin

Hence, the growth rate is given by the relationship expressed in Equation 1.25:

$$R = \frac{V \cos \alpha}{\cos(\alpha - \beta)} \quad (1.25)$$

In many cases, the value of  $(\alpha - \beta)$  is small so that  $\cos(\alpha - \beta) \approx 1$ , and the relation between the growth rate and heat-source travel speed is given simply as (Equation 1.26):

$$R = V \cos \alpha \quad (1.26)$$

Therefore, the variation of the scan speed between the different scan track zones influences the R value:  $R \approx 0$  at the scan track boundaries and  $R \approx V$  at the scan track centerline. The angular relationships between the scan speed, the normal solidification interface, and the grain growth direction are schematically represented in Figure 1.69 [91,92].

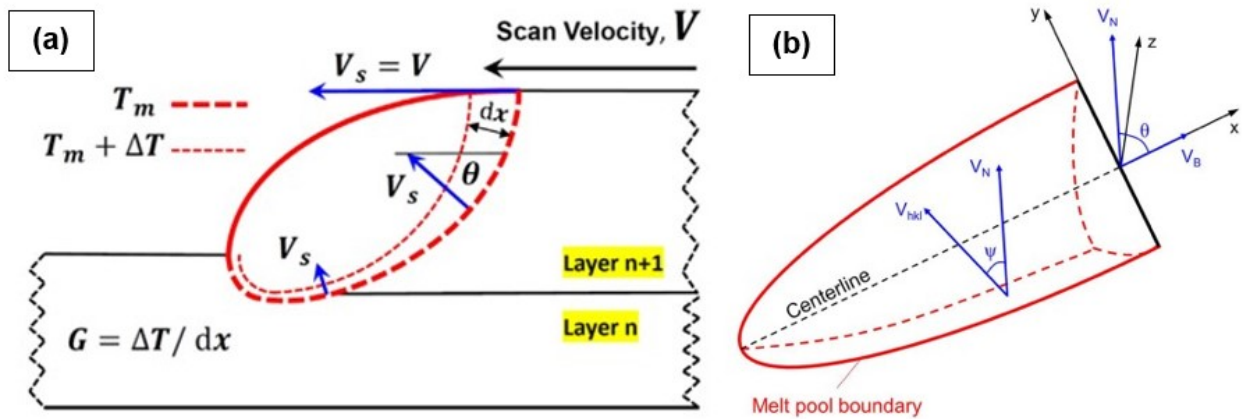


**Fig. 1.69.** Change of the local grain growth velocity ( $V_s$ ) and temperature gradient ( $G$ ) along the MPB (a). The  $T_M$  isotherm curve represents the estimated locus of the MPB. The temperature gradient along the MPB is defined as  $G = \Delta T/dx$ , estimated by the locus of the two isotherms shown above, i.e.,  $T_M$  and  $T_M + \Delta T$ . The relationship between the beam speed ( $V_b$ ), the nominal growth rate ( $V_n$ ), and the grain growth rate ( $V_{hkl}$ ) is related to the solidification that occurred in the MP (b). Adapted by [91,92].

The direction of heat flow at any point on the solidification surface is normal to the surface. It influences the crystallographic orientations heavily and is dependent on the local curvature of the boundary of the MP (Figure 1.69(a)). Considering Figure 1.69(b), the direction of heat flow at any point on the solidification surface can be given by Equation 1.27:

$$\nabla T = \frac{\partial T}{\partial x} i + \frac{\partial T}{\partial y} j + \frac{\partial T}{\partial z} k \quad (1.27)$$

where  $T$  is temperature and  $i$ ,  $j$  and  $k$  are unit vectors in the scan, width, and vertical directions. The temperature gradient,  $G$ , can be calculated by Equation 1.28:

$$G = \|\nabla T\| \quad (1.28)$$

The angle  $\theta$ , including between the heat flow direction and the scanning direction, is defined as (Equation 1.29):

$$\cos \theta = \frac{\frac{\partial T}{\partial x}}{\sqrt{\left(\frac{\partial T}{\partial x}\right)^2 + \left(\frac{\partial T}{\partial z}\right)^2}} \quad (1.29)$$

The modulus of normal solidification velocity  $\bar{V}_n$  at the solid-liquid interface is geometrically linked to beam velocity  $\bar{V}_b$ , according to Equation 1.30:

$$|\bar{V}_n| = |\bar{V}_b| \cos \theta \quad (1.30)$$

From Equation 1.30, it is possible to define the growth velocity  $\bar{V}_{hkl}$  of grains along a specific crystallographic direction  $[h \ k \ l]$ , considering  $\Psi$  as the angle between the normal to the solidification interface and the preferred  $[h \ k \ l]$  crystallographic direction [8] (Equation 1.31):

$$|\overline{V}_{hkl}| = \frac{|\overline{V}_n|}{\cos\psi} = \frac{|\overline{V}_b|\cos\theta}{\cos\psi} \quad (1.31)$$

Equation 1.31 indicates that the grain may have a misorientation  $\Psi$  between its crystallographic direction and the maximum heat flow direction, which is represented by  $\overline{V}_n$ . In other words, the scan velocity  $\overline{V}_b$  influences the growth velocity of microstructure  $\overline{V}_{hkl}$ . The favorable orientation of grains tips reduces undercooling needed to ensure their growth; this condition is satisfied only if  $\overline{V}_{hkl}$  is higher than  $\overline{V}_n$  to keep up with the solidification interface of the MP (Figure 1.69(b)). Misoriented grains are characterized by slightly more undercooling and therefore are located behind the better-oriented grains [5].

In summary, the columnar grains epitaxially grow from the previously deposited layer, following the thermal gradient and parallel to the building direction. The growth direction depends on both the crystallographic orientation and the direction of the local heat flow, which affects the local curvature of the solidification interface. Therefore, the columnar grains continuously grow by shifting their direction to align with the most favorable one according to a "competitive growth" between grains with various crystallographic orientations, determining the final solidification structure. In particular, for the AlSi10Mg alloy, a fibrous texture  $\langle 100 \rangle$  can be observed, parallel to the building direction and the thermal gradient and attributable to the easy direction of growth (Table 1.4) and the chemical and crystalline affinity between liquid metal and solidified substrate (Figure 1.70) [72,93]. The competitive growth leads the grains characterized by crystallographic direction  $\langle 100 \rangle$  to be favorably oriented in the direction of maximum growth so that they continue the growth also for subsequent layers, up to the point where the misalignment due to a rotation or an unfavorable change in the scanning direction stops its growth at the expense of other grains [5]. The particular crystallographic texture of L-PBF AlSi10Mg characterizes the microstructure through a clear directionality, which induces a crucial anisotropic behavior in the alloy linked to the different grain boundary densities (GBD) in correspondence with different section planes; in fact, the thin and long columnar grains aligned to the building axis determine a higher GBD on the plane perpendicular to the building direction (Figure 1.70) [42,93].

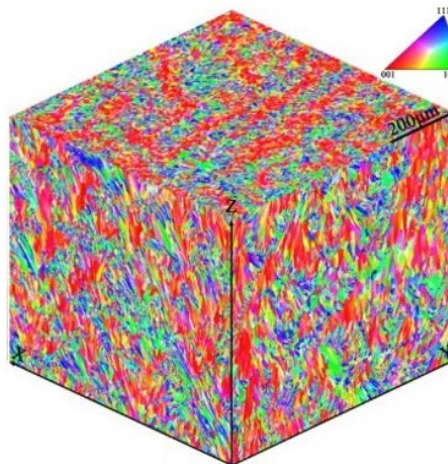


**Fig. 1.70.** 3D representation of the orientation and grain boundary in the L-PBF part [93]

The L-PBF AlSi10Mg alloy solidifies in non-equilibrium conditions, forming a fine sub-structure within grains. As shown by the phase diagram in Figure 1.71(a), forming a solid phase leads to the rejection of the solute into the liquid. The extent of solute enrichment in the liquid progresses as solidification proceeds, and the liquid composition follows the liquidus line. The solute rejected by the solid at the S/L interface must be transported away from the interface by diffusion or convection phenomena. If the growth rate of the S/L interface is relatively high (leading to a high rate of solute rejection) or the transport of solute into the liquid by diffusion or convection is low, then a boundary layer of the

solute can develop in the liquid near the S/L interface. Since solute enrichment leads to a reduction of the liquidus temperature, it follows that the presence of a solute boundary layer leads to a liquidus temperature gradient close to the S/L interface. This condition is shown schematically in Figures 1.71(b,c), where the liquidus temperature is relatively low at the S/L interface due to a large amount of solute in the liquid [48].

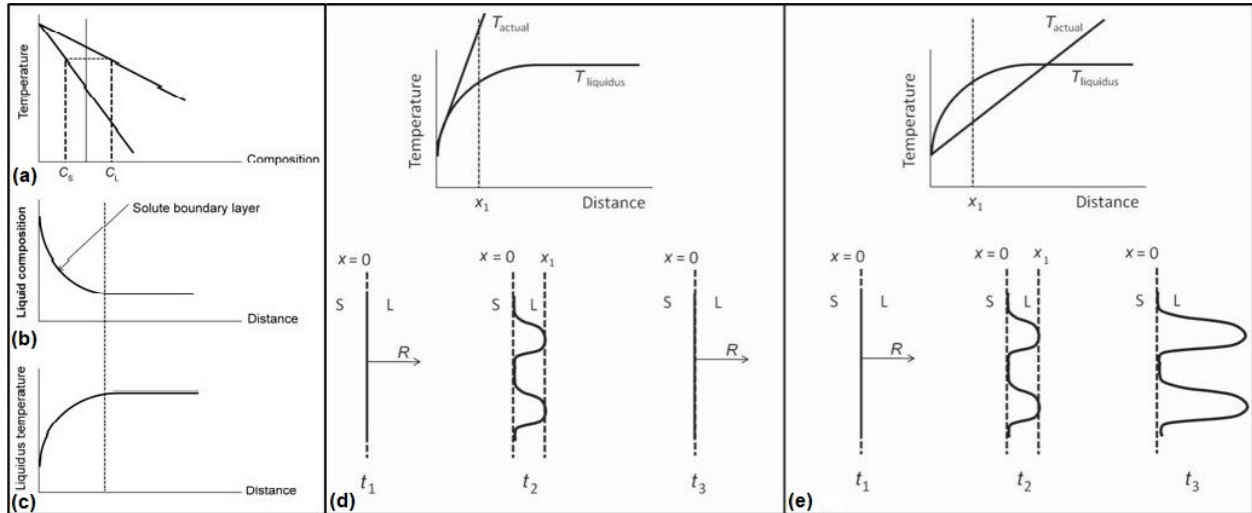


**Fig. 1.71.** Schematic illustration showing solute enrichment in liquid during solidification (a), formation of a solute boundary layer in the liquid (b), variation in liquidus temperature near the S/L interface due to formation of the solute boundary layer (c), stability condition of a planar S/L (d) and break condition of a planar interface (e) [48].

The growth process depends on the thermal and compositional gradients at the S/L interface, as they determine the morphology of the solidification front. The stability of the planar S/L interface in the early stages of solidification depends on the relationship between the liquidus temperature gradient ( $\frac{dT_L}{dx} = G_L$ ) and the actual temperature gradient in the liquid ( $\frac{dT_A}{dx} = G$ ). Two conditions can be defined:

- $G > G_L$  (Figure 1.71(d)): the planar interface shifts to the right and develops protrusions as it grows due to interface pinning effects from inclusions in the liquid or differences in the growth rate between neighboring grains. In this condition, the tip of the protrusion interfaces with a liquid characterized by a temperature higher than the liquidus temperature of the alloy (position  $x_1$  in Figure 1.71(d)), which makes the solid tip unstable, causing it to re-melt and the return to a stable planar interface.
- $G_L > G$  (Figure 1.72(e)): it is referred to the constitutional undercooling condition, where the liquid is cooled below its liquidus temperature. This condition generates the stability necessary for the tip growth in the liquid metal at a temperature below the liquidus value (position  $x_1$  in Figure 1.71(e)). Hence, the growth rate at the tips will be greater than at the protrusions' roots, proportional to the undercooling's contribution, leading to the disruption of the planar interface and the formation of a cellular interface. The solute can accumulate at the boundaries of adjacent cells as they converge and, depending on the cooling rate and diffusivity of the solute in the solid, lead to solute-enriched zones after solidification.

Therefore, the condition for the disruption of the planar S/L interface and the concomitant formation of a cellular substructure is given by the condition in which  $G_L > G$ . This relationship can be quantitatively determined by first developing an expression for the solute concentration gradient in the liquid ( $\frac{dC_L}{dx}$ ) and then converting  $\frac{dC_L}{dx}$  into  $\frac{dT_L}{dx}$  via the phase diagram [48]. A mass balance is obtained at the S/L interface, assuming a linear solute gradient in the liquid, as described in Equation 1.32:

$$R (C_L - C_0) = -D_L \frac{dC_L}{dx} \quad (1.32)$$

where  $D_L$  is the diffusivity of the solute in the liquid. In this way, it is possible to describe the solute flow into the interface due to the rejection of the solute by the solid ( $R (C_L - C_0)$ ), and the flow of solute along the gradient in the liquid ( $-D_L \frac{dC_L}{dx}$ ), assuming a linear concentration gradient. Under steady-state conditions, these two flows are balanced, and Equation 1.32 is verified. Considering a linear liquidus line in a phase diagram, a given value of  $\frac{dC_L}{dx}$  produces a corresponding change in the liquidus temperature  $\frac{dT_L}{dx}$  that is given by Equation 1.33:

$$G = m_L \frac{dC_L}{dx} \quad (1.33)$$

From Equations 1.22 and 1.33, the constitutional undercooling criterion is described by Equation 1.34:

$$G < -\frac{R * m_L * (C_L - C_0)}{D_L} \quad (1.34)$$

Considering that the value  $G$  is simply the temperature gradient, under steady-state conditions,  $C_L$  is equal to  $C_0/k$  [82]. Thus, the expression for constitutional undercooling can be expressed as (Equation 1.35):

$$\frac{G}{R} < -\frac{m_L * C_0 * (1-k)}{k * D_L} \quad (1.35)$$

Equation 1.35 allows dividing the terms at the extremes of the equation: (i) the solidification parameters on the left and (ii) the parameters of the alloy on the right. In particular, the term  $m_L * C_0 * (1-k)$  represents the equilibrium solidification range of the alloy, so the constitutional undercooling ( $\Delta T$ ) condition can also be written as (Equation 1.36):

$$\frac{G}{R} < -\frac{\Delta T}{D_L} \quad (1.36)$$

This condition represents the onset of undercooling and the formation of a cellular-dendritic sub-structure (Figure 1.72) [48].

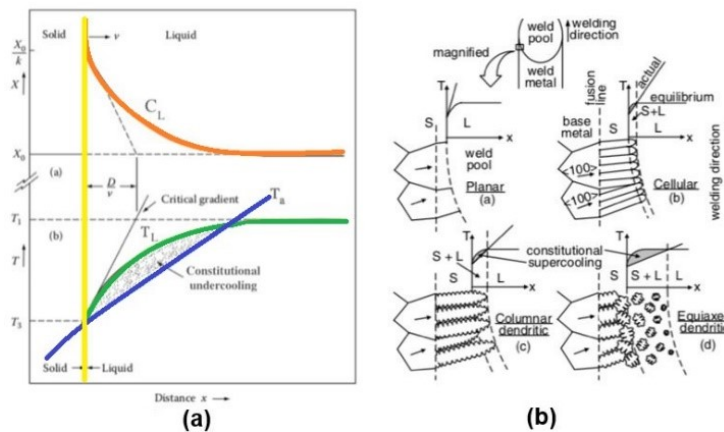


**Fig. 1.72.** Constitutional supercooling: definition (adapted from [82]) (a), effect of on grain morphology (b) [48].

The terms  $G$  and  $R$  can more carefully evaluate the solidification microstructures in their combined forms of  $G * R$  and  $G/R$ . In particular:

- The  $G/R$  ratio determines the mode of solidification;
- The  $G * R$  product governs the scale of the solidification microstructure.

Figure 1.73 shows the effect of  $G/R$  and  $G \cdot R$  values on the solidification microstructure [95]. The solidification microstructures can be planar, cellular, columnar dendritic, or equiaxed dendritic with decreasing  $G/R$  values:

- **Planar structure:** only in controlled solidification conditions, characterized by high  $G$  and low  $R$  values. For this reason, most alloys have a microstructural morphology deriving from non-planar solidification.
- **Cellular structure:** in solidification conditions where the  $G/R$  ratio is slightly lower than the  $\Delta T/D_L$  ratio. As the  $G/R$  ratio decreases, the interface becomes columnar dendritic. The liquid regions left between cells and dendrites are enriched with solute and produce micro-segregation at the end of solidification.
- **Dendritic structures:** Its formation is closely linked to a high constitutional undercooling concerning an increase in the solute and a consequent reduction in the  $G/R$  ratio, which determines a greater degree of segregation than the previously described morphologies. The columnar or equiaxed morphology depends on the undercooling rate undergone by the liquidus at the S/L interface.

The dimension of all four solidification microstructures decreases with increasing cooling rate  $G \cdot R$ .

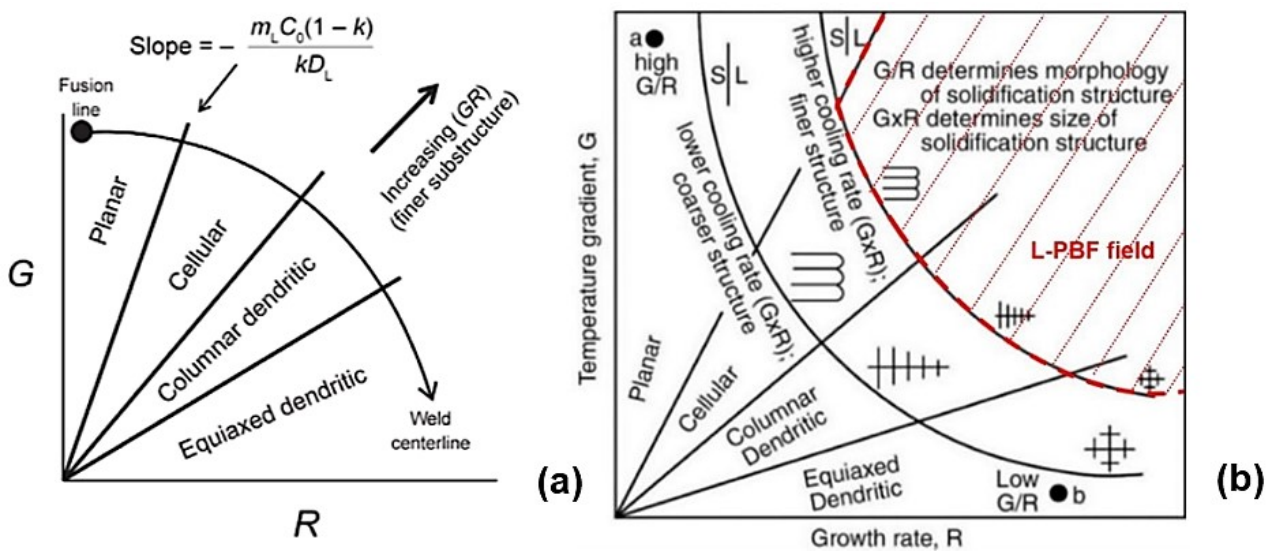
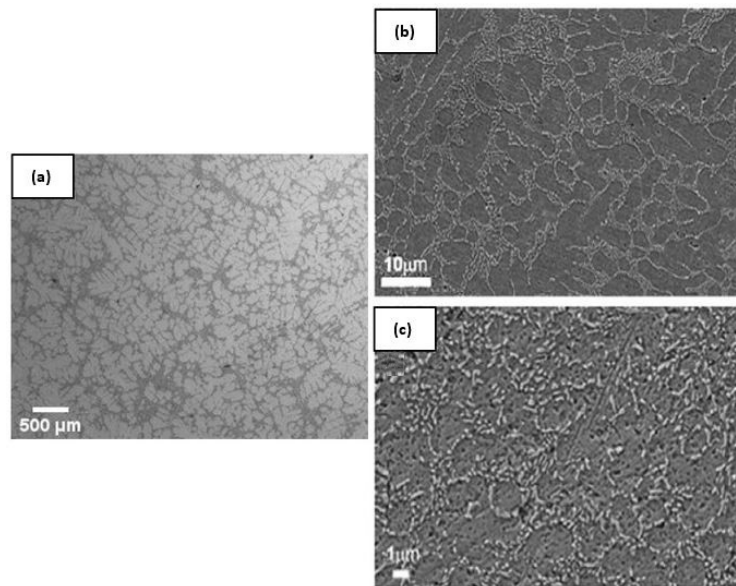


Fig. 1.73. Schematic representation of the effect of temperature gradient  $G$  and growth rate  $R$  on the morphology of solidification microstructure (a). More elaborate scheme of the effect of the  $G/R$  and  $G \cdot R$  factors on the size and morphology of the substructure (b). Adapted from [48,82].

It is essential to consider that the alloys are made up of base metals, such as Fe, Al, Cu, or Ni, to which other elements (solutes) are added to obtain the desired properties. The transformation from liquid to solid (solidification) can occur when the liquid solution is transformed into a solid solution or through different processes such as eutectic, peritectic, or monotectic reactions. How solidification of the solid solution occurs is crucial as they determine the final substructure and, thus, the properties of the component, as will be described below.

### 1.5.3 L-PBF AlSi10Mg microstructure

The term rapid solidification is historically applied to casting processes in which the cooling rate of the liquid exceeds  $10^2$  K/s, such as copper mold casting (CMC) or melt spinning (MS) [95]. The different cooling rates lead to different microstructures: the AlSi10Mg cast alloy is characterized by  $\alpha$ -Al dendrites surrounded by an aggregated AlSi eutectic phase (Figure 1.74(a)) [96,97]. On the contrary, the AlSi10Mg alloy made with MC and MS technologies is characterized by a primary phase consisting of  $\alpha$ -Al cells surrounded by a fibrous eutectic-Si network in the intercellular regions (Figures 1.74(b,c)) [95]. This peculiar microstructure derives from micro-segregation and limited diffusion phenomena due to the high cooling rates that determine the L-to-S phase transformation without significant change in composition.



**Fig. 1.74.** Microstructures of AlSi10Mg alloy solidified by different solidification techniques: Casting (a); MC (b); MS (c). Adapted from [95]

The solidification rate in the L-PBF process quickly reaches high cooling rates ( $10^5 - 10^8$  K/s) thanks to the high energy density and laser scan speed [83]. Consequently, the L-PBF AlSi10Mg microstructure differs from that observed in the AlSi10Mg alloy produced by MS and MC, and it is hugely finer than the AlSi10Mg cast alloy up to two orders of magnitude. The non-equilibrium solidification conditions during the printing process significantly affect the morphology of the microstructure within the columnar epitaxial grains solidified into the MPs [42,98]. In particular, they affect the solute entrapment rate in the Al lattice at the S/L interface, thus increasing the solid solution limit of the alloying elements in the matrix. In this way, a fine metastable cellular microstructure solidifies within the columnar epitaxial grains, characterized by sub-micrometric supersaturated  $\alpha$ -Al cells, surrounded by a fibrous eutectic-Si network and by limited precipitation of strengthening phases (Figure 1.75) [73,99].

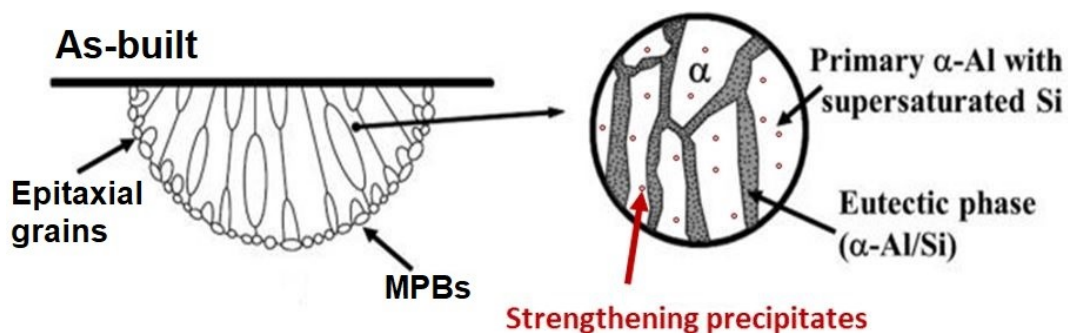


**Fig. 1.75.** L-PBF AlSi10Mg alloy as-built microstructure. Adapted from [100]

As described above, the theory of constitutional undercooling can be used to explain the solidification phenomena that lead to this peculiar microstructure [48]. The microstructure variation from planar to cellular or dendritic morphology depends on the relationship between the temperature gradient and the grain growth rate, suggesting the importance of thermodynamic aspects in dictating the morphology of the solidification microstructure [101]. On the other hand, the theory of interfacial stability suggests that the morphology of the microstructure depends, in particular, on the interfacial kinetics, the heat transfer, and the entrapment rate of the solute at the solid-liquid interface (kinetic aspects) [102]. For these reasons, the solidification of the metastable cellular microstructure is kinetically rather than thermodynamically favored [83]. The  $\alpha$ -Al phase begins to solidify into a cellular structure due to the high cooling rate, which simultaneously results in an extended solubility of the Si atoms within the Al crystal lattice (at 573 K is observed to be 0.06% by weight under almost steady-state cooling conditions [103]) via an entrapment mechanism. The Si phase is rejected by the solidification front in the liquid at the S/L interface, thus increasing the Si concentration in the liquid by the local surface tension-driven process. The residual free Si content concentrates along the boundaries and forms a eutectic-Si phase around the  $\alpha$ -Al cells (Figure 1.76) [104].

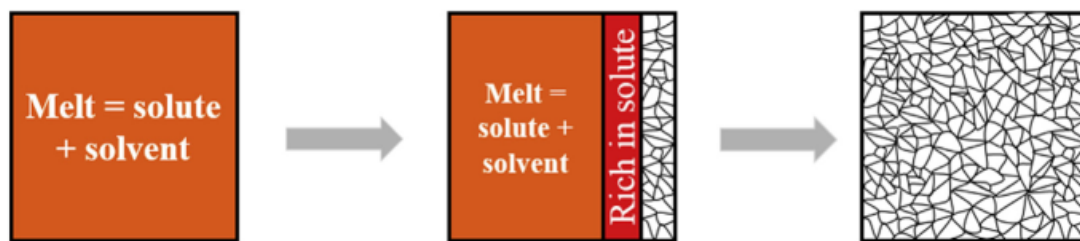


**Fig. 1.76.** Schematic illustration describing the formation of a cellular microstructure from the melt [83]

In addition to the thermodynamic and kinetic considerations, other physical aspects should also be considered to explain in-depth the ultrafine metastable microstructure obtainable from the L-PBF process. In particular, as described in section 1.3.3, the instability within the MP induced by the surface tension gradient (Marangoni force-driven instability) causes a diffusive transport of the solute whose role in rapid solidification is still unknown [92].

The L-PBF solidification conditions lead to the development of a metastable ultrafine cellular microstructure within the columnar grains characterized by sub-micrometric cells of supersaturated  $\alpha$ -Al solution surrounded by a eutectic Si network (Figure 1.77) [42]. Microstructural anisotropy characterizes the cellular structure: the eutectic-Si network appears to be branched and oriented towards the direction growth, which is parallel to the building direction, with highly elongated  $\alpha$ -Al cells, while in a section parallel to the building platform, the  $\alpha$ -Al cells are found in a honeycomb arrangement, which is underlined by the distribution of the eutectic-Si network around the single  $\alpha$ -Al cell. The width of the submicron-sized cellular microstructure is between 500 and 1000 nm, and the cellular boundaries are found to be  $\sim 10^2$  nm thick (Figure 1.77) [83].

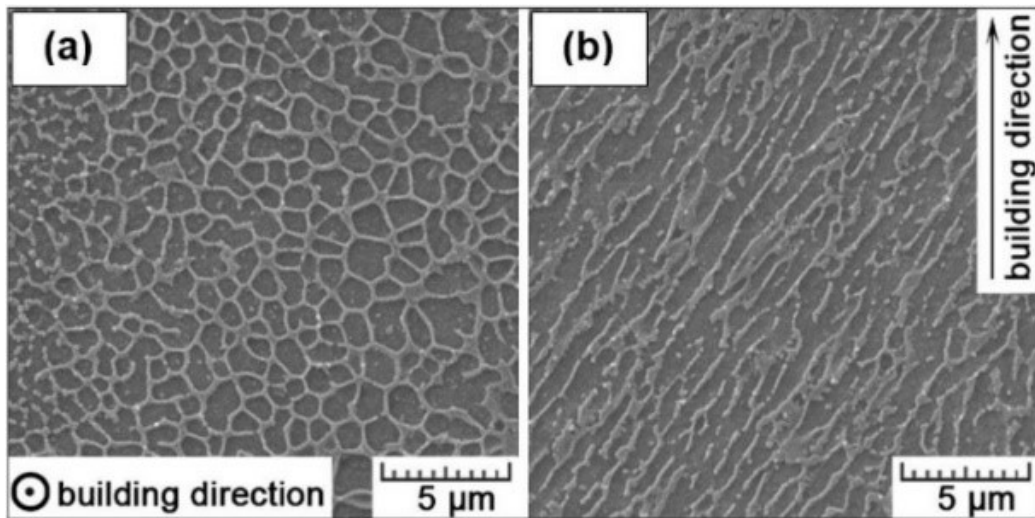


Fig. 1.77 Fine cellular substructure in (a) transversal and (b) longitudinal section [105]

Furthermore, Mg segregates in the intercellular network along cell boundaries and tends to form  $Mg_2Si$  precursors phases ( $\beta'$  and  $\beta''$ ) by reaction with Si following the heating processes associated with the subsequent deposition steps. For the same reason, nano-sized Si particles precipitate inside the  $\alpha$ -Al cells (Figure 1.78) [99,100,106].

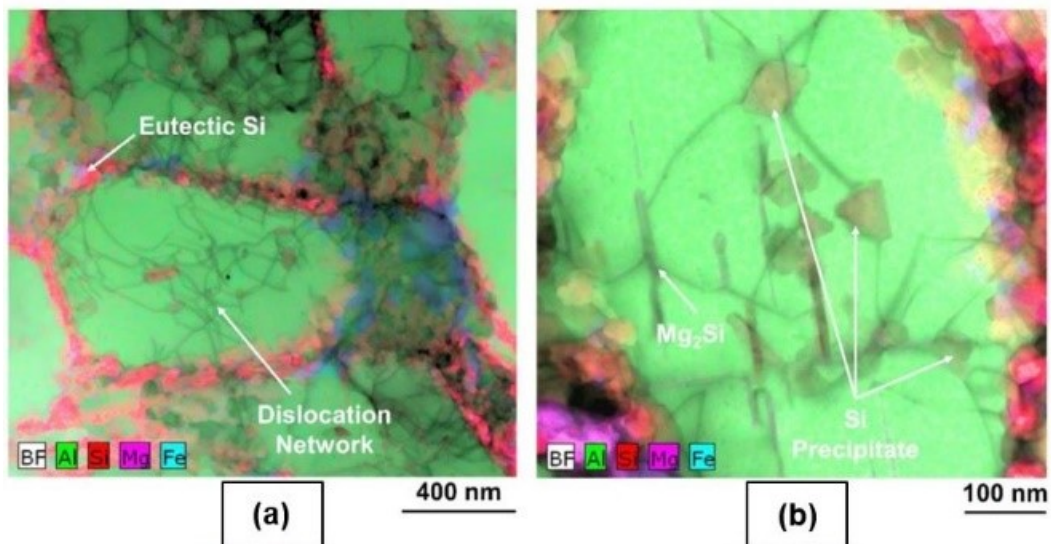
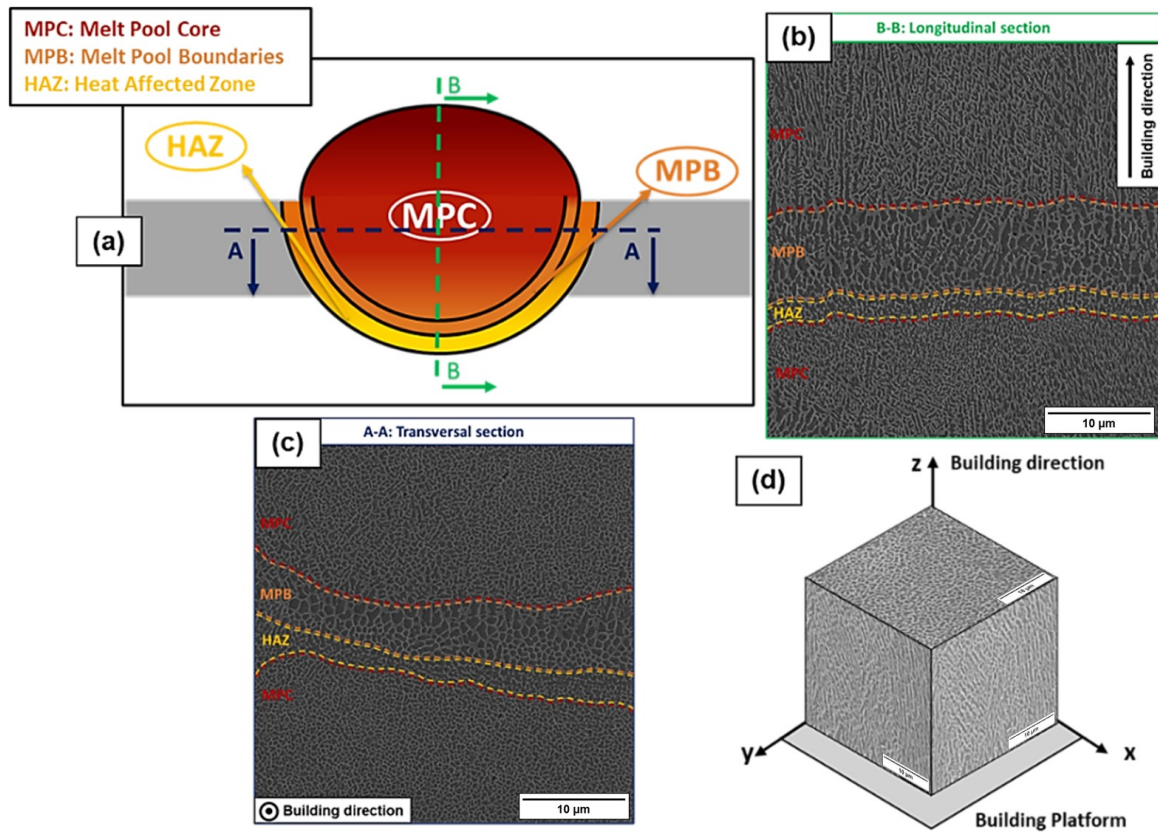


Fig. 1.78. STEM-BF microstructure of the as-built sample (a); details of dislocation networks and Si and  $Mg_2Si$  precipitates (b) [99].

The distribution, morphology, and size of  $\alpha$ -Al cells depend on the continuous heating and cooling cycles necessary to produce the 3D component; in fact, the eutectic-Si network presents different morphologies within the MP structure: highly uniform in the Melt Pool Core (MPC), where the  $\alpha$ -Al cells appear fine and equiaxial, coarser and elongated in the areas adjacent to the MPBs, extremely discontinuous in the HAZ adjacent to the MPB, where it appears jagged, inhomogeneous and characterized by the formation of small agglomerated Si particles (Figure 1.79) [42]. Furthermore, the thermal exposure of the solidified material influences the dimensions and morphology of the  $\alpha$ -Al cells on which the mechanical properties of the as-built (AB) alloy depend. A longer-lasting MP that cools more slowly produces a coarser microstructure with larger grains, broader  $\alpha$ -Al cells, and thicker eutectic Si. At the same time, the extension of the HAZ and the fragmentation of the eutectic-Si network increase [107,108].



**Fig. 1.79** Different microstructural zones (MPC, MPB, and HAZ) within the MP (a), cellular structure in cross section (b); cellular structure in transversal section (c). The coarser microstructure along the MPBs and the eutectic-Si network fragmentation at the HAZs are due to the partial remelting of the previously deposited layers. 3D representation of the AISi10Mg cellular microstructure in the L-PBF part (d)

The microstructural anisotropy characterizing the AB alloy influences its mechanical properties; in fact, the orientation of the MBPs and HAZs to the load direction determines a different mechanical response of the material (Figure 1.80) [107]. According to several authors [72,79,107,108], these regions represent the weakest part of the AB microstructure due to the coarser size of the  $\alpha$ -Al cells and the disaggregated eutectic-Si network, which promote crack initiation and propagation. In particular, as Xiong et al. [107] described, the samples produced parallel to the building platform (Figure 1.80 (a)) show a good combination of strength and elongation to failure ( $\epsilon_f$ ) caused by a smaller number of MPs interested in crack propagation; in fact, in this condition fracture propagates across the MP, encountering higher resistance by the finer equiaxed microstructure within the MPC. However, as highlighted by several authors [80,109,110], hardness and yield strength (YS) show a negligible anisotropy since it is mainly due to more easily propagation of the fracture inside the material in the plastic range.

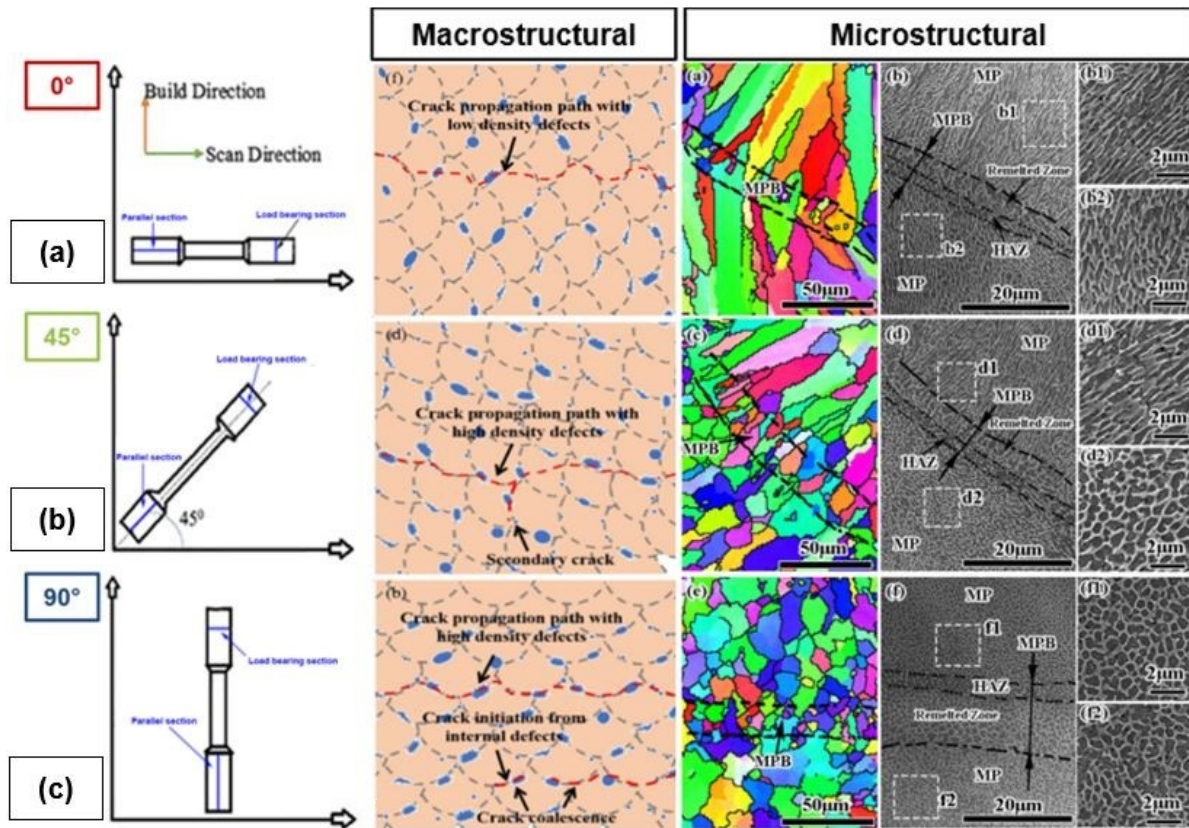


**Fig. 1.80.** Different failure propagation conditions according to the building and the load directions: Parallel to the layers, the fracture propagates along the plane perpendicular to the layers, leading to an inter and trans-track fracture (a); At 45° to the layers, the fracture propagates along the plane perpendicular to the layers, leading to a mixed inter-layer, inter and trans-track fracture (b); Perpendicular to the layers, the fracture preferentially propagates along the MPB, producing an inter-layer fracture and trans-track fracture (c). Adapted from [107]

A comparable phenomenon was analyzed for the impact toughness of the as-built L-PBF AlSi10Mg alloy: in specimens oriented at 90° (Figures 1.81(a,c)), the fracture preferentially propagates along the MPB, producing an inter-layer fracture and trans-track fracture, while in specimens oriented at 0° (Figures 1.81(b,d)), the fracture propagates along the plane perpendicular to the layers, leading to a mixed inter and trans-track fracture and leading to a higher value of the impact energy absorbed by the alloy [123,131,143].

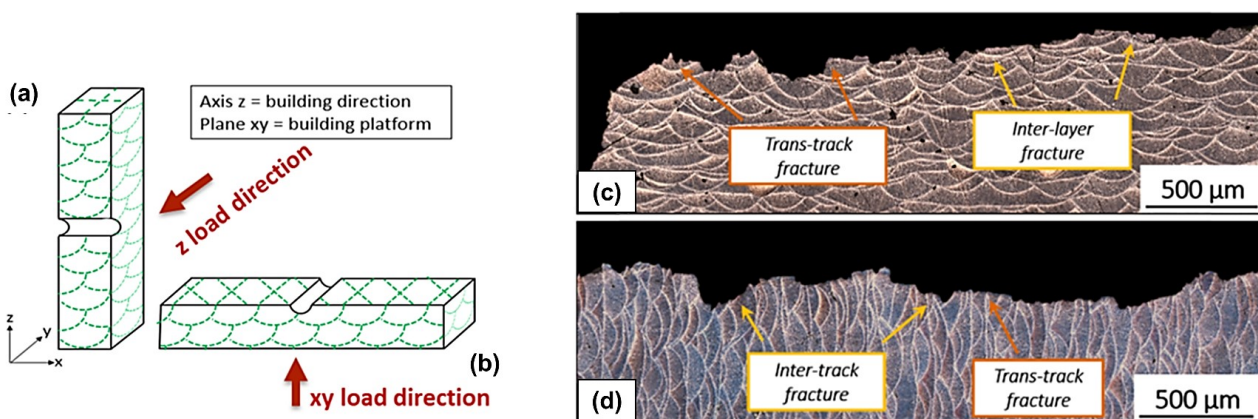


**Fig. 1.81** Diagram of the orientation of L-PBF samples on the building platform, vertical (a) and horizontal (b). Fracture profiles for L-PBF samples in as-built condition, perpendicular to the notch, in vertical (c) and horizontal (d) orientations. Adapted from [143].

Contrary to what has been seen for the static mechanical properties and toughness, the fatigue specimens characterized by different building directions have a comparable fatigue strength. The specimens characterized by an axis parallel to the building direction (Figure 1.80(c)) have a higher GBD on the XY plane (Figure 1.82), which balances the negative effect of MP orientation (Figures 1.82(a,b)) [56,79,111].

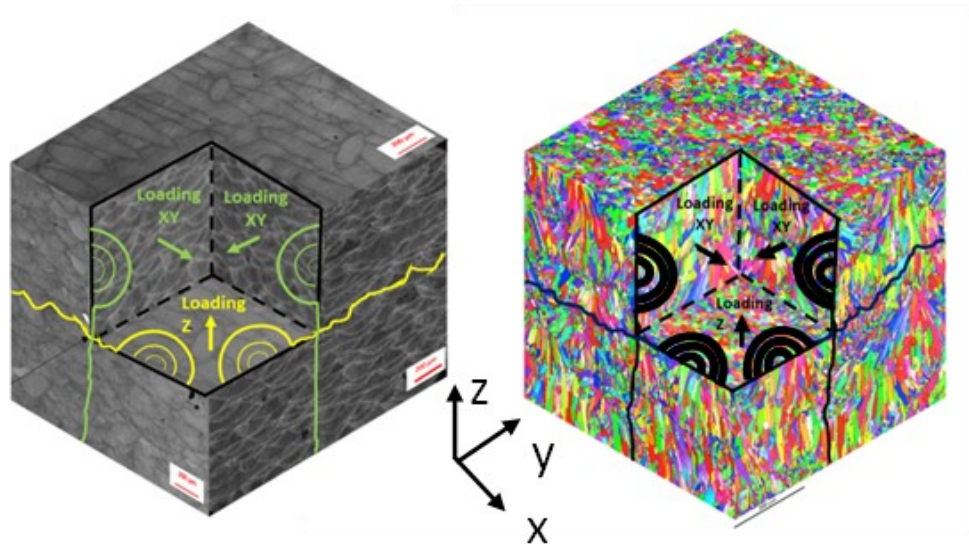


**Fig. 1.82** Sketch explaining the difference observed in fatigue properties between XY and Z, fatigue crack related to the MP's size (a), and fatigue crack related to the grain size (b). Adapted from [79].

The indicative range of the mechanical properties of the AB alloy will be described in the following section.

### 1.5.4 L-PBF process parameters: influence on microstructure and strengthening mechanisms

The peculiar microstructure of the AB alloy is characterized by microstructural refinement (according to the Hall-Petch law) and solid solution strengthening (Figure 1.83(a)) [100,112,113]. In addition, the high GBD and the morphology of the aggregated second phase (eutectic-Si network) further reduce the dislocation motion, increasing the mechanical performance of the AB alloy. The small interphase (Si/ $\alpha$ -Al) distance results in high strain gradients, contributing to the enhancement of dislocation density by the Orowan looping mechanism around the eutectic-Si phase (Figure 1.83(b)). Therefore, the ultrafine cellular structure of the AB alloy acts as a barrier to dislocation motion and increases the strain-hardening mechanism [135]. In addition, the precipitation hardening induced by  $\beta$ -Mg<sub>2</sub>Si phases and nano-sized Si particles determines a further strengthening of the AB alloy, the extent of which is linked to the applied process parameters that promote the precipitation hardening due to the high solute content in the Al crystal lattice (Figure 1.78) [100,106].

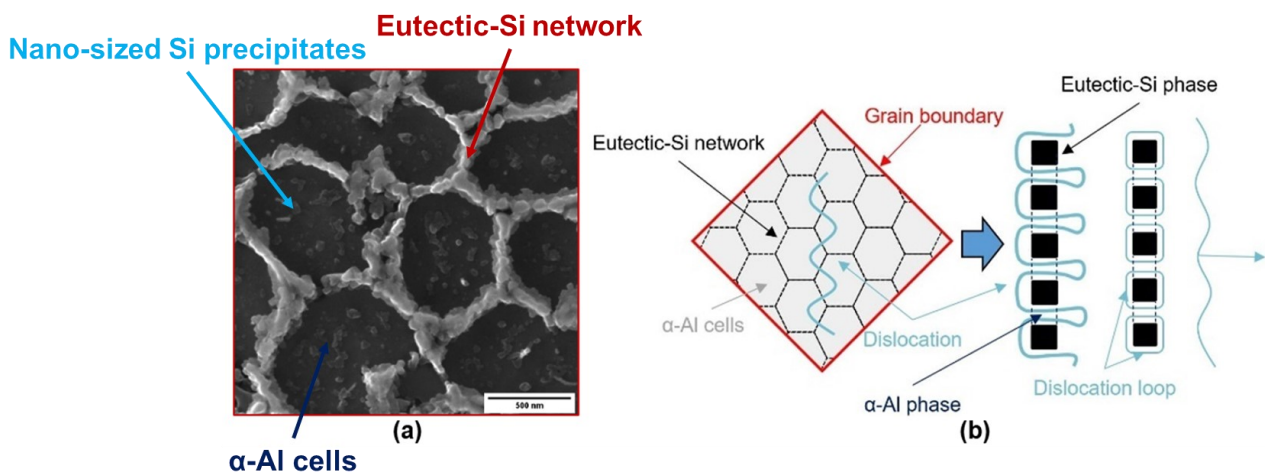


**Fig. 1.83** SEM image at high magnification of the cellular substructure (a). Interaction between the dislocations and the cell boundary via Orowan looping in hierarchically structured L-PBF AlSi10Mg alloy under loading: dislocations pass through the cell boundary, producing dislocation loops around boundary phases (b).

Therefore, the ultra-fine cellular microstructure characterizing the AB alloy leads to the synergistic effect of multiple strengthening mechanisms, including microstructural refinement, solid solution, aggregated second phases (eutectic Si network), high dislocation density, and limited precipitation hardening. Consequently, higher hardness and tensile strength are generally obtained in the AB alloy, although with lower ductility and toughness, than the as-cast Al alloys [42,99,106,112].

The L-PBF process parameters, such as laser parameters, build platform temperature, and scan strategy, play a key role in the microstructural characteristics and, consequently, in the strengthening mechanisms of the AlSi10Mg alloy. In particular, as described above, the morphology and size of the microstructure are closely related to the thermal gradient and the solidification (or growth) rate, which highly depend on process parameters [8].

The  $ED_v$  value cannot be used as a direct indicator to evaluate the effect of process parameters on the morphology and size of the AlSi10Mg microstructure since it can have different combinations of laser power, scan speed, hatch spacing, and layer thickness, which can individually affect the microstructure differently [42,44,60,70]. Moses et al. [72] studied the effect of hatch spacing and layer thickness at  $ED_v$  value constant, revealing that the increase in hatch spacing and layer thickness results in larger columnar grains with a broader cellular structure. However, the laser power and scan speed were varied to ensure a constant energy density, and a direct correlation between microstructure thickness and hatch spacing, and layer thickness cannot be considered. At the same time, Thijs et al. [73] demonstrated that hatch

spacing and layer thickness mainly affected crystal texture; a smaller hatch spacing or layer thickness leads to a higher amount of partial remelting of neighboring tracks, therefore generating a stronger  $\langle 100 \rangle$  texture. Liu et al. [114] fixed the hatch spacing and layer thickness and investigated the influences of laser power and scan speed on the microstructure, showing a coarser Si-rich network for higher laser power or a lower scan speed (Figure 1.84). Liu et al. [42] also showed that a higher laser power would promote a larger mean grain size. These trends can be related to the cooling rate, which increases and decreases with the increase in scan speed and laser power. Tang et al. [115] and Hyer et al. [113] highlighted a close correlation between  $\alpha$ -Al cell size and cooling rate: a faster scan rate and, consequently, a faster cooling rate leads to a more refined cell structure. However, starting from the analysis of several studies [99,105,112,116], the morphology, shape, and size of the nano-sized Si particles within Al cells do not seem to depend on laser energy density or cooling rate. The cooling rate determines the solute content in the Al lattice upon solidification. In contrast, the precipitation hardening is expected to be more closely related to the thermal history after solidification, i.e., the solid-state thermal cycling from subsequent tracks/layers. Lastly, it is difficult to determine the exact thermal history to which the solidified microstructure is subjected due to the several parameters involved [117].

Name	subgroups	Laser Power (W)	Scan speed (mm/s)	Energy Density (J/mm <sup>3</sup> )
E38	1	264	2320	38
E51/P300*	1,2	300	1960	51
E70	1	355	1690	70
P200	2	200	1307	51
P355	2	355	2320	51

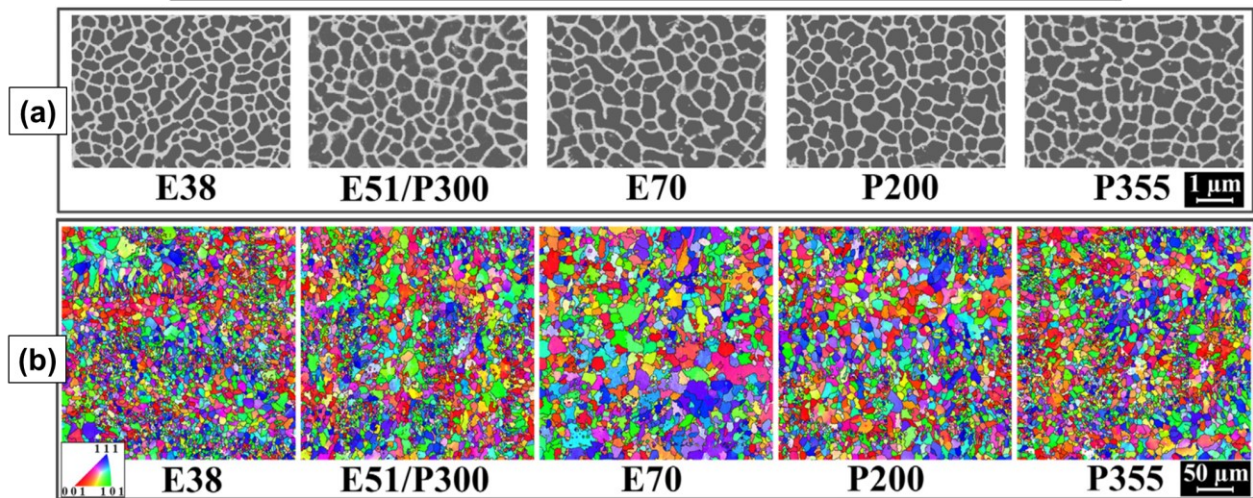


**Fig. 1.84.** SEM images (a) and EBSD maps (b) show the microstructures in the L-PBF AlSi10Mg produced using five different processing conditions, which are reported in the table at the top. The color code representing the crystal orientation is included. Adapted from [114]

Another important factor that highly influences the microstructure is the build platform temperature, which is a useful strategy to reduce RS, distortions, and hot-tearing cracks by reducing the cooling rate and thermal gradient [44,115,118]. As the substrate's temperature rises, the fluidity of the liquid metal increases, thus reducing the problems associated with the formation of hot cracking and LoFs but increasing the gas porosity inside the material proportionally to the higher solubility gas in the MP [119,120]. A wide range of build platform temperatures was tried in literature, from 35 °C to 300 °C [67,92,116,119,121-123]. The Si-rich eutectic always manifests as an interconnected network, whereas the microstructure fineness varies with the level of the temperature gradient. Santos Macías et al. [124] showed that the increase in the build platform temperature (from 35 °C to 200 °C while maintaining the rest process parameters) leads to (i) enlargement of the MPB and HAZ regions, (ii) coarsening of the cellular structure within the MPC and the Si-rich eutectic network in terms of equivalent cell diameter and network thickness, respectively, and (iii) coalescence of the Si-rich particles inside the Al cells and coarsening of the nano-sized Si particles (Figure 1.85).

Nevertheless, the build platform temperature did not affect the grain size and morphology. Similar observations were reported by Casati et al. [116] comparing build platform temperatures of 25 °C and 160 °C. It is noteworthy that if a higher build platform temperature than 160 °C was used, the microstructure could be further coarsened. In addition to coarsening of Si-rich eutectic and nanoparticles, the building platform preheating can also lead to in-situ aging effects, reducing Si solute concentration (i.e., causing Si precipitation) and forming Mg<sub>2</sub>Si precipitates within Al cells. These microstructural changes result in a higher  $e_f$ , but lower strength properties (YS and ultimate tensile strength (UTS)) compared to samples produced with a no-heated platform and subjected to artificial aging to induce the precipitation hardening. Van Cauwenbergh et al. [125] showed that 200 °C preheating could reduce the Si concentration from 2.7 wt.% (without preheating) to 0.5 wt.%. Hadadzadeh et al. [92] demonstrated the presence of Mg<sub>2</sub>Si precipitates in as-built L-PBF AlSi10Mg alloy with a build platform temperature of 200 °C. However, such in-situ precipitation slightly contributes to strengthening due to its low content, given a significant amount of no-free Mg in the eutectic network [125]. It is noteworthy that no systematic studies have been devoted to identifying the critical build platform temperature at which Mg<sub>2</sub>Si precipitate starts to form [126].

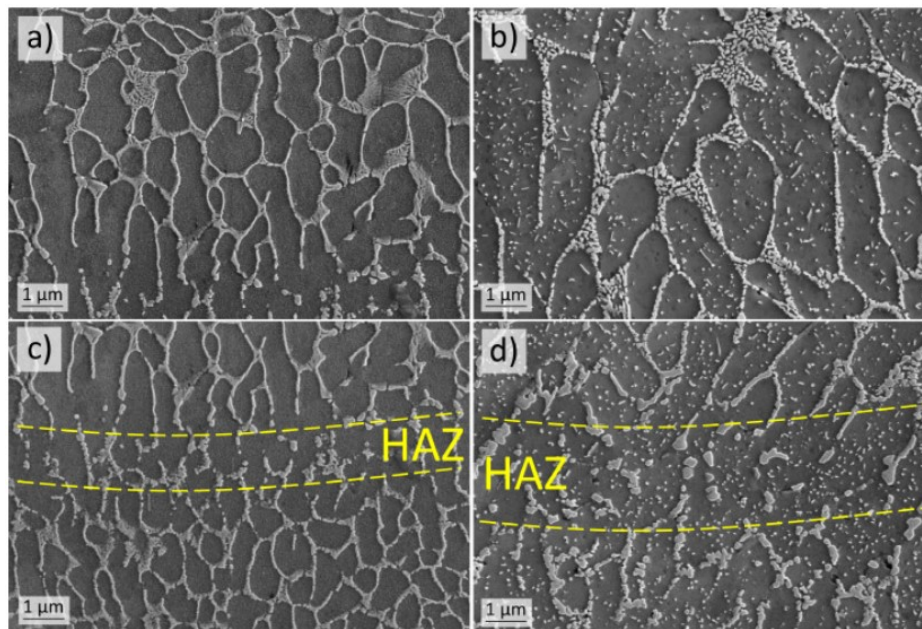


**Fig. 1.85.** SEM micrographs of the MPC zone of L-PBF AlSi10Mg with build platform temperatures of 35°C (a) and 200°C (b) and of the HAZ zone (in between the two yellow dashed lines) with build platform temperature of 35°C (c) and 200°C (d) [124].

The scan strategy can also induce a high impact on microstructure, mainly in grain orientation and MP structure arrangement. Thijs et al. [73] studied the influence of the scan strategy on the crystallographic texture. They showed that a strong  $\langle 100 \rangle$  fiber texture along the scanning direction was present when no rotation of scanning direction in the layer (i.e., islands) or between layers was applied. In contrast, when a 90° rotation was employed, a weak  $\langle 100 \rangle$  cube texture along the building direction was formed. These results indicate that rotations of scanning vectors can control the texture of L-PBF AlSi10Mg. Moses et al. [72] demonstrated that the scan strategy could also control the MP arrangement by comparing 67° and 90° rotations. The 67° rotation case shows a similar MP morphology for any side view (i. e., sections parallel to the building direction), whereas the 90° rotation leads to a quite variable morphology. The counter-clockwise rotation of the scan vector by 67° upon completion of each layer determines a relatively randomized that helps to homogenize the microstructure. The application of this scanning strategy produces several advantages compared to the commonly used bidirectional or island-based scanning regimes with 90° rotation associated with a more tortuous crack propagation path in the material due to a random MP arrangement (Figure 1.86).

**Table 1**

Processing parameters used for the four batches of LPBF produced AlSi10Mg alloy. Gas atomized AlSi10Mg powders with particle size range between  $\sim 20\text{--}65\ \mu\text{m}$  were used; energy density was kept constant at  $\sim 50\ \text{J}/\text{mm}^3$ .

Parameters	60LT/190HS /67SS	30LT/190HS /67SS	30LT/100HS /67SS	30LT/100HS /90SS
Layer Thickness ( $\mu\text{m}$ )	60	30	30	30
Hatch Spacing ( $\mu\text{m}$ )	190	190	100	100
Scan Strategy ( $^\circ$ )	67	67	67	90
Relative Density (%)	98.9	98.7	99.5	99.6

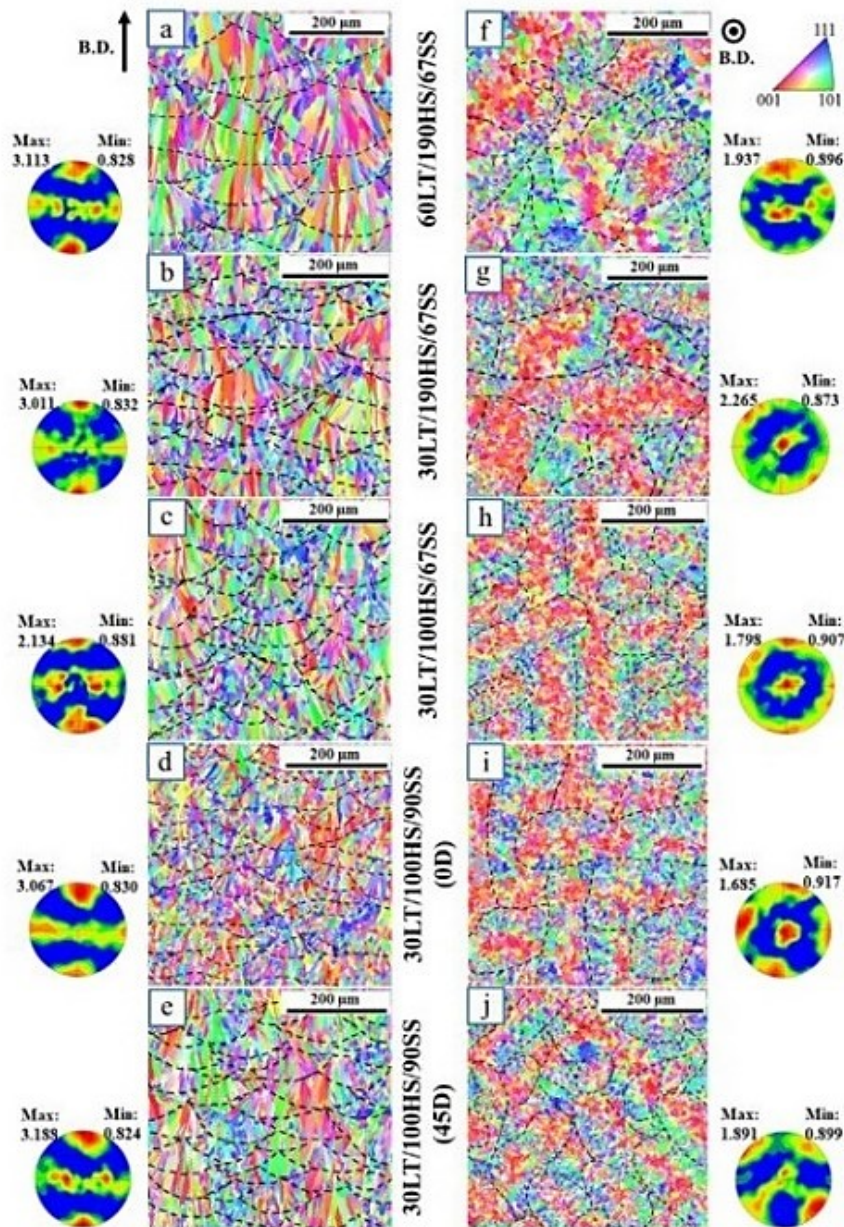


**Fig. 1.86** Processing parameters used for the four batches of L-PBF-produced AlSi10Mg alloy (top). IPF maps to the MP (a-e) and the scan track (f-j) for all build conditions; corresponding  $\langle 001 \rangle$  pole figures are placed adjacent to the images. MP boundaries are drawn as dashed lines from superimposing optical microscopy images taken from the same area [72].

The effects of the process parameters on microstructure and strengthening mechanisms are resumed in Table 1.5.

Table 1.5. Relationship between process parameters, microstructure, and strengthening mechanisms.

Strengthening mechanisms / Process parameters	Microstructural refinement	Solid solution	Aggregate second phase	High dislocation density	Precipitation hardening
Laser power ↑	* Coarser microstructure	* lower super-saturated $\alpha$ -Al cells	≈ higher quantity, less tortuous morphology	* Lower value due to lower solidification rate	-
Scan Speed ↑	✓ Finer microstructure	✓ High super-saturated $\alpha$ -Al cells	≈ smaller quantity, more tortuous morphology	✓ Higher value due to higher solidification rate	-
Hatch spacing ↑	* Coarser microstructure	-	-	-	-
Layer Thickness ↑	* Coarser microstructure	-	-	-	-
Platform Temperature ↑	* Coarser microstructure	* lower super-saturated $\alpha$ -Al cells	-	* Lower value due to stress relief	✓ Higher due to direct artificial aging
Scan strategy ↑	≈ depends on the scan strategy	-	≈ depends on the scan strategy	-	-

### 1.5.5 Heat treatment: influence on microstructure and mechanical properties

Several post-process heat treatments can be applied to improve the balance between static and dynamic mechanical properties. In particular, the most applied heat treatments are direct aging, also called T5 heat treatment (T5), stress relieving treatment (SR), and solution and artificial aging treatment, also called T6 heat treatment (T6). The heat treatments induce different microstructural changes in the AB alloy as a function of the different thermal exposure to which it is subjected [127,142].

In reason of the solidification conditions discussed above, the microstructure of the AB alloy is metastable and may decompose at high temperatures for different soaking times. In particular, the cellular metastable microstructure transforms into a composite-like microstructure when annealed over specific temperature and soaking time conditions (Figure 1.87) [126]. The inter-connected Si phase along the cellular boundaries acts as nucleation sites for the formation of Si particles, and the excess of Si atoms in the Al lattice diffuses out, thus contributing to the growth of the Si particles at these nucleation sites. As a result, a composite-like microstructure constituted by Si particles embedded into an Al-based matrix is observed [112,123], whose size is purely a function of the annealing temperature and soaking time [127,128].

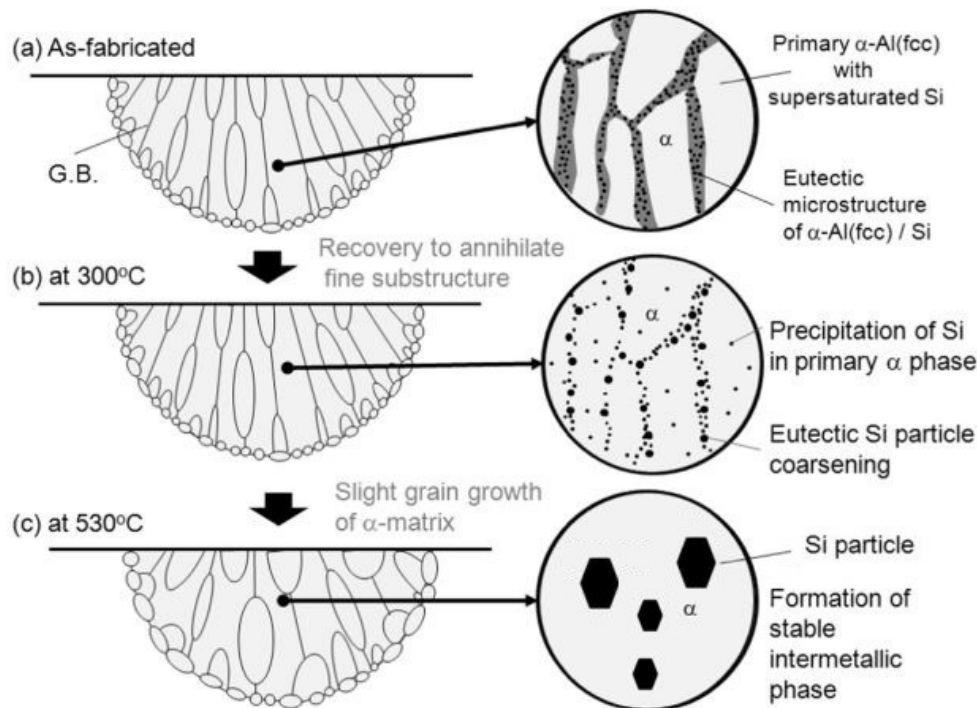
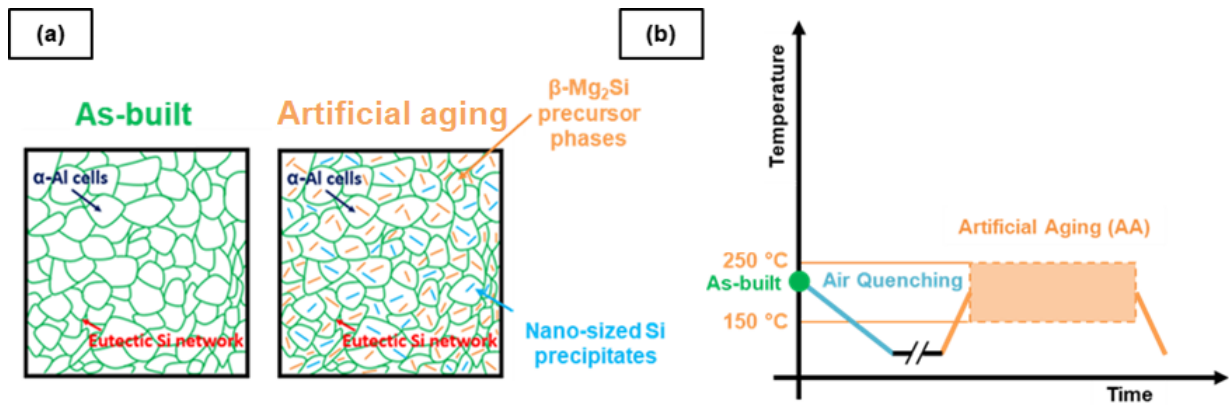


Fig. 1.87. Schematic showing the change in the microstructure of the AB L-PBF AlSi10Mg alloy induced by heat treatment. Adapted from [137]

**T5 heat treatment** is widely adopted to promote fine precipitation of the  $\beta$ -Mg<sub>2</sub>Si precursor phases, and nano-sized Si precipitates inside the  $\alpha$ -Al cells by exploiting the supersaturated Si solution in the Al lattice (Figure 1.88(a)), especially for conditions of zero or moderate preheating of the building platform, and to slightly reduce the RS, thus increasing the ductility of the L-PBF-produced part [116,129-131]. The T5 heat treatment is generally carried out at aging temperatures ( $T_{AA}$ ) between 150 and 250 °C and aging time ( $t_{AA}$ ) between 2 and 6 h to promote precipitation hardening and stress relieving (Figure 1.88(b)) [67,106,121,122,132].



**Fig. 1.88** Scheme of the microstructural evolution induced by the T5 heat treatment: fine precipitation of the  $\beta$ - $Mg_2Si$  precursor phases and nano-sized Si precipitates inside the  $\alpha$ -Al cells (a). Time-temperature diagram of the T5 heat treatment (b).

Focusing on the T5 heat treatment conditions, they do not lead to macroscopic changes in the microstructure, thus leaving unaltered the MP structure and the cellular sub-structure of the AB alloy due to the relatively low thermal exposure (Figures 1.89(a,b)). However, as described above, the short diffusion distances of Si atoms from the supersaturated Al lattice allow the precipitation of the Si precipitates inside the  $\alpha$ -Al cells (Figure 1.89(c)) [105,131,133].

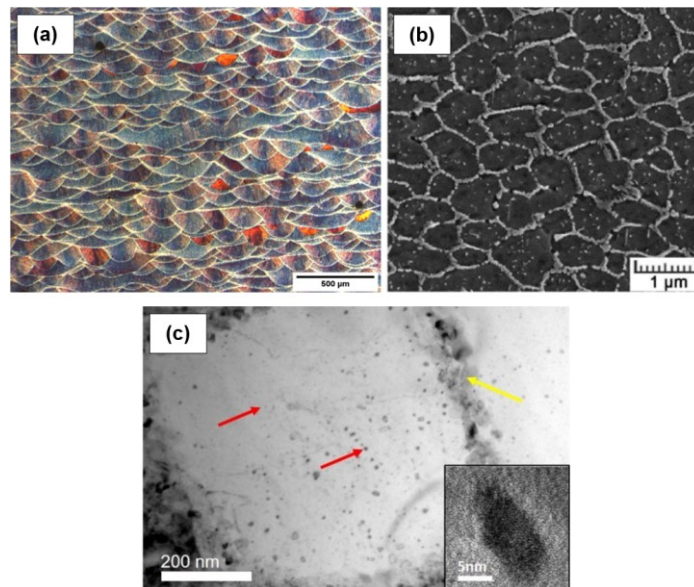


**Fig. 1.89** T5 heat-treated (160 °C for 5 h) microstructure observed at OM (a), SEM-FEG (b), and TEM views of microstructure. Red arrows indicate Si precipitates, while yellow arrows indicate eutectic ribbons. Adapted from [106,129].

In addition, as reported by Fite et al. [129], the low  $T_{AA}$  of the T5 heat treatment does not statistically affect the average grain size and the GBD of the L-PBF AlSi10Mg alloy, even for highly long  $t_{AA}$  (Figure 1.90).

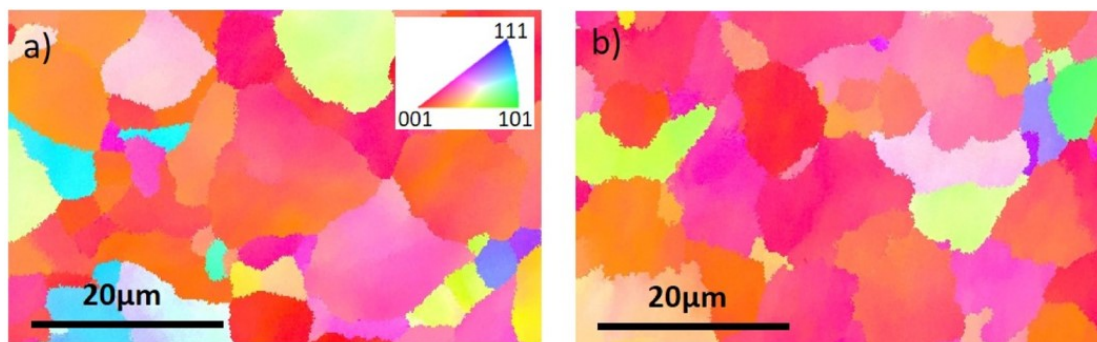


**Fig. 1.90** EBSD maps of the L-PBF AlSi10Mg alloy in the direction parallel to the building platform for L-PBF AlSi10Mg alloy in AB condition (a) and after 604 h at 170 °C aging (b). The IPF legend inset in (a) applies for (a-b). Adapted from [129]. The IPF legend inset in (a) applies for (a-b). Adapted from [129].

The choice of the  $T_{AA}$  and  $t_{AA}$  of the T5 heat treatment are critical to maximizing the mechanical response of the T5 alloy; as described by Zhang et al. [136], a higher  $T_{AA}$  accelerates the precipitation kinetics but increasing the size of the reinforcing precipitates beyond a critical value leads to a reduction in the precipitation hardening effect. The same effect occurs for excessively long  $t_{AA}$ ; in this case, a more prolonged thermal exposure leads to the coalescence of the  $Mg_2Si$  and Si precipitates due to diffusion phenomena, which is associated with an increase in the size of the reinforcing precipitates and a reduction in the reinforcement precipitation [106].

There is probably a thermal exposure threshold value beyond which the total or partial dissolution of the eutectic-Si network and the formation of numerous irregular and coarse Si-rich particles occur and, consequently, a net reduction of the strengthening mechanisms associated with the microstructural refinement and the fine aggregated second phases. According to [126], the Si-rich eutectic phase remains nearly unchanged below 160 °C, while it starts to coarsen and become spherical when the  $T_{AA}$  is higher than 200 °C. However, the network feature is still well retained at 260 °C, whereas a full network breakdown occurs at around 300 °C. The effect of the  $T_{AA}$  appears predominant over the  $t_{AA}$ ; as reported by Fite et al. [129], for example, 604 h at 170 °C is insufficient to dissolve the eutectic-Si network and to produce a significant coarsening of the cellular microstructure in the T5 alloy. Therefore, the optimization of the  $T_{AA}$  and  $t_{AA}$  is necessary to avoid both the fragmentation of the Si eutectic network and the processes of formation and coarsening of the Si particles, maximizing, at the same time, the precipitation hardening.

Ultimately, a correct T5 heat treatment preserves the main strengthening mechanisms of the AB condition (microstructural refinement, solid solution, aggregated second phases) but increases the contribution provided by the precipitation hardening. At the same time, it relieves the RS and reduces the dislocation density, thus slightly improving the ductility [67,136]. In this way, obtaining a higher mechanical property trade-off is possible compared to the AB alloy [116,132]. An example was provided by Fioocchi et al.: in a first paper [137], they described a slight decrease in RS of about 35% and an increase in hardness of about 8% compared to the AB alloy through a relatively low thermal exposure (170 °C for 1.5 h), while, in subsequent work [67] they showed a complete relieving of the RS associated with more severe T5 conditions (3 h at 244 °C), preserving at the same time the eutectic-Si network. However, the latter condition induced a slight strength decrease of about 15% and 10% for YS and UTS values, respectively, due to the excessive coarsening of the strengthening precipitates. In the same way, Rosenthal et al. [131] found a significant strengthening effect on the AB alloy induced by the T5 heat treatment applied at relatively low temperatures, 200 °C for 2 h, associated with an increase of about 5% and 15% in hardness and YS respectively. Tonelli et al. [133] also observed an increase in hardness of approximately 20% for the A357 alloy and a significant relief of the RS post-T5 heat treatment (170 °C for 4 h).

Comparable effects of the T5 heat treatment can be obtained using a heated build platform during the processing of the L-PBF AlSi10Mg alloy; however, this solution can produce a coarser microstructure due to the low thermal gradient and a slight decrease in tensile strength [116,126]. Furthermore, the preheating platform appears to induce microstructural differences along the Z axis for as-built samples due to different thermal gradients associated with inhomogeneous values of UTS and hardness [147,148].

**Stress Relieving** is applied to relieve the RS entirely and increase the AB alloy's ductility significantly. However, these results are accompanied by a significant loss of hardness and strength properties [33,67,100,122,125,131]. The SR is characterized by an annealing temperature ( $T_{SR}$ ) of about 300 °C for a soaking time ( $t_{SR}$ ) between 1 and 2 h (Figure 1.91 (b)). These heat treatment conditions induce the dissolution of the eutectic-Si network and the growth of the initial nano-sized Si particles by the Ostwald ripening mechanism: the Si atoms come out of the supersaturated Al lattice and

move from the eutectic-Si network, thus spreading into the Al matrix to minimize the internal energy of the system [112,127]. As a result, the Si network begins to shrink while the Si particles continue to coalesce, especially along the Al/Si cellular interfaces, thus keeping the memory of the disappearing structure (Figure 1.91(a)) [67,132,138].

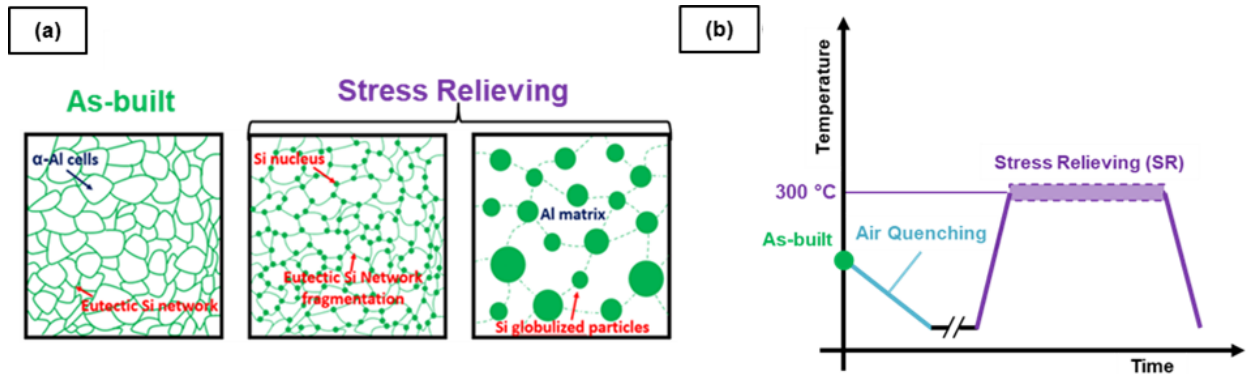


**Fig. 1.91** Scheme of the microstructural evolution induced by the SR heat treatment: the thermal exposure leads to the dissolution of the eutectic-Si network and the consequent formation of the first Si nucleus, which coarsen as the thermal exposure continues, bringing to the formation of coarse Si particles embedded into the  $\alpha$ -Al matrix (a). Time-Temperature diagram of the SR heat treatment (b).

The high temperatures of SR not only affect the metastable cellular structure of the AB alloy but also lead to the partial disappearance of MPs, leaving them still visible (Figures 1.92(a,b)) [33]. However, it does not affect the grain structure, whose microstructural features remain unchanged after annealing at 300 °C (Figure 1.93) [138].

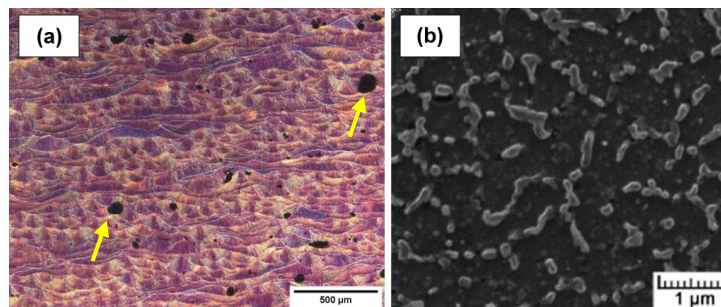


**Fig. 1.92** SR heat-treated (160 °C for 5 h) microstructure observed at optical microscope (a), SEM-FEG (b). Yellow arrows indicate defects located in the bulk material. Adapted from [106].

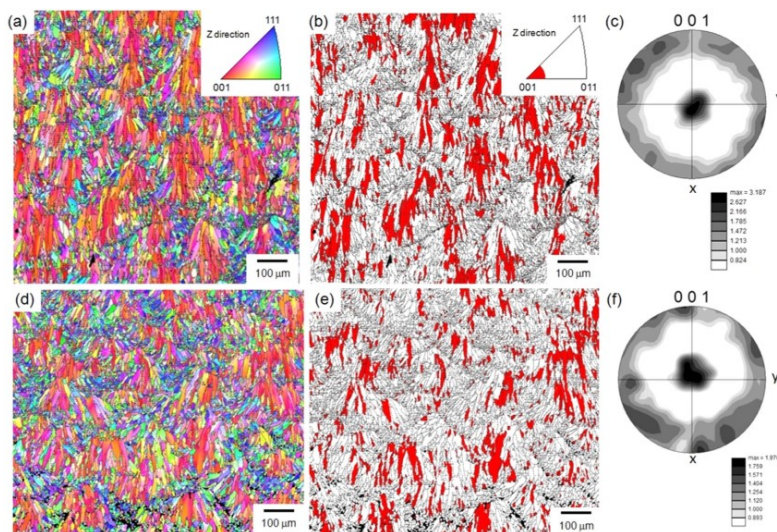


**Fig. 1.93.** Orientation color maps (a,d), distribution maps of [001] oriented regions (less than a 15° deviation was tolerated from the [001] direction parallel to the Z direction) (b,e), and 001 pole figures (c,f) of the AlSi10Mg alloy samples: AB (a-c), and SR (300 °C for 2 h) (d-e). Adapted from [138].

The SR affects the mechanical properties of the AB alloy through the change of the strengthening mechanisms associated with the microstructural evolution induced by the high  $T_{SR}$ , as described above, and the complete relieving of

the RS [122,138,139]. This results in a significant ductility improvement but a decrease in the YS and UTS values [106,31,138]. Prashanth et al. [149] and Takata et al. [138] reported that the mechanical property evolution is attributable to the complete microstructural rearrangement induced by thermally-activated diffusion processes, which affect both the dispersed (nano-sized Si precipitates) and aggregated (eutectic-Si network) strengthening phases. This process leads to forming a composite-like microstructure consisting of spherical Si particles incorporated in an  $\alpha$ -Al matrix and the loss of the strengthening mechanisms linked to the AB microstructure (Figure 1.92(b)). Furthermore, the reinforcement contribution of the second dispersed phase (coarse Si particles) is limited by the coarse size of the Si particles (Orowan looping mechanism) [137], while the drastic decrease of the Si content in solution in Al cells, less than 0.3 wt.% leads to the near disappearance of the solid solution strengthening mechanism [132]. Therefore, both effects increase the ductility of the SR alloy at the expense of tensile strength and fatigue [140,141].

**T6 Heat Treatment** is applied to homogenize the microstructure, increase ductility and reduce the anisotropy of the mechanical behavior and residual stresses of the L-PBF AlSi10Mg alloy while inducing precipitation hardening to avoid a significant decrease in mechanical strength associated with the loss of subcellular structure of the AB alloy. This microstructural evolution improves the compromise between the alloy's static and dynamic mechanical properties [123,128,141]. The high temperatures of the solution step (SHT) first promote the dissolution of the eutectic Si network and then the Si particles' coalescence due to Si diffusion from the supersaturated  $\alpha$ -Al phase [127,142]. It is possible to schematically describe the microstructural evolution of the L-PBF AlSi10Mg alloy during the T6 heat treatment, as shown in Figure 1.94(a). As discussed above, the AB alloy displays a microstructure consisting of a supersaturated Al matrix surrounded by a fibrous eutectic-Si network. During the solution treatment, the Si atoms are rejected from the supersaturated Al matrix and the dissolved eutectic-Si network to form small Si particles. At this stage, the cellular boundaries become blurred. With increasing solution temperature ( $T_{\text{SHT}}$ ), the Si particles generally form along the Al/Si cellular boundaries and grow up with their number decreasing significantly. Then, the coarse Si particles are evenly distributed on the Al matrix. Finally, during artificial aging (AA), the precipitation of both  $\beta''$  and  $\beta'$  strengthening phases (precursors of the  $\text{Mg}_2\text{Si}$  equilibrium phase) occurs, inducing the precipitation hardening by coherent and semi-coherent strengthening phases. Therefore, the T6 heat treatment makes it possible to obtain a balance of the mechanical properties by improving toughness and ductility (thanks to the composite-like microstructure) without inducing a decrease in yield strength (due to the increased contribution of the precipitation hardening) and simultaneously improving the fatigue behavior, as described in [79,83,106,122]. The T6 heat treatment consists of different steps: (i) high-temperature SHT ( $T_{\text{SHT}}$  between 510 and 550 °C, solution soaking time ( $t_{\text{SHT}}$ ) between 1 and 8 h), (ii) water quenching, (iii) AA treatment (aging temperature ( $T_{\text{AA}}$ ) between 160 and 190 °C, and aging time ( $t_{\text{AA}}$ ) between 4 and 12 h (Figure 1.94(b)) [80,122,123,139].

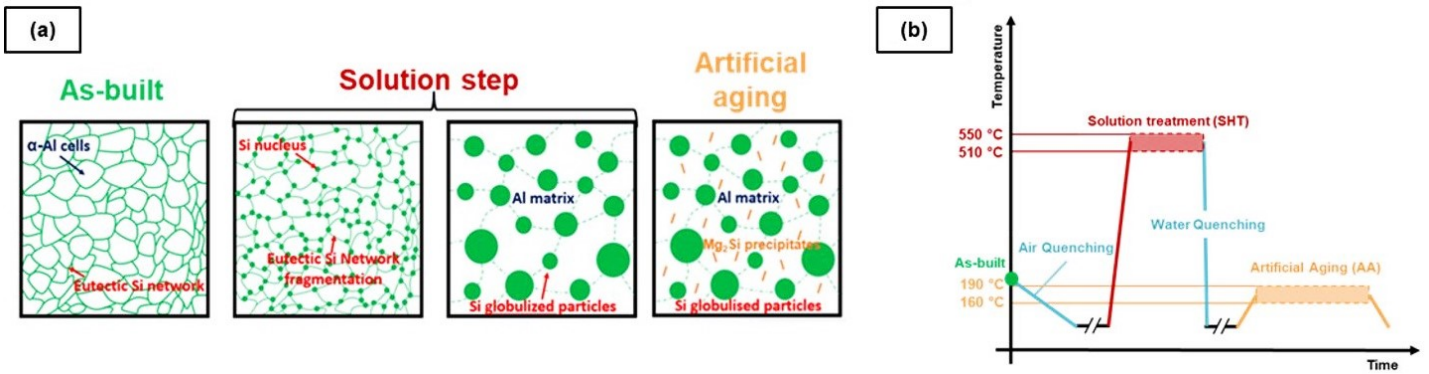


**Fig. 1.94** Scheme of the microstructural evolution induced by the T6 heat treatment: the SHT leads to the dissolution of the eutectic-Si network and the consequent formation of the first Si nucleus, which coarse during the SHT, bringing to the formation of coarse Si particles embedded into the  $\alpha$ -Al matrix. Ultimately, the AA leads to forming of the Mg<sub>2</sub>Si precursor phases (a). Time-Temperature diagram of the T6 heat treatment (b).

The T6 heat treatment induces a complete rearrangement of the AB microstructure. In particular, it deletes the MP structure (Figure 1.95(a)) and forms a more homogeneous composite-like microstructure of Si particles embedded in the  $\alpha$ -Al phase matrix (Figure 1.95(b)) [106,112,127]. These changes are promoted by the high temperatures and the long soaking time of SHT, which cause the dissolution of the eutectic Si network firstly and then the coalescence of the Si particles due to Si diffusion from the supersaturated  $\alpha$ -Al phase [127,128].

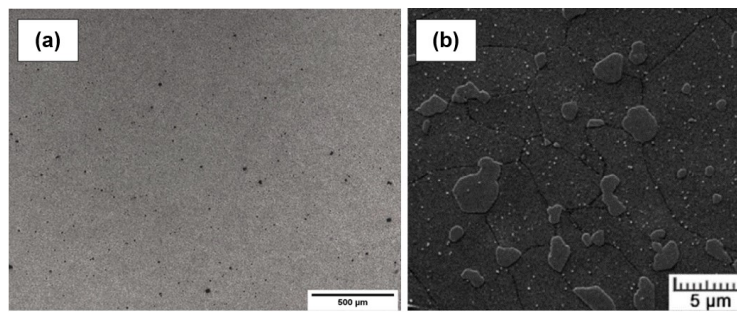


**Fig. 1.95** T6 heat-treated (SHT 510 °C for 6 h, AA 170°C for 4 h) microstructure observed at optical microscope (a), and SEM-FEG (b).

However, it does not induce appreciable modification of the grain structure, which preserves the texture and microstructural features of the AB alloy. However, long  $t_{\text{SHT}}$  promotes a little crystallographic rearrangement linked to a slight coarsening of the grains (Figures 1.96 and 1.97) [79,129,138].

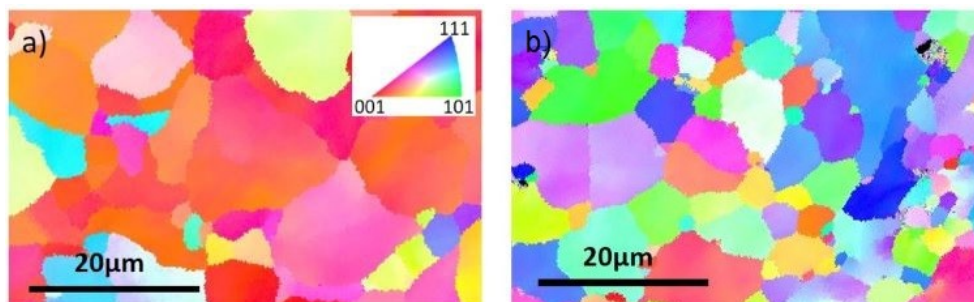


**Fig. 1.96** EBSD maps of the L-PBF AlSi10Mg alloy in the direction parallel to the building platform for L-PBF AlSi10Mg alloy in AB condition (a), and after SHT at 530 °C for 5 h and AA at 170 °C for 604 h (b). The IPF legend inset in (a) applies for (a-b). Adapted from [129].

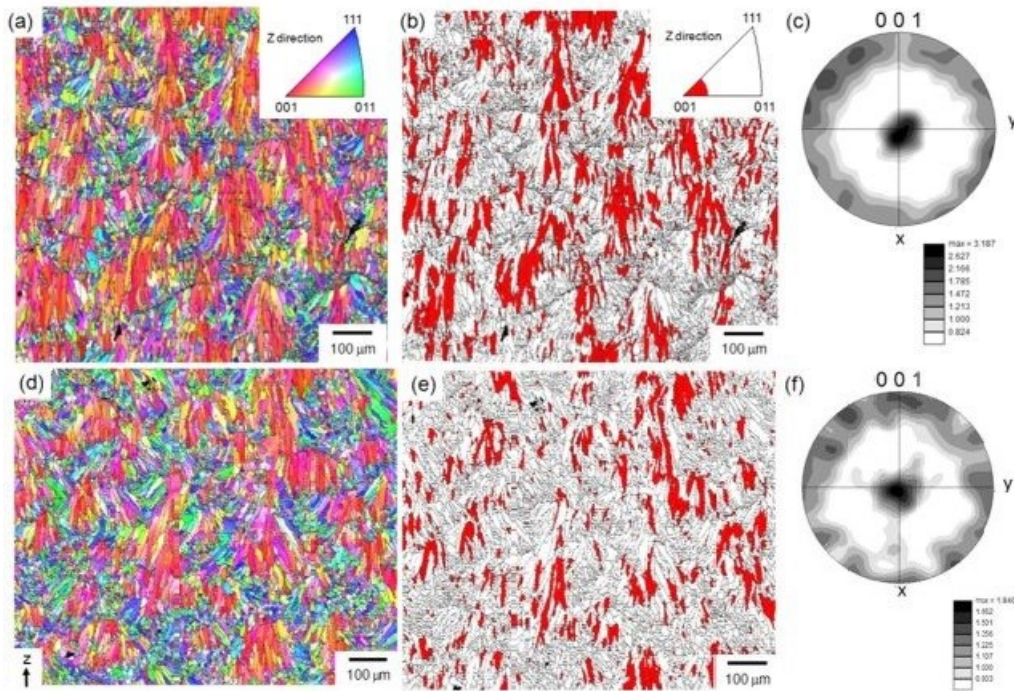


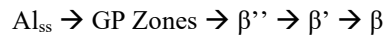
**Fig. 1.97.** Orientation color maps (a,d), distribution maps of [001] oriented regions (less than a 15° deviation was tolerated from the [001] direction parallel to the Z direction) (b,e), and 001 pole figures of the AlSi10Mg alloy samples (c f) for AB (a,b,c), and SHT (530 °C for 6 h) (d,e,f). Adapted from [138].

The effects of the SHT are not limited to microstructural rearrangement; in fact, as described by Tonelli et al. [133], the high  $T_{\text{SHT}}$  makes it possible to homogenize the AB microstructure and to relieve the RS after only 10 min completely. However, the SHT leads to a gas porosity volumetric increase due to the expansion of the gas occluded within them [118,141].

Greater thermal exposure affects the growth of Si particles, which is more significant with increasing  $T_{\text{SHT}}$  or  $t_{\text{SHT}}$ . Therefore, to limit the negative effect on the mechanical properties of the coarse Si particles and maximize the mechanical properties of the T6 alloy, the control, and optimization of the SHT parameters become extremely important. Most researchers [112,127,128,141] proposed that the Si particles' distribution, size, and morphology represent the essential microstructural aspects that influence the mechanical properties of the T6 alloy. In their studies, Tocci et al. [141] and Wang et al. [78] described the detrimental effects of the coarsening of the Si particles on the strength of the T6 heat-treated alloy due to the decrease in the contribution of the Orowan reinforcement mechanism. Iturrioz et al. [128] and Zhang et al. [150] also underlined the importance of limiting the Si particle size to improve cohesion between the Si particles and the Al matrix, suggesting that a homogeneous distribution of fine Si particles could lead to a concurrent increase of both the alloy strength and ductility, induced by the higher cohesion between Si particles and Al matrix. However, as reported by Domfang et al. [79] and Alghamdi et al. [112], the detrimental effects of a higher thermal exposure during the SHT phase do not seem to influence the size and morphology of the grain structure, consequently not negatively affecting the static and dynamic mechanical response of the T6 alloy.

As already mentioned, the nanometric coherent  $\text{Mg}_2\text{Si}$  precipitates are mainly responsible for the high mechanical strength obtained in the T6 condition. The SHT step is fundamental to releasing Mg and Si in the Al matrix and dissolving the coarse  $\text{Mg}_2\text{Si}$  particles previously formed during the L-PBF solidification, thus providing the elements to promote the fine precipitation of the  $\beta\text{-Mg}_2\text{Si}$  precursor phases during the AA [99,112,129]. For this to happen, it is first necessary to retain the dissolved Mg in the Al matrix through rapid quenching from the  $T_{\text{SHT}}$ , usually performed in water ( $T \ll 100 \text{ }^\circ\text{C}$ ). The rapid cooling promotes the formation of a supersaturated Al solid solution ( $\text{Al}_{\text{ss}}$ ) and a high

density of vacancies in the crystal structure. Lastly, the artificial aging treatment stimulates the formation of fine precipitates following a specific precipitation sequence:



Precipitation starts with fully coherent solute-rich clusters termed GP (Guinier-Preston) zones. GP zones are the first to homogeneously nucleate due to their coherency with the matrix and their atomic size. In this stage, vacancies play a significant role in the nucleation of coherent precipitates by promoting diffusion and relieving local strain in the lattice [134]. During aging, solute-rich clusters transform and eventually evolve in an equilibrium phase ( $\beta$ ). However, before reaching the equilibrium phase, two metastable intermediate phases, also termed transition phases, exist: (i)  $\beta''$ , a coherent phase that strongly contributes to the strengthening of the alloy, and (ii)  $\beta'$ , a semi-coherent phase occurring in the first phase of softening. The trend of the alloy strength as a function of aging time and precipitates is given in Figure 1.98. Two main conditions can be recognized: peak-aging, which corresponds to the highest strength that can be reached, and an over-aging condition, where softening occurs due to the formation of the stable incoherent  $\beta$  phase.

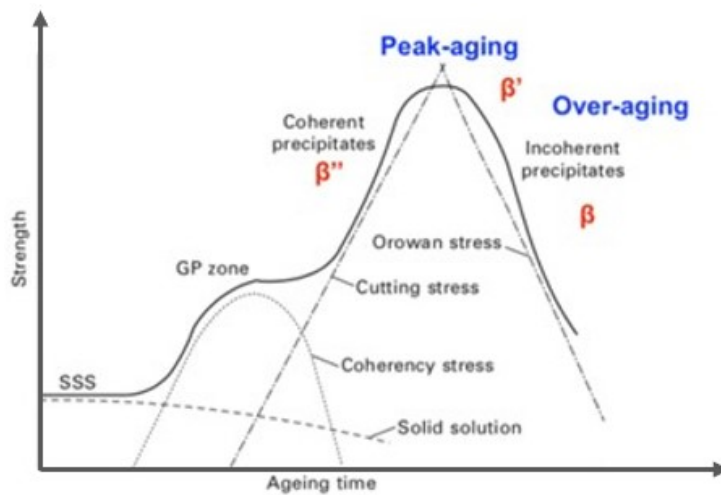


**Fig. 1.98.** The qualitative trend of alloy strength as a function of aging time for an AlSiMg alloy with details of precipitations stages and strengthening mechanisms (adapted from [135])

The nature and distribution of the precipitates of the T6 L-PBF AlSi10Mg alloy were thoroughly analyzed by Zhou et al. [142], which showed the existence of the same precipitation hardening sequence (GP zones  $\rightarrow$   $\beta'' \rightarrow \beta'$ -Mg<sub>2</sub>Si precursor phases) that characterizes the T6 heat-treated AlSiMg cast alloys.

As widely reported in the literature [106,116,122,123,127,141], the T6 heat treatment applied on the L-PBF AlSi10Mg alloy reduces its strength properties, in particular the UTS value, and increases its ductility. The different microstructure leads to different strengthening mechanisms, which entail a different balance between the mechanical properties.

In the T6 alloy, the dissolution of the eutectic-Si network and the disappearance of the fine cellular substructure promote the formation of a coarser microstructure, which are the result of the diffusive processes activated by  $T_{\text{SHT}}$  and lead to the loss of strengthening from the second aggregated phases and microstructural refinement. The composite-like microstructure, consisting of Si particles incorporated in the Al matrix, contributes instead by reinforcement from the second dispersed phases; in particular, the characteristics of the Si particles (distribution, size, and morphology) directly influence the mechanical properties and the fracture mechanisms. The different elastoplastic behavior of the Si particles and the Al matrix influences the crack growth rate and the failure mechanism of the T6 alloy; in fact, the non-homogeneous stress state developed around the larger Si particles promotes the detachment of the  $\alpha$ -Al matrix along the Si particle borders due to the concentration of the plastic flow, accelerating the failure of T6 alloy [100,151]. Therefore,

finer and more numerous Si particles, substantially spherical and homogeneously distributed within the Al matrix, increase the mechanical properties of the alloy both in terms of strength and ductility [128,141].

Precipitation hardening introduced by the AA phase increases the obstacle to the dislocation motion by the Orowan looping mechanism, thus avoiding a significant drop in YS [142]. In addition, the increase in dislocation motion, the stress relieving, and the reduction of the microstructural anisotropy of the L-PBF AlSi10Mg alloy increase both toughness and ductility [116,122,141]. However, the loss of the ultrafine cellular structure of the AB alloy, which acts as a barrier to the dislocation motion and increases the strain-hardening mechanism (Figure 1.83), leads to a significant decrease in the UTS value [113]. This condition limits the formation of high dislocation density and determines lower n-index values of the T6 alloy compared to the AB one.

The microstructural homogenization induced by the T6 heat treatment leads to a higher strength-ductility balance than the AB alloy, thus increasing the fatigue resistance and toughness of the L-PBF AlSi10Mg alloy [79,144]. At the same time, it almost wholly attenuates the mechanical anisotropy typical of the AB alloy [123], which remains only for the different GBD in the cross-sectional plane and parallel to the building direction due to the grain directional structure (Figure 1.97) [138]. This microstructural evolution allows the best compromise among the mechanical properties compared to the other heat treatment conditions of the L-PBF AlSi10Mg alloy, erasing at the same time the problems linked to the directional solidification of the L-PBF technology.

In summarizing, the strengthening mechanisms associated with the different microstructures in the as-built and differently heat-treated alloy are reported in Figure 1.99.

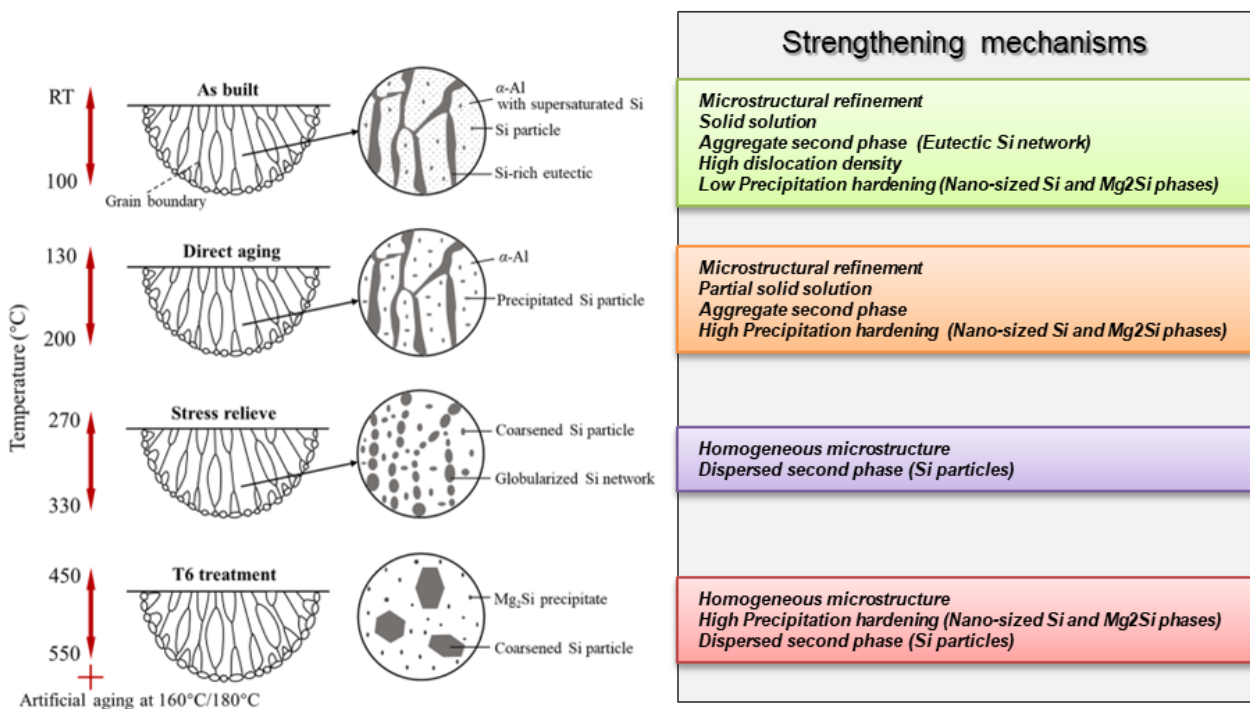


Fig. 1.99 Influence of post-printing heat treatment on the microstructure and strengthening mechanisms of the heat-treated L-PBF AlSi10Mg. Adapted from [126]

The peculiar microstructure of the AB alloy and the microstructural evolution involved during the heat treatments lead to different mechanical properties such as hardness, tensile strength, fatigue resistance, and impact toughness. To understand the effects of microstructural modifications on the reinforcement mechanisms and the mechanical behavior

of the L-PBF AlSi10Mg alloy, the indicative ranges of the different mechanical properties from the literature [21,30,56,66,67,73,78,79,80,106,109,111,116, 118,121-124,126,127-131,137-146] are reported in Table 1.6.

**Table 1.6.** Indicative range of the hardness values for the as-built (AB) and heat-treated (SR, T5, and T6) L-PBF AlSi10Mg alloy. The hardness data reported in the table are converted into HV values according to ASTM E140 (2019) to ease the analysis [139]

	<b>AB</b>	<b>T5</b>	<b>SR</b>	<b>T6</b>
<b>Hardness [HV]</b>	<b>110 - 150</b>	<b>110 - 160</b>	<b>80 - 105</b>	<b>90 - 130</b>
<b>YS [MPa]</b>	<b>170 - 320</b>	<b>260 - 320</b>	<b>150 - 180</b>	<b>160 - 270</b>
<b>UTS [MPa]</b>	<b>280 - 480</b>	<b>310 - 510</b>	<b>250 - 300</b>	<b>250 - 320</b>
<b><math>\epsilon_f</math> [%]</b>	<b>1.0 - 8.0</b>	<b>1.5 - 8.0</b>	<b>5.0 - 18.0</b>	<b>3.0 - 16.0</b>
<b>Fatigue <math>\sigma_{max}</math> [MPa] – Rotating bending R = -1, <math>10^6</math> - <math>10^7</math> cycles</b>	<b>75 - 125</b>	<b>75 - 125</b>	<b>70 - 85</b>	<b>100 - 140</b>
<b>Fatigue <math>\sigma_{max}</math> [MPa] – Axial load R= 0.1, <math>10^7</math> cycles</b>	<b>65 - 135</b>	<b>75 - 125</b>	<b>90 - 120</b>	<b>105 - 165</b>
<b>Toughness [J]</b>	<b>2 - 6</b>	<b>7 - 10</b>	<b>4 - 12</b>	<b>3 - 8</b>

## References

1. International, A. Committee F42 on Additive Manufacturing Technologies. 2009.
2. ASTM International. ISO/ASTM52900-15 Standard Terminology for Additive Manufacturing. West Conshohocken, PA, 2015.
3. N.T. Aboulkhair, M. Simonelli, L. Parry, I. Ashcroft, C. Tuck, R. Hague, 3D printing of Aluminium alloys: Additive Manufacturing of Aluminium alloys using selective laser melting, *Progress in Materials Science*, 106 (2019) 100578. <https://doi.org/10.1016/j.pmatsci.2019.100578>.
4. D. Herzog, V. Seyda, E. Wycisk, C. Emmelmann, Additive manufacturing of metals, *Acta Materialia*, 117 (2016) 371-392. <https://doi.org/10.1016/j.actamat.2016.07.019>.
5. T. DebRoy, H.L. Wei, J.S. Zuback, T. Mukherjee, J.W. Elmer, J.O. Milewski, A.M. Beese, A. Wilson-Heid, A. De, W. Zhang, Additive manufacturing of metallic components – Process, structure and properties, *Progress in Materials Science*, 92 (2018) 112-224. <https://doi.org/10.1016/j.pmatsci.2017.10.001>.
6. W.E. Frazier, Metal Additive Manufacturing: A Review. *J. of Mater Eng and Perform* 23 (2014) 1917–1928. <https://doi.org/10.1007/s11665-014-0958-z>
7. Y. Zhang, L. Wu, X. Guo, S. Kane, Y. Deng, Y.G. Jung, J.H. Lee, J. Zhang. Additive Manufacturing of Metallic Materials: A Review. *J. of Mater Eng and Perform*, 27 (2028) 1–13. <https://doi.org/10.1007/s11665-017-2747-y>.
8. Pola A., Overview on Metal Additive Manufacturing, AIM Winter School of Metallurgy, 2020.
9. A. Vafadar, F. Guzzomi, A. Rassau, K. Hayward, Advances in Metal Additive Manufacturing: A Review of Common Processes, Industrial Applications, and Current Challenges. *Appl. Sci.* 11 (2021) 1213. <https://doi.org/10.3390/app11031213>.
10. I. Gibson, D.W. Rosen, B. Stucker, Additive Manufacturing Technologies 3d Printing, Rapid Prototyping, and Direct Digital Manufacturing, Springer Verlag (2016).
11. C.Y. Yap, K. Chua, Z. Dong, Z. Liu, D. Zhang, L.E. Loh, S.L. Sing, Review of selective laser melting: Materials and applications. *Applied Physics Reviews*, 2 (2015) 041101. <https://doi.org/10.1063/1.4935926>.
12. E.O. Olakanmi, R.F. Cochrane, K.W. Dalgarno, A review on selective laser sintering/melting (SLS/SLM) of aluminium alloy powders: Processing, microstructure, and properties, *Progress in Materials Science*, 74 (2015) 401-477. <https://doi.org/10.1016/j.pmatsci.2015.03.002>.
13. R.J. Herbert, Viewpoint: metallurgical aspects of powder bed metal additive manufacturing, *J Mater Sci*, 51 (2016) 1165–1175. <https://doi.org/10.1007/s10853-015-9479-x>.
14. J. Zhang, B. Song, Q. Wei, D. Bourell, Y. Shi, A review of selective laser melting of aluminum alloys: Processing, microstructure, property and developing trends, *Journal of Materials Science & Technology*, 35(2) (2019) 270-284. <https://doi.org/10.1016/j.jmst.2018.09.004>.
15. <https://additivemanufacturingindia.blogspot.com/2018/04/cad-conversion-and-stl-file-in-additive.html>
16. N.T. Aboulkhair, N.M. Everitt, I. Ashcroft, C. Tuck, Reducing porosity in AlSi10Mg parts processed by selective laser melting, Additive Manufacturing, Volumes 1–4, 2014, Pages 77-86, ISSN 2214-8604, <https://doi.org/10.1016/j.addma.2014.08.001>.
17. A. Sola, A. Nouri, Microstructural porosity in additive manufacturing: The formation and detection of pores in metal parts fabricated by powder bed fusion; *Journal of Advanced Manufacturing and Processing*, 1 (2019) e10021. <https://doi.org/10.1002/amp2.100>.
18. J.P. Kruth, P. Mercelis, J. Van Vaerenbergh, L. Froyen, M. Rombouts, Binding mechanisms in selective laser sintering and selective laser melting, *Rapid Prototyping Journal*, 11(1) (2005) 26-36. <https://doi.org/10.1108/13552540510573365>.
19. T.G. Spears, S.A. Gold, In-process sensing in selective laser melting (SLM) additive manufacturing. *Integr Mater Manuf Innov.* 5 (2016) 16–40. <https://doi.org/10.1186/s40192-016-0045-4>.
20. C. Lun A. Leung, S. Marussi, M. Towrie, J. Val Garcia, R.C. Atwood, A.J. Bodey, J. R. Jones, P.J. Withers, P.D. Lee, Laser-matter interactions in additive manufacturing of stainless steel SS316L and 13-93 bioactive glass revealed by in situ X-ray imaging, *Additive Manufacturing*, 24 (2018) 647-657. <https://doi.org/10.1016/j.addma.2018.08.025>.
21. S. Bagherifard, N. Beretta, S. Monti, M. Riccio, M. Bandini, M. Guagliano, On the fatigue strength enhancement of additive manufactured AlSi10Mg parts by mechanical and thermal post-processing, *Materials & Design*, 145 (2018) 28-41. <https://doi.org/10.1016/j.matdes.2018.02.055>.
22. A. Pantarelli, Trattamenti termici della lega AlSi10Mg realizzata mediante Additive Manufacturing: microstruttura e proprietà meccaniche, Politecnico di Torino, (2019).
23. L. Markusson, Powder Characterization for Additive Manufacturing Processes, Luleå University of Technology, (2017).
24. J.A. Slotwinski, E.J. Garboczi, P.E. Stutzman, C.F. Ferraris, S.S. Watson, M.A. Peltz, Characterization of Metal Powders Used for Additive Manufacturing. *J Res Natl Inst Stand Technol.*, 19 (2014) 460–493. <https://doi.org/10.6028/jres.119.018>.
25. K. Riemer, N. Albrecht, S. Ziegelmeier, R. Ramakrishnan, L. Haferkamp, A.B. Spierings, G.J. Leichtfried, Influence of particle size distribution and morphology on the properties of the powder feedstock as well as of AlSi10Mg parts produced by laser powder bed fusion (LPBF). *Addit. Manuf.*, 34 (2020) 101286. <https://doi.org/10.1016/j.addma.2020.101286>.
26. Zhong, C.; Biermann, T.; Gasser, A.; Poprawe, R. Experimental study of effects of main process parameters on porosity, track geometry, deposition rate, and powder efficiency for high deposition rate laser metal deposition. *J. Laser Appl.*, 27(4) (2015) 042003. <https://doi.org/10.2351/1.4923335>.
27. T.M. Wischeropp, C. Emmelmann, M. Brandt, A. Pateras, Measurement of actual powder layer height and packing density in a single layer in selective laser melting, *Additive Manufacturing*, 28 (2019) 176-183, <https://doi.org/10.1016/j.addma.2019.04.019>.
28. D. Huck-Jones, C. Langley, Beyond particle size: Exploring the influence of particle shape on metal powder performance, *Metal AM - The Magazine For The Metal Additive Manufacturing Industry*, 3(4) (2017).
29. J. Dawes, R. Bowerman, R. Trepleton, Introduction to the Additive Manufacturing Powder Metallurgy Supply Chain. *Johnson Matthey Technology Review*, 59 (2015), 243-256. <https://doi.org/10.1595/205651315X688686>.
30. N. Read, W. Wang, K. Essa, M. M. Attallah, Selective laser melting of AlSi10Mg alloy: Process optimisation and mechanical properties development, *Materials & Design* (1980-2015), 65 (2015) 417-424. <https://doi.org/10.1016/j.matdes.2014.09.044>.
31. T. Laumer, T. Stichel, K. Nagulin, M. Schmidt, Optical analysis of polymer powder materials for Selective Laser Sintering. *Polym. Test.*, 56 (2016) 207–213. <https://doi.org/10.1016/j.polymertesting.2016.10.010>.

32. S.L. Sing, W.Y. Yeong, Laser powder bed fusion for metal additive manufacturing: perspectives on recent developments, *Virtual and Physical Prototyping*, 15(3) (2020) 359-370, <https://doi.org/10.1080/17452759.2020.1779999>.
33. A.H. Maamoun, M. Elbestawi, G.K. Dosbaeva, S.C. Veldhuis, Thermal post-processing of AlSi10Mg parts produced by Selective Laser Melting using recycled powder, *Additive Manufacturing*, 21 (2018) 234-247, <https://doi.org/10.1016/j.addma.2018.03.014>.
34. H. Asgari, C. Baxter, K. Hosseinkhani, M. Mohammadi, On microstructure and mechanical properties of additively manufactured AlSi10Mg 200C using recycled powder, *Materials Science and Engineering: A*, 707 (2017) 148-158, <https://doi.org/10.1016/j.msea.2017.09.041>.
35. H. Lee, C.H.J. Lim, M.J. Low, V.M. Murukeshan, Y.J. Kim, Lasers in additive manufacturing: A review. *Int. J. of Precis. Eng. and Manuf.-Green Tech.*, 4 (2017) 307-322. <https://doi.org/10.1007/s40684-017-0037-7>.
36. G. Veerhaeghe, P. Hilton, Battle of the sources – using a high power Yb-fibre laser for welding steel and aluminium. In: Junek L, editor. *Proceedings of the IIW Conference on Benefits of New Methods and Trends in Welding to Economy, Productivity and Quality*, 10-15 July, Prague, Czech Republic, (2005) 188-200.
37. L. Quintino, R. Miranda, U. Dilthey, D. Iordachescu, M. Banasik, S. Stano, Laser Welding of Structural Aluminium. In: Moreira, P., da Silva, L., de Castro, P. (eds) *Structural Connections for Lightweight Metallic Structures*. *Advanced Structured Materials*, 8 (2010) Springer, Berlin, Heidelberg. [https://doi.org/10.1007/8611\\_2010\\_46](https://doi.org/10.1007/8611_2010_46).
38. A. Basak, S. Das, Epitaxy and microstructure evolution in metal additive manufacturing. *Annu. Rev. Mater. Res.*, 46 (2016) 125-149. <https://doi.org/10.1146/annurev-matsci-070115-031728>.
39. M. Balbaa, S. Mekhiel, M. Elbestawi, J. McIsaac, On selective laser melting of Inconel 718: Densification, surface roughness, and residual stress, *Materials & Design*, 193 (2020) 108818, <https://doi.org/10.1016/j.matdes.2020.108818>.
40. Q. Shi, D. Gu, M. Xia, S. Cao, T. Rong Effects of laser processing parameters on thermal behaviour and melting/solidification mechanism during selective laser melting of TiC/Inconel 718 composites *Optics and Laser Technology*, 84 (2016) 9-22. <https://doi.org/10.1016/j.optlastec.2016.04.009>.
41. T. Qi, H. Zhu, H. Zhang, J. Yin, L. Ke, X. Zeng, Selective laser melting of Al7050 powder: Melting mode transition and comparison of the characteristics between the keyhole and conduction mode, *Materials & Design*, 135 (2017) 257-266, <https://doi.org/10.1016/j.matdes.2017.09.014>.
42. X. Liu, C. Zhao, X. Zhou, Z. Shen, W. Liu, Microstructure of selective laser melted AlSi10Mg alloy, *Materials & Design*, 168 (2019) 107677. <https://doi.org/10.1016/j.matdes.2019.107677>.
43. P. Hanzl, M. Zetek, T. Bakša, T. Kroupa, The Influence of Processing Parameters on the Mechanical Properties of SLM Parts, *Procedia Engineering*, 100 (2015) 1405-1413. <https://doi.org/10.1016/j.proeng.2015.01.510>.
44. P.C. Collins, D.A. Brice, P. Samimi, I. Ghamarian, H.L. Fraser Microstructural control of additively manufactured metallic materials *Ann Rev Mater Res*, 46 (2016) 63-91. <https://doi.org/10.1146/annurev-matsci-070115-031816>.
45. X. Xiao, C. Lu, Y. Fu, X. Ye, L. Song, Progress on Experimental Study of Melt Pool Flow Dynamics in Laser Material Processing, in *Liquid Metals*, London, United Kingdom: IntechOpen, (2021) <https://www.intechopen.com/chapters/76127> doi: 10.5772/intechopen.97205.
46. J. Mazumder, Overview of melt dynamics in laser processing. *Optical Engineering*, 30(8) (1991) 1208. DOI:10.1117/12.55899.
47. P.S. Cook, A.B. Murphy. Simulation of Melt Pool Behaviour during Additive Manufacturing: Underlying Physics and Progress. *Additive Manufacturing*, 31 (2019) 100909. <https://doi.org/10.1016/j.addma.2019.100909>.
48. S. Kou, Fluid Flow and Metal Evaporation in Welding, in: *Weld. Metall.*, Second edi, John Wiley & Sons, Hoboken, New Jersey, (2003) 97-122.
49. L. Tonelli, Additive manufacturing by LPBF and WAAM of metals: correlation between production process, microstructure and mechanical properties. *Università di Bologna* (2021).
50. X. Zhou, X. Liu, D. Zhang, Z. Shen, W. Liu, Balling phenomena in selective laser melted tungsten, *J. Mater. Process. Technol.* 222 (2015) 33-42. <https://doi.org/10.1016/j.jmatprotec.2015.02.032>.
51. S. Zou, H. Xiao, F. Ye, Z. Li, W. Tang, F. Zhu, C. Chen, C. Zhu, Numerical analysis of the effect of the scan strategy on the residual stress in the multi-laser selective laser melting, *Results in Physics*, 16 (2020) 103005, <https://doi.org/10.1016/j.rinp.2020.103005>.
52. C. Galy, E.L. Guen, E. Lacoste, C. Arvieu, Main defects observed in aluminum alloy parts produced by SLM: From causes to consequences, *Additive Manufacturing*, 22 (2018) 165-175. <https://doi.org/10.1016/j.addma.2018.05.005>.
53. Z. Dong, Y. Liu, W. Li, J. Liang, Orientation dependency for microstructure, geometric accuracy and mechanical properties of selective laser melting AlSi10Mg lattices, *Journal of Alloys and Compounds*, 791 (2019) 490-500, <https://doi.org/10.1016/j.jallcom.2019.03.344>.
54. J.P. Oliveira, A.D. LaLonde, J. Ma, Processing parameters in laser powder bed fusion metal additive manufacturing, *Materials & Design*, 193 (2020) 108762, <https://doi.org/10.1016/j.matdes.2020.108762>.
55. B. Zhang, Y. Li, Q. Bai, Defect Formation Mechanisms in Selective Laser Melting: A Review. *Chin. J. Mech. Eng.* 30 (2017) 515-527. <https://doi.org/10.1007/s10033-017-0121-5>.
56. M. Tang, P.C. Pistorius, Oxides, porosity and fatigue performance of AlSi10Mg parts produced by selective laser melting, *International Journal of Fatigue*, 94(2) (2017) 192-201, <https://doi.org/10.1016/j.ijfatigue.2016.06.002>.
57. S. Pauly, P. Wang, U. Kühn, K. Kosiba, Experimental determination of cooling rates in selectively laser-melted eutectic Al-33Cu, *Addit Manuf*, 22 (2018) 753-757. <https://doi.org/10.1016/j.addma.2018.05.034>.
58. C. Panwisawas, Y.T. Tang, R.C. Reed, Metal 3D printing as a disruptive technology for superalloys, *Nat. Commun.* 11 (2020) 2327. <https://doi.org/10.1038/s41467-020-16188-7>.
59. S. Shrestha, T. Starr, K. Chou, A Study of Keyhole Porosity in Selective Laser Melting: Single-Track Scanning With Micro-CT Analysis" *ASME. J. Manuf. Sci. Eng.*, 141(7) (2019) 071004. <https://doi.org/10.1115/1.4043622>.
60. Q. Tan, Y. Liu, Z. Fan, J. Zhang, Y. Yin, M.X. Zhang, Effect of processing parameters on the densification of an additively manufactured 2024 Al alloy, *Journal of Materials Science & Technology*, 58 (2020) 34-45. <https://doi.org/10.1016/j.jmst.2020.03.070>.
61. Thibaut de Terris, Olivier Andreau, Patrice Peyre, Frédéric Adamski, Imade Koutiri, Cyril Gorny, Corinne Dupuy, Optimization and comparison of porosity rate measurement methods of Selective Laser Melted metallic parts, *Additive Manufacturing*, Volume 28, 2019, Pages 802-813, ISSN 2214-8604, <https://doi.org/10.1016/j.addma.2019.05.035>.

62. D. Wang, S. Wu, F. Fu, S. Mai, Y. Yang, Y. Liu, C. Song, Mechanisms and characteristics of spatter generation in SLM processing and its effect on the properties, *Materials & Design*, 117 (2017) 121-130, <https://doi.org/10.1016/j.matdes.2016.12.060>.
63. A. Salmi, E. Atzeni (2017) History of residual stress during the production phases of AlSi10Mg parts processed by powder bed additive manufacturing technology, *Virtual and Physical Prototyping*, 12(2) (2017) 153-160. <https://doi.org/10.1080/17452759.2017.1310439>.
64. J.L. Bartlett, X. Li, An overview of residual stress in metal powder bed fusion, *Additive Manufacturing*, 27 (2019) 131-149, <https://doi.org/10.1016/j.addma.2019.02.020>.
65. S. Marola, D. Manfredi, G. Fiore, M. G. Poletti, M. Lombardi, P. Fino, L. Battezzati, A comparison of Selective Laser Melting with bulk rapid solidification of AlSi10Mg alloy, *Journal of Alloys and Compounds*, 742 (2018) 271-279. <https://doi.org/10.1016/j.jallcom.2018.01.309>.
66. L. Wang, X. Jiang, Y. Zhu, Z. Ding, X. Zhu, J. Sun, B. Yan, Investigation of performance and residual stress generation of AlSi10Mg processed by selective laser melting. *Advances in Materials Science and Engineering*, 12 (2018) 7814039. <https://doi.org/10.1155/2018/7814039>.
67. J. Fiochi, C.A. Biffi, C. Colombo, L.M. Vergani, A. Tuissi. Ad Hoc Heat Treatments for Selective Laser Melted Alsi10mg Alloy Aimed at Stress-Relieving and Enhancing Mechanical Performances. *JOM* 72, 1118–1127 (2020). <https://doi.org/10.1007/s11837-019-03973-z>.
68. <https://www.metal-am.com/articles/70927-2/>
69. D. Koutny, D. Palousek, L. Pantelejev, C. Hoeller, R. Pichler, L. Tesicky, J. Kaiser, Influence of Scanning Strategies on Processing of Aluminum Alloy EN AW 2618 Using Selective Laser Melting, *Materials*, 11(2) (2018) 298. <https://doi.org/10.3390/ma11020298>.
70. U. Patakham, A. Palasay, P. Wila, R. Tongsri, MPB characteristics and Si morphologies on mechanical properties and fracture behavior of SLM AlSi10Mg, *Materials Science and Engineering: A*, 821 (2021) 141602. <https://doi.org/10.1016/j.msea.2021.141602>.
71. J. Delahaye, J. Tchoufang Tchuidjang, J. Lecomte-Beckers, O. Rigo, A.M. Habraken, A. Mertens, Influence of Si precipitates on fracture mechanisms of AlSi10Mg parts processed by Selective Laser Melting, *Acta Materialia*, 175 (2019) 160-170, <https://doi.org/10.1016/j.actamat.2019.06.013>.
72. M.J. Paul, Q. Liu, J.P. Best, X. Li, J.J. Kruzic, U. Ramamurty, B. Gludovatz, Fracture resistance of AlSi10Mg fabricated by laser powder bed fusion, *Acta Materialia*, 211 (2021) 116869. <https://doi.org/10.1016/j.actamat.2021.116869>.
73. L. Thijs, K. Kempen, J.P. Kruth, J. Van Humbeeck, Fine-structured aluminium products with controllable texture by selective laser melting of pre-alloyed AlSi10Mg powder, *Acta Mater.*, 61 (2013) 1809–1819. <https://doi.org/10.1016/j.actamat.2012.11.052>.
74. E. Beevers, A.D. Brandão, J. Gumpinger, M.Gschweilt, C. Seyfert, P. Hofbauer, T. Rohr, T. Ghidini, Fatigue properties and material characteristics of additively manufactured AlSi10Mg – Effect of the contour parameter on the microstructure, density, residual stress, roughness and mechanical properties, *International Journal of Fatigue*, 117 (2018) 148-162. <https://doi.org/10.1016/j.ijfatigue.2018.08.023>.
75. A.P. Babu, A. Huang, N. Birbilis, On the heat treatment and mechanical properties of a high solute Al–Zn–Mg alloy processed through laser powder bed fusion process, *Materials Science and Engineering: A*, 807 (2021) 140857. <https://doi.org/10.1016/j.msea.2021.140857>.
76. M. S. Kenevisi, Y. Yu, F. Lin, A review on additive manufacturing of Al–Cu (2xxx) aluminium alloys, processes and defects, *Materials Science and Technology*, Volume 37(9) 805-829 (2021). <https://doi.org/10.1080/02670836.2021.1958487>.
77. F. Trevisan, F. Calignano, M. Lorusso, J. Pakkanen, A. Aversa, E.P. Ambrosio, M. Lombardi, P. Fino, D. Manfredi, On the Selective Laser Melting (SLM) of the AlSi10Mg Alloy: Process, Microstructure, and Mechanical Properties, *Materials* 10(1) (2017) 76. <https://doi.org/10.3390/ma10010076>.
78. L.F. Wang, J. Sun, X.L. Yu, Y. Shi, X.G. Zhu, L.Y. Cheng, H.H. Liang, B. Yan, L.J. Guo, Enhancement in mechanical properties of selectively laser-melted AlSi10Mg aluminum alloys by T6-like heat treatment, *Materials Science and Engineering: A*, 734 (2018) 299-310. <https://doi.org/10.1016/j.msea.2018.07.103>.
79. J. N. Domfang Ngnekou, Y. Nadot, G. Henaff, J. Nicolai, W. H. Kan, J. M. Cairney, L. Ridosz, *International Journal of Fatigue*, 119 (2019) 160-172. <https://doi.org/10.1016/j.ijfatigue.2018.09.029>
80. N. T. Aboulkhair, I. Maskery, C. Tuck, I. Ashcroft, N.M. Everitt, The microstructure and mechanical properties of selectively laser melted AlSi10Mg: The effect of a conventional T6-like heat treatment, *Materials Science and Engineering: A*, 667 (2016) 139-146. <https://doi.org/10.1016/j.msea.2016.04.092>.
81. D.M. Stefanescu, R. Ruxanda, *ASM International Volume 9, Fundamentals of Solidification, Metallography and Microstructures*, Editor(s): Vander Voort, George F., (2004) 71-92.
82. J.N. DuPont, *Fundamentals of Weld Solidification*. In *Welding Fundamentals and Processes*; Lienert, T., Siewert, T., Babu, S., Acoff, V., Eds.; ASM International: Almere, The Netherlands, (2011) 96-114. <https://doi.org/10.31399/asm.hb.v06a.a0005609>.
83. K.G. Prashanth, J. Eckert, Formation of metastable cellular microstructures in selective laser melted alloys, *Journal of Alloys and Compounds*, 707 (2017) 27-34, <https://doi.org/10.1016/j.jallcom.2016.12.209>.
84. W.J. Boettinger, D.K. Banerjee, Chapter 7 - Solidification, Editor(s): David E. Laughlin, Kazuhiro Hono, *Physical Metallurgy* (Fifth Edition), Elsevier, (2014) 639-850. <https://doi.org/10.1016/B978-0-444-53770-6.00007-1>.
85. R.E. Smallman, A.H.W. Ngan, Chapter 3 - Solidification, Editor(s): R.E. Smallman, A.H.W. Ngan, *Modern Physical Metallurgy* (Eighth Edition), Butterworth-Heinemann, (2014) 93-119. <https://doi.org/10.1016/B978-0-08-098204-5.00003-1>.
86. R.A. Michelin, A. Munari, Chapter 7 – Termodinamica e principi di termodinamica chimica, Editor(s): CEDAM, *Fondamenti di chimica* (II edizione), Wolters Kluwer Italia srl, (2011) 215-241, ISBN 978-88-13-31401-9.
87. Fredriksson, Hasse, and Ulla Åkerlind. *Solidification and Crystallization Processing in Metals and Alloys*, John Wiley & Sons, Incorporated, 2012. ProQuest Ebook Central, <http://ebookcentral.proquest.com/lib/unibo/detail.action?docID=956555>.
88. <http://people.virginia.edu/~lj2n/mse305/notes/Nucleation.pdf>
89. R. Abbaschian, L. Abbaschian, R. E. Reed-Hill, *Physical Metallurgy Principles* 4ed. (Cengage Learning 2009)
90. F. Pochly, S. Fialová, M. Kozubkova, L. Zavadil, Lukas. Study of the Adhesive Coefficient Effect on the Hydraulic Losses and Cavitation. *International Journal of Fluid Machinery and Systems*, 3 (2010) 386–395. <https://doi.org/10.5293/IJFMS.2010.3.4.386>.

91. G. Yu, D. Gu, D. Dai, M. Xia, C. Ma, Q. Shi, On the role of processing parameters in thermal behavior, surface morphology and accuracy during laser 3D printing of aluminum alloy. *J. Phys. D: Appl. Phys.* 49 (2016) 135501. <http://dx.doi.org/10.1088/0022-3727/49/13/135501>.
92. A. Hadadzadeh, B.S. Amirkhiz, J. Li, M. Mohammadi, Columnar to equiaxed transition during direct metal laser sintering of AlSi10Mg alloy: Effect of building direction, *Additive Manufacturing*, 23 (2018) 121-131. <https://doi.org/10.1016/j.addma.2018.08.00>.
93. H. Qin, V. Fallah, Q. Dong, M. Brochu, M. R. Daymond, M. Gallerneault, Solidification pattern, microstructure and texture development in Laser Powder Bed Fusion (L-PBF) of Al10SiMg alloy, *Materials Characterization*, 145 (2018) 29-38. <https://doi.org/10.1016/j.matchar.2018.08.025>.
94. Trivedi, R. & Kurz, W. Dendritic growth. *Int. Mater. Rev.* 39 (1994) 49–74. <https://doi.org/10.1179/imr.1994.39.2.49>.
95. S. Marola, S. Bosia, A. Veltro, G. Fiore, D. Manfredi, M. Lombardi, G. Amato, M. Baricco, L. Battezzati, Residual stress in additively manufactured AlSi10Mg: Raman spectroscopy and X-ray diffraction analysis, *Materials & Design*, 202 (2021) 109550, <https://doi.org/10.1016/j.matdes.2021.109550>.
96. M. Javidani, D. Larouche D, Application of cast Al–Si alloys in internal combustion engine components. *International Materials Reviews*, 59(3) (2014) 132-158. <https://doi.org/10.1179/1743280413Y.0000000027>.
97. G.E. Totten, D.S. MacKenzie, editors. *Handbook of Aluminum: Volume 2: Alloy Production and Materials Manufacturing*. Volume 2 CRC Press; Boca Raton, FL, USA (2003).
98. J. Wu, X.Q. Wang, W. Wang, M.M. Attallah, M.H. Loretto, Microstructure and strength of selectively laser melted AlSi10Mg, *Acta Materialia*, 117 (2016) 311-320, <https://doi.org/10.1016/j.actamat.2016.07.012>.
99. A. Hadadzadeh, B. S. Amirkhiz, M. Mohammadi, Contribution of Mg2Si precipitates to the strength of direct metal laser sintered AlSi10Mg, *Materials Science and Engineering: A*, 739 (2019) 295-300. <https://doi.org/10.1016/j.msea.2018.10.055>.
100. N. Takata, M. Liu, H. Kodaira, A. Suzuki, M. Kobashi, Anomalous strengthening by supersaturated solid solutions of selectively laser melted Al–Si-based alloys, *Additive Manufacturing*, 33 (2020) 101152. <https://doi.org/10.1016/j.addma.2020.101152>.
101. M. Gäumann, S. Henry, F. Cléton, J.D. Wagnière, W. Kurz, Epitaxial laser metal forming: analysis of microstructure formation, *Materials Science and Engineering: A*, 271(1–2) (1999) 232-241, [https://doi.org/10.1016/S0921-5093\(99\)00202-6](https://doi.org/10.1016/S0921-5093(99)00202-6).
102. M. Asta, C. Beckermann, A. Karma, W. Kurz, R. Napolitano, M. Plapp, G. Purdy, M. Rappaz, R. Trivedi, Solidification microstructures and solid-state parallels: recent developments, future directions, *Acta Mater.* 57 (2009) 941-971 <https://doi.org/10.1016/j.actamat.2008.10.020>.
103. S.K. Bose, R. Kumar, Structure of rapidly solidified aluminium-silicon alloys. *J Mater Sci*, 8 (1973) 1795–1799. <https://doi.org/10.1007/BF02403532>.
104. T. Maeshima, K. Oh-ishi. Solute clustering and supersaturated solid solution of AlSi10Mg alloy fabricated by selective laser melting. *Heliyon* 5(2) (2019) e01186. <https://doi.org/10.1016/j.heliyon.2019.e01186>.
105. Fousova, M.; Dvorsky, D.; Vronka, M.; Vojtech, D.; Lejcek, P. The Use of Selective Laser Melting to Increase the Performance of AlSi9Cu3Fe Alloy. *Materials* 11 (2018) 1918. <https://doi.org/10.3390/ma11101918>
106. M. Fousová, D. Dvorský, A. Michalcová, D. Vojtěch, Changes in the microstructure and mechanical properties of additively manufactured AlSi10Mg alloy after exposure to elevated temperatures, *Materials Characterization*, 137 (2018) 119-126. <https://doi.org/10.1016/j.matchar.2018.01.028>.
107. Z.H. Xiong, S.L. Liu, S.F. Li, Y. Shi, Y.F. Yang, R.D.K. Misra, Role of melt pool boundary condition in determining the mechanical properties of selective laser melting AlSi10Mg alloy, *Materials Science and Engineering: A*, 740–741 (2019) 148-156. <https://doi.org/10.1016/j.msea.2018.10.083>.
108. Y. Kok, X.P. Tan, P. Wang, M.L.S. Nai, N.H. Loh, E. Liu, S.B. Tor, Anisotropy and heterogeneity of microstructure and mechanical properties in metal additive manufacturing: A critical review, *Materials & Design*, 139 (2018) 565-586. <https://doi.org/10.1016/j.matdes.2017.11.021>.
109. K. Kempen, L. Thijs, J. Van Humbeeck, J.-P. Kruth, Mechanical Properties of AlSi10Mg Produced by Selective Laser Melting, *Physics Procedia*, 39 (2012) 439-446. <https://doi.org/10.1016/j.phpro.2012.10.059>.
110. W. H. Kan, Y. Nadot, M. Foley, L. Ridosz, G. Proust, J. M. Cairney, Factors that affect the properties of additively-manufactured AlSi10Mg: Porosity versus microstructure, *Additive Manufacturing*, 29 (2019) 100805, <https://doi.org/10.1016/j.addma.2019.100805>.
111. E. Brandl, U. Heckenberger, V. Holzinger, D. Buchbinder. Additive manufactured AlSi10Mg samples using Selective Laser Melting (SLM): Microstructure, high cycle fatigue, and fracture behavior. *Materials & Design*, 34 (2012) 159-169. <https://doi.org/10.1016/j.matdes.2011.07.067>.
112. F. Alghamdi, X. Song, A. Hadadzadeh, B. Shalchi-Amirkhiz, M. Mohammadi, M. Haghshenas, Post heat treatment of additive manufactured AlSi10Mg: On silicon morphology, texture and small-scale properties, *Materials Science and Engineering: A*, 783 (2020) 139296. <https://doi.org/10.1016/j.msea.2020.139296>.
113. B. Chen, S.K. Moon, X. Yao, G. Bi, J. Shen, J. Umeda, K. Kondoh, Strength and strain hardening of a selective laser melted AlSi10Mg alloy, *Scripta Materialia*, 141 (2017) 45-49. <https://doi.org/10.1016/j.scriptamat.2017.07.025>.
114. Q. Liu, H. Wu, M.J. Paul, P. He, Z. Peng, B. Gludovatz, J.J. Kruczic, C.H. Wang, X. Liu, Machine-learning assisted laser powder bed fusion process optimization for AlSi10Mg: New microstructure description indices and fracture mechanisms, *Acta Mater.* 201 (2020) 316–328. <https://doi.org/10.1016/j.actamat.2020.10.010>.
115. M. Tang, P.C. Pistorius, S. Narra, J.L. Beuth, Rapid Solidification: Selective Laser Melting of AlSi10Mg. *JOM* 68, 960–966 (2016). <https://doi.org/10.1007/s11837-015-1763-3>.
116. R. Casati, M.N. Hamidi, M. Coduri, V. Tirelli, M. Vedani, Effects of Platform Pre-Heating and Thermal-Treatment Strategies on Properties of AlSi10Mg Alloy Processed by Selective Laser Melting. *Metals*, 8(11) (2018) 954. <https://doi.org/10.3390/met8110954>.
117. H. Qin, V. Fallah, Q. Dong, M. Brochu, M. R. Daymond, M. Gallerneault, Solidification pattern, microstructure and texture development in Laser Powder Bed Fusion (L-PBF) of Al10SiMg alloy, *Materials Characterization*, 145 (2018) 29-38. <https://doi.org/10.1016/j.matchar.2018.08.025>.

118. J.H. Rao, Y. Zhang, K. Zhang, X. Wu, A. Huang, Selective laser melted Al-7Si-0.6Mg alloy with in-situ precipitation via platform heating for residual strain removal, *Materials & Design*, 182 (2019) 108005. <https://doi.org/10.1016/j.matdes.2019.108005>.
119. D. Buchbinder, W. Meiners, K. Wissenbach, R. Poprawe, Selective laser melting of aluminum die-cast alloy—correlations between process parameters, solidification conditions, and resulting mechanical properties, *J. Laser Appl.* 27 (2015) S29205. <https://doi.org/10.2351/1.4906389>.
120. Wang, L., Jiang, X., Zhu, Y., Ding, Z., Zhu, X., Sun, J., & Yan, B. (2018). Investigation of performance and residual stress generation of AlSi10Mg processed by selective laser melting. *Advances in Materials Science and Engineering*, 2018 (2018) 7814039. <https://doi.org/10.1155/2018/7814039>.
121. T. Maconachie, M. Leary, J. Zhang, A. Medvedev, A. Sarker, D. Ruan, G. Lu, O. Faruque, M. Brandt, Effect of build orientation on the quasi-static and dynamic response of SLM AlSi10Mg, *Mater. Sci. Eng. A* 788 (2020), 139445. <https://doi.org/10.1016/j.msea.2020.139445>.
122. E. Padovano, C. Badini, A. Pantarelli, F. Gili, F. D’Aiuto, A comparative study of the effects of thermal treatments on AlSi10Mg produced by laser powder bed fusion, *Journal of Alloys and Compounds*, 831 (2020) 154822. <https://doi.org/10.1016/j.jallcom.2020.154822>.
123. L. Girelli, M. Tocci, M. Gelfi, A. Pola, Study of heat treatment parameters for additively manufactured AlSi10Mg in comparison with corresponding cast alloy, *Mater. Sci. Eng. A* 739 (2019) 317–328. <https://doi.org/10.1016/j.msea.2018.10.026>.
124. J.G. Santos Macías, T. Douillard, L. Zhao, E. Maire, G. Pyka, A. Simar, Influence on microstructure, strength and ductility of build platform temperature during laser powder bed fusion of AlSi10Mg, *Acta Mater.* 201 (2020) 231–243. <https://doi.org/10.1016/j.actamat.2020.10.001>.
125. P. Van Cauwenbergh, V. Samae, L. Thijs, J. Nejezchlebova, P. Sedlak, A. Ivekovic, D. Schryvers, B. Van Hooreweder, K. Vanmeensel, Unravelling the multi-scale structure–property relationship of laser powder bed fusion processed and heat-treated AlSi10Mg, *Sci. Rep.* 11 (2021) 6423. <https://doi.org/10.1038/s41598-021-85047-2>.
126. L. Zhao, L. Song, J.G. Santos Macías, Y. Zhu, M. Huang, A. Simar, Z. Li, Review on the correlation between microstructure and mechanical performance for laser powder bed fusion AlSi10Mg, *Additive Manufacturing*, 56 (2022) 102914, <https://doi.org/10.1016/j.addma.2022.102914>.
127. W. Li, S. Li, J. Liu, A. Zhang, Y. Zhou, Q. Wei, C. Yan, Y. Shi, Effect of heat treatment on AlSi10Mg alloy fabricated by selective laser melting: Microstructure evolution, mechanical properties and fracture mechanism, *Materials Science and Engineering: A*, 663 (2016) 116–125. <https://doi.org/10.1016/j.msea.2016.03.088>.
128. A. Iturrioz, E. Gil, M.M. Petite, F. Garciandia, A. M. Mancisor, M. San Sebastian, Selective laser melting of AlSi10Mg alloy: influence of heat treatment condition on mechanical properties and microstructure, *Weld World*, 62 (2018) 885–892. <https://doi.org/10.1007/s40194-018-0592-8>.
129. J. Fite, S. E. Prameela, J. A. Slotwinski, T. P. Weihs, Evolution of the microstructure and mechanical properties of additively manufactured AlSi10Mg during room temperature holds and low temperature aging, *Additive Manufacturing*, 36 (2020) 101429. <https://doi.org/10.1016/j.addma.2020.101429>.
130. T.H. Park, M.S. Baek, H. Hyer, Y. Sohn, K.A. Lee, Effect of direct aging on the microstructure and tensile properties of AlSi10Mg alloy manufactured by selective laser melting process, *Materials Characterization*, 176 (2021) 111113, <https://doi.org/10.1016/j.matchar.2021.111113>.
131. I. Rosenthal, R. Shneck, A. Stern, Heat treatment effect on the mechanical properties and fracture mechanism in AlSi10Mg fabricated by additive manufacturing selective laser melting process, *Materials Science and Engineering: A*, 729 (2018) 310–322, <https://doi.org/10.1016/j.msea.2018.05.074>.
132. L. Zhao, J.G. Santos Macías, L. Ding, H. Idrissi, A. Simar, Damage mechanisms in selective laser melted AlSi10Mg under as built and different post-treatment conditions, *Materials Science and Engineering: A*, 764 (2019) 138210. <https://doi.org/10.1016/j.msea.2019.138210>.
133. L. Tonelli, E. Liverani, A. Morri, L. Ceschini, Role of Direct Aging and Solution Treatment on Hardness, Microstructure and Residual Stress of the A357 (AlSi7Mg0.6) Alloy Produced by Powder Bed Fusion. *Metall Mater Trans B*, 52 (2021) 2484–2496. <https://doi.org/10.1007/s11663-021-02179-6>.
134. M. Epler, Structures by Precipitation from Solid Solution, in: G.F. Vander Voort (Ed.), *Metallogr. Microstruct.*, ASM International, (2004) 134–139. <https://doi.org/10.31399/asm.hb.v09.a0003731>.
135. Editor(s): A.P. Mouritz, Strengthening of metal alloys, *Introduction to Aerospace Materials*, Woodhead Publishing, 2012, 57–90, <https://doi.org/10.1533/9780857095152.57>.
136. H. Zhang, Y. Wang, J.J. Wang, D.R. Ni, D. Wang, B.L. Xiao, Z.Y. Ma, Achieving superior mechanical properties of selective laser melted AlSi10Mg via direct aging treatment, *J. Mater. Sci. Technol.* 108 (2022) 226–235. <https://doi.org/10.1016/j.jmst.2021.07.059>.
137. J. Fiocchi, A. Tuissi, P. Bassani, C.A. Biffi, Low temperature annealing dedicated to AlSi10Mg selective laser melting products, *Journal of Alloys and Compounds*, 695 (2017) 3402–3409, <https://doi.org/10.1016/j.jallcom.2016.12.019>.
138. N. Takata, H. Kodaira, K. Sekizawa, A. Suzuki, M. Kobashi, Change in microstructure of selectively laser melted AlSi10Mg alloy with heat treatments, *Mater. Sci. Eng. A* 704 (2017) 218–228. <https://doi.org/10.1016/j.msea.2017.08.029>.
139. N.E. Uzan, R. Shneck, O. Yeheskel, N. Frage, Fatigue of AlSi10Mg specimens fabricated by additive manufacturing selective laser melting (AM-SLM), *Materials Science and Engineering: A*, 704 (2017) 229–237 <https://doi.org/10.1016/j.msea.2017.08.027>.
140. Matjeke, V.J., Moopanar, C., Bolokang, A.S. et al. Effect of heat treatment time on the microstructure and mechanical deformation behavior of additive-manufactured AlSi10Mg components. *Prog Addit Manuf*, 5 (2020) 379–385. <https://doi.org/10.1007/s40964-020-00139-1>.
141. M. Tocci, A. Pola, M. Gelfi, G. M. La Vecchia, Effect of a New High-Pressure Heat Treatment on Additively Manufactured AlSi10Mg Alloy, *Metall Mater Trans A* 51 (2020) 4799–4811. <https://doi.org/10.1007/s11661-020-05905-y>.
142. L. Zhou, A. Mehta, E. Schulz, B. McWilliams, K. Cho, Y. Sohn, Microstructure, precipitates and hardness of selectively laser melted AlSi10Mg alloy before and after heat treatment, *Materials Characterization*, 143 (2018) 5–17. <https://doi.org/10.1016/j.matchar.2018.04.022>.

143. L. Girelli, M. Giovagnoli, M. Tocci, A. Pola, A. Fortini, M. Merlin, G.M. La Vecchia, Evaluation of the impact behaviour of AlSi10Mg alloy produced using laser additive manufacturing, *Materials Science and Engineering: A*, 748 (2019) 38-51. <https://doi.org/10.1016/j.msea.2019.01.078>.
144. N. T. Aboulkhair, I. Maskery, C. Tuck, I. Ashcroft, N.M. Everitt, Improving the fatigue behaviour of a selectively laser melted aluminium alloy: Influence of heat treatment and surface quality, *Materials & Design*, 104 (2016) 174-182. <https://doi.org/10.1016/j.matdes.2016.05.041>.
145. Q. Yan, B. Song, Y. Shi, Comparative study of performance comparison of AlSi10Mg alloy prepared by selective laser melting and casting, *Journal of Materials Science & Technology*, 41 (2020) 199-208, <https://doi.org/10.1016/j.jmst.2019.08.049>.
146. J. Damon, S. Dietrich, F. Vollert, J. Gibmeier, V. Schulze, Process dependent porosity and the influence of shot peening on porosity morphology regarding selective laser melted AlSi10Mg parts, *Additive Manufacturing*, 20 (2018) 77-89. <https://doi.org/10.1016/j.addma.2018.01.001>.
147. E. Cerri, E. Ghio, G. Bolelli, Effect of the Distance from Build Platform and Post-Heat Treatment of AlSi10Mg Alloy Manufactured by Single- and Multi-Laser Selective Laser Melting. *J. of Materi Eng and Perform* 30 (2021) 4981–4992 . <https://doi.org/10.1007/s11665-021-05577-8>
148. B. Amir, E. Grinberg, Y. Gale, O. Sadot, S. Samuha, Influences of platform heating and post-processing stress relief treatment on the mechanical properties and microstructure of selective-laser-melted AlSi10Mg alloys, *Materials Science and Engineering: A*, 822 (2021) 141612. <https://doi.org/10.1016/j.msea.2021.141612>.
149. K.G. Prashanth, S. Scudino, H.J. Klauss, K.B. Surreddi, L. Löber, Z. Wang, A.K. Chaubey, U. Kühn, J. Eckert, Microstructure and mechanical properties of Al–12Si produced by selective laser melting: Effect of heat treatment, *Materials Science and Engineering: A*, 590 (2014) 153-160, <https://doi.org/10.1016/j.msea.2013.10.023>.
150. C. Zhang, H. Zhu, H. Liao, Y. Cheng, Z. Hu, X. Zeng, Effect of heat treatments on fatigue property of selective laser melting AlSi10Mg, *International Journal of Fatigue*, 116 (2018) 513-522. <https://doi.org/10.1016/j.ijfatigue.2018.07.016>.
151. K. Kim, J.H. Hwang, E.Y. Kim, Y.U. Heo, W. Woo, S.H. Choi. Evaluation of the stress-strain relationship of constituent phases in AlSi10Mg alloy produced by selective laser melting using crystal plasticity FEM, *Journal of Alloys and Compounds*, 714 (2017) 687-697, <https://doi.org/10.1016/j.jallcom.2017.04.264>.

## Chapter 2 - Optimization of innovative heat treatments for the L-PBF AlSi10Mg alloy: a new perspective

1. This section contains selected parts of the manuscript:



Original Research Article | Published: 07 January 2022

### A Novel T6 Rapid Heat Treatment for AlSi10Mg Alloy Produced by Laser-Based Powder Bed Fusion: Comparison with T5 and Conventional T6 Heat Treatments

Gianluca Di Egidio , Lorella Ceschini, Alessandro Morri, Carla Martini & Mattia Merlin

*Metallurgical and Materials Transactions B* **53**, 284–303 (2022) | [Cite this article](#)

768 Accesses | [Metrics](#)

The following link can access the published version of the paper:  
<https://doi.org/10.1007/s11663-021-02365-6>

The authors thank Metallurgical and Materials Transactions B for granting permission to re-use the manuscript titled “A Novel T6 Rapid Heat Treatment for AlSi10Mg Alloy Produced by Laser-Based Powder Bed Fusion: Comparison with T5 and Conventional T6 Heat Treatments” in the present Ph.D. thesis (<https://www.springer.com/gp/open-access/publication-policies/copyright-transfer>).

2. This section contains selected parts of the manuscript:

La Metallurgia Italiana  
International Journal of the Italian Association for Metallurgy

Memorie scientifiche - **Trattamenti Termici**

### Evaluation by nanoindentation of the influence of heat treatments and the consequent induced microstructure on the mechanical response of the heat-treated L-PBF AlSi10Mg alloy

G. Di Egidio

**Winner of the “Elio Giannotti” prize - Edition 2022**

The published version of the paper is accessible on:

G. Di Egidio, Evaluation by nanoindentation of the influence of heat treatments and the consequent induced microstructure on the mechanical response of the heat-treated L-PBF AlSi10Mg alloy, *La Metallurgia Italiana*, Vol. 6 (2022), pp,8–15.

The authors wish to thank La Metallurgia Italiana for granting permission to re-use the manuscript titled “Evaluation by nanoindentation of the influence of heat treatments and the consequently induced microstructure on the mechanical response of the heat-treated L-PBF AlSi10Mg alloy” in the present Ph.D. thesis ( <https://www.metallurgia-italiana.net/publicazioni.php?idc=11> ).

3. This section reports selected parts of the manuscript:

## **Room- and High-Temperature Fatigue Strength of the T5 and Rapid T6 Heat-Treated AlSi10Mg Alloy Produced by Laser-Based Powder Bed Fusion**

by  Gianluca Di Egidio \*  ,  Lorella Ceschini ,  Alessandro Morri  and  Mattia Zanni 

Department of Industrial Engineering (DIN), Alma Mater Studiorum, University of Bologna, Viale Risorgimento 4, 40136 Bologna, Italy

\* Author to whom correspondence should be addressed.

*Metals* **2023**, *13*(2), 263; <https://doi.org/10.3390/met13020263>

**Received: 5 January 2023 / Revised: 20 January 2023 / Accepted: 26 January 2023 /**

**Published: 29 January 2023**

(This article belongs to the Special Issue **Mechanical Behaviors and Damage Mechanisms of Metallic Materials**)

The following link can access the published version of the paper:

<https://doi.org/10.3390/met13020263>

The authors thank Metals for granting permission to re-use the manuscript titled “Room- and High-Temperature Fatigue Strength of the T5 and Rapid T6 Heat-Treated AlSi10Mg Alloy Produced by Laser-Based Powder Bed Fusion” in the present Ph.D. thesis (<https://www.mdpi.com/authors/rights>).

4. This section reports selected parts of the manuscript:

## **Influence of microstructure on fracture mechanisms of the heat-treated AlSi10Mg alloy produced by Laser-based Powder Bed Fusion**

G. Di Egidio, C. Martini, J. Börjesson, E. Ghassemali, L. Ceschini, A. Morri

Paper currently under review in Materials – MDPI

## 2.1 Aim

As widely reported in Chapter 1, the AlSi10Mg alloy satisfies both the technological requirements (excellent thermal conductivity, fluidity, and weldability) and, after adequate heat treatment, the mechanical ones (excellent mechanical strength/weight ratio, good fatigue resistance, and impact resistance) for the production of high-tech mechanical parts. These properties allowed the AlSi10Mg alloy to become the most widely studied Al alloy used to make parts by the L-PBF process [1-4]. Given this material's importance in producing components with high-added value, several papers in the literature have already investigated the effects of conventional heat treatments on the microstructure and mechanical behavior of the L-PBF AlSi10Mg alloy. However, they often neglect the metastable and peculiar starting microstructure induced by rapid solidification.

As extensively described in the previous chapter, the highly rapid solidification that characterizes the L-PBF technology leads to the formation of a hierarchical microstructure within the semicircular MP consisting of grains aligned with the direction of the maximum heat flow at the solid/liquid interface and a metastable and extremely fine cellular substructure. The submicrometric cells of supersaturated  $\alpha$ -Al solution are surrounded by a eutectic-Si network and by limited precipitation of  $Mg_2Si$  and Si particles [5-7]. The synergistic effect of multiple reinforcement mechanisms linked to this peculiar as-built microstructure leads to higher strength properties than Al cast alloys. However, the microstructural inhomogeneity due to continuous heating and cooling cycles, which are necessary for the complete printing of the 3D component, and the high density of defects due to the limited control over the solidification of the material, induce a generally low ductility, toughness, and fatigue resistance [8-10]. Therefore, several heat treatments have been recently applied to the AB alloy to improve the balance of mechanical properties, including T5, SR, T6 heat treatments [7]. In particular, the T6 heat treatment achieves the best balance of mechanical properties by improving ductility, toughness, and fatigue strength (thanks to the homogeneous composite-like microstructure) without inducing a decrease in YS (due to the contribution of precipitation hardening) as described in [10-12].

For these reasons, optimizing the T6 heat treatment parameters is still widely studied. Focusing on the grain structure, Domfarg et al. [13] and Alghamdi et al. [14] highlighted the following points: (i) the T6 heat treatment marginally affects the grain size and morphology; (ii) the modification of grain size and morphology do not induce appreciable effects on the static mechanical response of the L-PBF AlSi10Mg alloy. On the contrary, according to most of the research [12,15,16], the Si particles' distribution, size, and morphology significantly influence the mechanical properties of the T6 alloy. Tocci et al. [12] and Wang et al. [17] described the detrimental effects of the Si particle coarsening on the strength properties of the T6 alloy, while Iturrioz et al. [15] and Mertens et al. [18] underlined the importance of limiting the Si particle size to improve cohesion between the Si particles and the Al matrix, hence increasing the ductility. Furthermore, Zhang et al. [16] reported a concurrent increase in strength and ductility due to the homogeneous distribution of fine Si particles induced by the T6 heat treatment. Based on the above considerations, the strength-ductility trade-off in the T6 alloy can be improved by reducing the size and homogenizing the distribution of the Si particles, and avoiding the growth of gas pores during the high-temperature SHT treatment.

Up to now, the research has primarily focused on assessing the T6 heat treatment effects characterized by the typical parameters used for cast alloys without thoroughly investigating possible modification of the solution or aging parameters to induce a customized microstructure and, therefore, optimize the mechanical properties. To the best of our knowledge, only Li et al. [11] and Iturrioz et al. [15] have systematically studied the influence of the  $T_{SHT}$  on the T6 alloy, but the effects of a rapid solution ( $t_{SHT}$  significantly shorter than 1 h) have not been analyzed yet.

For these reasons, this chapter focused on developing an innovative T6 rapid heat treatment for the L-PBF AlSi10Mg alloy based on a rapid SHT capable of homogenizing the AB microstructure without losing its peculiar fineness and the strengthening mechanisms associated with it. Our attention was focused on the effects of the  $T_{\text{SHT}}$  and the short  $t_{\text{SHT}}$  on (i) size, morphology, and distribution of Si particles; (ii) gas pores size; (iii) Al matrix supersaturation. In particular, the short  $t_{\text{SHT}}$  reduced the typical porosity growth at high temperatures and led to a homogeneous distribution of fine spheroidal Si particles in the Al matrix. In addition, it limited the diffusion processes, increasing the amount of Mg and Si atoms available in solid solution for precipitation hardening and avoiding microstructural coarsening. Understanding these aspects has enabled the definition of customized heat treatment parameters for the L-PBF AlSi10Mg alloy, capable of improving the material's mechanical performance of the L-PBF AlSi10Mg. The influence of heat treatment on RS was not analyzed in detail; as widely reported in the literature, the synergistic effect of the high-temperature preheating platform used during the L-PBF process [4,19] and the heat treatments carried out in the 290 - 540 °C range allow to relieve the RS entirely in a short soaking time: 45 min at 290 °C and 10 min at 540 °C [20,21].

Different typologies of mechanical characterization were used to evaluate the effects of the optimized rapid solution heat treatment (T6R) on the mechanical properties of the L-PBF AlSi10Mg alloy: static (section 2.3.2), nano (section 2.3.3), in-situ (section 2.3.4), and cyclic (section 2.3.5). These analyses allowed having a complete view of the advantages introduced by the rapid solution (SHTR) compared to different heat treatment conditions, such as AB, T5, and T6 benchmark (T6B) heat treatments. In particular, the latter was considered able to induce the best strength-ductility trade-off among those reported in the literature.

## 2.2 Experimental procedure

The production of rod samples (diameter of 9 mm and height of 77 mm) (Figure 2.1(a)) and discs (diameter  $\Phi = 46$  mm and thickness  $h = 5$  mm) (Figure 2.1(c)) employed gas atomized powders of AlSi10Mg alloy (chemical composition in Table 2.1 and physical properties in Table 2.2). The specimens were produced with the longitudinal axis and the flat surface parallel to the building direction (z-axis). In particular, this solution was used to consider the worst-case scenario in terms of mechanical strength and reduce costs by increasing the number of components on a single platform, as commonly occurs in industrial production. Glow Discharge Optical Emission Spectroscopy (GD-OES) was used to check the chemical composition of the as-built specimens (Table 2.1) according to ISO 14707:2015 [22]. Their composition matched the requirements given by the EN AC-43000 data sheet for AlSi10Mg (Table 2.1). The chemical composition of the L-PBF samples does not show significant differences

**Table 2.1.** Chemical compositions (wt.%) of the AlSi10Mg alloy according to EN AC-43000 (i) and AlSi10Mg powders supplied by the producer (ii). Nominal chemical compositions (wt.%) of rod specimens (iii) and disks (iv) evaluated by GD-OES.

Element (wt%)	Al	Si	Mg	Fe	Cu	Mn	Ni	Pb	Sn	Ti	Zn
EN AC-43000	Bal.	9-11	0.20-0.45	<0.55	<0.05	<0.45	<0.05	<0.05	<0.05	<0.15	<0.10
Powders	Bal.	9.21	0.27	0.15	0.001	0.006	0.003	0.001	<0.001	0.05	0.002
Rod specimens	Bal.	9.66 $\pm 0.103$	0.29 $\pm 0.02$	0.12 $\pm 0.02$	-	0.006 $\pm 0.001$	-	0.008 $\pm 0.002$	0.025 $\pm 0.010$	0.017 $\pm 0.003$	0.042 $\pm 0.009$
Disks	Bal.	9.74 $\pm 0.086$	0.30 $\pm 0.03$	0.13 $\pm 0.01$	-	0.005 $\pm 0.001$	-	0.008 $\pm 0.001$	0.020 $\pm 0.010$	0.020 $\pm 0.002$	0.040 $\pm 0.005$

**Table 2.2.** Physical properties of the AlSi10Mg powders supplied by the producer.

Tap density [g/cm <sup>3</sup> ] ASTM B527	Carney Apparent density [g/cm <sup>3</sup> ] ASTM B417	Relative humidity [%]	Static Carney Flow test [s/150g] ASTM B964	Powders range size [ $\mu$ m] ASTM B822, B221, B214
1.8	1.49	4.6%	32	20-63

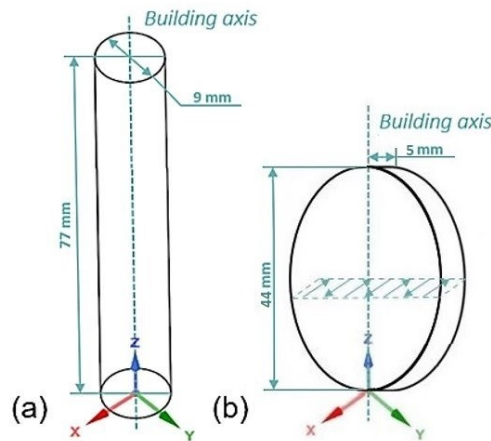


**Figure 2.1.** Schematic illustration of the building orientation of the rod specimens (a) and disk (b).

SLM500 system (SLM Solution Group AG, DE [23]), including a build chamber of 500x280x365 mm<sup>3</sup> and four Yttrium fiber laser sources (4x400 W), was used for manufacturing the samples (Figure 2.2).



Figure 2.2 SLM500 system used to produce the specimens [23]

The specimens were made on a heated platform (150 °C) using a bidirectional stripes scan strategy of 67° rotation between subsequent layers and a re-melted contour zone strategy at the end of each scanning (Figure 2.3). Ar with low O<sub>2</sub> content (<0.2 vol.%) backfilled the build chamber. The samples were removed from the platform through wire electrical discharge machining. The L-PBF process parameters are reported in Table 2.3.

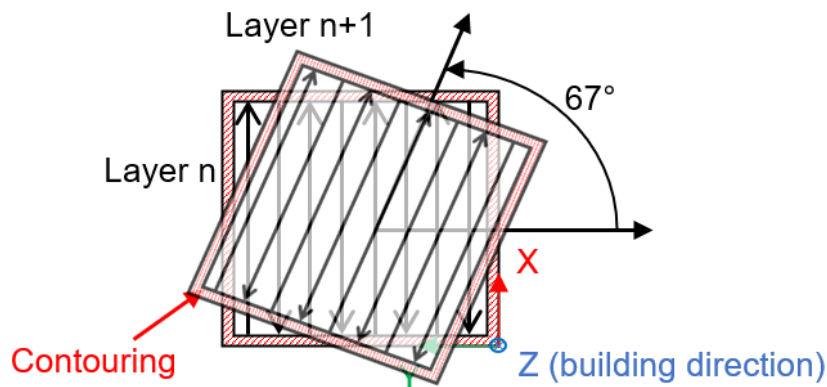


Figure 2.3. Scan strategy adopted to make the specimens by the SLM500 system.

Table 2.3. L-PBF process parameters set for building AlSi10Mg samples.

Atmosphere	Heated platform [°C]	Laser power [W]	Scan speed [mm/s]	Spot diameter [μm]	Layer thickness [μm]	Hatch distance [μm]	Energy density [J/mm <sup>3</sup> ]
Argon, O <sub>2</sub> <0,2%	150	350	1150	80	50	170	36

The present study aims to identify the optimal T6 heat treatment conditions for the L-PBF AlSi10Mg alloy considering its peculiar microstructure. For this reason, a preliminary study was carried out to assess the effect of the heat treatment parameters on the main microstructural features. The static mechanical performances of the optimized T6R were investigated and compared to the AB, T5, and T6B conditions, as summarized in Table 2.4.

Table 2.4. Heat treatment conditions investigated for the L-PBF AlSi10Mg alloy by tensile test.

Condition	Acronym	Heat treatment
As-built	AB	-
T5 direct artificial aging	T5	(AA) at 160 °C for 4h, air cooling
T6 benchmark heat treatment	T6B	(SHT) at 540 °C for 1h, water quenching at room temperature, (AA) at 160 °C for 4h, air cooling
T6 rapid heat treatment	T6R	(SHT) at 510 °C for 10 min, water quenching at room temperature, (AA) at 160 °C for 6 h, air cooling

The T6B heat treatment conditions were selected based on an extensive bibliographic investigation using two different quality indices (Drouzy, Jacob e Richard Index ( $Q_{DJR}$ ), and Din, Rashid e Campbell Index ( $Q_{DRC}$ )) [25,26] to evaluate the balance of the different mechanical properties (YS, UTS, and  $e_f$ ) obtainable post-T6 heat treatment (Figure 2.4). In particular, the data reported by Casati et al. [27] showed the best strength-ductility trade-off for the reported T6 heat treatment conditions among those reported in the literature [7,12,15-18,22,28-36], and they were selected as the benchmark.

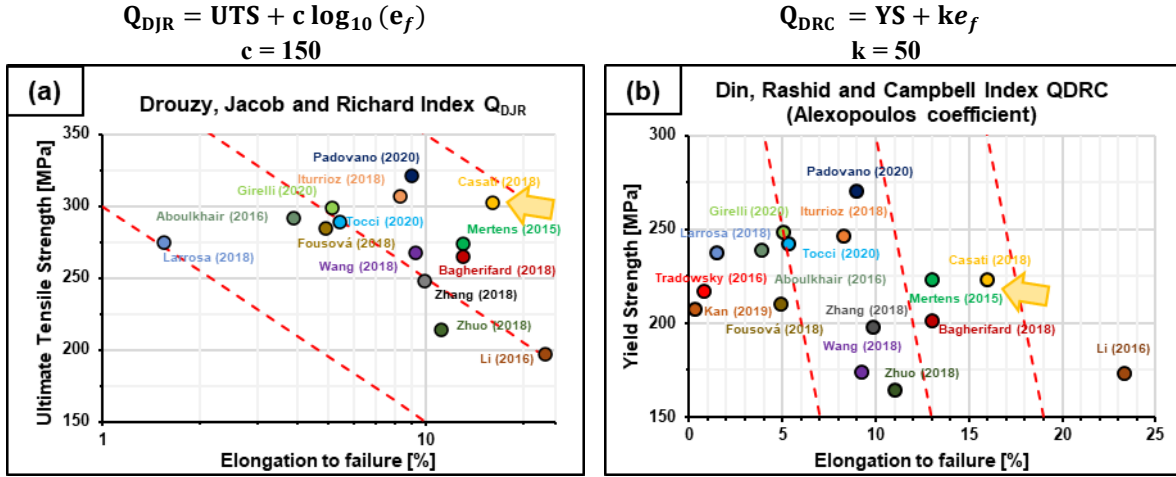


**Figure 2.4.** Comparison of the results related to T6 heat-treatments reported in the [7,12,15-18,22,28-36] using two different quality indices: Drouzy, Jacob e Richard Index ( $Q_{DJR}$ ) (a), and Din, Rashid e Campbell Index ( $Q_{DRC}$ ) (b). Only the results concerning a building orientation comparable to the sample produced for this work were considered. The best compromise between the mechanical properties is related to the T6 heat treatment conditions reported by Casati et al. [27].

The  $T_{SHT}$  and  $t_{SHT}$  (Table 2.5) investigated in the present work were defined based on a comprehensive literature survey, starting from the results reported in [11,15,27,28,37]. The  $t_{SHT}$  was evaluated when the target value for  $T_{SHT}$  was reached after positioning the samples in the furnace. Microstructural analyses were performed after quenching the samples in water at room temperature.

**Table 2.5.** Investigated SHT conditions for L-PBF AlSi10Mg specimens.

Temperature ( $T_{SHT}$ )	Soaking time ( $t_{SHT}$ )						
450 °C	-	-	-	-	-	-	60 min    120 min
510 °C	5 min	10 min	15 min	20 min	30 min	60 min	-
540 °C	-	-	-	-	-	60 min	-

Density measurements were carried out by Archimedes' principle on AB and SHTed samples (Table 2.5), according to ASTM B962 [38]. Four samples were analyzed for each condition. To reduce the influence of surface roughness, emery papers up to 1200 grits ground the specimens before the test. The weight measurement was repeated three times in air and distilled water. The effective density  $\rho_{eff}$  was elaborated according to the following equation (Equation 2.1):

$$\rho_{eff} = \frac{\omega_{air}}{\omega_{air} - \omega_{water}} \rho_{water} \quad (2.1)$$

where  $\omega_{air}$  and  $\omega_{water}$  are the weight of the samples in air and distilled water, respectively. Considering the density of bulk material ( $\rho_{bulk}$ ) equal to 2.68 g/cm<sup>3</sup> for the AlSi10Mg alloy [29], the relative porosity P in terms of volume percentage was evaluated as follows (Equation 2.2):

$$P = \left(1 - \frac{\rho_{eff}}{\rho_{bulk}}\right) \cdot 100 \quad (2.2)$$

X-ray diffraction (XRD) was performed in Bragg-Brentano geometry with a PANalytical X'Pert PRO diffractometer using a Cu K $\alpha$  radiation source ( $\lambda_{\text{Cu}}=0.15418$  nm). Patterns were acquired in the  $2\theta$  range from  $20^\circ$  to  $110^\circ$  with a  $0.02^\circ$  step size and a 4 s dwell time. After phase identification, differences induced by heat treatment parameters were evaluated by semi-quantitative analysis of the lattice parameters, the full width at half maximum (FWHM), and the ratio between Si and Al main peak counts [40,41].

Microstructural analyses were carried out on the as-built and heat-treated samples using optical microscopy (OM) and field emission-gun scanning electron (FEG-SEM) microscopy. FEG-SEM (MIRA3, TESCAN) was equipped with energy-dispersive X-ray spectroscopy (EDS). Metallographic samples were embedded in conductive resin, ground by emery papers up to 1200 grit, polished by diamond suspensions from  $9\ \mu\text{m}$  to  $1\ \mu\text{m}$ , according to ASTM E3 [42], and then etched with Weck's reagent (3g NH $_4$  HF $_2$ , 4 mL HCl, 100 mL H $_2$ O) according to ASTM E407 [43]. EBSD analysis (Hikari Plus, EDAX) coupled with FEG-SEM (LYRA3, TESCAN) was carried out to characterize the crystallographic structure. Before EBSD analysis, the mechanically polished specimens were not etched, but further polished with OP-S colloidal silica

Image analysis was carried out by the ImageJ software to identify morphology, size, spatial distribution, and average near-neighbor distance of the eutectic Si particles embedded in the Al matrix. For each solution condition, five FEG-SEM images were analyzed for a total area of about  $4 \times 10^{-3}$  mm $^2$ . The image analysis procedure included the microstructure tessellation by a particle surface-based algorithm into a mesh of Voronoi cells (ImageJ plug-in), each containing an individual particle, as suggested by Li et al. [43]. The Voronoi tessellation allowed the division of the analyzed region into sub-regions so that each Si particle was associated with an area closer to it than any other. This analysis makes it possible to estimate the average nearest-neighbor distance among the Si particles [43]. The analysis process was standardized to guarantee repeatable results. The FEG-SEM images (Figure 2.5(a)) were elaborated through a threshold function to identify the Si particles (Figure 2.5(b)). Subsequently, the images were processed to define the Voronoi tessellation resulting from Si particle distribution (Figure 2.5(d)), and the average nearest-neighbor distance for each image was calculated. Particular attention was paid to different quantitative parameters: (i) average area of Si particles; (ii) Si particle number per unit area; (iii) average near-neighbor distance.

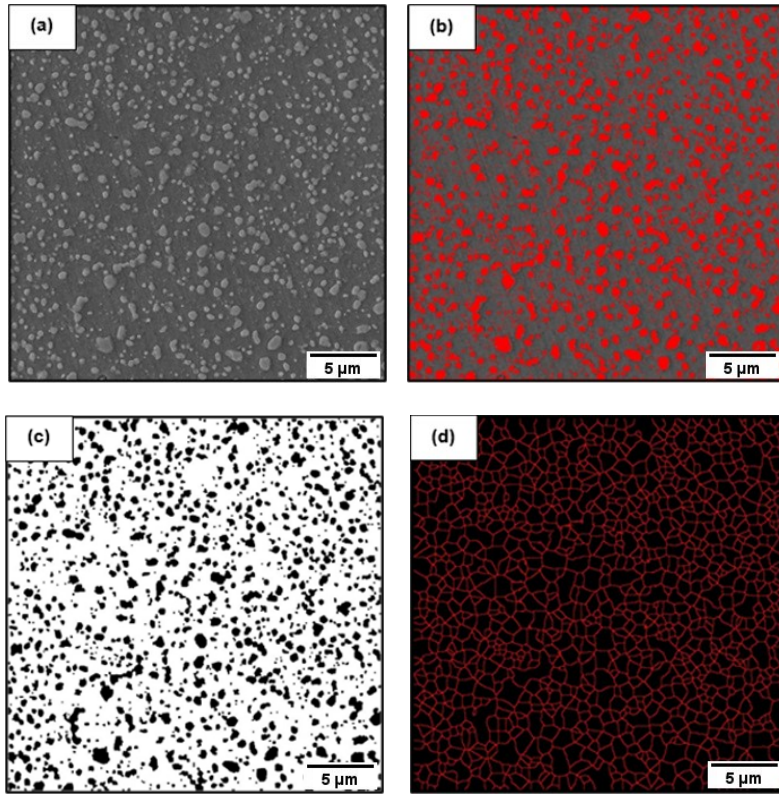


**Figure 2.5.** Example of the image processing path comprising: (a) the original FEG-SEM image; (b) identification of Si particles by threshold function; (c) conversion into a binary image; (d) the Voronoi tessellation (red lines define the average nearest-neighbor distance for each Si particle).

$T_{\text{SHT}} = 510 \text{ }^{\circ}\text{C}$  and  $t_{\text{SHT}} = 10 \text{ min}$  were identified as the SHT conditions and hereafter referred to as SHTR. The SHTR treatment was applied to the samples that underwent further artificial aging and the subsequent mechanical characterization.

AA curves were evaluated for both AB and SHTR alloys according to the temperature-time conditions listed in Table 2.6. Vickers hardness ( $\text{HV}_1$ ) tests were performed on the heat-treated samples, according to ASTM E92 [44], to determine hardness as a function of aging time and temperature.

**Table 2.6.** Artificial aging conditions for T5 and T6R heat treatments

Initial alloy condition	Heat treatment	Artificial aging conditions	
		Temperature ( $T_{\text{AA}}$ )	Soaking time ( $t_{\text{AA}}$ )
As-built (AB)	T5	160 $^{\circ}\text{C}$ / 170 $^{\circ}\text{C}$ / 180 $^{\circ}\text{C}$	1 - 8 h
Solution treated (SHTR) and quenched (510 $^{\circ}\text{C}$ for 10 min)	T6R	160 $^{\circ}\text{C}$ / 170 $^{\circ}\text{C}$ / 180 $^{\circ}\text{C}$	1 - 10 h

Tensile and  $\text{HV}_1$  hardness tests were performed on samples that underwent different heat treatments. Each tested condition is reported in Table 2.4. Round dog-bone tensile samples (gauge length  $L_0 = 25 \text{ mm}$ , gauge diameter  $d_0 = 5 \text{ mm}$ ) were machined from the heat-treated specimens (Figure 2.6). Tensile tests were carried out at room temperature on a screw-testing machine at a strain rate of  $3.3 \times 10^{-3} \text{ s}^{-1}$  according to ISO 6892-1 and ISO 6892-2 [45,46]. Yield strength (YS), ultimate tensile strength (UTS), and elongation to failure ( $\epsilon_f$ ) were evaluated as the average of at least four samples for each investigated condition.

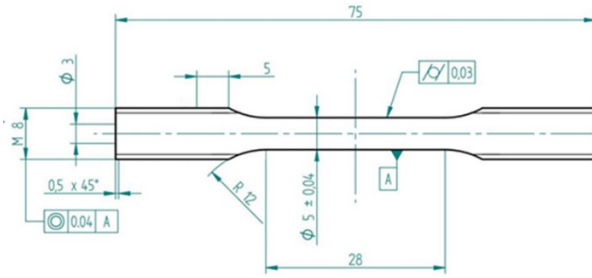


Figure 2.6. Tensile sample geometry (dimensions in mm).

The nanoindentation tests were carried out using a NanoTest Vantage from Micromaterials equipped with a Berkovich indenter (Centerline-to-face angle,  $\alpha = 65,27^\circ$ , Young's Module,  $E_o = 1141$  GPa e Poisson coefficient,  $\nu_o = 0.07$ ) according to ISO 14577-1 [47]. A load speed of 1 mN/s, a maximum load of 10 mN, and a holding time of 5 s at the load peak were used. The analysis was carried out using maps with dimensions of  $400 \times 200 \mu\text{m}$  to afford the characterization of a large area of material through equidistant indentations at  $40 \mu\text{m}$ . In total, the number of points analyzed in each map was 66.

The hardness (H) and elastic recovery parameter (ERP) data were processed by Matlab software to create the related maps. The first is the ratio between the maximum applied load ( $P_{max}$ ) and the projected contact area at that load ( $A(h_c)$ ) (Figure 2.7) [48], which is expressed by Equation 2.3:

$$H = \frac{P_{max}}{A(h_c)} \quad (2.3)$$

The elastic recovery parameter (ERP) is a dimensionless index that is indicative of the slope (S) of the unloading curve and consequently related to the ratio between H and Young's modulus (E) of the material (Figure 2.7) [49]:

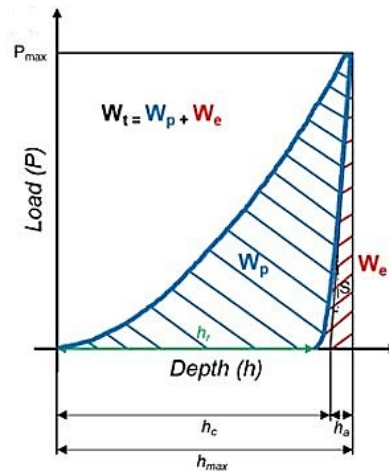


Figure 2.7. Load-unload curve for the instrumented indentation technique.

In Equation 2.4,  $h_{max}$  defines the depth at the maximum load, while  $h_c$  is the contact depth. The ERP coefficient highlights the elastoplastic behavior of the material: as ERP increases, the elastic work ( $W_e$ ) increases. Conversely, its decrease in value corresponds to an increase in plastic work ( $W_p$ ) [49].

$$ERP = \frac{h_{max} - h_c}{h_{max}} \quad (2.4)$$

The samples preparation and the data acquisition followed this procedure: (i) cutting of the samples parallel to the building axis of the specimens, (ii) embedding of the samples in conductive resin, and subsequent metallographic preparation up to polishing with a diamond suspension of 1  $\mu\text{m}$ , according to the ASTM E3 [41] standard, (iii) performing nanoindentation tests according to ISO 14577-1 [47], (iv) chemical etching of samples using Weck's reagent, according to ASTM E407 [42], (v) image acquisition using OM and FEG-SEM microscopes.

In-situ tensile tests were performed on a tensile/compression module (Kammrath & Weiss) (Figure 2.8) inside a FEG-SEM (LYRA3, TESCAN) at room temperature following the ASTM E8 standard [50] with a constant crosshead speed of 0.5 mm/min.

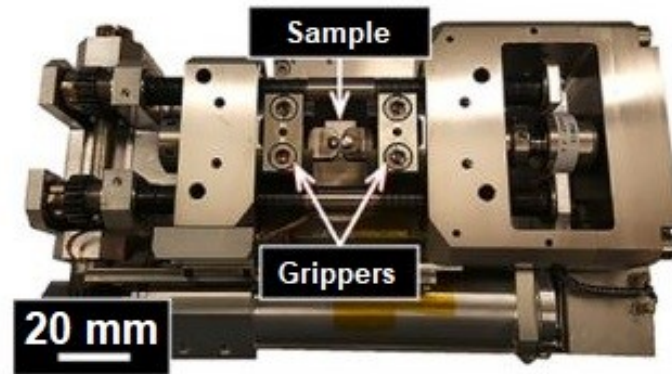


**Figure 2.8.** Tensile/compression module for In-situ tensile tests.

Miniaturized Tensile (MT) samples were cut using electric discharge machining with a 0.25 mm wire from the disk reported in Figure 2.1. The miniaturized MT samples (Figure 2.9(a)) were machined from the disc in two different directions: parallel to the building direction (Sample -V) and perpendicular to the building direction (Sample -H) (Figure 2.9(b)). Therefore, the analysis of the micromechanical performance and the fracture propagation was performed for (i) AB (AB-H and AB-V), (ii) T5 (T5-H and T5-V), (iii) optimized T6R (T6R-H and T6R-V), and (iv) T6B (T6B-H and T6B-V).

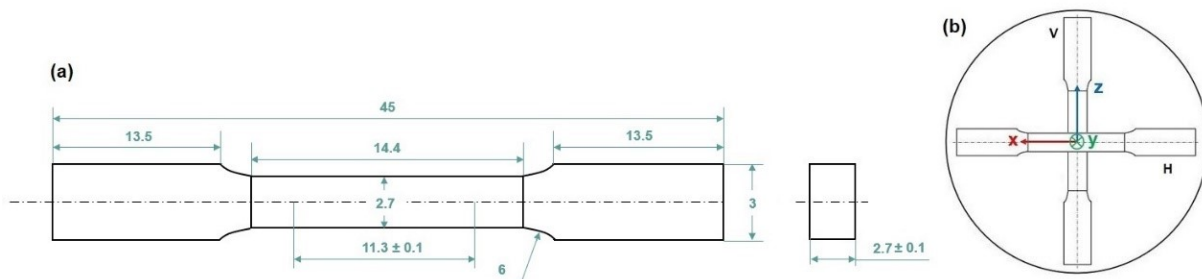


**Figure 2.9.** Miniaturized Tensile (MT) sample geometry (dimensions in mm) (a). Samples were machined from disc (b) in two different directions: parallel to the building direction (Sample -V) and perpendicular to the building direction (Sample -H).

MT samples for microstructural analysis were embedded in resin, ground by emery papers up to 1200 grit, and polished by diamond suspensions from 9 to 1  $\mu\text{m}$ , according to ASTM E3 [41]. This process was performed to preserve the plane parallelism of the samples. Following the extraction of the MT samples from the resin, they were etched with Weck's reagent according to ASTM E407 [42] to ensure observation of the crack propagation within the microstructure of the L-PBF AlSi10Mg alloy. Fractographic analyses were carried out by optical microscope (OLYMPUS DSX1000) and field emission-gun scanning electron (FEG-SEM) microscopy.

Room temperature rotating bending fatigue tests ( $R = -1$ ) were performed by the staircase method according to ISO 12107:2012 [51] standard, with a step size of 10 MPa to evaluate the 50% reliability endurance limit. Tests were carried out on hourglass specimens (Figure 2.10) at 33 Hz frequency setting the run-out to  $2 \times 10^6$  cycles.

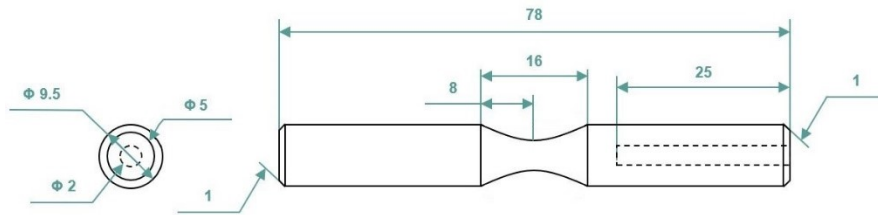


**Figure 2.10.** Shape and dimensions (mm) of the fatigue specimens.

For each staircase, fifteen samples were tested. TP Engineering machine in bending moment controlled mode was used; in particular, the force was logged by a load cell, which is loaded via the lever arm (Figure 2.11) and converted to the applied moment.

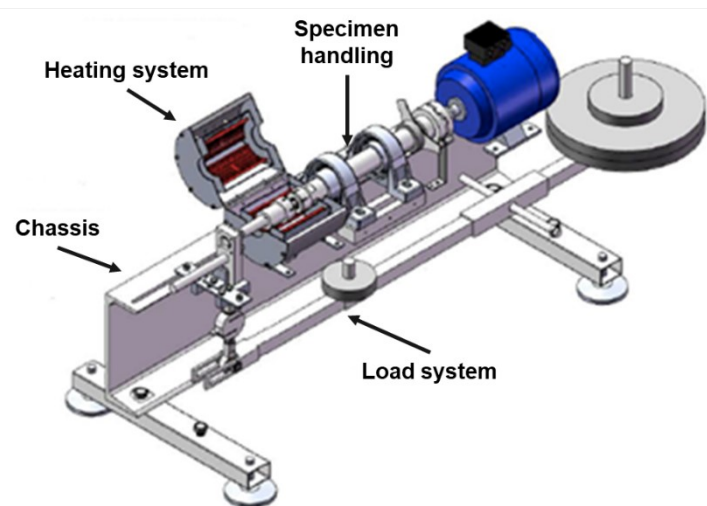


**Figure 2.11.** Scheme of the fatigue machine.

Considering the anisotropy induced by the building direction, the fatigue samples were made by the L-PBF machine with the longitudinal axis perpendicular to the platform, comparable to the position of the rod specimens shown in Figure 2.1, for considering the worst-case scenario in terms of mechanical strength [22]. The gauge section of the fatigue samples was directly polished on the as-built specimen using emery papers with a mesh ranging from 250 to 2500 to obtain a smooth surface roughness. This condition is close to the production of near-net-shape components that require extremely low roughness on certain surfaces ( $R_a \approx 0.2 \mu\text{m}$ ) to guarantee the deposition of a protective or lubricant coating, as occurs in the deposition of the multilayer coating on the piston skirt. 3D-digital microscope (Hirox KH 7700) and FEG-SEM/EDS were used to identify the dominant fracture mechanisms.

## 2.3 Results and discussion

### 2.3.1 Rapid solution optimization

#### 2.3.1.1 Density measurement

Density measurements were carried out on each specimen before and after the SHT step to evaluate the effect of the  $T_{\text{SHT}}$  and  $t_{\text{SHT}}$  conditions on the gas porosity content (Figure 2.12). The protective gases (Ar) in the building chamber, the presence of  $\text{H}_2$  in moisture on the powder surface, and the air in the voids within the powder bed are the leading causes of gas porosity. The average density of the AB samples was  $2.656 \pm 0.003 \text{ g/cm}^3$  with a consequent porosity content of 0.91%. The average increase of the porosity induced by different  $T_{\text{SHT}}$  or  $t_{\text{SHT}}$  is reported in Figure 2.12. These data clearly show that porosity content rises with an increase in both  $T_{\text{SHT}}$  and  $t_{\text{SHT}}$ . At 510 °C the porosity increases from 13.3%, after 5 min, to 31.6% after 1 h.

Similarly, the porosity increases from 18.6% at 450 °C to 41.0% at 540 °C for a  $t_{\text{SHT}}$  of 1 h. The latter represents the worst possible analyzed SHT condition, leading to the highest porosity content. As expected, the increase of porosity is more affected by  $T_{\text{SHT}}$  than  $t_{\text{SHT}}$ . At high temperatures, the gas pressure in the pores increases, the alloy strength decreases, and consequently, porosities can grow [37,52]. However, based on these results, it is possible to infer that the  $T_{\text{SHT}}$  of 510 °C and  $t_{\text{SHT}}$  of up to 15 min can limit the porosity content increase.

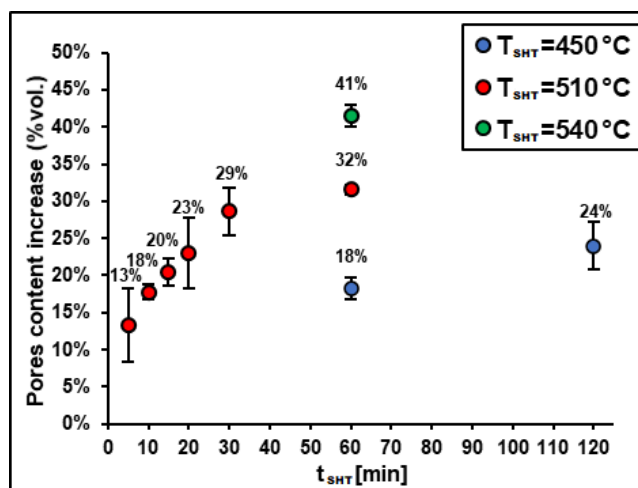


Figure 2.12. Effect of  $T_{\text{SHT}}$  and  $t_{\text{SHT}}$  on the increase of pores content in the heat-treated compared with the AB samples.

### 2.3.1.2 X-ray diffraction

The main parameters derived from XRD patterns of the L-PBF AlSi10Mg alloy are summarized in Table 2.7 as a function of different SHT conditions. The Si/Al ratio was determined by Equation 2.5, as the ratio between the area under the Si  $\langle 111 \rangle$  peak and the Al  $\langle 111 \rangle$  peak,

$$\frac{Si}{Al} = \frac{Area_{Si(111)}}{Area_{Al(111)}} \quad (2.5)$$

while the effect of the different SHT conditions on the amount of the Si dissolved in Al was assessed using Vergard's law (Equation 2.6) [53]:

$$a = -0.0174x_{Si} + 0.40491 \quad (2.6)$$

where  $a$  is the lattice parameter of FCC Al and  $X_{Si}$  is the atomic fraction of dissolved Si.

FCC Al and diamond cubic Si phases were identified in the XRD patterns of all the samples, with lower intensity for Si than for Al. FCC Al reflections were always sharp, indicating the presence of large crystallites, while no texture was observed. As reported by [5], the bidirectional stripes scan strategy of  $67^\circ$  rotation between subsequent layers, the significant hatch distance (170  $\mu\text{m}$ ), and the high layer thickness (50  $\mu\text{m}$ ) used for the production of the L-PBF samples can lead to the absence of texture, conversely from unidirectional or bidirectional scan strategy.

The Si FWHM values indicate the presence of finer Si crystallites in AB than in the heat-treated alloy due to the high cooling rate during the L-PBF process, as also observed by [54]. Among the SHTed specimens heat treated at 510  $^\circ\text{C}$ , those that underwent the shorter solution time of 5 and 10 min have a higher FWHM than the others due to the retention of smaller Si crystallites. The FWHM of these samples is also broader than that of SHT specimens that underwent low  $T_{SHT}$  (450  $^\circ\text{C}$ ) but longer  $t_{SHT}$  (1 - 2 h). For  $t_{SHT}$  equal to 1 h, the FWHM decreases, and the Si/Al ratio increases with rising  $T_{SHT}$ , indicating an increase in eutectic Si particle size and amount, respectively. These data agree with the microstructural analyses reported in the following sections.

**Table 2.7.** Si  $\langle 111 \rangle$  peak FWHM and Si/Al ratio for AB and SHTed samples.

Heat Treatment	$T_{SHT}$ [ $^\circ\text{C}$ ]	$t_{SHT}$ [min]	Si $\langle 111 \rangle$ FWHM	Si/Al	$X_{Si}$ [%]
None (AB)	-	-	0.394	0.08	4.17
SHT	450	60	0.148	0.13	3.14
SHT	450	120	0.148	0.25	2.81
SHT	510	5	0.197	0.02	5.90
SHT	510	10	0.197	0.03	6.90
SHT	510	15	0.148	0.04	5.56
SHT	510	20	0.148	0.08	4.55
SHT	510	30	0.148	0.14	3.64
SHT	510	60	0.148	0.15	3.34
SHT	540	60	0.148	0.19	3.34

The plot in Figure 2.13 clearly shows that the highest amount of Si dissolved in Al ( $X_{Si}$ ) is present in the samples subjected to SHTR for 10 min at 510  $^\circ\text{C}$ , while longer  $t_{SHT}$  leads to a decrease in Al saturation. However, as expected, the lowest amount of Si in solid solution was detected in the aged samples ( $X_{Si} = 0.19$  at.% for T6R). Hence the aging treatment, as expected, led to the formation of  $\text{Mg}_2\text{Si}$  hardening precipitates and the consequent reduction of the Si supersaturation in the Al-rich matrix [9].

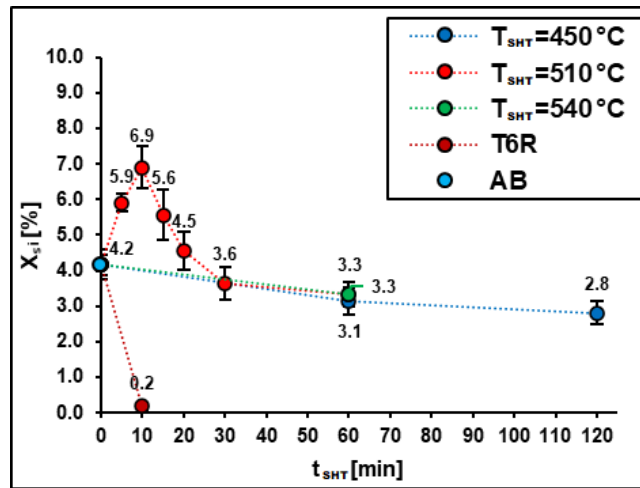
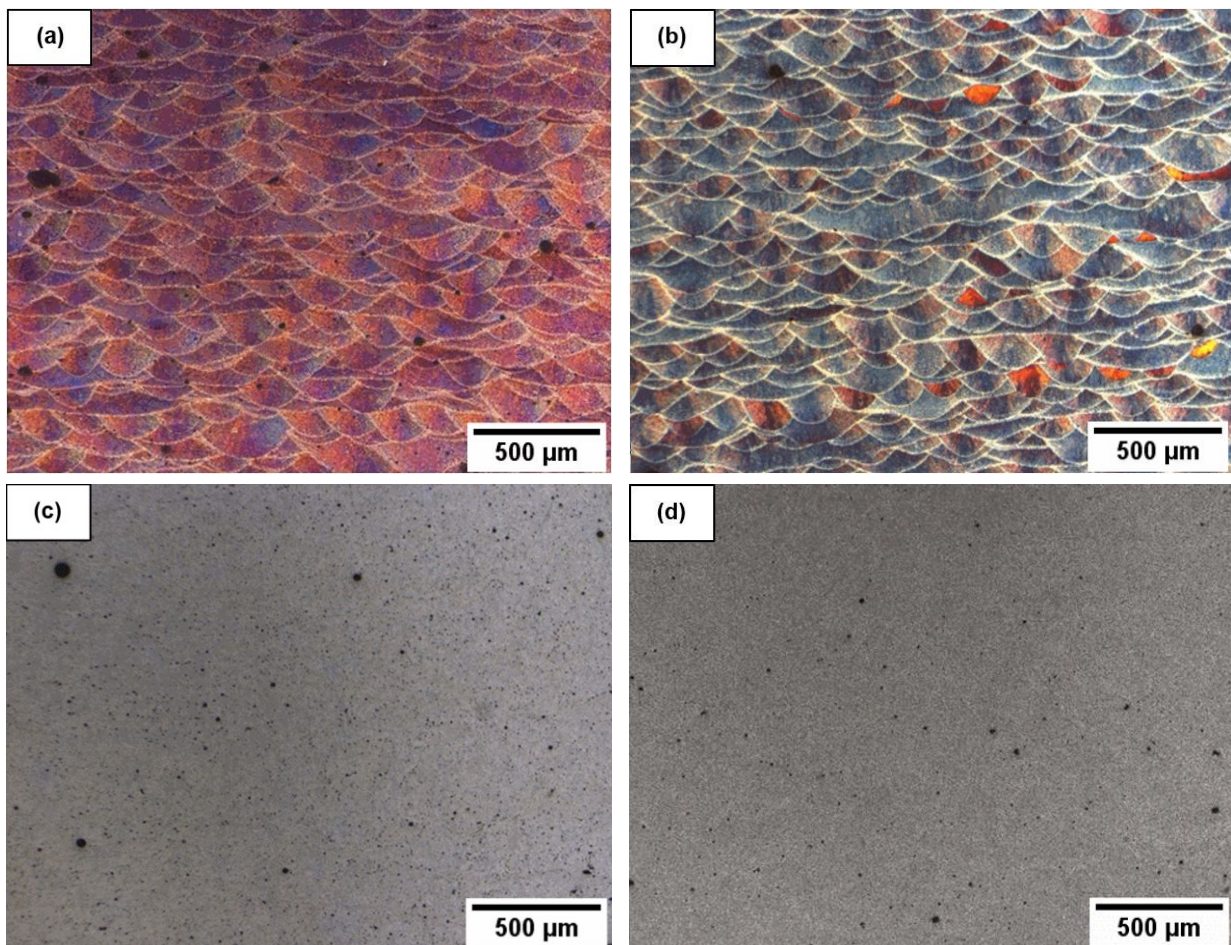


Figure 2.13. Si dissolved in FCC Al ( $X_{Si}$ ) estimated by Vergard's law for SHTed samples with different  $T_{SHT}$  and  $t_{SHT}$  and a T6R sample.

### 2.3.1.3 Microstructure

The microstructural analyses aimed to identify the optimal SHT conditions by comparing the effect of different heat treatments on MP structure, cellular microstructure, porosity, size, amount, and distribution of Si particles.

The OM images reported in Figure 2.14 show the evolution of the MP structure as a function of the heat treatment temperature. The T5 heat treatment ( $T_{AA} = 160\text{ °C}$ ,  $t_{AA} = 4\text{ h}$ ) has no remarkable effect (Figure 2.14(b)) on the MP structure characterizing the AB samples (Figure 2.14(a)). The diffusion processes at the aging temperatures (in this study ranging between  $160\text{ °C}$  and  $180\text{ °C}$ ) are negligible; consequently, their effects on the microstructure are also negligible [7,20,55]. The microstructure, in contrast, is affected by the SHT, as evident in Figures 2.14(c) and 2.14(d). In SHTed samples, the MP structure disappears, leading to similar homogeneous microstructures both in the samples subjected to the benchmark solution treatment (SHTB) used in the T6B (Figure 2.14(c)) and the SHTR (Figure 2.14(d)).



**Figure 2.14.** OM images of the L-PBF AlSi10Mg microstructure: AB (a); T5:  $T_{AA} = 160\text{ °C}$   $t_{AA} = 4\text{ h}$  (b); T6B:  $T_{SHT} = 540\text{ °C}$   $t_{SHT} = 1\text{ h}$ ,  $T_{AA} = 160\text{ °C}$   $t_{AA} = 4\text{ h}$  (c); T6R:  $T_{SHT} = 510\text{ °C}$   $t_{SHT} = 10\text{ min}$ ,  $T_{AA} = 160\text{ °C}$   $t_{AA} = 6\text{ h}$  (d). The T5 did not affect the MP structure, which was deleted by the SHTR and conventional SHT.

The layer-by-layer deposition strategy promotes the formation of a preferentially oriented crystallographic texture. Inverse Pole Figure (IPF) maps (Figures 2.15 (a,c,e,g)) show elongated columnar grains near the center line of the MP and then aligned with the direction of the heat flow. Pole Figures (PF) and Inverse Pole Figures (IPF) (Figures 2.15 (b,d,f,h)) reveal a solid crystallographic texture along the building direction (z-axis) for each condition due to the predominant  $\langle 100 \rangle$  orientation of the columnar grains, as clearly evidenced by the high intensities of the diffraction peaks  $\langle 100 \rangle$  in the IPF maps. The cell solidification mode of cubic materials occurs along the  $\langle 100 \rangle$  direction, following a higher accommodation coefficient than other crystallographic directions of the FCC structure [56].

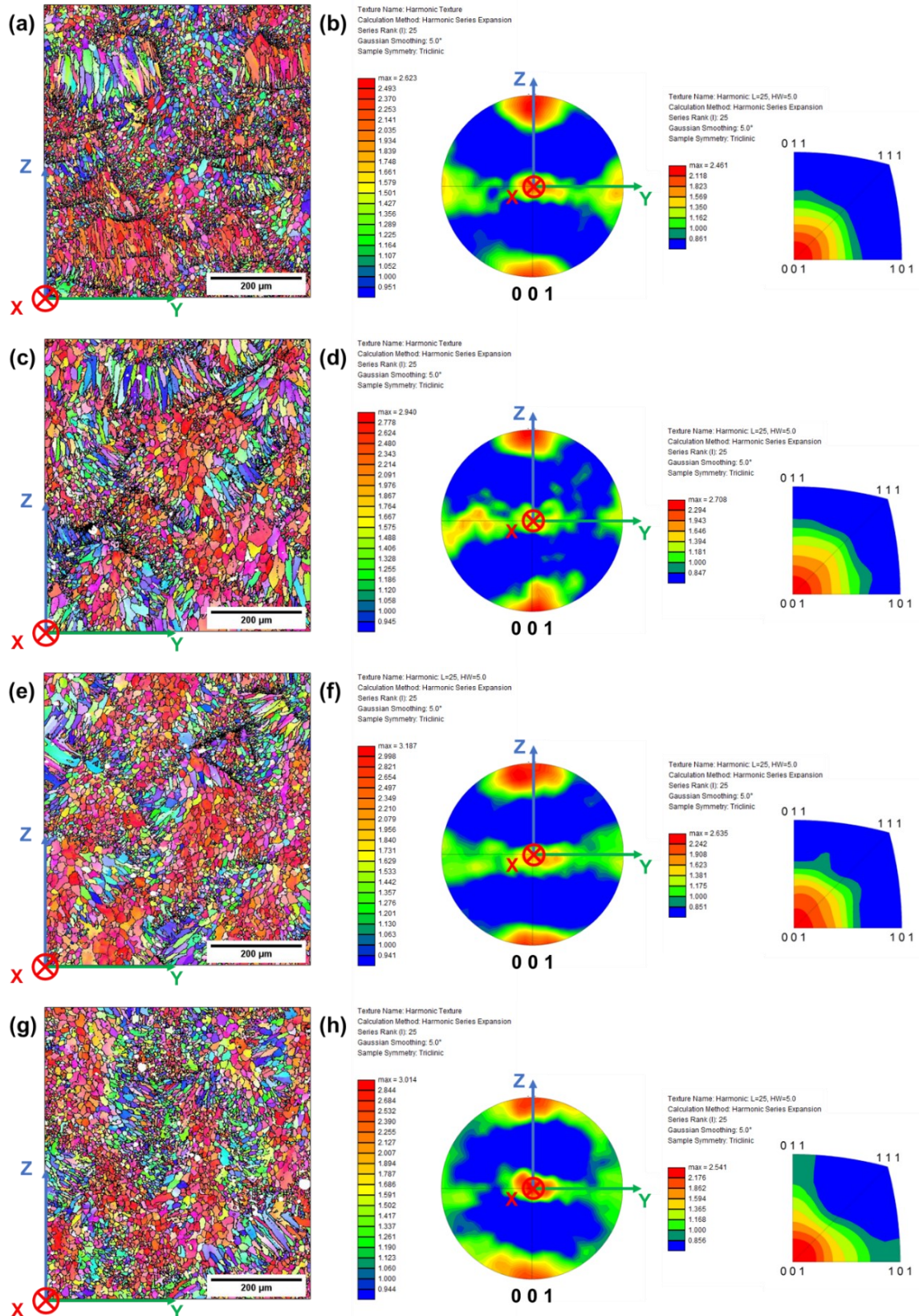


**Figure 2.15.** IPF maps, PF, and IPF of the L-PBF AlSi10Mg alloy in AB (a,b), T5 (c,d), T6R (e,f), and T6B (g,h). In GB maps, the misorientation values higher than 15° are marked by black lines, while lower misorientation was characterized only by a variation in color intensity.

The effect of the 67° rotating scanning strategy is detectable by a moderate  $\langle 100 \rangle$  crystallographic orientation along the y-axis (Figures 2.15(b,d,f,h)); in fact, the local direction of the epitaxial grain can tilt to the z-axis along the entire MPB,

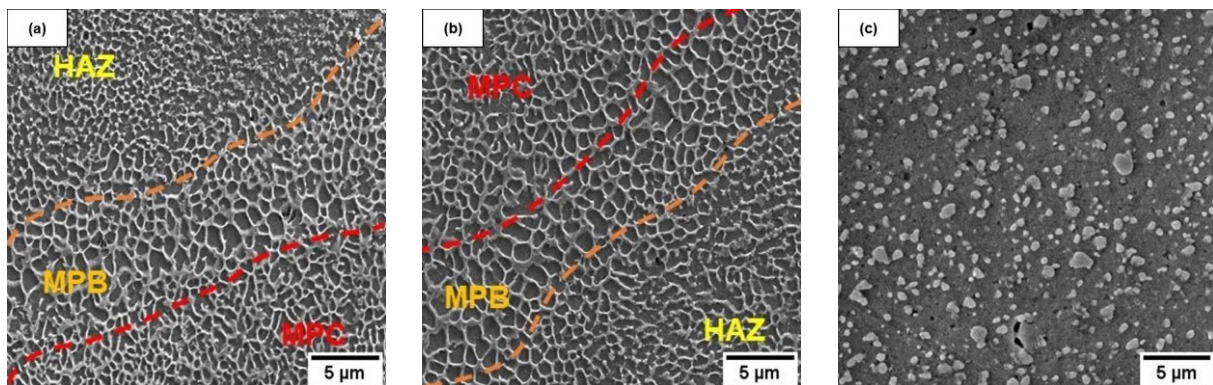
also promoted by the high scanning speed (1150 mm/s). The rotating scanning strategy induces a more isotropic microstructure, as reported by Qin et al. [57] and Moses et al. [56], as also described in Figure 2.16.



**Figure 2.16.** Light optical microscopy (LOM) image of the plane parallel to the building direction of the L-PBF AlSi10Mg alloy. In particular, the superimposition with the grain boundaries (GBs) obtained by EBSD shows equiaxed grains and columnar grains passing through the individual layers. The rotating scanning strategy induces randomly distributed MPs.

Weak  $\langle 110 \rangle$  and  $\langle 111 \rangle$  texture components are observable in IPF of the T6B condition (Figure 2.15(h)). It could be due to the recovery process induced by the high temperatures (540 °C) and long soaking times (1 h) [8]. In particular, the high content of Si segregated along cell boundaries of the L-PBF AlSi10Mg alloy may induce thermal stresses caused by the thermal expansion coefficient mismatch between Al and Si. The stress encourages dislocation formation in cellular boundaries, which can act as nucleation sites for recrystallization [58]. Therefore, the recovery process could lead to higher high-angle grain boundaries (HAGBs, with a misorientation angle higher than 15°) [59]. A more extensive discussion will be given in section 3.3.1. Furthermore, the high volume of remelted base metal promotes the crystallization of equiaxed grains along the MPBs (Figures 2.15(a,c,e,g)), whose growth during the L-PBF printing is limited by the competitive growth of large columnar grains of  $\langle 100 \rangle$  orientation. In any case, all samples show comparable crystallographic characteristics: consequently, the T5 and T6 heat treatments did not significantly influence the crystallographic texture, as reported by other authors [79,112,129]

Further investigations on the effect of different  $T_{SHT}$  and  $t_{SHT}$  on the microstructure evolution were carried out by FEG-SEM (Figure 2.17).



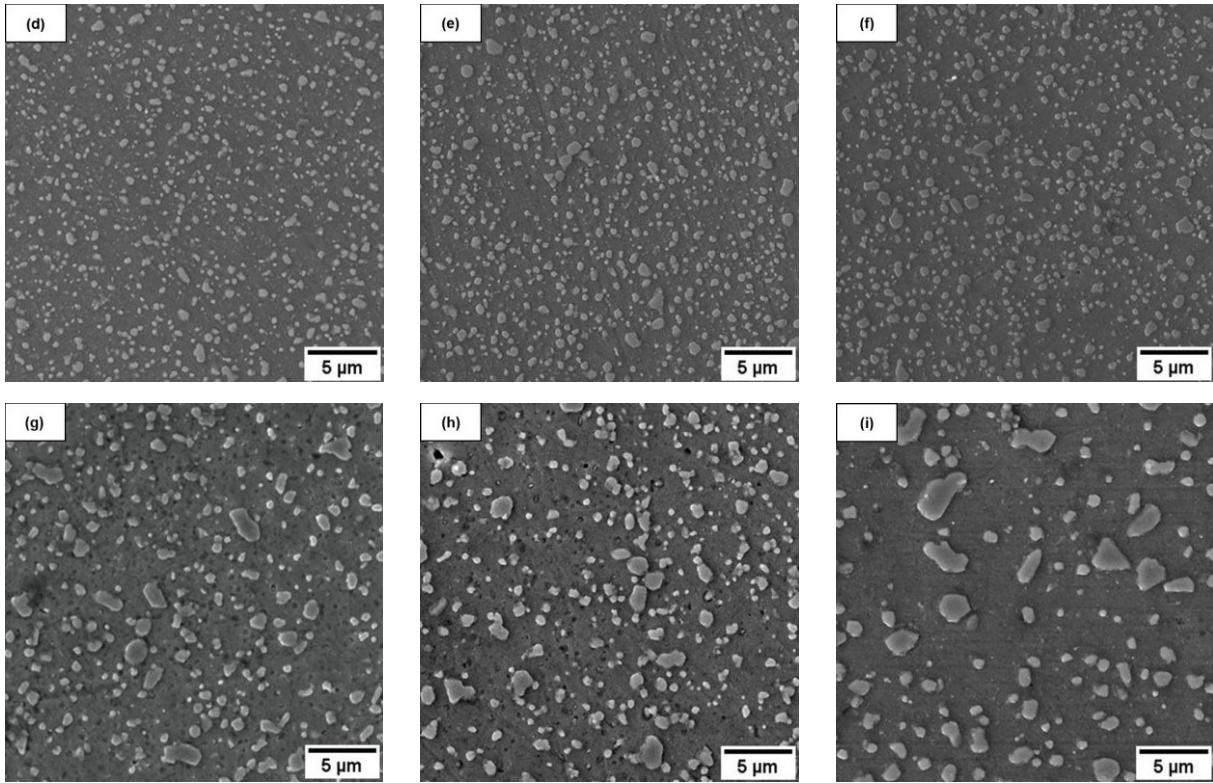


**Figure 2.17.** L-PBF AlSi10Mg microstructures: AB (a); T5:  $T_{AA} = 160\text{ °C}$   $t_{AA} = 4\text{ h}$  (b); after solution phase:  $T_{SHT} = 450\text{ °C}$   $t_{SHT} = 1\text{ h}$  (c);  $T_{SHT} = 510\text{ °C}$   $t_{SHT} = 5\text{ min}$  (d);  $T_{SHT} = 510\text{ °C}$   $t_{SHT} = 10\text{ min}$  (e);  $T_{SHT} = 510\text{ °C}$   $t_{SHT} = 15\text{ min}$  (f);  $T_{SHT} = 510\text{ °C}$   $t_{SHT} = 30\text{ min}$  (g);  $T_{SHT} = 510\text{ °C}$   $t_{SHT} = 1\text{ h}$  (h);  $T_{SHT} = 540\text{ °C}$   $t_{SHT} = 1\text{ h}$  (i).

In AB and T5 samples, the particular solidification conditions led to the formation of sub-micrometric cells of supersaturated  $\alpha$ -Al solution surrounded by a eutectic Si network (Figures 2.17(a,b)). The Figures show equiaxed and uniform cells corresponding to the MPC and coarser and elongated cells next to the MPB, as described in [6,14]. Moreover, at higher magnification (Figure 2.18), the presence of acicular nano-sized Si precipitates within the cells of the Al matrix is visible, both in the AB and T5 samples. The prolonged exposure to high temperature induces their formation due to the use of a heated platform ( $150\text{ °C}$  for 30 h), while the following artificial aging ( $160\text{ °C}$  for 4 h) did not have remarkable effects on Si precipitate size and distribution [7,27].

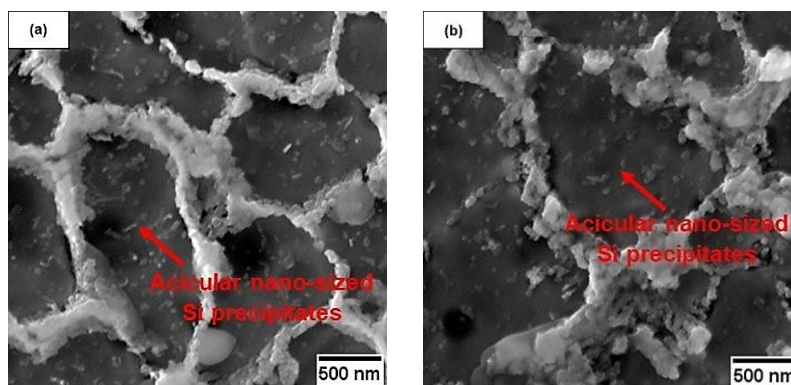


**Figure 2.18.** L-PBF AlSi10Mg alloy microstructures: AB (a); T5:  $T_{AA}=160\text{ °C}$   $t_{AA}=4\text{ h}$  (b).

During the SHT step, the AB microstructure evolved from the ultrafine cellular structure to a composite-like microstructure of eutectic Si particles embedded into the  $\alpha$ -Al matrix (Figures 2.17(c-k)). The dissolution of the eutectic Si network and the nucleation of the first nano-sized Si particles can take less than 5 min at high temperatures (Figure 2.17(e)). However, the final size and distribution of the Si particles is a function of both  $T_{SHT}$  and  $t_{SHT}$  in agreement with the findings of [11,15-17], confirming the importance of Si diffusion processes in particle growth and coalescence.

Complete image analysis of the Si particles was carried out to assess the effects of SHT conditions on the microstructure and, after that, on the mechanical properties. Figure 2.19 shows the average area of the Si particles (Figure 2.19(a)) and their number per unit area (Figure 2.19(b)) for each SHT condition. The lowest Si particle area and the highest density of Si particles per unit area were observed for SHT carried out at  $T_{SHT}$  of 510 °C and for  $t_{SHT}$  in the range of 5 - 15 min, indicating that a very short SHT leads both to smaller and more homogeneously distributed Si particles in the Al matrix, as also confirmed by their lower distance (Table 2.8).

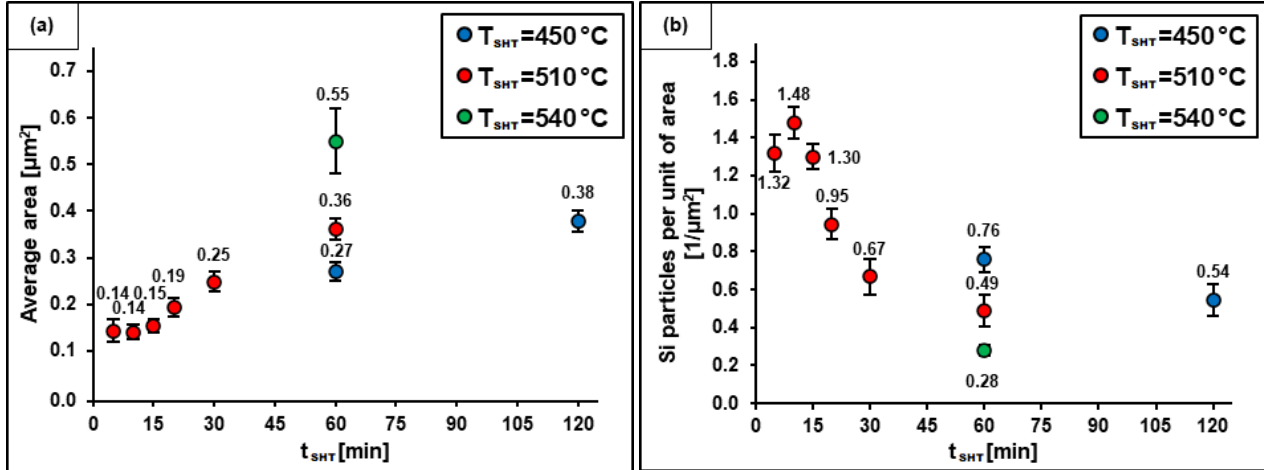


Figure 2.19. Effects of different SHT conditions on (a) Si particle average area; (b) number of Si particles per unit of area.

As reported by Chen [8], reducing the inter-particle distance can induce an increase in the alloy strength contributed by Orowan looping due to the higher stress required to unlock dislocations motion through the nano and micrometric Si particles [14,60-62]. Accordingly, Si particle size and distribution also play a vital role in the strengthening process of the alloy. The increase in stress is mainly due to the Orowan strengthening mechanism and can be estimated by the following equation:

$$\Delta\sigma = \frac{MGb}{\lambda} \quad (2.7)$$

In Equation 2.7, M is the Taylor factor (3.06 for FCC crystals), G is the shear modulus (25.4 GPa for Al), b is the Burger's vector (0.286 nm for Al), and  $\lambda$  is the inter-particle spacing ( $\mu\text{m}$ ) [8]. The results in Table 8 show the correlation between a more homogeneous distribution of Si particles into the Al matrix and a higher strengthening level due to dispersed second phases. Table 2.8 reports the increased strength due to the Orowan mechanism, evaluated for each SHT condition, and the comparison with SHTB ( $T_{SHT} = 540$  °C and  $t_{SHT} = 1$  h) to focus on the increased strength introduced by the finer microstructure and to minimize possible systematic errors due to the analysis process. According to Equation 2.7, the SHTR (510 °C for 10 min) could lead to the maximum improvement of YS of 20 MPa, compared to SHTB.

Table 2.8. Inter-particle spacing ( $\lambda$ ) and increase in strength due to the Orowan mechanism for different SHT conditions.

Temperature ( $T_{SHT}$ )	Soaking time ( $t_{SHT}$ )	$\lambda$ [ $\mu\text{m}$ ]	$\Delta\sigma_{th}$ [Mpa]	$\Delta\sigma_{th} - \Delta\sigma_{540^\circ\text{C}-1h}$ [Mpa]
450 °C	1h	$0.78 \pm 0.01$	$30 \pm 0.2$	9
	2h	$0.93 \pm 0.02$	$25 \pm 0.4$	4
510 °C	5min	$0.59 \pm 0.02$	$39 \pm 1.6$	18
	10min	$0.57 \pm 0.02$	$41 \pm 1.3$	20
	15min	$0.60 \pm 0.01$	$39 \pm 0.8$	18
	20min	$0.67 \pm 0.02$	$35 \pm 0.8$	14

	<b>30min</b>	0.81 ± 0.04	29 ± 1.5	8
	<b>1h</b>	0.86 ± 0.01	27 ± 0.4	6
<b>540 °C</b>	<b>1h</b>	1.11 ± 0.06	21 ± 1.1	x

Several authors [12,15,16] reported a positive effect on the mechanical performance of the L-PBF AlSi10Mg of a homogeneous distribution of small Si particles in the  $\alpha$ -Al matrix. Moreover, a finer microstructure can further improve the mechanical performance of the alloy since a small Si particle size means higher cohesion of the particles with the  $\alpha$ -Al matrix and hence higher alloy strength and ductility. However, to the authors' knowledge, a quantitative evaluation was yet to be carried out.

The size distribution of the Si particles for the samples which underwent SHTR and SHTB is reported in Figure 2.20. These results show the difference between the Si particle area in the two analyzed conditions: (i) SHTR microstructure consists of approximately 98% of the Si particle area below 0.5  $\mu\text{m}^2$ , while (ii) SHTB microstructure shows the distribution of the Si particle area displaced at 5  $\mu\text{m}^2$ .

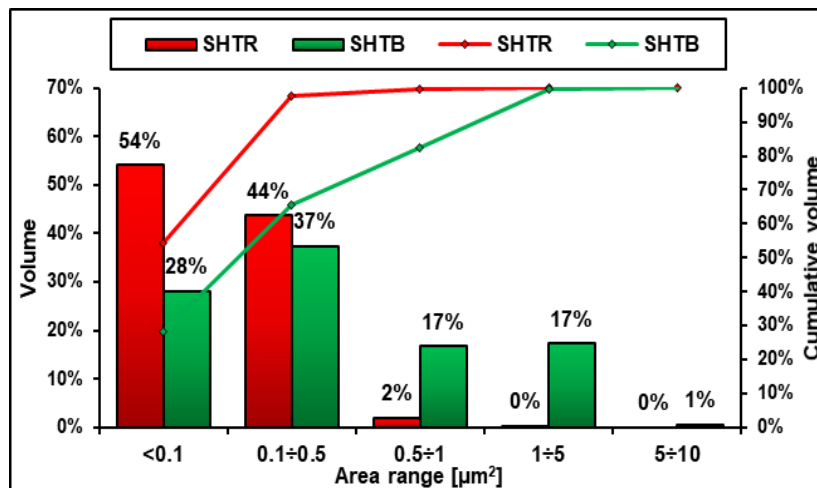


**Figure 2.20.** Area distribution of Si particles for SHTR ( $T_{\text{SHT}} = 510\text{ °C}$  and  $t_{\text{SHT}} = 10\text{ min}$ ) and SHTB ( $T_{\text{SHT}} = 540\text{ °C}$  and  $t_{\text{SHT}} = 1\text{ h}$ ) conditions.

From the results of density measurements, XRD, and microstructural analyses, SHTR offers several advantages in comparison with the other SHT conditions as (i) limiting the increase in the porosity content due to high-temperature exposure, (ii) leading to more refined and more homogeneous microstructure in terms of eutectic Si particles, (iii) promoting the development of a more supersaturated  $\alpha$ -Al matrix. These effects should induce both higher strength and ductility after subsequent aging. Therefore, the SHTR has been identified in this study as the optimal SHT for the L-PBF AlSi10Mg alloy.

### 2.3.1.4 Aging curves

The aging curves on AB samples at 160 °C, 170 °C, and 180 °C for times up to 8 h are reported in Figure 2.21(a). The curves highlight that the hardness decreases post AA compared with the AB alloy. The reduction is negligible up to 4 h at 160 °C, while at higher temperatures, the hardness decreased after only 1 h. At 160 °C and 170 °C, the maximum hardness drop is 4% and 6% after 8 h, respectively. Conversely, at 180 °C a significant hardness drop of about 15% already occurs after 5 h. This behavior can be explained considering that the L-PBF printing of the samples is carried out using a heated platform (150 °C) and takes about 30 h. The heated platform promotes the precipitation of strengthening acicular nano-sized Si phases within the cells of the  $\alpha$ -Al matrix, as observed in Figure 2.21(a). Depending on the  $T_{AA}$  and  $t_{AA}$ , the AA may not have appreciable effects on Si precipitates, or it may induce their coarsening with a consequent decrease of the material hardness at temperatures higher than 150 °C.

The aging curves (Figure 2.21(b)) of the alloy after SHTR (T6R heat treatment) show the typical trend for solution-treated and quenched Al alloys, where hardness increases with increasing  $t_{AA}$  and the peak aging condition shifts to shorter aging times with increasing aging temperature. It is worth noting that the SHTR, because of its effects on microstructure (described in section 2.3.2) causes a hardness drop of about 45% compared to the AB condition. This drop is only partially recovered after the aging treatment because of the precipitation of  $\beta''$  and  $\beta'$  strengthening phases [28,30,63].

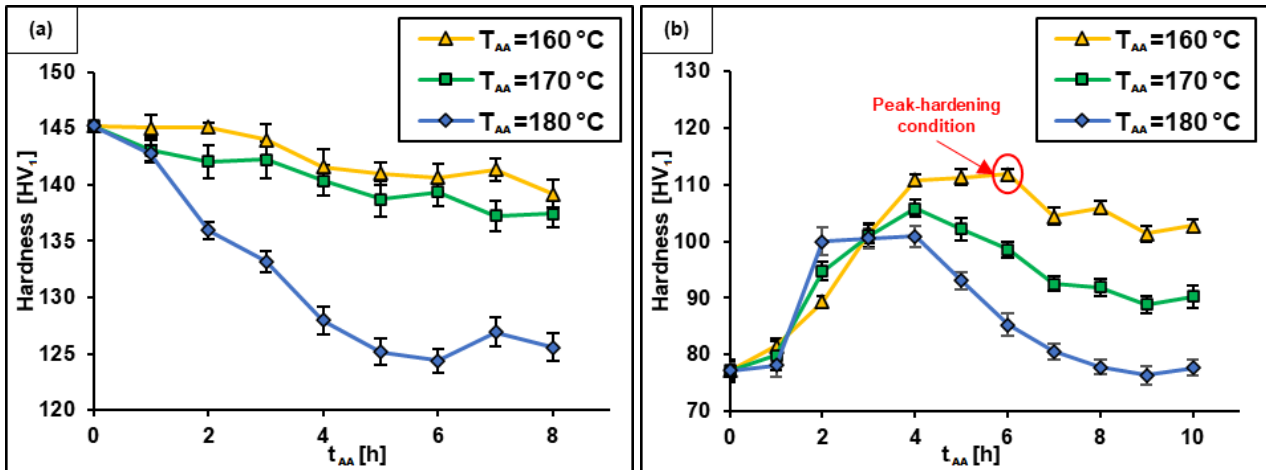


Figure 2.21. Aging curves for the AB (a) and SHTR (b) conditions at 160 °C, 170 °C, and 180 °C.

Even in the peak-aged condition ( $T_{AA} = 160$  °C and  $t_{AA} = 6$  h), the hardness drop equals 23% compared with the AB alloy. Despite the hardness reduction, these data agree with data already published [7,12,18,31] for T6 heat-treated L-PBF AlSi10Mg alloy, further confirming the effectiveness of the SHTR compared with a conventional SHT. Similar trends in the aging curves have been identified by different authors [12,30,31], even if peak-hardening conditions have been identified for a longer time. Zhou et al. [28], starting from conventional T6 solution treatment conditions ( $T_{SHT} = 520$  °C and  $t_{SHT} = 2$  h and  $T_{AA} = 160$  °C), identified the peak-hardening condition at 10 h. Comparable results were obtained by Padovano et al. [30] in the same T6 heat treatment conditions. However, the aging curves in the present paper show that the peak-hardening conditions move towards a shorter aging time, occurring after 6 h. Probably this behavior is due to the higher Si supersaturation induced by SHTR compared to conventional SHT, which accelerates the precipitation kinetics hardening after quenching [64]. This finding agrees with [17] and [30]: precipitation kinetic is closely related to the SHT conditions.

The aging curves at 170 °C and 180 °C compared with the curve at 160 °C show: (i) a shift of the peak hardness to a shorter  $t_{AA}$  (3 h instead of 6 h); (ii) a lower peak hardness (7 and 11%, respectively); (iii) a faster overaging, with a residual hardness after 8 h at 180 °C equal to the hardness of the alloy after SHTR. In addition, for these  $T_{AA}$  the hardness trends agree with those reported in the literature [18,28,30], but the peak hardness shifted to shorter  $t_{AA}$  because of the faster precipitation kinetics. Moreover, it is worth noting that after 8 h at 180 °C the residual hardness is comparable to the SHTRed alloy.

In light of the above, the influence of the following heat treatment conditions on the mechanical behavior and the fracture mechanisms of the L-PBF AlSi10Mg alloy was assessed:

- (i) Direct artificial aging (T5): 160 °C for 4 h followed by air cooling, slightly increases the ductility of the alloy compared with AB alloy.
- (ii) Rapid solution treatment (T6R): SHTR at 510 °C for 10 min, water quenching at room temperature, artificial aging at 160 °C for 6 h, and air cooling, to test the peak-hardening condition.

### 2.3.2 Static mechanical characterization

Tensile properties and hardness of the T5 and T6R alloys were compared with the AB and T6B alloys, as described in section 2.2. The hardness ( $HV_1$ ) of the tensile samples and the results of the tests are reported in Figure 2.22, while representative stress-strain curves are reported in Figure 2.23.

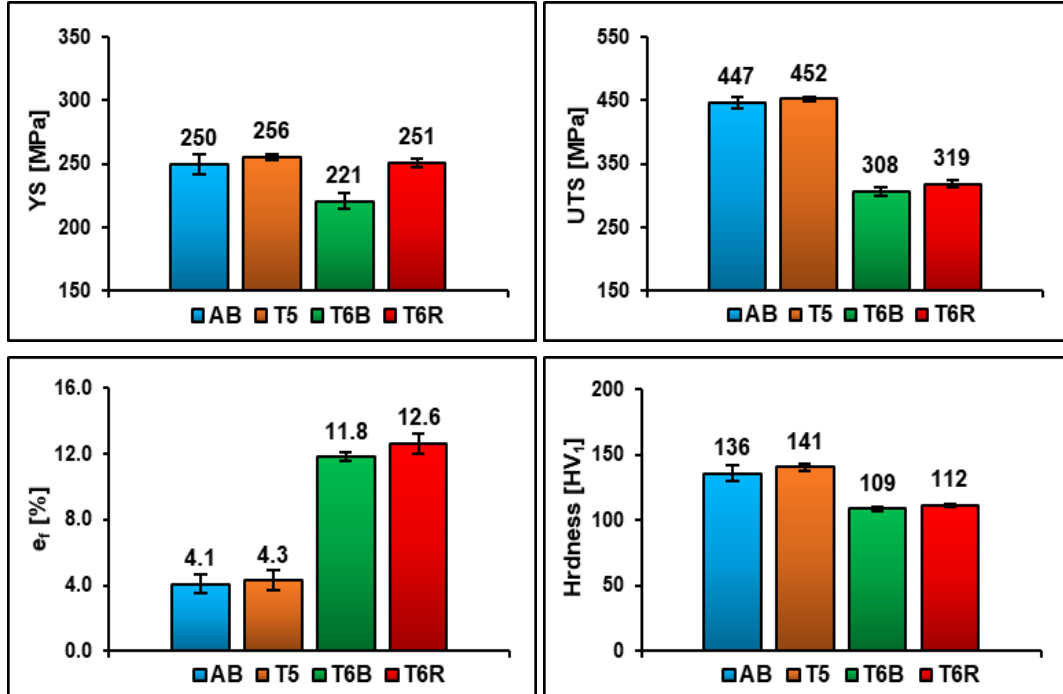


**Figure 2.22.** Tensile properties and hardness of the L-PBF AlSi10Mg alloy related to the conditions: AB (i), T5 (AA at 160 °C for 4 h) (ii), T6B (SHTB at 540 °C for 1 h and AA at 160 °C for 4 h) (iii) and T6R (SHTR at 510 °C for 10min and AA at 160 °C for 6 h) (iv).

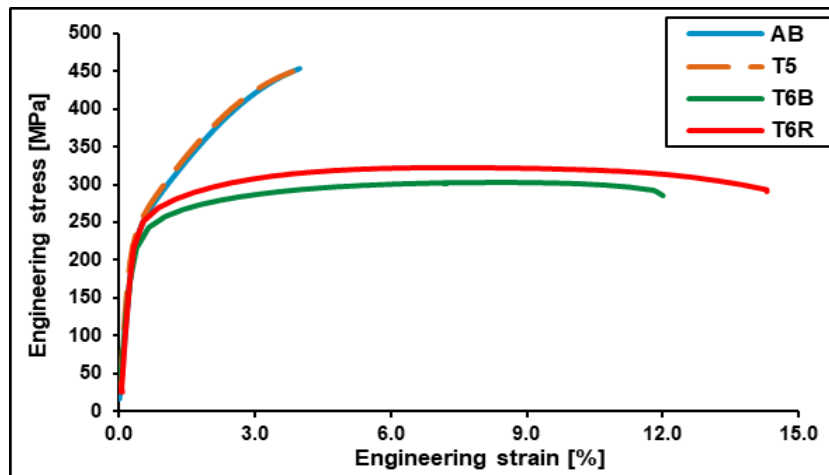


**Figure 2.23** Representative tensile stress-strain curves of the L-PBF AlSi10Mg alloy related to the conditions: AB (i), T5 (AA at 160 °C for 4 h) (ii), T6B (SHTB at 540 °C for 1 h and AA at 160 °C for 4 h) (iii) and T6R (SHTR at 510 °C for 10min and AA at 160 °C for 6 h) (iv).

Among the tested samples, the AB and T5 samples show the highest strength but the lowest  $e_f$  (Figure 2.22) due to the concurrent effect of several strengthening mechanisms typical of their peculiar microstructure: microstructural refinement, solid solution, aggregated second phase (eutectic Si network), high dislocation density and precipitation hardening.

The T5 heat treatment leads to a slight increase of the tensile properties compared with the AB condition, respectively equal to 3.7% for hardness, 1.1% and 2.4% for UTS and YS, and 4.8% for  $e_f$ . According to the literature survey [7,20,24], this slight improvement in mechanical performances of the T5 alloy could be related to (i) the formation of

acicular nano-sized Si precipitates within the cells of the Al matrix, (ii) the partial stress relief occurring during the T5 and (iii) the preservation of the AB microstructure with its main strengthening mechanisms. It is worth mentioning that the more significant improvement of the mechanical performance reported in the literature by the T5 heat treatment [7,27] is attributable to the use of a not heated platform in these studies, while, in the present work, the platform was heated to 150 °C. Platform heating increases the amount of acicular nano-sized Si strengthening precipitates that already form during the printing of the samples in the cells of the  $\alpha$ -Al matrix, as confirmed by the previously reported microstructural analyses (Figures 2.18(a,b)). Therefore, it can be inferred that the T5 performed in the present study had a lower effect on the amount of Si precipitates and, consequently, on their strength compared to [7,27] due to the heated platform. The T5 heat treatment, moreover, had no beneficial effects on the ductility due to its negligible effect on the MPB, which ensures a preferential path for crack growth during the tensile tests analogous to that observed in the AB samples, as described below

Conversely, T6B induces a decrease in strength properties (10% for the YS and 45% for the UTS) and an approximately 200% increase in  $\epsilon_f$  compared to both the AB and T5 alloys.

These findings agreed with the results reported in [12,15,59] and were widely explained in the light of the microstructural changes which take place mainly during the SHT, such as the disappearance of the MP structure or the development of the composite-like microstructure of Si particles in  $\alpha$ -Al phase matrix in place of the cellular structure [9,11,15]. These microstructural changes induce a remarkable reduction of the solid solution reinforcement, the loss of both microstructural refinement and aggregate second-phase strengthening mechanisms, and a drop in the dislocation density. The loss of the main strengthening mechanisms active in the AB alloy is partially balanced by the precipitation of both  $\beta''$  and  $\beta'$  strengthening phases and the dispersed second phase reinforcement due to the presence of spherical Si particles inside the  $\alpha$ -Al matrix. Conversely, the disappearance of scan tracks, MPBs, and HAZs, besides an overall reduction of the inhomogeneity inside the microstructure and of the internal residual stresses, leads to an increase in the alloy's ductility.

The new proposed T6R heat treatment induces an increase of both strength (about 14% and 4% for YS and UTS, respectively) and ductility (about 7% for  $\epsilon_f$ ) compared with the T6B, while comparison with AB and T5 samples show similar YS and significantly higher elongation to failure (more than 200%), while UTS is lower of about 30%. The increase in mechanical performance in terms of strength and ductility of the T6R compared to the T6B can be mainly ascribed to its more refined and homogeneous microstructure. Smaller Si particles allow (i) an increase in the effect of the Orowan strengthening mechanism; (ii) an increase in the cohesion between Si particles and  $\alpha$ -Al matrix; (iii) a reduction in the tendency of the Si particles to fracture; (iv) a reduction in the gas porosity content [12,15,16]. These considerations are confirmed by Equation 2.7, which estimates the increase of the alloy strength due to the Orowan mechanism. In particular, Equation 2.7 could evaluate with good approximation the effect on the YS of the alloy of the different composite-like microstructures induced by T6R and T6B. According to equation 5, the T6R samples have a higher YS of 20 MPa than T6B ones, a value in agreement with the results of the tensile tests that highlighted a difference ( $\Delta$ YS) of 30 MPa between the YS of the T6R and T6B samples. This slight difference between calculated and measured  $\Delta$ YS could be ascribed to the effects of the other microstructural changes on the above-reported strengthening or failure mechanisms.

It is worth noting how the microstructure also affects the strain-hardening ability of the L-PBF AlSi10Mg alloy. The AB and T5 alloys, as highlighted by the stress-strain curves in Figure 2.23, show a higher strain hardening than that of the T6R and T6B samples. According to Chen et al. [8], this behavior is mainly due to the ultrafine cellular structure

and indicates the possibility for ultrafine cellular structures of the L-PBF AlSi10Mg alloy to achieve large uniform elongations. However, the presence of an inhomogeneous microstructure constituted by MPBs, HAZs, and defects such as gas pores and LoF reduces the theoretical  $\epsilon_f$  of the AB and T5 samples so that it is lower than T6B and T6R samples, which have a coarser but more homogeneous microstructure.

To highlight the effect of the heat treatment conditions on the fracture mechanisms of L-PBF AlSi10Mg alloy, the analysis of the fracture surfaces was carried out both by OM (Figures 2.24 and 2.25) and by SEM (Figures 2.25, 2.26, and 2.25) to identify the main failure mechanisms.

In the AB and T5 samples (Figure 2.24), the fracture propagates preferentially along the MPBs. These regions are characterized by a coarser microstructure, lower Si content (for the larger  $\alpha$ -Al cells area), and higher density of defects (like LoFs), representing the weakest zones of the microstructure [65]. No significant differences in the macro and microfracture features have been observed between T5 and AB samples, further confirming that the direct aging treatment at low temperature (lower than 300 °C) has no substantial effects on the alloy microstructure.

In contrast, in both T6B and T6R samples (Figure 2.25), the fracture propagates by joining the pores present at the Si particles/ $\alpha$ -Al matrix interface, originating from the detachment of the Si particles from the matrix [66]. The fracture mechanism is comparable to AlSi cast alloys, where the nucleation of the micro-voids occurs at the soft Al-matrix/hard Si-phase interface, followed by growth and coalescence of the voids. However, because of the finer and more homogeneous Si particle distribution, it is possible to observe a smoother crack path in the failed T6R compared to the T6B samples (Figures 2.25(c,d)). The larger and more irregular Si particles and the higher amount of gas porosities in the T6B compared to the T6R samples induce the formation of larger pores (Figures 2.25(b,d)), which promote failure under tensile loading with the development of rougher fracture surfaces.

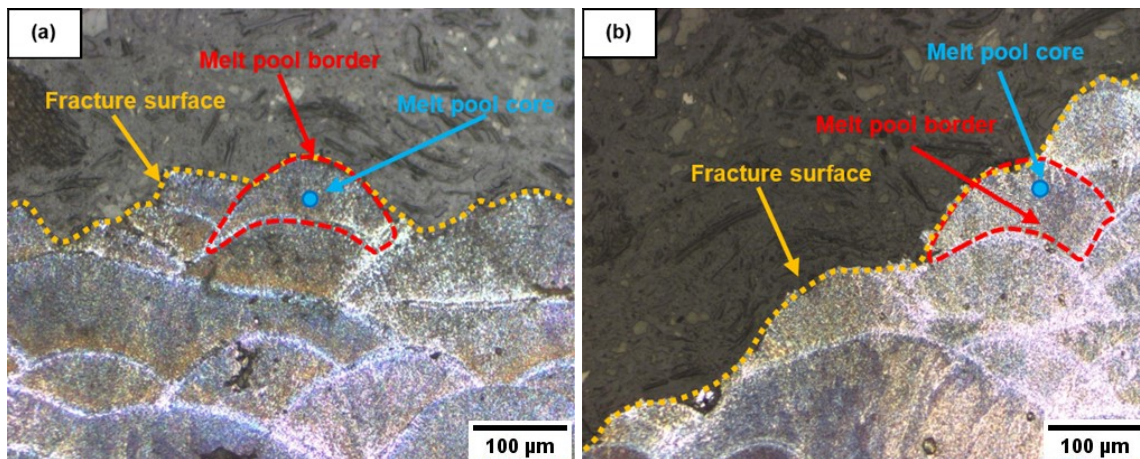


**Figure 2.24.** Longitudinal section of the fracture surface relative to the AB (a) and T5 (b) conditions. Each optical micrograph shows the same crack propagation path along the MPB.

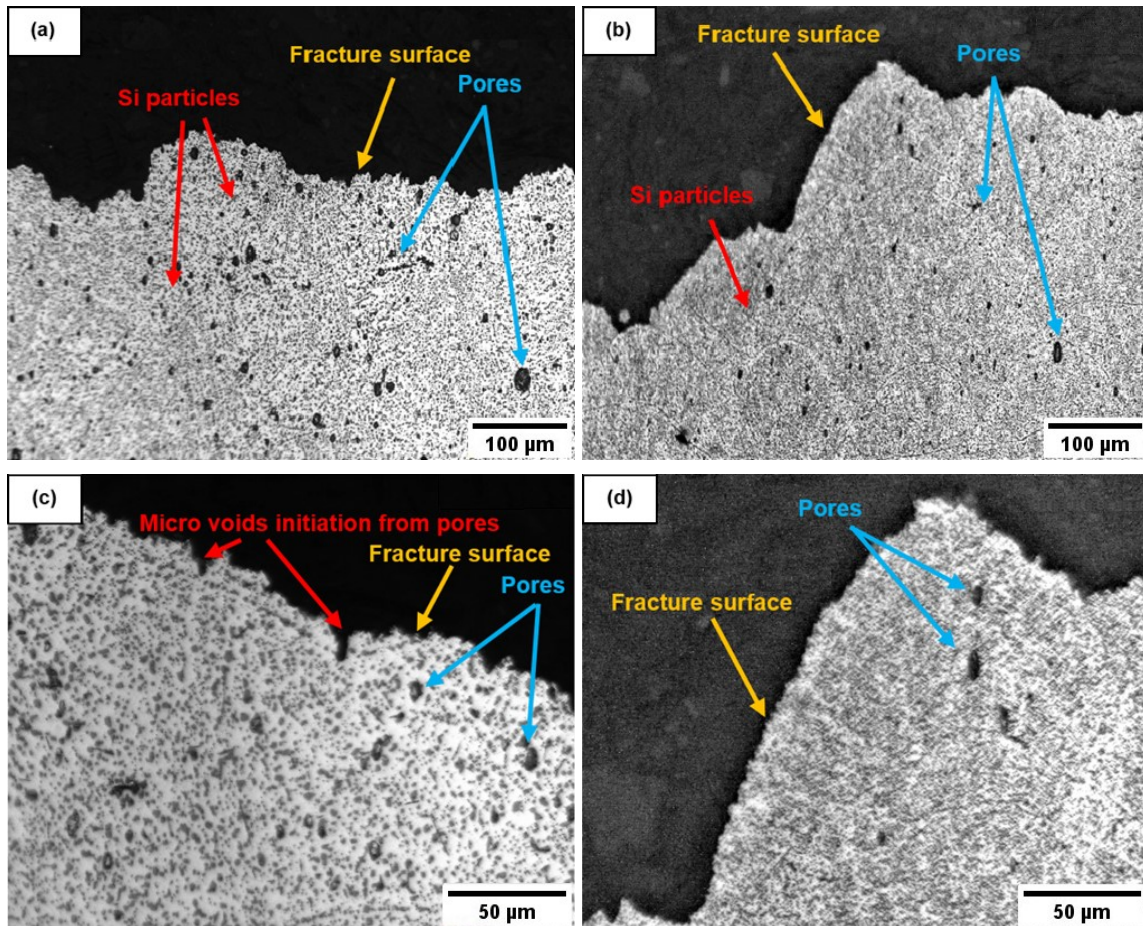


**Figure 2.25.** Longitudinal section of the fracture surface relative to the T6B (a,c) and T6R (b,d) conditions. The T6B samples show larger Si particles, higher internal pore density, and higher fracture surface roughness than the T6R samples.

As described above, AB and T5 samples show identical fracture surface morphologies. Focusing on the AB condition, the low magnification SEM images of the fracture surfaces (Figures 2.26(a,b)) highlight: (i) an interlayer fracture path, (ii) significant defects (LoF and pores), (iii) flat zones where scan-track segments are visible and (iv) a crack path that develops due to detachment at the interface between the Si eutectic network and the  $\alpha$ -Al matrix [11]. These images agree with the previous observations, highlighting the fracture path's development mainly through the microstructure's weakest zones, such as MPB, HAZ, and defects. This preferential fracture path induces an inter-layer fracture with consequent low  $e_f$ . Fracture surfaces at higher magnification (Figure 2.26(c,d)) are characterized by shallow micro and sub-micrometric dimples with a jagged, sharp, and irregular morphology. This morphology is probably due to the tear-fracture mechanism at the Si network/ $\alpha$ -Al cells interface, which leads to the formation of dimples with size and morphology that mirrors the sub-cellular microstructure of the alloy and reflects the high strength and low ductility of the material. The presence of Si nanoparticles within the center of the cellular eutectic cells, which further increase the strength of  $\alpha$ -Al and reduce its ductility, accentuates the fracture mechanisms [55,67].

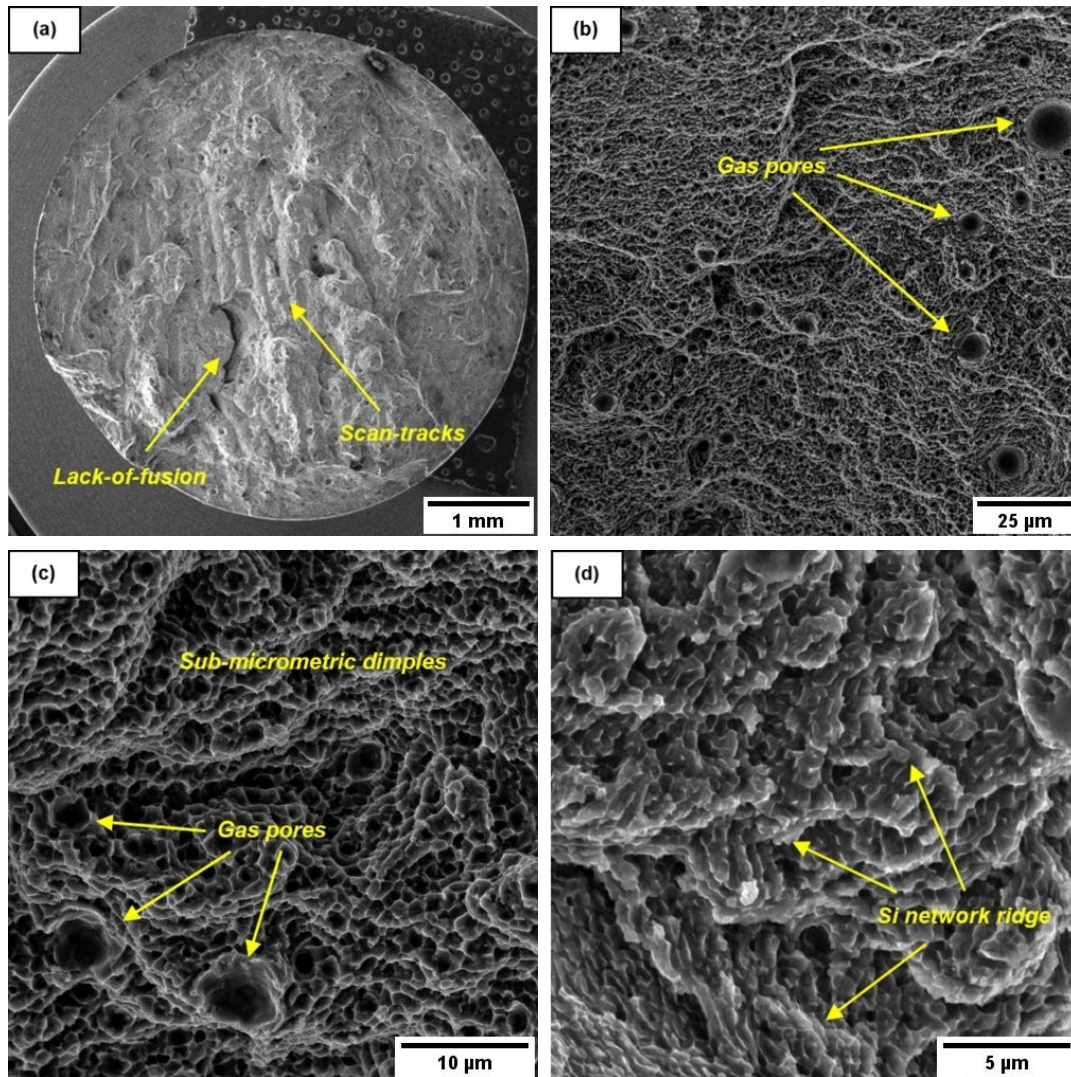


**Figure 2.26.** FEG-SEM images of the fracture surfaces of the L-PBF AlSi10Mg parts in AB condition at different magnifications: (a) 40x, (b) 1.50kx, (c) 5.00kx, (d) 10.00kx.

The microstructure evolution induced by the T6 heat treatments also significantly modified the fracture morphology of both T6B and T6R samples compared with AB and T5 samples, mainly at high magnification. At low magnification (Figures 2.27(a,b) and 2.28(a,b)), irregular surfaces and significant defects, mainly pores, characterized the fracture surfaces of both T6B and T6R. Even if the T6 heat treatments homogenize the microstructure and delete the MPB and HAZ [16,29], which represent a preferential crack path, some scan tracks are still observed, in agreement with the findings of Girelli et al. [34]. In contrast, the fracture surface analyses cannot highlight an apparent increase in gas porosity in the T6 alloy compared with AB or T5 samples, as pointed out by the density measurements reported in the previous section. The differences in the amount and size of gas pores appear negligible among the AB, T5, T6R, and T6B samples, and this can be explained considering that, independently from the condition of the samples, the crack propagates through the weakest path with the highest number of defects.

Fracture surface analyses at high magnification of both T6B and T6R samples show a completely ductile failure mode, characterized by deep dimples (Figures 2.27(c) and 2.28(c)), instead of the shallow dimples observed in the AB and T5 samples. However, despite the similar fracture mechanism, the different sizes and distribution of the Si particles in the T6B or T6R alloy affect dimple feature. In the T6B samples, the coarse and inhomogeneously distributed Si particles form large and very deep dimples and tear ridges (Figure 2.27(d)). The first is caused by the detachment between Si

particles and the Al matrix or the fracture of the larger Si particles [11,68], while the latter is caused by local plastic flow induced by the presence of large particles or pores close to each other. In the T6R samples, the Si particles are less prone to fracture because of their smaller size and spheroidal morphology, and therefore the dimples mainly nucleate at the Si particle/ $\alpha$ -Al matrix interface rather than by cracked particles (Figure 2.28(d)). The homogeneous distribution of the fine Si particles induces the development of finer dimples and more uniform plastic deformation than the T6B alloy.

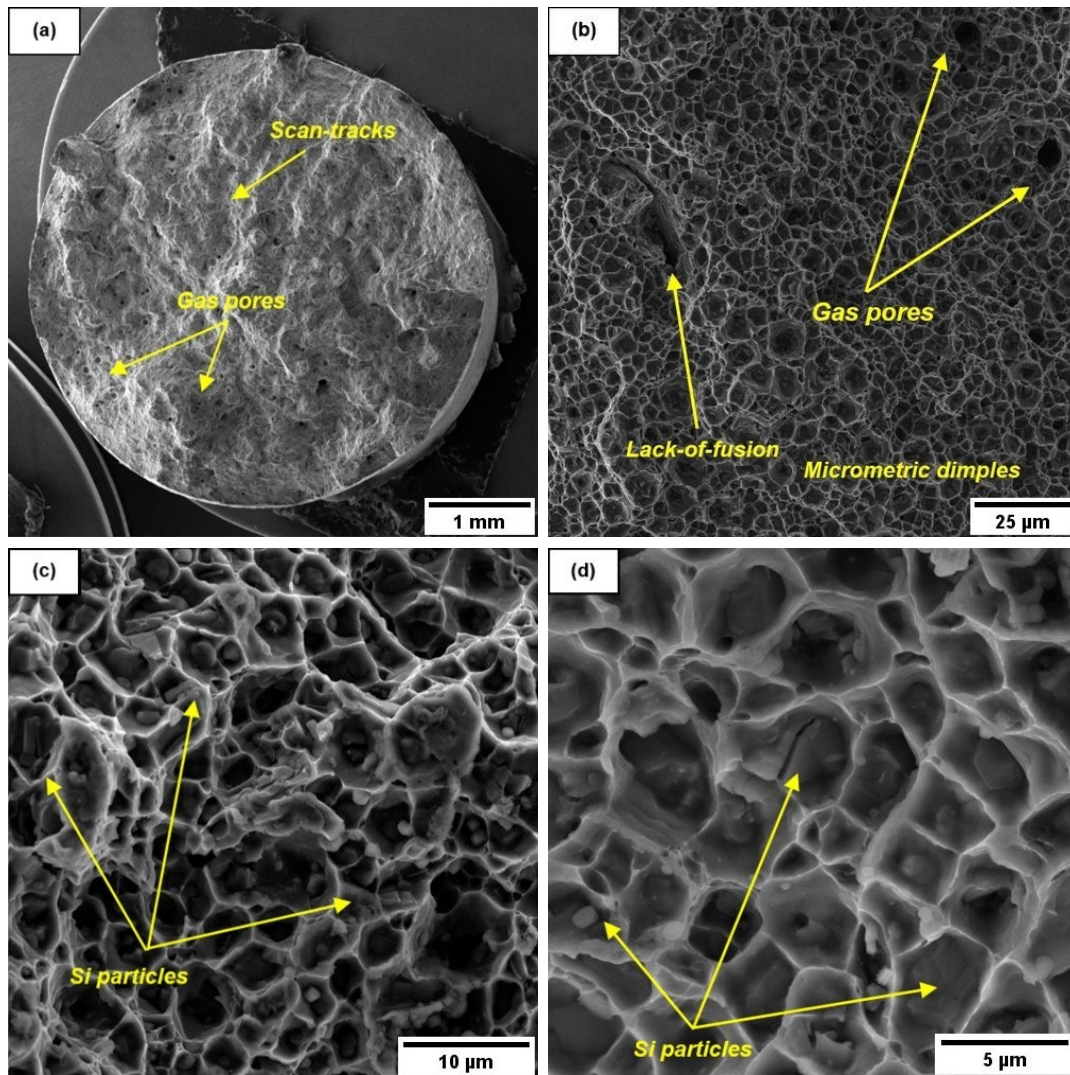


**Figure 2.27.** FEG-SEM images of the fracture surfaces of the L-PBF AlSi10Mg parts in T6B condition at different magnifications: (a) 40x, (b) 1.50kx, (c) 5.00kx, (d) 10.00kx.

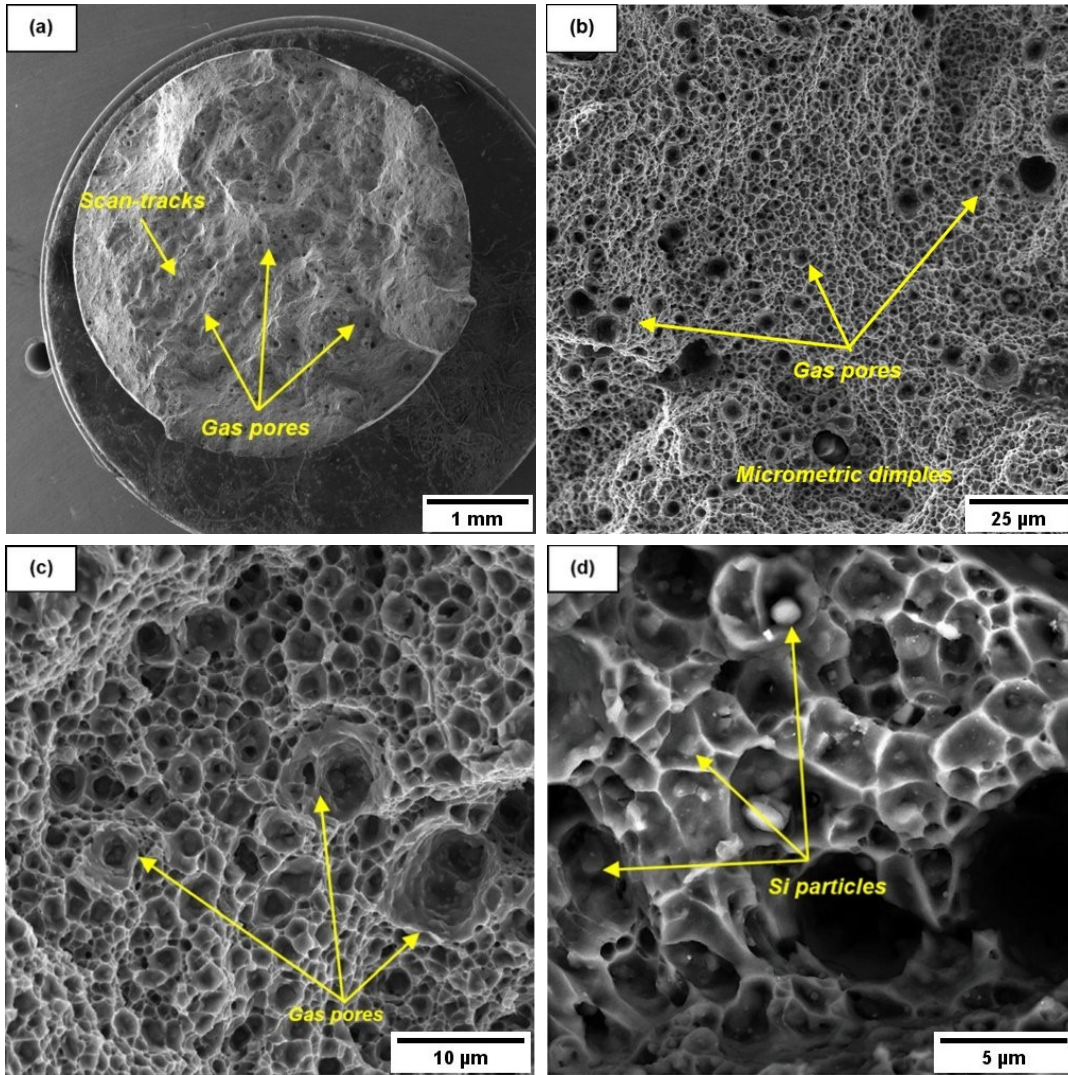


**Figure 2.28.** FEG-SEM images of the fracture surfaces of the L-PBF AlSi10Mg parts in T6R condition at different magnifications: (a) 40x, (b) 1.50kx, (c) 5.00kx, (d) 10.00kx.

### 2.3.3 Nano-mechanical characterization

The nanoindentation test investigated the influence of the morphology and size of the microstructural characteristics on the local mechanical behavior and, consequently, how this reflects on the mechanical performance of the component. To the best of the author's knowledge, a detailed analysis of the effects of the substructure on local mechanical behavior is lacking in the literature. For example, Moses et al. [56] and Zhuo et al. [59] performed nanoindentation tests on AB and heat-treated samples. However, without reporting, neither a precise mapping of the influence of the different phases and features that characterize the microstructure of the L-PBF AlSi10Mg alloy nor a direct correlation between local and macroscopic mechanical properties.

As described in the previous section, the T5 heat treatment has no remarkable effects on the microstructure and hardness of the AB alloy. Therefore the analyses carried out on T5 samples reported in the following can be considered representative of both conditions. A macrostructure of overlapping MPs and a substructure of submicrometric cells of supersaturated  $\alpha$ -Al surrounded by a eutectic-Si network characterizes the T5 alloy (Figures 2.29(a,b) and 2.17(b)).

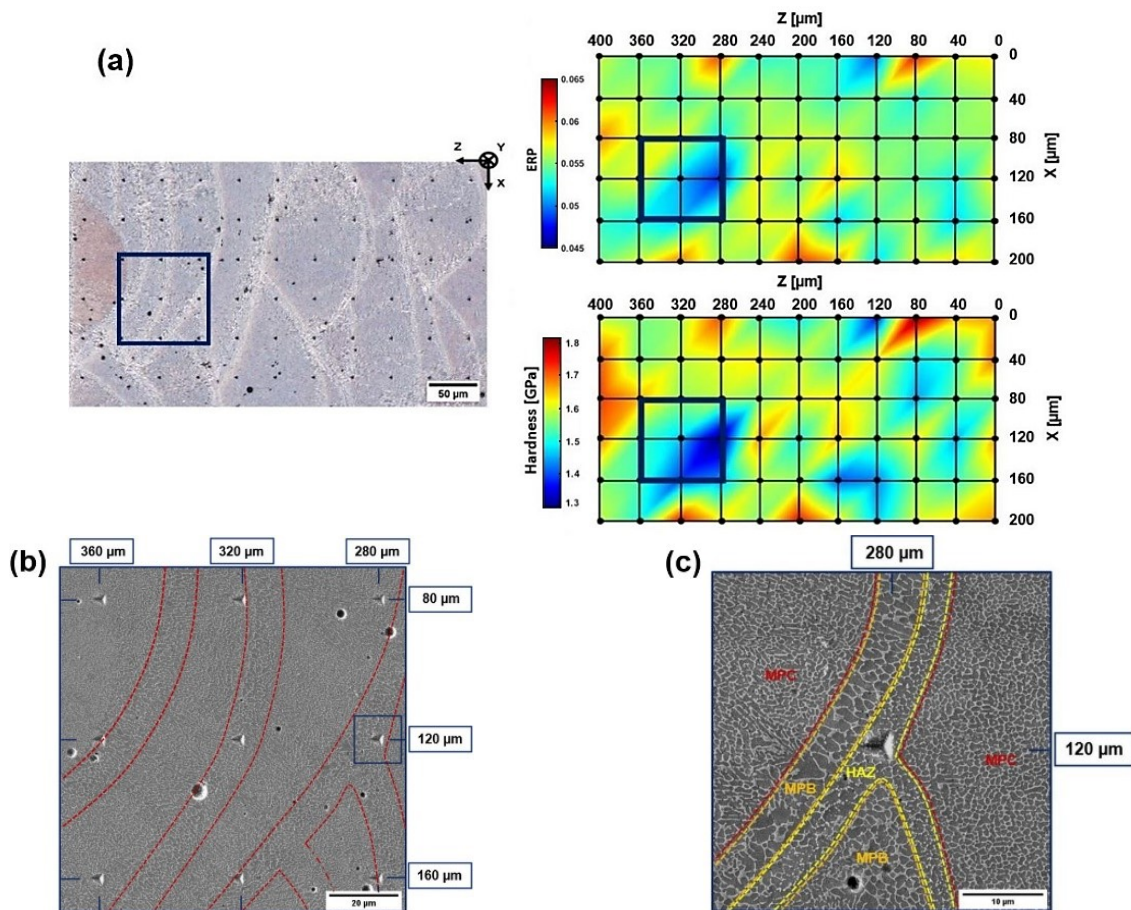


**Figure 2.29.** OM acquisition of the microstructure and nanoindentation matrix for the T5 alloy (a). High-magnification microstructures acquired at FEG-SEM: region characterized by a high density of MPB and low hardness and elastic recovery parameter values (b), HAZ characterized by deep indenter penetration into the Al matrix promoted by the disgregation of the eutectic-Si (c).

The continuous heating and cooling cycles during L-PBF printing affected the ultrafine cellular structure, as described in section 2.1. In particular, the eutectic-Si network presents different morphologies within the MP structure: (i) relatively uniform in the MPC, where the  $\alpha$ -Al cells are fine and equiaxial; (ii) coarser and more elongated in the areas adjacent to the MPB; (iii) highly discontinuous in HAZ, where it appears fragmented and constituted by small agglomerated Si particles (Figure 2.29(c)). The hardness and ERP coefficient maps clearly show the effects of the non-uniform microstructure on the mechanical response of the T5 alloy [69]. In particular, it is possible to observe H and

ERP values in large HAZ that are approximately 20 - 30% lower than the maximum measured value ( $H = 1.75$  GPa and  $ERP = 0.062$ ). This result confirms the relationship between lower local mechanical properties and a coarser and more inhomogeneous microstructure. As described by Kim et al. [70], upon loading, dislocations in the Al matrix pile up near the Si-rich interface and lead to stacking defects resulting in twinning in Si nanoparticles located at the boundaries of Si-rich cells. The morphology and size of the cellular structure influence the hindering mechanism at the eutectic-Si network/ $\alpha$ -Al cell interface and, consequently, the mechanical properties of the alloy. The lower Si content in the cellular boundaries of the HAZ, resulting from Si decomposing associated with the thermal history of the alloy [71], compared to the fine (MPC) and coarse (MPB) cellular zones (Figure 2.17), entails less effect in inhibiting dislocation slip. Since dislocations can quickly move in the HAZ, hardness decreases while plastic deformation increases. In the tensile test, the plastic deformation is mainly located within the HAZ zones, constrained by the high strength zone (MPC) and minimally by coarser zones (MPB), which prevents the dislocation motion. This condition leads to a stress-triaxiality condition and microvoids formation and coalescence [72,73]. Micro-void coalescence and deformation accumulation within the HAZ reduce  $\epsilon_f$  (Figure 2.22) and impact toughness of the material [74].

The T6R and T6B samples have a homogeneous composite-like microstructure of Si particles incorporated into the  $\alpha$ -Al phase matrix resulting from the SHT phase (Figures 2.30 and 2.31, respectively). However, the different SHT parameters determines variations in the morphology, size, and distribution of the Si particles and, consequently, a different mechanical response, both on the macro and microscale.

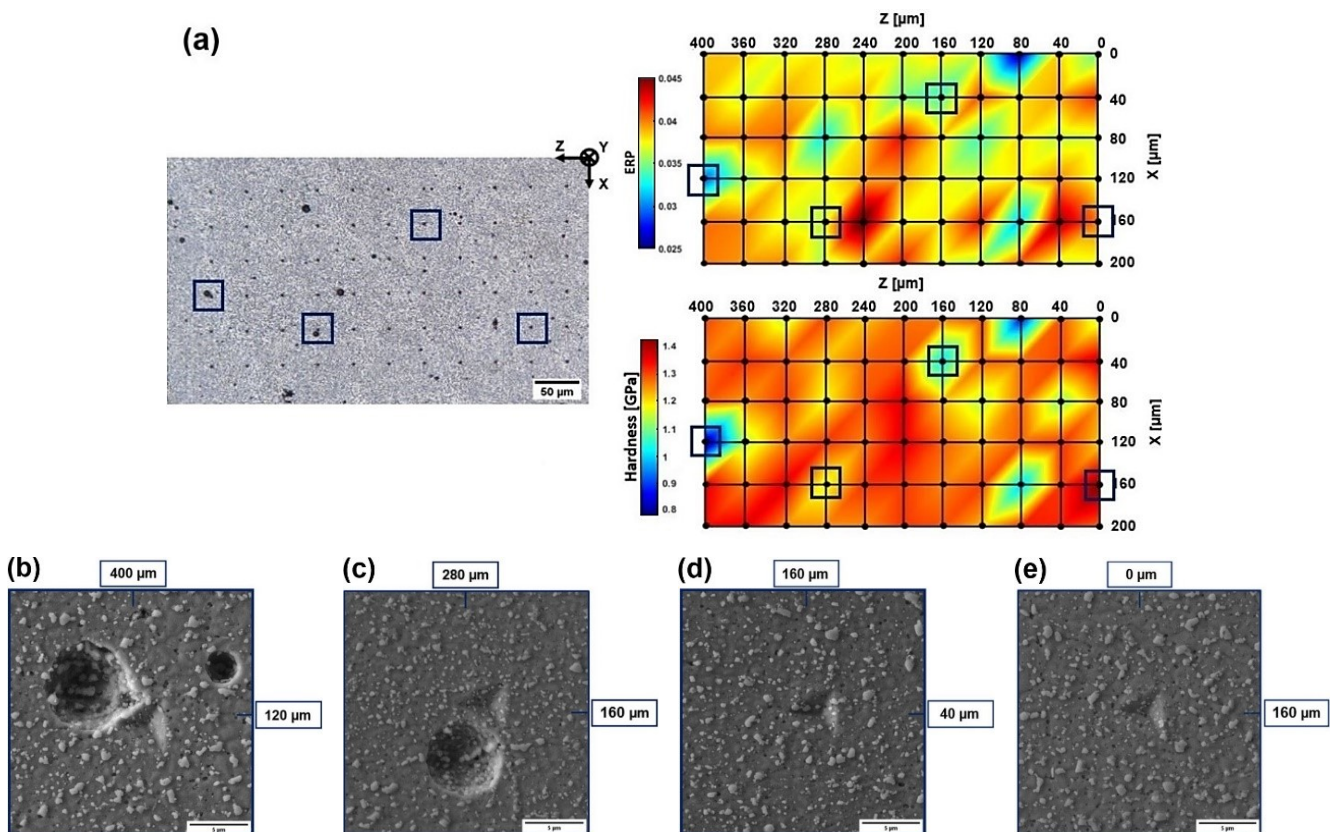


**Figure 2.30.** OM acquisition of the microstructure and nanoindentation matrix for the T6R alloy (a). High-magnification microstructures acquired at FEG-SEM: measurements close to porosity and characterized by low hardness and ERP values (b) (c), areas characterized by a fine dispersion of Si particles, and uniform H and ERP values (d) (e).

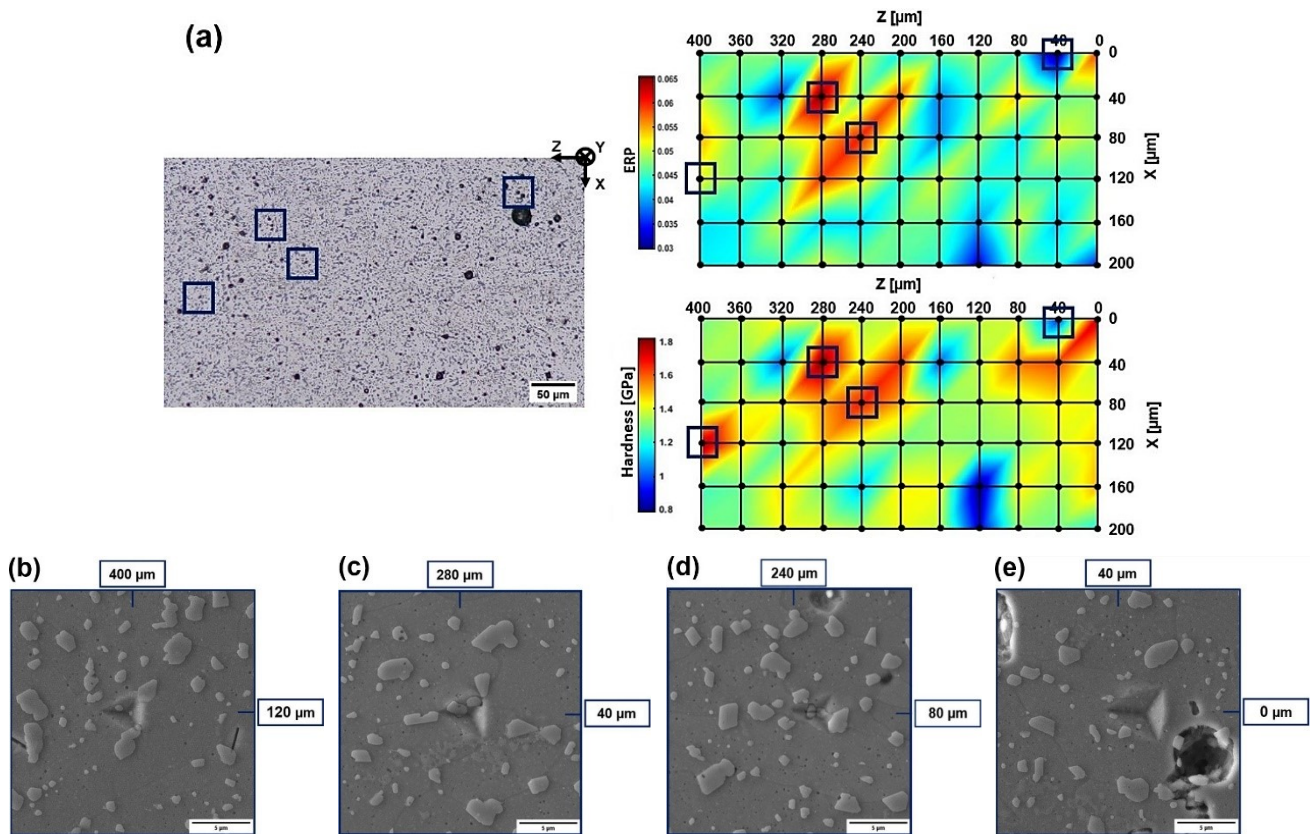


**Figure 2.31.** OM acquisition of the microstructure and nanoindentation matrix for the T6B alloy (a). High-magnification microstructures acquired at FEG-SEM: out-of-scale measurements corresponding to areas characterized by clusters of large Si particles (b) (c) (d), measurement on an area free of large Si particles interacting with the indenter and therefore characterized by low hardness and ERP values (e).

In the T6R samples, the homogeneous distribution of the small-sized Si particles and the high cohesion with the  $\alpha$ -Al matrix led to the indenter always fully penetrating the  $\alpha$ -Al matrix (Figures 2.30(d,e)), and therefore the measurements were not affected by scattering, with values between 1.3 and 1.4 GPa (Figure 2.30(a)). The only off-scale peak values were due to the presence of pores (Figures 2.30(b,c)) with a reduction of about 25% in terms of H and ERP.

Conversely, in the T6B samples, the heterogeneous size and distribution of Si particles led to a high difference in both H and ERP values between the particle-free zones ( $H = 0.9 - 1.1$  GPa,  $ERP = 0.035 - 0.045$ ) (Figure 2.31(e)) and the zones full of large Si particles and/or Si particles clusters in the material ( $H = 1.4 - 1.7$  GPa,  $ERP = 0.055 - 0.065$ ) (Figures 2.31(b-d)). The direct interaction of the Berkovich indenter with large Si particles influenced the measurements on the T6B. However, in the presence of large Si particles or clusters, the material always showed higher hardness and lower ductility than Si particle-free zones, even if no direct interaction of the indenter and the Si particles was observed. This consideration is in line with the results of the tensile tests (Figure 2.22) and the fractographic analysis described above. The fractographic analysis highlighted that the presence of large Si particles induced a concentration of the plastic flow, the detachment of the  $\alpha$ -Al matrix along their borders, and the nucleation of large dimples after the Si particle failure due to the local stress field. In the particle-free zones, instead, the presence of homogenous plastic deformation with small dimples was observed [74]. The lower hardness and, therefore, the tendency to undergo plastic deformation under lower stresses of the particle-free zones could explain the lower  $Y_S$  and  $e_f$  of the T6B alloy compared to the T6R alloy [75].

More information on these aspects will be provided in the next section.

### 2.3.4 In-situ mechanical characterization

The correlation between the fracture path (or crack propagation path) and the microstructure is crucial for understanding the fracture mechanisms of metallic materials and evaluating possible solutions to increase the mechanical response [4]. For this reason, in-situ tensile tests were also performed to analyze the microstructural features influencing the crack initiation and fracture propagation, thus investigating the failure mechanisms.

In AB and T5 alloys, the interference area between neighboring MPBs and HAZs constitutes a coarse and inhomogeneous microstructural region characterized by limited effect in hindering dislocation motion, thus representing the weakest part of the material and the dominant contributor at the nucleation and propagation of the fracture [76,77]. Therefore, the distribution of the MPBs and HAZs on the load-bearing area strongly influences micro- and macroscopic plastic behavior and fracture mode [65,78]. In particular, the main effect is a different fracture mode depending on the reciprocal direction of the building and load directions (Figure 2.32).

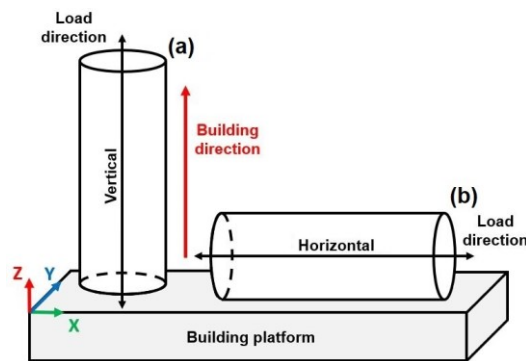


**Figure 2.32.** Reciprocal positioning between load and building direction. Vertical (a) and horizontal (b) conditions.

As Moses et al. [56] and Araújo et al. [79] described, the crack which propagates parallel to the building direction mainly crosses the MPs and presents a tortuous path induced by deflection at the MPBs. In contrast, when the crack propagates perpendicular to the building direction, it mainly follows the MPBs, where the fracture resistance is lower (Figure 2.33). The difference in fracture resistance between the MPB and MPC is responsible for the anisotropy of the mechanical response [56]; consequently, the MP arrangements strongly influence the ductility of the L-PBF AlSi10Mg alloy.

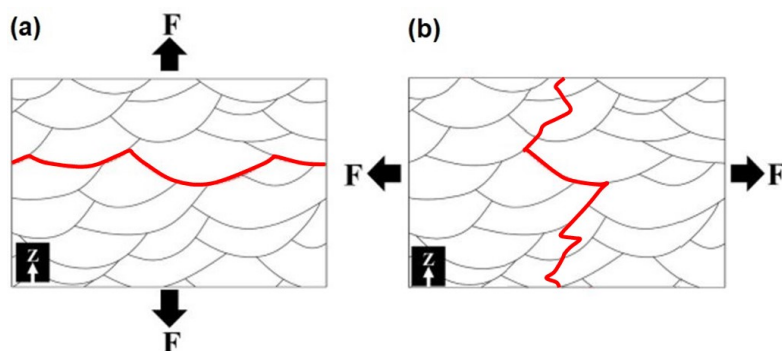


**Figure 2.33.** Crack propagation scheme on the fracture surfaces of specimens loaded parallel (a) or perpendicular (b) to the building direction. Adapted from [60].

As reported in the literature [4], an appropriate scan strategy reduces the anisotropic mechanical behavior of the L-PBF AlSi10Mg parts by modifying the MPB distribution on the load-bearing area. One of the most adopted solutions uses a bidirectional stripes scan strategy of  $67^\circ$  rotation between subsequent layers [56,57,70], which results in randomly

distributed MPs (Figure 2.16) that promote more tortuous crack propagation [65,70]. This solution significantly reduces the anisotropy in mechanical response. However, it does not significantly increase the ductility of the alloy [56,57]

Another solution to eliminate the anisotropy of the mechanical response and simultaneously increase the AB alloy's ductility is using suitable heat treatments. The T6 heat treatment promotes microstructural homogenization due to the disappearance of MP and cellular sub-structure, a more isotropic mechanical behavior, and an increased ductility, as described in section 2.3.2. Unfortunately, the different elastoplastic behavior of the Si particles and the Al matrix also promotes a local extensive plastic deformation of the Al matrix around the Si particles, influencing the crack growth rate. Coarser Si particles amplify the non-homogeneous stress state at Si/Al interface, increasing the local plastic flow and promoting the detachment between the Al matrix and Si particles due to the plastic relieving of the Al matrix near the Si particles [80].

In this section, the micromechanical performance and fracture propagation analysis were performed on samples characterized by horizontal (-H) and vertical (-V) building direction for each heat-treated condition evaluated in section 2.3.2, as reported in Table 2.9.

**Table 2.9.** Heat treatment conditions investigated by in-situ tensile test.

Condition	Building direction	
	Horizontal	Vertical
As-built	AB-H	AB-V
T5 direct artificial aging	T5-H	T5-V
T6 benchmark heat treatment	T6B-H	T6B-V
T6 rapid heat treatment	T6R-H	T6R-V

Starting from the AB and T5 samples, the AB-H and T5-H samples (Figures 2.34(a,c)) show the fracture propagation along the plane perpendicular to the layers, leading to a mixed inter- and intra-MP fracture mode. In contrast, the AB-V and T5-V samples (Figures 2.34(b,d)) are characterized by fracture propagation along the MPBs, producing an inter-layer and inter-MP fracture mode. The T6 samples (Figures 2.34(e-h)) show necking and higher ductility than the AB and T5 alloys. The interconnected eutectic-Si network of the AB and T5 alloys fosters damage at low strain because, at the onset of damage, the Si network transfers the load to the enclosed Al phase, which then fractures quickly under high stress, thus leading to low material ductility. In contrast, in the presence of spheroidal Si particles, the ductility is highly increased, resulting from the delay in void nucleation at the interface between the Al matrix and Si particles and the resistance to the growth of voids. In particular, the T6R samples (Figures 2.34(e,f)) show higher necking compared to the T6B ones (Figures 2.34(g,h)) due to the finer Si particles and their more homogeneous distribution, which promotes an increase in ductility of the T6R alloy, as described in the previous sections.

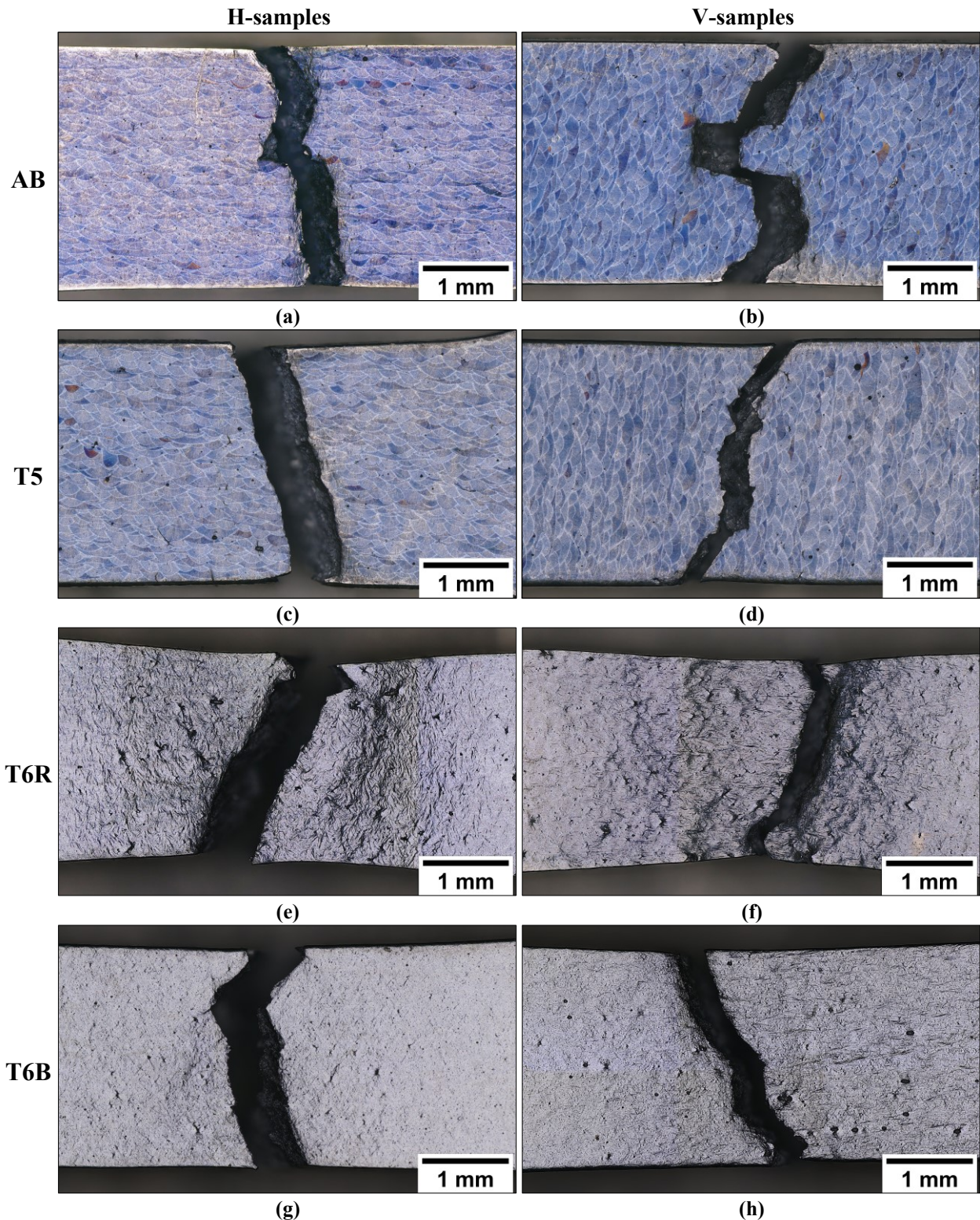


**Figure 2.34.** OM images of the fracture area of the in-situ tensile samples: AB (a,b); T5:  $T_{AA} = 160\text{ }^{\circ}\text{C}$   $t_{AA} = 4\text{ h}$  (c,d); T6R:  $T_{SHT} = 510\text{ }^{\circ}\text{C}$   $t_{SHT} = 10\text{ min}$ ,  $T_{AA} = 160\text{ }^{\circ}\text{C}$   $t_{AA} = 6\text{ h}$  (e,f); T6B:  $T_{SHT} = 540\text{ }^{\circ}\text{C}$   $t_{SHT} = 1\text{ h}$ ,  $T_{AA} = 160\text{ }^{\circ}\text{C}$   $t_{AA} = 4\text{ h}$  (g,h). H and V indicate the different building orientations of the samples.

Higher plastic strain in T6B and T6R allows a more accurate observation of grain orientation influence on material deformation. In particular, the T6R-H, T6B-H, T6R-V, and T6B-V samples (Figure 2.34(e-h)) exhibit different strain levels based on the influence of building orientation and microstructure on mechanical behavior.

As schematized in Figure 2.35, the V-oriented specimens have a more significant strain than the H-oriented ones due to the favorable orientation of the grain within the MP. In particular, a load direction perpendicular to the building

direction (Figure 2.35(b)) promotes mutual sliding along the GBs in an unfavorable direction to the load. This condition promotes a lower plastic deformation and generates depressions and protrusions in bulk material (Figure 2.36(a,c)). For building direction parallel to the load direction condition (Figure 2.35(c)), the applied load encourages the grain to slide along favorably oriented GBs, creating ripples in the bulk material (Figure 2.36(b,d)).

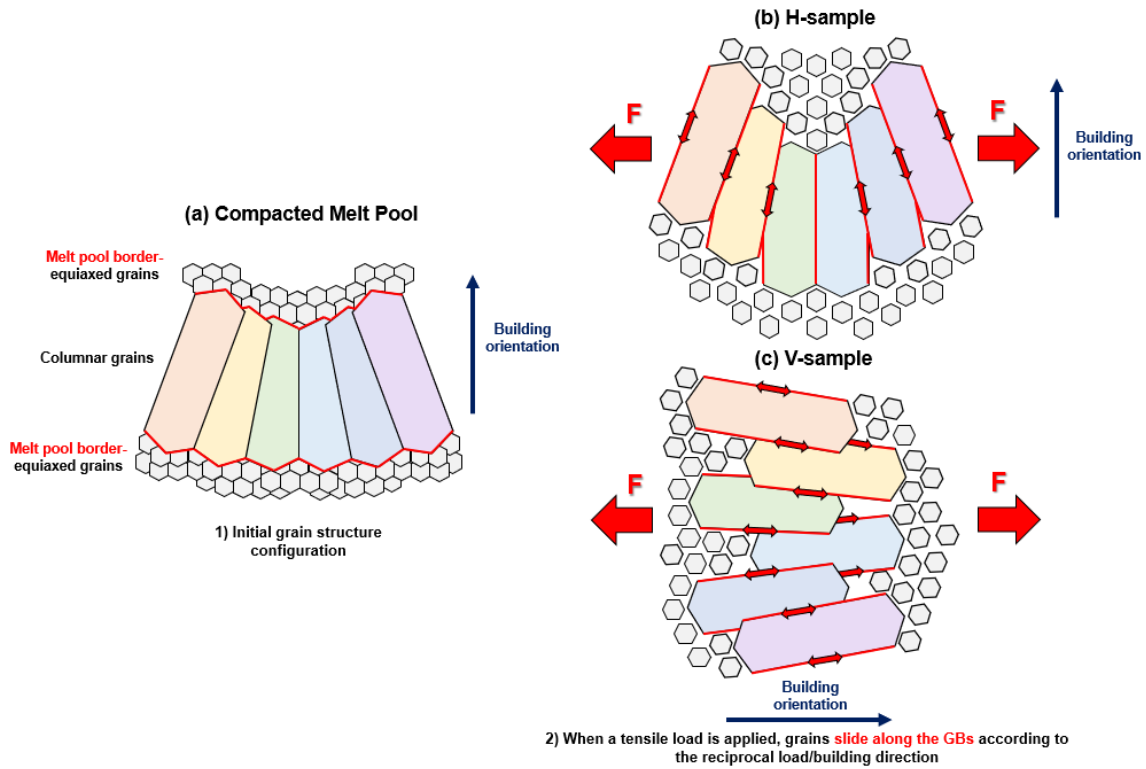


Figure 2.35.: Initial grain structure configuration (a). Evolution of the grain structure under tensile load: grain sliding movement (b), and mutual grain spacing movement (c)

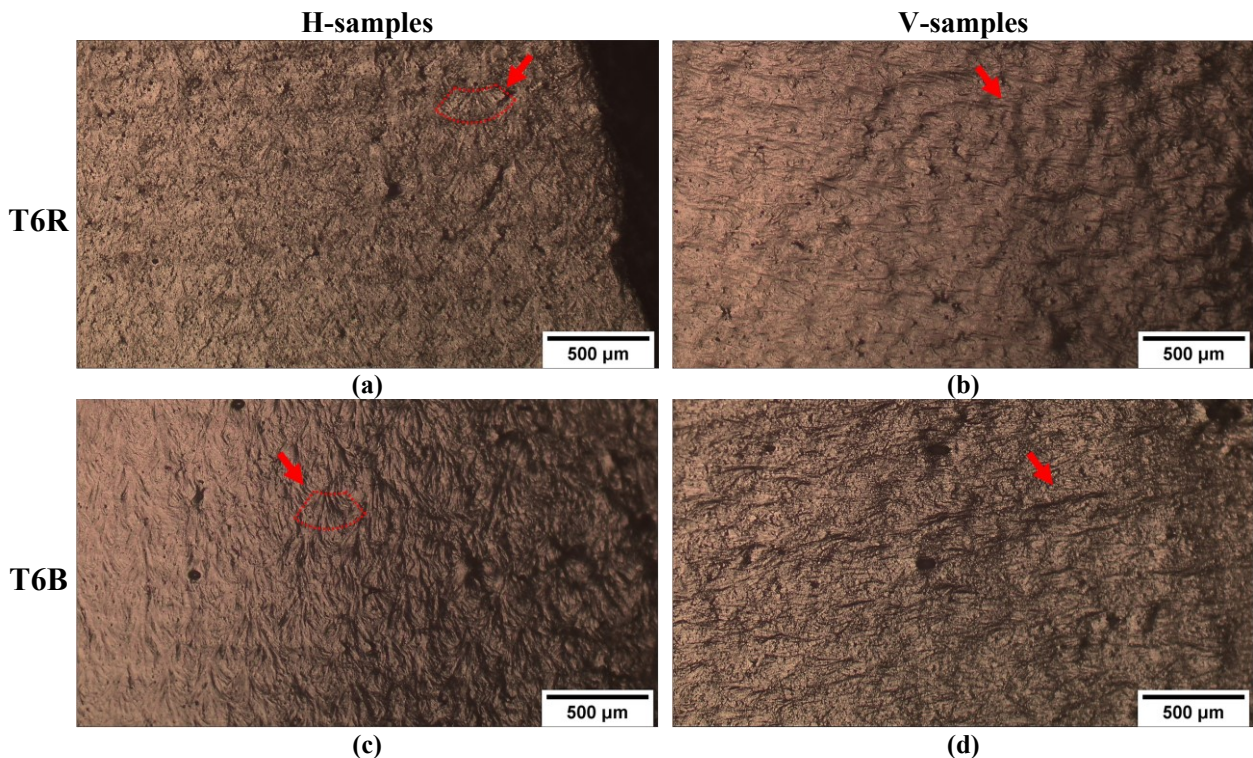
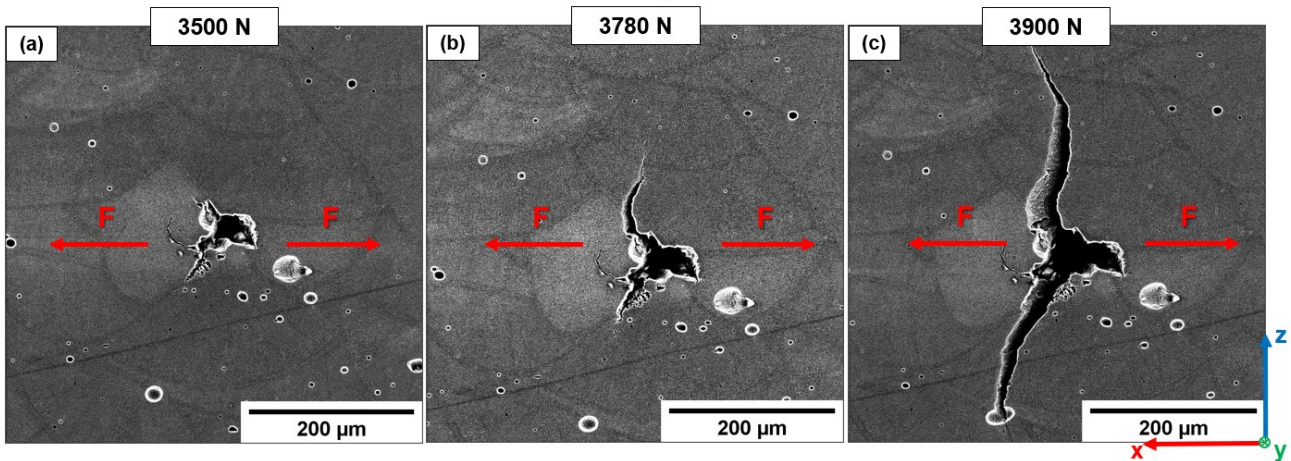


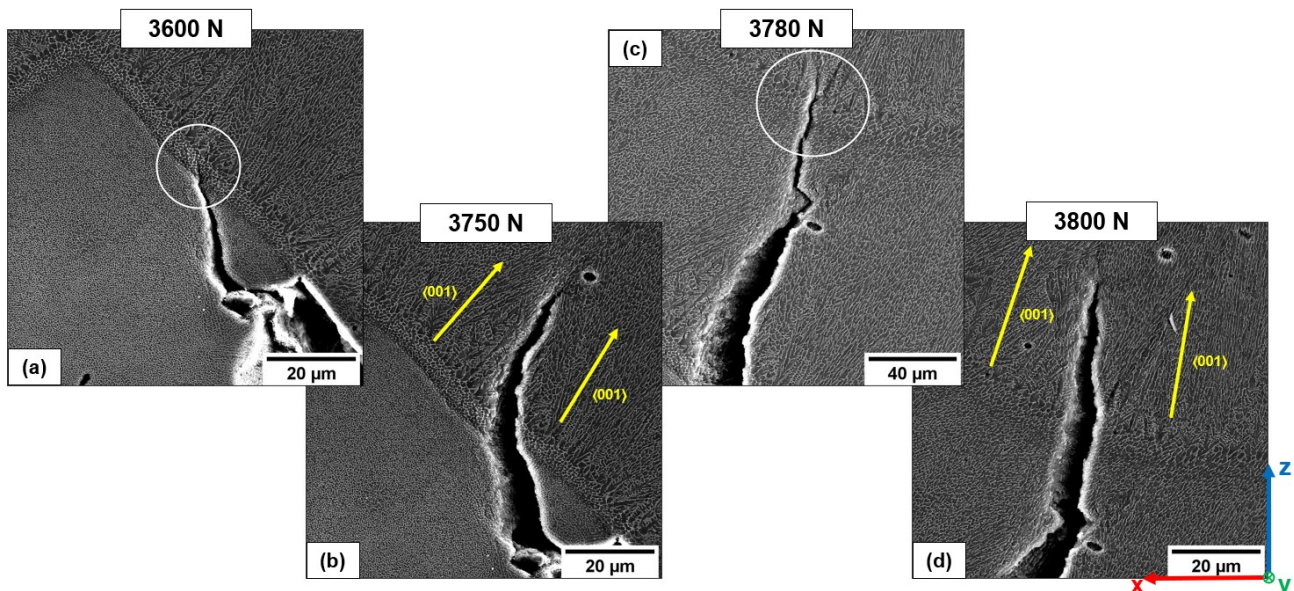
Figure 2.36. Detail of the fracture surface of T6R (a,b) and T6B (c,d). Red arrows indicate examples of grains moving away from each other or sliding along the GBs. In particular, in the red dotted line (a) and (c), the morphology of MP is evident due to the motion mechanisms of the grains

Observing the crack nucleation and propagation within the bulk material during tensile loading provides information on the influence of microstructural features on sample failure. Figure 2.37 shows the nucleation and propagation step of a crack in a T5-H sample. As expected, the crack nucleates from a LoFs and then propagates perpendicular to the load direction.



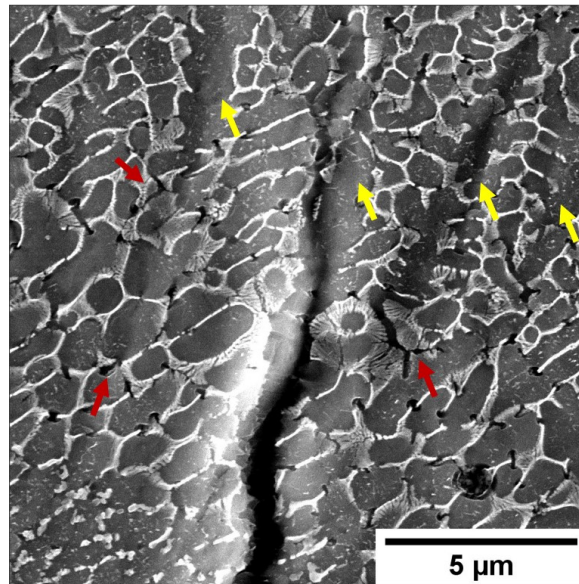
**Figure 2.37.** Fracture propagation within the T5 -H samples. Significant LoF defect is identified at the intersection of several MP (a); as load increases, the crack propagates perpendicular to the load direction (b); fracture continues along planes of maximum sliding, 45° oriented to the load direction (c).

However, it does not grow through the inhomogeneous and coarse microstructure that characterizes MPBs and HAZs, but through the MPC (Figures 2.38(a,b)). The observation of the microstructure around the crack (Figures 2.38(c,d)) highlights that the fracture crack path in the MPC follows the grain texture orientation (GBs), which is characterized by a direction parallel to the building direction and perpendicular to the load direction (as widely described in Chapter 1).



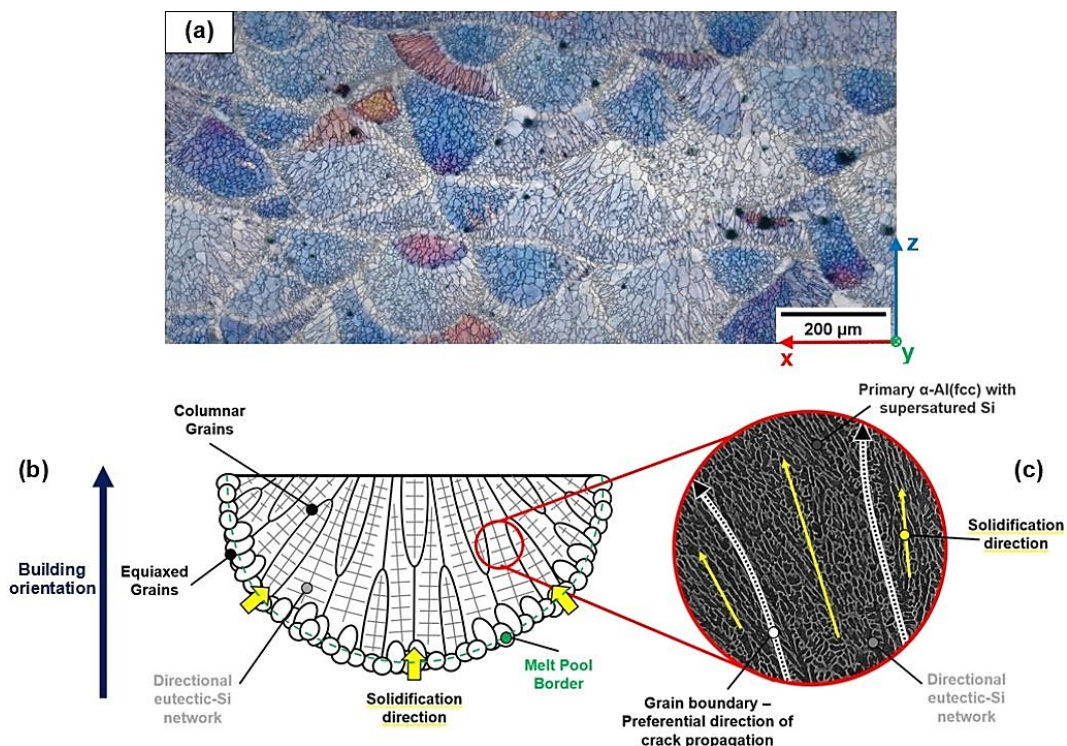
**Figure 2.38.** Detail of the fracture propagation reported in Figure 2.32: crack tip starts the propagation as the load increases (a); fracture deviates toward the MPC of the overlying layer (b), crosses the zone of discontinuity of the MPB, characterized by a coarse microstructure (c), and continues toward the MPC of the overlying layer (d).

In addition, Figure 2.39 shows a detail of the crack propagation reported in Figure 2.38(c): the intense deformation at the crack tip leads to the formation of microcracks at the interface between the Si and Al phases due to the formation of voids at the Al/Si interface by the triaxial stress condition and the crack through the softer Al phase and the deformation of the material along the adjacent GBs.

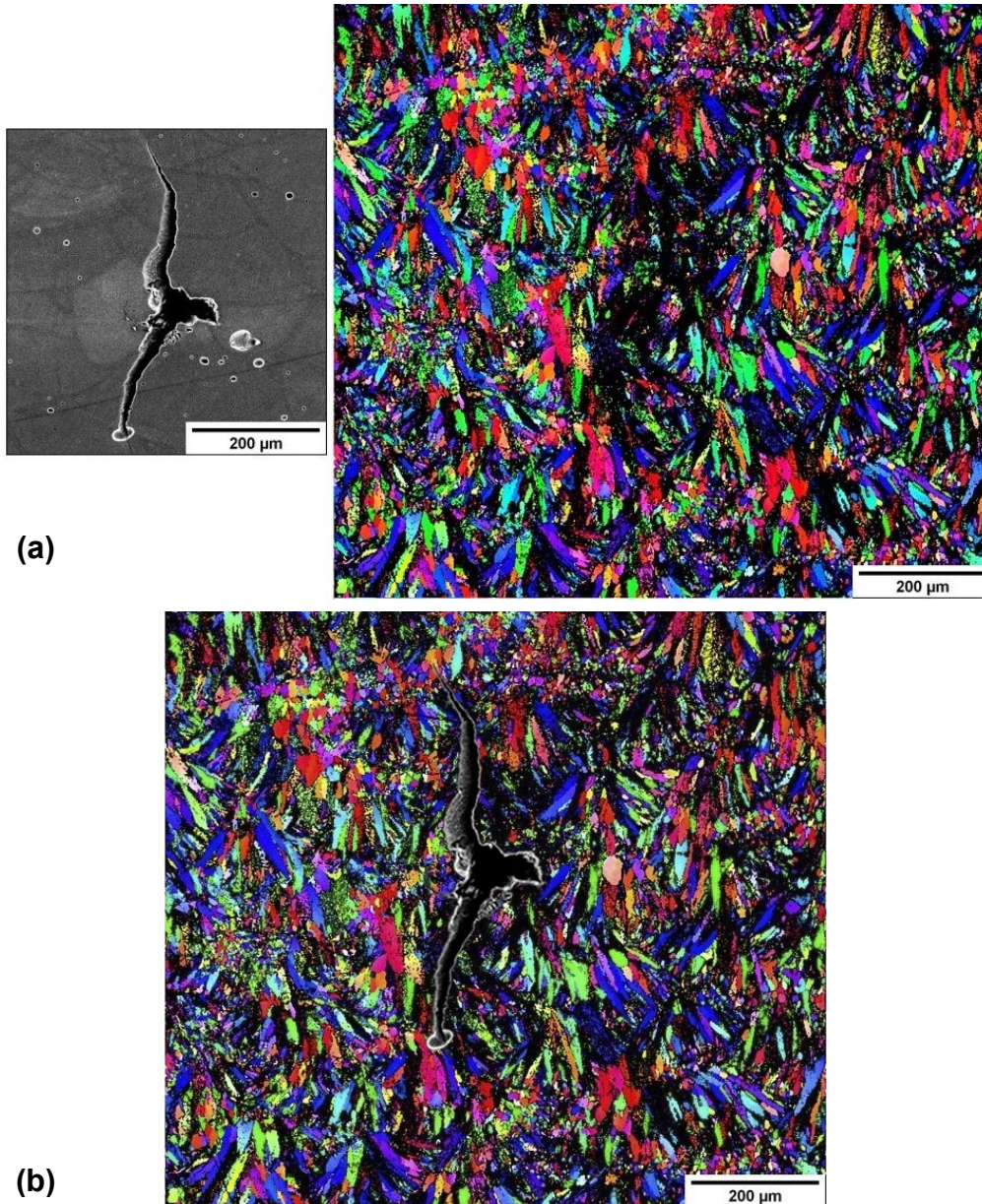


**Figure 2.39.** Detail of the effects of the intensified stress at the crack tip. Red arrows show the formation of voids at the Al/Si interface by the triaxial stress condition and the crack through the softer Al phase. Yellow arrows indicate the intense plastic deformation at the crack tip.

As reported in Figure 2.40, the alignment between the sub-microstructure and the grain texture orientation promotes crack propagation along the weak points of the microstructure, i.e., the GBs and the low-density region of the eutectic-Si network. Therefore, the grain texture orientation deeply affects the crack propagation direction (Figure 2.41) by influencing the shear stress direction acting at the eutectic-Si network/primary  $\alpha$ -Al cells, as theorized by [65,81]. Consequently, the fracture does not propagate only through the coarse microstructure (MPBs and HAZs) but also through the fine microstructure of the MPC along the borders of the columnar grains 45° oriented to the load direction (Figure 2.41).

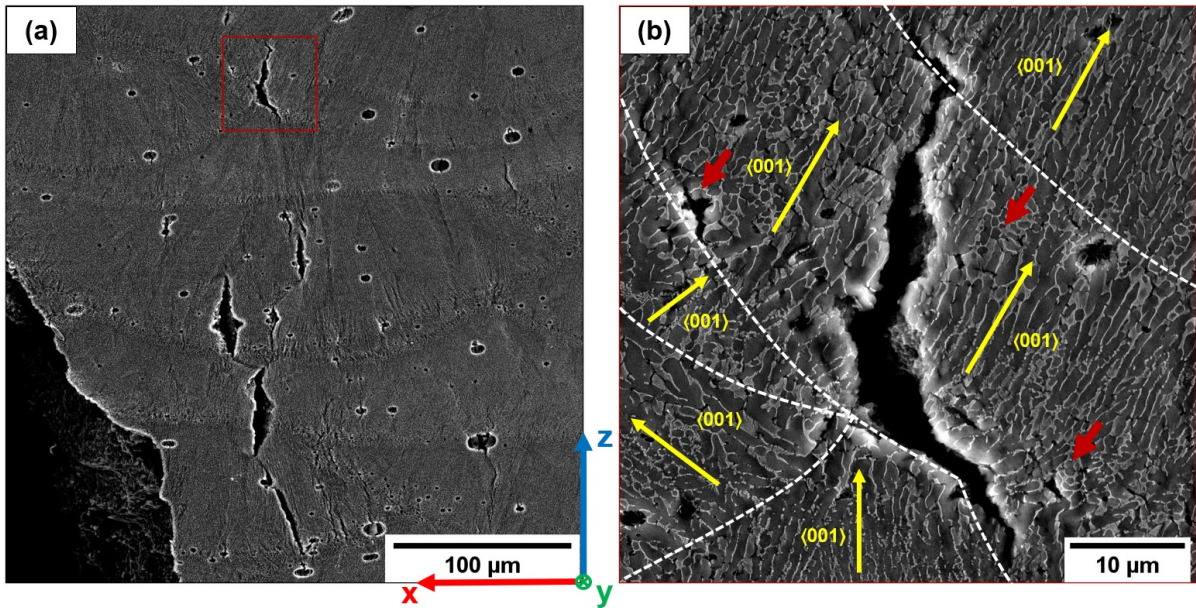


**Figure 2.40.** Light optical microscopy (LOM) image of the plane parallel to the building direction of the L-PBF AlSi10Mg alloy (a). The superimposition with the grain boundaries (GBs) obtained by EBSD shows equiaxial grains and columnar grains passing through the individual layers. Scheme of the preferential orientation of the single microstructural components inside a MP (b): the misorientation of the cellular sub-structure between adjacent columnar grains promotes the propagation of the fracture along the GBs (c).



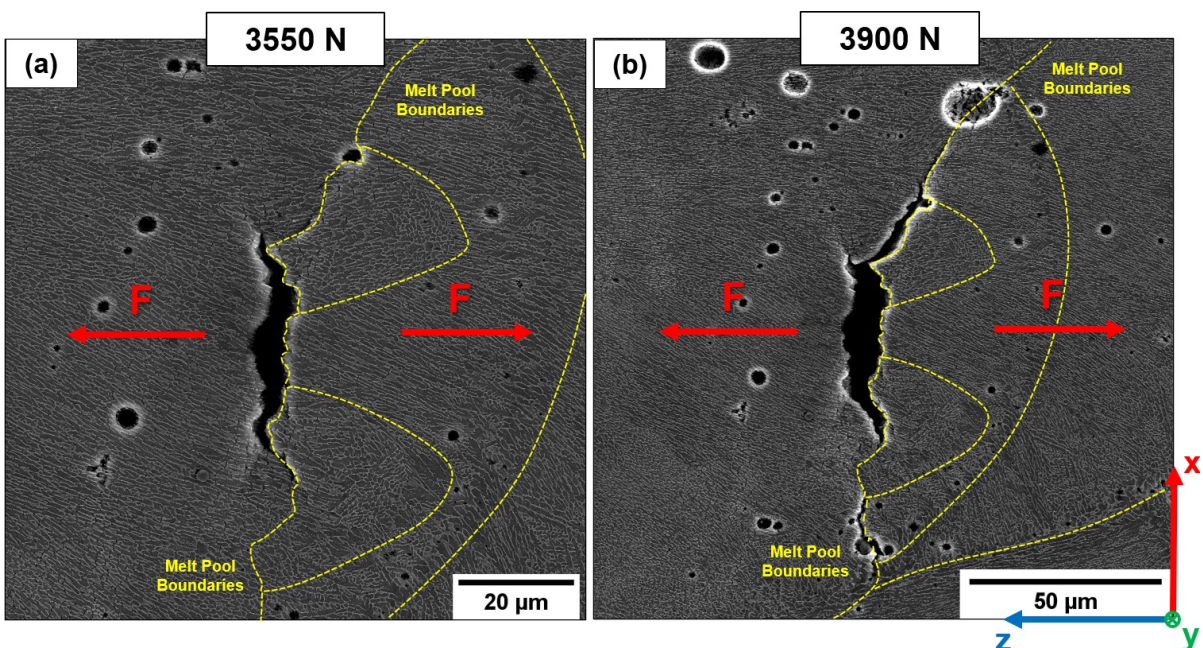
**Figure 2.41.** Comparison between the in-situ crack propagation within the T5 -H samples and relative IPF map (a). Superimposition between the two images (b): the crack is parallel to the crystallographic texture and propagates following the misorientation of the columnar grains.

The intense plastic deformation close to the fracture region highlights the phenomenon just described, as shown by the detail of the AB-H sample in Figure 2.42(a). Crack propagation occurs perpendicular to the load direction following the misorientation of the substructure within the columnar grains (Figure 2.42(b)). The crack path first deviates in the direction of the MPBs, encountering less resistance to propagation due to the coarse microstructure, then moves towards the MPC in more favorable GBs directions. As described previously, the voids within the bulk material due to the distancing between the columnar grains highlight the GBs (Figure 2.42(a)).



**Figure 2.42.** AB-H sample. Crack formation along the GBs close to the fracture surface (a). Crack propagation along favorable grain direction within the MPC (b). White dotted lines highlight the MPBs. Yellow arrows indicate the solidification direction of the cellular sub-structure. Red arrows show the formation of voids at the Al/Si interface and cracks through the softer Al phase

Otherwise, the AB-V and T5-V samples show a crack path mainly oriented along the MPBs and HAZs; as the load increases, the propagation of failure occurs in the coarser and inhomogeneous microstructure, where the strength properties of the alloy are lower (Figure 2.43(a,b)). In this condition, the favorable orientation of the coarser cellular structure along the MPBs and the HAZs stimulates the fracture's propagation perpendicular to the load's direction, reducing the effect of the grain texture orientation. However, the fracture path is not perfectly perpendicular to the load direction due to the presence of defects in the bulk material (Figure 2.43(b)) and the intertwined morphology of the microstructure generated by the adopted scan strategy (bidirectional stripes of  $67^\circ$  rotation) to reduce the microstructural anisotropy [56,57]. As described previously, the cracks occur from the eutectic-Si network's breakage and the cracks' propagation through the softer  $\alpha$ -Al phase, inducing the plastic deformation of the material (Figure 2.43(c,d)).



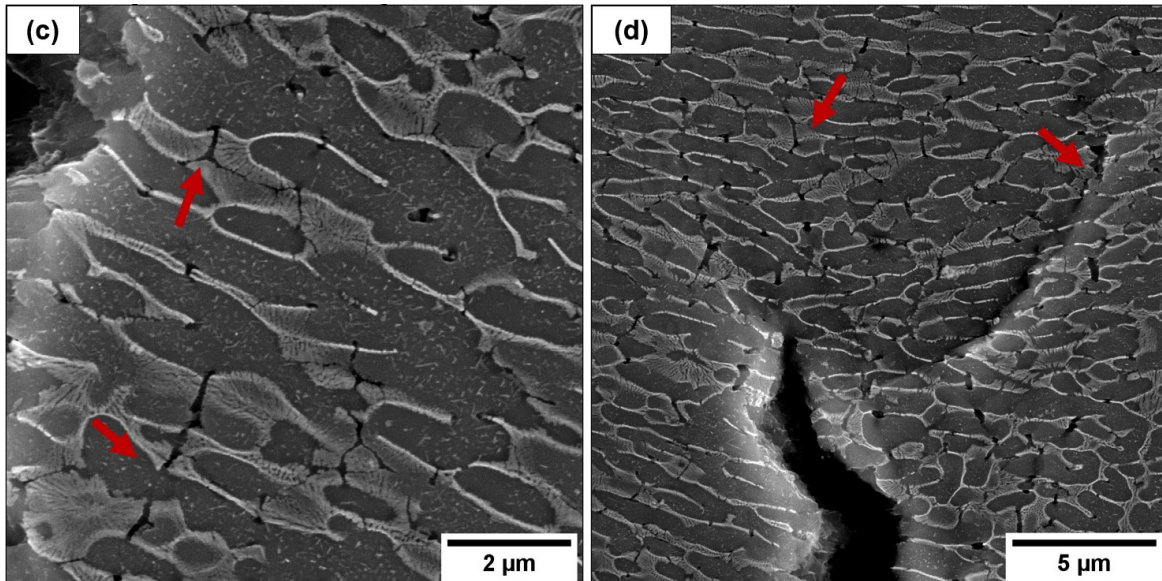


**Figure 2.43.** Fracture propagates through the coarser structure (a) and along the MPBs (b). Details of the severe plastic deformation at the crack tip (c) (d). Red arrows indicate the eutectic-Si network's breakage and the formation of cracks through the softer Al phase.

The weakness of the regions delimiting the MP is probably related to the uneven distribution of stress concentration caused by the coarser and elongated microstructure in the MPBs and the fragmented eutectic-Si network located in the HAZs (Figure 2.44).

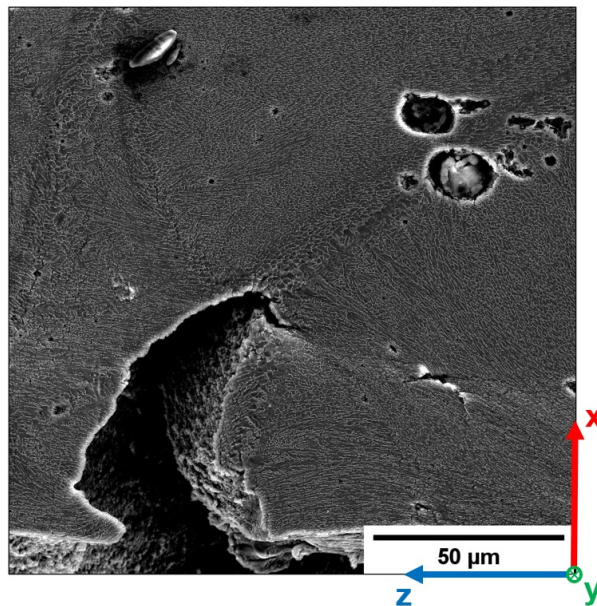


**Figure 2.44.** Detail of the propagation of the fracture in the AB-V sample. The fracture starts from the sample surface, preferably from MPB and HAZ, where the microstructure appears coarser.

The effects are shown in Figure 2.45. In the areas close to the crack tip, the high-stress condition leads to the fracture of the microstructure due to the tearing mechanism at the Si network/ $\alpha$ -Al cell interface related to the different elastoplastic behavior of the two phases. In particular, the void initiation at the Si network/ $\alpha$ -Al cell interface is an energy-consuming process where a threshold value of work “W” is necessary to create the crack between the aggregated second phase and the Al matrix (Equation 2.8). W depends on three factors, i.e., the surface energy of the matrix  $\gamma_{Al}$ , the surface energy of the aggregate second phase  $\gamma_{Si}$ , and the interface energy  $\gamma_{Al-Si}$  (2.8) [71].

$$W \propto \gamma_{Al} + \gamma_{Si} + \gamma_{(Al-Si)} \quad (2.8)$$

The coarser  $\alpha$ -Al cell and the thinner eutectic-Si network along the MPBs increase the strain field in the proximity of the second phase due to the difference in the lattice parameters between Si and Al, promoting the loss of coherency between the hard Si phase and the soft Al matrix [65]. This condition increases the contribution of the  $\gamma_{Al-Si}$  value, thus reducing the work necessary to nucleate a void at the  $\alpha$ -Al/Si interface (Figure 2.45(b)). The fragmented eutectic-Si network in the HAZs further emphasizes this phenomenon, as described above in section 2.3.3 [71].

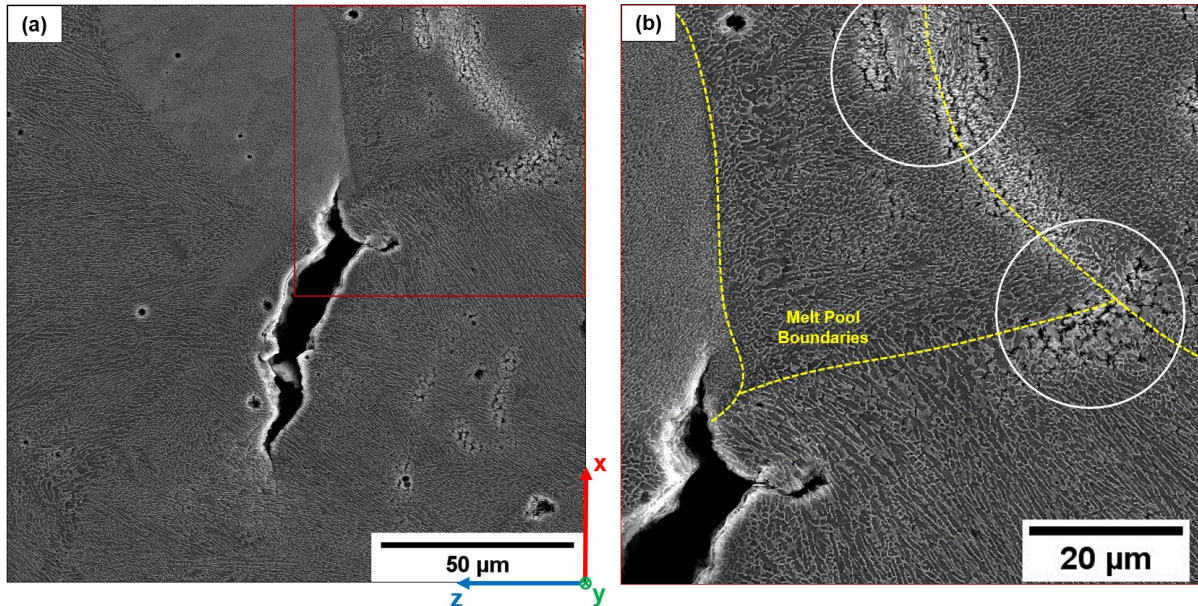


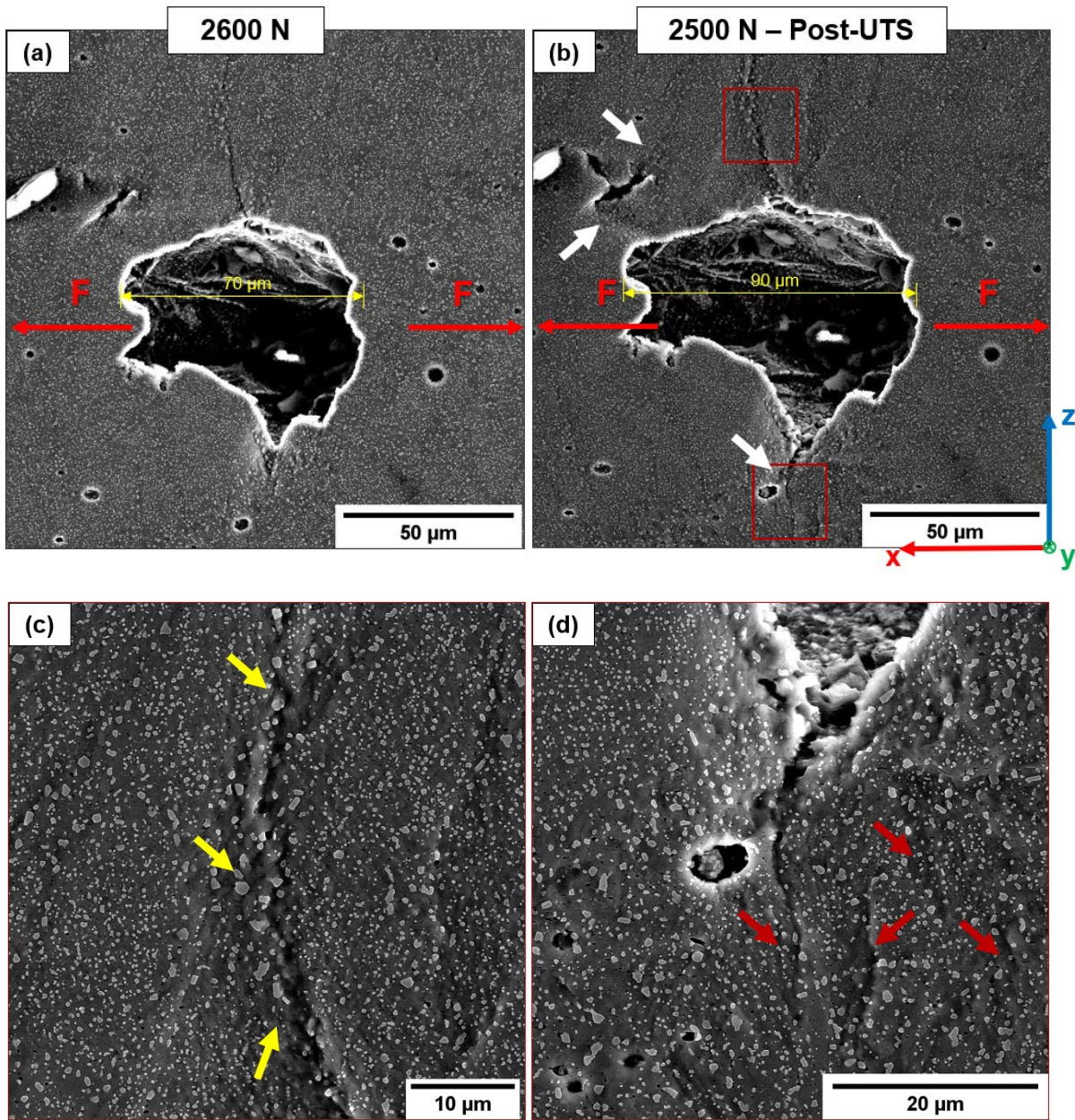
**Figure 2.45.** Fracture propagation in the T5-V sample. The crack tip is oriented to the coarser microstructure of the MPBs (a); Detail of the fracture propagation due to the tearing mechanisms (b). White circles indicate the void formation at the Si network/ $\alpha$ -Al cell interface along the MPBs and HAZs.

When the Si network is present (AB and T5), excessive damage nucleates on the Si network at a low strain since the Si phase is interconnected and cannot withstand high strain before failure. As described above, the high strength of AB and T5 alloys is due to the load-bearing capacity of the Si network. However, once damage initiates, the Si network will simultaneously transfer the load to the enclosed Al phase and the part of the network without damage, which fractures quickly and connects the voids. It is worth noting that the damage mechanism mentioned above is different from the void-sheet scenario [4], which involves a coalescence of voids wide apart through shear bands.

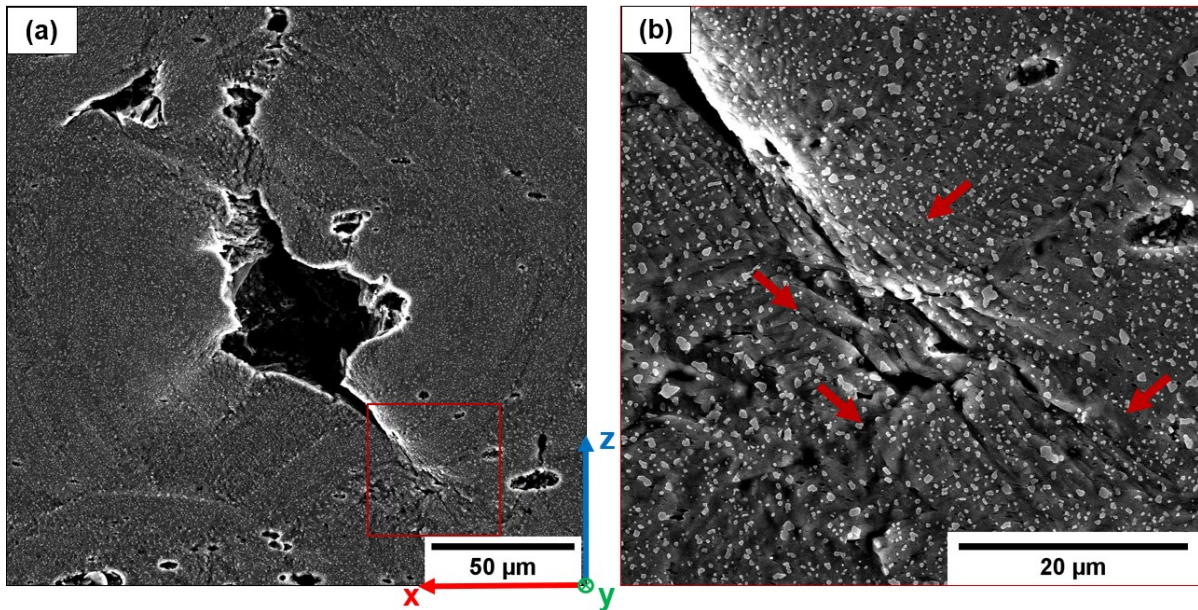
Applying the tensile load on the T6 alloy generates an entirely different crack propagation than the AB and T5 alloys. The higher ductility of the T6R alloy determines defect plastic deformation and the void opening due to the discontinuity at the Si particles/ $\alpha$ -Al matrix interface (Figures 2.46(a,b)). In tensile loading, spherical Si particles cause localized shearing at an early stage of plastic deformation. The different elastoplastic behavior of the Si particles and the Al matrix leads to the formation of initial voids at the Si/Al interface due to the local extensive plastic deformation of the Al matrix around the Si particles. Stress intensification at the crack tip leads to the void opening (Figure 2.47). In particular, a non-homogeneous stress state develops around the larger Si particles due to the increase in local plastic flow as the load increases, inducing the detachment between the Al matrix and Si particles. At the same time, free-Si particle zones inside the Al matrix offer less resistance to dislocation motion, promoting crack propagation (Figures 2.46(c-e)).

Restructuring the starting eutectic-Si phase into large, distant globular Si particles forces the crack to propagate across the tough  $\alpha$ -Al matrix, enhancing the crack propagation resistance by the higher alloy's ductility [77]. Therefore, the deformation and opening of the defects and the material necking during the load application promote the void

coalescence within the bulk material and the decrease in the residual resistance area, thus inducing sample failure [34,73].

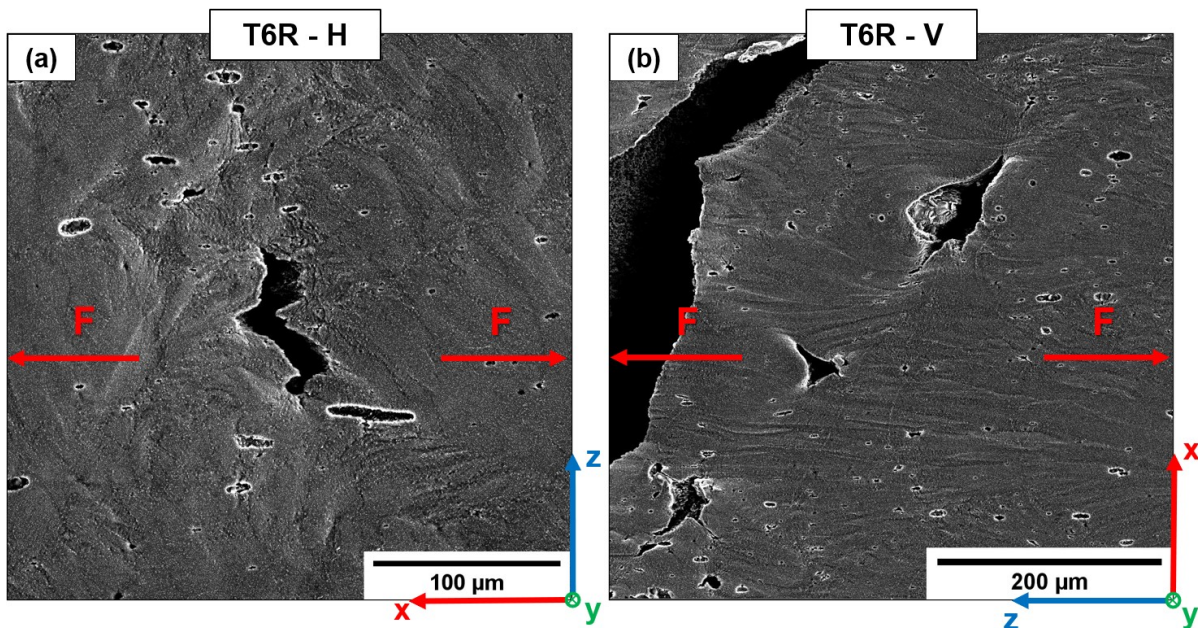


**Figure 2.47.** Failure mechanism in the T6R microstructure (T6R-H sample). Defects evolution during the in-situ tensile test (a,b). White arrows highlight strongly localized deformation in the region between the defects. High magnification of the plastic deformation at the crack tip as tensile load increases (c) (d). Yellow arrows indicate regions characterized by large Si particle clusters (limited hindering dislocation motion). Red arrows indicate secondary cracks.



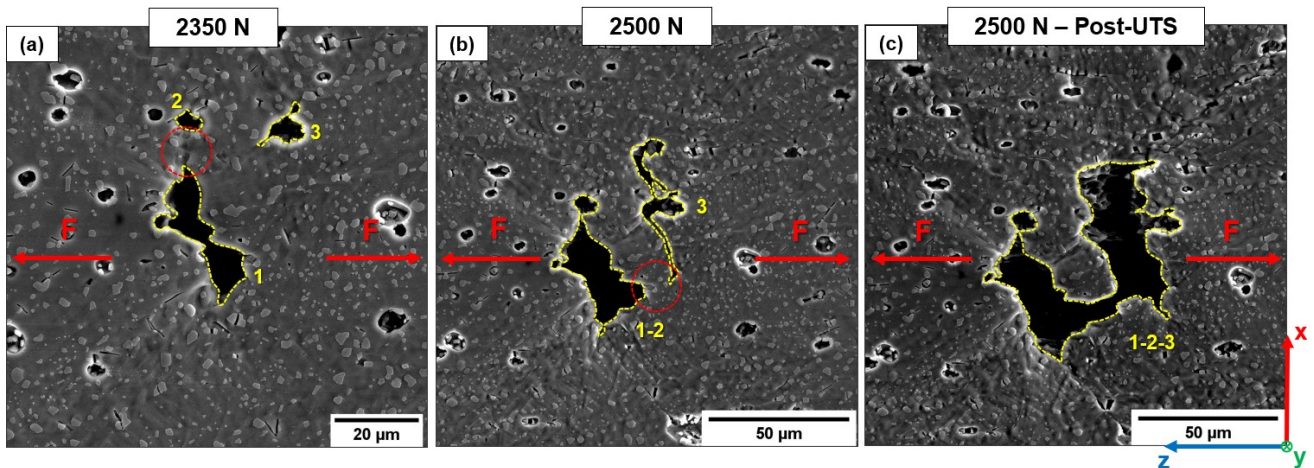
**Figure 2.47.** Void opening within the bulk material (a). Plastic deformation at the crack tip due to the stress intensification (b).

After the T6 heat treatment, the microstructural homogenization minimizes the differences in void opening and crack propagation between the T6R-H and T6R-V samples. In particular, as described above (Figure 2.35), the material's plastic deformation makes only the different grain texture orientations visible: the T6R-H sample shows slightly curved grain oriented perpendicular to the load direction (Figure 2.48(a)), while the T6R-V highlight columnar grain aligned to the load direction (Figures 2.48(b)).



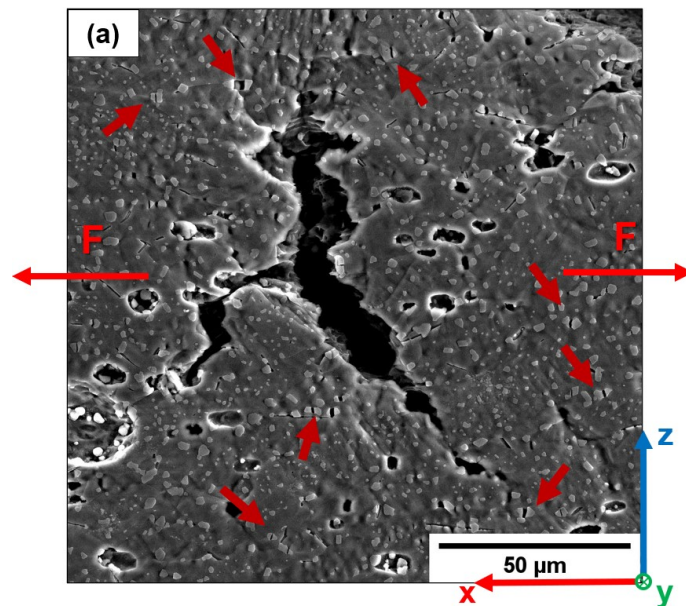
**Figure 2.48.** Grain texture orientation highlighted by plastic deformation: perpendicular to load direction in T6R-H condition (a), parallel to load direction in T6R-V condition (b).

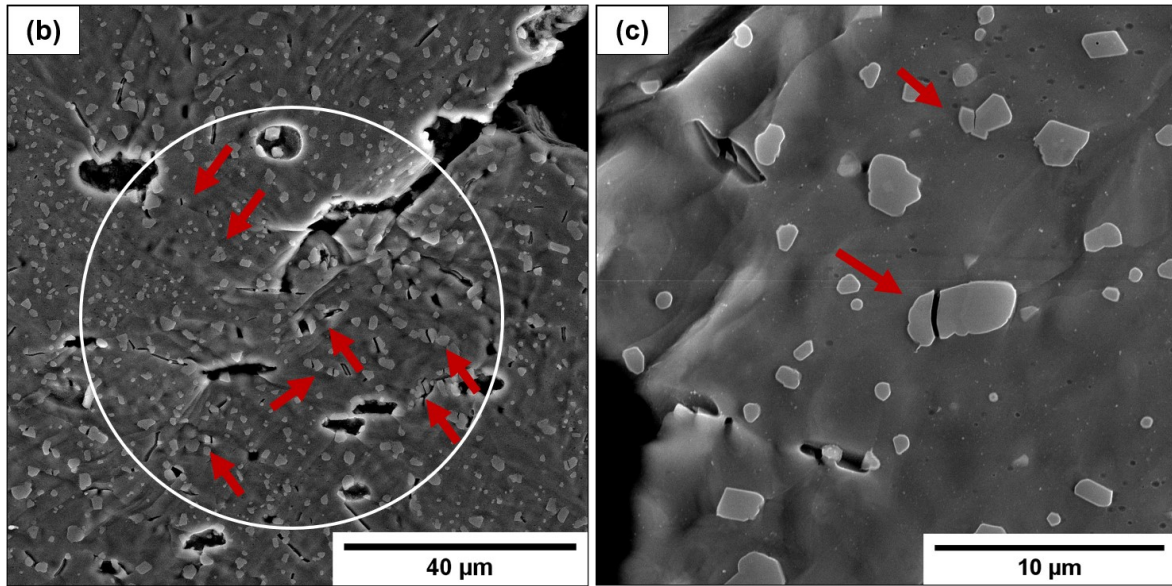
The T6B alloy shows the exact mechanism described for the T6R alloy. In particular, starting from separated voids (Figure 2.49(a)), the deformation and opening of the defects occur as the load increase due to the high stresses at the void tips (Figure 2.49(b)). Consequently, the plastic deformation forms a single large void through coalescence phenomena among adjacent pores (Figure 2.49(c)).



**Figure 2.49.** Void coalescence within the T6B-V sample. Separated voids (1, 2, and 3) (a); deformation and coalescence of the voids 1 and 2 (b); void coalescence and formation of a single large void consisting (c). Dashed red circle highlights the zone of intensified stress at the crack tip and junction between the pores.

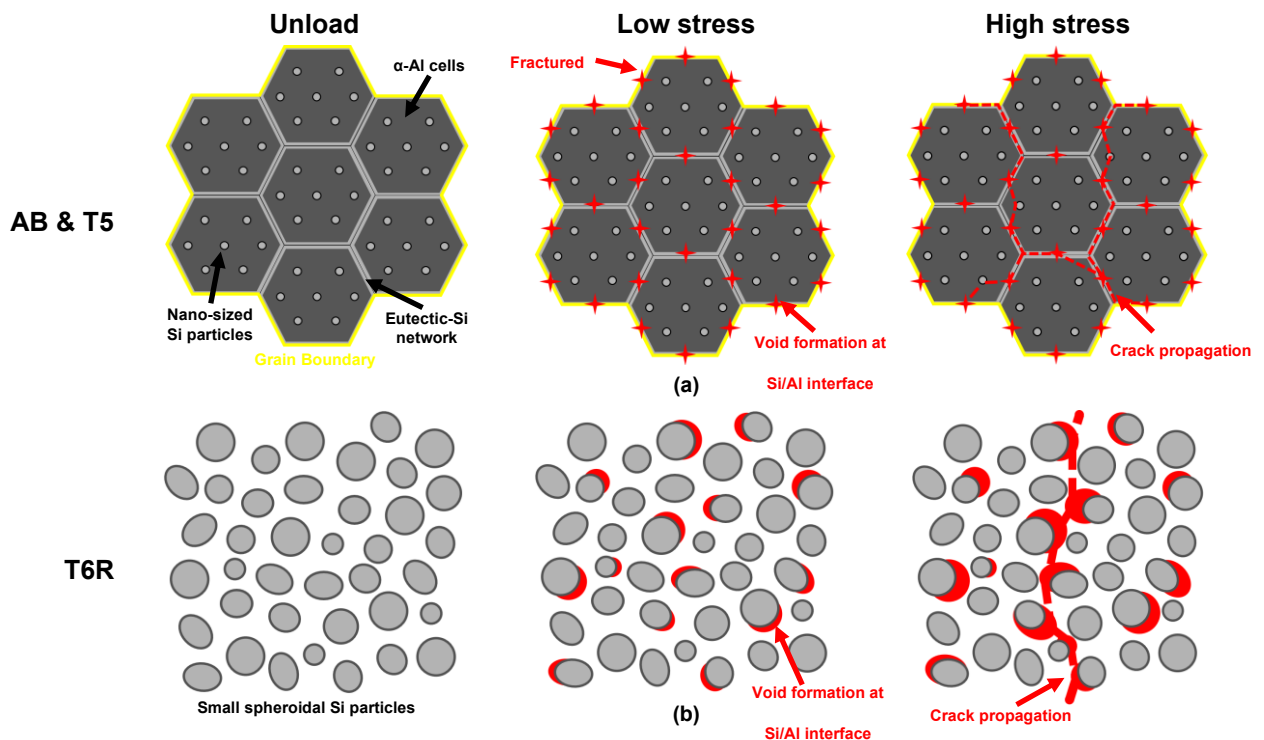
Despite a microstructure comparable to the T6R alloy, the T6B alloy shows a lower plastic deformation and ductility (Figures 2.34(g,h)) due to the presence of coarser Si particles embedded into the Al matrix. According to T. H. Park et al. [72], the size and morphology of the eutectic Si particles impact the mechanical properties of the T6 alloy: the damage nucleates on the Si particles by both particle fracture and Si particle/Al matrix detachment. In particular, intensified stress at the crack tip and the pile-up dislocation phenomena at the Al/Si interphase boundary cause the shearing of the Si particles (Figure 2.50) [69]. In particular, because the large Si particles contain a statistically higher density of internal defects, their failure stress is lower than small Si particles.





**Figure 2.50.** Void coalescence within the T6B-H sample (a). Detail of the Si particle cracking at the crack tip caused by intensified stress (b); detail of Si particle cracking (c).

Therefore in the T6B alloy, the damage can nucleate at a lower macroscopic strain: the Si particle spacing is much larger than T6R alloy, and there is more space for void growth and coalescence. On the other hand, crack nucleates late in the T6R sample, and the small inter-particle spacing delays the void coalescence (Figure 2.51). Conversely, when the Si network is present, such as in the AB and T5 alloys (Figure 2.51), excessive damage nucleates on the eutectic network at a low strain since the Si phase is mostly interconnected and cannot bear high strain before failure. Once damage initiates, the Si network will transfer the load to the enclosed Al phase and the part of the network without damage, which quickly breaks and connects the voids. It is worth noting that the damage mechanism mentioned above is different from the void-sheet scenario of the T6 alloys, which involves a coalescence of voids wide apart through shear bands [59]. As a result, the T6R presents higher ductility than the other heat-treated conditions alloy due to different void nucleation, growth, and coalescence kinematics that occurred during the application of tensile load.



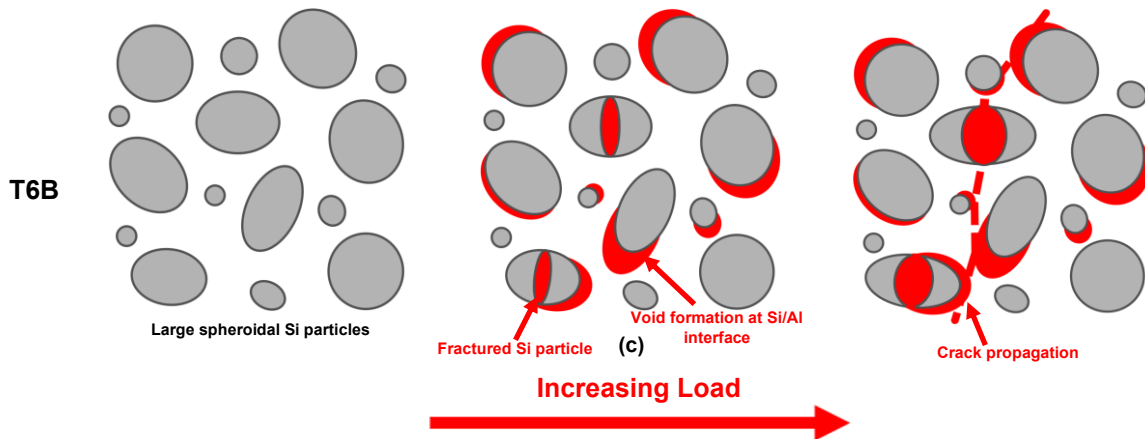


**Figure 2.51.** Failure evolution scheme characterizing different microstructures: eutectic-Si network fracturing and void formation and coalescence at Al cell/Si network interface (AB and T5); void nucleation at Al matrix/Si particles interface (T6R and T6B) and fractured Si particles (T6B), and propagation through shear bands.

When examining fracture surfaces after the tensile test, AB-V and T5-V samples exhibit step-like features due to inter-layer crack propagation, reminiscent of the laser scan tracks (Figures 2.52(c,g)). The fracture surfaces of the AB-H and T5-H samples do not show signs of the MP scan strategy, evidence of a more tortuous, trans-track fracture propagation mechanism (Figures 2.52(a,e)). The response of characteristic MPBs to the stress at different tensile directions can explain the difference between the fracture surfaces of the AB-V and T5-V samples compared to the AB-H and T5-H [65,81]. Under a tensile load, the MPBs slipping surface in the V-samples is perpendicular to the tensile load direction. When a tensile load reaches a specific value, cracks extend along the MPBs, showing evidence of the scan strategy. Crack deflection at the interface of the individual MPs can be observed in regions where it is energetically more favorable than crossing MPs. However, for the H-samples, the tensile load direction is parallel to the MPBs. When a tensile load increases to a certain level, cracks propagate trans-MP, not showing traces of the scan strategy on the fracture surface.

At higher magnification (Figure 2.52), the fracture surfaces exhibit dimples associated with the detachment between the Si network and the Al matrix induced by the plastic deformation. The Si-rich boundaries impede dislocation motion in the Al-matrix, thereby increasing the strength of the material. With increasing load, plastic deformation occurs in the Al-matrix, debonding at the Si-rich cell interface and causing the nucleation of dimple-like cavities on the fracture surface. The dimple size matches the cell dimensions observed in the microstructural analysis. While AB-H and T5-H samples show a failure by shear resulting in dimples inclined to the tensile direction (Figures 2.50(b,f)), the AB-V and T5-V samples resemble cup-and-cone-type dimples characteristics (Figures 2.50(d,h)). The inclined dimple surface of the H-samples can be associated with a lack of stress-triaxiality [56].

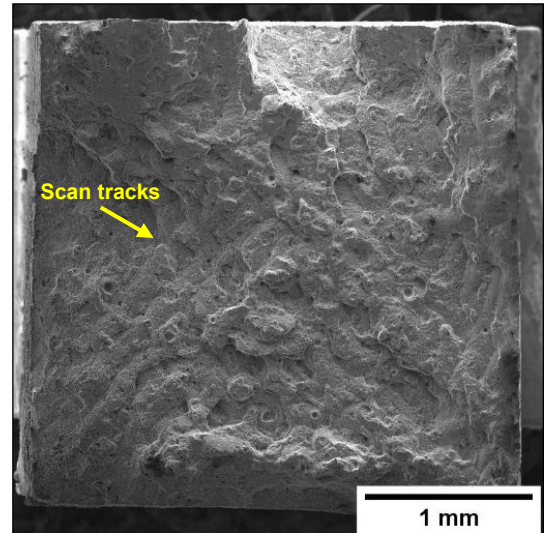
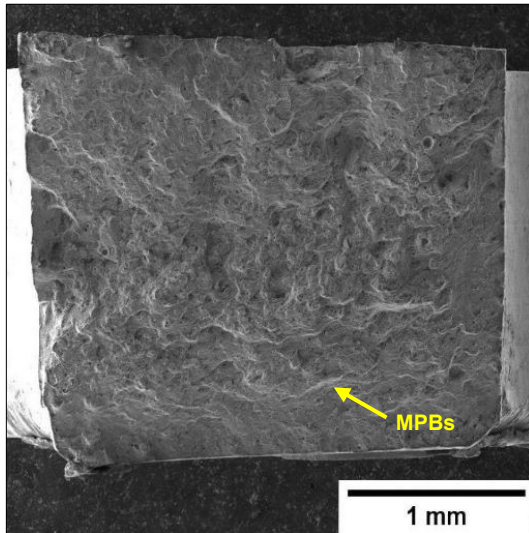
Even though the T6 heat treatment homogenizes the microstructure and deletes the MPBs and HAZs [16,29], which represent a preferential crack path, some scan track marks are still observed (Figures 2.52(i,m,o,q)), in agreement with the findings of Girelli et al. [34]. Zones characterized by less or more Si particle density may cause this phenomenon: high Si phase content zones of the AB alloy, like the MPCs, promote a higher density of Si particles than low Si phase content zones of the MPBs and HAZs. Minimal differences in silicon content between these areas lead to minimal differences in the distribution of silicon particles and result in the persistence of scan track signs on the fracture surface

T6B and T6R samples show a completely ductile failure mode, characterized by deep dimples (Figures 2.52(j,l,n,p)) instead of the shallow dimples observed in the AB and T5 samples. However, in the T6B samples, the coarse and inhomogeneously distributed Si particles form large and very deep dimples caused by the detachment between Si

particles and the Al matrix or the fracture of the larger Si particles. In the T6R samples, the Si particles are less prone to fracture because of their smaller size and spheroidal morphology, and therefore the dimples mainly nucleate at the Si particle/ $\alpha$ -Al matrix interface rather than by cracked particles (Figures 2.52(j,l)). The homogeneous distribution of the fine Si particles induces the development of finer dimples and more uniform plastic deformation than the T6B alloy (Figures 2.52(n,p)).

### H-samples

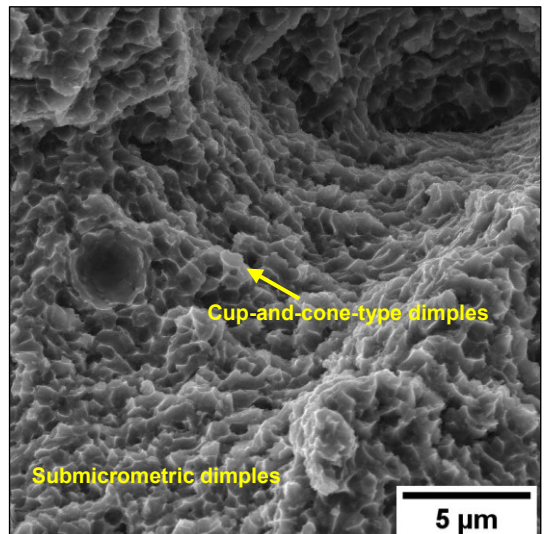
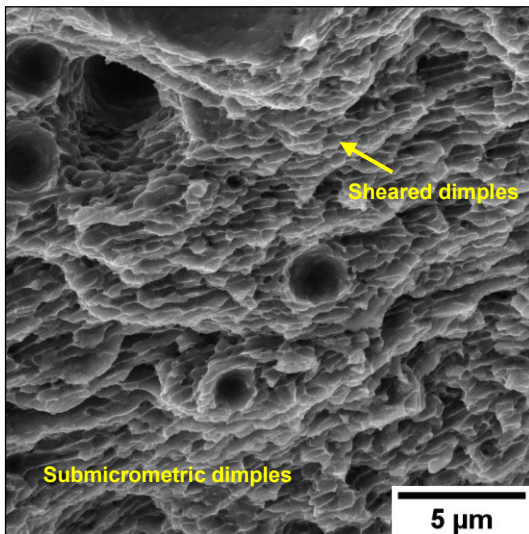
### V-samples



AB

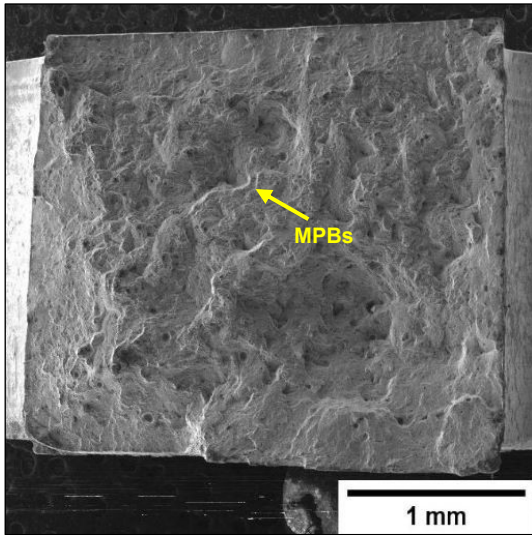
(a)

(b)

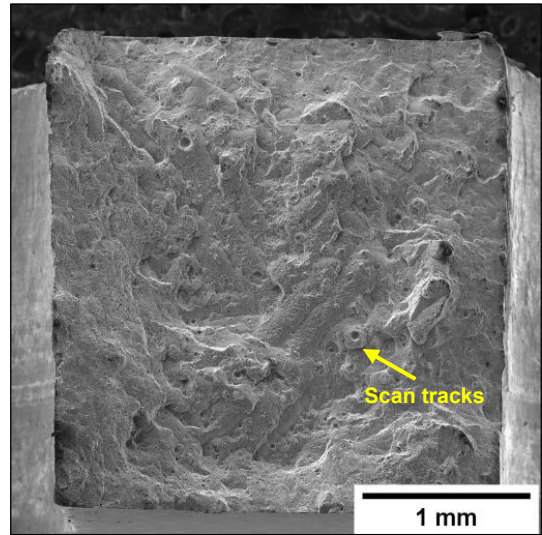


(c)

(d)

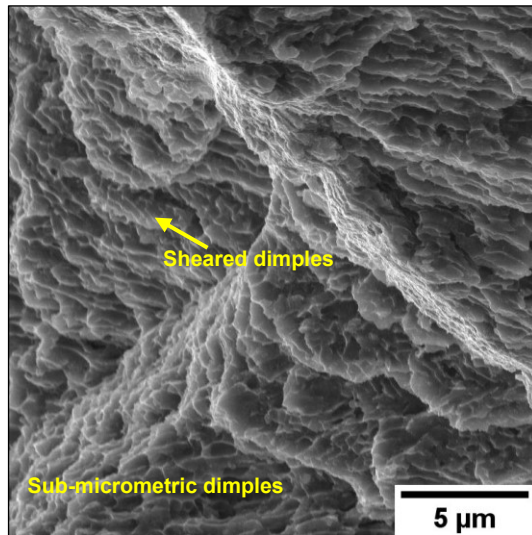


(e)

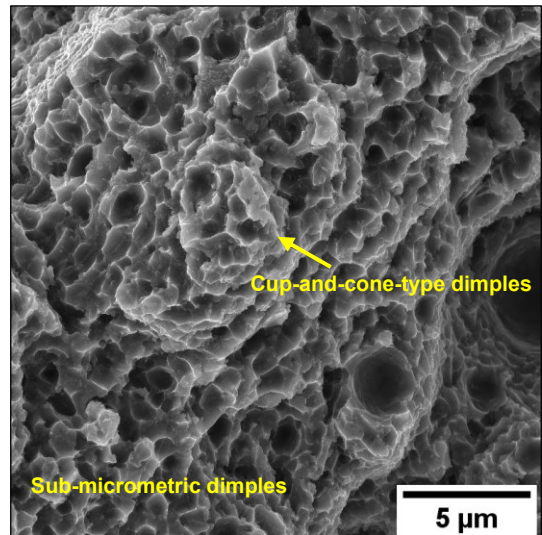


(f)

T5

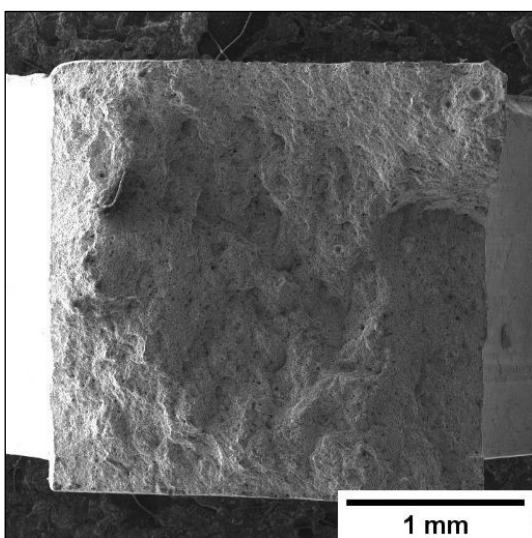


(g)

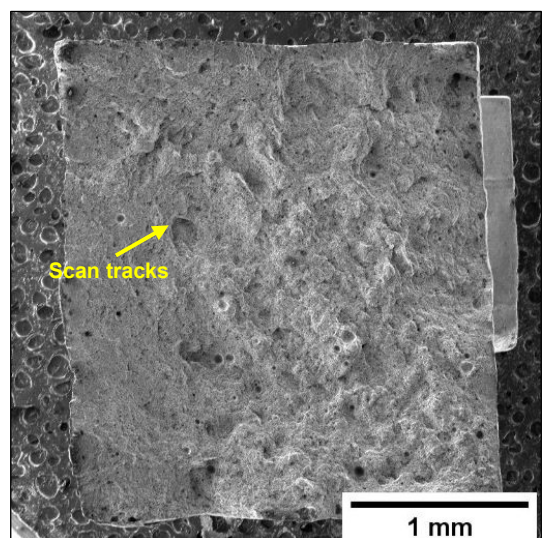


(h)

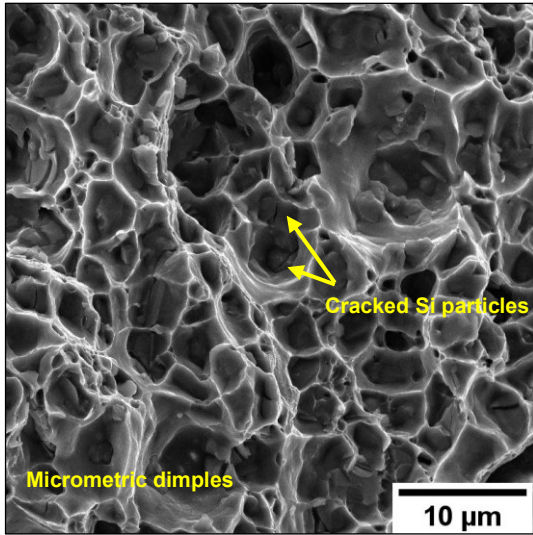
T6R



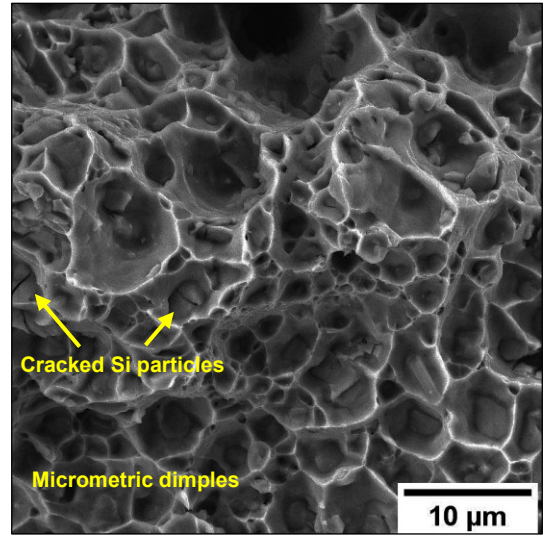
(i)



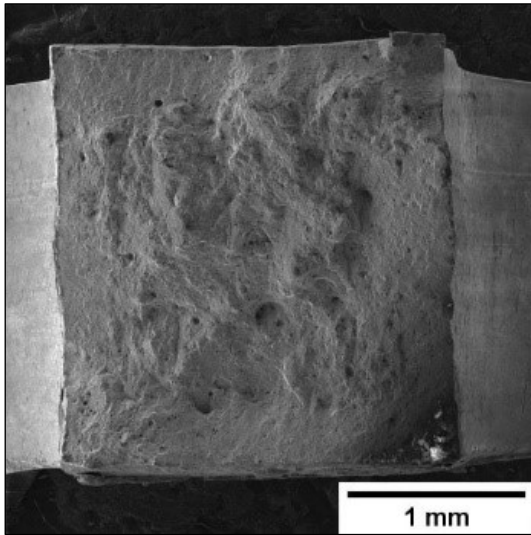
(j)



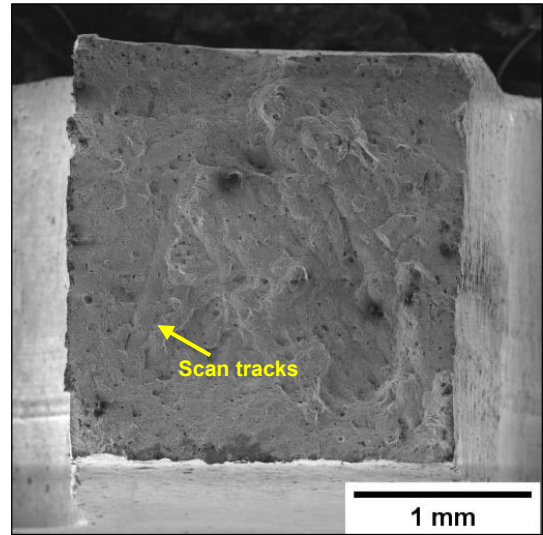
(k)



(l)

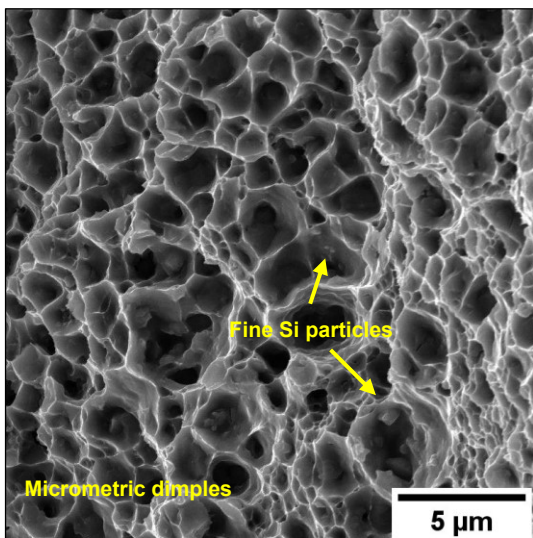


(m)

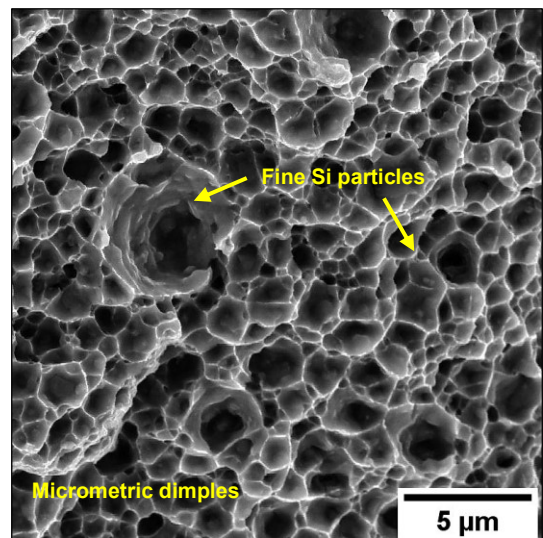


(n)

T6B



(o)



(p)

**Figure 2.52.** Fracture surfaces at different magnifications of the AB-H (a,b), AB-V (c,d), T5-H (e,f), T5-V (g,h), T6B-H (i,j), T6B-V (k,l), T6R-H (m,n), and T6R-V (o,p).

### 2.3.5 Cyclic mechanical characterization

Fatigue is the most common failure mode of engineering structures subjected to repeated loads. High fatigue strength is generally required, especially for the aerospace and automotive sectors, where the L-PBF AlSi10Mg alloy has many potential applications. However, material defects commonly in the L-PBF AlSi10Mg alloy, such as internal pores, inclusions, and surface roughness, act as stress concentrators and promote fatigue crack nucleation, thus limiting a broader application [29,32].

Based on the results of the static mechanical characterization, the fatigue behavior of the L-PBF AlSi10Mg alloy was assessed on samples that underwent: (i) T5 (Figure 2.53(a)) and (ii) T6R (Figure 2.53(b)) heat treatments.

According to the staircase method, the test results highlighted a fatigue strength at  $2 \times 10^6$  cycles at 50% survival probability ( $\sigma_{fs}$ ) equal to  $92 \pm 14.9$  MPa for the T5 alloy and  $108 \pm 3.8$  MPa for the T6R alloy (Figure 2.54). The lower ductility and the presence of coarser and inhomogeneous zones (MPBs and HAZs) in the T5 microstructure promote a high deviation of  $\sigma_{fs}$  value due to a minor obstacle to nucleation and fracture propagation under low stresses. The results agree with the data reported by [22,82-85] for rotating bending tests characterized by  $\sigma_{max}/\sigma_{min}$  ratio equal to -1. These results confirm the effectiveness of the optimized heat treatments.

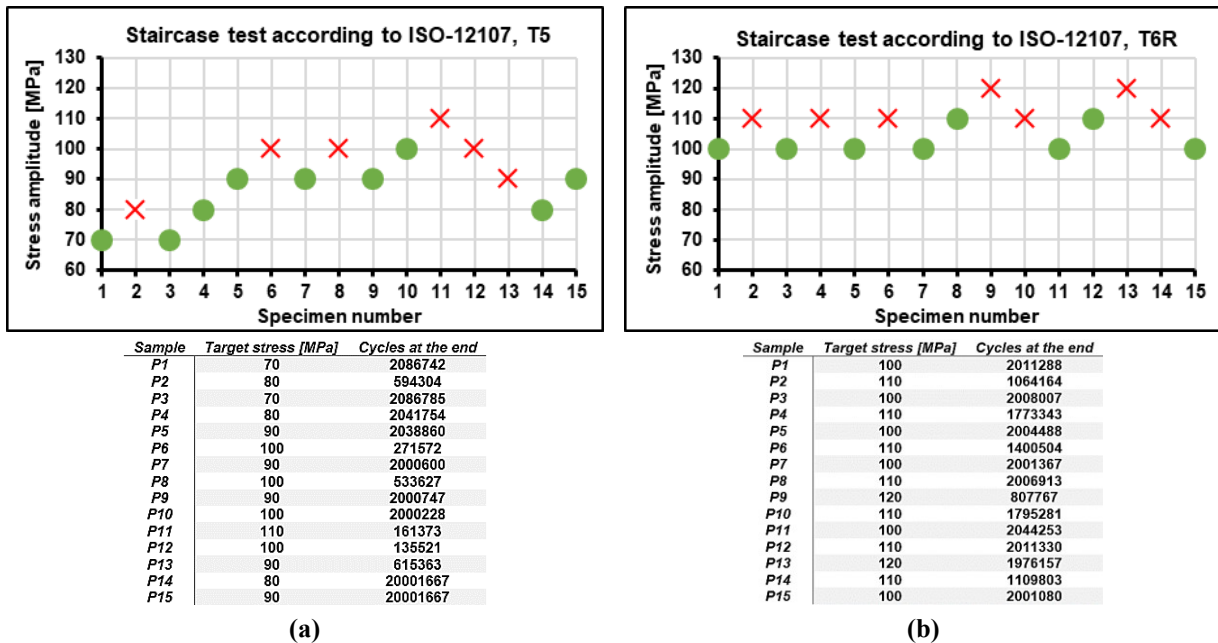


Figure 2.53. Staircase of the T5 (a) and T6R (b) alloys. The T5 condition shows all failures between 100 and 600 thousand cycles. The T6R condition shows all failures over 1 million cycles at 110 Mpa, about 800,000 cycles at 120 MPa.

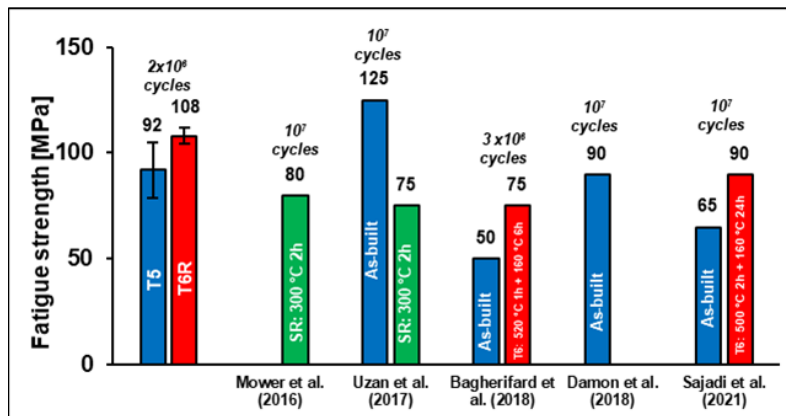
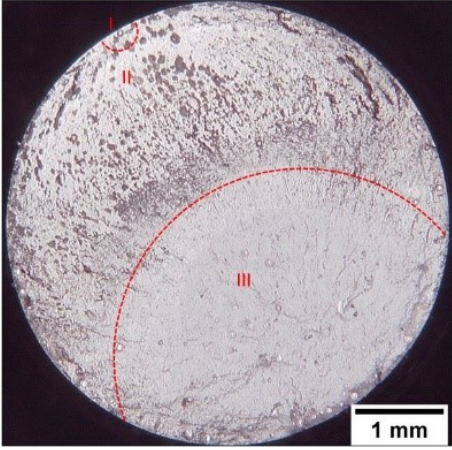
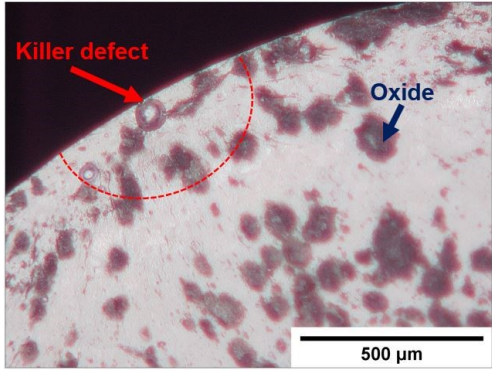
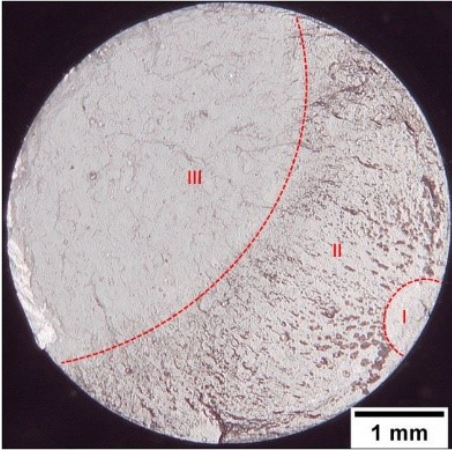
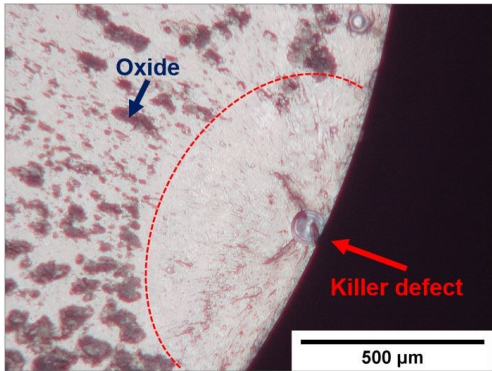
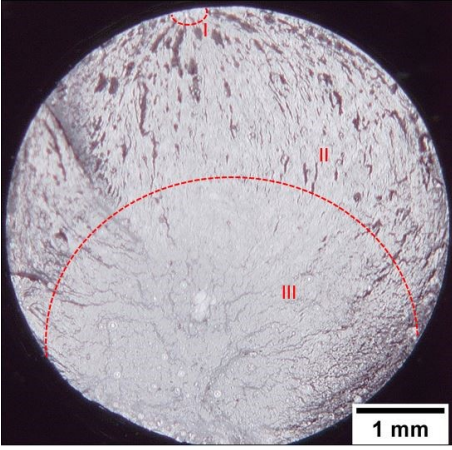
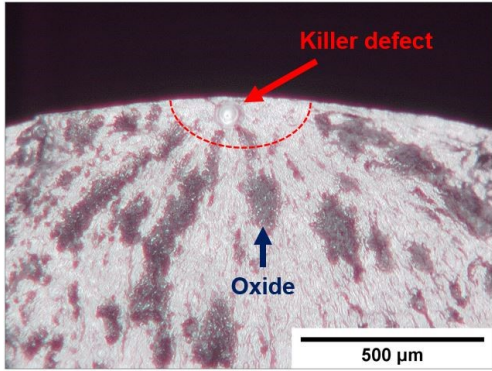
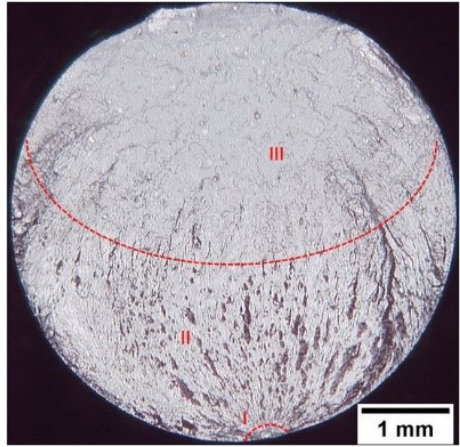


Figure 2.54. Comparison of fatigue strength of the T5 and T6R alloys compared to the literature data [22,32,33,35,84].

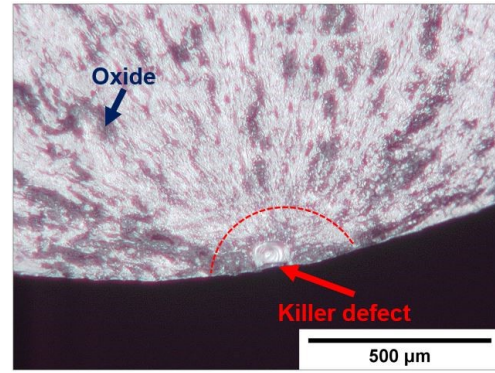
Low-magnification multi-focus images of the fracture surfaces of fatigue specimens are reported in Figure 2.55(a,c,e,g). Fracture morphology was investigated to find the crack nucleation site (Figures 2.55(b,d,f,h)) and study the fracture propagation during failure. In the failed samples, the fracture develops in three stages, namely (i) crack initiation, (ii) crack propagation, (iii) and final overload fracture [86,87]. The applied stress amplitude ( $\sigma_a$ ) influences the fracture morphology: higher stresses induce less extensive fatigue crack propagation area and more extensive final overload fracture zones. Large oxidized zones characterize the fracture propagation zone due to the heat generated by the surface contact, as highlighted by EDS maps (Figure 2.56). This phenomenon will be more evident in Chapter 3.

Sample	Macro	Crack initiation site
<b>P13 T5</b> 90 MPa 615363 cycles	 <p style="text-align: center;">(a)</p>	 <p style="text-align: center;">(b)</p>
<b>P6 T5</b> 100 MPa 271572 cycles	 <p style="text-align: center;">(c)</p>	 <p style="text-align: center;">(d)</p>
<b>P6 T6R</b> 110 MPa 1400504 cycles	 <p style="text-align: center;">(e)</p>	 <p style="text-align: center;">(f)</p>

**P9 T6R**  
120 MPa  
807767 cycles



(g)



(h)

**Figure 2.55.** Low magnification multi-focus images for T5 (a,b,c,d) and T6R heat-treated alloy (e,f,g,h). Fracture surface regions of interest: (i) crack initiation, (ii) crack propagation, (iii) and final overload fracture

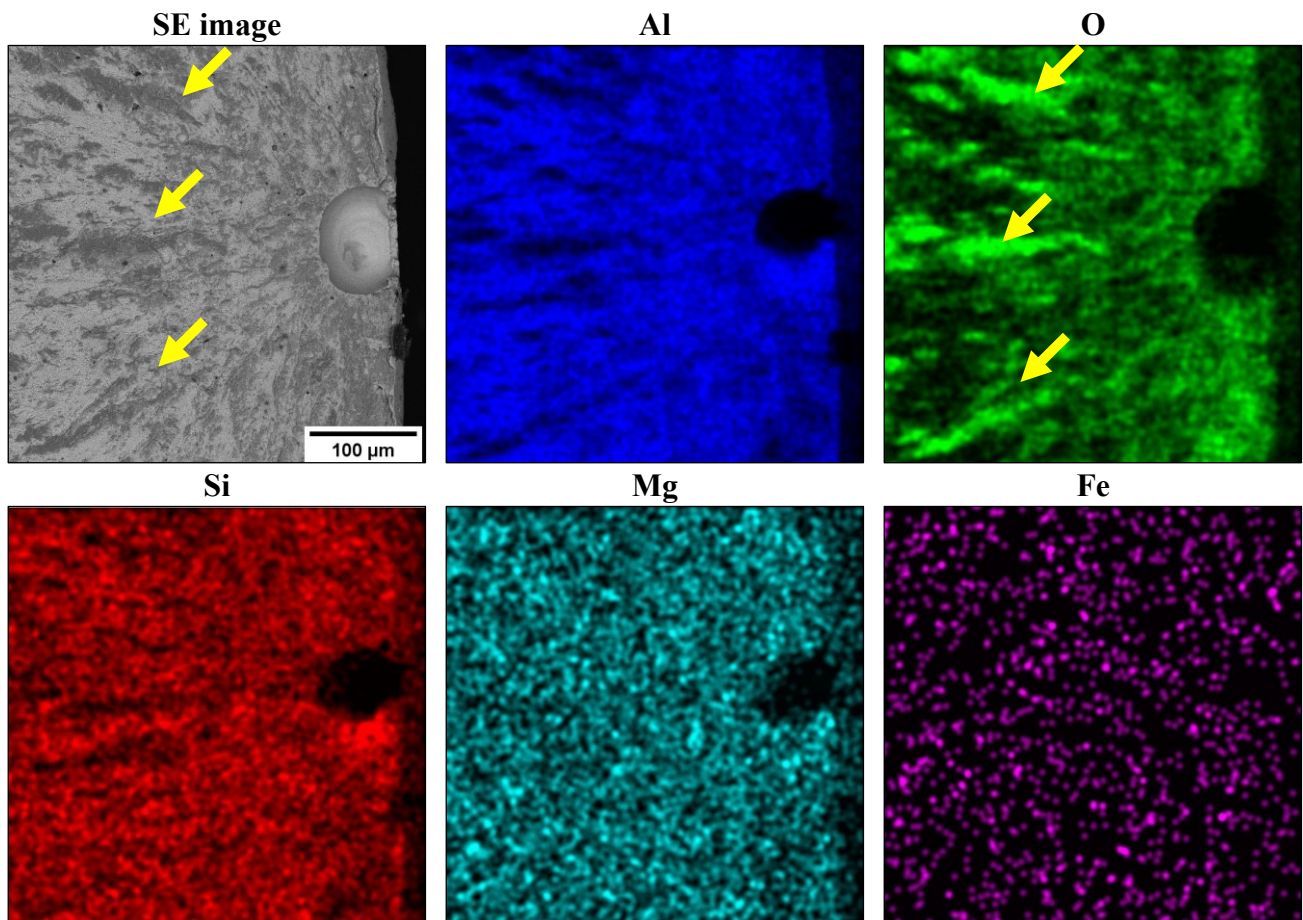


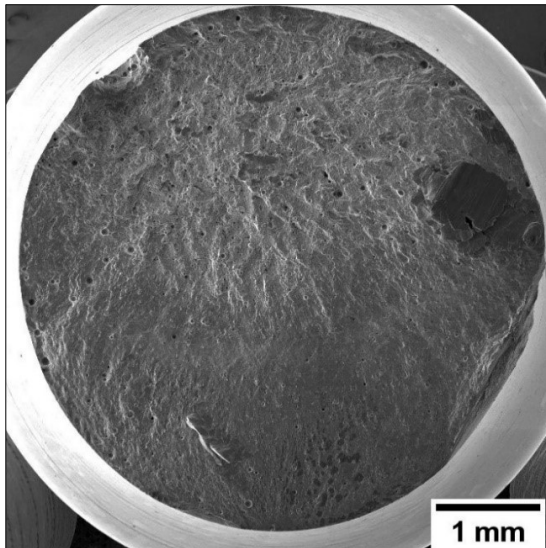
**Figure 2.56.** BSE image of the crack initiation of the T6R alloy (Sample 10). EDS elemental maps of Al (blue), O (green), Si (red), Mg (cyan), and Fe (violet), respectively. The yellow arrows in the BSE image and the O maps highlight the correspondence between dark areas and areas with high oxygen content, identifying the large dark areas in the propagation region as strongly oxidized areas.

At high magnification (Figures 2.57 and 2.58), it is possible to observe the crack initiation sites, which start from a sub-surface spherical void, such as gas or key-hole pores, with an area between 50 and 100 (Figures 2.57(b) and 2.58(b)). In particular, keyhole and gas pores were identified around the entire boundary of the fracture surface (Figure 2.59). Although the polished samples did not suffer from surface irregularities, the removal of 0.2 mm on the diameter approached sub-surface pores induced by the contour strategy to the surface, leaving sub-surface defects highly susceptible to fatigue cracking [89]. Using a contour strategy to increase geometrical accuracy and surface quality can lead to a high density of sub-surface pores, which can act as fatigue nucleation sites (Figure 2.60), as confirmed by

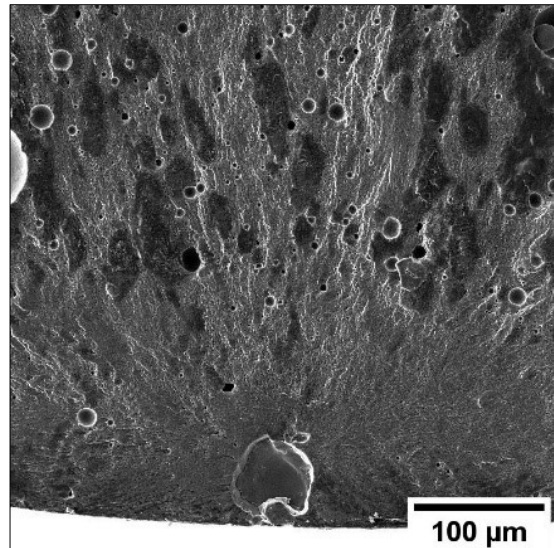
[86,94]. In particular, the presence of pores close to the surface increases the chance of revealing them by machining or polishing [90], and high energy density used in the contour strategy should be avoided instead because it induces the formation in the subsurface area of gas defects ascribable to the molten metal turbulent flow [93]. Several authors confirm these considerations. As Beevers et al. [87] described, the samples produced with contour show lower fatigue behavior due to the larger gas pores close to the outer surface than samples produced without contour. In addition, the optimum level of ED for low roughness was found to be at the onset of the keyhole conditions, bringing a higher volume of porosities induced by keyhole laser conditions [78-80]. Therefore, a contour strategy can negatively affect the fatigue resistance of the L-PBF AlSi10Mg alloy, and post-process treatments such as sandblasting or shot-peening that can replace the contour strategy should be considered [91,92].

The early stages of fatigue fracture are accompanied by significant plastic strain, as evidenced by torn rivulets and linked cavities radiating outward from the origin (Figures 2.57(c) and 2.58(c)) [84]. The defects located away from the primary initiating defect induce the initiation and propagation of minor cracks, which can merge with the primary crack propagation on a different plane [88]. In particular, the tendency of the cracks to deflect in the Al matrix forms secondary cracks, fatigue striations, and small parabolic stripes around the defects in the fatigue crack propagation regions, highlighting the effects of the secondary defects on fatigue failure [86]. The fatigue crack surface results planar, as occurs in samples subjected to rotating bending and fatigue striations, as well as micro-tearing (Figures 2.57(d) and 2.58(d)) in the fatigue propagation region, can be observed. In particular, these parabolic stripes identify the striation lines' direction and are characteristic features of stable crack propagation [22]. The zones of overload fracture, shown in Figures 2.57(e,f) and 2.58(e,f), exhibit a ductile behavior. In particular, the T5 alloy (Figure 2.57(e,f)) showed shallow dimples inside the Si cellular eutectic, typical of relatively brittle materials. The scale of the dimples is comparable to the cellular eutectic microstructure. In particular small cleavage facets and dense shear ridges mixed with dimple regions, typical of quasi-brittle fracture, are visible.

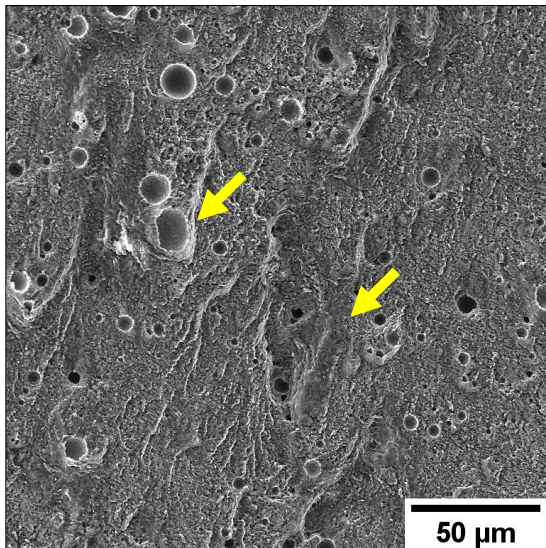
Moreover, it is possible to identify the tearing damage along scan tracks, which represent the weakest areas in the alloy and, therefore, the preferential fatigue crack path (Figure 2.57(e)). In the T6R alloy, the cellular  $\alpha$ -Al cells are not present, and the eutectic Si network evolves into larger Si particles. The final fracture area displayed a ductile fracture with relatively deep dimples compared to the T5 specimens (Figure 2.58(f)) and larger gas pores (Figure 2.58(e)). Large and deep dimples on the fracture surface of the T6R specimens indicate more ductility than the T5 specimens, as widely described above.



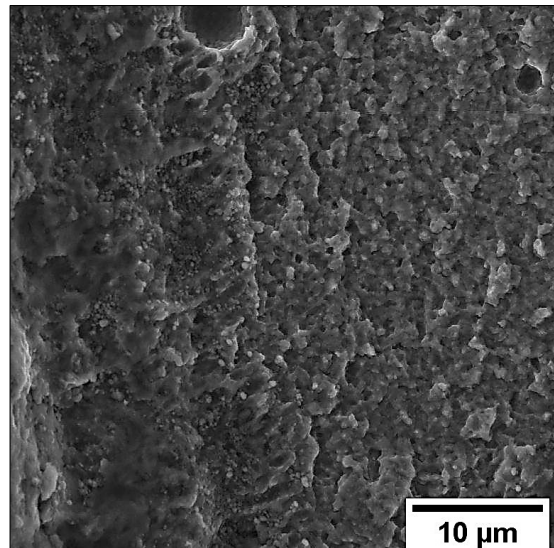
(a)



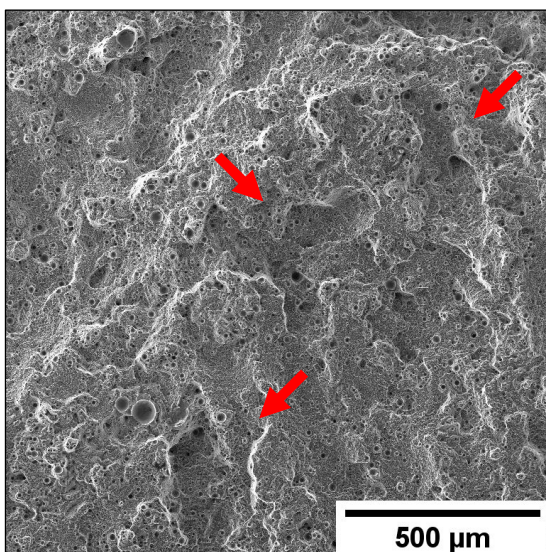
(b)



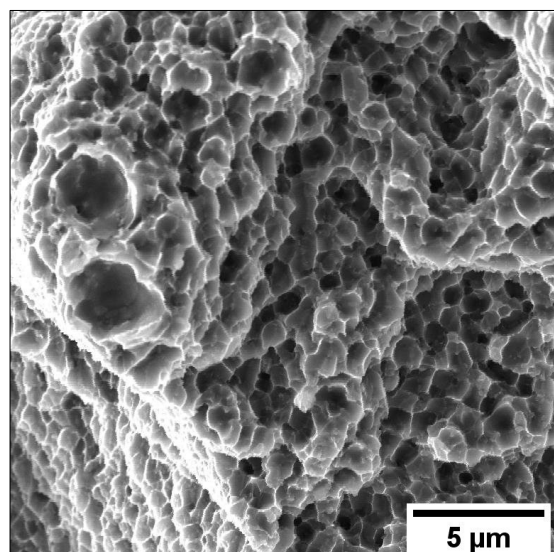
(c)



(d)

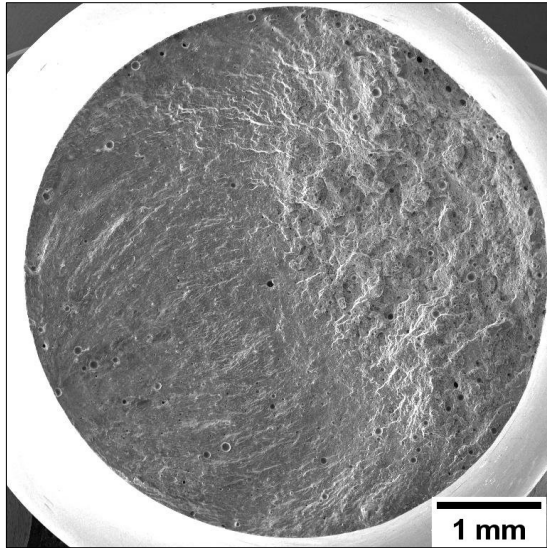


(e)

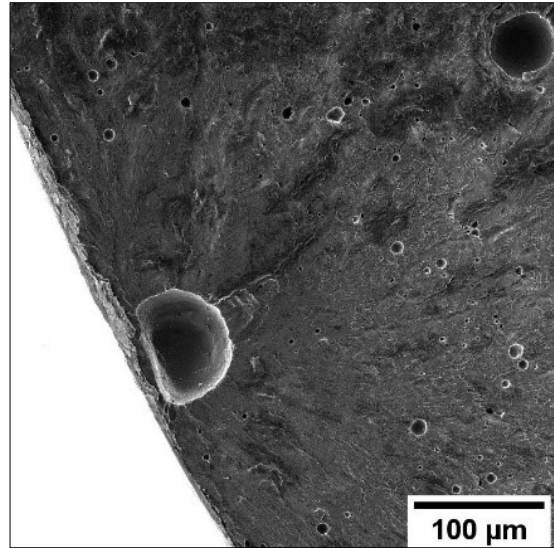


(f)

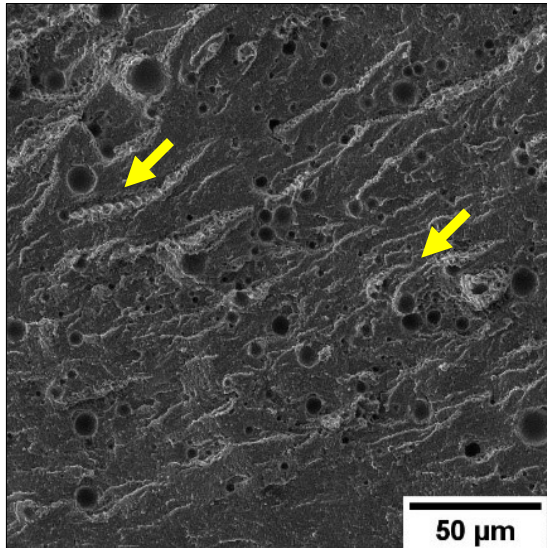
**Figure 2.55.** SE image of the T5 alloy (Sample 11). Low magnification (a); killer defect (b) crack propagation; (c) micro-tearing in the fatigue propagation region (d) final overload fracture; (e) dimple voids. Yellow arrows indicate parabolic stripes around the defects in the fatigue crack propagation regions. Red arrows indicate the scan track marks in the overload fracture zone.



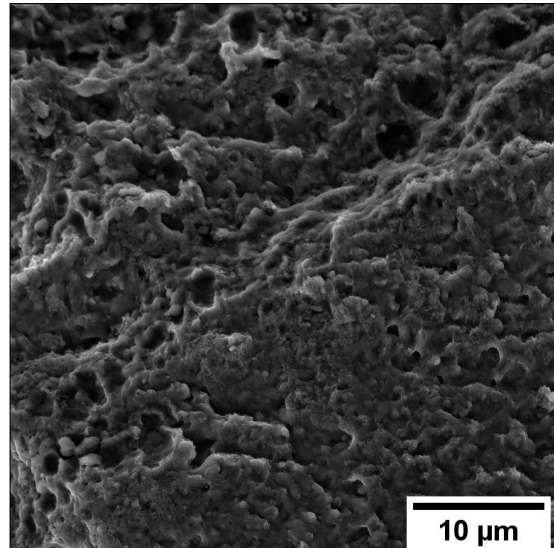
(a)



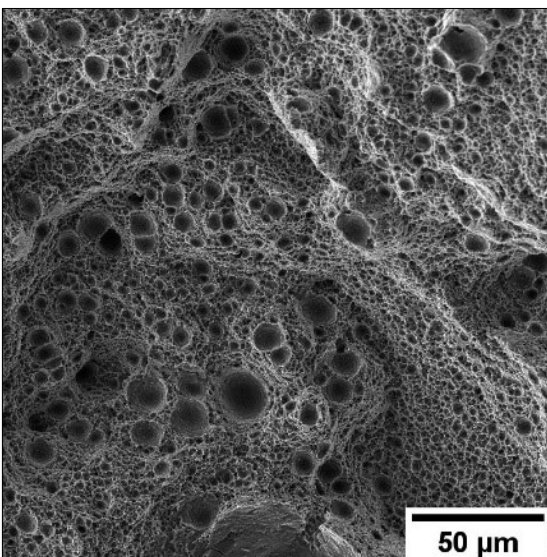
(b)



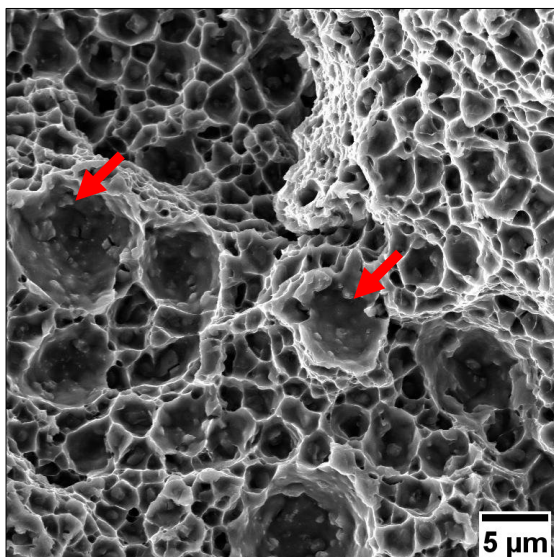
(c)



(d)



(e)



(f)

**Figure 2.56.** SE image of the T6R alloy (Sample 10). Low magnification (a); killer defect (b) crack propagation; (c) micro-tearing in the fatigue propagation region (d) final overload fracture; (e) dimple voids. Yellow arrows indicate parabolic stripes around the defects in the fatigue crack propagation regions. Red arrows indicate the Si particles inside the large dimples.

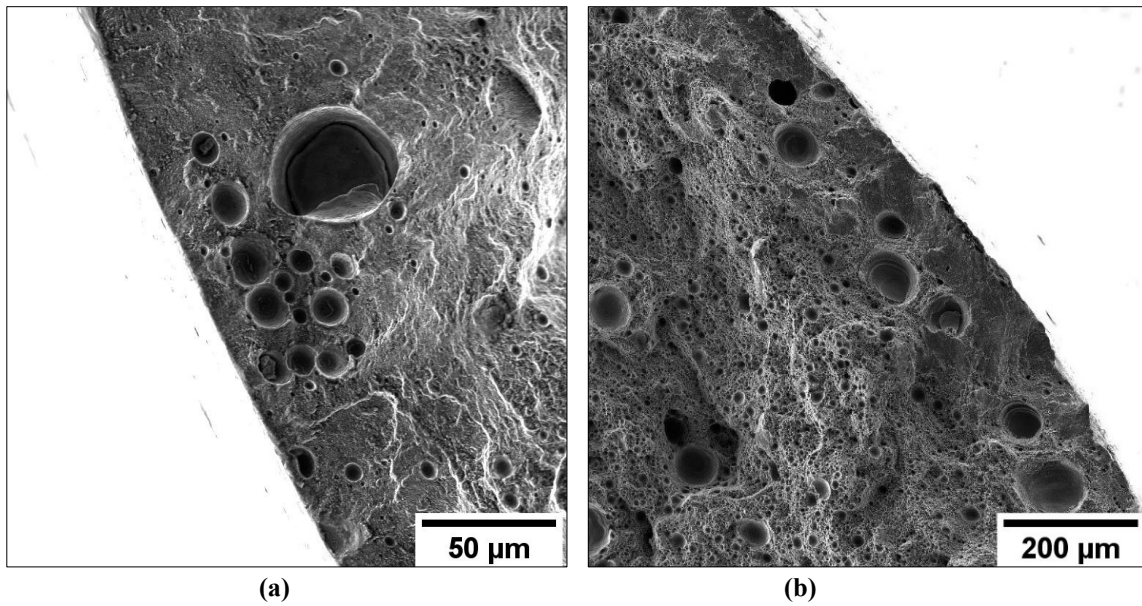


**Figure 2.57.** Detail of contouring zone for T5 alloy (Sample 13) (a) and T6R alloy (Sample 6) (b).

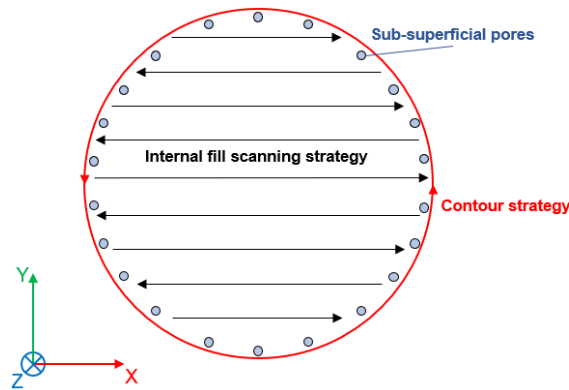


**Figure 2.58.** Scheme of contour strategy. It forms a circular crown of gas and keyhole porosities around the bulk material.

The T6 heat treatment improved fatigue strength, although the porosity measurements revealed slightly higher porosity than the T5 ones (Figure 2.12). Thus, the synergistic effects of increased ductility and microstructural homogenization can increase the capacity of the material to sustain the presence of cracks, limiting the detrimental effect of the increased porosity [22]. In addition, according to Brandl et al. [68], the fatigue improvement of the T6 alloy is also the consequence of the microstructural evolution of the eutectic-Si network that would limit crack initiation and propagation because the fatigue failure does not lead to Si particle fracture. The integrity of the Si particles helps the deformation of the Al matrix, delaying the collapse of the microstructure and the sample failure. Conversely, under tension-compression cyclic loading of the fully reversed rotating bending test, in the T5 alloy, the dislocation density rises with the increase of cycle times. The dislocation pile-up leads to microcracks at the Al cell/eutectic-Si network interface, easing the failure of the softer Al phase of the Si network and the crack propagation. The higher ductility of the T6R microstructure than the T5 one induces a slower fatigue crack initiation due to the more energy-consuming failure mechanism, as described in sections 2.3.2 and 2.3.3 [77]. In this way, the T6 heat treatment improves fatigue resistance, even in higher defect density [13].

## 2.4 Conclusion

This chapter aims to customize optimized heat treatment to the L-PBF AlSi10Mg alloy. In particular, an innovative T6R heat treatment consisting of a rapid SHT (510 °C for 10 min) followed by AA (160 °C for 6 h) was developed. The performances of the T6R alloy were compared with other heat treatment conditions: AB; optimized T5 (direct artificial aging of the AB alloy at 160 °C for 4 h); benchmark T6 (T6B), consisting of SHT (540 °C for 1 h) followed by AA (160 °C for 4 h). A variety of mechanical characterization techniques (static (section 2.3.2), nano (section 2.3.3), in-situ (section 2.3.4), and cyclic (section 2.3.5) tests) were used to understand a bottom the advantage and disadvantages of the T6R heat treatment.

The following conclusions can be drawn:

- The SHTR (temperature 510 °C and time between 5 and 20 min) allows obtaining a higher level of Si supersaturation in the  $\alpha$ -Al matrix and less gas pore growth than higher temperature or more prolonged soaking time conditions. In addition, the SHTR accelerates the kinetics of precipitation hardening, moving the peak-hardening condition towards a shorter artificial aging soaking time.
- The SHTR develops a composite-like microstructure of Si particles embedded into the  $\alpha$ -Al phase matrix. Compared with the Si particles induced by conventional SHT, these are finer and more homogeneous in size and distribution. The microstructural features induced by the T6R heat treatment increase the Orowan strengthening mechanism, the cohesion between Si particles and  $\alpha$ -Al matrix, and the fracture resistance of the alloy.
- The T5 alloy shows a local microstructural anisotropy that affected the local mechanical behavior of the alloy: lower nano-hardness and ERP values characterize HAZs and MPBs, which are less effective in inhibiting dislocation slip than the MPC.
- The T6B and T6R alloys are characterized by lower nano-hardness and ERP values, indicating a softer alloy than the T5 alloy. Moreover, the different distribution and sizes of the Si particles embedded into the  $\alpha$ -Al matrix affect the local mechanical response of the two conditions. While the T6R samples show a homogeneous mechanical response due to the fine dispersion of Si particles, larger Si particles or clusters in the T6B samples led to a local inhomogeneous mechanical behavior.
- The microstructural characteristics of the T6R alloy lead to the highest static mechanical property balance and fatigue strength compared to the T5 alloy. However, the high pore density in the sub-surface zones due to the contour strategy reduced the fatigue strength obtainable.
- The tensile fracture surfaces show shallow dimples in the AB and T5 alloys and deep dimples in the T6 alloys, whose extension is proportional to the size of the Si particles. The morphology of the fatigue fracture surfaces of the T5 and T6R alloys consists of crack initiation, crack propagation, and final overload fracture zone. However, the T5 alloy shows thinner dimples in the overload fracture zone than the T6R alloy due to the finer microstructure
- The AB and T5 alloys present similar fracture path, which develops preferentially along the coarser and inhomogeneous zones (MPBs and HAZs). Crack nucleates on the eutectic-Si network at a low strain since the harder Si phase transfers the load to the enclosed softer Al phase, leading to a fast sample failure.
- The crack propagation in the T6R and T6B alloys shows a void-sheet scenario involving the coalescence of the inner pores and voids at the Si particles/ $\alpha$ -Al matrix interface. The particle fracture stress and the Si particle/ $\alpha$ -

Al matrix detachment highly depend on the Si particle size and distribution, determining the lower ductility of the T6B alloy than the T6R one.

- The failure mechanisms induced by the rotating bending fatigue tests are comparable in the T5 and T6R alloys. They consist of detachment or cracking of brittle eutectic Si phase and Si particles, generation of shear bands with consequent formation of microcracks, and final fracture generated by linkage of microcracks and their propagation.

In conclusion, the rapid solution induced a microstructural refinement compared to the conventional solution, improving the mechanical response of the T6 heat-treated L-PBF AlSi10Mg alloy. Considering the decrease in anisotropy, the better balance of static and cyclic mechanical properties, and the nano- and micro-mechanical response induced by the T6R heat treatment, it represents an optimal solution to produce reliable structural components.

## References

1. T. DebRoy, H.L. Wei, J.S. Zuback, T. Mukherjee, J.W. Elmer, J.O. Milewski, A.M. Beese, A. Wilson-Heid, A. De, W. Zhang, Additive manufacturing of metallic components – Process, structure and properties, *Progress in Materials Science*, 92 (2018) 112-224. <https://doi.org/10.1016/j.pmatsci.2017.10.001>.
2. N. T. Aboulkhair, M. Simonelli, L. Parry, I. Ashcroft, C. Tuck, R. Hague, 3D printing of Aluminium alloys: Additive Manufacturing of Aluminium alloys using selective laser melting, *Progress in Materials Science*, 106 (2019) 100578. <https://doi.org/10.1016/j.pmatsci.2019.100578>.
3. E.O. Olakanmi, R.F. Cochrane, K.W. Dalgarno, A review on selective laser sintering/melting (SLS/SLM) of aluminium alloy powders: Processing, microstructure, and properties, *Progress in Materials Science*, 74 (2015) 401-477. <https://doi.org/10.1016/j.pmatsci.2015.03.002>.
4. Lv Zhao, L. Song, J. G. Santos Macías, Y. Zhu, M. Huang, A. Simar, Z. Li, Review on the correlation between microstructure and mechanical performance for laser powder bed fusion AlSi10Mg, *Additive Manufacturing*, 56 (2022) 102914. <https://doi.org/10.1016/j.addma.2022.102914>.
5. L. Thijs, K. Kempen, J.P. Kruth, J. Van Humbeeck, Fine-structured aluminium products with controllable texture by selective laser melting of pre-alloyed AlSi10Mg powder, *Acta Mater.*, 61 (2013) 1809–1819, doi:10.1016/j.actamat.2012.11.052.
6. A. Hadadzadeh, B. S. Amirkhiz, M. Mohammadi, Contribution of Mg<sub>2</sub>Si precipitates to the strength of direct metal laser sintered AlSi10Mg, *Materials Science and Engineering: A*, 739 (2019) 295-300, <https://doi.org/10.1016/j.msea.2018.10.055>.
7. M. Fousová, D. Dvorský, A. Michalcová, D. Vojtěch, Changes in the microstructure and mechanical properties of additively manufactured AlSi10Mg alloy after exposure to elevated temperatures, *Materials Characterization*, 137 (2018) 119-126. <https://doi.org/10.1016/j.matchar.2018.01.028>.
8. B. Chen, S.K. Moon, X. Yao, G. Bi, J. Shen, J. Umeda, K. Kondoh, Strength and strain hardening of a selective laser melted AlSi10Mg alloy, *Scripta Materialia*, 141 (2017) 45-49. <https://doi.org/10.1016/j.scriptamat.2017.07.025>.
9. J. Fite, S. E. Premeela, J. A. Slotwinski, T. P. Weihs, Evolution of the microstructure and mechanical properties of additively manufactured AlSi10Mg during room temperature holds and low temperature aging, *Additive Manufacturing*, 36 (2020) 101429. <https://doi.org/10.1016/j.addma.2020.101429>.
10. K.G. Prashanth, J. Eckert, Formation of metastable cellular microstructures in selective laser melted alloys, *Journal of Alloys and Compounds*, 707 (2017) 27-34, <https://doi.org/10.1016/j.jallcom.2016.12.209>.
11. W. Li, S. Li, J. Liu, A. Zhang, Y. Zhou, Q. Wei, C. Yan, Y. Shi, Effect of heat treatment on AlSi10Mg alloy fabricated by selective laser melting: Microstructure evolution, mechanical properties and fracture mechanism, *Materials Science and Engineering: A*, 663 (2016) 116-125. <https://doi.org/10.1016/j.msea.2016.03.088>.
12. M. Tocci, A. Pola, M. Gelfi, G. M. La Vecchia, Effect of a New High-Pressure Heat Treatment on Additively Manufactured AlSi10Mg Alloy, *Metall Mater Trans A* 51 (2020) 4799–4811. <https://doi.org/10.1007/s11661-020-05905-y>
13. J. N. Domfang Ngnokou, Y. Nadot, G. Henaff, J. Nicolai, W. H. Kan, J. M. Cairney, L. Ridosz, *International Journal of Fatigue*, 119 (2019) 160-172.. <https://doi.org/10.1016/j.ijfatigue.2018.09.029>.
14. F. Alghamdi, X. Song, A. Hadadzadeh, B. Shalchi-Amirkhiz, M. Mohammadi, M. Haghshenas, Post heat treatment of additive manufactured AlSi10Mg: On silicon morphology, texture and small-scale properties, *Materials Science and Engineering: A*, 783 (2020) 139296. <https://doi.org/10.1016/j.msea.2020.139296>.
15. A. Iturrioz, E. Gil, M.M. Petite, F. Garcíandia, A. M. Mancisidor, M. San Sebastian. Selective laser melting of AlSi10Mg alloy: influence of heat treatment condition on mechanical properties and microstructure, *Weld World*, 62 (2018) 885–892. <https://doi.org/10.1007/s40194-018-0592-8>.
16. C. Zhang, H. Zhu, H. Liao, Y. Cheng, Z. Hu, X. Zeng, Effect of heat treatments on fatigue property of selective laser melting AlSi10Mg, *International Journal of Fatigue*, 116 (2018) 513-522. <https://doi.org/10.1016/j.ijfatigue.2018.07.016>.
17. L.F. Wang, J. Sun, X.L. Yu, Y. Shi, X.G. Zhu, L.Y. Cheng, H.H. Liang, B. Yan, L.J. Guo, Enhancement in mechanical properties of selectively laser-melted AlSi10Mg aluminum alloys by T6-like heat treatment, *Materials Science and Engineering: A*, 734 (2018) 299-310. <https://doi.org/10.1016/j.msea.2018.07.103>.
18. A. Mertens, O. Dedry, D. Reuter, O. Rigo, J. Lecomte-Beckers, Thermal Treatments of AlSi10Mg Processed By Laser Beam Melting, In *Proceedings of the 26th International Solid Freeform Fabrication Symposium*, Dayton, OH, USA, 23–26 June 2015, 1007–1016.
19. B. Amir, E. Grinberg, Y. Gale, O. Sadot, S. Samuha, Influences of platform heating and post-processing stress relief treatment on the mechanical properties and microstructure of selective-laser-melted AlSi10Mg alloys, *Materials Science and Engineering: A*, 822 (2021) 141612. <https://doi.org/10.1016/j.msea.2021.141612>.
20. J. Fiocchi, C.A. Biffi, C. Colombo, L. M. Vergani, A. Tuissi, Ad Hoc Heat Treatments for Selective Laser Melted Alsi10mg Alloy Aimed at Stress-Relieving and Enhancing Mechanical Performances. *JOM*, 72 (2020) 1118–1127. <https://doi.org/10.1007/s11837-019-03973-z>.
21. L. Tonelli, E. Liverani, A. Morri, L. Ceschini, Role of Direct Aging and Solution Treatment on Hardness, Microstructure and Residual Stress of the A357 (AlSi7Mg0.6) Alloy Produced by Powder Bed Fusion. *Metall Mater Trans B*, 52 (2021) 2484–2496. <https://doi.org/10.1007/s11663-021-02179-6>
22. S. Bagherifard, N. Beretta, S. Monti, M. Riccio, M. Bandini, M. Guagliano, On the fatigue strength enhancement of additive manufactured AlSi10Mg parts by mechanical and thermal post-processing, *Materials & Design*, 145 (2018) 28-41. <https://doi.org/10.1016/j.matdes.2018.02.055>.
23. SLM Solution Group AG, DE, [Online]. Available: <https://www.slm-solutions.com/it/prodotti/machines/slmr500/>

24. International Organization for Standardization: ISO 14707:2015: Surface chemical analysis— Glow discharge optical emission spectrometry (GD-OES) — Introduction to use; International Organization for Standardization: Geneva, Switzerland, 2015.
25. M. Tiryakioğlu, J. Campbell, N.D. Alexopoulos, Quality Indices for Aluminum Alloy Castings: A Critical Review. *Metall Mater Trans B*, 40 (2009) 802. <https://doi.org/10.1007/s11663-009-9304-5>
26. N.D. Alexopoulos, Definition of quality in cast aluminum alloys and its characterization with appropriate indices. *J. of Materi Eng and Perform*, 15 (2006) 59–66. <https://doi.org/10.1361/105994906X83547>
27. R. Casati, M.N. Hamidi, M. Coduri, V. Tirelli, M. Vedani, Effects of Platform Pre-Heating and Thermal-Treatment Strategies on Properties of AlSi10Mg Alloy Processed by Selective Laser Melting. *Metals*, 8(11) (2018) 954. <https://doi.org/10.3390/met8110954>.
28. L. Zhou, A. Mehta, E. Schulz, B. McWilliams, K. Cho, Y. Sohn, Microstructure, precipitates and hardness of selectively laser melted AlSi10Mg alloy before and after heat treatment, *Materials Characterization*, 143 (2018) 5-17. <https://doi.org/10.1016/j.matchar.2018.04.022>.
29. W. H. Kan, Y. Nadot, M. Foley, L. Ridosz, G. Proust, J. M. Cairney, Factors that affect the properties of additively-manufactured AlSi10Mg: Porosity versus microstructure, *Additive Manufacturing*, 29 (2019) 100805, <https://doi.org/10.1016/j.addma.2019.100805>.
30. E. Padovano, C. Badini, A. Pantarelli, F. Gili, F. D'Aiuto, A comparative study of the effects of thermal treatments on AlSi10Mg produced by laser powder bed fusion, *Journal of Alloys and Compounds*, 831 (2020) 154822. <https://doi.org/10.1016/j.jallcom.2020.154822>.
31. N. T. Aboulkhair, I. Maskery, C. Tuck, I. Ashcroft, N.M. Everitt, The microstructure and mechanical properties of selectively laser melted AlSi10Mg: The effect of a conventional T6-like heat treatment, *Materials Science and Engineering: A*, 667 (2016) 139-146. <https://doi.org/10.1016/j.msea.2016.04.092>.
32. N.O. Larrosa, W. Wang, N. Read, M.H. Loretto, C. Evans, J. Carr, U. Tradowsky, M.M. Attallah, P.J. Withers, Linking microstructure and processing defects to mechanical properties of selectively laser melted AlSi10Mg alloy, *Theoretical and Applied Fracture Mechanics*, Volume 98, 2018, Pages 123-133, <https://doi.org/10.1016/j.tafmec.2018.09.011>.
33. U. Tradowsky, J. White, R.M. Ward, N. Read, W. Reimers, M.M. Attallah, Selective laser melting of AlSi10Mg: Influence of post-processing on the microstructural and tensile properties development, *Materials & Design*, 105 (2016) 212-222. <https://doi.org/10.1016/j.matdes.2016.05.066>.
34. L. Girelli, M. Tocci, M. Gelfi, A. Pola, Study of heat treatment parameters for additively manufactured AlSi10Mg in comparison with corresponding cast alloy, *Materials Science and Engineering: A*, 739 (2019) 317-328. <https://doi.org/10.1016/j.msea.2018.10.026>.
35. Longchao Zhuo, Zeyu Wang, Hongjia Zhang, Enhuai Yin, Yanlin Wang, Tao Xu, Chao Li, Effect of post-process heat treatment on microstructure and properties of selective laser melted AlSi10Mg alloy, *Materials Letters*, Volume 234, 2019, Pages 196-200, <https://doi.org/10.1016/j.matlet.2018.09.109>.
36. W. Li, S. Li, J. Liu, A. Zhang, Y. Zhou, Q. Wei, C. Yan, Y. Shi, Effect of heat treatment on AlSi10Mg alloy fabricated by selective laser melting: Microstructure evolution, mechanical properties and fracture mechanism, *Materials Science and Engineering: A*, 663 (2016) 116-125. <https://doi.org/10.1016/j.msea.2016.03.088>
37. Lumley, R., O'Donnell, R., D.R. Gunasegaram, M. Givord, Heat Treatment of High-Pressure Die Castings. *Metall Mater Trans A*, 38 (2007) 2564–2574. <https://doi.org/10.1007/s11661-007-9285-4>.
38. ASM International. ASTM B962–17: Standard Test Methods for Density of Compacted or Sintered Powder Metallurgy (PM) Products Using Archimedes' Principle, ASM International: West Conshohocken, PA, USA, 2017.
39. K.H. Eckelmeyer, X-Ray Diffraction for Bulk Structural Analysis, *Metals Handbook Desk Edition*, Second Edition, 1998.
40. G. Poli, R. Sola, P. Veronesi, Microwave-assisted combustion synthesis of NiAl intermetallics in a single mode applicator: Modeling and optimisation, *Materials Science and Engineering: A*, 441 1–2 (2006) 149-156. <https://doi.org/10.1016/j.msea.2006.08.114>.
41. ASM International. ASTM E3-11(2017): Standard Guide for Preparation of Metallographic Specimens, ASM International: West Conshohocken, PA, USA, 2017.
42. ASM International. ASTM E407-07(2015): Standard Practice for Microetching Metals and Alloys, ASM International: West Conshohocken, PA, USA, 2015.
43. M Li, S Ghosh, O Richmond, H Weiland, T.N Rouns, Three dimensional characterization and modeling of particle reinforced metal matrix composites: part I: Quantitative description of microstructural morphology, *Materials Science and Engineering: A*, 265 1–2 (1999) 153-173. [https://doi.org/10.1016/S0921-5093\(98\)01132-0](https://doi.org/10.1016/S0921-5093(98)01132-0).
44. ASM International. ASTM E92-17: Standard Test Methods for Vickers Hardness and Knoop Hardness of Metallic Materials, ASM International: West Conshohocken, PA, USA, 2017.
45. International Organization for Standardization. ISO 6892-1:2009, *Metallic Materials–Tensile Testing–Part 1: Method of Test at Room Temperature*; International Organization for Standardization: Geneva, Switzerland, 2009.
46. International Organization for Standardization. ISO 6892-2:2011, *Metallic Materials–Tensile Testing–Part 2: Method of Test at Elevated Temperature*; International Organization for Standardization: Geneva, Switzerland, 2011.
47. International Organization for Standardization. ISO 14577-1:2015, *Metallic materials — Instrumented indentation test for hardness and materials parameters — Part 1: Test method*; International Organization for Standardization: Geneva, Switzerland, 2011.
48. J.L. Hay, G.M. Pharr, *ASM Handbook Vol. 8: Mechanical Testing and Evaluation*, 10th Edition, ASM International, Materials Park, OH, (2000) 232–243.
49. Muhammad, M., Pegues, J.W., Shamsaei, N. et al. Effect of heat treatments on microstructure/small-scale properties of additive manufactured Ti-6Al-4V. *Int J Adv Manuf Technol*, 103 (2019) 4161–4172. <https://doi.org/10.1007/s00170-019-03789-w>

50. ASM International. ASTM E8/E8M-21: Standard Test Methods for Tension Testing of Metallic Materials, ASM International: West Conshohocken, PA, USA, 2021.
51. International Organization for Standardization. ISO 12107:2012 Metallic materials. Fatigue testing. Statistical planning and analysis of data; International Organization for Standardization: Geneva, Switzerland, 2012.
52. R.N. Lumley, I.J. Polmear, P.R. Curtis, Rapid Heat Treatment of Aluminum High-Pressure Diecastings. *Metall Mater Trans A*, 40 (2009) 1716–1726. <https://doi.org/10.1007/s11661-009-9836-y>.
53. A. Bendijk, R. Delhez, L. Katgerman, Th. H. De Keijser, E. J. Mittemeijer, N. M. Van Der Pers Characterization of Al-Si alloys rapidly quenched from the melt. *J Mater Sci*, 15 (1980) 2803–2810. <https://doi.org/10.1007/BF00550549>
54. S. Marola, D. Manfredi, G. Fiore, M. G. Poletti, M. Lombardi, P. Fino, L. Battezzati, A comparison of Selective Laser Melting with bulk rapid solidification of AlSi10Mg alloy, *Journal of Alloys and Compounds*, 742 (2018) 271-279, <https://doi.org/10.1016/j.jallcom.2018.01.309>.
55. I. Rosenthal, R. Shneck, A. Stern, I. Rosenthal, R. Shneck, A. Stern, Heat treatment effect on the mechanical properties and fracture mechanism in AlSi10Mg fabricated by additive manufacturing selective laser melting process, *Materials Science and Engineering: A*, 729 (2018) 310-322, <https://doi.org/10.1016/j.msea.2018.05.074>.
56. J.P. Moses, Q. Liu, J. P. Best, X. Li, J. J. Kruzic, U. Ramamurty, B. Gludovatz, Fracture resistance of AlSi10Mg fabricated by laser powder bed fusion, *Acta Materialia*, 211 (2021) 116869. <https://doi.org/10.1016/j.actamat.2021.116869>.
57. H. Qin, V. Fallah, Q. Dong, M. Brochu, M. R. Daymond, M. Gallemeault, Solidification pattern, microstructure and texture development in Laser Powder Bed Fusion (L-PBF) of Al10SiMg alloy, *Materials Characterization*, 145 (2018) 29-38. <https://doi.org/10.1016/j.matchar.2018.08.025>.
58. P. Wei, Z. Chen, S. Zhang, X. Fang, B. Lu, L. Zhang, Z. Wei, Effect of T6 heat treatment on the surface tribological and corrosion properties of AlSi10Mg samples produced by selective laser melting, *Materials Characterization*, 171 (2021) 110769. <https://doi.org/10.1016/j.matchar.2020.110769>.
59. Lv Zhao, Juan Guillermo Santos Macias, Lipeng Ding, Hosni Idrissi, Aude Simar, Damage mechanisms in selective laser melted AlSi10Mg under as built and different post-treatment conditions, *Materials Science and Engineering: A*, 764 (2019) 138210. <https://doi.org/10.1016/j.msea.2019.138210>.
60. Z. Zhang, D.L. Chen, Contribution of Orowan strengthening effect in particulate-reinforced metal matrix nanocomposites, *Materials Science and Engineering: A*, 483–484 (2008) 148-152, <https://doi.org/10.1016/j.msea.2006.10.184>.
61. Y. Tao, W. Kuaishu, W. Wen, P. Pai, H. Liying, Q. Ke, J. Yuanyuan, Effect of Friction Stir Processing on Microstructure and Mechanical Properties of AlSi10Mg Aluminum Alloy Produced by Selective Laser Melting. *JOM*, 71 (2019) 1737–1747. <https://doi.org/10.1007/s11837-019-03343-9>.
62. Z. Yang, J. Fan, Y. Liu, J. Nie, Z. Yang, Y. Kang, Strengthening and Weakening Effects of Particles on Strength and Ductility of SiC Particle Reinforced Al-Cu-Mg Alloys Matrix Composites. *Materials* 2021, 14, 1219. <https://doi.org/10.3390/ma14051219>.
63. G. Özer, G. Tarakçı, M.S. Yilmaz, Z.Ç. Öter, Ö. Sürmen, Y. Akça, M. Coşkun, E. Koç. Investigation of the effects of different heat treatment parameters on the corrosion and mechanical properties of the AlSi10Mg alloy produced with direct metal laser sintering. *Mater. Corros.*, 71 (2020) 365–373. <https://doi.org/10.1002/maco.201911171>
64. A.K. Gupta, D.J. Lloyd, S.A. Precipitation hardening in Al–Mg–Si alloys with and without excess Si, *Materials Science and Engineering: A*, 316 1–2 (2001) 11-17. [https://doi.org/10.1016/S0921-5093\(01\)01247-3](https://doi.org/10.1016/S0921-5093(01)01247-3).
65. Z.H. Xiong, S.L. Liu, S.F. Li, Y. Shi, Y.F. Yang, R.D.K. Misra, Role of melt pool boundary condition in determining the mechanical properties of selective laser melting AlSi10Mg alloy, *Materials Science and Engineering: A*, 740–741 (2019) 148-156. <https://doi.org/10.1016/j.msea.2018.10.083>.
66. N. Read, W. Wang, K. Essa, M. M. Attallah, Selective laser melting of AlSi10Mg alloy: Process optimisation and mechanical properties development, *Materials & Design* (1980-2015), 65 (2015) 417-424. <https://doi.org/10.1016/j.matdes.2014.09.044>.
67. N. Takata, H. Kodaira, K. Sekizawa, A. Suzuki, M. Kobashi, Change in microstructure of selectively laser melted AlSi10Mg alloy with heat treatments, *Materials Science and Engineering: A*, 704 (2017) 218-228. <https://doi.org/10.1016/j.msea.2017.08.029>.
68. E. Brandl, U. Heckenberger, V. Holzinger, D. Buchbinder. Additive manufactured AlSi10Mg samples using Selective Laser Melting (SLM): Microstructure, high cycle fatigue, and fracture behavior. *Materials & Design*, 34 (2012) 159-169. doi: 10.1016/J.MATDES.2011.07.067D.
69. K. Kim, J.H. Hwang, E.Y. Kim, Y.U. Heo, W. Woo, S.H. Choi. Evaluation of the stress-strain relationship of constituent phases in AlSi10Mg alloy produced by selective laser melting using crystal plasticity FEM, *Journal of Alloys and Compounds*, 714 (2017) 687-697, <https://doi.org/10.1016/j.jallcom.2017.04.264>.
70. U. Patakham, A. Palasay, P. Wila, R. Tongsrri, MPB characteristics and Si morphologies on mechanical properties and fracture behavior of SLM AlSi10Mg, *Materials Science and Engineering: A*, 821 (2021) 141602, <https://doi.org/10.1016/j.msea.2021.141602>.
71. J. Delahaye, J. Tchoufang Tchoundjang, J. Lecomte-Beckers, O. Rigo, A.M. Habraken, A. Mertens, Influence of Si precipitates on fracture mechanisms of AlSi10Mg parts processed by Selective Laser Melting, *Acta Materialia*, 175 (2019) 160-170, <https://doi.org/10.1016/j.actamat.2019.06.013>.
72. T.H. Park, M.S. Baek, H. Hyer, Y. Sohn, K.A. Lee, Effect of direct aging on the microstructure and tensile properties of AlSi10Mg alloy manufactured by selective laser melting process, *Materials Characterization*, 176 (2021) 111113, <https://doi.org/10.1016/j.matchar.2021.111113>.
73. L. Lattanzi, M. Merlin, A. Fortini, A. Morri, G.L. Garagnani, Effect of Thermal Exposure Simulating Vapor Deposition on the Impact Behavior of Additively Manufactured AlSi10Mg Alloy. *J. of Materi Eng and Perform*, 31 (2022) 2859–2869. <https://doi.org/10.1007/s11665-021-06414-8>

74. N. Takata, M. Liu, H. Kodaira, A. Suzuki, M. Kobashi, Anomalous strengthening by supersaturated solid solutions of selectively laser melted Al–Si-based alloys, *Additive Manufacturing*, 33 (2020) 101152. <https://doi.org/10.1016/j.addma.2020.101152>.
75. S. Joseph, S. Kumar, A systematic investigation of fracture mechanisms in Al–Si based eutectic alloy—Effect of Si modification, *Materials Science and Engineering: A*, 588 (2013) 111-124. <https://doi.org/10.1016/j.msea.2013.09.019>.
76. H. Hyer, L. Zhou, A. Mehta, S. Park, T. Huynh, S. Song, Y. Bai, K. Cho, B. McWilliams, Y. Sohn, Composition-dependent solidification cracking of aluminum-silicon alloys during laser powder bed fusion, *Acta Mater.* 208 (2021) 116698, <https://doi.org/10.1016/j.actamat.2021.116698>
77. M. T. Di Giovanni, J. T. Oliveira de Menezes, G. Bolelli, E. Cerri, E. M. Castrodeza, Fatigue crack growth behavior of a selective laser melted AlSi10Mg, *Engineering Fracture Mechanics*, 217 (2019) 106564, <https://doi.org/10.1016/j.engfracmech.2019.106564>.
78. P. Ashwath, M. Anthony Xavier, Andre Batako, P. Jeyapandiarajan, J. Joel, Selective laser melting of Al–Si–10Mg alloy: microstructural studies and mechanical properties assessment, *Journal of Materials Research and Technology*, 17 (2022) 2249-2258, <https://doi.org/10.1016/j.jmrt.2022.01.135>.
79. L.C. Araújo, A.H.G. Gabriel, E.B. da Fonseca, J.A. Avila, A.L. Jardini, R. Seno Júnior, E.S.N. Lopes, Effects of build orientation and heat treatments on the tensile and fracture toughness properties of additively manufactured AlSi10Mg, *Int. J. Mech. Sci.* 213 (2022), 106868. <https://doi.org/10.1016/j.ijmecsci.2021.106868>
80. C.H. Caceres. A rationale for the quality index of Al-Si-Mg casting alloys. *International Journal of Cast Metals Research*. 12 6 (2000) 385-391. <https://doi.org/10.1080/13640461.2000.11819376>.
81. W. Shifeng, L. Shuai, W. Qingsong, C. Yan, Z. Sheng, S. Yusheng, Effect of molten pool boundaries on the mechanical properties of selective laser melting parts, *Journal of Materials Processing Technology*, 214 11 (2014) 2660-2667. <https://doi.org/10.1016/j.jmatprotec.2014.06.002>.
82. N.E. Uzan, R. Shneck, O. Yeheskel, N. Frage, Fatigue of AlSi10Mg specimens fabricated by additive manufacturing selective laser melting (AM-SLM), *Materials Science and Engineering: A*, 704 (2017) 229-237 <https://doi.org/10.1016/j.msea.2017.08.027>.
83. F. Sajadi, J.M. Tiemann, N. Bandari, A. Cheloe Darabi, J. Mola, S. Schmauder. Fatigue Improvement of AlSi10Mg Fabricated by Laser-Based Powder Bed Fusion through Heat Treatment. *Metals* 11 (2021) 683. <https://doi.org/10.3390/met11050683>
84. T. M. Mower, M. J. Long, Mechanical behavior of additive manufactured, powder-bed laser-fused materials, *Materials Science and Engineering: A*, 651 (2016) 198-213, <https://doi.org/10.1016/j.msea.2015.10.068>
85. J. Damon, S. Dietrich, F. Vollert, J. Gibmeier, V. Schulze, Process dependent porosity and the influence of shot peening on porosity morphology regarding selective laser melted AlSi10Mg parts, *Additive Manufacturing*, 20 (2018) 77-89. <https://doi.org/10.1016/j.addma.2018.01.001>.
86. Z.W. Xu, Q. Wang, X.S. Wang, C.H. Tan, M.H. Guo, P.B. Gao, High cycle fatigue performance of AlSi10mg alloy produced by selective laser melting, *Mechanics of Materials*, 148 (2020) 103499. <https://doi.org/10.1016/j.mechmat.2020.103499>.
87. E. Beevers, A. D. Brandão, J. Gumpinger, M. Gschweilt, C. Seyfert, P. Hofbauer, T. Rohr, T. Ghidini, Fatigue properties and material characteristics of additively manufactured AlSi10Mg – Effect of the contour parameter on the microstructure, density, residual stress, roughness and mechanical properties, *International Journal of Fatigue*, 117 (2018) 148-162. <https://doi.org/10.1016/j.ijfatigue.2018.08.023>.
88. L. Ceschini, A. Morri, S. Toschi, S. Seifeddine, Room and high temperature fatigue behaviour of the A354 and C355 (Al–Si–Cu–Mg) alloys: Role of microstructure and heat treatment, *Materials Science and Engineering: A*, 653 (2016) 129-138. <https://doi.org/10.1016/j.msea.2015.12.015>.
89. N. T. Aboulkhair, I. Maskery, C. Tuck, I. Ashcroft, N.M. Everitt, Improving the fatigue behaviour of a selectively laser melted aluminium alloy: Influence of heat treatment and surface quality, *Materials & Design*, 104 (2016) 174-182. <https://doi.org/10.1016/j.matdes.2016.05.041>.
90. K. Kempen, L. Thijs, J. Van Humbeeck, J.-P. Kruth, Mechanical Properties of AlSi10Mg Produced by Selective Laser Melting, *Physics Procedia*, 39 (2012) 439-446. <https://doi.org/10.1016/j.phpro.2012.10.059>.
91. O. Poncelet, M. Marteleur, C. van der Rest, O. Rigo, J. Adrien, S. Dancette, P.J. Jacques, A. Simar, Critical assessment of the impact of process parameters on vertical roughness and hardness of thin walls of AlSi10Mg processed by laser powder bed fusion, *Additive Manufacturing*, 38 (2021) 101801. <https://doi.org/10.1016/j.addma.2020.101801>.
92. A. Boschetto, L. Bottini, D. Piloni. Effect of laser remelting on surface roughness and microstructure of AlSi10Mg selective laser melting manufactured parts. *Int J Adv Manuf Technol*, 113 (2021) 2739–2759. <https://doi.org/10.1007/s00170-021-06775-3>
93. Q. Yan, B. Song, Y. Shi, Comparative study of performance comparison of AlSi10Mg alloy prepared by selective laser melting and casting, *Journal of Materials Science & Technology*, 41 (2020) 199-208. <https://doi.org/10.1016/j.jmst.2019.08.049>.
94. F. Sausto, C. Tezzele, S. Beretta. Analysis of Fatigue Strength of L-PBF AlSi10Mg with Different Surface Post-Processes: Effect of Residual Stresses. *Metals*. 12(6) (2022) 898. <https://doi.org/10.3390/met12060898>.

# Chapter 3 – Tribological behavior of the as-built and heat-treated L-PBF AlSi10Mg alloy

1. This section contains selected parts of the manuscript:



Wear  
Volumes 516–517, 15 March 2023, 204602



## Dry sliding behavior of AlSi10Mg alloy produced by Laser-based Powder Bed Fusion: influence of heat treatment and microstructure

G. Di Egidio<sup>a</sup>  , C. Martini<sup>a</sup> , J. Börjesson<sup>b</sup> , E. Ghassemali<sup>b</sup> , L. Ceschini<sup>a</sup> ,  
A. Morri<sup>a</sup> 

The following link can access the published version of the paper:  
<https://doi.org/10.1016/j.wear.2022.204602>

The authors thank Wear for granting permission to re-use the manuscript titled “Dry sliding behavior of AlSi10Mg alloy produced by Laser-based Powder Bed Fusion: influence of heat treatment and microstructure” in the present Ph.D. thesis (<https://www.elsevier.com/journals/wear/0043-1648/guide-for-authors>).

### 3.1 Aim

Engineering sliding contact applications frequently use AlSi cast alloys [1,2]. The increasingly stringent regulations on CO<sub>2</sub> emissions, in fact, have led the transport sector to consider a significant reduction in weight and greater fuel efficiency as guidelines for the research and development of new materials, thus favoring continuous growth in the production and use of AlSi components produced by innovative technologies [3,4].

As widely described in Chapter 1, AlSi alloys are highly suitable to be produced by the L-PBF technology [5,6] and are used for the realization of high-performance parts, such as fuel injectors, valves, pistons, and cylinder liners, which can be strongly subject to heavy abrasive phenomena linked to sliding contact [7-9]. In particular, the L-PBF AlSi alloys present a relatively lower hardness in as-built and heat-treated conditions than other counterpart materials and could suffer high wear rates in heavy-duty applications [1,8-10]. For this reason, it is necessary to deepen their tribological behavior under severe operating conditions to expand the use of these alloys in high-technology sectors.

There is currently limited literature on the tribological behavior of the L-PBF AlSi alloys compared to the published articles on analyzing the static and dynamic mechanical response [9]. Most literature on L-PBF AlSi alloys focused on the AlSi12 and AlSi10Mg alloys in the AB condition [11-18], which shows a wear resistance higher than the corresponding cast alloys. In particular, Prashanth et al. [12] and Rathod et al. [13] reported a lower wear rate of the AB L-PBF AlSi12 alloy than the AlSi12 cast alloy in dry sliding test conditions carried out against hard-faced stainless steel and GCr15 bearing steel (equivalent to 100Cr6), respectively. Kang et al. [17] confirmed this trend also for an optimized AB L-PBF AlSi12 alloy, which was enriched in Si content and tested against Al<sub>2</sub>O<sub>3</sub> counterpart. However, the brittle behavior and degraded mechanical properties limited its future structural applications, even though it exhibited better tribological performance than the corresponding cast alloy. Wu et al. [18] confirmed these promising results also for the AB L-PBF AlSi10Mg alloy, reporting a lower wear rate than the AlSi10Mg cast alloy in unlubricated conditions against GCr15 bearing steel. However, Thasleem et al. [16] described that in the dry sliding test performed against EN31 steel (equivalent to 100Cr6), the microstructural refinement induced by the L-PBF process increased the coefficient of friction of the AB L-PBF AlSi10Mg alloy compared to the AlSi10Mg cast alloy. Furthermore, several authors [11,14,16] observed the onset of abrasive wear induced by hard Si phases and Al<sub>2</sub>O<sub>3</sub> debris formed on the wear track, in addition to adhesive wear and tribooxidation phenomena typical of AlSi cast alloys.

Even though the AB L-PBF AlSi alloys yield promising tribological results, many structural components require an adequate balance between tensile strength and ductility, achievable only by applying appropriate heat treatments [19,20]. In particular, two heat treatments are usually carried out to improve the mechanical response of AlSiMg alloys, direct artificial aging (T5) and solution treatment (T6), which modify the microstructural characteristics of the AB alloy, as widely discussed in the previous chapter.

Currently, only a few researches focused on the influence of heat treatment on the dry sliding behavior of the L-PBF AlSi10Mg alloy. Wei et al. [11] reported on the detrimental influence of the T6 on friction coefficient and wear depth in the dry sliding test against Si<sub>3</sub>N<sub>4</sub>, showing an increase in the wear rate proportional to the solution temperature and the Si particle size. Likewise, Prashanth et al. [12] stated that the microstructural coarsening induced by annealing performed between 200 and 500 °C increased the wear rate proportionally to the temperature during the dry sliding test against hard-faced stainless steel. Conversely, Park et al. [21] reported a higher wear resistance of the T6 heat-treated L-PBF AlSi10Mg alloy against 100Cr6 than the AB condition. They attributed this result to the higher load-bearing

capacity provided by the fine Si particles, which are more strongly bound than the fibrous eutectic-Si network to the  $\alpha$ -Al matrix.

A comprehensive work by Kan et al. [14] recently discussed how stress-relieving (210 °C for 1 h) and conventional T6 (solution treatment at 540 °C for 8 h in a salt pot furnace, water quenching, and artificial aging for 10 h at 160 °C in an oil bath) affected the dry sliding behavior of the L-PBF AlSi10Mg alloy, considering both AISI440C martensitic stainless steel and SiC as counterparts. This work highlighted that, when sliding against a ceramic counter-material, conventional T6 heat treatment was extremely detrimental (hence unnecessary) to the wear rate of the L-PBF AlSi10Mg alloy due to the impossibility of forming a stable, protective oxide layer on the worn surface.

However, the innovative T6R heat treatment introduced and analyzed in Chapter 2 could increase the tribological behavior of the L-PBF AlSi10Mg alloy compared to the T6 heat treatments characterized by higher  $T_{SHT}$  and longer solution soaking times  $t_{SHT}$ . In particular, the application of the rapid solution on the L-PBF AlSi10Mg alloy showed several advantages: (i) improvement of Si particle features (size, morphology, and distribution), (ii) decrease in the volumetric expansion of the gas pores, and (iii) increase in the supersaturation of the Al matrix, thus accelerating precipitation hardening kinetic. In addition, the T6R heat treatment ensured a more homogeneous distribution of smaller Si particles and improved adhesion between the Al matrix and Si particles. All these factors could significantly favor an increase in the tribological behavior of the T6 heat-treated alloy.

Always in Chapter 2, the effects of the T5 heat treatment on the metastable microstructure of the AB L-PBF AlSi10Mg alloy were investigated, focusing in particular on the precipitation of nano-acicular Si precipitates and  $\beta$ -Mg<sub>2</sub>Si precursor phases from the supersaturated Al lattice due to the short diffusion distances of the Si atoms. The T5 optimization (artificial aging in air at 160 °C for 6 h) led to a slight increase in strength and ductility and a consequent improvement of the mechanical response of the AB alloy without, however, achieving the best balance among the mechanical properties afforded by the innovative T6 heat treatment.

Considering the beneficial influence of a shorter solution in T6 on the mechanical properties, the effects of T6R on the tribological behavior must be assessed. In particular, the significant reduction in the distance among the Si particles embedded into the  $\alpha$ -Al matrix induced by T6R can give rise to high strain gradients which contribute to an enhancement of the dislocation density and may consequently increase the wear resistance. In addition, the more homogeneous dispersion of Si particles can provide a higher load-bearing capacity [22].

Therefore, this chapter aims to assess the influence of the T6R heat treatment on the tribological behavior of the L-PBF AlSi10Mg alloy by comparing the following conditions: AB, T5, T6R, and T6B, the last considered as a benchmark [20]. The tribological tests were performed on the plane parallel to the building axis of the L-PBF specimens for two reasons: (i) more severe test conditions induced by lower load capacity due to larger melt pool overlap and coarser microstructure [14,23,24]; (ii) greater industrial relevance [4,5,8] by reducing costs through the positioning of large surfaces parallel to the building direction to increase the number of components on a single platform. Microstructural evolution in subsurface regions of the wear tracks was monitored in each heat-treated sample by different microscopy techniques (including FEG-SEM coupled with Focused Ion Beam (FIB) milling). At the same time, nanoindentation was used to evaluate possible work-hardening or softening effects and the load-bearing capacity provided by the eutectic-Si network (in the AB and T5 conditions) and the globulized Si particles (in the T6 heat-treated conditions) [9,25]. The thermo-mechanical analysis supported this analysis to highlight the effects of contact temperature on tribological behavior and microstructural evolution [26].

## 3.2 Experimental procedure

### 3.2.1 Samples production and characterization

L-PBF AlSi10Mg alloy disks (Figure 3.1) (diameter  $\Phi = 46$  mm and thickness  $h = 5$  mm) were produced by a SLM500 printing system, using the following parameters: 50  $\mu\text{m}$  layer thickness, 350 W laser power, 1150 mm/s scan speed, 170  $\mu\text{m}$  hatch distance, and 150 °C heated-platform temperature. The build chamber was filled with high-purity Ar gas to reduce the O<sub>2</sub> level to 0.2 vol.%. Bidirectional stripes scan strategy of 67° counter-clockwise rotation between subsequent layers and a re-melted contour zone strategy at the end of each scanning were used to increase the density and the microstructural isotropy of the L-PBF-produced parts [27]. The gas atomized powder diameter ranged from 20 to 63  $\mu\text{m}$ , and its chemical composition, given by the supplier, is reported in Table 3.1. The chemical composition of the L-PBF samples was verified by a GD-OES (Spectrumba Analytik GDA 650) with a Grimm-style glow discharge lamp in DC mode. The analyzed area was about 5 mm<sup>2</sup>, corresponding to the internal area of the tubular anode (2.5 mm diameter) (Table 3.1).

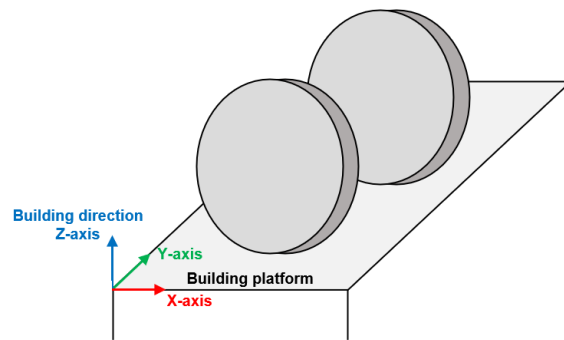


**Figure 3.1.** Representative scheme of the L-PBF disks used for the tribological tests: building axis (z) and plane parallel to the building platform (xy).

**Table 3.1.** Chemical compositions (wt.%) of (i) AlSi10Mg feedstock powder supplied by the producer and (ii) L-PBF AlSi10Mg samples.

	Al	Si	Mg	Fe	Mn	Pb	Sn	Ti	Zn
<b>Powders</b>	Bal.	9.21	0.27	0.15	0.006	0.001	<0.001	0.050	0.002
<b>Disks</b>	Bal.	9.74	0.30	0.13	0.005	0.008	0.002	0.020	0.004

Three different heat treatments were carried out on the samples: (i) direct artificial aging at 160 °C for 4 h and subsequent air cooling (hereafter T5); (ii) rapid T6 solution treatment consisting of solutionizing at 510 °C for 10 min, water quenching, and artificial aging at 160 °C for 6 h (hereafter T6R); and (iii) conventional T6 solution treatment consisting of solutionizing at 540 °C for 1 h, water quenching, and artificial aging at 160 °C for 4 h (hereafter T6B). SHT and AA were carried out in air in an electric furnace with a temperature control of  $\pm 5$  °C. More details on heat treatment optimization can be found in Chapter 2. Metallographic samples for microstructural analysis were embedded in conductive resin, ground by emery papers up to 1200 grit, polished by diamond suspensions from 9 to 1  $\mu\text{m}$ , according to ASTM E3 [28], and then etched with Weck's reagent (3g NH<sub>4</sub> HF<sub>2</sub>, 4 mL HCl, 100 mL H<sub>2</sub>O) according to ASTM E407 [29]. Microstructural analyses were carried out by optical microscope (OLYMPUS DSX1000) and FEG-SEM (MIRA3, TESCAN) with Energy-Dispersive X-ray Spectroscopy (EDS, Bruker Quantax 200/30 mm<sup>2</sup>). In addition, EBSD analysis (Hikari Plus, EDAX) coupled with FEG-SEM (LYRA3, TESCAN) was carried out to characterize the crystallographic structure. Before EBSD analysis, the mechanically polished specimens were not etched, but further polished with OP-S colloidal silica. HV<sub>0.1</sub> hardness tests (Isoscan Galileo) were performed on random areas of polished cross sections of the samples according to ASTM E92 to check the mechanical response of the L-PBF AlSi10Mg alloy post-heat treatment.

### 3.2.2 Dry sliding tests

The tribological behavior of the as-built and heat-treated L-PBF AlSi10Mg alloy was investigated using a ball-on-disk test (THT, CSM) according to ASTM G-99 [30]. The L-PBF AlSi10Mg samples were used as rotating disks (tribo-element 1) ( $R_a = 0.2 \mu\text{m}$  and  $R_q = 0.3 \mu\text{m}$ , after grinding) and the counterpart (tribo-element 2) was a 3 mm radius ( $R_2$ )  $\text{Al}_2\text{O}_3$  ball (hardness 1360  $\text{HV}_{0.1}$ ,  $R_a = 0.1 \mu\text{m}$ , elastic modulus  $E_2 = 360 \text{ GPa}$ , Poisson's ratio  $\nu_2 = 0.22$ ). The samples were subjected to a preliminary ultrasonic washing in acetone for 5 minutes to remove contaminants. Applied load (maximum Hertzian contact pressures in Table 2), sliding speed, and counter material were selected to highlight the differences in the wear performance of the heat-treated L-PBF AlSi10Mg alloy, resulting from the microstructural evolution of the Si phase in the form of eutectic network (AB and T5) and spherical particles (T6R and T6B) [31]. The influence of variations in the Si phase on the wear performance of AlSi alloys is reported to be more prominent under relatively severe conditions [32]. Dry conditions were chosen to exclude the effects of the lubricant, which would have significantly attenuated the interaction between the counterparts [1,14]. A ceramic counter-material ( $\text{Al}_2\text{O}_3$ ) was used to avoid the formation of mixed iron-rich oxide protective layers that typically form against steel, thus highlighting only the interactions between the AlSi10Mg microstructure and the Al oxide layer [1] and inducing more severe contact conditions. For these reasons, dry sliding tests were carried out in an ambient environment (humidity between 45 and 55 %, temperature between 19 and 22 °C), at a fixed sliding speed ( $v = 0.1 \text{ m/s}$ ), under a normal load ( $F_n$ ) of 5 N, over a distance of 250 m. Three repetitions were performed for each condition: average values and the corresponding standard deviation are reported for the measured Coefficient of Friction (CoF) and Wear Depth (WD) values. The friction force and the vertical displacement, related to total wear, were measured during the tests by a loading cell and a vertical displacement transducer, respectively. Friction values were firstly averaged over the steady-state regime (50-250 m) for each test, then averaged again over the three repetitions of each test. A K-type thermocouple was used to evaluate the bulk temperature of the material ( $T_o$ ). After the sliding tests and the ultrasonic washing in acetone for 5 minutes of the samples, maximum wear track depths on disks were separately evaluated by stylus profilometry (Hommelwerke T2000, radius of curvature of the stylus tip equal to 5  $\mu\text{m}$ ), by a set of 8 measurements spaced 45° from each other along the worn track of each specimen. The average value of the measurements for each sample was considered.

### 3.2.3 Microstructural and micromechanical characterization after dry sliding

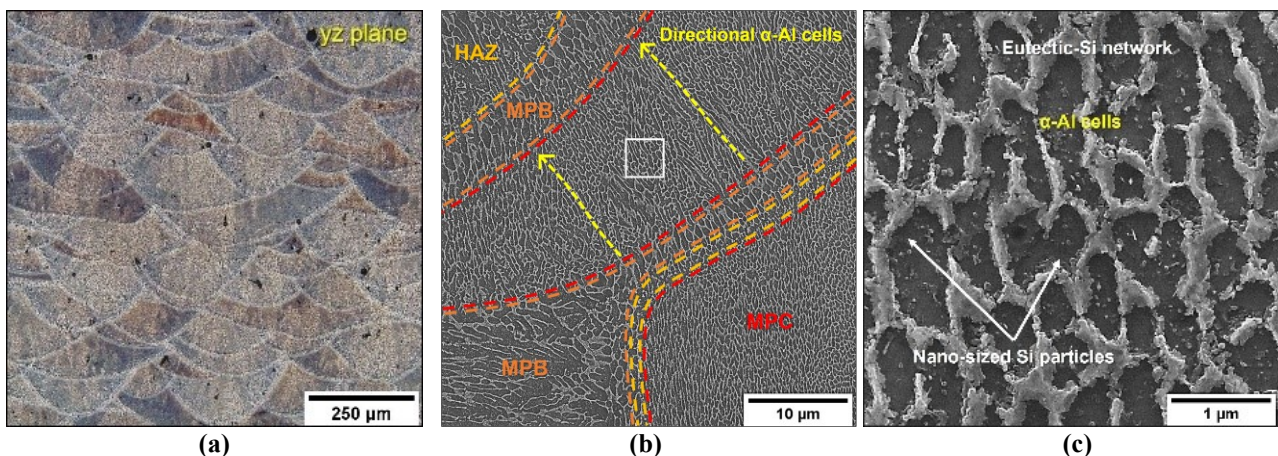
3D-digital microscope (Hirox KH 7700) and FEG-SEM/EDS were used to identify the dominant wear mechanisms. Moreover, sub-surface analyses below wear tracks were carried out on cross-section specimens embedded in conductive resin and prepared according to the same procedure described in section 3.2.1. Microstructural analyses in cross section were carried out by optical microscope and FEG-SEM with EDS. Sub-surface damage mechanisms were also investigated by Focused Ion Beam analysis (FIB, COBRA, res. down to 2.5 nm) coupled with FEG-SEM (LYRA3, TESCAN). Cross section trenches were milled using FIB ( $< 12\mu\text{A}$  at 30keV) along the sliding direction and perpendicular to it. The cross-sectional surfaces were then polished using lower FIB currents ( $> 120\text{nA}$  at 30 keV). Subsequently, the specimens were observed by FEG-SEM after chemical etching with Weck's reagent to highlight microstructural evolution after tribological tests. Nanoindentation tests analyzed the local mechanical response of the material below the wear tracks and were carried out through a NanoTest Vantage (Micromaterials Ltd.) equipped with a Berkovich indenter (Centerline-to-face angle,  $\alpha = 65,27^\circ$ , Young's Module,  $E_o = 1141$  GPa, Poisson coefficient,  $\nu_o = 0.07$ ). Pulse-echo ultrasonic measurements of the disk were conducted along the build direction (Z) and along X and Y to evaluate the Poisson coefficient,  $\nu_1$ , of the AB and heat-treated AlSi10Mg alloy. The nanoindentation test was performed with 1 mN/s of load speed, 10 mN maximum load, and 5 s holding time at peak load. Indentation maps with dimensions of 400 x 200  $\mu\text{m}$ , characterized by equidistant indentations in steps of 40  $\mu\text{m}$ , were performed. Nano-indentation points were elaborated by Matlab® software

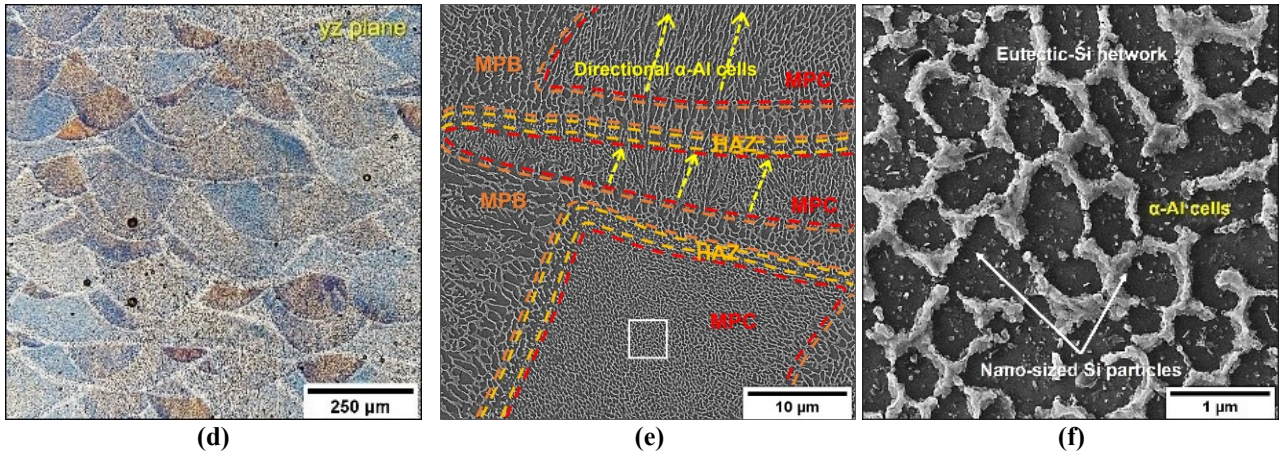
## 3.3 Results and discussion

### 3.3.1 Microstructural analysis

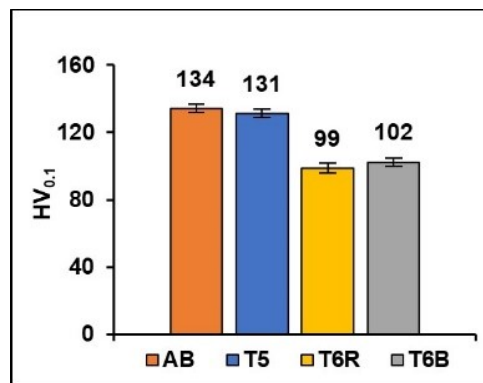
As already observed in Chapter 2, the AB microstructure consists of a randomized cusp-like pattern of Melt Pools (MP) (Figure 3.2(a)) with differences in depth and shape. The 67° counter-clockwise rotation of the scan strategy induced the intertwined structure in the material, thus promoting a less anisotropic microstructure, as described by [33-35]. A coarser microstructure than the MPC characterizes the MPBs due to the partial remelting of the previously deposited layers, which also induces the formation of HAZs due to the thermal cycles typically induced by the L-PBF process (Figure 3.2(b)). The morphology of the cell structure varies from directional to non-directional inside and across the MPs, following the heat flux and scan direction [26]. Therefore, as reported in section 2.3.4, the growth rate of the primary Al is faster in the direction parallel to the thermal gradient, thus resulting in an elongated columnar structure due to the strong thermal gradient between MPC and MPB. However, it is also possible to identify equiaxial cells within the MPC due to the direction of randomized solidification induced by the scanning strategy (Figure 3.2(b)). At higher magnification, the substructure shows submicrometric  $\alpha$ -Al cells characterized by areas lower than  $1 \mu\text{m}^2$  within the MPC and up to  $5 \mu\text{m}^2$  in the MPB (Figure 3.2(c)), which are surrounded by a fibrous eutectic-Si network. The heated platform (150 °C) promotes the formation of nanoscale Si particles found within the Al matrix, which leads to an increase in the hardness (Figure 3.3) of the AB alloy compared to the unheated platform condition [37].

The T5 does not induce particular macrostructural modifications, preserving the hierarchical structure already observed in the AB condition (Figures 3.2(d,e)). In addition, the diffusion processes activated by the aging temperature promoted the precipitation of the nano-sized Si particles embedded into the  $\alpha$ -Al matrix, thus reducing the amount of Si atoms in solid solution [38,39] (Figure 3.2(f)). The aging conditions (4 h at 160 °C) are insufficient to induce the dissolution of the eutectic-Si network or the significant coarsening of the Si particles and, therefore, do not lead to a significant hardness variation compared to the AB condition (Figure 3.3).



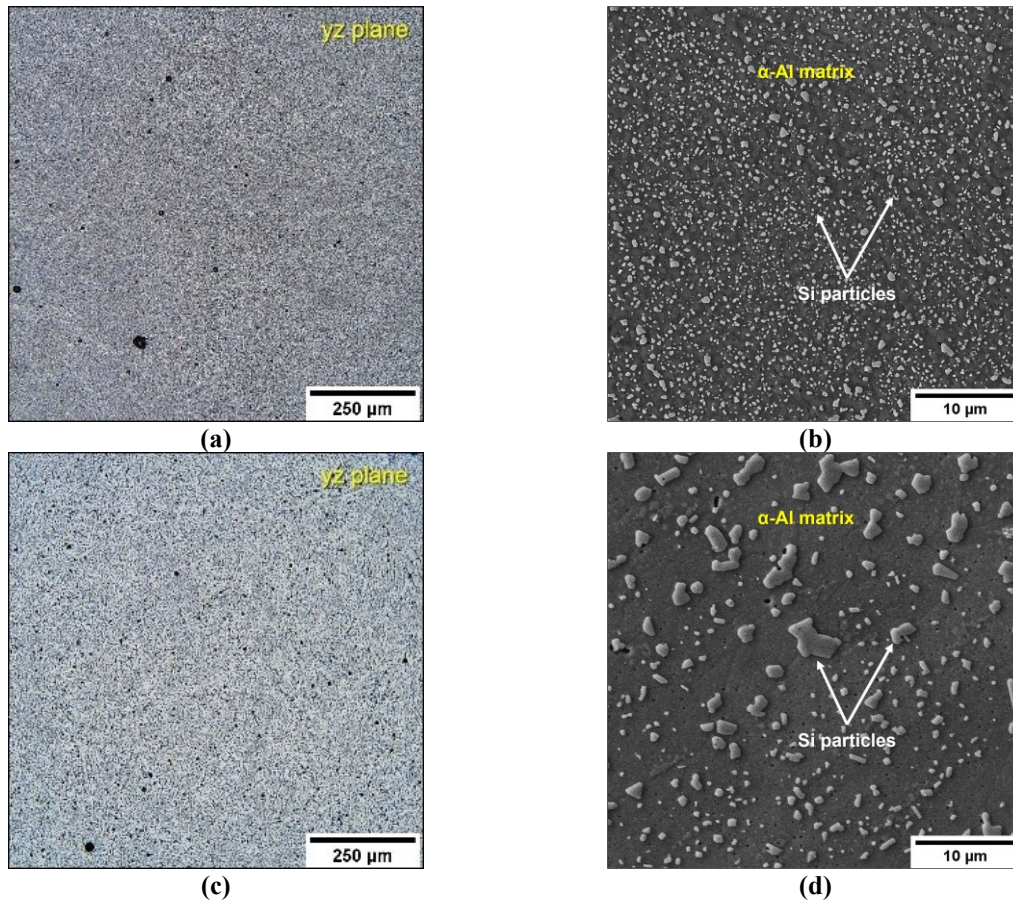


**Figure 3.2.** OM and FEG-SEM images showing the microstructure of the sliding surface of the L-PBF AlSi10Mg alloy discs (yz plane): AB (a,b,c) and T5: 4 h at 160 °C (d,e,f).



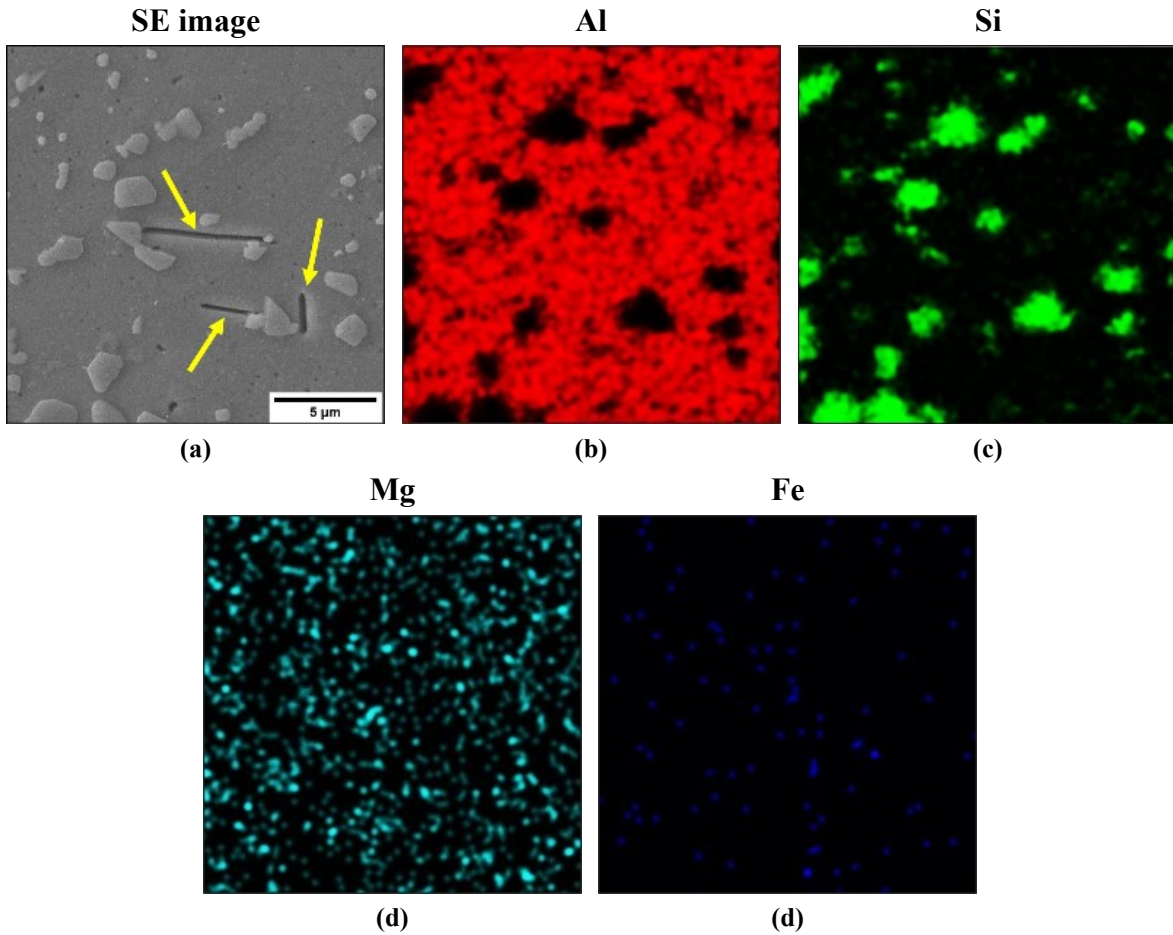
**Figure 3.3.** Microhardness (HV<sub>0.1</sub>) values for the L-PBF AlSi10Mg alloy in AB and heat-treated conditions (T5, T6R, and T6B).

On the contrary, both T6 heat treatments, T6R and T6B, erase the MP structure and ultimately modify the sub-structure, which results in a composite-like microstructure consisting of a homogeneous distribution of Si particles embedded in the  $\alpha$ -Al matrix (Figures 3.4(a,b)). The diffusion-driven mechanisms promoted by the solution step lead to the fragmentation of the eutectic-Si network and the spheroidization of the Si phase, causing a complete microstructural rearrangement. At higher magnification (Figures 3.4(b,d)), the microstructures show different features, which depend on the conditions applied in the SHT phase. The  $T_{SHT}$  and  $t_{SHT}$  influence the coarsening of the Si particles embedded into the  $\alpha$ -Al matrix, which is related to thermal exposure. As reported in section 2.3.1, moving from T6R solution conditions to T6B ones, the Si particle density decreases from 1.48 particles/ $\mu\text{m}^2$  to 0.28 particles/ $\mu\text{m}^2$  and the mean area increases from 0.14  $\mu\text{m}^2$  to 0.55  $\mu\text{m}^2$ . Therefore, a lower  $T_{SHT}$  for extremely short  $t_{SHT}$  leads to a more homogeneous distribution of smaller Si particles, which can contribute to a better balance between strength properties, ductility, and toughness due to the higher adhesion between the Al matrix and the Si particles as well as to the improved strengthening effect of the second dispersed phases [5,6]. As described by [11,12], the marked difference in size, number, and distribution of the second dispersed phases could lead to significant differences in the tribological behavior of the T6B and T6R conditions, despite the comparable hardness.



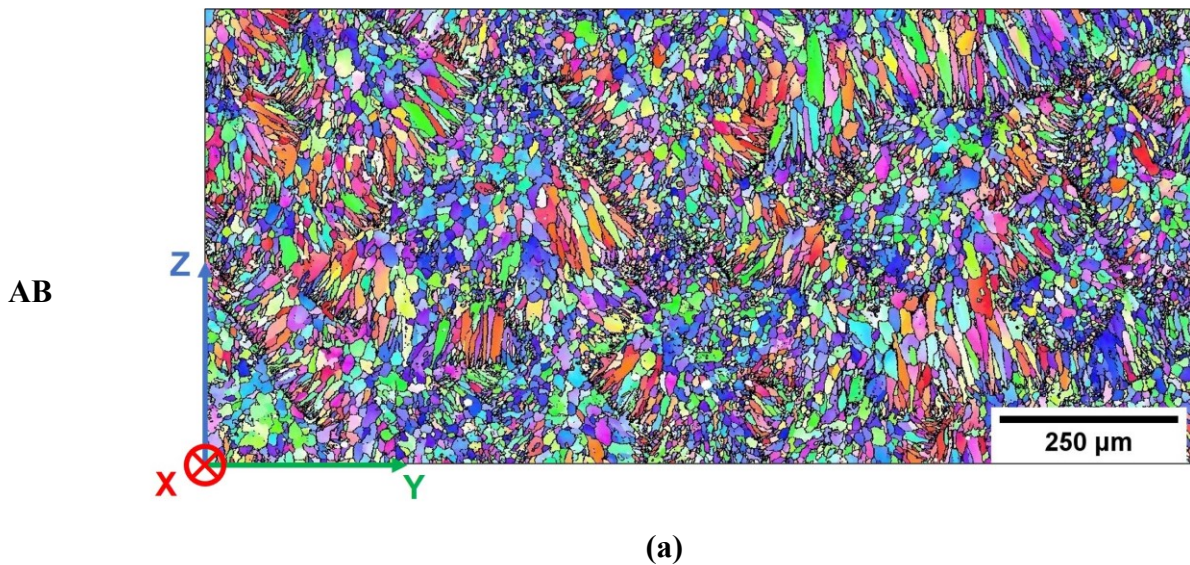
**Figure 3.4.** OM and FEG-SEM images showing the microstructure of the sliding surface of the L-PBF AlSi10Mg alloy discs (yz plane): T6R: 10 min at 510 °C (SHT) and 6 h at 160 °C (AA) (a,b); T6B: 1 h at 540 °C (SHT) and 4 h at 160 °C (AA) (c,d).

EDS elemental maps (Figure 3.5) do not show the presence of plate-like Fe-rich intermetallic induced by the T6B heat treatment, like the  $\beta$ -Al<sub>5</sub>SiFe or other possible precipitates which negatively affect tribological behavior [1,40], as pointed out by [5,39,41,42]. The voids are probably ploughing artifacts attributable to the detachment of Si particles during the metallographic preparation.



**Figure 3.5.** Detail of the T6B microstructure by FEG-SEM and EDS elemental maps of Al (red), Si (green), Mg (cyan), and Fe (blue), respectively. The arrows in the SE image indicate the supposed plate-like features, which are artifacts attributable to the detachment of Si particles during the metallographic preparation.

The layer-by-layer deposition strategy promotes the formation of a preferentially oriented crystallographic texture. IPF maps (Figure 3.6) show elongated columnar grains near the center line of the MP and then aligned along the direction of the heat flow generated by the laser source. Furthermore, the high volume of remelted base metal promotes the recrystallization of equiaxed grains along the MPBs (Figure 3.6(a)), whose growth is hindered by the competitive growth of large columnar grains of  $\langle 100 \rangle$  orientation, as widely reported in the literature [27,34].



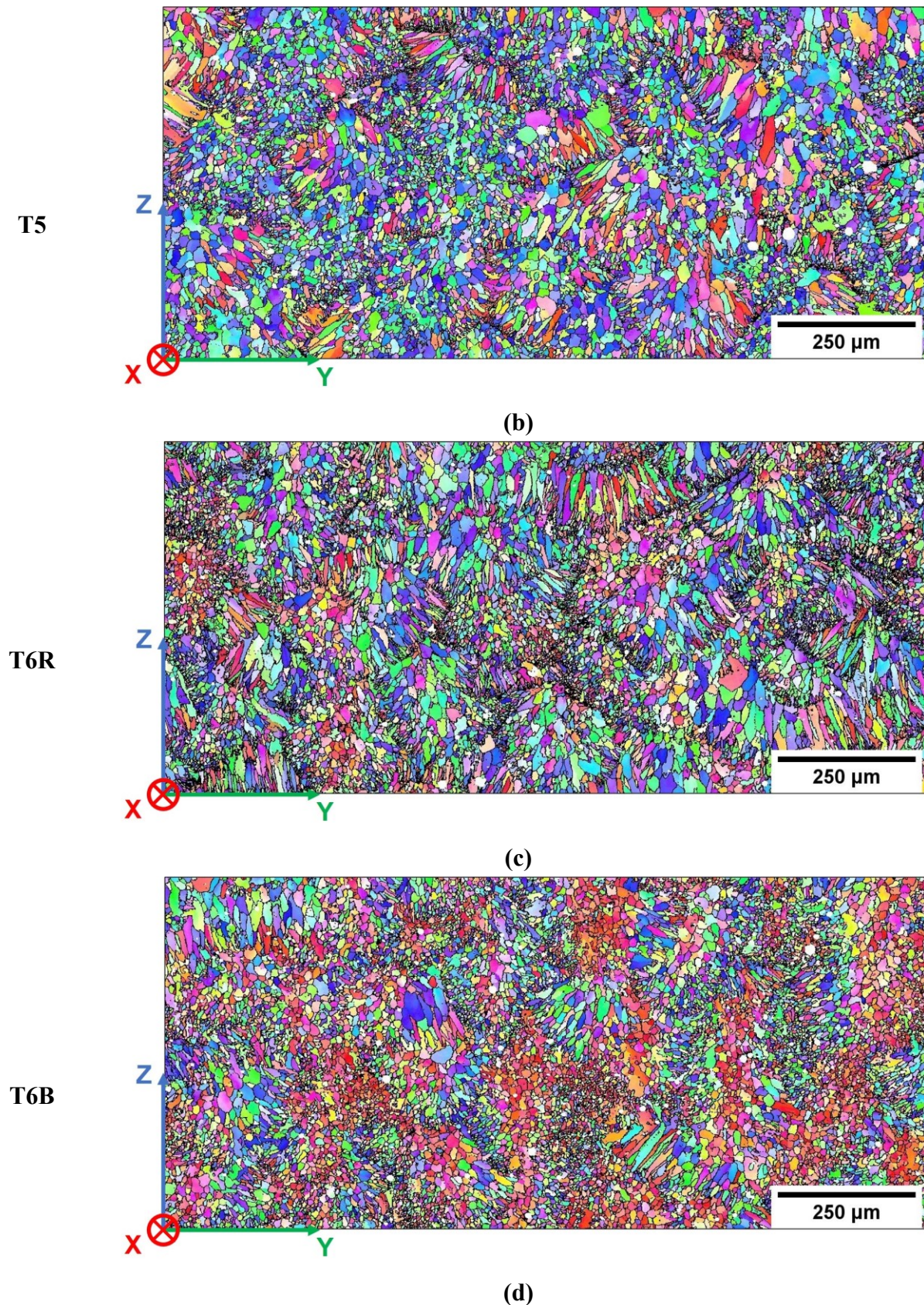


**Figure 3.6.** IPF maps of the L-PBF AlSi10Mg alloy in AB (a), T5 (b), T6R (c), and T6B (d). In IPF maps, the misorientation values higher than  $15^\circ$  are marked by black lines, while lower misorientation was characterized only by a variation in color intensity.

The EBSD data show a grain diameter ranging from 4 to 30 μm for the AB, T5, and T6R conditions, while the grain diameter ranged between 4 and 25 μm for the T6B condition (Figure 3.7). This result confirms the absence of grain coarsening induced by the T5 and T6 heat treatment, in agreement with [43,44]. The slight grain refinement

characterizing the T6B condition could be due to the recovery process induced by the high temperatures (540 °C) and long soaking times (1 h) [43]. The high content of Si segregated along cell boundaries of the L-PBF AlSi10Mg alloy may induce thermal stresses caused by the thermal expansion coefficient mismatch between Al and Si. The stress encourages dislocation formation in cellular boundaries, which can act as nucleation sites for recrystallization [11]. Therefore, the recovery process and the consequent gradual increase in the size of the sub-grain structure within the columnar grain, which is related to  $T_{SHT}$  and  $t_{SHT}$ , could lead to a higher number of high-angle boundaries (HAGBs, with a misorientation angle higher than  $15^\circ$ ) measured by the grain size analysis [23,39]. In particular, the T6B condition has a percentage value of HAGBs equal to 61.5%, compared to the values for AB, T5, and T6R conditions, equal to 57.0%, 56.8%, and 58.1%, respectively.

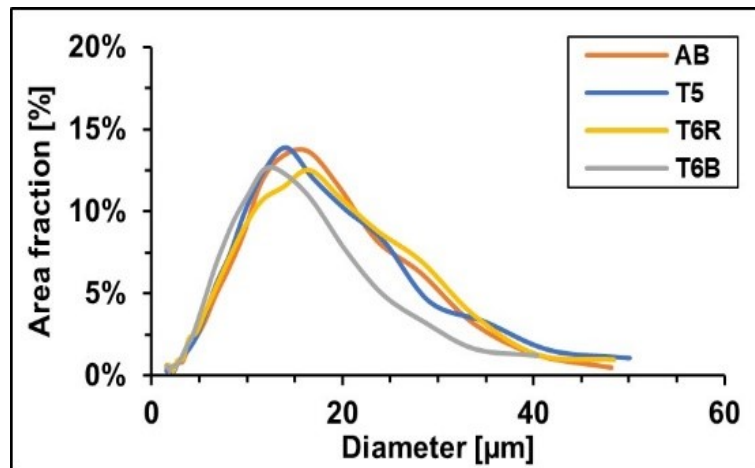
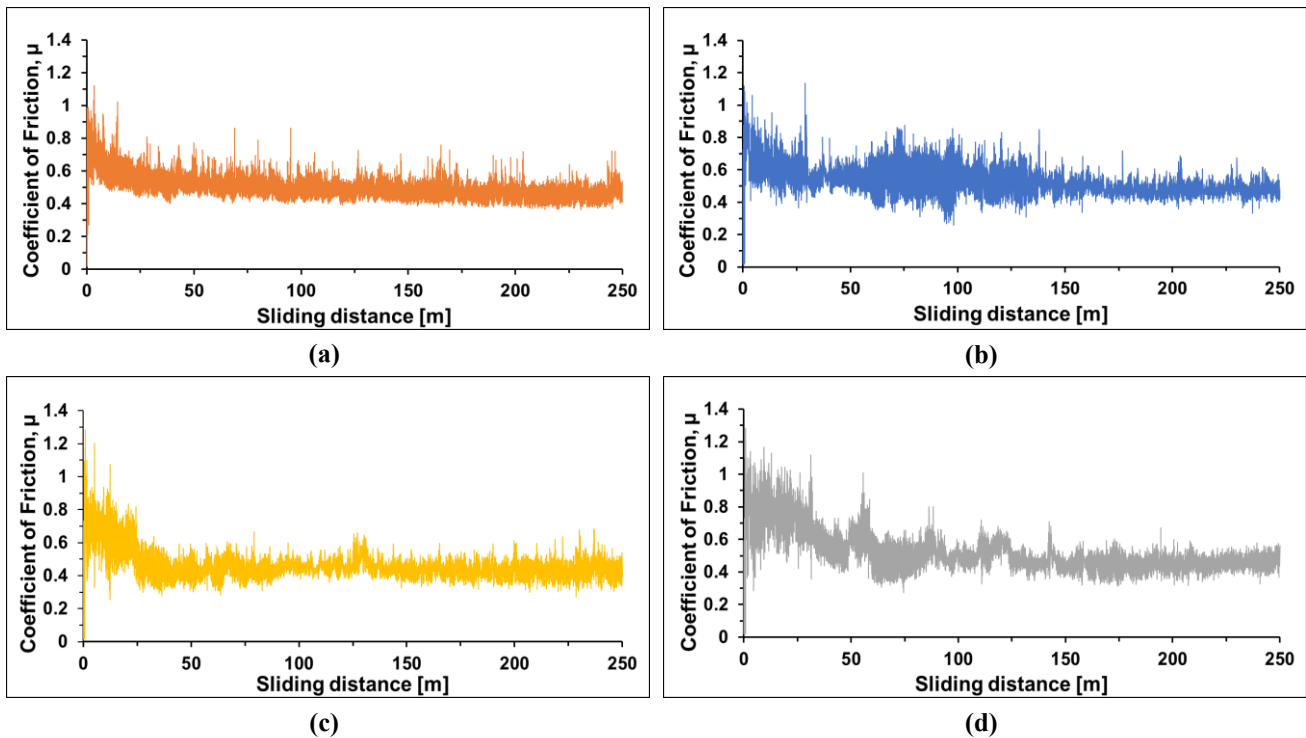


Figure 3.7. Grain size distribution of the L-PBF AlSi10Mg alloy in AB, T5, T6R, and T6B conditions.

### 3.3.2 Dry sliding tests

Figure 3.8 shows representative plots of the dry sliding tests ( $v = 0.1$  m/s,  $F_n = 5$  N, distance = 250 m) performed on AB and heat-treated samples in terms of the CoF value as a function of sliding distance. For each condition tested, the CoF trends are comparable between the three repetitions performed and reveal for all samples a rapid increase in friction at the start of the test (up to 20 m), followed by a decrease until it reaches the steady-state value. Wide fluctuations (stick-slip phenomena) characterize the evolution of the COF of each sample due to the high adhesion work and the formation of a transfer layer on both the counterparts that generally occurs in dry sliding of Al vs.  $Al_2O_3$  at low speed ( $v = 0.1$  m/s) [1]. All tested conditions show a comparable CoF evolution; however, heat-treated samples appear to be characterized by wider oscillations (T5, Figure 7.3(b)) or more irregular fluctuations (T6R and T6B, Figures 7.3(c) and 7.3(d) respectively) than AB (Figure 7.3(a)). These tribological phenomena may indicate the different processes of formation, stabilization, and detachment of the transfer layer on the wear track, which is discussed below and observed on L-PBF AlSi10Mg vs. ceramic counterparts also by other Authors [11,14]. The differences tend to disappear, and the CoF curves overlap beyond a distance of about 150 m.

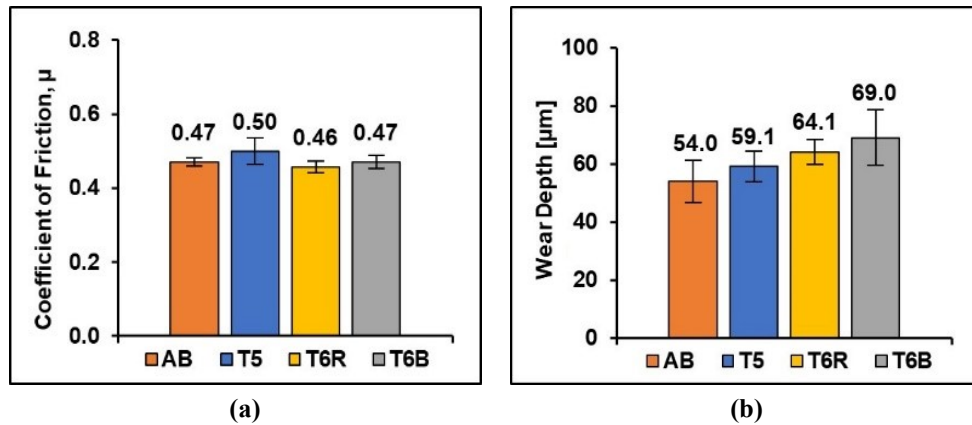


**Figure 3.8.** Representative evolution of the CoF value for L-PBF AlSi10Mg as a function of sliding distance: (a) AB, (b) T5, (c) T6R, and (d) T6B.

A comparison between the average steady-state CoF values of the AB, T5, T6R, and T6B samples are reported in Figure 3.9(a). All samples showed values between 0.46 and 0.50, with no significant differences except for a slightly higher value for T5. All the CoF values fall within the range of the Al cast alloy in dry sliding conditions, which generally goes from 0.4 to 0.6 depending on the test conditions and the alloy [40]. The heat treatment conditions and hence the different microstructures and hardness values of the L-PBF AlSi10Mg alloy (Figures 3.2 and 3.3) do not significantly affect CoF, as observed by [17]. However, the differences in CoF trends in Figure 3.8 will be discussed in the following sections based on the stability of transfer layers at the contact interface.

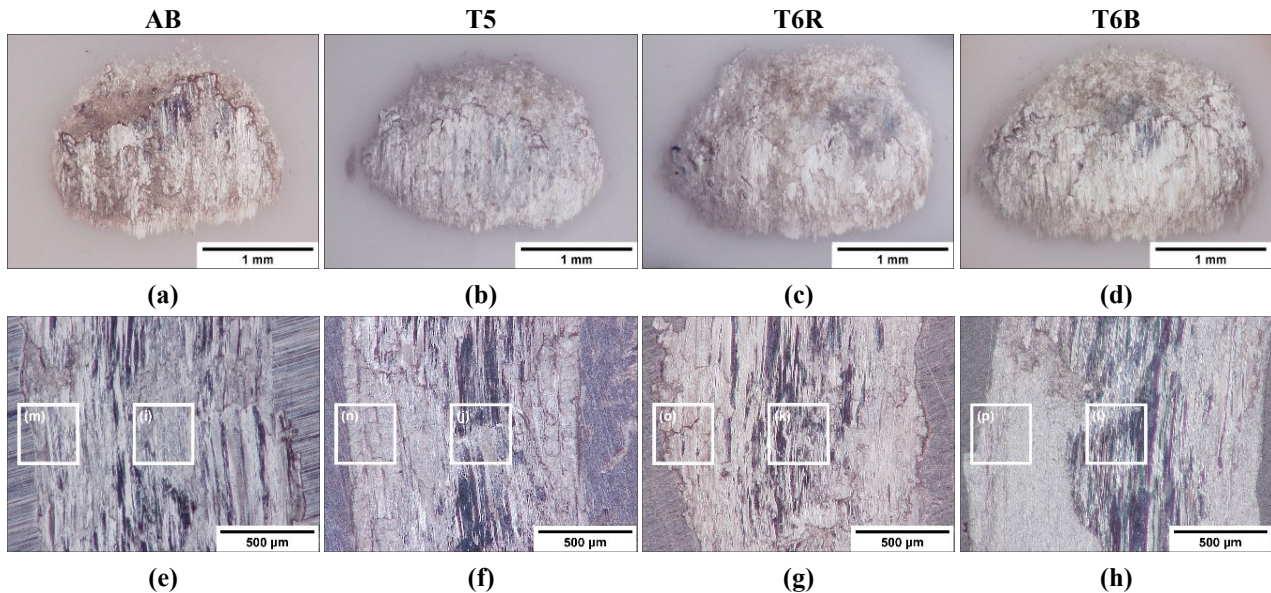
Figure 3.9(b) shows average values of WD, it is lower for AB and T5 than the T6 conditions (T6R and T6B). Therefore, WD tends to increase with decreasing hardness (Figure 3.3). However, despite the slightly higher hardness than T6R, the WD for T6B does not decrease, probably due to the unfavorable morphology and distribution of the second hard

phase (Si particles), which may favor localized fracture phenomena and prevent the formation of a protective transfer layer on the worn surface, as described with more detail in section 3.3.3.



**Figure 3.9.** Average (a) steady-state CoF and (b) WD values for the L-PBF AlSi10Mg samples dry sliding vs.  $\text{Al}_2\text{O}_3$ .

Figures 3.10 (a-d) show a thick transfer layer on the surface of each  $\text{Al}_2\text{O}_3$  sphere due to severe adhesive wear of the L-PBF AlSi10Mg disk (Figures 9(e-h)). In most cases, the formation of transfer layers on the  $\text{Al}_2\text{O}_3$  ball led to negative ball weight variations, which may be randomly affected by partial detachment while disassembling the ball from the testing device. However, the area covered by the transfer layer on the sphere increases with increasing WD on the disk (Figure 3.9). EDS analysis carried out on the  $\text{Al}_2\text{O}_3$  sphere (Figures 3.11(a,b)) reveals the presence of both Al and O in the transfer layer, which consists of heavily deformed and partly oxidized Al-based material from the rotating disk. Correspondingly, on the worn surface of the disks, typical signs of severe adhesive wear can be observed at the bottom of the wear track in high-magnification SEM images (Figure 3.10(i-l)): heavy plastic deformation, rough patches due to material pile-up (Figures 3.10(m-p)), as described by [45], and loose flake-like debris sticking on some areas of the wear track.



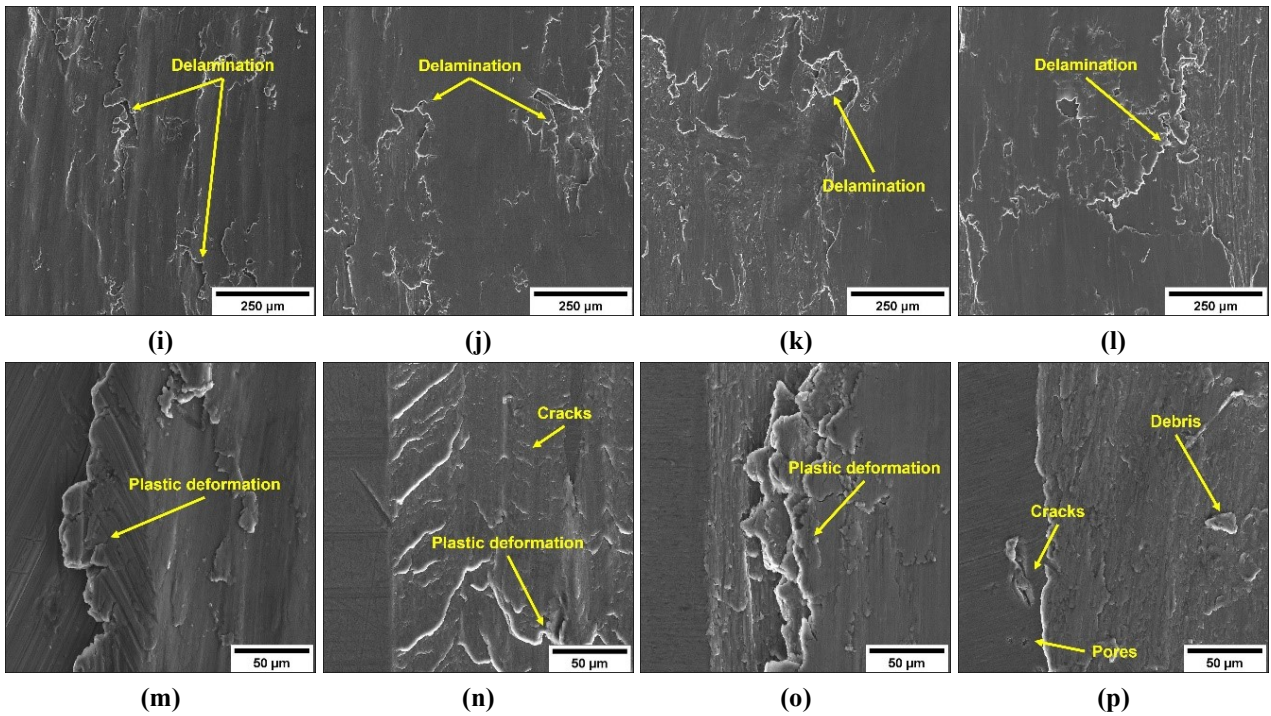


**Figure 3.10.** Transfer layers on the  $\text{Al}_2\text{O}_3$  spheres after dry sliding against AB (a), T5 (b), T6R (c), and T6B samples (d). Wear tracks at low (e-h) and high magnification (i-p) on the AB (e,i,m), T5 (f,j,n), T6R (g,k,o), and T6B (h,l,p) disks. The worn surfaces of disks are characterized by severe adhesive wear, heavy plastic deformation, delamination, and forming rough patches.

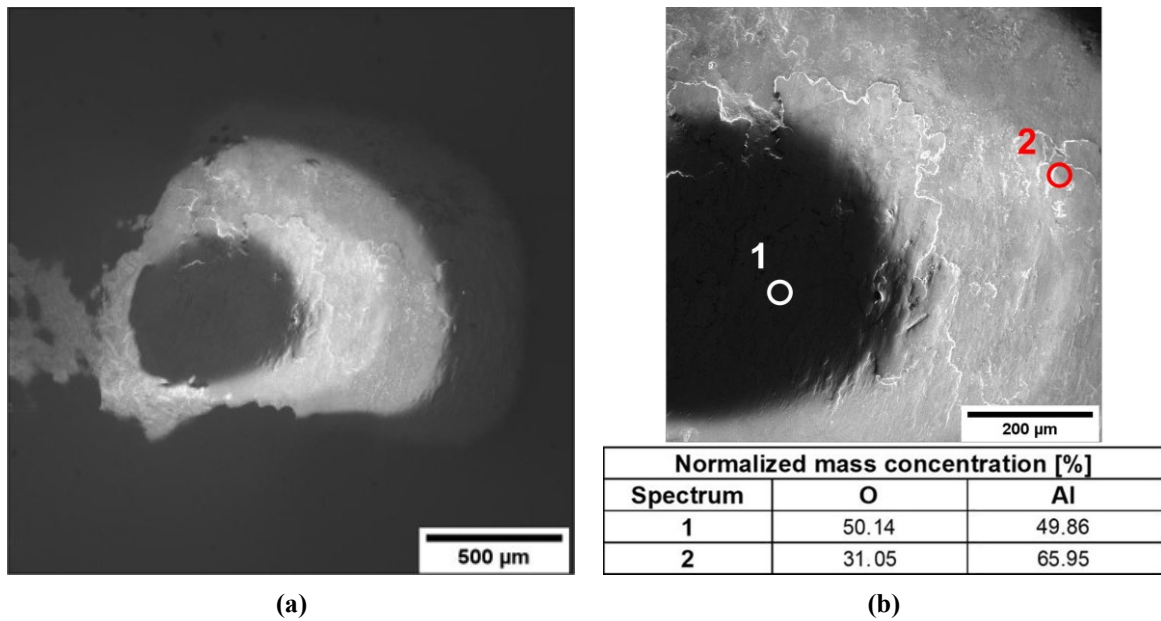


**Figure 3.11.** Transfer layer on the  $\text{Al}_2\text{O}_3$  sphere: general view (BSE image) (a) and localized EDS analysis (b): the dark region at the center of the image corresponds to the thinner portion of the layer transferred onto the sphere, while the light annular area corresponds to a thicker layer with a higher Al concentration.

EDS analysis reveals the presence of O on the wear tracks of all the samples, thus confirming the presence of oxide-based compounds in the transfer layer. The detection of O on the wear tracks does not appear to be related to a coherent and uniform tribo-layer, but rather to the presence of localized areas with a high concentration of O. High-magnification BSE images of wear tracks (Figures 3.12(a-d)) show areas characterized by a darker shade of gray, suggesting the discontinuous presence of an oxide layer above the worn surfaces, as also observed by [16]. The oxide layer on the wear tracks of AB and T5 samples (Figures 3.12 (a,b)) is less fragmented and more continuous compared to the T6R and T6B ones (Figures 3.12 (c,d)), thus contributing to lowering the wear rate.

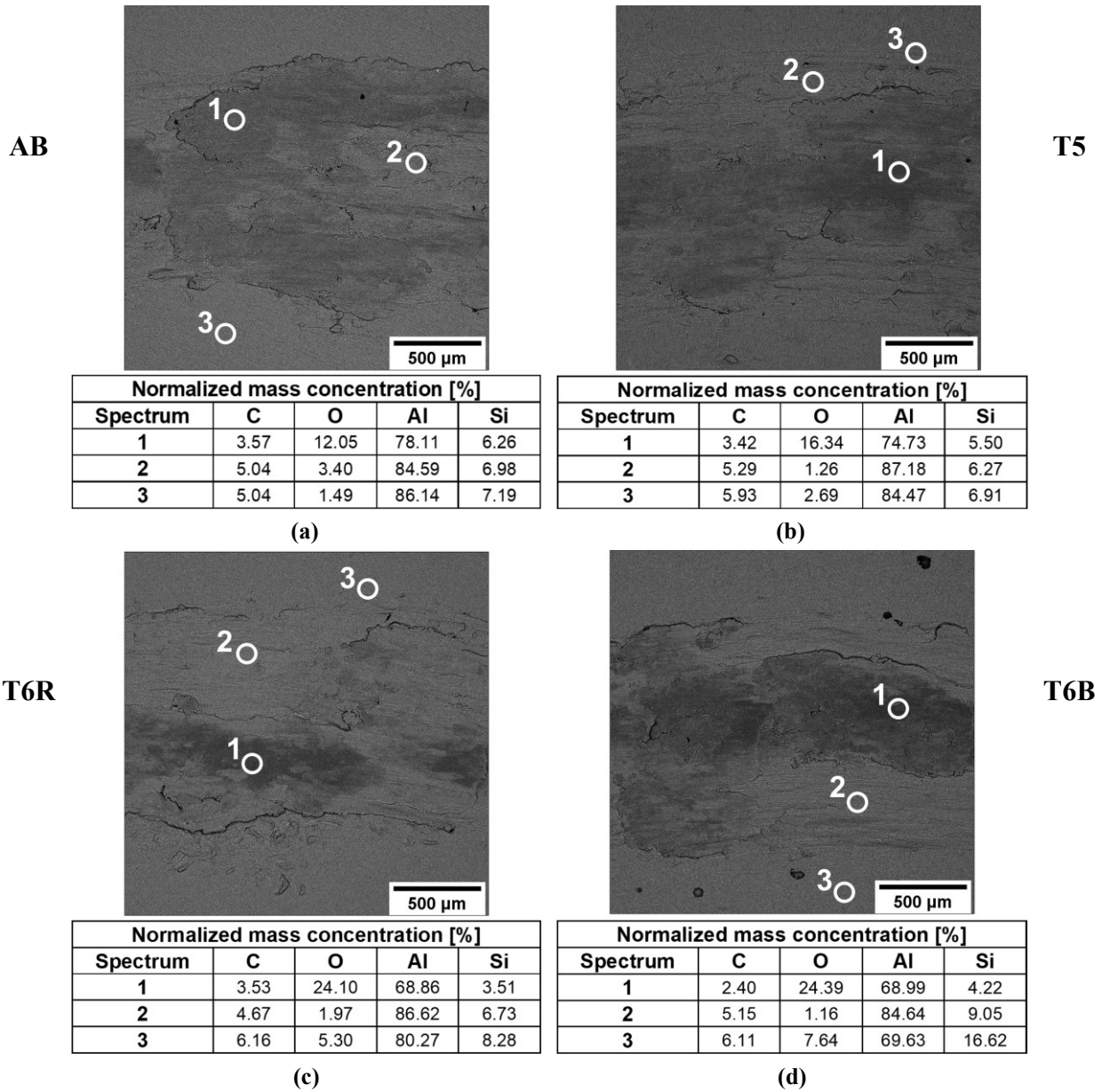


Figure 3.12. BSE images and EDS analysis of the wear tracks of each sample: AB (a), T5 (b), T6R (c), and T6B (d).

Based on the observation of the worn surfaces, the dominant wear mechanism is severe adhesion with a moderate tribo-oxidative contribution. However, the following section presents a sub-surface analysis of the wear tracks to better understand transfer layers' role and how their stability is affected by heat treatment conditions.

### 3.3.3 Sub-surface characterization

#### 3.3.3.1 Thermo-mechanical analysis

During the dry sliding test, the material undergoes high thermo-mechanical stresses, which generate different wear mechanisms depending on the stress distribution and temperature below the contact interface. In particular, considering the non-conformal contact between the Al<sub>2</sub>O<sub>3</sub> ball and L-PBF AlSi10Mg disk, the radius of the contact region ( $r$ ) and the maximum Hertzian contact pressure ( $p_{max}$ ), were estimated according to Equations 3.1 and 3.2 [46]:

$$r = (3F_n R / 4E)^{\frac{1}{3}} \quad (3.1)$$

$$p_{max} = 3F_n / 2\pi r^2 \quad (3.2)$$

Where  $E$  is the contact modulus, defined according to Equation 3.3, and  $R$  is the reduced radius of curvature, defined according to Equation 3.5 [47]:

$$1/E = 1 - \nu_1^2/E_1 + 1 - \nu_2^2/E_2 \quad (3.3)$$

$$1/R = 1/R_1 + 1/R_2 \quad (3.5)$$

$E_1$  and  $\nu_1$  were determined on L-PBF AlSi10Mg samples by nanoindentation and non-destructive ultrasonic evaluation according to the methods described in [39] and [47], respectively. The area of contact ( $A_n$ ), the maximum shear stress ( $\tau_{max}$ ), the average pressure ( $p_{average}$ ), and the distance from the surface corresponding to  $\tau_{max}$  value ( $z\tau_{max}$ ) were evaluated according to [26]. Table 3.2 summarizes the results obtained.

**Table 3.2.** Contact parameters for each heat-treatment condition.

	$E_1$ [GPa]	$\nu_1$	$r$ [mm]	$A_n$ [mm <sup>2</sup> ]	$p_{max}$ [MPa]	$p_{average}$ [MPa]	$\tau_{max}$ [MPa]	$z\tau_{max}$ [mm]
<b>AB</b>	91.7	0.337	0.0517	0.0084	892	594	268	0.0264
<b>T5</b>	91.2	0.337	0.0518	0.0084	889	593	267	0.0264
<b>T6R</b>	93.1	0.337	0.0515	0.0083	899	599	270	0.0263
<b>T6B</b>	93.7	0.337	0.0514	0.0083	901	601	270	0.0262

The bulk temperature ( $T_o$ ), which was monitored by a K-type thermocouple located in the tribometer, is used to assess the average surface temperature ( $T_s$ ) and the flash temperature ( $T_f$ ) at the contact interface, according to [48]. The  $T_s$  value is evaluated according to Equation 3.6:

$$T_s = T_o + \mu F_n v / A_n * 1 / (\frac{k_1}{l_1} + \frac{k_2}{l_2}) \quad (3.6)$$

Where  $k_1$  (30 W/m\*K) [49] and  $k_2$  (120 W/m\*K) [48] are the thermal conductivities of the two bodies in contact, and  $l_1$  and  $l_2$  are the equivalent heat diffusion distances for the tribological system. The first one ( $l_1$ ) can be expressed by Equation 3.7, considering that heat flow is not one-dimensional but has a spherical symmetry [45]:

$$l_1 = \sqrt{\pi} * r / 2 \quad (3.7)$$

The second one ( $l_2$ ) depends on the typology of the contact. If the ball's sliding speed ( $v$ ) is sufficiently lower than the disk's thermal diffusivity ( $a$ ), the temperature profile can be considered constant with time. This condition can be determined by the Peclet number,  $Pe$ , given by Equation 3.8:

$$Pe = v * r / 2a \quad (3.8)$$

The  $Pe$  value is approximately 0.05, considering a thermal diffusivity value equal to 50 mm<sup>2</sup>/s [41], and therefore sufficiently lower than the limit value of 0.1 necessary to consider a steady-state model for the tribological system. Consequently,  $l_2$  can be expressed according to Equation 3.9:

$$l_2 = k_2 l_1 / k_1 \quad (3.9)$$

$T_f$  was evaluated according to Equation 3.10, considering a plastic contact at the asperities of the two bodies:

$$T_f = T_s + 8.8 * 10^4 * \mu / (1 + 12\mu^2)^{1/2} * v / (k_1 + k_2) \quad (3.10)$$

However, the distinction between the  $T_f$  and  $T_s$  disappears if the real area of contact ( $A_r$ ) tends to the nominal area of contact ( $A_n$ ), i.e., the normal load  $F_n$  tends to the seizure load ( $F_s$ ).  $F_s$  is defined by Equation 3.11:

$$F_s = HV_{0.1} * A_n / (1 + 12\mu^2)^{1/2} \quad (3.11)$$

Where  $HV_{0.1}$  is the measured hardness value of each heat-treated sample. The results are reported in Table 3.3.

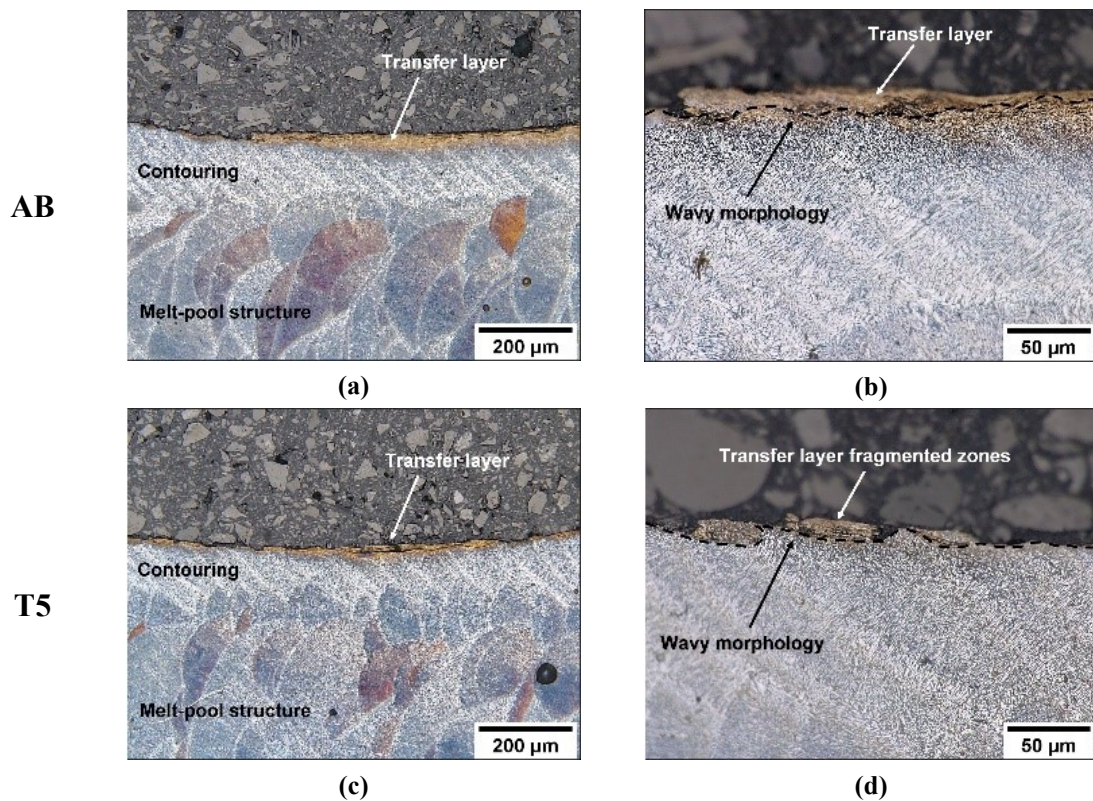
**Table 3.3.** Surface and flash temperatures at the contact interface for each heat-treatment condition were evaluated according to Equations 5 and 9, respectively.

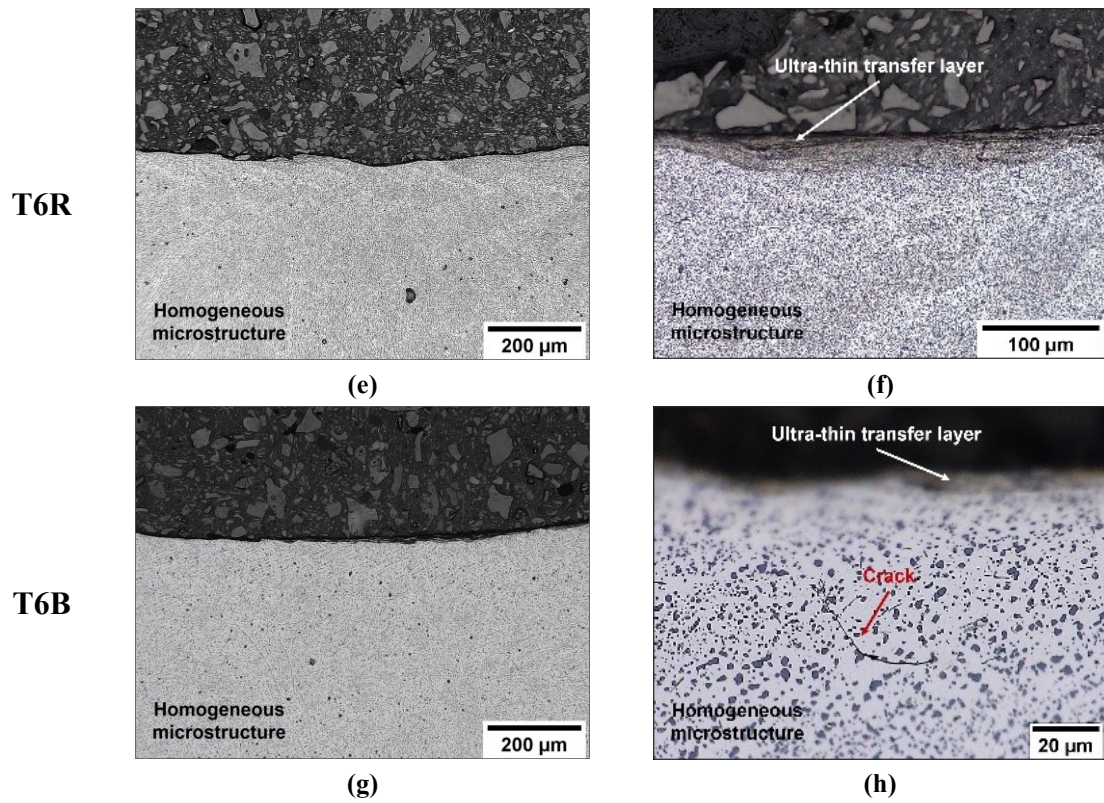
	<b>HV<sub>0.1</sub> [MPa]</b>	<b>μ</b>	<b>F<sub>s</sub> [N]</b>	<b>T<sub>s</sub> [K]</b>	<b>T<sub>f</sub> [K]</b>
<b>AB</b>	1350	0.47	5.9	319	334
<b>T5</b>	1310	0.50	5.5	321	336
<b>T6R</b>	990	0.46	4.4	319	319
<b>T6B</b>	1020	0.47	4.4	320	320

Considering the values reported in Table 3,  $F_n$  (5 N) is close to the seizure load in all the analyzed conditions. In particular, for the T6 heat-treated conditions (both T6R and T6B), the true contact area approached the nominal contact area because  $F_s < F_n$ , and the seizure condition occurred, in agreement with the heavy material transfer from the disk to the ball and the low coverage by protective oxides shown in Figures 3.12(a-d).

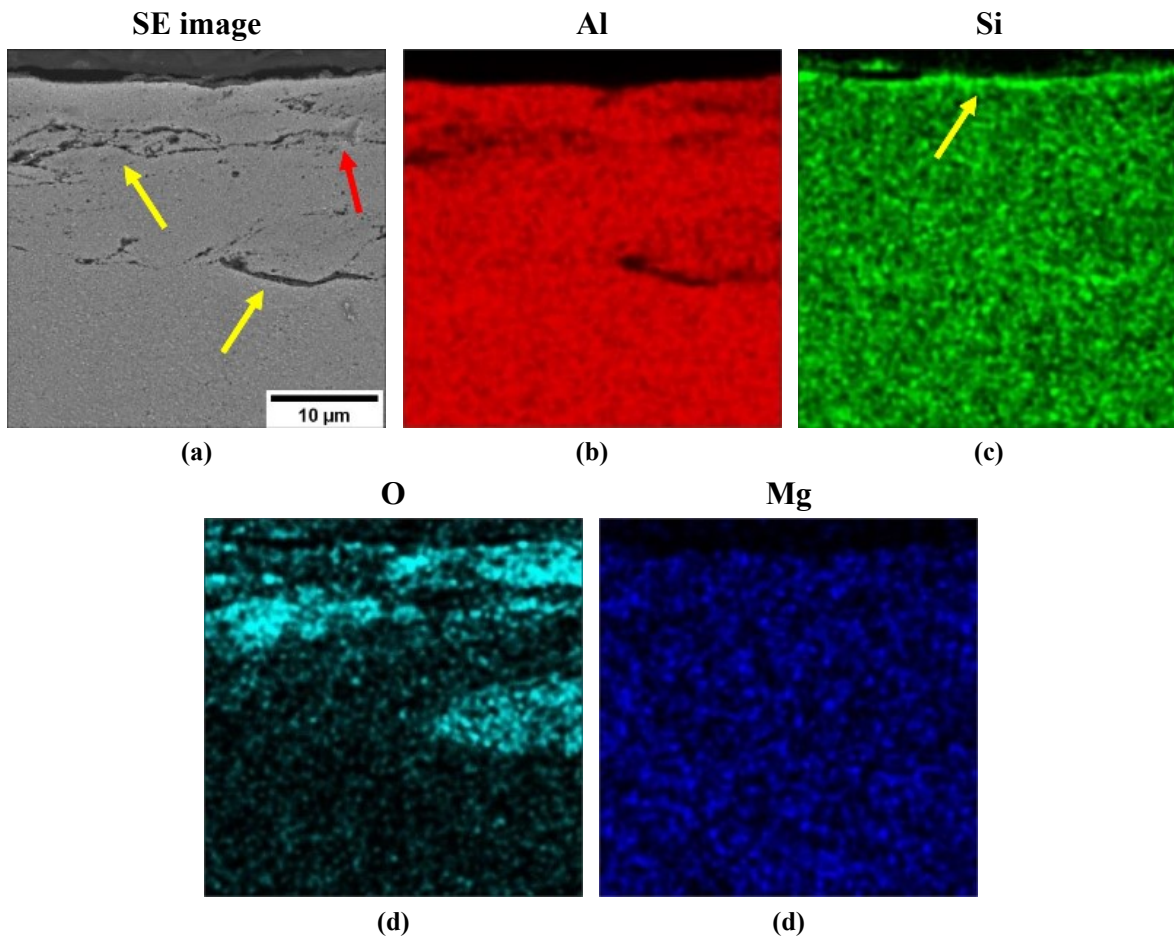
### 3.3.3.2 Morphological and micromechanical analysis of the sub-surface zone

As shown by the EDS analysis (Figures 3.12(a-d)), each L-PBF AlSi10Mg sample is characterized by the presence of oxidized material on the worn surface due to the high reactivity of Al in the air as well as to the combined action of mechanical stresses and frictional heating during dry sliding. The transfer layer's role in the tribological behavior of the L-PBF AlSi10Mg alloy, its morphology, and the microstructure and micromechanical characteristics of the sub-surface area are investigated in cross section. A thicker and more continuous transfer layer is observed on the wear tracks of the AB and T5 (Figures 12(a,c)) than on T6R and T6B (Figures 3.13(e,g)). EDS maps in cross section (Figure 3.14) show that this transfer layer consists of Al- and Si-rich phases, which are mechanically mixed with oxidized material and distributed in large O-rich patches. A continuous thin layer of Si is found in the outermost region of the transfer layer, probably due to the accumulation of particles from the harder eutectic fibrous-Si network. If the transfer layer is adherent and correctly supported by the substrate, its delamination does not occur, as described by [14,31]. The wavy morphology of the material below the transfer layer (Figures 3.13(b,d)) due to the height difference between the protruding MPC, characterized by a finer microstructure, and the recessing MPBs, where the microstructure is coarser than the MPBs and HAZs, affords improved adhesion by mechanical interlocking. Upon reaching a critical layer thickness, the transfer layer breaks away, leading to material removal from the wear track. The higher WD value of T5 compared to AB may be attributable to more extensive detachment phenomena from the transfer layer detected in some areas, as shown in Figures 3.13(b,d).





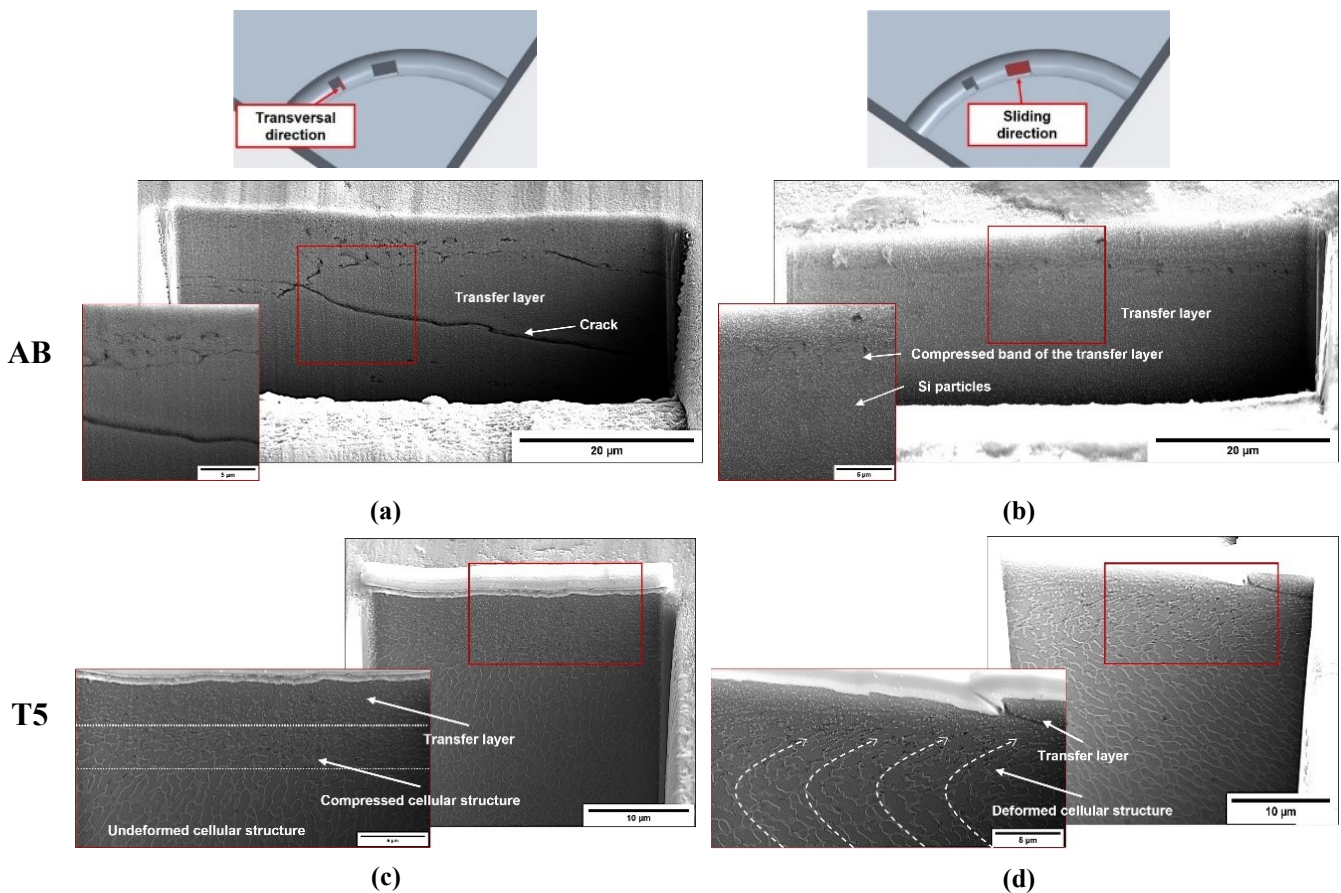
**Figure 3.13.** Cross section below the wear track of the L-PBF AlSi10Mg specimens in each tested condition: AB (a, b), T5 (c, d) T6R (e, f), T6B, (g, h).



**Figure 3.14.** EDS X-ray maps of the transfer layer on the AB disk: SE image (a), Al (b), Si (c), O (d), and Mg (e) elemental distribution. The yellow arrows in the SE image indicate the interfaces between oxide-based patches and Al-, Si-rich zones, while the red arrow indicates a nanoindentation mark. In the Si map, the yellow arrow indicates the Si-rich top layer.

This phenomenon is explained in more detail by the results of the FIB analysis. The transfer layer on AB (Figures 3.15(a,b)) is the thickest among all samples (from 20 to 30  $\mu\text{m}$ ), as already reported in Figure 3.13, and shows a compact and adherent morphology, both in the sliding and transverse directions. However, the frictional force at the sliding interface is sufficiently high to shear the material off the wear track partly. The  $\tau_{\text{max}}$  value achieved at a  $z\tau_{\text{max}}$  distance of about 26  $\mu\text{m}$  from the contact interface (Table 3.2) may lead to localized detachment of the transfer layer (Figures 3.13(b) and 3.16(a)).

The transfer layer on T5 is thinner than on AB ( $< 5 \mu\text{m}$ , Figures 3.15(c,d)) and adheres to the cellular substructure without showing cracks or signs of delamination (Figures 3.15(c,d)). Below the oxide layer, the eutectic-Si network appears fragmented and deformed due to thermomechanical stresses induced by dry sliding. In particular, the elongated cells (Figure 3.15(d)) in the transverse section suggest that deformation of the eutectic-Si fibrous structure occurred mainly along the sliding direction, while the cross section shows the compressive effect induced by the contact pressure on the cellular structure (Figure 3.15(c)), as described by [31]. The high contact pressure plastically deforms the  $\alpha$ -Al matrix and may activate sliding movements at the interface between the hard Si phase and the soft Al phase. This condition leads to the disintegration of the eutectic-Si network by forming voids at the Al/Si interface and propagating cracks, preferably through the softer Al phase (Figure 3.16(b)). Finally, the hard Si phase is mechanically mixed with the Al-rich material and forms the protective transfer layer on the worn surfaces. The nanometric Si-rich particles in the top layer of the transfer layer (Figure 3.16(b)) may be attributed only to the crushing effect rather than the microstructural evolution induced by high temperatures, considering the low contact temperature and the high contact pressure (Table 3.3).



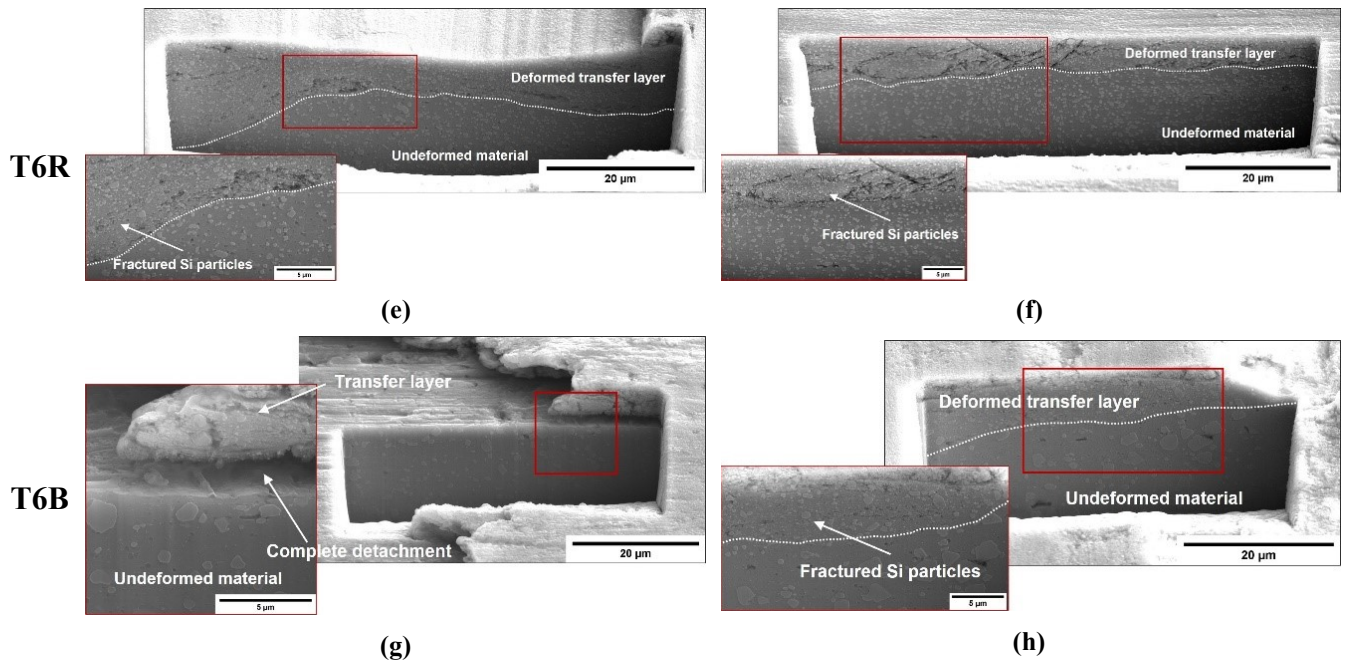


**Figure 3.15.** FEG-SEM images of FIB cross sections of the wear tracks in the transverse and sliding direction: AB (a,b), T5 (c,d), T6R (e,f), T6B (g,h). Images in (a,b) show the morphology and fragmentation of the oxide film, (c,d) the deformation mechanisms of the eutectic-Si network under load, (e,f) the mechanically deformed layer of the T6R sample, (g,h) the lack of adhesion of the oxide layer on the T6B sample and the crushing of the large Si particles, respectively.

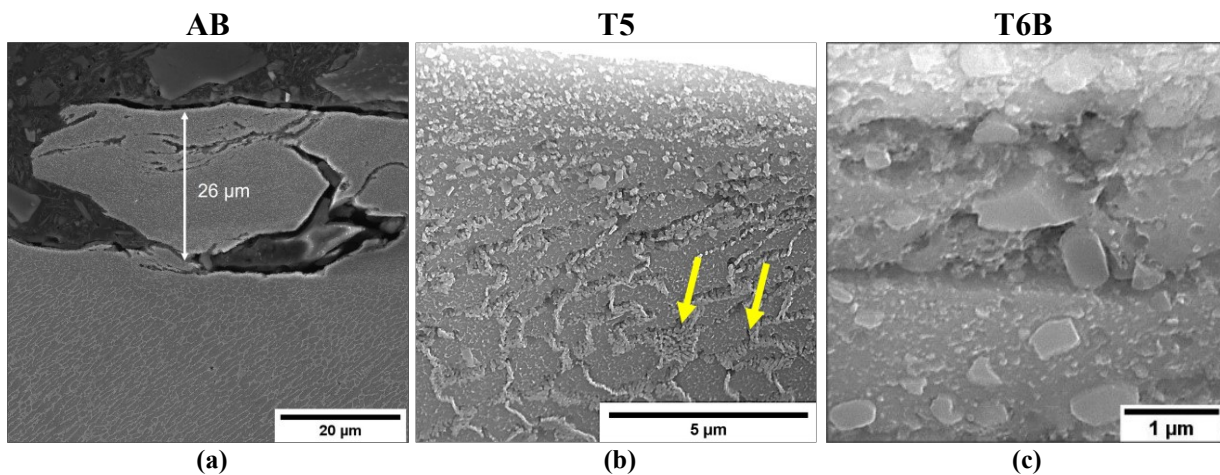
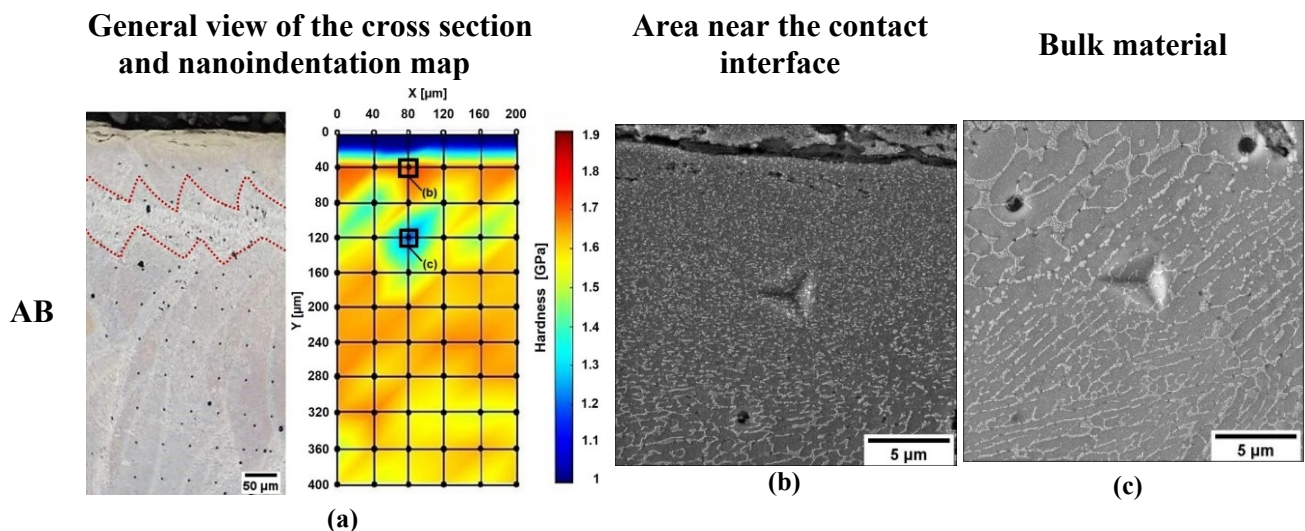


**Figure 3.16.** Cross-section FEG-SEM images with details below the wear tracks: localized detachment of the thick transfer layer on AB (a), sliding phenomena between the hard (Si) and the soft phase (Al) in the eutectic-Si network induced by contact pressure (b) and cracking of the Si particles incorporated and mixed in the deformed layer (c). In (b), yellow arrows indicate the propagation of cracks through the softer Al cells.

The T6R and T6B samples have a very smooth and flat surface (Figures 3.13(e,g)) in which the beneficial wavy interface, previously described for AB and T5, is not present anymore: hence, only a skinny transfer layer is barely detectable (Figures 3.13(f,h)). Moreover, the dispersed and coarse Si particles within the microstructure of T6R and T6B act as a less efficient load-bearing phase compared to the fine eutectic-Si network that characterizes AB and T5, as also reported by [45,50]. The cellular substructure of AB and T5 is similar to a fiber-reinforced metal matrix composite, which is typically more effective in terms of load support by comparison to a particulate-reinforced metal matrix composite when fibers are favorably oriented to the applied stress, as in this case. On the contrary, the T6R and T6B samples are characterized by debonding and pull-out of Si particles from the  $\alpha$ -Al matrix, which typically occurs during dry sliding of AlSi alloys, as also observed by [43], and the formation of mechanically-mixed transfer layers (Figures 3.15(e-h)). In particular, Si particles are first fractured and subsequently incorporated and mixed in the transfer layer with the oxidized material (Figure 15(c)), indicating that the softer Al wore out quickly while the harder Si particles stuck to the surface (Figures 3.15(e,f,h)).

Furthermore, as described in [20], the different elastoplastic behavior between the Si particles and the Al matrix may promote the growth of cracks inside the softer material due to the inhomogeneous stress state developed close to the Si particles and the local extensive plastic deformation of the Al matrix. The cracking of the Si particles inside the  $\alpha$ -Al matrix samples and the formation of microcracks at the interface between the Si and Al phase by a triaxial stress condition make the transfer layer of the T6R and T6B samples less adherent than on AB and T5 (Figures 3.15(g)), as also reported by [31,50]. This phenomenon depends on the size and distribution of the Si particles; in fact, the coarser and non-uniformly distributed Si particles of the T6B sample represent a preferential site for cracking at the Si particles/ $\alpha$ -Al matrix interface, thus promoting fragmentation and delamination of both the metal substrate (Figure 3.13(h)) and the transfer layer. As Takata [22] reported, the decrease in stress concentration at the Si particle/Al matrix interface increases the ability to transfer load from the soft Al matrix to the harder Si particles and prevents detachment or particle cracking. Small-sized and well-dispersed Si particles, such as those in T6R, generally improve the wear resistance of the alloy, being less prone to detachment and reduction of the adhesive wear, preserving part of the transfer layer. Small particles are less prone to forming cracks, which may cause subsurface delamination. The low grip of the transfer layer from the composite-like microstructure induced by the T6 heat treatments promotes the transfer layer decomposition and removal at a depth lower than  $z_{\tau_{max}}$  compared to the AB and T5 samples (Figure 3.15(g)). The crushing of Si particles dramatically reduces their size and prevents them from acting as an effective third abrasive body, making abrasive wear extremely difficult. The dominant effects on the tribological behavior of the anti-wear oxide layer and the microstructural evolution induced by the contact pressure under the worn surface made the slight differences observed in the EBSD analysis negligible (Figures 3.6 and 3.7). Furthermore, unlike what other authors pointed out [11,14,50], no apparent effect of the defects on the detachment mechanism of the oxide layer is observed, probably due to the low density of the defects and the small volume of the gas pores, as evaluated in Chapter 2.

The stability of the transfer layer is also affected by softening or work-hardening phenomena in the underlying alloy, related to contact temperature and pressure (Table 3.2 and Table 3.3). The nanoindentation maps (Figure 3.17) show the differences in the local mechanical response in the different regions of interest.



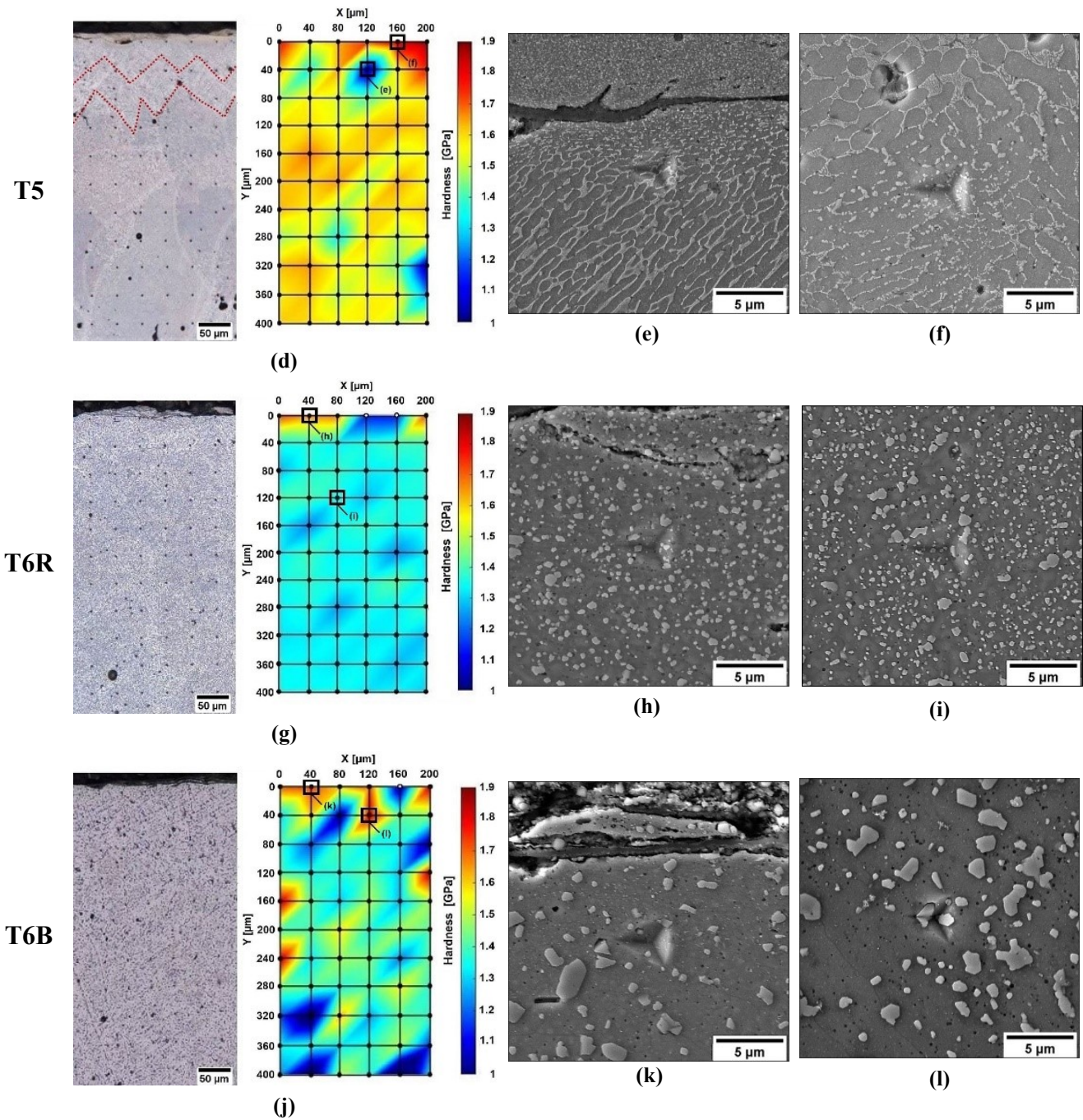


**Figure 3.17.** Sub-surface nanoindentation: general view of the cross section (OM images), nanoindentation maps in the area shown by OM images, and FEG-SEM images of indentations in specific points of the maps (near the contact interface (b,e,h,l) or in the bulk material (c,f,i,l)). The red dotted line highlights the contour zone boundaries in AB and T5 samples. White row and point on nanoindentation maps describe out-of-range values due to the very low hardness characterizing the oxide layer.

Firstly, the samples obtained in different heat treatment conditions are compared in bulk nanoindentation response. AB and T5 show an inhomogeneous mechanical behavior compared to T6R and T6B as a function of the indentation position, related to their peculiar microstructure. As described in the previous sections, the eutectic-Si network in AB and T5 shows different morphologies within the MP structure: (i) finely distributed in the MPC; (ii) coarser and more inhomogeneous along the MPBs; (iii) fragmented and extremely discontinuous in the HAZs (Figures 3.2(b,e)). Furthermore, the contour strategy applied to improve the surface finish of the samples results in a coarser cellular microstructure along the entire boundary of the contour zone (CZB) (area between red dotted lines in Figures 16(a,d)), as typically observed [53]. The areas characterized by coarser and inhomogeneous microstructure (MPBs, HAZs, and CZBs) have a decrease in hardness of about 20% compared to the values measured in the MPC are about 1.6 – 1.7 GPa.

Kim et al. [54] described that upon nanoindentation loading, dislocations in the Al matrix pile up at the eutectic-Si network/Al cell interface, which is highly effective in hindering dislocation slip and in reducing the plastic deformation area due to its continuity and fineness within the MPC. Conversely, the coarser and fragmented Si content, resulting from the Si decomposition associated with the different thermal history in MPBs, HAZs, and CZBs (Figures 3.17(c,f)), has a minor effect on inhibiting dislocation motion, thus reducing the local hardness.

Two different conditions are observable in the area below the wear track: (i) near the contact interface, a transfer layer with very low hardness (about 0.6 GPa) compared to the average of the bulk material (1.6 GPa) (Figure 3.17(a)); (ii) below the transfer layer, an area with higher hardness (1.8 - 1.9 GPa) than the bulk material, both in MPC (between 1.6 and 1.7 GPa) and in MPBs, HAZs, and CBZs (1.1 - 1.4 GPa) (Figure 3.17(d)). In the first case, the transfer layer consisting of Al oxides and dispersed Si lost all the AB and T5 microstructure characteristics, and the indenter found a low resistance to penetration (Figure 3.17(b)). In the second case, the high contact pressure during the test exceeds the elastic limit of the material, thus inducing plastic deformation and hence work-hardening (Figure 13.7(e)), as reported by Mahato et al. [31]. This phenomenon, typical of AlSi alloys [53], is furtherly emphasized by the high work-hardening ability of the cellular microstructure of L-PBF AlSi10Mg: the small interphase (Si/ $\alpha$ -Al) distance results in high strain gradients, contributing to the enhancement of dislocation density by Orowan looping mechanism around the eutectic Si phase [52] (Figure 3.18).

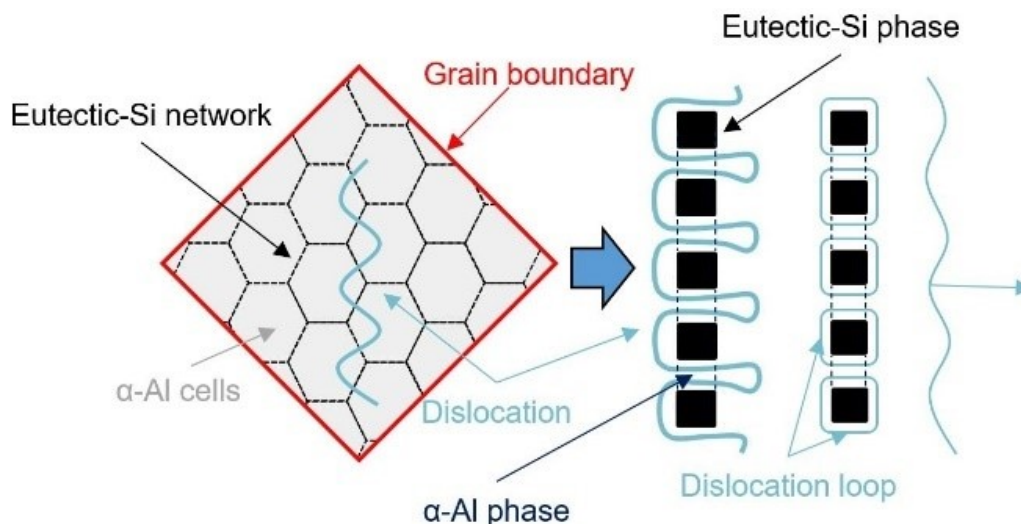


**Figure 3.18.** Interaction between the dislocations and the cell boundary via Orowan looping in hierarchically structured L-PBF AlSi10Mg alloy under loading: dislocations pass through the cell boundary, producing dislocation loops around boundary phases.

The work-hardened layer attains a higher load-bearing capacity, limiting delamination of the oxide layer, as localized strain-hardening also improves shear resistance [14]. In addition, the transfer layer protects the underlying material from continuous contact with the  $\text{Al}_2\text{O}_3$  counterpart [1], explaining the thicker transfer layer and the lower wear rate of the AB and T5 samples. This hypothesis is valid up to specific values of normal load and sliding speed, above which the contact pressure leads to the softening of the Al alloy due to the frictional heating, which in this case is dominant. However, as reported in Table 3.3, the  $T_f$  and  $T_s$  values are relatively low, and the thermal relieving of the microstructure is not expected to occur.

The shorter SHT step of the T6R heat treatment induces Si particle refinement compared to the T6B heat treatment and beneficially affects microstructural homogenization and local mechanical response (Figures 3.17(g-i)). In the T6R sample, the homogeneous distribution of the small-sized Si particles and the high cohesion with the  $\alpha$ -Al matrix lead to the involvement of both the Si particles and the  $\alpha$ -Al matrix in the indentation response (Figure 3.17(h)). Therefore, the

measurements in the area below the contact interface are not affected by high scattering, and the indentation map shows an extremely homogeneous hardness distribution, with values between 1.3 and 1.4 GPa (Figure 3.17(g)). Conversely, the less homogeneous size and distribution of Si particles in T6B lead to a high variation in hardness (Figure 16(j)) between the particle-free zones (1.0 - 1.2 GPa) (Figure 3.17(l)) and the zones with large Si particles or Si particles clusters in the material (1.5 -1.7 GPa) (Figure 3.17(k)).

The T6R and T6B samples (Figures 3.17(g,j)) show the presence of residual patches of the oxide layer (hardness of about 0.7 GPa) and work-hardened material (about 1.7 GPa) below the wear track. The T6 heat-treated alloys are characterized by comparable work-hardening mechanisms described above for AB and T5. However, the coarser size and the less homogeneous distribution of the dispersed second phase reduce the effect of the Orowan looping mechanism compared to the cellular microstructure, as described by [51] and [52]. Consequently, the lower hardness of the areas below the wear track in T6R and T6B could contribute to a lower load-bearing capacity, leading to the detachment of the protective oxide layer, thus lowering the wear resistance.

### 3.4 Conclusions

This Chapter investigated the influence of different heat treatments on dry sliding against  $\text{Al}_2\text{O}_3$  of AlSi10Mg alloy produced by Laser-based Powder Bed Fusion (L-PBF). The following heat treatment conditions were assessed: T5 (artificial aging (AA) at 160 °C for 4 h), T6R (rapid solution (SHTR) at 510 °C for 10 min followed by artificial aging (AA) at 160 °C for 6 h), and T6B (solution (SHT) at 540 °C for 1 h followed by artificial aging (AA) at 160 °C for 4 h) and compared with the as-built (AB) condition. The sliding tests were carried out on the plane parallel to the building axis of the specimen. The following conclusions can be drawn:

- AB, T5, T6R, and T6B alloys show comparable friction coefficient values between 0.46 and 0.50. The wear depth follows the hardness trend, starting from the lowest value, 54  $\mu\text{m}$ , of the AB, displaying the higher hardness (134  $\text{HV}_{0.1}$ ) up to the highest value, 69  $\mu\text{m}$ , of the T6B (102  $\text{HV}_{0.1}$ ). Despite a slightly lower hardness than the T6B, the T6R alloy (99  $\text{HV}_{0.1}$ ) shows a lower wear depth equal to 64  $\mu\text{m}$ .
- The ability to retain an anti-wear oxide layer on the AB and T5 samples and the higher hardness induces lower wear depth values than the T6R and T6B samples.
- The submicrometric size of the Si particles and the lower interparticle distance of the T6R microstructure increase the wear resistance compared to the T6B through higher cohesion between the hard Si phase and the Al matrix.
- Strong adhesive and mild tribooxidation wear mechanisms are observed on worn surfaces. No abrasive wear mechanism is identified due to the grinding and mixing processes involving the extremely fine Si phase.
- Contact pressure induces strain-hardening, microstructural deformation, and Si-phase cracking under the worn surface. The low contact temperature does not induce overaging or stress-relieving phenomena.

In conclusion, the rapid solution induced a microstructural refinement compared to the conventional solution, improving the tribological behavior of the T6 heat-treated L-PBF AlSi10Mg alloy and bringing it closer to that of the AB alloy. Considering the decrease in anisotropy and the better balance of mechanical (strength and ductility) and tribological properties induced by T6R, this heat treatment can produce a reliable structural component. Further investigations will be carried out to verify these advantages even in more severe conditions.

## References

1. L. Ceschini, S. Toschi, Friction and Wear of Aluminum Alloys and Composites, *Frict. Lubr. Wear Technol.* 18 (2018) 509–532. <https://doi.org/10.31399/asm.hb.v18.a0006388>
2. D. Kumar Dwivedi, Wear behaviour of cast hypereutectic aluminium silicon alloys, *Materials & Design*, 27 (7) (2006) 610–616. <https://doi.org/10.1016/j.matdes.2004.11.029>.
3. Å. Kastensson, Developing lightweight concepts in the automotive industry: taking on the environmental challenge with the SÄNätt project, *Journal of Cleaner Production*, 66 (2014) 337–346. <https://doi.org/10.1016/j.jclepro.2013.12.007>.
4. A. Vafadar, F. Guzzomi, A. Rassau, K. Hayward, Advances in Metal Additive Manufacturing: A Review of Common Processes, Industrial Applications, and Current Challenges. *Appl. Sci.*, 11 (3) 2021 1213. <https://doi.org/10.3390/app11031213>.
5. A. Iturrioz, E. Gil, M.M. Petite, F. Garciandia, A. M. Mancisidor, M. San Sebastian. Selective laser melting of AlSi10Mg alloy: influence of heat treatment condition on mechanical properties and microstructure, *Weld World*, 62 (2018) 885–892. <https://doi.org/10.1007/s40194-018-0592-8>.
6. W. Li, S. Li, J. Liu, A. Zhang, Y. Zhou, Q. Wei, C. Yan, Y. Shi, Effect of heat treatment on AlSi10Mg alloy fabricated by selective laser melting: Microstructure evolution, mechanical properties and fracture mechanism, *Materials Science and Engineering: A*, 663 (2016) 116–125. <https://doi.org/10.1016/j.msea.2016.03.088>.
7. E.O. Olakanmi, R.F. Cochrane, K.W. Dalgarno, A review on selective laser sintering/melting (SLS/SLM) of aluminium alloy powders: Processing, microstructure, and properties, *Progress in Materials Science*, 74 (2015) 401–477. <https://doi.org/10.1016/j.pmatsci.2015.03.002>.
8. N. T. Aboulkhair, M. Simonelli, L. Parry, I. Ashcroft, C. Tuck, R. Hague, 3D printing of Aluminium alloys: Additive Manufacturing of Aluminium alloys using selective laser melting, *Progress in Materials Science*, 106 (2019) 100578. <https://doi.org/10.1016/j.pmatsci.2019.100578>.
9. Y. Zhu, J. Zou, H. Yang, Wear performance of metal parts fabricated by selective laser melting: a literature review. *J. Zhejiang Univ. Sci. A*, 19 (2018) 95–110. <https://doi.org/10.1631/jzus.A1700328>.
10. Erfan Maleki, Sara Bagherifard, Michele Bandini and Mario Guagliano, Surface post-treatments for metal additive manufacturing: progress, challenges, and opportunities, *Additive Manufacturing*, (2020) doi:<https://doi.org/10.1016/j.addma.2020.101619>.
11. P. Wei, Z. Chen, S. Zhang, X. Fang, B. Lu, L. Zhang, Z. Wei, Effect of T6 heat treatment on the surface tribological and corrosion properties of AlSi10Mg samples produced by selective laser melting, *Materials Characterization*, 171 (2021) 110769. <https://doi.org/10.1016/j.matchar.2020.110769>.
12. K.G. Prashanth, B. Debalina, Z. Wang, P.F. Gostin, A. Gebert, M. Calin, U. Kühn, M. Kamaraj, S. Scudino, J. Eckert, Tribological and corrosion properties of Al-12Si produced by selective laser melting, *J. Mater. Res.* 29(2014) 2044–2054. <https://doi.org/10.1557/jmr.2014.133>.
13. H.J. Rathod, T. Nagaraju, K.G. Prashanth, U. Ramamurty, Tribological properties of selective laser melted Al– 12Si alloy, *Tribol. Int.* 137 (2019) 94–101. <https://doi.org/10.1016/j.triboint.2019.04.038>
14. W.H. Kan, S. Huang, Z. Man, L. Yang, A. Huang, L. Chang, Y. Nadot, J.M. Cairney, G. Proust, Effect of T6 treatment on additively-manufactured AlSi10Mg sliding against ceramic and steel, *Wear.* 482–483 (2021). <https://doi.org/10.1016/j.wear.2021.203961>.
15. J. Liu, Y. Zhou, Y. Fan, X. Chen, Effect of laser hatch style on densification behavior, microstructure, and tribological performance of aluminum alloys by selective laser melting, *J. Mater. Res.* 33 (2018) 1713–1722. <https://doi.org/10.1557/jmr.2018.166>.
16. P. Thasleem, B. Kuriachen, D. Kumar, A. Ahmed, M.L. Joy, Effect of heat treatment and electric discharge alloying on the tribological performance of selective laser melted AlSi10Mg, *J. Tribol.* 143 (2021) 1–16. <https://doi.org/10.1115/1.4050897>.
17. N. Kang, P. Coddet, H. Liao, T. Baur, C. Coddet, Wear behavior and microstructure of hypereutectic Al-Si alloys prepared by selective laser melting, *Appl. Surf. Sci.* 378 (2016) 142–149. <https://doi.org/10.1016/j.apsusc.2016.03.221>.
18. H. Wu, Y. Ren, J. Ren, A. Cai, M. Song, Y. Liu, X. Wu, Q. Li, W. Huang, X. Wang, I. Baker, Effect of melting modes on microstructure and tribological properties of selective laser melted AlSi10Mg alloy, *Virtual Phys. Prototyp.* 15 (2020) 570–582. <https://doi.org/10.1080/17452759.2020.1811932>.
19. J. Fite, S. E. Prameela, J. A. Slotwinski, T. P. Weihs, Evolution of the microstructure and mechanical properties of additively manufactured AlSi10Mg during room temperature holds and low temperature aging, *Additive Manufacturing*, 36 (2020) 101429. <https://doi.org/10.1016/j.addma.2020.101429>.
20. G. Di Egidio, L. Ceschini, A. Morri, C. Martini, M. Merlin, A Novel T6 Rapid Heat Treatment for AlSi10Mg Alloy Produced by Laser-Based Powder Bed Fusion: Comparison with T5 and Conventional T6 Heat Treatments. *Metall Mater Trans B* 53 (2022) 284–303. <https://doi.org/10.1007/s11663-021-02365-6>
21. T.H. Park, M.S. Baek, Y. Sohn, K.A. Lee, Effect of post-heat treatment on the wear properties of AlSi10Mg alloy manufactured by selective laser melting, *Arch. Metall. Mater.* 65 (2020) 1073–1080. <https://doi.org/10.24425/amm.2020.133220>.
22. N. Takata, M. Liu, H. Kodaira, A. Suzuki, M. Kobashi, Anomalous strengthening by supersaturated solid solutions of selectively laser melted Al–Si-based alloys, *Additive Manufacturing*, 33 (2020) 101152. <https://doi.org/10.1016/j.addma.2020.101152>.
23. A.K. Mishra, R.K. Upadhyay, A. Kumar, Surface Wear Anisotropy in AlSi10Mg Alloy Sample Fabricated by Selective Laser Melting: Effect of Hatch Style, Scan Rotation and Use of Fresh and Recycled Powder, *J. Tribol.* 143 (2021) 1–17. <https://doi.org/10.1115/1.4047788>.
24. Z.H. Xiong, S.L. Liu, S.F. Li, Y. Shi, Y.F. Yang, R.D.K. Misra, Role of melt pool boundary condition in determining the mechanical properties of selective laser melting AlSi10Mg alloy, *Materials Science and Engineering: A*, 740–741 (2019) 148–156. <https://doi.org/10.1016/j.msea.2018.10.083>.

25. B.K. Prasad, K. Venkateswarlu, O.P. Modi, A. H. Yegneswaran, Influence of the size and morphology of silicon particles on the physical, mechanical and tribological properties of some aluminium – silicon alloys. *J Mater Sci Lett*, 15 (1996) 1773–1776. <https://doi.org/10.1007/BF00275338>.
26. M.F. Ashby, J. Abulawi, H.S. Kong Temperature maps for frictional heating in dry sliding *ASME Tribology Trans.*, 34 (1991), pp. 577-587. <https://doi.org/10.1080/10402009108982074>.
27. J.P. Moses, Q. Liu, J. P. Best, X. Li, J. J. Kruzic, U. Ramamurty, B. Gludovatz, Fracture resistance of AlSi10Mg fabricated by laser powder bed fusion, *Acta Materialia*, 211 (2021) 116869. <https://doi.org/10.1016/j.actamat.2021.116869>.
28. ASM International. ASTM E3-11(2017): Standard Guide for Preparation of Metallographic Specimens, ASM International: West Conshohocken, PA, USA, 2017.
29. ASM International. ASTM E407-07(2015): Standard Practice for Microetching Metals and Alloys, ASM International: West Conshohocken, PA, USA, 2015.
30. ASM International. ASTM G99-17(2017): Standard Practice for Microetching Metals and Alloys, ASM International: West Conshohocken, PA, USA, 2017.
31. A. Mahato, N. Verma, V. Jayaram, S.K. Biswas, Severe wear of a near eutectic aluminium–silicon alloy, *Acta Materialia*, 59(15) (2011) 6069-6082. <https://doi.org/10.1016/j.actamat.2011.06.016>.
32. D.K. Dwivedi, Adhesive wear behaviour of cast aluminium–silicon alloys: Overview, *Materials & Design* (1980-2015), 31 5 (2010), 2517-2531, <https://doi.org/10.1016/j.matdes.2009.11.038>.
33. X. Liu, C. Zhao, X. Zhou, Z. Shen, W. Liu, Microstructure of selective laser melted AlSi10Mg alloy, *Materials & Design*, 168 (2019) 107677. <https://doi.org/10.1016/j.matdes.2019.107677>.
34. H. Qin, V. Fallah, Q. Dong, M. Brochu, M. R. Daymond, M. Gallemeault, Solidification pattern, microstructure and texture development in Laser Powder Bed Fusion (LPBF) of Al10SiMg alloy, *Materials Characterization*, 145 (2018) 29-38. <https://doi.org/10.1016/j.matchar.2018.08.025>.
35. L. Thijs, K. Kempen, J.P. Kruth, J. Van Humbeeck, Fine-structured aluminium products with controllable texture by selective laser melting of pre-alloyed AlSi10Mg powder, *Acta Mater.*, 61 (2013) 1809–1819, doi:10.1016/j.actamat.2012.11.052.
36. L. Tonelli, Revealing the Hierarchical Microstructure of Innovative Additively Manufactured Metal Parts with Conventional Light Microscopy. *Metallogr. Microstruct. Anal.*, 10 (2021) 278–282. <https://doi.org/10.1007/s13632-021-00721-1>.
37. R. Casati, M.N. Hamidi, M. Coduri, V. Tirelli, M. Vedani, Effects of Platform Pre-Heating and Thermal-Treatment Strategies on Properties of AlSi10Mg Alloy Processed by Selective Laser Melting. *Metals*, 8(11) (2018) 954. <https://doi.org/10.3390/met8110954>.
38. M. Fousová, D. Dvorský, A. Michalcová, D. Vojtěch, Changes in the microstructure and mechanical properties of additively manufactured AlSi10Mg alloy after exposure to elevated temperatures, *Materials Characterization*, 137 (2018) 119-126. <https://doi.org/10.1016/j.matchar.2018.01.028>.
39. L. Zhuo, Z. Wang, H. Zhang, E. Yin, Y. Wang, T. Xu, C. Li, Effect of post-process heat treatment on microstructure and properties of selective laser melted AlSi10Mg alloy, *Materials Letters*, 234 (2019) 196-200. <https://doi.org/10.1016/j.matlet.2018.09.109>.
40. Dong, H., *Surface engineering of light alloys: Aluminium, magnesium and titanium alloys*. Chapter 2. (2010). Elsevier. <https://doi.org/10.1533/9781845699451>.
41. K. V. Yang, P. Rometsch, C.H.J. Davies, A. Huang, X. Wu, Effect of heat treatment on the microstructure and anisotropy in mechanical properties of A357 alloy produced by selective laser melting, *Mater. Des.* 154 (2018) 275–290. <https://doi.org/10.1016/j.matdes.2018.05.026>.
42. L. Zhou, A. Mehta, E. Schulz, B. McWilliams, K. Cho, Y. Sohn, Microstructure, precipitates and hardness of selectively laser melted AlSi10Mg alloy before and after heat treatment, *Materials Characterization*, 143 (2018) 5-17. <https://doi.org/10.1016/j.matchar.2018.04.022>.
43. F. Alghamdi, X. Song, A. Hadadzadeh, B. Shalchi-Amirkhiz, M. Mohammadi, M. Haghshenas, Post heat treatment of additive manufactured AlSi10Mg: On silicon morphology, texture and small-scale properties, *Materials Science and Engineering: A*, 783 (2020) 139296. <https://doi.org/10.1016/j.msea.2020.139296>.
44. J. N. Domfang Ngnenkou, Y. Nadot, G. Henaff, J. Nicolai, W. H. Kan, J. M. Cairney, L. Ridosz, *International Journal of Fatigue*, 119 (2019). <https://doi.org/10.1016/j.ijfatigue.2018.09.029>.
45. M.L. Rahaman, Liangchi Zhang, An investigation into the friction and wear mechanisms of aluminium high silicon alloy under contact sliding, *Wear*, 376–377(B) (2017) 940-946. <https://doi.org/10.1016/j.wear.2016.10.026>.
46. J.A. Williams, R.B Dwyer-Joyce, *Modern Tribology Handbook*. Chapter 3. (2001). Ed. Bharat Bhusan. CRC Press.
47. T. Sol, S. Hayun, D. Noiman, E. Tiferet, O. Yeheskel, O. Tevet, Nondestructive Ultrasonic Evaluation of Additively Manufactured AlSi10Mg Samples, *Additive Manufacturing*, 22 (2018) 700–707. doi: 10.1016/j.addma.2018.06.016.
48. G. Straffelini, *Wear mechanisms*. In: *Friction and wear*. Springer tracts in mechanical engineering, 11 (2015) 85–113. [https://doi.org/10.1007/978-3-319-05894-8\\_4](https://doi.org/10.1007/978-3-319-05894-8_4).
49. D. Martínez-Maradiaga, O.V. Mishin, K. Engelbrecht, Thermal Properties of Selectively Laser-Melted AlSi10Mg Products with Different Densities. *J. of Materi Eng and Perform*, 29 (2020) 7125–7130. <https://doi.org/10.1007/s11665-020-05192-z>.
50. P. Tonolini, L. Montesano, M. Tocci, A. Pola, M. Gelfi, Wear Behavior of AlSi10Mg Alloy Produced by Laser- Based Powder Bed Fusion and Gravity Casting, *Adv. Eng. Mater.*, 2100147 (2021) 2100147. <https://doi.org/10.1002/adem.202100147>.
51. U.F. Kocks, H. Mecking, Physics and phenomenology of strain hardening: the FCC case, *Progress in Materials Science*, 48 (3) (2003), 171-273, [https://doi.org/10.1016/S0079-6425\(02\)00003-8](https://doi.org/10.1016/S0079-6425(02)00003-8).
52. B. Chen, S.K. Moon, X. Yao, G. Bi, J. Shen, J. Umeda, K. Kondoh, Strength and strain hardening of a selective laser melted AlSi10Mg alloy, *Scripta Materialia*, 141 (2017) 45-49. <https://doi.org/10.1016/j.scriptamat.2017.07.025>.
53. E. Beevers, A.D. Brandão, J. Gumpinger, M. Gschweidl, C. Seyfert, P. Hofbauer, T. Rohr, T. Ghidini, Fatigue properties and material characteristics of additively manufactured AlSi10Mg – Effect of the contour parameter on the microstructure, density, residual stress, roughness and mechanical properties, *International Journal of Fatigue*, 117 (2018) 148-162. <https://doi.org/10.1016/j.ijfatigue.2018.08.023>.

54. D. Kim, J. Hwang, E. Kim, Y. Heo, W. Woo, S. Choi, Evaluation of the stress-strain relationship of constituent phases in AlSi10Mg alloy produced by selective laser melting using crystal plasticity FEM, Journal of Alloys and Compounds, 714 (2017) 687-697. <https://doi.org/10.1016/j.jallcom.2017.04.264>.

# Chapter 4 – High-temperature behavior of the heat-treated and overaged L-PBF AlSi10Mg Alloy

1. This section contains selected parts of the manuscript:



May 18 - 20, 2022, Brno, Czech Republic, EU

## EVALUATION OF HIGH-TEMPERATURE TENSILE PROPERTIES OF HEAT-TREATED AlSi10Mg ALLOY PRODUCED BY LASER-BASED POWDER BED FUSION

\*Gianluca DI EGIDIO, Alessandro MORRI, Lorella CESCHINI

*Department of Industrial Engineering (DIN), Alma Mater Studiorum, University of Bologna, Viale Risorgimento 4, 40136 Bologna, Italy, \* [gianluca.diegidio2@unibo.it](mailto:gianluca.diegidio2@unibo.it)*

The published version of the paper is accessible on:

<https://www.confer.cz/metal/2022>

Proceedings of the conference METAL 2022 will be indexed on the Web of Science and Scopus.

The authors wish to thank for granting permission to re-use the manuscript titled “Evaluation of high-temperature tensile properties of heat-treated alloy produced by Laser-based Powder Bed Fusion” in the present Ph.D. thesis (<https://www.confer.cz/metal/2022>).

2. This section reports selected parts of the manuscript:

## ADVANCED ENGINEERING MATERIALS

Research Article | Open Access |

### High-Temperature Behavior of the Heat-Treated and Overaged AlSi10Mg Alloy Produced by Laser-Based Powder Bed Fusion and Comparison with Conventional Al–Si–Mg-Casting Alloys

Gianluca Di Egidio , Alessandro Morri, Lorella Ceschini, Lavinia Tonelli

First published: 26 January 2023 | <https://doi.org/10.1002/adem.202201238>

The published version of the paper is accessible on:

<https://doi.org/10.1002/adem.202201238>

The authors thank Wear for granting permission to re-use the manuscript titled “Dry sliding behavior of AlSi10Mg alloy produced by Laser-based Powder Bed Fusion: influence of heat treatment and microstructure” in the present Ph.D. thesis (<https://onlinelibrary.wiley.com/page/journal/15272648/homepage/author-guidelines>).

3. This section reports selected parts of the manuscript:

## **Room- and High-Temperature Fatigue Strength of the T5 and Rapid T6 Heat-Treated AlSi10Mg Alloy Produced by Laser-Based Powder Bed Fusion**

by  Gianluca Di Egidio \*  ,  Lorella Ceschini ,  Alessandro Morri  and  Mattia Zanni 

Department of Industrial Engineering (DIN), Alma Mater Studiorum, University of Bologna, Viale Risorgimento 4, 40136 Bologna, Italy

\* Author to whom correspondence should be addressed.

*Metals* **2023**, *13*(2), 263; <https://doi.org/10.3390/met13020263>

**Received: 5 January 2023 / Revised: 20 January 2023 / Accepted: 26 January 2023 /**

**Published: 29 January 2023**

(This article belongs to the Special Issue **Mechanical Behaviors and Damage Mechanisms of Metallic Materials**)

The following link can access the published version of the paper:

<https://doi.org/10.3390/met13020263>

The authors thank Metals for granting permission to re-use the manuscript titled “Room- and High-Temperature Fatigue Strength of the T5 and Rapid T6 Heat-Treated AlSi10Mg Alloy Produced by Laser-Based Powder Bed Fusion” in the present Ph.D. thesis (<https://www.mdpi.com/authors/rights>).

## 4.1 Aim

Transportation and energy are probably the main industrial sectors that could greatly benefit from the L-PBF technology by reducing the mass and size of mechanical parts to reduce their environmental impact [1,2]. Fuel injectors, heat sinks, mixing and swirling burner tips, pistons, gas turbines, and aerodynamic parts are possible L-PBF-produced components [3-5]. However, the thin-walled and lattice design solutions require the continuous development of new thermally stable materials capable of withstanding the thermomechanical stresses caused by the severe operating conditions (high temperatures and long service times) that occur in automotive, aeronautical, aerospace, and energy applications [6-8].

As extensively reported in previous chapters, the AlSiMg alloys produced by the L-PBF technology represent an up-and-coming solution for producing structural components due to their mechanical and production requirements [5,9]. In particular, the improved laser absorption of the powder and the narrowed solidification range compared to other Al cast alloys, such as the heat-resistant AlCu and AlZn alloys, ease the production by AM technique [10-14]. Among the AlSiMg alloys, the AlSi10Mg alloy is currently the most commonly used in the L-PBF process. Unfortunately, the lack of knowledge concerning its high-temperature mechanical behavior limits its use in producing high-tech components directly or indirectly exposed to heating [15-17].

From the literature, the metastable cellular structure of the AB L-PBF AlSi10Mg alloy, consisting of sub-micrometric cells of supersaturated  $\alpha$ -Al phase surrounded by a eutectic-Si network, evolves into a more stable condition after prolonged exposure to high temperatures during specific heat treatments, such as SR [18,19] or T6 solution treatment [14,19,20]. As widely described by the authors in Chapter 1, the thermal exposure alters the microstructure of the AB alloy due to thermally activated diffusion processes which affect both the dispersed (nano-sized Si precipitates and precursors of the  $Mg_2Si$  equilibrium phase) and aggregated (eutectic-Si network) strengthening phases. Consequently, given the complexity of the topic, the literature in recent years has mainly focused on the effects of process parameters and heat treatments on the microstructure and the mechanical properties at room temperature of the L-PBF AlSi10Mg alloy, omitting the analysis of the effect of long-term exposure at high working temperatures (near or higher than 200 °C) on microstructure and mechanical behavior. However, increasing the data concerning the high-temperature mechanical properties of the L-PBF AlSi10Mg alloy is essential to spread its use.

Currently, only a few studies focused on the high-temperature mechanical behavior of the L-PBF AlSi10Mg alloy in AB or heat-treated conditions. Uzan et al. [21] evaluated the high-temperature mechanical properties of the L-PBF AlSi10Mg alloy subjected to SR (300 °C for 2 h) in a temperature range between 25 °C and 400 °C, observing a significant decrease in mechanical strength (YS and UTS) and an increase in  $e_f$  as the temperature rises. Furthermore, the analysis of the true stress-true strain curves showed strain-hardening phenomena only at temperatures below 200 °C. Tocci et al. [22], instead, performed high-temperature tensile tests at 100 °C and 150 °C on L-PBF AlSi10Mg alloy in AB and T5 (100 °C and 150 °C for 10 h) conditions, identifying a good response of the alloy at high temperatures with a slight decrease in UTS, no effect on YS and an increase in  $e_f$ .

This Chapter aims to fill the knowledge gap on the effects of overaging and high temperatures on the peculiar microstructure and mechanical properties of the L-PBF AlSi10Mg alloy subjected to the optimized direct aging treatment and the novel rapid solution treatment reported in Chapter 2. In summary, the T5 heat treatment (artificial aging at 160 °C for 4 h and subsequent air cooling) slightly increased the mechanical properties of the AB alloy, preserving its microstructure and strengthening mechanisms. The T6R treatment (solutionizing at 510 °C for 10 min in

air, water quenching, and aging for 6 h at 160 °C in air) obtained the best compromise between strength and ductility compared to other conditions assessed (AB, T5, and T6B (solutionizing at 540 °C for 1 h, water quenching, and artificial aging at 160 °C for 4 h)). In particular, high-temperature tensile tests on overaged alloys (210 °C for 41 h) and high-temperature fatigue tests were performed to study the static and cyclic mechanical properties at high temperatures (200 °C) of the T5 and T6R alloy and to evaluate the effects of thermomechanical stresses caused by severe operating conditions.

Lastly, the results of the high-temperature mechanical characterization were compared to those of previous studies carried out by the Metallurgy Group of the Department of Industrial Engineering (DIN) of the University of Bologna on several HIPped Al cast alloys developed for high-temperature applications [23-25].

## 4.2 Experimental procedure

The samples were produced according to the specifications in Chapter 2 and Chapter 3. The chemical composition, the physical properties of feedstock powder, and the L-PBF process parameters are resumed in Table 4.1.

**Table 4.1.** Chemical composition (wt.%) and physical properties of the AlSi10Mg powder supplied by the producer; L-PBF process parameters and scan strategy conditions.

Chemical composition											
Element (wt.%)	<i>Al</i>	<i>Si</i>	<i>Mg</i>	<i>Fe</i>	<i>Cu</i>	<i>Mn</i>	<i>Ni</i>	<i>Pb</i>	<i>Sn</i>	<i>Ti</i>	<i>Zn</i>
<b>Powders</b>	Bal.	9.210	0.270	0.150	0.001	0.006	0.003	0.001	<0.001	0.05	0.002
Powder physical properties											
Tap density [g cm <sup>-3</sup> ] ASTM B527	Carney Apparent density [g cm <sup>-3</sup> ] ASTM B417		Relative humidity [%]			Static Carney Flow test [s (150g) <sup>-1</sup> ] ASTM B964		Powders range size [μm] ASTM B822, B221, B214			
1.80	1.49		4.6%			32		20 - 63			
L-PBF Process parameters											
Atmosphere	Heated platform [°C]	Laser power [W]	Scan speed [mm s <sup>-1</sup> ]	Spot diameter [μm]	Layer thickness [μm]	Hatch distance [μm]	Energy density [J mm <sup>-3</sup> ]				
Ar, O <sub>2</sub> < 0,2 vol.%	150	350	1150	80	50	170	36				
L-PBF Scan strategy											
Bidirectional stripes scan strategy of 67° rotation between subsequent layers and a re-melted contour zone strategy at the end of each scanning											

Samples produced with L-PBF were subjected to T5 and T6R heat treatment according to the conditions optimized in section 2.3.1 and reported in Table 4.2. SHT and AA were carried out in air, in an electric furnace with temperature control of ± 5 °C.

**Table 4.2.** Heat treatment conditions for the L-PBF AlSi10Mg.

Condition	T5	T6R
<b>Heat treatment sequence</b>	(AA) at 160 °C for 4h, air cooling	(SHT) at 510 °C for 10 min, water quenching at room temperature, (AA) at 160 °C for 6 h, air cooling

The effects of thermal exposure on the T5 and T6R heat-treated alloy were evaluated by overaging (OA) curves (hardness as a function of temperature and time) at exposure temperatures ( $T_{OA}$ ) equal to 200 °C, 210 °C, and 245 °C for a soaking time ( $t_{OA}$ ) up to 48 h. The OA conditions analyze both the effects on the investigated alloy of the typical average temperatures (200 °C and 210 °C) experienced by a high-performance motorbike engine during a race [26] and the effects on the metastable microstructure of a low-temperature (245 °C) stress-relieving [27].

Brinell test (hereinafter HB<sub>10</sub>) measured hardness values with a 2.5 mm diameter steel ball and a 62.5 kgf load, according to the ASTM E10-18 standard [28]. At least five measurements were performed for each time-temperature combination, then average values and standard deviations were reported in the OA curves. A FEG-SEM (TESCAN MIRA3) equipped with energy-dispersive X-ray spectral analysis was used for microstructural analysis. Microstructural characterization was conducted on overaged conditions after 48 h of exposure time to highlight the microstructural modification induced by the investigated temperatures (200 °C, 210 °C, and 245 °C). Metallographic samples were embedded in resin, grounded and polished according to ASTM E3 [29], and chemically etched with Weck's reagent (3g NH<sub>4</sub>HF<sub>2</sub>, 4 mL HCl, 100 mL H<sub>2</sub>O) according to ASTM E407 [30]. Image analysis, aimed at determining quantitative

parameters of the Si particles present in the T6R heat-treated alloy, was carried out by the ImageJ software on 5 images at 7.5kx magnification for a total area of about  $4 \times 10^{-3} \text{ mm}^2$ , according to [31].

High-temperature ( $200 \pm 5 \text{ }^\circ\text{C}$ ) tensile tests were carried out on both T5 and T6R heat-treated alloy post-OA performed at  $210 \text{ }^\circ\text{C}$  for 41 h ( $T5_{OA}$  and  $T6R_{OA}$ ). OA conditions for tensile tests were chosen to reproduce the average operating conditions typical of racing engine heads [26]. Four round dog bone specimens for each tested condition were considered and machined from L-PBF-produced bars (Figure 4.1). The tests, at a strain rate of  $3.3 \times 10^{-3} \text{ s}^{-1}$ , were performed with a screw testing machine equipped with a resistance furnace and a high-temperature strain gauge, according to ISO 6892-1 and ISO 6892-2 [32,33]. The heating rate in the furnace reached the testing temperature ( $200 \pm 5 \text{ }^\circ\text{C}$ ) within 30 min, and the specimens were maintained at  $200 \text{ }^\circ\text{C}$  for 30 min before starting the tensile test to homogenize the temperature of the specimen. Two K-type thermocouples were placed next to the specimen in the upper and bottom zones of the calibrated gauge length to check the temperature's uniformity during the furnace's holding time. The temperature was maintained at  $200 \text{ }^\circ\text{C}$  until the failure of the sample. After the high-temperature tensile tests, the residual hardness of the samples was evaluated by five  $HB_{10}$  measurements.

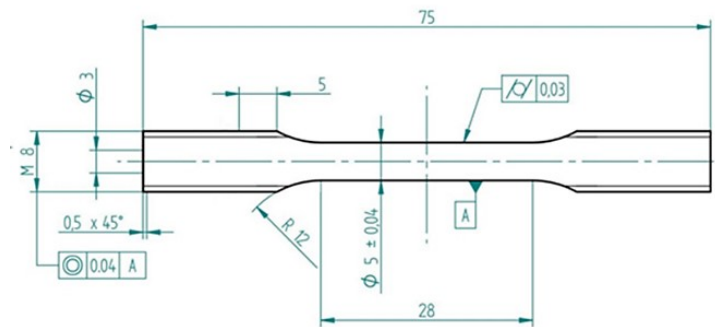


**Figure 4.1.** Tensile sample geometry (dimensions in mm). The specimens have the exact dimensions used for room-temperature tensile samples.

Results of high-temperature tensile tests were compared to room-temperature tensile and fatigue properties reported in sections 2.3.2 and 2.3.5, respectively, and to previous mechanical characterizations carried out on AlSi cast alloys [25,26]. The plastic behavior of the L-PBF AlSi10Mg alloy was described by Hollomon's equation (Equation 4.1) to study the effects of OA and high-temperature test on the strain-hardening ability of L-PBF AlSi10Mg alloy [4,39]:

$$\sigma = K \varepsilon^n \quad (4.1)$$

The elastic strain was subtracted from the total strain for calculation of the true strain according to ISO 10275:2020 standard [35]. The strength coefficient  $K$  and the hardening exponent  $n$  were evaluated using true stress-true strain data between 2% plastic strain and the percentage plastic extension at maximum force [35].

Fractographic analyses, carried out using the FEG-SEM microscope, highlighted the differences in fracture mechanisms among samples tested at room and high temperatures.

High-temperature ( $200 \text{ }^\circ\text{C}$ ) rotating bending fatigue tests ( $R = -1$ ) were performed by the staircase method according to ISO 12107:2012 [36] standard with a step size of 10 MPa to evaluate the 50% reliability endurance limit. The temperature of  $200 \text{ }^\circ\text{C}$  was held for 60 min before running the test to homogenize the sample temperature. Tests were carried out on hourglass specimens (Figure 4.2) at 33 Hz frequency setting the run-out to  $2 \times 10^6$  cycles.

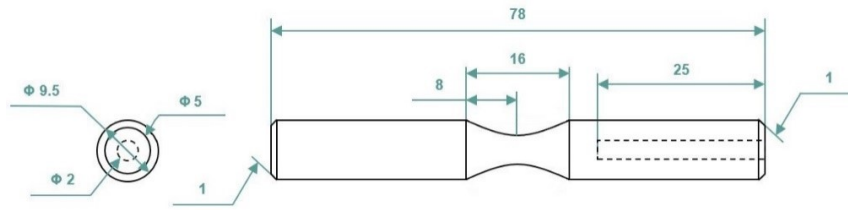


**Figure 4.2.** Shape and dimensions (mm) of the fatigue specimens. The specimens have the exact dimensions used for room-temperature tensile samples.

For each staircase, fifteen samples were tested. In bending moment controlled mode, the TP Engineering machine was used. In particular, the force was logged by a load cell, loaded via the lever arm (Figure 4.3), and converted to the applied moment.

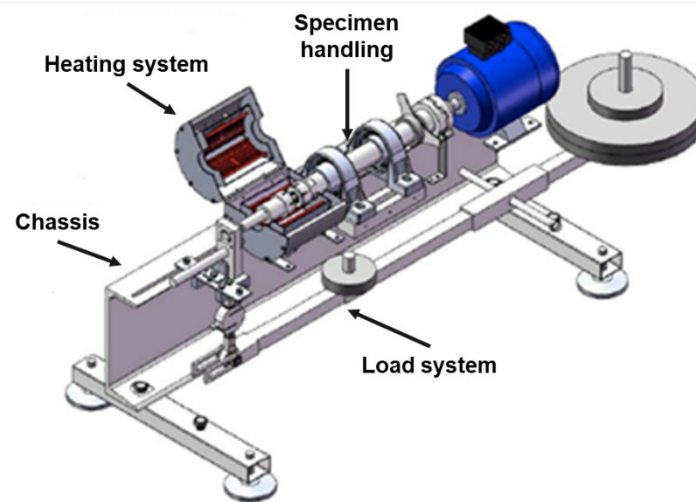


**Figure 4.3.** Scheme of the fatigue machine.

Considering the anisotropy induced by the building direction, the fatigue samples were made by the L-PBF machine with the longitudinal axis perpendicular to the platform to consider the worst-case scenario in terms of mechanical strength [37]. The gauge section of the fatigue samples was directly polished on the as-built specimen using emery paper with a mesh ranging from 250 to 2500 to obtain a smooth surface roughness. This condition is close to the production of near-net-shape components that require extremely low roughness on certain surfaces ( $R_a \approx 0.2$ ) to guarantee high tribological behavior, as described in Chapter 3, and the deposition of a protective or lubricant coating, as occurs in the deposition of the multilayer coating on the piston skirt. 3D-digital microscope (Hirox KH 7700) and FEG-SEM/EDS microscope were used to identify the dominant fracture mechanisms.

## 4.3 Results and discussion

### 4.3.1 Effects of overaging on hardness and microstructure

The effects of high-temperature exposure on the hardness of the L-PBF AlSi10Mg alloy are highlighted by the OA curves (Figure 4.4). The hardness measurements were carried out on T5 (Figure 4.4(a)) and T6R (Figure 4.4(b)) samples exposed at 200 °C, 210 °C, and 245 °C for an exposure time of up to 48 h.

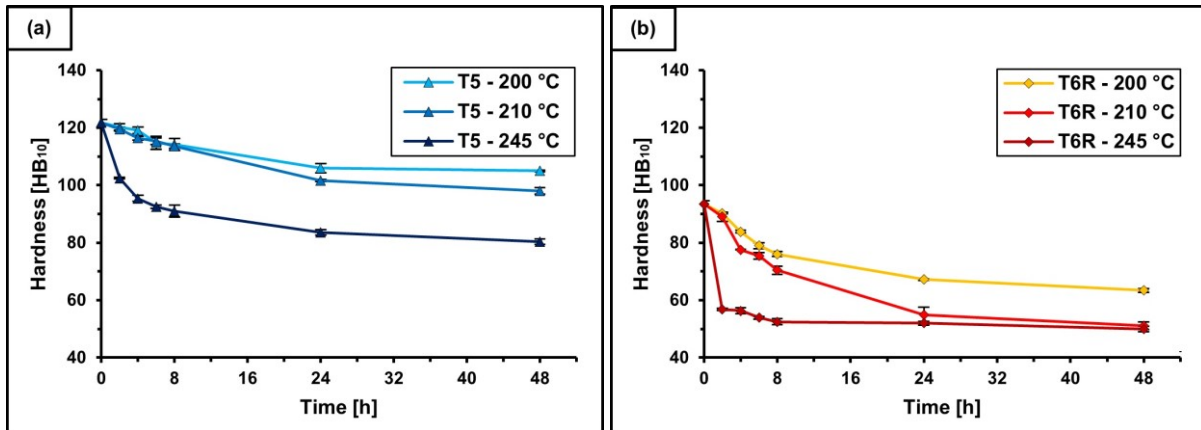


Figure 4.4. OA curves at 200 °C, 210 °C, and 245 °C for the T5 (a) and T6R alloy (b).

At 200 °C and 210 °C, the T5 alloy shows a comparable slight decrease (about 1 HB<sub>10</sub> h<sup>-1</sup>) in the first 8 h from the initial hardness (122 HB<sub>10</sub>). However, for longer exposure times (up to 48 h), the drop is more significant at 200 °C (106 HB<sub>10</sub> (- 13%)) than at 210 °C (98 HB<sub>10</sub> (- 20%)). Instead, at 245 °C, the T5 alloy reaches 91 HB<sub>10</sub> in just 8 h (- 25%), while in the following 40 h arrives at the minimum value of 80 HB<sub>10</sub> (- 35%) (Figure 4.4(a)). These different performances can be explained in light of the microstructural evolution induced by OA [39,40]. Therefore, AB and T5 microstructures before and after exposure to 200 °C, 210 °C, and 245 °C for 48 h (hereafter T5 - 200 °C, T5 - 210 °C, and T5 - 245 °C respectively) are shown in Figure 4.5.

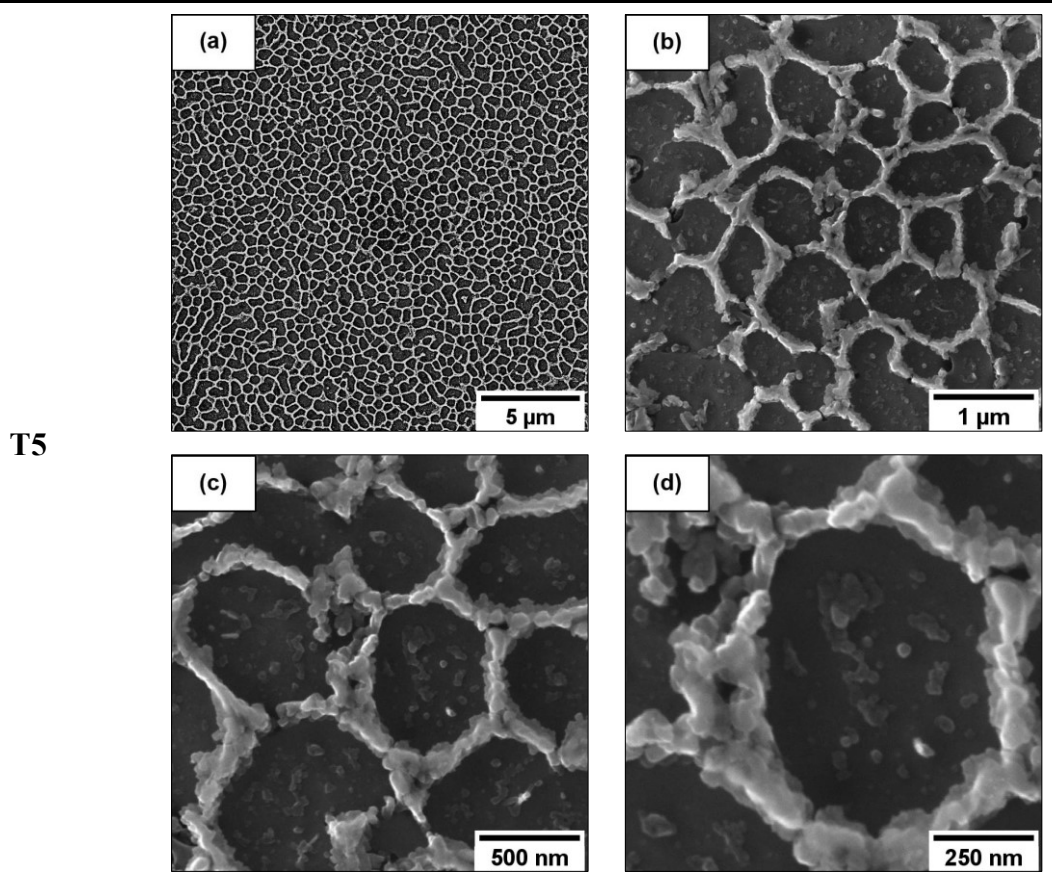
As described in Chapter 2, the T5 alloy has a microstructure comparable to the AB alloy constituted by an ultrafine sub-micrometric structure of supersaturated  $\alpha$ -Al cells surrounded by a eutectic-Si network (Figures 4.5(a,b)), resulting from the high solidification rate [40,41]. Moreover, the Si forms nano-sized precipitates inside the  $\alpha$ -Al cells [36,40] and Mg<sub>2</sub>Si precursors phases ( $\beta'$  and  $\beta''$ ) by reacting with the Mg, which mainly segregates in the intercellular network along cell boundaries [45,47]. Unfortunately, this microstructure, which provides high strength to the material, is highly metastable and, during prolonged exposure to high temperatures, evolves towards a more stable state but less performing one [20,39,42].

At low magnification (Figures 4.5(a,e,i,m)), microstructural modifications become appreciable only post-OA at 245 °C. In this case, the dissolution of the Si network leads to its complete fragmentation into numerous irregular Si-rich particles and to a consequent decrease in the strengthening effect due to the fine microstructure and presence of second phases (Figure 4.5(n)). The evolution in the microstructure, which is schematized in Figure 4.6, is close to the one observed in the L-PBF AlSi10Mg alloy subjected to SR heat treatment, generally performed at 300 °C for 1 - 2 h [18,19,44]. Furthermore, the diffusion processes of Si atoms, activated by the highest  $T_{OA}$ , lead to the coarsening of the nano-sized Si particles in the  $\alpha$ -Al matrix (Figures 4.5(o,p)).

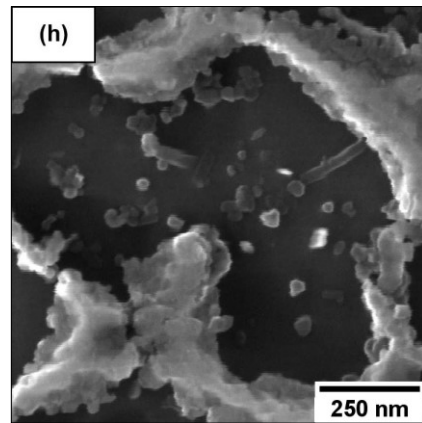
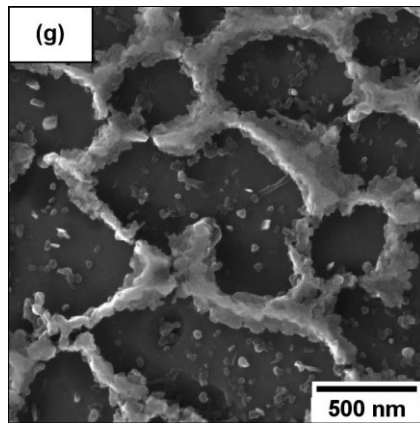
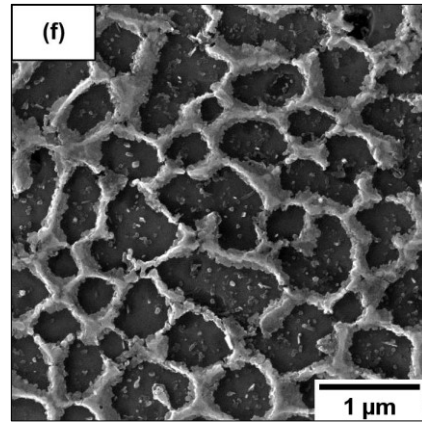
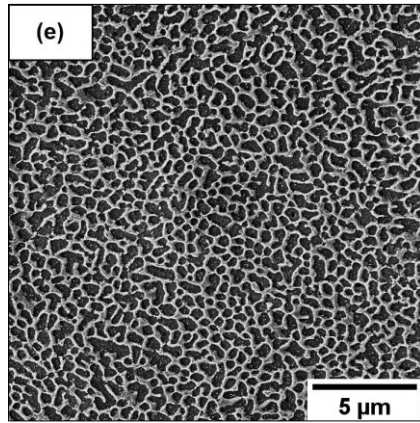
At higher magnifications, the eutectic-Si network shows microstructural evolutions starting from OA at 210 °C. Figures 4.5(k) and 4.5(l) show the initial dissolution step of the eutectic-Si network. The eutectic-Si network appears partially

fragmented, showing the Si nanoparticles anchored to the eutectic-Si network due to the activation of diffusion processes, which promotes the formation of globular Si-rich particles in the  $\alpha$ -Al matrix. During the diffusion processes, the Si atoms also move from the eutectic-Si network to the Al matrix to form new Si particles and coarse pre-existing nano-sized Si particles to minimize the internal energy of the microstructure [20,43]. As a result, the Si network begins to shrink while the Si particles continue to coalesce and develop [45]. Furthermore, the diffusion processes of Si atoms from the supersaturated  $\alpha$ -Al cells contribute to further Si particle coarsening. This aspect of the eutectic-Si network is not detected in the alloy overaged at 200 °C (Figures 4.5(g,h)), where the Si network has a homogeneous and smooth structure, similar to the T5 condition (Figures 4.5(c,d)). However, despite the different morphology of the eutectic-Si network between the alloy overaged at 200 °C and 210 °C (Figures 4.5(b,f,j,n)), the micrographs show a similar density of Si particles within the  $\alpha$ -Al cells, confirming that the diffusion of Si atoms from the eutectic-Si network and the Al lattice took place also at 200 °C [38,39,46]. The higher diffusion rate in the T5 - 245 °C alloy promotes the coarsening of the nano-sized Si particles larger than those observed in the T5 - 200 °C and T5 - 210 °C conditions.

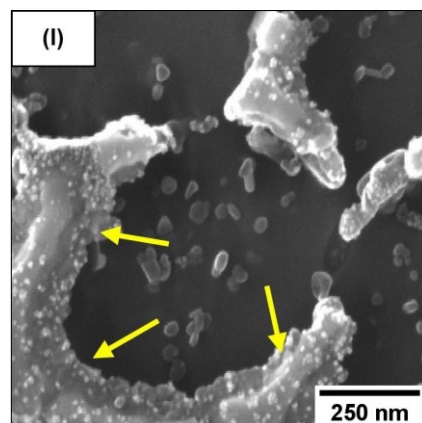
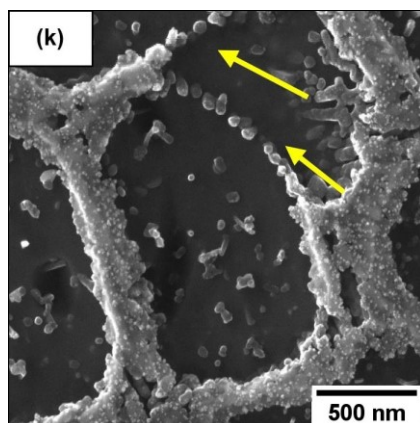
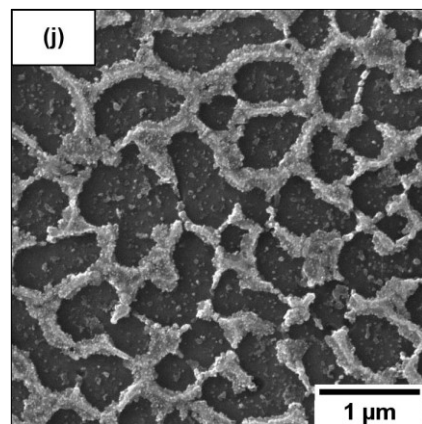
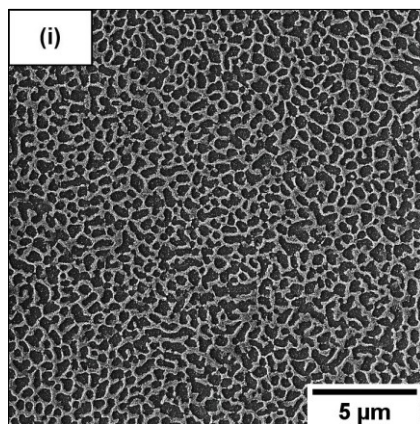
A deep understanding of the effect of the OA on both Si and Mg<sub>2</sub>Si strengthening precipitates may be provided only by performing TEM analyses. However, several authors agree that prolonged exposure at high temperatures of heat-treated Al cast alloys [6,7,23,25,26] and heat-treated L-PBF AlSi10Mg alloy [19,46,47] generates a diffusion-driven phenomenon governed by the Ostwald ripening mechanism, which can induce a rapid coarsening of the reinforcing precipitates. This process leads to a microstructure containing larger but fewer precipitates that offer less contribution to alloy strengthening and hardness due to: (i) the reduction of the precipitate/matrix interfacial area; (ii) the lower density of obstacle to dislocation motion, and (iii) the loss of coherence between the strengthening precipitates and  $\alpha$ -Al matrix.



T5 - 200 °C



T5 - 210 °C



T5 - 245 °C

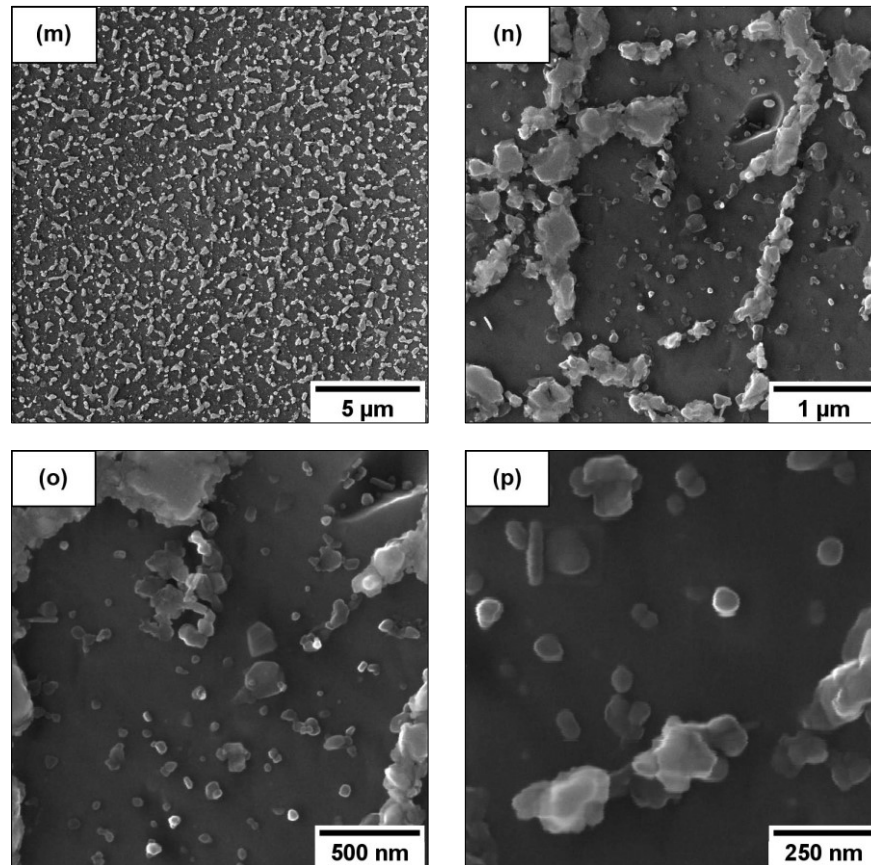


**Figure 4.5.** Microstructures of the T5 alloy: before OA (a) (b) (c) (d), T5 - 200 °C condition (e) (f) (g) (h), T5 - 210 °C condition (i) (j) (k) (l), T5 - 245 °C condition (m) (n) (o) (p). Yellow arrows in (k) and (l) show the Si nanoparticles anchored to the eutectic-Si network due to the activation of diffusion processes, which promoted the formation of spherical Si-rich particles in the  $\alpha$ -Al matrix.

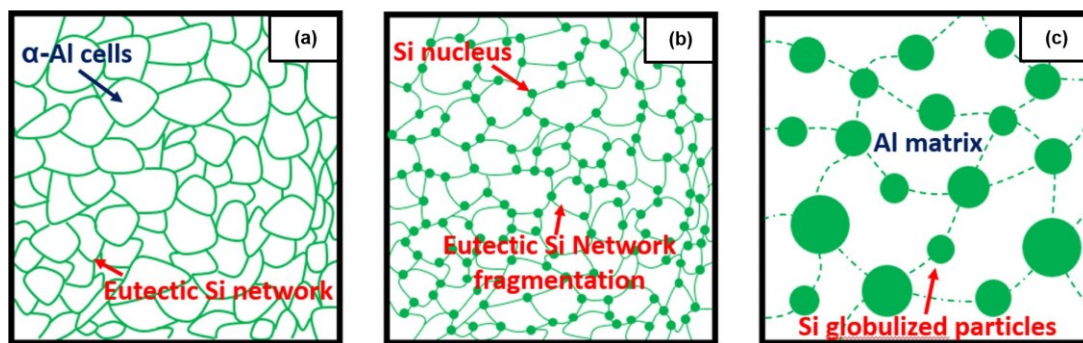


**Figure 4.6.** Scheme of the microstructural evolution of the T5 alloy during high-temperature exposure: before OA, the continuous eutectic-Si network surrounds the sub-micrometric cells of supersaturated  $\alpha$ -Al phase (a); during the first phases of thermal degradation, fragmentation of the eutectic-Si network and the consequent formation of the first Si nucleus occur (b); as the thermal exposure continues, coarsening of the first Si nucleus brings to the formation of the Si particles embedded into the  $\alpha$ -Al matrix (if  $T_{OA}$  and  $t_{OA}$  are sufficient) (c).

The T6R alloy (Figure 4.4(b)) shows a significant decrease in hardness for all the investigated OA temperatures equal to 19% at 200 °C, 25% at 210 °C, and 44% at 245 °C. In the latter case, this decrease mainly occurs after the first 2 h; the residual hardness after 2 h of OA is 57 HB<sub>10</sub>, close to the minimum value of 51 HB<sub>10</sub> measured after 48 h. It is also worth noting the different trends of the OA curves evaluated at 200 °C and 210 °C. They show a comparable decrease in hardness of about 2.2 - 2.9 HB<sub>10</sub> h<sup>-1</sup> up to 8 h, but a significant difference for longer soaking times. Specifically, at 200 °C, the T6R alloy decreases hardness from 8 h to 48 h by about 17%, with a minimum of 63 HB<sub>10</sub>. Instead, at 210 °C, it shows a hardness drop from 8 h to 48 h of about 27 %, with a minimum of 51 HB<sub>10</sub>. In particular, at 210 °C, a hardness value (55 HB<sub>10</sub>) very close to the residual hardness at 48 h (51 HB<sub>10</sub>) is reached after 24 h.

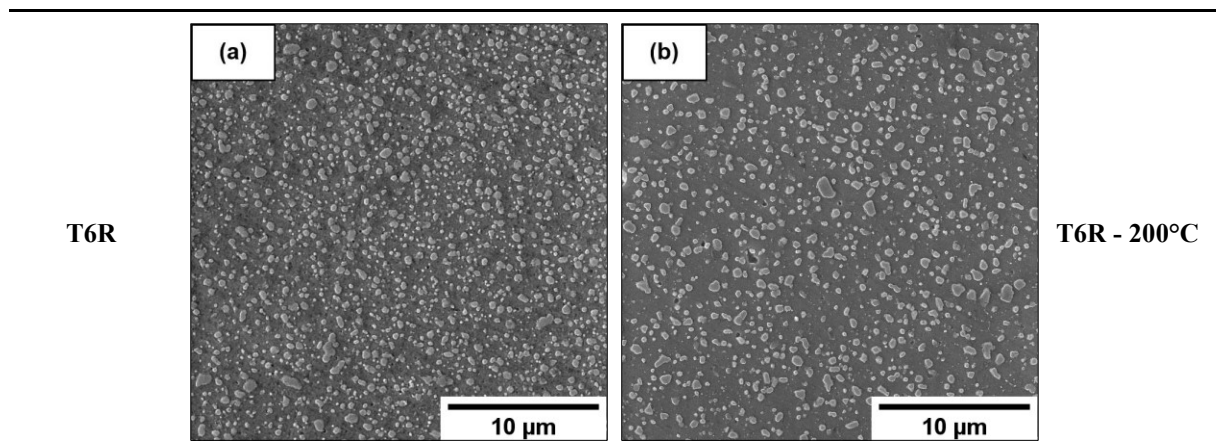
The SEM metallographies of the T6R alloy before and post-OA at 200 °C, 210 °C, and 245 °C for 48 h (hereafter T6R - 200°C, T6R - 210°C, and T6R - 245°C, respectively) are reported in Figure 4.7 to evaluate the effects of the OA conditions on the microstructure.

The microstructure of the T6R alloy consists of a composite-like microstructure of Si-rich particles embedded into the  $\alpha$ -Al matrix (Figure 4.7(a)). During the SHT step, two different solid-state diffusion-driven mechanisms lead to the fragmentation of the eutectic-Si network, the spheroidization of Si, and the coarsening of the nano-Si precipitates, i.e., (i) the surface self-diffusion, in which the atoms move by surface diffusion, and (ii) the interdiffusion at the Al/Si interface, in which the Si atoms move through the Al matrix [43]. In addition, during the AA step, the precipitation of both  $\beta''$  and  $\beta'$  strengthening phases (precursors of the  $Mg_2Si$  equilibrium phase) occurs, introducing the precipitation hardening [41,47]. Therefore, the OA could have two main effects on the microstructure: (i) modification of the size of the Si particles developed during the SHT [14,20,45], and (ii) coarsening of the  $Mg_2Si$  coherent precipitates obtained during the AA [11,43,48].

In the T6R - 200 °C alloy, negligible modification in the Si particle size and distribution (Figures 4.8(a,b)) is visible, as also confirmed by the Si inter-particle spacing (Table 4.3). Instead, despite the low increase in the  $T_{OA}$ , the T6R - 210 °C alloy (Figure 4.7(c)) shows a remarkable increase (about 14%) in the Si particle size (Figure 4.8(a)), a decrease in the number of particles per unit area of about 18% (Figure 4.8(b)) and an increase in the Si particles inter-spacing of about 9% (Table 4.3) if compared to the T6R alloy before OA. As expected, the effect of the OA on the microstructure is more evident in the T6R - 245 °C condition. The higher  $T_{OA}$  leads to an increase of the Si particle size of about 21% (Figure 4.8(a)), a decrease in the number of Si particles per unit area of about 32% (Figure 4.8(b)), and an increase of the Si particles inter-spacing of only about 14% (Table 4.3).

Although the coalescence of the Si particles can be easily observed using microstructural analyses, its effect on the hardness of the T6R alloy is negligible compared to the coarsening of the strengthening precipitates. In fact, in section 2.3.1.4, the increase of the Si particle size up to 300% from the T6R condition to the T6B condition, both under peak aging conditions, led to a decrease in the hardness of the alloy by only 3%.

Therefore, the decrease in hardness of the overaged T6R alloy is probably mainly due to the coarsening of the  $Mg_2Si$  strengthening precipitates. The OA curves and the higher hardness of the T6R - 200°C condition suggest that the thermal exposure at 210 °C for 24 h or at 245 °C for 8 h provides the thermal energy needed to complete the formation of incoherent  $\beta$ - $Mg_2Si$  phase, while at 200 °C only a partial coarsening of the strengthening precipitates occur, even after 48 h.



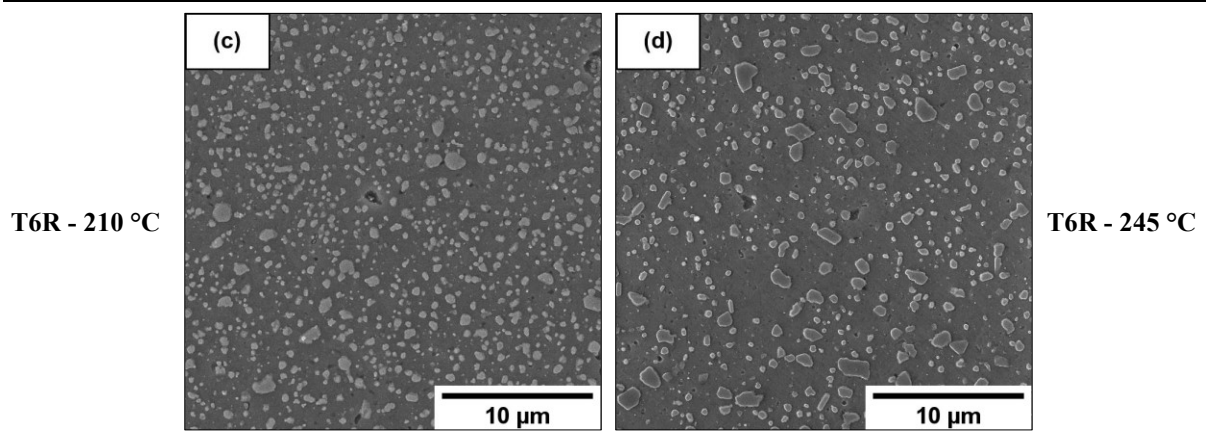


Figure 4.7. Si particle characterization of the T6R alloy evaluated: before OA (a), post-OA at 200 °C (b), 210 °C (c), and 245°C (d) for 48 h.

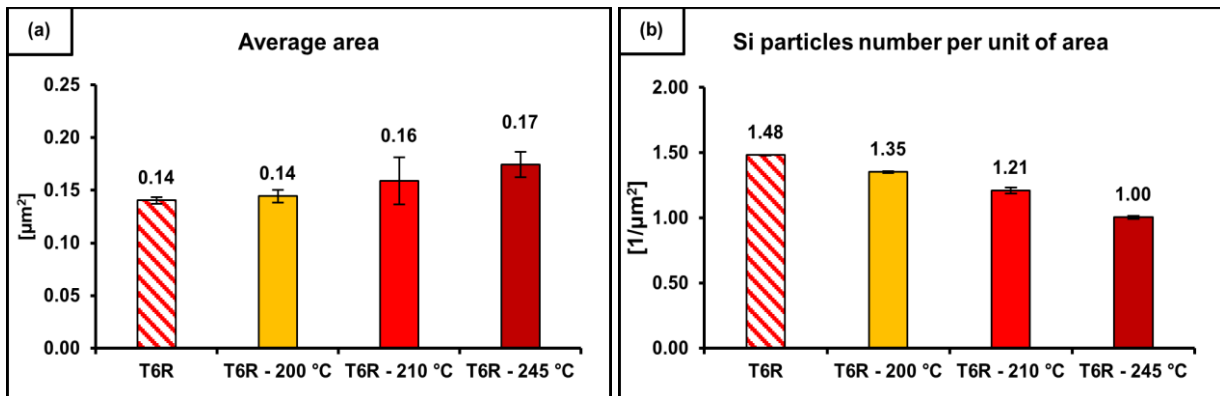


Figure 4.8. Effects of OA (200 °C, 210 °C, and 245 °C for 48 h) on the T6R alloy: Si particle average area (a) and number of Si particles per unit of area (b).

Table 4.3. Inter-particle spacing ( $\lambda$ ) and inter-particle spacing variation ( $\Delta\lambda$ ) compared to the T6R alloy for the different OA conditions.

Condition	$\lambda$ [ $\mu\text{m}$ ]	$\Delta\lambda$ [ $\mu\text{m}$ ]	Percentage increase
T6R	$0.57 \pm 0.02$	-	-
T6R - 200°C	$0.58 \pm 0.01$	0.01	1.8%
T6R - 210°C	$0.62 \pm 0.03$	0.05	8.8%
T6R - 245°C	$0.65 \pm 0.04$	0.08	14.0%

In summary, for the same  $T_{OA}$  and  $t_{OA}$  conditions, the T5 alloy shows a lower hardness decrease than the T6R alloy. Therefore the sub-micrometric cellular structure of the T5 alloy appears to be more capable of hindering the dislocation motion even after long thermal exposure than the composite-like microstructure of the T6 alloy, which extensively undergoes the coarsening of the strengthening precipitates induced by OA.

### 4.3.2 Static mechanical characterization

The tensile tests were performed at 200 °C on overaged (210 °C for 41 h) samples to compare the results of the tests with the experimental data of previous mechanical characterizations carried out by the authors on Al cast alloys [23-26,51]. The results of tensile tests at room (T5 - RT and T6R - RT condition) and high temperature (T5<sub>OA</sub> - 200T and T6R<sub>OA</sub> - 200T condition) carried out on the L-PBF AlSi10Mg alloy are compared in Figure 4.9. Hardness measurements were carried out on all specimens after tests. Representative engineering stress-strain curves and corresponding true stress-true strain curves are reported in Figure 4.10.

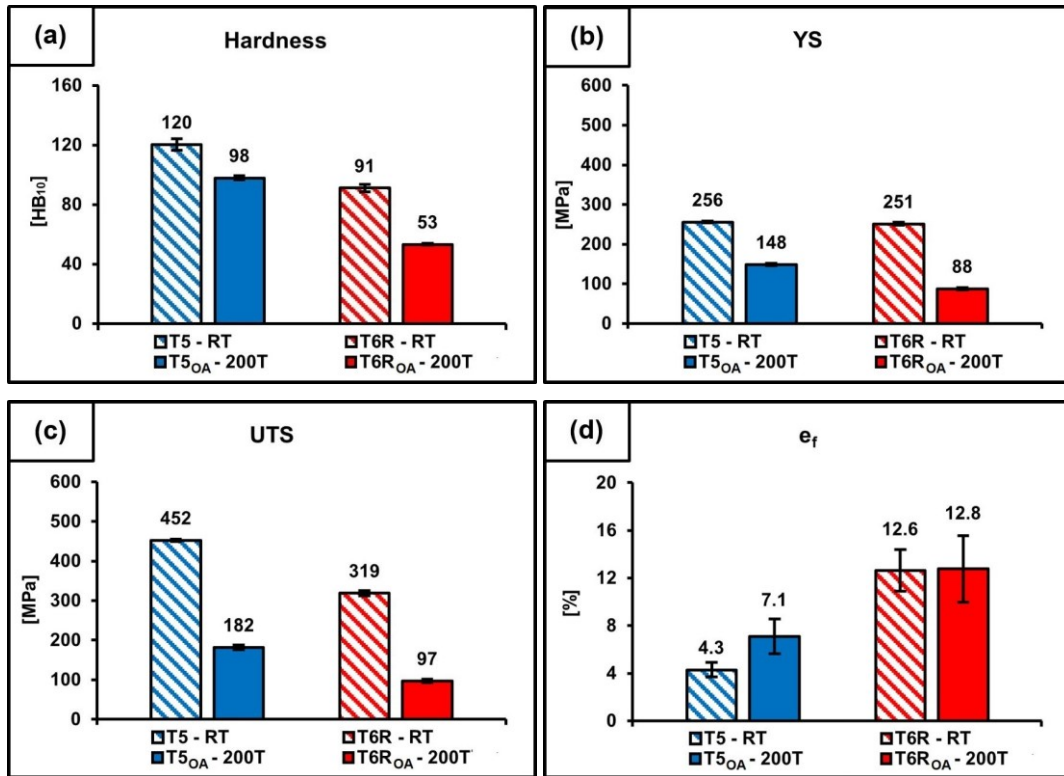
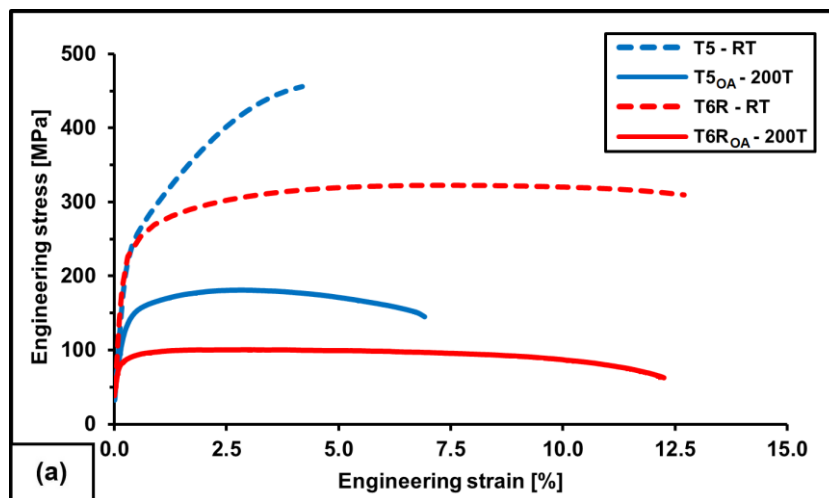
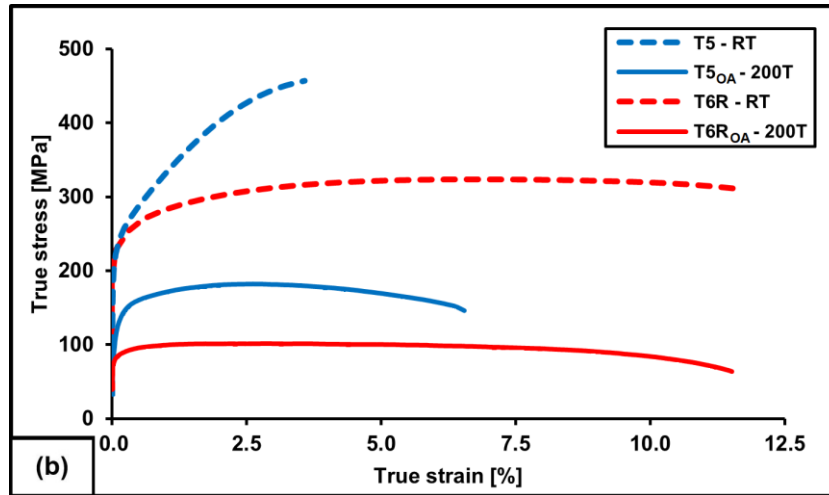


Figure 4.9. Hardness (a) and tensile properties (YS (b), UTS (c), and e<sub>f</sub>(d)) of the T5 and T6R alloys tested at (i) room temperature (T5 - RT and T6R - RT) and (ii) high temperature (T5<sub>OA</sub> - 200T and T6R<sub>OA</sub> - 200T) after overaging (OA).





**Figure 4.10.** Representative engineering stress-strain curves (a) and true stress-true strain curves (b) of the T5 and T6R alloys tested at (i) room temperature (T5 - RT and T6R - RT) (dashed lines) and (ii) high temperature (T5<sub>OA</sub> - 200T and T6R<sub>OA</sub> - 200T) (solid lines). The elastic strain was subtracted from the total strain for calculation of the true strain according to ISO 10275:2020 standard [35].

As expected, the specimens overaged and tested at 200 °C show a significant decrease in YS, UTS, and hardness values compared to the RT condition of about 42%, 60%, and 18% for the T5<sub>OA</sub> - 200T condition and 65%, 70%, and 42% for the T6R<sub>OA</sub> - 200T condition, respectively. Conversely, the  $e_f$  shows a significant increase (about 65%) for the T5<sub>OA</sub> - 200T samples but a negligible increase for the T6R<sub>OA</sub> - 200T samples.

According to the microstructural analyses of the overaged samples (Figure 4.5), the decrease in tensile properties (YS and UTS) for the T5<sub>OA</sub> - 200T condition is mainly due to: (i) the partial or total fragmentation of the eutectic-Si network, (ii) the coarsening of the strengthening precipitates (nano-sized Si precipitates and precursors of the Mg<sub>2</sub>Si equilibrium phase), and (iii) the reduction of Si atoms in solid solution. Change in the strengthening mechanisms leads to a decrease in strength and an increase in ductility consequent to the reduction of the pinning effects on the dislocation motion. Moreover, during the high-temperature tensile test, softening of the Al matrix occurs, resulting in a decrease in the activation energy for the dislocation motion and an increase in the number of activated sliding planes. This phenomenon stimulates the dislocation motion by climbing and gliding, leading to increased ductility [49,51].

For the T6R<sub>OA</sub> - 200T condition, the loss of efficiency of the precipitation hardening is the leading cause of the decrease in YS, UTS, and hardness values. Conversely, the negligible effect of the OA and high temperature on the  $e_f$  is probably attributable to an inhomogeneous and localized plastic deformation of the  $\alpha$ -Al matrix that, from a macroscopic point of view, does not lead to an increase in the uniform deformation as observed in the T5<sub>OA</sub> - 200T condition. This aspect will be described in the following sections concerning the plastic behavior of the material and the fracture surface analyses.

The T5 and T6R alloys show a different mechanical behavior evidenced both by the work-hardening exponent (Figure 4.11), which was assessed by the true stress-true strain curves in Figure 4.10(b), and the analysis of the elastic, plastic, and necking fields (Figure 4.12), which was evaluated by the engineering stress-strain curves (Figure 4.10(a)).

Engineering stress-strain curves, as it is well-known, can be divided into three fields: elastic (up to YS), plastic (uniform strain) from YS to UTS, and necking (localized strain) from UTS to failure (Figure 4.12(a)). The stress-strain ratio increases linearly in the elastic range until the dislocation slip. Due to dislocations' interactions, uniform plastic deformation and work-hardening occur until necking [36]. The difference in the extension of these three regions of the tested samples is shown in Figure 4.12(b) as the ratio between the single strain field and the total strain field.

In the T5 - RT samples, necking is substantially absent (Figures 4.10(b) and 4.12(b)). In particular, the high percentage of uniform elongation compared to the total elongation (85%) is evidence of the high strain-hardening ability (Figure 4.11). As described by Considère's criterion [41], strain-hardening delays the localized deformation and, therefore, the necking phenomenon. In the T5 - RT samples, failure occurs during the strain-hardening phase and before necking due to the high dislocation density and defects (gas porosities or LoF) [41,52,53]. Conversely, the T6R - RT condition shows a low strain-hardening value (Figure 4.11) and a significant tendency to necking (Figures 4.10(b) and 4.12(b)). The microstructure of the T6R samples is, in fact, less effective in hindering the dislocation motion than the microstructure of the T5 ones, thus inducing lower n-index values [39].

The T5<sub>OA</sub> - 200T and T6R<sub>OA</sub> - 200T conditions are characterized by: (i) lower n-index values than T5 - RT and T6R - RT ones, with a reduction of 77% and 80%, respectively (Figure 4.11); (ii) higher necking, with an increase of 55% and 76% of the total strain field, respectively (Figure 4.12(b)). The combined effects of OA and high temperature applied during the tensile test modify the plastic deformation mechanisms. They increase the localized deformation phenomenon because of (i) the thermal softening of the  $\alpha$ -Al matrix occurring at high temperatures, (ii) the increase of vacancies by diffusion phenomena, and (iii) the loss in efficiency of the strengthening mechanisms [36,54,55].

However, the T5<sub>OA</sub> - 200T condition also preserves a significant strain-hardening ability, thanks to the action of the ultrafine cellular structure still present at high temperatures (Figure 4.5(i)) [42], while the T6R<sub>OA</sub> - 200T condition loses almost wholly the strain-hardening ability due to the reduction of the strengthening effect, mainly of Mg<sub>2</sub>Si precipitates, induced by the high temperature [21,24,36].

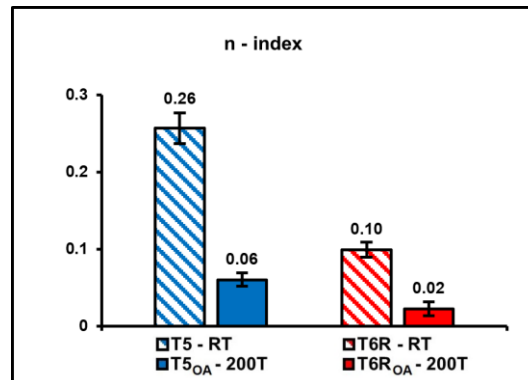


Figure 4.11. Work-hardening exponent evaluated for the T5 and T6R alloys tested at room temperature (T5 - RT and T6R - RT) (i) and high temperature (T5<sub>OA</sub> - 200T and T6R<sub>OA</sub> - 200T) (ii).

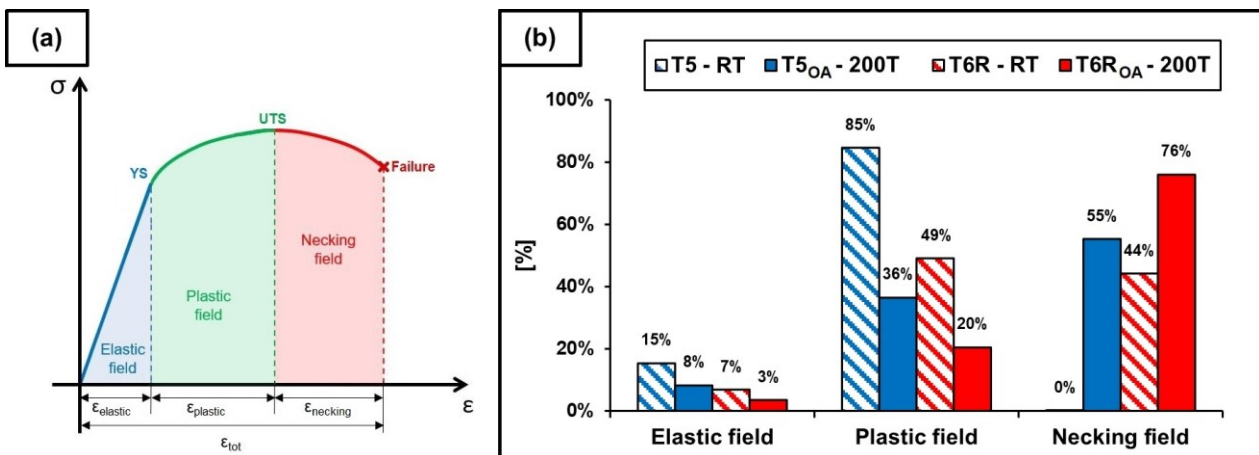


Figure 4.12. Schematic subdivision in the engineering stress-strain curves of the total strain ( $\epsilon_{tot}$ ) into elastic ( $\epsilon_{elastic}$ ), plastic ( $\epsilon_{plastic}$ ), and necking ( $\epsilon_{necking}$ ) fields (a). Percentage sub-division of the stress-strain curves into elastic, plastic, and necking fields for the T5 and T6R alloys tested at room temperature (T5 - RT and T6R - RT) and high temperature (T5<sub>OA</sub> - 200T and T6R<sub>OA</sub> - 200T) (b).

At low magnification, the fracture surfaces of the T5 - RT and T5<sub>OA</sub> - 200T samples show similar fracture morphology (Figures 4.13(a,b,e,f)), consisting of (i) interlayer fracture path at the eutectic-Si network/Al matrix interface, (ii) presence of defects, in particular gas pores, and (iii) flat fracture morphology in correspondence of the scan-track segments [18]. However, the effects promoted by OA and thermal exposure during the tensile test, including the softening of the Al matrix and the lower cohesion between the Al matrix and the eutectic-Si network, determine more remarkable plasticity of the alloy and the formation of larger dimples in correspondence to the discontinuities within the eutectic-Si network [26,36,48].

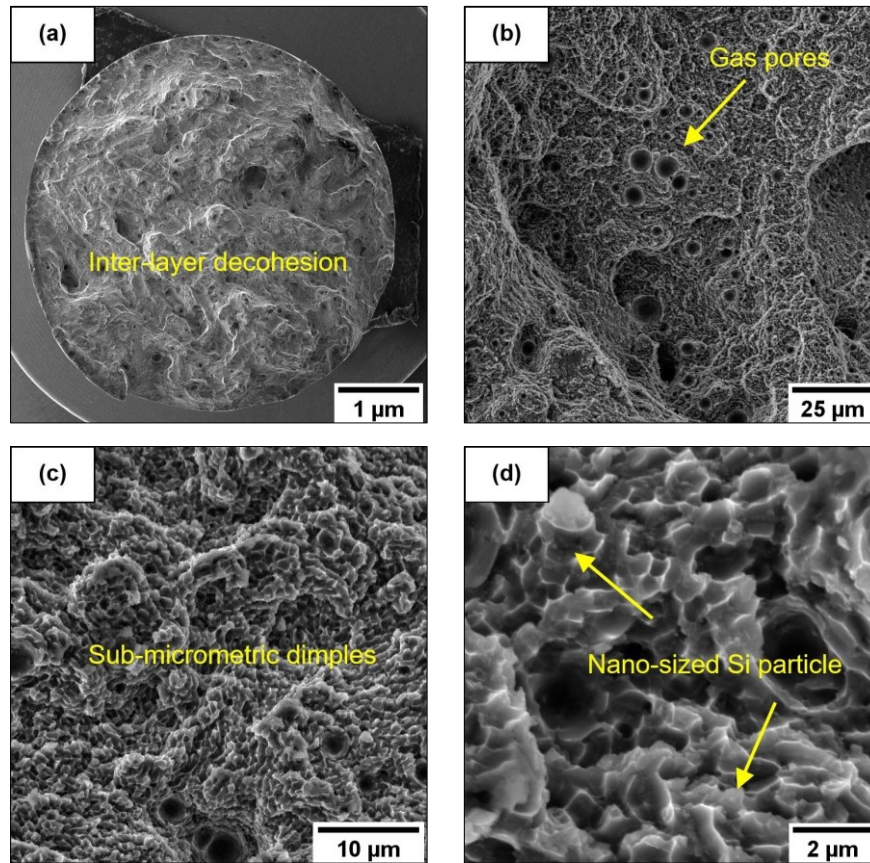
At higher magnification (Figures 4.13(c,d,g,h)), the T5 - RT and T5<sub>OA</sub> - 200T samples show shallow micro and sub-micrometric dimples, reflecting the sub-cellular microstructure. Where the eutectic-Si network is continuous and not fragmented, the microstructure is more effective in hindering dislocation slip and reducing the plastic deformation area [55], with the consequent development of small dimples, whose sizes are proportional to the secondary phase spacing [56]. A partially fragmented and coarsened cellular structure and material softening lead to the formation of larger dimples, as observed in the T5<sub>OA</sub> - 200T samples. To explain this fracture behavior, it is worth noting that the void initiation at the Si network/ $\alpha$ -Al cell interface is an energetic process where a threshold value of work “W” is necessary to create the crack between the aggregated second phase and the Al matrix. W depends on three factors: the surface energy of the matrix  $\gamma_{Al}$ , the surface energy of the aggregate second phase  $\gamma_{Si}$ , and the interface energy  $\gamma_{Al-Si}$  (Equation 4.2) [52].

$$W \propto \gamma_{Al} + \gamma_{Si} + \gamma_{Al-Si} \quad (4.2)$$

The eutectic-Si network dissolution occurring at high temperatures induces the increase of the strain field in the proximity of the second phase, which is due to the difference in the lattice parameters between Si and Al, and the loss of coherency with the matrix [50,52]. Those two phenomena increase  $\gamma_{Al-Si}$ , thus reducing the work necessary to nucleate a void at the  $\alpha$ -Al matrix/second phase interface.

The effectiveness of this microstructure at high temperatures explains the lower percentage decrease in strength properties of the T5<sub>OA</sub> - 200T compared to the T6R<sub>OA</sub> - 200T samples. At the same time, the local increase in plastic flow at the  $\alpha$ -Al matrix/eutectic-Si network interface, and in particular around the fragmented zones where larger dimples are present (Figures 4.13(e,f)), is likely the cause of the necking phenomenon and increase in the  $e_f$  value for the T5<sub>OA</sub> - 200T condition compared to the T5 – RT reported in the previous section.

T5 - RT



T5<sub>0A</sub> - 200T

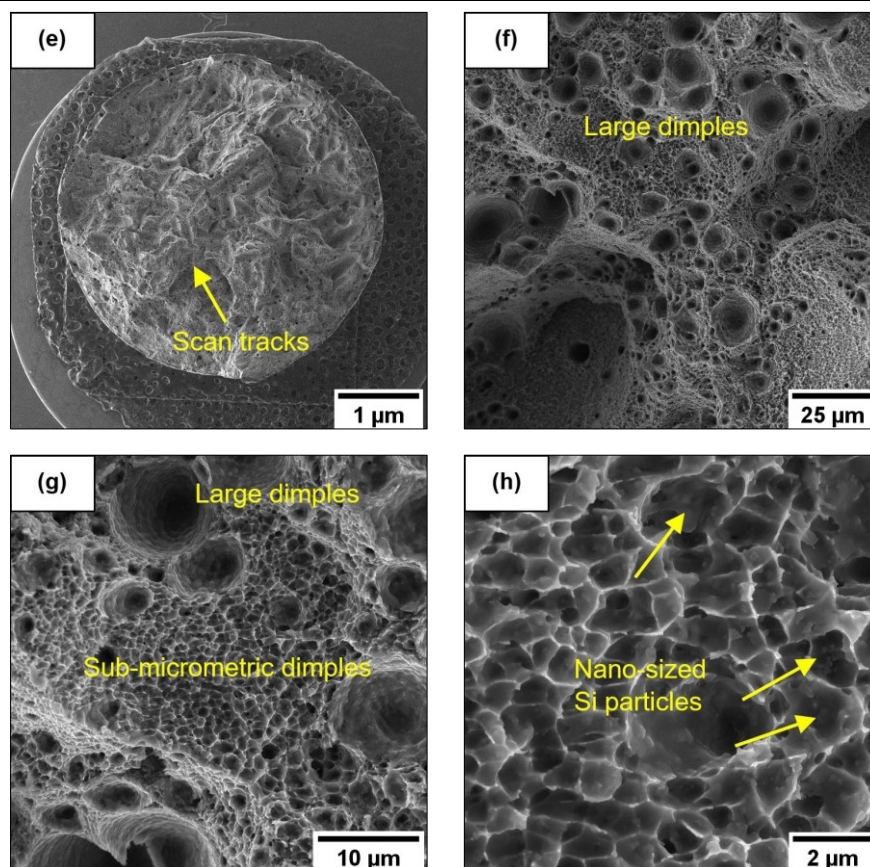
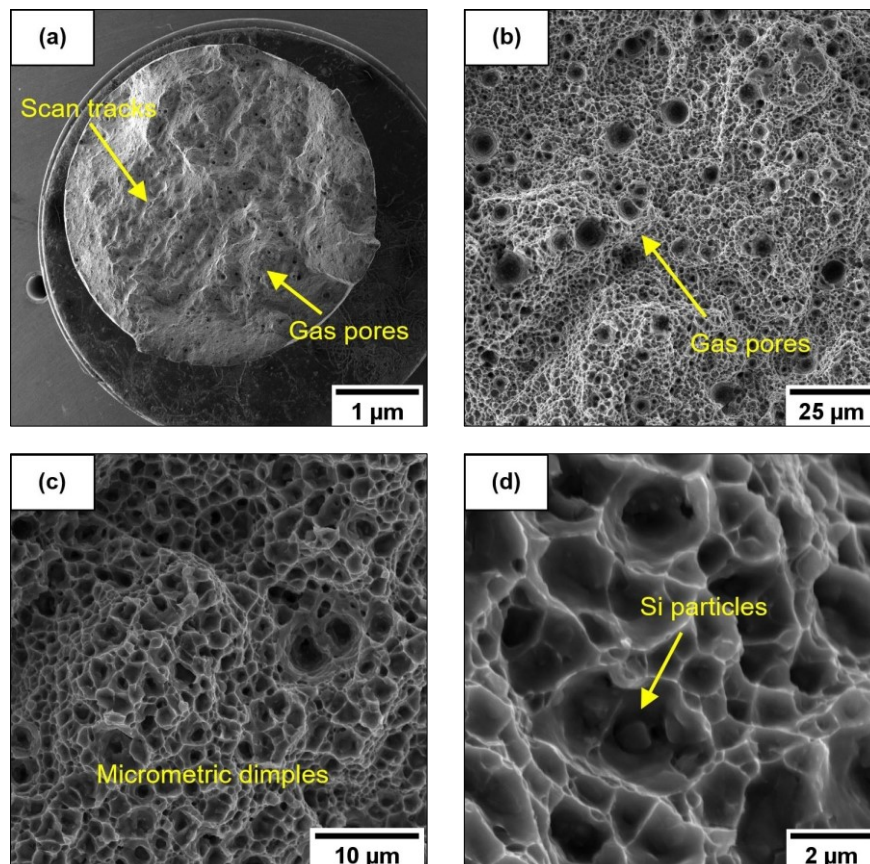


**Figure 4.13.** FEG-SEM images of the fracture surfaces of the T5 - RT and T5<sub>0A</sub> - 200T samples at different magnifications: 40x (a) (e), 1.50kx (b) (f), 5.00kx (c) (g), and 20.0kx (d) (h), respectively.

The T6R - RT and T6R<sub>OA</sub> - 200T samples at low magnification (Figures 4.14(a,b,e,f)) exhibit a higher gas pore density on the fracture surfaces compared to the T5<sub>OA</sub> - 200T and T5 - RT conditions, probably due to the effects of the SHT [57]. The T6R - RT samples show scan tracks on the fracture surfaces, which are not detected on the T6R<sub>OA</sub> - 200T ones due to the irregular morphology induced by the necking.

For both the T6R - RT and the T6R<sub>OA</sub> - 200T samples, the fracture propagates by joining gas pores and the voids present at the Si particles/ $\alpha$ -Al matrix interface with the mechanism described for the T5<sub>OA</sub> - 200T samples and also reported in Chapter 2. The morphology, size, number, and distribution of the Si particles strongly influence the decohesion phenomena and the size and depth of the dimples (Figures 4.14(c,d,g,h)) [58,59]. The coarsening of Si particles and the material softening leads to larger dimples in the T6R<sub>OA</sub> - 200T condition than in the T6R - RT condition. The effect of the large Si particles on the local plastic deformation of the alloy can be observed in Figures 4.14(g) and 4.14(h); these clearly show the plastic flow of the matrix around the Si particles located at the center of the dimples. The formation of larger dimples in the T6R<sub>OA</sub> - 200T may explain the negligible increase in  $\epsilon_f$  of the T6R<sub>OA</sub> - 200T compared to T6R - RT samples, despite the softening of the matrix [59]. The deformation in the T6R<sub>OA</sub> - 200T samples is not homogeneous and concentrated around the largest Si particles due to the higher local plastic flow (Figure 4.14(e)) [33,50]. This process promotes a non-homogeneous deformation of the material, highlighted by the necking phenomena and a decrease in uniform deformation, as evidenced by the data shown in Figure 4.12.

T6R - RT



T6R<sub>OA</sub> - 200T

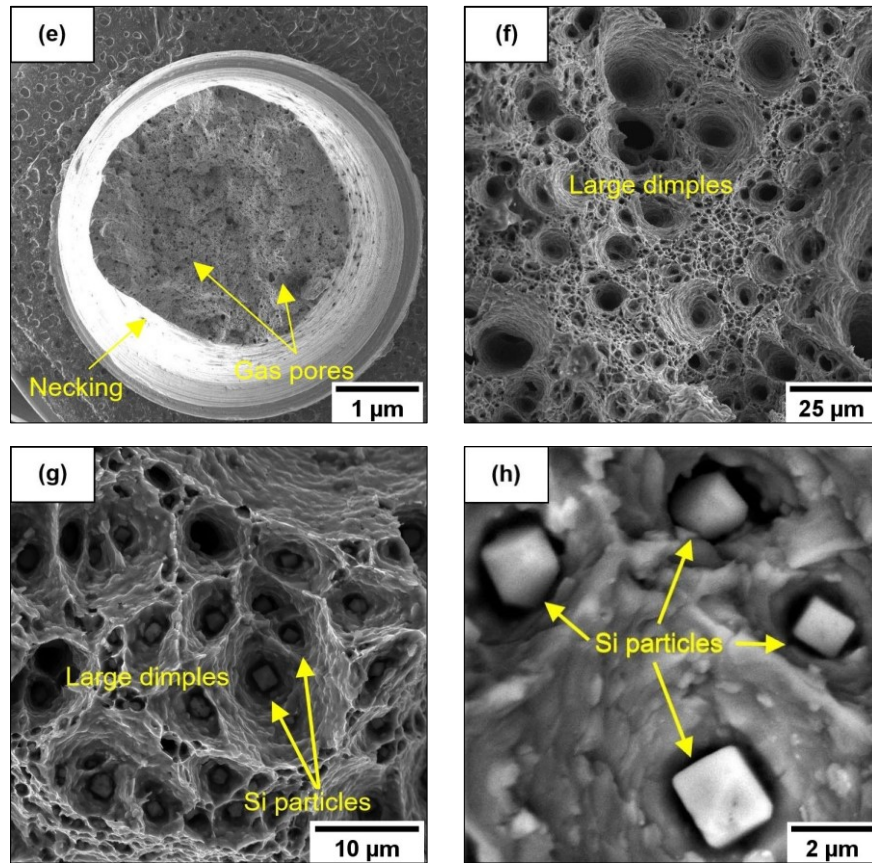


**Figure 4.14.** FEG-SEM images of the fracture surfaces of the in T6R - RT and T6R<sub>OA</sub> - 200T samples at different magnifications: 40x (a) (e), 1.50kx (b) (f), 5.00kx (c) (g), and 20.0kx (d) (h), respectively.

### 4.3.3 Cyclic mechanical characterization

Several structural components in the transportation industry undergo high-temperature cyclic loads over a wide range of temperature distribution and mechanical load conditions [60]. In particular, thin-walled and lattice structures produced by the L-PBF technology and introduced to reduce weight in aerodynamic components and thermal systems must be able to withstand high-temperature fatigue stresses caused by the severe operating conditions to meet the durability requirements of applications up to 200 °C [61,62].

Farkoosh et al. [63] found that under specific operating conditions involving cyclic heating-cooling loads, the materials used should be characterized by an optimal balance between strength and ductility to avoid premature failures. Despite the remarkable room-temperature mechanical performance of the L-PBF AlSi10Mg alloy described in Chapter 2, the progressive loss of the strengthening mechanisms above 200 °C and consequent drop of the mechanical properties of the T5 and T6R alloys at high temperatures (described in section 4.3.2) make it necessary to assess the fatigue behavior of the alloys at high temperature.

In light of the possible application of L-PBF components in combustion engines, it was decided to simulate the typical average temperature operating conditions of a racing engine head [26], and therefore the fatigue tests were performed at 200 °C. The YS value drops by approximately 42% and 65%, and the UTS value by approximately 60% and 70% for the T5<sub>OA</sub> - 200T and T6R<sub>OA</sub> - 200T conditions, respectively. Considering the effect of overaging on the high-temperature tensile properties of the L-PBF AlSi10Mg alloy is essential due to the testing duration of the fatigue tests and the long soaking time at high temperatures. In particular, the loss of efficiency of the strengthening mechanisms in these operating conditions, such as those induced by aggregated second phase and precipitation hardening for the T5<sub>OA</sub> - 200T alloy and dispersed second phase and precipitation hardening for the T6R<sub>OA</sub> - 200T alloy, are the leading causes of the decrease in strength properties. The softening of the Al matrix at 200 °C involves a decrease in the activation energy for the dislocation motion, stimulating climbing and gliding relative to pile-up phenomena, and therefore induces an increase in the  $\epsilon_f$ . However, only the T5<sub>OA</sub> - 200T alloy is subjected to an increase in  $\epsilon_f$  (about 65%), while the T6R<sub>OA</sub> - 200T alloy shows values comparable to the T6R - RT alloy tested at room temperature. The inhomogeneous and localized plastic deformation of the  $\alpha$ -Al matrix, which, from a macroscopic point of view, leads to a decrease in uniform deformation and premature failure of the samples, is probably the leading cause of this phenomenon.

The fatigue test results are reported in Figure 4.15: at 200 °C, the fatigue strength at  $2 \times 10^6$  cycles at 50% survival probability ( $\sigma_{fs}$ ) equals  $74 \pm 11.7$  MPa for the T5 - 200T and  $91 \pm 4.4$  MPa for the T6R - 200T (Figure 4.16) and the detrimental effect of high temperature is evident, considering a decrease of the fatigue strength of 20% and 15%, respectively. As described in section 2.3.5 for the tests carried out at room temperature, the microstructure of the T5 alloy appears less effective in hindering crack initiation. Moreover, its lower ductility and higher inhomogeneity at 200 °C, compared to the T6 alloy, lead to a high deviation of  $\sigma_{fs}$  value.

However, the ultrafine sub-micrometric structure of the T5 - 200T alloy and the composite-like microstructure of the T6R - 200T alloy appear more prone to withstand crack nucleation and propagation during cyclic loading at high temperatures than during static loading. The negative effect of high temperatures is less evident on the fatigue strength than on the static mechanical properties, particularly for the UTS value, which is strongly affected by the softening of the Al matrix and the more effortless dislocation motion (section 4.3.4).

The metallic material deformation mechanisms are strongly affected by temperature [50]. In the T5 - 200T alloy, under tension-compression cyclic loading, the dislocation density rises with the increase of loading cycles, and this leads to dislocation pile-up, which induces the nucleation of microcracks at the Al cell/eutectic-Si network interface [61]. At the same time, the eutectic-Si network dissolution occurring at high temperatures increases the strain field in the proximity of the Al phase and promotes an inhomogeneous deformation state, thus easing the crack initiation [52].

However, microstructural degradation is not the only factor influencing fatigue resistance: as described by Romano et al. [64], several variables can affect the nucleation and propagation of fatigue cracks, e.g., surface finish, defects, residual stresses, and anisotropy. In particular, defects control crack initiation in high-cycle fatigue tests and play a key role in sample failure, as described in section 2.3.5. Therefore, the effect of the high temperature on the strengthening mechanisms reduces the material's strength in opposition to the crack initiation, which, in the presence of a defect, can occur at a lower stress level than in room-temperature conditions.

Similar considerations can be drawn for the T6R alloy. In detail, the high density of possible killer defects along the contour of the samples controls crack initiation (Figure 2.57). The effect of the high temperature on the strengthening mechanisms reduces the material's strength in opposition to the crack initiation, which can occur at a lower stress level than in room-temperature conditions.

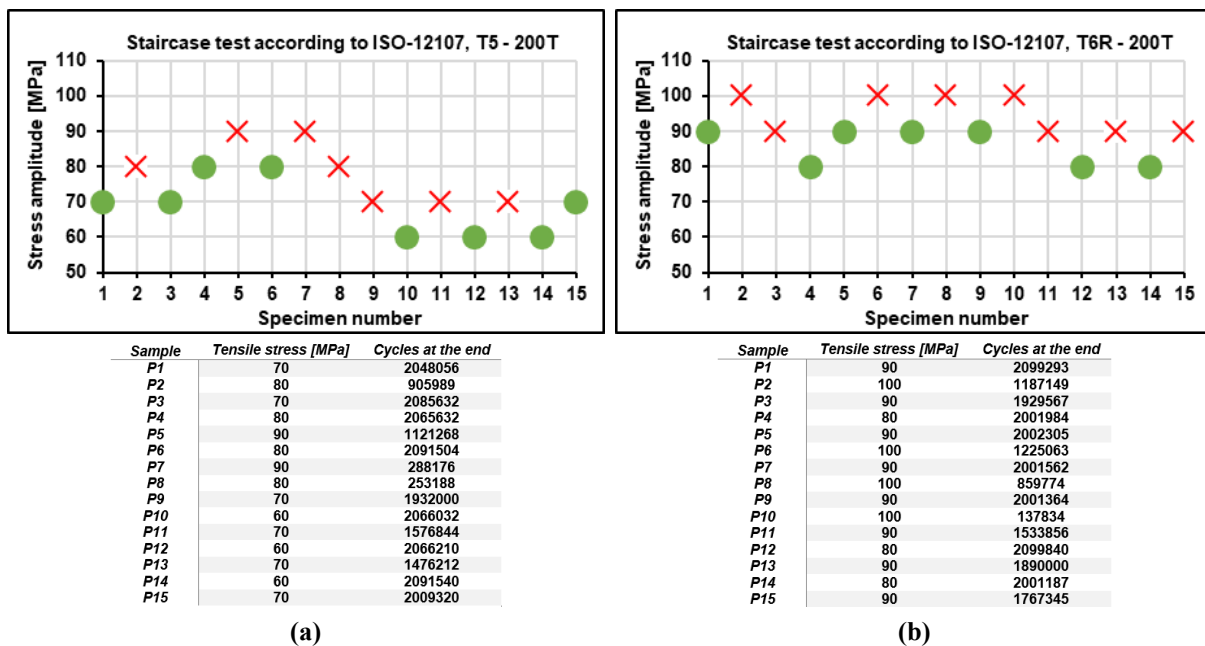


Figure 4.15. Staircase of the T5 - 200T (a) and T6R - 200T (b) conditions. Both conditions show low cycle failure at high load and high cycle failure at low load.

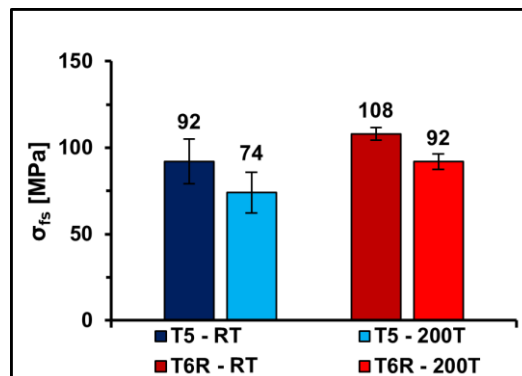
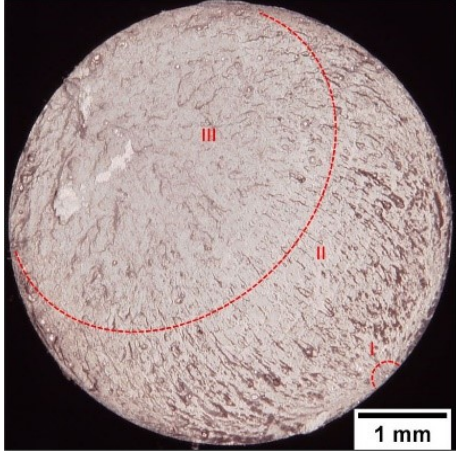
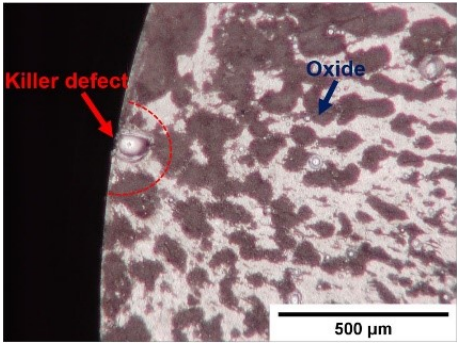
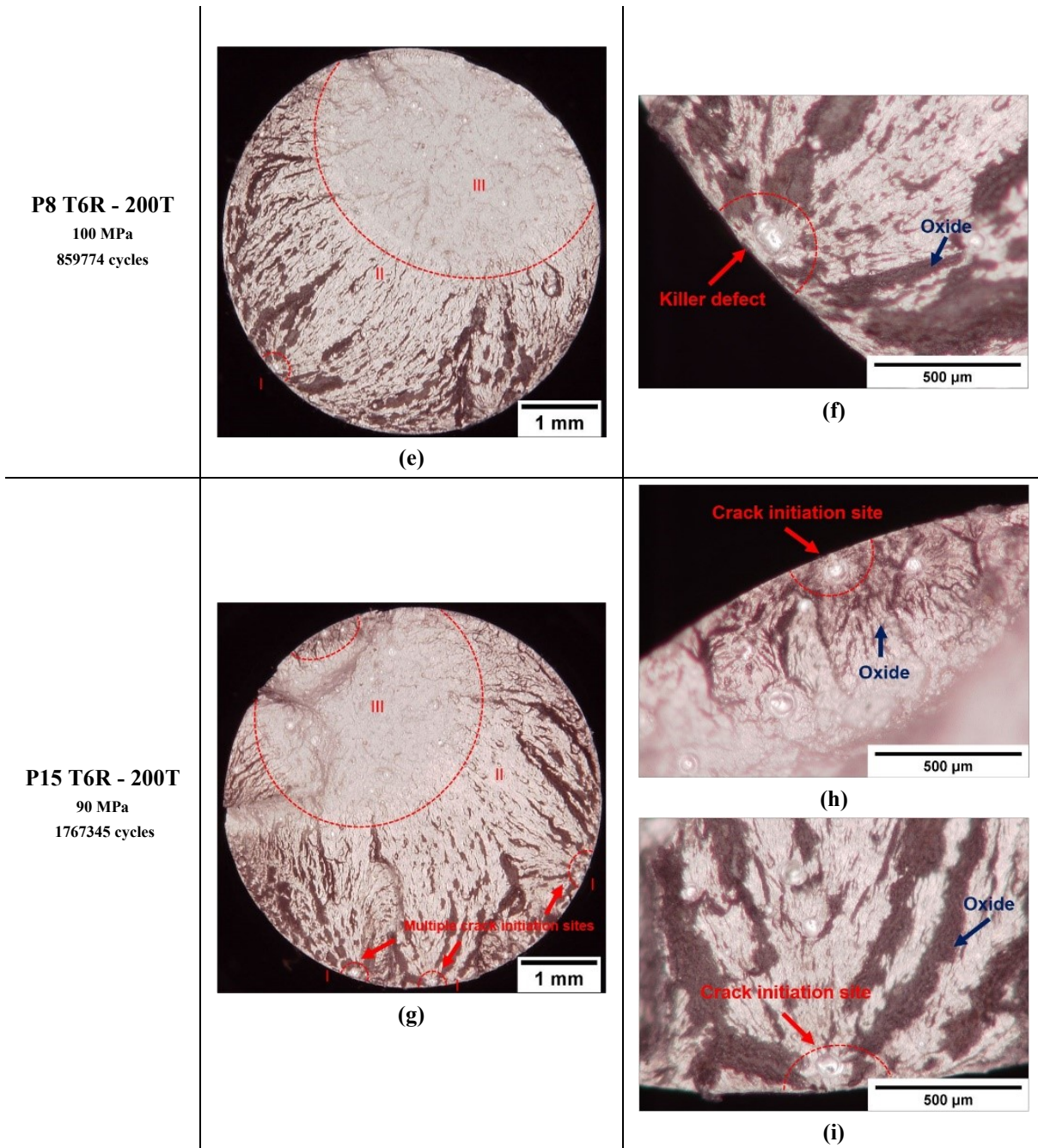


Figure 4.16. Comparison of fatigue strength of the T5 and T6 alloys tested at: (i) room temperature (T5-R and T6R-R) and (ii) high temperature (T5-200T and T6R-200T)

Low-magnification multi-focus images allowed a starting fracture surface analysis (Figure 4.17). These images show similar failure mechanisms between the room, shown in section 2.3.5, and high-temperature fatigue specimens. As described in [24,49], this can also occur in AlSi cast alloys. The fracture surface is subdivided into (i) crack initiation, (ii) crack propagation, (iii) and final overload fracture. The extension of the crack propagation and final overload fracture depends on the applied stress amplitude ( $\sigma_a$ ): low stresses determine more extensive fatigue crack propagation and a smaller final overload fracture. High stresses lead to small fatigue crack propagation regions and more extensive final overload fracture. The analyzed fracture surfaces show very extensive oxide regions, which are larger than those observed on the room-temperature fracture surfaces (Figure 2.53), especially for tests that reach a high number of cycles (Figures 4.17(e,g)). This result confirms the effect of the high test temperature (200 °C) on the oxidation of the fracture surface.

Observing multiple crack initiation sites on several T6R - 200T samples, as shown in Figure 4.17(h), is interesting. The high surface stress concentration induced by sub-superficial defects and the lower strength of the alloy at high temperatures promoted their triggering. The cracks usually develop on different planes and connect during the final failure of the specimen. The decrease in the mechanical properties of the alloy induced by thermal exposure allows reaching the stress conditions necessary for crack initiation in correspondence with the defects. The resistant area decreases as the crack propagation area and the effective stress increase, thus promoting the formation of multiple crack initiation sites and activating the onset of crack initiation sites even in the final overload fracture zone.

Sample	Macro	Crack initiation site
<p><b>P7 T5 - 200T</b> 90 MPa 288176 cycles</p>	 <p>(a)</p>	 <p>(b)</p>
<p><b>P11 T5 - 200T</b> 70 MPa 1576844 cycles</p>	 <p>(c)</p>	 <p>(d)</p>



**Figure 4.17.** Low magnification multi-focus images for T5 - 200T (a,b,c,d) and T6R-200T heat-treated alloy (e,f,g,h,i)

FEG-SEM analyses do not highlight substantial differences in the failure mechanisms observed between the samples tested at room (section 2.3.5) and high temperature (Figures 4.18 and 4.19). In particular, the fracture surfaces of the high-temperature fatigue specimens do not show creep phenomena that could occur under the tested conditions. The absence of creep phenomena is probably due to the high frequency of fatigue tests and the short exposure time at high temperatures, which agrees with previous work on AlSi cast alloys for high-temperature applications [34,49].

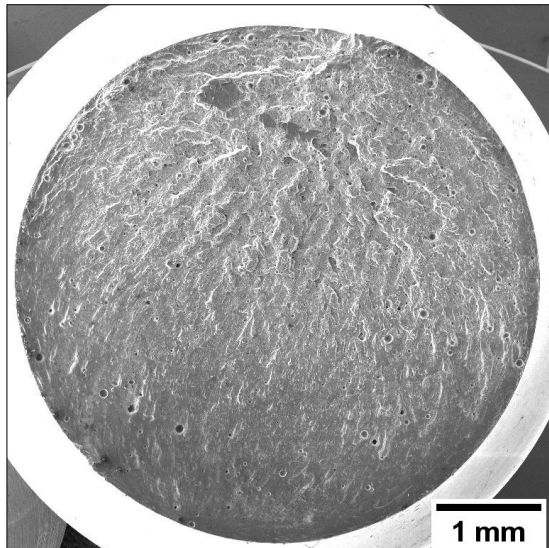
The analyses of the crack initiation sites indicate comparable crack nucleation at room (Figures 2.55(b) and 2.56(b)) and high temperature (Figures 4.18(b) and 4.19(b)). In each analyzed condition, the crack starts from a sub-surface spherical void (50 and 100 μm), such as a keyhole or gas pore. The crack propagation mechanism at high temperatures is comparable to that observed at room temperature: the surface displays a high density of fatigue striations deriving from the tendency of the cracks to deflect in the Al matrix and to form secondary cracks around gas porosities (Figures

4.18(c) and 4.19(c)). The fatigue striations show a micro-tearing fracture, which are characteristics of stable crack evolution and identify the direction of fracture propagation in a pattern that radiates away from the central defect into the outer circular region (Figures 4.18(d) and 4.18(d)) [37,65].

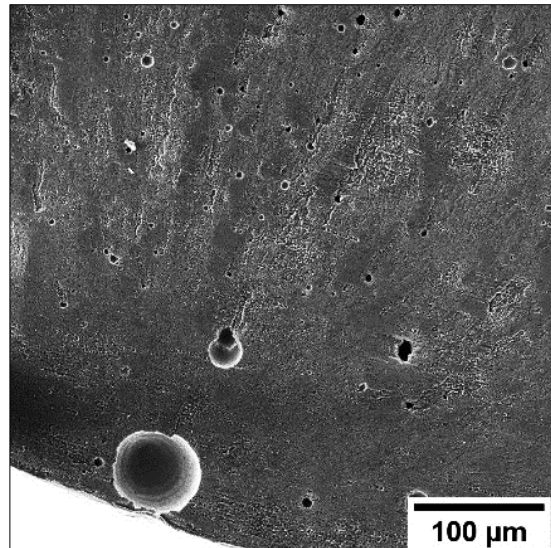
The fracture surface of the final failure regions (Figures 4.18(e,f) and 4.19(e,f)) shows pronounced ductile morphology characterized by more extensive and deeper dimples compared to room temperature specimens (Figures 2.55(e,f) and 2.56(e,f)). In the T5 - 200T alloy (Figure 4.18(e,f)), the softening of the Al matrix, the loss of efficiency of the strengthening mechanisms, and the lower cohesion between the Al matrix/eutectic-Si network promote higher plasticity and the formation of larger dimples at the eutectic-Si network/Al matrix interface. In particular, the extension of the dimples is largely more extensive than the cellular eutectic microstructure. As observed in section 4.3.2, the nucleation and growth of the voids at the  $\alpha$ -Al matrix/second phase interface need less work at high temperatures, promoting the formation of large dimples, especially in correspondence of partially fragmented and coarsened cellular structure where the microstructure is less effective in hindering dislocation slip and reducing the plastic deformation area [53].

The final fracture area of the T6R - 200T alloy displays a ductile fracture with dimples more extensive than the T6R - RT (Figures 2.56(e,f)) and the T5 - 200T alloy (Figures 4.18(e,f)). This phenomenon is related to the different elastoplastic behavior of the Si particles and the Al matrix that influences the formation of dimples; in fact, the Al matrix undergoes local extensive plastic deformation around the Si particles, not observed in the samples tested at room temperature. Therefore, the increase in local plastic flow promotes a non-homogeneous stress state around the larger Si particles, thus inducing the detachment between the Al matrix and Si particles and forming large dimples due to the plastic relieving of the Al matrix near the Si particles [66].

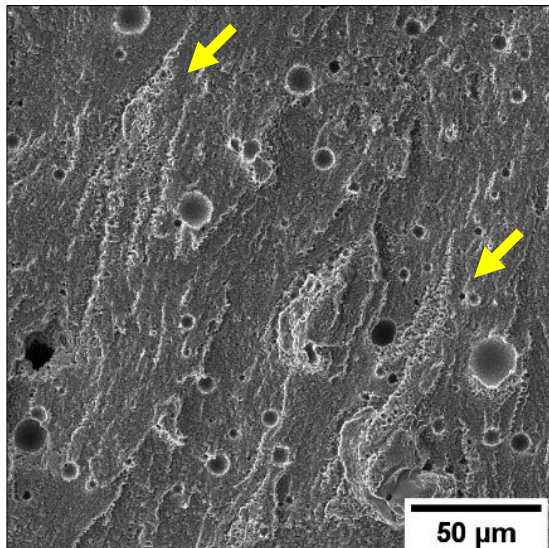
As described in section 2.3.5, the higher fatigue strength of the T6R - 200T than the T5 - 200T samples at high temperatures is due to the synergistic effects of increased ductility and microstructural homogenization that increase the withstand of the alloy to crack initiation, overshadowing the detrimental effect of the increased porosity volume [37,67].



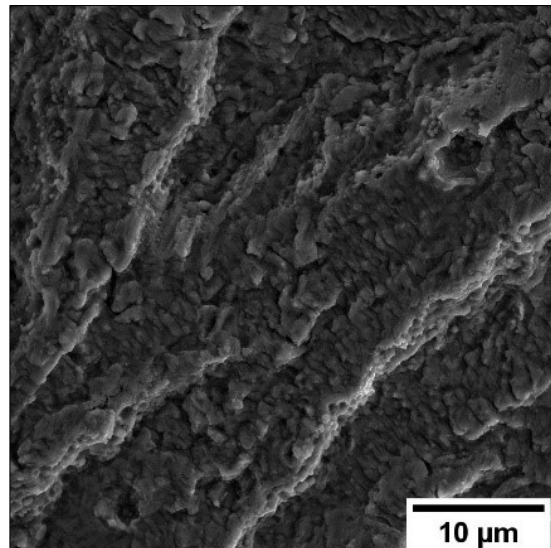
(a)



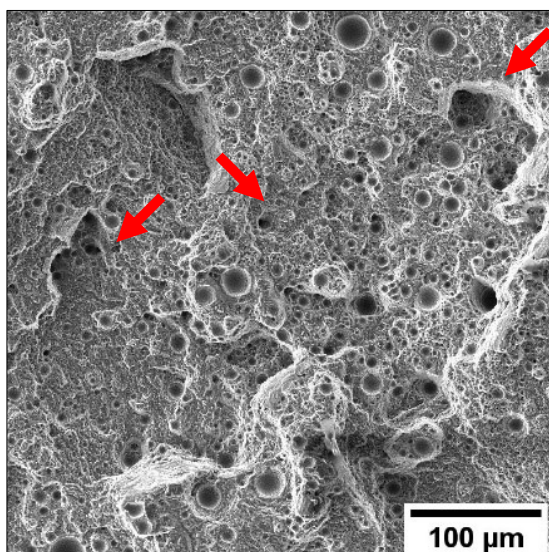
(b)



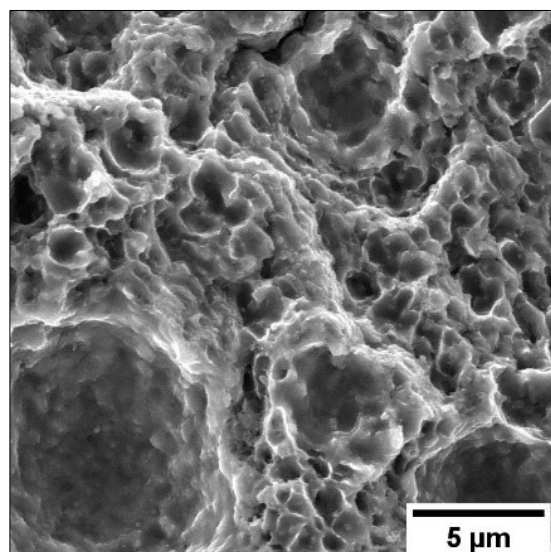
(c)



(d)

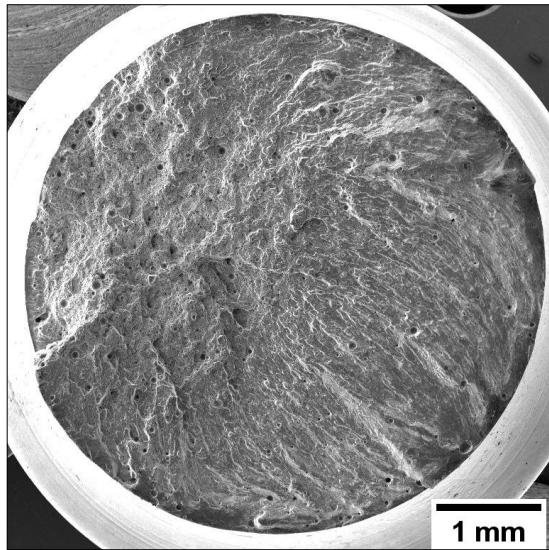


(e)

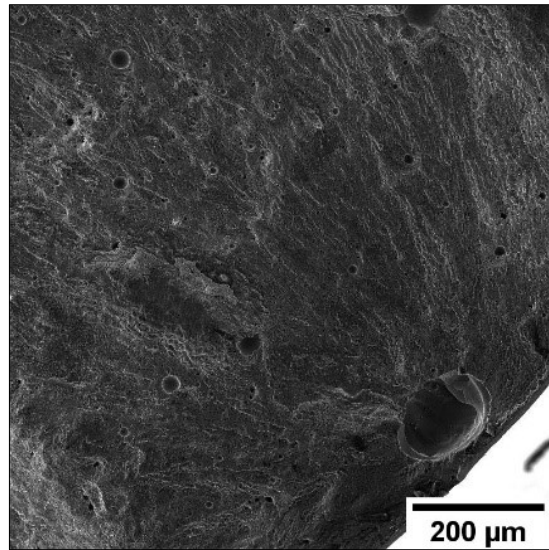


(f)

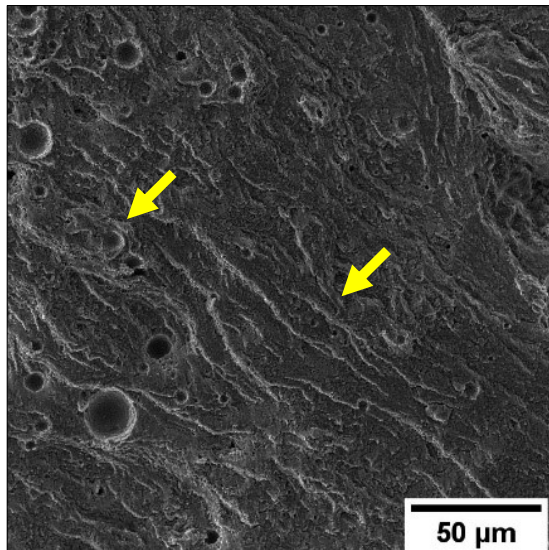
**Figure 4.17.** SE image of the T5 - 200 alloy (Sample P5). Low magnification (a); killer defect (b) crack propagation; (c) micro-tearing in the fatigue propagation region (d) final overload fracture; (e) dimple voids. Yellow arrows indicate parabolic stripes close to the defects in the fatigue crack propagation regions. Red arrows indicate the scan track marks in the overload fracture zone.



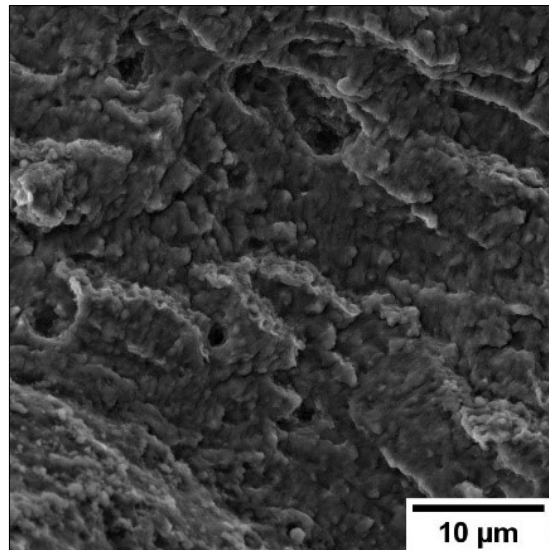
(a)



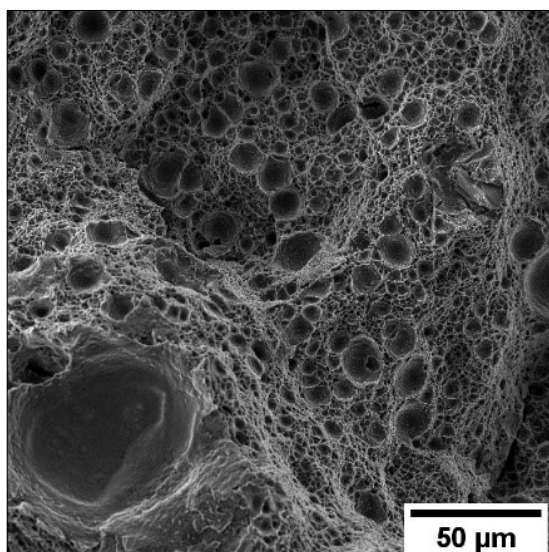
(b)



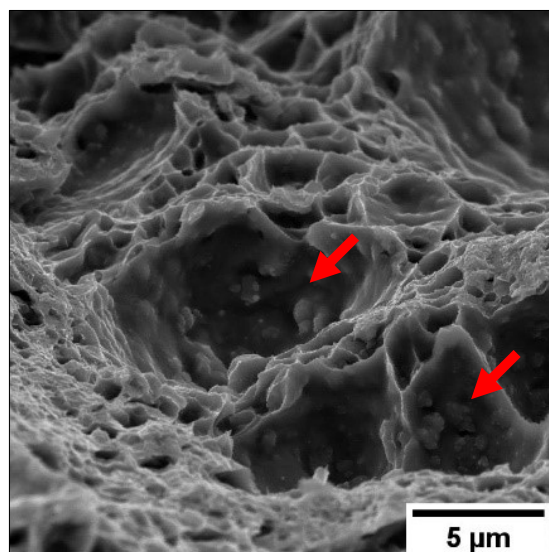
(c)



(d)



(e)



(f)

**Figure 4.18.** SE image of the T6R - 200T alloy (Sample P10). Low magnification (a); killer defect (b) crack propagation; (c) micro-tearing in the fatigue propagation region (d) final overload fracture; (e) dimple voids. Yellow arrows indicate parabolic stripes around the defects in the fatigue crack propagation regions. Red arrows indicate the Si particles inside the large dimples.

#### 4.3.4 Comparison between the high-temperature performance of the L-PBF AlSi10Mg alloy and AlSi cast alloys

In this section, the mechanical performance at room and high temperature of the T5 and T6R alloy is compared to the A356 (AlSiMg ternary alloy), A354, C355, and A357+Cu (AlSiMgCu quaternary alloys) cast alloys, whose composition are reported in Table 4.4. The cast alloys considered in this comparison were subjected to the Hot Isostatic Pressure (HIP) process, which is commonly used in the production of high-value-added cast components to reduce the internal volume of solidification defects (e.g. gas pores or interdendritic shrinkages), and to the T6 heat treatment [23-26].

**Table 4.4.** Average chemical compositions (wt.%) of A354, A356, A357 + Cu, and C355 cast alloys reported in [17,26] and L-PBF AlSi10Mg alloy used in this study.

Chemical composition												
Element (wt.%)	Al	Si	Mg	Fe	Cu	Mn	Pb	Sn	Sr	Ti	B	Zn
A354	Bal.	8.470	0.444	0.135	1.57	0.001	-	-	0.0240	0.126	<0.0002	-
A356	Bal.	7.240	0.420	0.138	<0.001	0.007	-	-	150 ppm	0.120	-	-
A357 + Cu	Bal.	6.770	0.658	<0.03	1.290	<0.001			140 ppm	0.05	-	
C355	Bal.	4.990	0.470	0.138	1.050	0.021	-	-	210 ppm	0.133	0.001	-
L-PBF AlSi10Mg	Bal.	9.662	0.285	0.120	-	0.006	0.008	0.025	-	0.017	-	0.042

Different chemical compositions directly affect the mechanical behavior of the cast alloys. The T6 heat-treated AlSiMg alloys have excellent strength-ductility balance and technological properties [6], but they exhibit a higher mechanical performance drop than AlSiMgCu alloys after long-term exposure at high temperatures [23]. The Mg<sub>2</sub>Si precipitates ( $\beta''$  and  $\beta'$  phases), in fact, readily undergo a diffusion-controlled coarsening, which leads to a progressive loss of their effectiveness in hindering the dislocation slip and to a consequent loss of mechanical strength during exposure at high temperatures [26]. Conversely, in the T6 heat-treated AlSiMgCu alloys, the presence of Cu and Mg leads to the formation of the  $\beta''$  and  $\beta'$  phases, but above all of binary CuAl<sub>2</sub> ( $\theta''$  and  $\theta'$ ), ternary Al<sub>2</sub>CuMg ( $S''$  and  $S'$  phases) and quaternary Al<sub>5</sub>Mg<sub>8</sub>Cu<sub>2</sub>Si<sub>6</sub> ( $Q''$  and  $Q'$ ) precipitates, which are characterized by higher resistance to thermal coarsening than the Mg<sub>2</sub>Si ones [63,68].

The comparison of the residual hardness post-OA at 200 °C and 245 °C for 48 h and the mechanical properties at room temperature (RT) and post-OA at high temperatures (200 °C) (OA - 200T) highlights that the T5 L-PBF AlSi10Mg alloy is characterized by: (i) a residual hardness post-OA, higher than the AlSiMg and comparable to the AlSiMgCu alloys (Figures 4.19(a,b)); (ii) lower YS than AlSiMgCu and higher than AlSiMg alloys in both conditions (RT and OA) (Figure 4.20(a)); (iii) higher UTS than AlSiMgCu and AlSiMg alloys value in RT condition, lower UTS than AlSiMgCu and higher than AlSiMg alloys in OA condition (Figure 4.20(b)); (iv) lower  $e_f$  than AlSiMgCu and AlSiMg alloys in both conditions (RT and OA - 200T), except for A354+Cu cast alloy (Figure 4.20(c)).

The additional strengthening mechanisms (aggregated second phases and solid solution) in the T5 alloy are more effective than the strengthening mechanisms of the A356-T6 alloy in maintaining a high YS value even at high temperatures but less effective than the strengthening mechanisms of the T6 heat-treated AlSiCuMg alloys. At the same time, the different UTS and  $e_f$  values of the T5 - RT condition compared to the HiPped cast alloys considered in this study may be attributable to the higher defect density [41].

The residual hardness post-OA and the mechanical properties at RT and OA - 200T conditions of the T6R alloy are characterized by: (i) the lowest values of residual hardness post-OA (Figures 4.19(a,b)), which is comparable only to

the A356-T6 alloy; (ii) lower YS and UTS values and higher  $e_f$  than AlSiMgCu alloys in both tested conditions (RT and OA-200T) (Figures 4.20(a,b,c)); (iii) higher tensile properties (YS and UTS) than the A356-T6 alloy and similar  $e_f$  in RT condition, but lower mechanical properties (YS, UTS, and  $e_f$ ) than the A356-T6 alloy in OA - 200T condition (Figures 4.20(a,b,c)). Probably at high temperatures, the Al cast microstructure hinders the dislocation motions more than the Si particles embedded in the  $\alpha$ -Al phase matrix of the T6R alloy. At the same time, the higher density of defects in the T6R alloy could lead to a decrease in the maximum possible  $e_f$  value. However, to corroborate these theories, it will be necessary to compare cast and L-PBF alloys under different high-temperature test conditions in future studies.

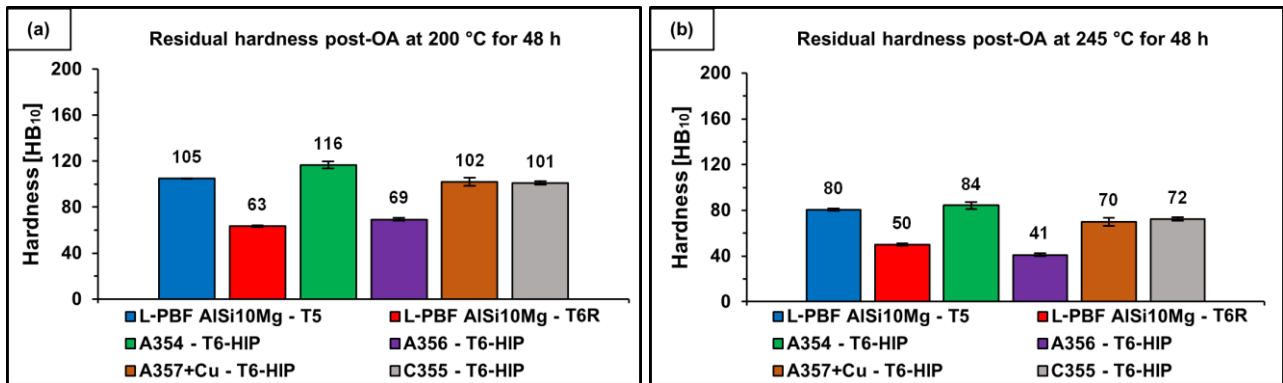


Figure 4.19. Compare the hardness values measured on the T5 and T6R alloys and the T6-HIP AlSi cast alloys [25,26]. The analyzed conditions are post-OA at 200 °C (a) and 245 °C (b) for 48 h.

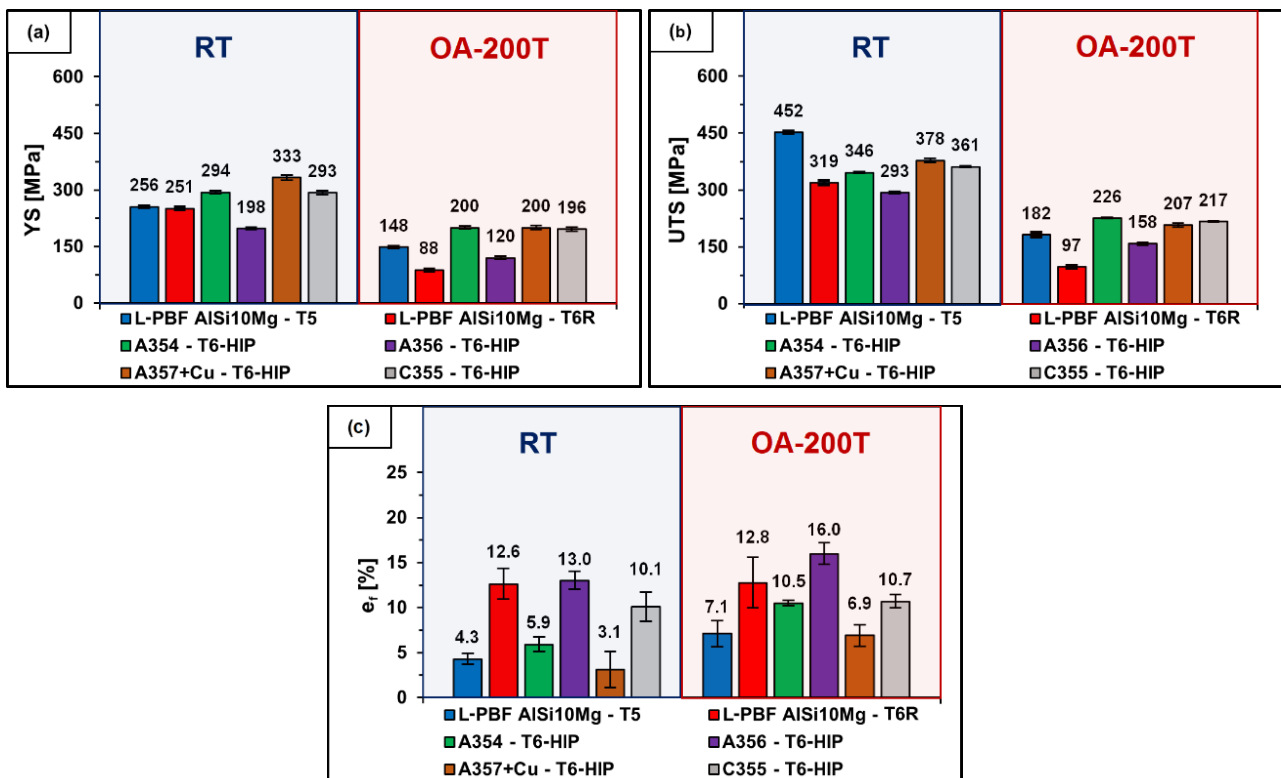


Figure 4.20. Room temperature (RT) and high-temperature tensile properties (YS (a), UTS (b), and  $e_f$  (c)) in overaged conditions (210 °C for 41 h) (OA-200T) of the T5 and T6R alloys and the T6-HIP AlSi cast alloys [25,26].

Similarly, the fatigue strength at room temperature (RT) and 200 °C (200T) of the T5 and T6R alloys is compared with the A357+Cu-T6-HIP alloy (Figure 4.21). The A357+Cu-T6-HIP alloy shows the highest fatigue strength in each test condition, confirming the above considerations for the static mechanical properties. However, the percentage reduction of the fatigue strength is similar for all conditions evaluated: 20% for T5 alloy, 15% for T6R alloy, and 22% for

A357+Cu-T6-HIP alloy, and could indicate that high testing temperature has comparable effects on the fatigue strength of the analyzed alloys, despite the different strengthening mechanisms and defect volumetric density.

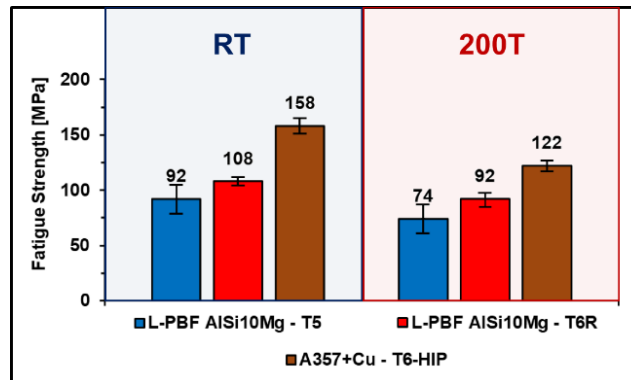


Figure 4.21. Room temperature (RT) and high-temperature (200T) fatigue strength of the T5 and T6R alloys and the A357+Cu -T6-HIP alloy [26].

## 4.4 Conclusion

This Chapter aimed to identify the effects of overaging (OA) and high temperatures (200 °C) on the microstructure and the mechanical properties of the L-PBF AlSi10Mg alloy, which underwent two different heat treatments: T5 (artificial aging at 160 °C for 4 h) and T6R (rapid solution at 510 °C for 10 min followed by artificial aging at 160 °C for 6 h). The effects of high-temperature exposure on residual hardness and microstructure were observed at different temperatures (200 °C, 210 °C, and 245 °C) and for soaking times up to 48 h. The tensile properties of the alloy were evaluated at 200 °C on T5 and T6R samples overaged for 41 h at 210 °C (T5<sub>OA</sub> - 200T and T6R<sub>OA</sub> - 200T). The fatigue tests at 200 °C were carried out on the T5 and T6R alloy not overaged. Fractographic analysis was carried out to identify the effect of OA and high temperature on the failure mechanisms. Furthermore, the mechanical characterization results were compared to previous works on conventional AlSiMg and AlSiMgCu cast alloys.

The following conclusions can be drawn:

- The T5 alloy shows an appreciable residual hardness with a minimum value of about 80 HB<sub>10</sub> after thermal exposure at 245 °C for 48 h. Under the same conditions, the T6R alloy shows a marked hardness decrease, up to a minimum value of about 50 HB<sub>10</sub>.
- T5 and T6R alloys subjected to OA and tested at high temperatures show decreased mechanical strength. However, the decrease is less evident in the case of the T5<sub>OA</sub> - 200T (- 42% in YS value and - 60% in UTS value) than in T6R<sub>OA</sub> - 200T (- 65% in YS value and 70% in UTS) alloy. On the contrary, ductility increases marginally for T6R<sub>OA</sub> - 200T (+ 2% in  $\epsilon_f$ ) and significantly for T5<sub>OA</sub> - 200T (+ 65% in  $\epsilon_f$ ).
- During the tensile test, the T5 - RT condition shows a complete elastic-plastic behavior, while the T6R - RT, T5<sub>OA</sub> - 200T, and T6R<sub>OA</sub> - 200T conditions are characterized by significant necking. At high temperatures, the strain hardening coefficients value decreases by 77% and 80% for the T5<sub>OA</sub> - 200T and T6R<sub>OA</sub> - 200T conditions compared to T5 - RT and T6R - RT ones, respectively.
- The higher effectiveness of the sub-micrometric cellular structure of the T5 alloy to hinder the dislocation motion at high temperatures compared to the composite-like microstructure of the T6R one determines the higher high-temperature mechanical properties of the T5<sub>OA</sub> - 200T compared to the T6R<sub>OA</sub> - 200T
- The T5 and T6R alloys show fatigue strength at 200 °C of  $74 \pm 11.7$  MPa and  $91 \pm 4.4$  MPa, respectively. This difference is probably due to the higher ductility and homogeneous microstructure of the T6 - 200T alloy compared to the T5 - 200T alloy.
- The T5 alloy achieves mechanical properties superior to conventional AlSiMg cast alloys and slightly inferior to AlSiCuMg alloys in both tested conditions (T5 - RT and T5<sub>OA</sub> - 200T). However, the UTS of the T5 - RT alloy demonstrates the highest value. The T6R - RT shows higher mechanical properties than AlSiMg alloys. However, the strength properties reveal inferior at high temperatures.
- The T5 and T6R alloys show a decrease in fatigue strength at high temperatures of 20% and 15%, respectively. These results align with the T6 heat-treated and HIPped A357+Cu alloy (- 22%), a quaternary AlSiMgCu cast alloy in high-temperature applications.

In conclusion, the T5 and T6R heat-treated L-PBF AlSi10Mg alloys provide good mechanical properties at high temperatures but are lower than quaternary AlSiMgCu cast alloys. Consequently, their application could only be considered for structural components operating at temperatures lower than 200 °C.

## References

1. M. Rogante, V.T. Lebedev, F. Nicolaie, E. Retfalvi, and L. Rosta, SANS Study of the Precipitates Microstructural Evolution in Al 4032 Car Engine Pistons, *Phys. B Condens. Matter*, 358 (2005) 224–231. <https://doi.org/10.1016/j.physb.2005.01.240>.
2. E. Balducci, L. Ceschini, A. Morri, A. Morri, EN AW-4032 T6 Piston Alloy After High-Temperature Exposure: Residual Strength and Microstructural Features, *J. of Materi Eng and Perform*, 26 (2017) 3802–3812 <https://doi.org/10.1007/s11665-017-2835-z>
3. M. Wong, S. Tsopanos, C. Sutcliffe, I. Owen, Selective laser melting of heat transfer devices, *Rapid Prototyping Journal*, 13 (2007) 291-297. <https://doi.org/10.1108/13552540710824797>.
4. E.O. Olakanmi, R.F. Cochrane, K.W. Dalgarno, A review on selective laser sintering/melting (SLS/SLM) of aluminium alloy powders: Processing, microstructure, and properties, *Progress in Materials Science*, 74 (2015) 401-477. <https://doi.org/10.1016/j.pmatsci.2015.03.002>.
5. T. DebRoy, H.L. Wei, J.S. Zuback, T. Mukherjee, J.W. Elmer, J.O. Milewski, A.M. Beese, A. Wilson-Heid, A. De, W. Zhang, Additive manufacturing of metallic components – Process, structure and properties, *Progress in Materials Science*, 92 (2018) 112-224. <https://doi.org/10.1016/j.pmatsci.2017.10.001>.
6. M. Javidani, D. Larouche, Application of cast Al–Si alloys in internal combustion engine components, *International Materials Reviews*, 59(3) (2014) 132-158. <https://doi.org/10.1179/1743280413Y.0000000027>.
7. E. Balducci, L. Ceschini, S. Messieri, High Temperature Tensile Tests of the Lightweight 2099 and 2055 Al-Cu-Li Alloy: A Comparison, *JOM*, 70 (2018) 2716–2725. <https://doi.org/10.1007/s11837-018-3006-x>.
8. S. Katsikis, B. Noble, S.J. Harris, Microstructural stability during low temperature exposure of alloys within the Al–Li–Cu–Mg system, *Mater. Sci. Eng. A*, 485 (2008) 613. <https://doi.org/10.1016/j.msea.2007.10.020>.
9. D. Herzog, V. Seyda, E. Wycisk, C. Emmelmann, Additive manufacturing of metals, *Acta Materialia*, 117 (2016) 371-392. <https://doi.org/10.1016/j.actamat.2016.07.019>.
10. E. Balducci, L. Ceschini, S. Messieri, S. Wenner, R. Holmestad, Thermal stability of the lightweight 2099 Al-Cu-Li alloy: Tensile tests and microstructural investigations after overaging, *Materials & Design*, 119 (2017) 54-64. <https://doi.org/10.1016/j.matdes.2017.01.058>.
11. A.P. Babu, A. Huang, N. Birbilis, On the heat treatment and mechanical properties of a high solute Al–Zn–Mg alloy processed through laser powder bed fusion process, *Materials Science and Engineering: A*, 807 (2021) 140857. <https://doi.org/10.1016/j.msea.2021.140857>.
12. M. S. Kenevisi, Y. Yu, F. Lin, A review on additive manufacturing of Al–Cu (2xxx) aluminium alloys, processes and defects, *Materials Science and Technology*, 37(9) (2021) 805-829. <https://doi.org/10.1080/02670836.2021.1958487>.
13. S. Toschi, E. Balducci, L. Ceschini, E.A. Mørtzell, A. Morri, M. Di Sabatino, Effect of Zr Addition on overaging and Tensile Behavior of 2618 Aluminum Alloy, *Metals*, 9 (2019) 130. <https://doi.org/10.3390/met9020130>.
14. A. Iturrioz, E. Gil, M.M. Petite, F. Garciandia, A. M. Mancisidor, M. San Sebastian, Selective laser melting of AlSi10Mg alloy: influence of heat treatment condition on mechanical properties and microstructure, *Weld World*, 62 (2018) 885–892. <https://doi.org/10.1007/s40194-018-0592-8>.
15. F. Czerwinski, W. Kasprzak, D. Sediako, D. Emadi, S. Shaha, J. Friedman, D. Chen, High-temperature aluminum alloys for automotive powertrains, *Adv. Mater. Process*, 174 (2016) 16–20.
16. F. Czerwinski, Thermal Stability of Aluminum Alloys, *Materials*, 13 (2020) 3441. <https://doi.org/10.3390/ma13153441>.
17. R. Konecna, G. Nicoletto, L. Kunz, and E. Riva, The Role of Elevated Temperature Exposure on Structural Evolution and Fatigue Strength of Eutectic AlSi12 Alloys, *Int. J. Fatigue*, 83 (2015) 24–35. <https://doi.org/10.1016/j.ijfatigue.2015.05.007>.
18. I. Rosenthal, R. Shneck, A. Stern, Heat treatment effect on the mechanical properties and fracture mechanism in AlSi10Mg fabricated by additive manufacturing selective laser melting process, *Materials Science and Engineering: A*, 729 (2018) 310-322. <https://doi.org/10.1016/j.msea.2018.05.074>.
19. E. Padovano, C. Badini, A. Pantarelli, F. Gili, F. D’Aiuto, A comparative study of the effects of thermal treatments on AlSi10Mg produced by laser powder bed fusion, *Journal of Alloys and Compounds*, 831 (2020) 154822. <https://doi.org/10.1016/j.jallcom.2020.154822>.
20. W. Li, S. Li, J. Liu, A. Zhang, Y. Zhou, Q. Wei, C. Yan, Y. Shi, Effect of heat treatment on AlSi10Mg alloy fabricated by selective laser melting: microstructure evolution, mechanical properties and fracture mechanism, *Mater. Sci. Eng. A*, 663 (2016) 116–125. <https://doi.org/10.1016/j.msea.2016.03.088>.
21. N. E. Uzan, R. Shneck, O. Yeheskel, N. Frage, High-temperature mechanical properties of AlSi10Mg specimens fabricated by additive manufacturing using selective laser melting technologies (AM-LPBF), *Additive Manufacturing*, 24 (2018) 257-263. <https://doi.org/10.1016/j.addma.2018.09.033>.
22. M. Tocci, A. Varone, R. Montanari, A. Pola, Study of High-Temperature Properties of AlSi10Mg Alloy Produced by Laser-Based Powder Bed Fusion. *Materials Science Forum*, 1016 (2021) 1485-1491. <https://doi.org/10.4028/www.scientific.net/MSF.1016.1485>
23. L. Ceschini, A. Morri, S. Toschi, S. Seifeddine, Room and high temperature fatigue behavior of the A354 and C355 (Al–Si–Cu–Mg) alloys: Role of microstructure and heat treatment, *Materials Science and Engineering: A*, 653 (2016) 129-138. <https://doi.org/10.1016/j.msea.2015.12.015>.
24. A. Morri, L. Ceschini, S. Messieri, E. Cerri, S. Toschi, Mo Addition to the A354 (Al–Si–Cu–Mg) Cast Alloy: Effects on Microstructure and Mechanical Properties at Room and High Temperature. *Metals*, 8(6) 2018 393. <https://doi.org/10.3390/met8060393>.
25. L. Ceschini, A. Morri, S. Toschi, S. Johansson, S. Seifeddine, Microstructural and mechanical properties characterization of heat-treated and overaged cast A354 alloy with various SDAS at room and elevated temperature, *Materials Science and Engineering: A*, 648 (2015) 340-349. <https://doi.org/10.1016/j.msea.2015.09.072>.
26. L. Ceschini, S. Messieri, A. Morri, S. Seifeddine, S.Toschi, M. Zamani. Effect of Cu addition on overaging behavior, room and high temperature tensile and fatigue properties of A357 alloy, *Transactions of Nonferrous Metals Society of China*, 30(11) (2020) 2861-2878. [https://doi.org/10.1016/S1003-6326\(20\)65427-9](https://doi.org/10.1016/S1003-6326(20)65427-9).
27. J. Fiocchi, C.A. Biffi, C. Colombo, L.M. Vergani, A. Tuissi, Ad-hoc heat treatments for Selective Laser melted AlSi10Mg alloy aimed at stress-relieving and enhancing mechanical performances, *JOM*, 72 (2020) 1118-1127. <https://doi.org/10.1007/s11837-019-03973-z>.
28. ASTM E10-18, Standard Test Method for Brinell Hardness of Metallic Materials, ASTM International, West Conshohocken, PA, (2018).
29. ASM International. ASTM E3-11(2017): Standard Guide for Preparation of Metallographic Specimens, ASM International: West Conshohocken, PA, USA, 2017.
30. ASM International. ASTM 407- 07(2015): Standard Practice for Microetching Metals and Alloys, ASM International: West Conshohocken, PA, USA, 2015.

31. M. Li, S. Ghosh, O. Richmond, H. Weiland, T.N Rouns, Three-dimensional characterization and modeling of particle reinforced metal matrix composites part II: damage characterization, *Materials Science and Engineering: A*, 265(1–2) (1999) 153-173. [https://doi.org/10.1016/S0921-5093\(98\)01133-2](https://doi.org/10.1016/S0921-5093(98)01133-2).
32. International Organization for Standardization. ISO 6892-1:2009, *Metallic Materials–Tensile Testing–Part 1: Method of Test at Room Temperature*; International Organization for Standardization: Geneva, Switzerland, 2009.
33. BSI Standards Publication. BS EN ISO 10275:2014, *Metallic Materials–Tensile Testing–Part 2: Method of Test at Elevated Temperature*; International Organization for Standardization: Geneva, Switzerland, 2011.
34. P. Dai, X. Luo, Y. Yang, Z. Kou, B. Huang, J. Zang, J. Ru, High temperature tensile properties, fracture behaviors and nanoscale precipitate variation of an Al–Zn–Mg–Cu alloy, *Progress in Natural Science: Materials International*, 30(1) (2020) 63-73. <https://doi.org/10.1016/j.pnsc.2020.01.007>.
35. International Organization for Standardization. ISO 6892-2:2011, *Metallic materials — Sheet and strip — Determination of tensile strain hardening exponent*; European Committee for Standardization: Brussels, Belgium, 2014.
36. International Organization for Standardization. ISO 12107:2012 *Metallic materials. Fatigue testing. Statistical planning and analysis of data*; International Organization for Standardization: Geneva, Switzerland, 2012.
37. S. Bagherifard, N. Beretta, S. Monti, M. Riccio, M. Bandini, M. Guagliano, On the fatigue strength enhancement of additive manufactured AlSi10Mg parts by mechanical and thermal post-processing, *Materials & Design*, 145 (2018) 28-41. <https://doi.org/10.1016/j.matdes.2018.02.055>.
38. M. Fousová, D. Dvorský, A. Michalcová, D. Vojtěch, Changes in the microstructure and mechanical properties of additively manufactured AlSi10Mg alloy after exposure to elevated temperatures, *Materials Characterization*, 137 (2018) 119-126. <https://doi.org/10.1016/j.matchar.2018.01.028>.
39. J. Fioocchi, A. Tuissi, P. Bassani, C.A. Biffi, Low-temperature annealing dedicated to AlSi10Mg selective laser melting products, *Journal of Alloys and Compounds*, 695 (2017) 3402-3409. <https://doi.org/10.1016/j.jallcom.2016.12.019>.
40. J. Fite, S. E. Prameela, J. A. Slotwinski, T. P. Weihs, Evolution of the microstructure and mechanical properties of additively manufactured AlSi10Mg during room temperature holds and low temperature aging, *Additive Manufacturing*, 36, (2020). <https://doi.org/10.1016/j.addma.2020.101429>.
41. B. Chen, S.K. Moon, X. Yao, G. Bi, J. Shen, J. Umeda, K. Kondoh, Strength and strain hardening of a selective laser melted AlSi10Mg alloy, *Scripta Materialia*, 141 (2017) 45-49. <https://doi.org/10.1016/j.scriptamat.2017.07.025>.
42. A. Hadadzadeh, B. S. Amirkhiz, M. Mohammadi, Contribution of Mg<sub>2</sub>Si precipitates to the strength of direct metal laser sintered AlSi10Mg, *Materials Science and Engineering: A*, 739 (2019) 295-300. <https://doi.org/10.1016/j.msea.2018.10.055>.
43. F. Alghamdi, X. Song, A. Hadadzadeh, B. Shalchi-Amirkhiz, M. Mohammadi, M. Haghsheenas, Post heat treatment of additive manufactured AlSi10Mg: On silicon morphology, texture and small-scale properties, *Materials Science and Engineering: A*, 783 (2020). <https://doi.org/10.1016/j.msea.2020.139296>.
44. M. Tocci, A. Pola, M. Gelfi, G.M. La Vecchia, Effect of a New High-Pressure Heat Treatment on Additively Manufactured AlSi10Mg Alloy, *Metall Mater Trans A*, 51 (2020) 4799–4811. <https://doi.org/10.1007/s11661-020-05905-y>.
45. L.F. Wang, J. Sun, X.L. Yu, Y. Shi, X.G. Zhu, L.Y. Cheng, H.H. Liang, B. Yan, L.J. Guo, Enhancement in mechanical properties of selectively laser-melted AlSi10Mg aluminum alloys by T6-like heat treatment, *Materials Science and Engineering: A*, 734 (2018) 299-310. <https://doi.org/10.1016/j.msea.2018.07.103>.
46. L. Tonelli, E. Liverani, A. Morri, L. Ceschini, Role of Direct Aging and Solution Treatment on Hardness, Microstructure and Residual Stress of the A357 (AlSi7Mg0.6) Alloy Produced by Powder Bed Fusion, *Metall Mater Trans B* 52 (2021) 2484–2496. <https://doi.org/10.1007/s11663-021-02179-6>.
47. L. Zhou, A. Mehta, E. Schulz, B. McWilliams, K. Cho, Y. Sohn, Microstructure, precipitates and hardness of selectively laser melted AlSi10Mg alloy before and after heat treatment, *Materials Characterization*, 143 (2018) 5-17. <https://doi.org/10.1016/j.matchar.2018.04.022>.
48. N. T. Aboulkhair, I. Maskery, C. Tuck, I. Ashcroft, N. M. Everitt, The microstructure and mechanical properties of selectively laser melted AlSi10Mg: The effect of a conventional T6-like heat treatment, *Materials Science and Engineering: A*, 667 (2016) 139-146. <https://doi.org/10.1016/j.msea.2016.04.092>.
49. L. Ceschini, A. Morri, A. Morri, S. Toschi, S. Johansson, S. Seifeddine, Effect of Microstructure and overaging on the Tensile Behavior at Room and Elevated Temperature of C355-T6 Cast Aluminum Alloy, *Mater. Des.*, 83 (2015) 626–634. <https://doi.org/10.1016/j.matdes.2015.06.031>.
50. M. Tocci, R. Donnini, G. Angella, E. Gariboldi, A. Pola, Tensile Properties of a Cast Al-Si-Mg Alloy with Reduced Si Content and Cr Addition at High Temperature. *J. of Mater Eng and Perform* 28 (2019) 7097–7108. <https://doi.org/10.1007/s11665-019-04438-9>.
51. E. Gariboldi, J.N. Lemke, L. Rovatti, O. Baer, G. Timelli, F. Bonollo, High-Temperature Behavior of High-Pressure Diecast Alloys Based on the Al-Si-Cu System: The Role Played by Chemical Composition. *Metals*, 8 (2018) 348. <https://doi.org/10.3390/met8050348>.
52. J. Delahaye, J. Tchoufang Tchuidjang, J. Lecomte-Beckers, O. Rigo, A.M. Habraken, A. Mertens, Influence of Si precipitates on fracture mechanisms of AlSi10Mg parts processed by Selective Laser Melting, *Acta Materialia*, 175 (2019) 160-170. <https://doi.org/10.1016/j.actamat.2019.06.013>.
53. P.J. Moses, Q. Liu, J. P. Best, X. Li, J. J. Kruzic, U. Ramamurty, B. Gludovatz, Fracture resistance of AlSi10Mg fabricated by laser powder bed fusion, *Acta Materialia*, 211 (2021) 116869. <https://doi.org/10.1016/j.actamat.2021.116869>.
54. G.E. Totten, D.S. MacKenzie, *Handbook of Aluminum - Volume 2: Alloy Production and Materials Manufacturing*, (2003).
55. M. Colombo, E. Gariboldi, A. Morri, Influences of Different Zr Additions on the Microstructure, Room and High Temperature Mechanical Properties of an Al-7Si-0.4 Mg Alloy Modified with 0.25%Er, *Mater. Sci. Eng. A*, 713 (2018) 151–160. <https://doi.org/10.1016/j.msea.2017.12.068>.
56. D. Broek, The role of inclusions in ductile fracture and fracture toughness, *Eng. Fract. Mech.* 5, 55-66, (1973). [https://doi.org/10.1016/0013-7944\(73\)90007-6](https://doi.org/10.1016/0013-7944(73)90007-6).
57. W. H. Kan, Y. Nadot, M. Foley, L. Ridosz, G. Proust, J. M. Cairney, Factors that affect the properties of additively manufactured AlSi10Mg: Porosity versus microstructure, *Additive Manufacturing*, 29 (2016) 100805. <https://doi.org/10.1016/j.addma.2019.100805>.
58. S. Joseph, S. Kumar, A Systematic Investigation of Fracture Mechanisms in Al-Si Based Eutectic Alloy-Effect of Si Modification, *Mater. Sci. Eng. A*, 588 111–124 (2013). <https://doi.org/10.1016/j.msea.2013.09.019>.
59. M.T. Di Giovanni, J.T. Oliveira de Menezes, G. Bolelli, E. Cerri, E.M. Castrodeza, Fatigue crack growth behavior of a selective laser melted AlSi10Mg, *Engineering Fracture Mechanics*, 217 (2019) 106564. <https://doi.org/10.1016/j.engfracmech.2019.106564>.
60. Cheng, X. Wang, Y. Ming, Z. Hongfei, et al., Thermal-mechanical Fatigue Analysis of Diesel Engine Cylinder Head Based on Fluid-Structure Interaction, *SAE Technical Paper* 2015-01-0558, 2015, doi:10.4271/2015-01-0558.

61. G. Ingarao, P.C. Priarone, Y. Deng, D. Paraskevas, Environmental modelling of aluminium based components manufacturing routes: Additive manufacturing versus machining versus forming. *Journal of Cleaner Production*. 176 (2018) 261-275. <https://doi.org/10.1016/j.jclepro.2017.12.115>.
62. R.A. Michi, A. Plotkowski, A. Shyam, R.R. Dehoff, S. Suresh Babu, Towards high-temperature applications of aluminium alloys enabled by additive manufacturing. *International Materials Reviews*. 67(3) (2021) 298-345. <https://doi.org/10.1080/09506608.2021.1951580>.
63. A. R. Farkoosh, M. Pegguleryuz, Enhanced mechanical properties of an Al–Si–Cu–Mg alloy at 300 °C: Effects of Mg and the Q-precipitate phase. *Materials Science and Engineering A*, 621 (2015) 277-286. <https://doi.org/10.1016/j.msea.2014.10.080>.
64. S. Romano, A. Brückner-Foit, A. Brandão, J. Gumpinger, T. Ghidini, S. Beretta, Fatigue properties of AlSi10Mg obtained by additive manufacturing: Defect-based modelling and prediction of fatigue strength, *Engineering Fracture Mechanics*, 187, (2018) 165-189. <https://doi.org/10.1016/j.engfracmech.2017.11.002>.
65. Z.W. Xu, Q. Wang, X.S. Wang, C.H. Tan, M.H. Guo, P.B. Gao. High cycle fatigue performance of AlSi10mg alloy produced by selective laser melting. *Mech. Mater.* 148 (2020) 103499. <https://doi.org/10.1016/j.mechmat.2020.103499>.
66. Julius N. Domfang Ngnokou, Y. Nadot, G. Henaff, J. Nicolai, W. H. Kan, J. M. Cairney, L. Ridosz, Fatigue properties of AlSi10Mg produced by Additive Layer Manufacturing, *International Journal of Fatigue*, 119 (2019) 160-172.. <https://doi.org/10.1016/j.ijfatigue.2018.09.029>.
67. C.H. Caceres, A rationale for the quality index of Al-Si-Mg cast alloys. *International Journal of Cast Metals Research*. 12(6), 2000 385-391. <https://doi.org/10.1080/13640461.2000.11819376>.
68. A. Aversa, G. Marchese, A. Saboori, E. Bassini, D. Manfredi, S. Biamino, D. Ugues, P. Fino, M. Lombardi, New Aluminum Alloys Specifically Designed for Laser Powder Bed Fusion: A Review. *Materials* 12 (2019) 1007. <https://doi.org/10.3390/ma12071007>

## Conclusion

The AlSi10Mg alloy produced by Laser-based Powder Bed Fusion (L-PBF) technology finds applications in many sectors, such as biomedical, energy, aerospace, and automotive, due to its excellent castability, high strength/weight ratio, good thermal properties and corrosion resistance, and relatively low cost. In recent years, significant efforts have been devoted to defining optimum process parameters to enhance mechanical performance, and further spread its use for mechanical applications. Even though numerous research papers focused on this alloy, a lack of knowledge concerning the relationships among heat treatment, microstructure, and mechanical behavior of the L-PBF AlSi10Mg alloy is still to be filled.

The heat treatment plays a crucial role in tuning the microstructural characteristics of the as-built parts and making them suitable for desired applications. However, most researchers investigated the heat treatment conditions typically used for conventional AlSiMg cast alloys, which do not consider the peculiar microstructure of the L-PBF-printed parts.

This Ph.D. project moved in this scenario, using a scientific approach to overcome the limits of the L-PBF AlSi10Mg alloy through tailored heat treatments. In particular, the work focused on developing an innovative T6 heat treatment consisting of a rapid solution capable of homogenizing the microstructure and relieving the residual stresses of the as-built microstructure, thus obtaining a finer microstructure and a consequent improvement of the strengthening mechanisms. The study allowed the definition of customized heat treatment (T6R) for the L-PBF AlSi10Mg alloy, consisting of a rapid solution (10 min at 510 °C) (SHTR) followed by artificial aging (6 h at 160 °C) (AA). The mechanical performances of the T6R heat-treated L-PBF AlSi10Mg alloy were compared with as-built condition (AB) and T5 (4 h at 160 °C), and conventional T6 (1 h at 540 °C and 4 h at 160 °C, hereafter T6B) heat treatments. Moreover, the central metallurgical-related aspect linked to the L-PBF process and the different heat treatments were examined to explain the material's mechanical behavior.

The microstructural characteristics and mechanical properties of the as-built L-PBF AlSi10Mg alloy were correlated to the peculiar solidification microstructures induced by the L-PBF process starting from the extensive literature review carried out to support the experimental activities. The following general conclusions have been drawn:

- The optimization of the process parameters influences the complex dynamics of the laser-powder interaction, which affect the defect content, the microstructural features, and, consequently, the mechanical behavior of the alloy (strength properties, work hardening, ductility, and fracture mechanisms). The rapid solidification and high cooling rates generate superior mechanical performance compared to conventional Al cast alloys due to the refined microstructure and high solute concentration. However, the microstructure experiences rapid and repeated thermal cycling leading to the formation of defects, residual stresses, and inhomogeneous microstructure, which lead to anisotropic mechanical behavior and a reduction of the potential fracture toughness, ductility, and fatigue resistance.
- The heat treatments currently adopted, direct aging (T5), stress relieving (SR), and solution and artificial aging treatment (T6), can effectively improve the mechanical performance of the L-PBF AlSi10Mg alloy. In particular, the post-heat treatment's mechanical performance depends on the temperature and soaking time effects on the microstructural evolution of the eutectic-Si network and the precipitation hardening. The T5 heat treatment is applied to slightly reduce residual stresses and increase material strength by forming acicular nano-sized Si precipitates and Mg<sub>2</sub>Si precursors within the cells of the Al matrix. The T6 heat treatment

obtains the best mechanical performances thanks to the peculiar composite-like microstructure without reducing yield strength due to the increased precipitation hardening contribution. Conversely, the SR completely relieves the residual stresses and increases ductility by forming spherical Si particles. However, it induces a noticeable decrease in strength properties due to the absence of significant reinforcement mechanisms.

Therefore, systematic experimental research was carried out to define the optimal heat treatment for the L-PBF AlSi10Mg alloy, considering its specific application. Based on the literature survey results, attention was paid to the T5 and T6 heat treatments, mainly focusing on the T6 one, which is considered able to induce the best strength-ductility trade-off among the heat treatment reported in the literature. In particular, the higher supersaturation of the as-built alloy compared to conventional AlSiMg cast alloy requires lower solution heat treatment times than typically used in conventional practice. Therefore, the activities on the T6 heat treatment were addressed to evaluate the effects of the solution temperatures and soaking time on (i) size, morphology, and distribution of Si particles; (ii) gas pores size; (iii) Al matrix supersaturation. Understanding these aspects enabled the definition of innovative rapid solution treatment for the L-PBF AlSi10Mg alloy, which could improve the material's strength-ductility balance. In detail:

- The SHTR allows obtaining a higher level of Si supersaturation in the  $\alpha$ -Al matrix, thus accelerating the kinetics of precipitation hardening and less gas pore growth. Furthermore, it develops a composite-like microstructure of Si particles embedded into the  $\alpha$ -Al phase matrix, characterized by a more homogeneous distribution of finer Si particles than the microstructure induced by conventional SHT. These microstructural characteristics increase the Orowan strengthening mechanism, the cohesion between Si particles and  $\alpha$ -Al matrix, and the fracture resistance of the alloy.
- The optimized T5 heat treatment increases the mechanical properties of the AB alloy by preserving the ultrafine cellular microstructure and part of the solid solution strengthening, promoting precipitation hardening and residual stress relief. However, the fracture path develops preferentially along the coarser and inhomogeneous zones (MPBs and HAZs), reducing the alloy's ductility. Crack nucleates on the eutectic-Si network at a low strain since the harder Si phase transfers the load to the enclosed softer Al phase, leading to a fast sample failure. The tensile fracture surfaces show shallow dimples formed starting from the eutectic-Si network, whose extension is proportional to the size of the  $\alpha$ -Al cells.
- The T6R heat treatment reduces the local mechanical anisotropy that affects the as-built microstructure due, for example, to Melt Pool Boundaries (MPBs) or Heat Affected Zones (HAZs). Conventional T6B alloy is characterized by larger Si particles and clusters embedded into the  $\alpha$ -Al matrix, compared to the T6R alloy, which leads to a local inhomogeneous mechanical behavior. The microstructural characteristics of the T6R alloy promote the highest static mechanical property balance and fatigue strength, introducing a crack propagation involving the coalescence of voids at the Si particles/ $\alpha$ -Al matrix interface and the formation of deep dimple extension proportional to the size of the Si particles. The particle fracture and the Si particle/ $\alpha$ -Al matrix decohesion highly depend on the Si particle size and distribution, determining the lower ductility of the T6B alloy than the T6R one. The morphology of the fatigue fracture is comparable with the T5 alloy: it consists of detachment or cracking of brittle Si particles and eutectic Si phase, respectively, and generation of shear bands with consequent formation of microcracks, and final fracture generated by linkage of microcracks and their propagation. The main important

differences are related to the final overload fracture zone: the T6R alloy is characterized by more profound and more extensive dimples than the T5 alloy, in line with the tensile fracture surfaces

The influence of T6R was also evaluated on the tribological behavior of the L-PBF AlSi10Mg alloy. The tribological tests and microstructural characterization highlighted that :

- T6R alloy has a comparable friction coefficient value to other analyzed conditions (AB, T5, and T6B) and a lower wear depth than the T6B alloy. In particular, the improved wear behavior of the T6R compared to the T6B alloys is due to the significant reduction of the Si particle inter-distance into the  $\alpha$ -Al matrix, giving rise to high deformation gradients and increasing the dislocation density and wear resistance. In addition, the more homogeneous dispersion of Si particles and higher cohesion between the hard Si phase and the soft Al matrix provides a higher load-bearing capacity. However, the AB and T5 alloy show higher wear resistance due to their ultrafine cellular microstructure, higher hardness, and ability to retain an anti-wear oxide layer,

The T5 and T6 alloys represent an up-and-coming solution for producing structural components, given their excellent mechanical and tribological behavior. The effects of overaging and high temperatures on the peculiar microstructure and mechanical properties of the L-PBF AlSi10Mg alloy were analyzed to extend their use in producing high-tech components directly or indirectly exposed to heating. Furthermore, the results were compared to previous studies carried out by the Metallurgy Group of Bologna on AlSiMg and AlSiMgCu cast alloys. In particular, it was observed that:

- The T6R and T5 alloys show a marked decrease in mechanical strength and hardness due to long soaking times (up to 48 h) at high temperatures (up to 245 °C). However, the higher effectiveness of the sub-micrometric cellular structure of the T5 alloy to hinder the dislocation motion at high temperatures determined better high-temperature tensile properties than the T6R alloy. The T5 alloy achieves mechanical properties superior to conventional AlSiMg cast alloys and slightly inferior to AlSiCuMg alloys in both room- and high-temperature tested conditions. However, the homogeneous microstructure and the higher ductility of the T6 alloy allow for preserving at high temperatures higher fatigue strength than the T5 alloy.

In conclusion, the innovative T6R heat treatment improves the overall balance of the mechanical and tribological response of the L-PBF AlSi10Mg alloy, representing an optimal solution for producing reliable structural components and fully exploiting the L-PBF technology. Furthermore, considering the good high-temperature mechanical properties, the L-PBF AlSi10Mg alloy could be adopted for structural components operating in mild service conditions at 200 °C, such as heat sinks, pistons, and aerodynamic parts.

Future research activities could be addressed to develop integrated post-process cycles constituted by heat treatment and surface modification processes to improve the tribological behavior of the L-PBF AlSi10Mg alloy; in fact, the lower hardness compared to the more common counterpart materials is the leading cause of high wear rates under severe service conditions in components produced in L-PBF AlSi10Mg alloy.